

AJNR

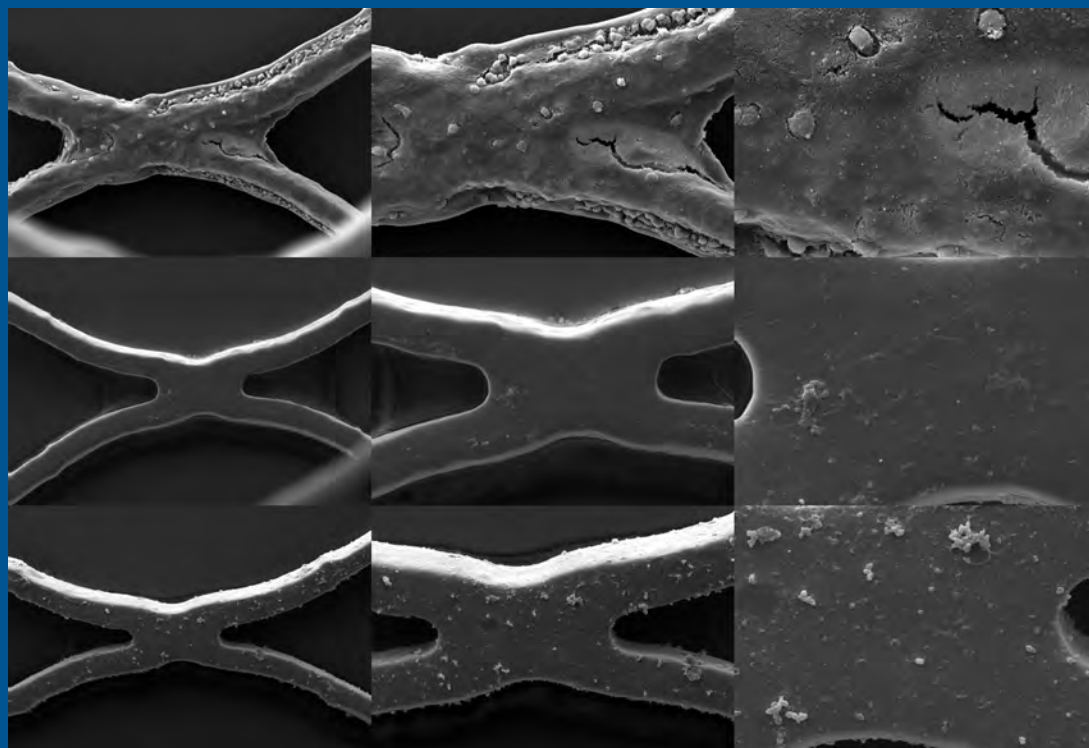
AMERICAN JOURNAL OF NEURORADIOLOGY

JANUARY 2015
VOLUME 36
NUMBER 1
WWW.AJNR.ORG

THE JOURNAL OF DIAGNOSTIC AND
INTERVENTIONAL NEURORADIOLOGY

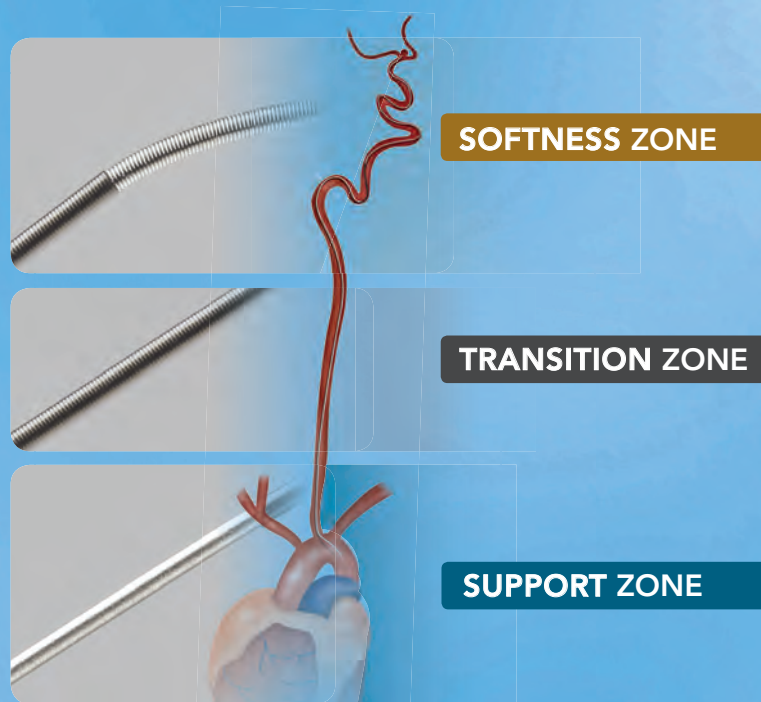
TRUTH results: gadobutrol vs. gadoteridol
Chronic codeine use and white matter integrity
DIR for spinal cord multiple sclerosis evaluation

Official Journal ASNR • ASFNR • ASHNR • ASPNR • ASSR



Advanced

by MicroVention



ENHANCED CONTROL TO MAXIMIZE COIL PERFORMANCE

The V-Trak[®] Advanced Coil System, the next generation to power the performance of our most technically advanced line of coils. Offering the optimal combination of support and flexibility.

microvention.com

MICROVENTION, V-Trak, LVIS and Headway are registered trademarks of MicroVention, Inc. Scientific and clinical data related to this document are on file at MicroVention, Inc. Refer to Instructions for Use for additional information. Federal (USA) law restricts this device for sale by or on the order of a physician.
© 2014 MicroVention, Inc. 11/14

Support

by MicroVention



LOW-PROFILE VISUALIZED INTRALUMINAL SUPPORT

The LVIS® and LVIS® Jr. devices are the next generation technology for optimal intraluminal support and coverage for stent-assist coil procedures.

Used with  Headway
Microcatheter

**Humanitarian Device:*

*Authorized by Federal Law for use in the treatment of wide-necked aneurysms in the neurovasculature.
The effectiveness of this device for this use has not been demonstrated.*

**For more information or a product demonstration,
contact your local MicroVention representative:**



MicroVention, Inc.

Worldwide Headquarters

1311 Valencia Avenue

Tustin, CA 92780 USA

MicroVention UK Limited

MicroVention Europe, S.A.R.L.

MicroVention Deutschland GmbH

PH +1.714.247.8000

PH +44 (0) 191 258 6777

PH +33 (1) 39 21 77 46

PH +49 211 210 798-0



BARRICADE™ COIL SYSTEM

PERFORMANCE AND VALUE DELIVERED



BLOCKADE
M E D I C A L

18 TECHNOLOGY DRIVE #169, IRVINE CA 92618 | P 949.788.1443
WWW.BLOCKADEMEDICAL.COM

 MADE IN AMERICA

CE
0297
MKTG-020 REV. B



AJNR

AMERICAN JOURNAL OF NEURORADIOLOGY

JANUARY 2015
VOLUME 36
NUMBER 1
WWW.AJNR.ORG

Publication Preview at www.ajnr.org features articles released in advance of print. Visit www.ajnrblog.org to comment on AJNR content and chat with colleagues and AJNR's News Digest at <http://ajnrndigest.org> to read the stories behind the latest research in neuroimaging.

EDITORIALS

PERSPECTIVES

- 1 **The 3 Pillars of Health** *M. Castillo*

EDITORIALS

- 2 **Point—TAR: A Useful Index to Follow-Up Coiled Intracranial Aneurysms?**
L. Pierot, J. Fiehler, and P. White
- 4 **Counterpoint—Target Aneurysm Recurrence: Measuring What Matters**
C.G. McDougall, S.C. Johnston, A. Gholkar, and A.S. Turk

REVIEW ARTICLE

- 7 **Cerebrovascular Reactivity Mapping: An Evolving Standard for Clinical Functional Imaging** *J.J. Pillai and D.J. Mikulis*

LEVEL 1 EBM EXPEDITED PUBLICATION

- 14 **Are There Differences between Macrocytic Gadolinium Contrast Agents for Brain Tumor Imaging? Results of a Multicenter Intraindividual Crossover Comparison of Gadobutrol with Gadoteridol (the TRUTH Study)** *K.R. Maravilla, M.P. Smith, J. Vymazal, M. Goyal, M. Herman, J.J. Baima, R. Babbel, M. Vaneckova, J. Žižka, C. Colosimo, M. Urbańczyk-Zawadzka, M. Mechl, A.K. Bag, S. Bastianello, E. Bueltmann, T. Hirai, T. Frattini, M.A. Kirchin, and G. Pirovano*

PRACTICE PERSPECTIVES

- 24 **Interobserver Agreement in the Interpretation of Outpatient Head CT Scans in an Academic Neuroradiology Practice** *G. Guérin, S. Jamali, C.A. Soto, F. Guilbert, and J. Raymond*

SOCIAL MEDIA VIGNETTE

- 30 **Social Media and the Neuroradiologist: A Brief Introduction** *A. Radmanesh and R.T. Fitzgerald*

BRAIN

- 32 **Patient Selection for Stroke Endovascular Therapy—DWI-ASPECTS Thresholds Should Vary among Age Groups: Insights from the RECOST Study** *F. Danière, K. Lobotesis, P. Machi, O. Eker, I. Mourand, C. Riquelme, X. Ayriagnac, J.F. Vendrell, G. Gascou, J. Fendeleur, C. Dargazanli, R. Schaub, H. Brunel, C. Arquizan, A. Bonafé, and V. Costalat*
- 40 **Percentage Insula Ribbon Infarction of >50% Identifies Patients Likely to Have Poor Clinical Outcome Despite Small DWI Infarct Volume** *V.M. Timpone, M.H. Lev, S. Kamalian, L.T. Morais, A.M. Franceschi, L. Souza, and P.W. Schaefer*

★ Indicates Editor's Choices selection

✍ Indicates Fellows' Journal Club selection

🔑 Indicates open access to non-subscribers at www.ajnr.org

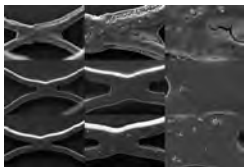
☰ Indicates article with supplemental on-line table

🖼 Indicates article with supplemental on-line photo

📺 Indicates article with supplemental on-line video

EBM 1 Indicates Evidence-Based Medicine Level 1

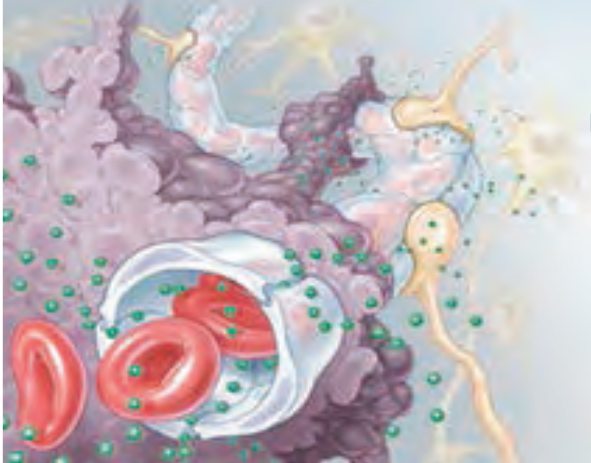
EBM 2 Indicates Evidence-Based Medicine Level 2



Surface electron microscopy shows decreased thrombogenicity of albumin- and heparin-coated stents (mid and bottom rows).

21st Annual Blood-Brain Barrier Consortium Meeting
March 19-21, 2015
Skamania Lodge in Stevenson, Washington

The 2015 Annual Blood-Brain Barrier Consortium Meeting will be held March 19-21 at Skamania Lodge in Stevenson, Washington. The meeting will include a state-of-the-art pre-clinical and clinical neuroimaging session titled "Imaging the Neurovascular Unit: Permeability, Blood Volume, and Functional Imaging". The meeting is partially funded by a National Institutes of Health R13 grant, with support from the National Cancer Institute, National Institute of Neurological Disorders and Stroke, and National Institute of Deafness and Communication Disorders, and is organized in collaboration with the International Brain Barriers Society.



For more information, please visit www.ohsu.edu/bbb



Simplify
the MOC Process

CMEgateway.org



Manage
your CME Credits Online



It's Easy and Free!

Log on to CME Gateway to:

- View or print reports of your CME credits from multiple societies from a single access point.
- Print an aggregated report or certificate from each participating organization.
- Link to SAMs and other tools to help with maintenance of certification.

American Board of Radiology (ABR) participation!

By activating ABR in your organizational profile, your MOC-fulfilling CME and SAM credits can be transferred to your own personalized database on the ABR Web site.

Sign Up Today!

go to CMEgateway.org

Available to Members of Participating Societies

American Board of Radiology (ABR)	Radiological Society of North America (RSNA)
American College of Radiology (ACR)	Society of Interventional Radiology (SIR)
American Roentgen Ray Society (ARRS)	SNM
American Society of Neuroradiology (ASNR)	The Society for Pediatric Radiology (SPR)
Commission on Accreditation of Medical Physics Educational Programs, Inc. (CAMPEP)	

- 46 **Middle Cerebral Artery Stenosis in Patients with Acute Ischemic Stroke and TIA in Israel** *G. Telman, H. Hurani, E. Sprecher, and E. Kouperberg*
-   50 **Abnormal White Matter Integrity in Chronic Users of Codeine-Containing Cough Syrups: A Tract-Based Spatial Statistics Study** *Y.-w. Qiu, H.-h. Su, X.-f. Lv, and G.-h. Jiang*
- 57 **Iron and Volume in the Deep Gray Matter: Association with Cognitive Impairment in Multiple Sclerosis** *C.M. Modica, R. Zivadinov, M.G. Dwyer, N. Bergsland, A.R. Weeks, and R.H.B. Benedict*
- 63 **Preoperative Prognostic Value of Dynamic Contrast-Enhanced MRI-Derived Contrast Transfer Coefficient and Plasma Volume in Patients with Cerebral Gliomas** *T.B. Nguyen, G.O. Cron, J.F. Mercier, C. Footitt, C.H. Torres, S. Chakraborty, J. Woulfe, G.H. Jansen, J.M. Caudrelier, J. Sinclair, M.J. Hogan, R.E. Thornhill, and I.G. Cameron*
-    70 **Mapping p53 Mutations in Low-Grade Glioma: A Voxel-Based Neuroimaging Analysis** *Y.Y. Wang, T. Zhang, S.W. Li, T.Y. Qian, X. Fan, X.X. Peng, J. Ma, L. Wang, and T. Jiang*
- 77 **MRI Grading versus Histology: Predicting Survival of World Health Organization Grade II–IV Astrocytomas** *A. Lasocki, A. Tsui, M.A. Tacey, K.J. Drummond, K.M. Field, and F. Gaillard*
-  84 **Macro- and Microstructural Changes in Patients with Spinocerebellar Ataxia Type 6: Assessment of Phylogenetic Subdivisions of the Cerebellum and the Brain Stem** *K. Sato, K. Ishigame, S.H. Ying, K. Oishi, M.I. Miller, and S. Mori*
-  91 **3T MRI Reveals Extra- and Intracranial Involvement in Giant Cell Arteritis** *S. Siemonsen, C. Brekenfeld, B. Holst, A.-K. Kaufmann-Buehler, J. Fiehler, and T.A. Bley*

INTERVENTIONAL *Published in collaboration with
Interventional Neuroradiology*

-  98 **Surpass Flow Diverter in the Treatment of Intracranial Aneurysms: A Prospective Multicenter Study** *A.K. Wakhloo, P. Lylyk, J. de Vries, C. Taschner, J. Lundquist, A. Biondi, M. Hartmann, I. Szikora, L. Pierot, N. Sakai, H. Imamura, N. Sourour, I. Rennie, M. Skalej, O. Beuing, A. Bonafé, F. Mery, F. Turjman, P. Brouwer, E. Boccardi, L. Valvassori, S. Derakhshani, M.W. Litzenberg, and M.J. Gounis, for the Surpass Study Group*
-  108 **International Retrospective Study of the Pipeline Embolization Device: A Multicenter Aneurysm Treatment Study** *D.F. Kallmes, R. Hanel, D. Lopes, E. Boccardi, A. Bonafé, S. Cekirge, D. Fiorella, P. Jabbour, E. Levy, C. McDougall, A. Siddiqui, I. Szikora, H. Woo, F. Albuquerque, H. Bozorgchami, S.R. Dashti, J.E. Delgado Almandoz, M.E. Kelly, R. Turner IV, B.K. Woodward, W. Brinjikji, G. Lanzino, and P. Lylyk*
-  116 **Treatment of Poor-Grade Subarachnoid Hemorrhage Trial** *D. Mitra, B. Gregson, V. Jayakrishnan, A. Gholkar, A. Vincent, P. White, and P. Mitchell*
-   121 **Rescue Treatment of Thromboembolic Complications during Endovascular Treatment of Cerebral Aneurysms: A Meta-Analysis** *W. Brinjikji, S.F. Morales-Valero, M.H. Murad, H.J. Cloft, and D.F. Kallmes*
-  126 **One-Year MR Angiographic and Clinical Follow-Up after Intracranial Mechanical Thrombectomy Using a Stent Retriever Device** *F. Eugène, J.-Y. Gauvrit, J.-C. Ferré, J.-C. Gentric, A. Besseghir, T. Ronzière, and H. Raoult*
-  133 **Preclinical Evaluation of the Thrombogenicity and Endothelialization of Bare Metal and Surface-Coated Neurovascular Stents** *S. Krajewski, B. Neumann, J. Kurz, N. Perle, M. Avci-Adali, G. Cattaneo, and H.P. Wendel*
- 140 **Parent Artery Occlusion in Large, Giant, or Fusiform Aneurysms of the Carotid Siphon: Clinical and Imaging Results** *M.-A. Labeyrie, S. Lenck, D. Bresson, J.-P. Desilles, A. Bisdorff, J.-P. Saint-Maurice, and E. Houdart*

ASNR 53rd Annual Meeting & The Foundation of the ASNR Symposium 2015

Just released!! Check out the innovative cutting edge programming at The Foundation of the ASNR Weekend Symposium 2015: "Skull Base: Bridging the Gap.....". World-renowned speakers will be presenting the latest and greatest in clinical and imaging advances, and emphasizing the translation of this information into your daily clinical practice.

Also, the Sunday afternoon Foundation Symposium will continue by introducing new "Neuroradiologist-Clinician-Patient multidisciplinary symposiums" on mild TBI, head & neck cancer, brain cancer and more. Neuroradiologists and clinicians will be discussing the role of imaging and advances in treatment in the care of their patients, while patients and public representatives/ambassadors share their own personal experiences and journeys living with their disease.

What's New for the ASNR 53rd Annual Meeting?

- The Foundation of the ASNR Symposium 2015 "Skull Base: -Bridging the Gap....." on Saturday, April 25 & Sunday morning, April 26, 2015
- **New**...On Sunday afternoon, April 26 - "Neuroradiologist-Clinician-Patient Multidisciplinary Symposiums"
- Enjoy some fun on Sunday late afternoon with an ASNR Game of Jeopardy
- **Note**...For those submitting oral abstracts more slots will be available to present oral papers in Chicago
- Annual Meeting focuses on Value-Based Neuroradiology and much, much more...

**Online Meeting Registration & Housing
for ASNR 2015 coming soon...**

Request Programming and Registration Materials for the ASNR 53rd Annual Meeting, Contact:

ASNR 53rd Annual Meeting
c/o American Society of Neuroradiology
800 Enterprise Drive, Suite 205
Oak Brook, Illinois 60523-4216

Phone: 630-574-0220
Fax: 630-574-0661
Email: meetings@asnr.org
Website: www.asnr.org/2015

**Scan now
to visit our
website**



ASFNR ASHNR ASPNR ASSR SNIS
THE FOUNDATION OF THE ASNR



**ASNR 2015 Program Chair/President Elect
Laurie A. Loevner, MD**

Programming developed in cooperation with the:

American Society of Functional Neuroradiology (ASFNR)
Pratik Mukherjee, MD, PhD
American Society of Head and Neck Radiology (ASHNR)
Richard H. Wiggins, III, MD
American Society of Pediatric Neuroradiology (ASPNR)
Thierry A.G.M. Huisman, MD
American Society of Spine Radiology (ASSR)
Adam E. Flanders, MD
American Society of Neuroradiology (ASNR)
Health Policy Committee
Robert M. Barr, MD, FACR
Society of NeuroInterventional Surgery (SNIS)
Donald F. Frei, Jr. MD

SAVE THE DATES....April 25-30, 2015

- 146 **MR Imaging of Myeloperoxidase Activity in a Model of the Inflamed Aneurysm Wall** *M.J. Gounis, I.M.J. van der Bom, A.K. Wakhloo, S. Zheng, J.-Y. Chueh, A.L. Kühn, and A.A. Bogdanov Jr*
- 153 **Establishing a Rabbit Spinal Tumor Model for Nonvascular Interventional Therapy through CT-Guided Percutaneous Puncture Inoculation** *L. Chen, J. Xiao, I.-C. Su, Y.-W. Wu, B. Zhang, K.-Y. Ge, Y.-C. Chang, C. Yang, and C.-F. Ni*

HEAD & NECK

- 160 **Degeneration and Plasticity of the Optic Pathway in Alström Syndrome** *R. Manara, V. Citton, P. Maffei, J.D. Marshall, J.K. Naggert, G. Milan, R. Vettor, A. Baglione, A. Vitale, C. Briani, F. Di Salle, and A. Favaro*
- 166 **MRI Texture Analysis Predicts p53 Status in Head and Neck Squamous Cell Carcinoma** *M. Dang, J.T. Lysack, T. Wu, T.W. Matthews, S.P. Chandarana, N.T. Brockton, P. Bose, G. Bansal, H. Cheng, J.R. Mitchell, and J.C. Dort*
- 171 **Incomplete Endochondral Ossification of the Otic Capsule, A Variation in Children: Evaluation of Its Prevalence and Extent in Children with and without Sensorineural Hearing Loss** *S.E. Sanverdi, B. Ozgen, A. Dolgun, and S. Sarac*
- 176 **High-Resolution CT Findings in Children with a Normal Pinna or Grade I Microtia and Unilateral Mild Stenosis of the External Auditory Canal** *R. Jacob, S. Gupta, B. Isaacson, J.W. Kutz Jr, P. Roland, Y. Xi, and T.N. Booth*

PEDIATRICS

- 181 **Advanced Fiber Tracking in Early Acquired Brain Injury Causing Cerebral Palsy** *F. Lennartsson, L. Holmström, A.-C. Eliasson, O. Flodmark, H. Forssberg, J.-D. Tournier, and B. Vollmer*
- 188 **Apparent Diffusion Coefficient Scalars Correlate with Near-Infrared Spectroscopy Markers of Cerebrovascular Autoregulation in Neonates Cooled for Perinatal Hypoxic-Ischemic Injury** *A. Tekes, A. Poretti, M.M. Scheurkogel, T.A.G.M. Huisman, J.A. Howlett, E. Alqahtani, J.-H. Lee, C. Parkinson, K. Shapiro, S.-E. Chung, J.M. Jennings, M.M. Gilmore, C.W. Hogue, L.J. Martin, R.C. Koehler, F.J. Northington, and J.K. Lee*
- 194 **MRI Characteristics of Globus Pallidus Infarcts in Isolated Methylmalonic Acidemia** *E.H. Baker, J.L. Sloan, N.S. Hauser, A.L. Gropman, D.R. Adams, C. Toro, I. Manoli, and C.P. Venditti*

PERIPHERAL NERVOUS SYSTEM

- 202 **Diffusivity Measurements Differentiate Benign from Malignant Lesions in Patients with Peripheral Neuropathy or Plexopathy** *E.L. Yuh, S. Jain Palrecha, G.M. Lagemann, M. Kliot, P.R. Weinstein, N.M. Barbaro, and C.T. Chin*

SPINE

- 210 **Vertebral Augmentation for Neoplastic Lesions with Posterior Wall Erosion and Epidural Mass** *A. Cianfoni, E. Raz, S. Mauri, S. Di Lascio, M. Reinert, G. Pesce, and G. Bonaldi*
- 219 **Double Inversion Recovery Sequence of the Cervical Spinal Cord in Multiple Sclerosis and Related Inflammatory Diseases** *I. Riederer, D.C. Karampinos, M. Settles, C. Preibisch, J.S. Bauer, J.F. Kleine, M. Mühlau, and C. Zimmer*

BOOK REVIEWS *R.M. Quencer, Section Editor*

Please visit www.ajnrblog.org to read and comment on Book Reviews.

CALL FOR AJNR EDITORIAL FELLOWSHIP CANDIDATES

ASNR and AJNR are pleased once again to join efforts with other imaging-related journals that have training programs on editorial aspects of publishing for trainees or junior staff (3–5 years after training), including Radiology (Olmsted fellowship), AJR (Figley and Rogers fellowships), and Radiologia.

2015 Candidate Information and Requirements

GOALS

- Increase interest in “editorial” and publication-related activities in younger individuals.
- Increase understanding and participation in the AJNR review process.
- Incorporate into AJNR’s Editorial Board younger individuals who have previous experience in the review and publication process.
- Fill a specific need in neuroradiology not offered by other similar fellowships.
- Increase the relationship between “newer” generation of neuroradiologists and more established individuals.
- Increase visibility of AJNR among younger neuroradiologists.

ACTIVITIES OF THE FELLOWSHIP

- Serve as Editorial Fellow for one year. This individual will be listed on the masthead as such.
- Review at least one manuscript per month for 12 months. Evaluate all review articles submitted to AJNR.
- Access to our electronic manuscript review system will be granted so that the candidate can learn how these systems work.
- Be involved in the final decision of selected manuscripts together with the Editor-in-Chief.
- Participate in all monthly Senior Editor telephone conference calls.
- Participate in all meetings of the Editors and Publications Committee during the annual meetings of ASNR and RSNA as per candidate’s availability. AJNR/ASNR will not provide funding for this activity but may offer a discounted fee for its annual meeting.
- Evaluate progress and adjust program to specific needs in biannual meeting or telephone conference with the Editor-in-Chief.
- Write at least one editorial for AJNR.
- Embark on an editorial scientific or bibliometric project that will lead to the submission of an article to AJNR or another appropriate journal as determined by the Editor-in-Chief. This project will be presented by the Editorial Fellow at the ASNR annual meeting.
- Serve as liaison between AJNR and ASNR’s Young Professionals Network and the 3 YPs appointed to AJNR as special consultants. Participate in meetings and telephone calls with this group. Design one electronic survey/year polling the group regarding readership attitudes and wishes.
- Recruit trainees as reviewers as determined by the Editor-in-Chief.
- Participate in Web improvement projects.
- Potentially become a member of AJNR’s Editorial Board at the end of the fellowship.
- Invite Guest Editors for AJNR’s News Digest to cover a variety of timely topics.

QUALIFICATIONS

- Be a fellow in neuroradiology from North America, including Canada (this may be extended to include other countries).
- Be a junior faculty neuroradiology member (< 3 years) in either an academic and private environment.
- Provide an “end” of fellowship report to AJNR’s Editor-in-Chief and ASNR’s Publications Committee.
- Be an “in-training” or member of ASNR in any other category.

APPLICATION

- Include a short letter of intent with statement of goals and desired research project. CV must be included.
- Include a letter of recommendation from the Division Chief or fellowship program director. A statement of protected time to perform the functions outlined is desirable.
- Applications will be evaluated by AJNR’s Senior Editors and the Chair of the Publications Committee prior to the ASNR meeting. The name of the selected individual will be announced at the meeting.
- Applications should be received by March 3, 2015 and sent to Ms. Karen Halm, AJNR Managing Editor, electronically at khalm@asnr.org.

Official Journal:

American Society of Neuroradiology
American Society of Functional Neuroradiology
American Society of Head and Neck Radiology
American Society of Pediatric Neuroradiology
American Society of Spine Radiology

EDITOR-IN-CHIEF

Mauricio Castillo, MD

Professor of Radiology and Chief, Division of Neuroradiology, University of North Carolina, School of Medicine, Chapel Hill, North Carolina

SENIOR EDITORS

Harry J. Cloft, MD, PhD

Professor of Radiology and Neurosurgery, Department of Radiology, Mayo Clinic College of Medicine, Rochester, Minnesota

Nancy J. Fischbein, MD

Professor of Radiology, Otolaryngology-Head and Neck Surgery, Neurology, and Neurosurgery and Chief, Head and Neck Radiology, Department of Radiology, Stanford University Medical Center, Stanford, California

Jeffrey S. Ross, MD

Staff Neuroradiologist, Barrow Neurological Institute, St. Joseph's Hospital, Phoenix, Arizona

Pamela W. Schaefer, MD

Clinical Director of MRI and Associate Director of Neuroradiology, Massachusetts General Hospital, Boston, Massachusetts, and Associate Professor, Radiology, Harvard Medical School, Cambridge, Massachusetts

Charles M. Strother, MD

Professor of Radiology, Emeritus, University of Wisconsin, Madison, Wisconsin

Jody Tanabe, MD

Professor of Radiology and Psychiatry, Chief of Neuroradiology, University of Colorado, Denver, Colorado

EDITORIAL BOARD

Ashley H. Aiken, *Atlanta, Georgia*
A. James Barkovich, *San Francisco, California*
Walter S. Bartynski, *Charleston, South Carolina*
Barton F. Branstetter IV, *Pittsburgh, Pennsylvania*
Jonathan L. Brisman, *Lake Success, New York*
Julie Bykowski, *San Diego, California*
Donald W. Chakeres, *Columbus, Ohio*
Alessandro Cianfoni, *Lugano, Switzerland*
Colin Derdeyn, *St. Louis, Missouri*
Rahul S. Desikan, *San Diego, California*
Richard du Mesnil de Rochemont, *Frankfurt, Germany*
Clifford J. Eskey, *Hanover, New Hampshire*
Massimo Filippi, *Milan, Italy*
David Fiorella, *Cleveland, Ohio*
Allan J. Fox, *Toronto, Ontario, Canada*
Christine M. Glastonbury, *San Francisco, California*

John L. Go, *Los Angeles, California*
Wan-Yuo Guo, *Taipei, Taiwan*
Rakesh K. Gupta, *Lucknow, India*
Lotfi Hacein-Bey, *Sacramento, California*
David B. Hackney, *Boston, Massachusetts*
Christopher P. Hess, *San Francisco, California*
Andrei Holodny, *New York, New York*
Benjamin Huang, *Chapel Hill, North Carolina*
Thierry A.G.M. Huisman, *Baltimore, Maryland*
George J. Hunter, *Boston, Massachusetts*
Mahesh V. Jayaraman, *Providence, Rhode Island*
Valerie Jewells, *Chapel Hill, North Carolina*
Timothy J. Kaufmann, *Rochester, Minnesota*
Kenneth F. Layton, *Dallas, Texas*
Ting-Yim Lee, *London, Ontario, Canada*
Michael M. Lell, *Erlangen, Germany*
Michael Lev, *Boston, Massachusetts*
Karl-Olof Lovblad, *Geneva, Switzerland*
Franklin A. Marden, *Chicago, Illinois*
M. Gisele Matheus, *Charleston, South Carolina*
Joseph C. McGowan, *Merion Station, Pennsylvania*
Kevin R. Moore, *Salt Lake City, Utah*
Christopher J. Moran, *St. Louis, Missouri*
Takahisa Mori, *Kamakura City, Japan*

Suresh Mukherji, *Ann Arbor, Michigan*
Amanda Murphy, *Toronto, Ontario, Canada*
Alexander J. Nemeth, *Chicago, Illinois*
Laurent Pierot, *Reims, France*
Jay J. Pillai, *Baltimore, Maryland*
Whitney B. Pope, *Los Angeles, California*
M. Judith Donovan Post, *Miami, Florida*
Tina Young Poussaint, *Boston, Massachusetts*
Joana Ramalho, *Lisbon, Portugal*
Otto Rapalino, *Boston, Massachusetts*
Álex Rovira-Cañellas, *Barcelona, Spain*
Paul M. Ruggieri, *Cleveland, Ohio*
Zoran Rumboldt, *Rijeka, Croatia*
Amit M. Saindane, *Atlanta, Georgia*
Erin Simon Schwartz, *Philadelphia, Pennsylvania*
Aseem Sharma, *St. Louis, Missouri*
J. Keith Smith, *Chapel Hill, North Carolina*
Maria Vittoria Spampinato, *Charleston, South Carolina*
Gordon K. Sze, *New Haven, Connecticut*
Krishnamoorthy Thamburaj, *Hershey, Pennsylvania*
Kent R. Thielen, *Rochester, Minnesota*
Cheng Hong Toh, *Taipei, Taiwan*
Thomas A. Tomsick, *Cincinnati, Ohio*
Aquila S. Turk, *Charleston, South Carolina*
Willem Jan van Rooij, *Tilburg, Netherlands*
Arastoo Vossough, *Philadelphia, Pennsylvania*
Elysa Widjaja, *Toronto, Ontario, Canada*
Max Wintermark, *Charlottesville, Virginia*
Ronald L. Wolf, *Philadelphia, Pennsylvania*
Kei Yamada, *Kyoto, Japan*

EDITORIAL FELLOW

Asim F. Choudhri, *Memphis, Tennessee*

YOUNG PROFESSIONALS ADVISORY COMMITTEE

Asim K. Bag, *Birmingham, Alabama*
Anna E. Nidecker, *Sacramento, California*
Peter Yi Shen, *Sacramento, California*

HEALTH CARE AND SOCIOECONOMICS EDITOR

Pina C. Sanelli, *New York, New York*

Founding Editor

Juan M. Taveras

Editors Emeriti

Robert I. Grossman, Michael S. Huckman,
Robert M. Quencer

Special Consultants to the Editor
Sandy Cheng-Yu Chen, Girish Fatterpekar,
Ryan Fitzgerald, Katherine Freeman,
Yvonne Lui, Greg Zaharchuk

INR Liaisons

Timo Krings, Karel terBrugge

Managing Editor

Karen Halm

Electronic Publications Manager

Jason Gantenberg

Editorial Assistant

Mary Harder

Executive Director, ASNR

James B. Gantenberg

Director of Communications, ASNR

Angelo Artemakis



AJNR (Am J Neuroradiol) (ISSN 0195–6108) is a journal published monthly, owned and published by the American Society of Neuroradiology (ASNR), 800 Enterprise Drive, Suite 205, Oak Brook, IL 60523. Annual dues for the ASNR include \$170.00 for journal subscription. The journal is printed by Cadmus Journal Services, 5457 Twin Knolls Road, Suite 200, Columbia, MD 21045; Periodicals postage paid at Oak Brook, IL and additional mailing offices. Printed in the U.S.A. POSTMASTER: Please send address changes to American Journal of Neuroradiology, P.O. Box 3000, Denville, NJ 07834, U.S.A. Subscription rates: nonmember \$380 (\$450 foreign) print and online, \$305 online only; institutions \$440 (\$510 foreign) print and basic online, \$875 (\$940 foreign) print and extended online, \$365 online only (basic), extended online \$790; single copies are \$35 each (\$40 foreign). Indexed by PubMed/Medline, BIOSIS Previews, Current Contents (Clinical Medicine and Life Sciences), EMBASE, Google Scholar, HighWire Press, Q-Sensei, RefSeek, Science Citation Index, and SCI Expanded. Copyright © American Society of Neuroradiology.

Trevo® XP ProVue Retrievers

See package insert for complete indications, complications, warnings, and instructions for use.

INDICATIONS FOR USE

The Trevo Retriever is intended to restore blood flow in the neurovasculature by removing thrombus in patients experiencing ischemic stroke within 8 hours of symptom onset. Patients who are ineligible for intravenous tissue plasminogen activator (IV t-PA) or who fail IV t-PA therapy are candidates for treatment.

COMPLICATIONS

Procedures requiring percutaneous catheter introduction should not be attempted by physicians unfamiliar with possible complications which may occur during or after the procedure. Possible complications include, but are not limited to, the following: air embolism; hematoma or hemorrhage at puncture site; infection; distal embolization; pain/headache; vessel spasm, thrombosis, dissection, or perforation; emboli; acute occlusion; ischemia; intracranial hemorrhage; false aneurysm formation; neurological deficits including stroke; and death.

COMPATIBILITY

3x20 mm retrievers are compatible with Trevo® Pro 14 Microcatheters (REF 90231) and Trevo® Pro 18 Microcatheters (REF 90238). 4x20 mm retrievers are compatible with Trevo® Pro 18 Microcatheters (REF 90238). Compatibility of the Retriever with other microcatheters has not been established. Performance of the Retriever device may be impacted if a different microcatheter is used. The Merci® Balloon Guide Catheters are recommended for use during thrombus removal procedures. Retrievers are compatible with the Abbott Vascular DOC® Guide Wire Extension (REF 22260)

WARNINGS

- Contents supplied STERILE, using an ethylene oxide (EO) process. Nonpyrogenic.
- To reduce risk of vessel damage, adhere to the following recommendations:
 - Take care to appropriately size Retriever to vessel diameter at intended site of deployment.
 - Do not perform more than six (6) retrieval attempts in same vessel using Retriever devices.
 - Maintain Retriever position in vessel when removing or exchanging Microcatheter.
- To reduce risk of kinking/fracture, adhere to the following recommendations:
 - Immediately after unsheathing Retriever, position Microcatheter tip marker just proximal to shaped section. Maintain Microcatheter tip marker just proximal to shaped section of Retriever during manipulation and withdrawal.
 - Do not rotate or torque Retriever.
 - Use caution when passing Retriever through stented arteries.
- Do not resterilize and reuse. Structural integrity and/or function may be impaired by reuse or cleaning.
- The Retriever is a delicate instrument and should be handled carefully. Before use and when possible during procedure, inspect device carefully for damage. Do not use a device that shows signs of damage. Damage may prevent device from functioning and may cause complications.
- Do not advance or withdraw Retriever against resistance or significant vasospasm. Moving or torquing device against resistance or significant vasospasm may result in damage to vessel or device. Assess cause of resistance using fluoroscopy and if needed resheath the device to withdraw.

- If Retriever is difficult to withdraw from the vessel, do not torque Retriever. Advance Microcatheter distally, gently pull Retriever back into Microcatheter, and remove Retriever and Microcatheter as a unit. If undue resistance is met when withdrawing the Retriever into the Microcatheter, consider extending the Retriever using the Abbott Vascular DOC guidewire extension (REF 22260) so that the Microcatheter can be exchanged for a larger diameter catheter such as a DAC® catheter. Gently withdraw the Retriever into the larger diameter catheter.
- Administer anti-coagulation and anti-platelet medications per standard institutional guidelines.

PRECAUTIONS

- Prescription only – device restricted to use by or on order of a physician.
- Store in cool, dry, dark place.
- Do not use open or damaged packages.
- Use by “Use By” date.
- Exposure to temperatures above 54°C (130°F) may damage device and accessories. Do not autoclave.
- Do not expose Retriever to solvents.
- Use Retriever in conjunction with fluoroscopic visualization and proper anti-coagulation agents.
- To prevent thrombus formation and contrast media crystal formation, maintain a constant infusion of appropriate flush solution between guide catheter and Microcatheter and between Microcatheter and Retriever or guidewire.
- Do not attach a torque device to the shaped proximal end of DOC® Compatible Retriever. Damage may occur, preventing ability to attach DOC® Guide Wire Extension.



Concentric Medical
301 East Evelyn
Mountain View, CA 94041



EMERGO Europe
Molenstraat 15
2513 BH, The Hague
The Netherlands



Stryker Neurovascular
47900 Bayside Parkway
Fremont, CA 94538

stryker.com/neurovascular
stryker.com/emea/neurovascular

Date of Release: JUN/2014

EX_EN_GL

The 3 Pillars of Health

M. Castillo, *Editor-in-Chief*

For many years, I undervalued sleep. Why sleep when one can be up and about? Well, several things have recently caused me to change my mind. Our understanding of sleep and how it affects our brains and bodies is rapidly changing, and personal fitness devices help us keep track of these effects.

Approximately 2 months ago, I bought a personal fitness device; one of those plastic bands worn around a wrist that have lately been in the news. Most of these devices rely on accelerometers and altimeters (such as those used in the iPhone and iPad that allow one to play games by twisting and moving the devices) and store their data in small computers that then take this information to calculate different parameters. With regard to the types of physical activity analyzed, the performances of these devices vary and I tend to concentrate on trends rather than specific daily measures (but by now I know exactly how much I walk when on clinical service from my office to the reading room and how much I move during academic days).

With regard to sleep, my device does something called “sleep efficiency tracking.” After communicating via Bluetooth and Wi-Fi with my telephone, I get to see the following: total sleep time, hours of deep and light sleep, and times and duration of periods in which I was awake. Every few days, it gives me messages informing that I am sleeping well or need to sleep more such as, “If you sleep more than 7 hours today, tomorrow you will feel more rested, confident, beautiful, and smart!” How can one resist such messages?

In addition (I have not tried it yet), the device has a smart waking alarm, meaning that it will wake me within 30 minutes of a selected time based on my REM cycles. Apparently, this eliminates the disconcerted feeling of being woken up in the middle of a dream. In reality, I think that most sleep information it provides is fairly vague but, again, trends are what count.

One message that my device has sent me several times states that sleep (the National Sleep Foundation recommends 7–9 hours per day for adults) helps one lose weight, and this does make sense. If one is not sleeping well, one is spending more time awake, which increases the chance of eating and induces fatigue that leads to more eating (especially carbohydrates) and lesser physical activity. Sleep deprivation produces a “double hit” to the brain in this regard: there is a sharp reduction in frontal lobe activity leading one to misjudge hunger and eat more junk and also leading to an exaggerated activation of reward centers (mostly the amygdalae) after eating. One meta-analysis of nearly 700 published studies showed that both adults and children who are short sleepers have an increased risk of obesity.¹ In a different study, 12 men were allowed a full night of sleep (8 hours) followed by a partial night of sleep (4 hours); after the latter, the men were hungrier upon waking up and ate more during the day (22%).² Acute par-

tial sleep leads to increased serum levels of ghrelin (a hunger hormone) and decreased levels of leptin (a satiety hormone). Paradoxically, sleeping less leads to increased metabolism and extra burning of calories (but on average just a paltry 111 calories per day). However, the compensatory intake of food exceeds this amount and results in a net weight gain.³ Partial sleepers tend to consume approximately 600 more calories than full-night sleepers, with most of those calories coming from chocolate, desserts, and potato chips.⁴ Poor food choices are common in the sleep deprived. One of the authors of this last study speculated that adenosine, which is a brain metabolic by-product, possibly disrupts neural function by accumulating in the sleep-deprived brain.⁵ It is conceivable that adenosine accumulation affects the way we perceive food. Because sleep clears the brain of adenosine, sleep is the equivalent of chemically rebooting our brains.

Sleep must be terribly important because all animals on earth do it. A recent article published in *Science* starts to shed light on its importance. Rats undergoing natural sleep or sleep induced by anesthesia increased their brain’s interstitial spaces by 60%.⁶ This leads to significant exchanges between CSF and interstitial fluid that result in increased rates of beta-amyloid clearance during sleep. Apparently, amyloid accumulates during the day and sleep disposes of it at night. This system is thought to be analogous to the lymphatic system that clears metabolic waste from the rest of the body, hence its name: glymphatic system (glial + lymphatic). Sleep promotes memory consolidation and that is why this process is abnormal in the elderly (who sleep less) and in those with diseases such as Alzheimer, in which amyloid accumulates.

The term “glymphatic system” derives from the fact that the glial cells are the ones mostly responsible for the exchange of fluids through their membranes. The glymphatic system is a high-energy system and that is why it cannot work when the brain’s energy is being used for other activities such as being awake. Wakefulness decreases the brain’s fluid exchange capacity by approximately 95%. Norepinephrine probably serves to control this fluid exchange. The authors of the *Science* article speculated that increased norepinephrine when awake results in increased cell volume and conversely decreased interstitial volume. Animals given adrenergic receptor antagonists show increased CSF influx into their brain’s interstitial space. Thus, rather than sleep, it is probably wakefulness that primarily regulates the glymphatic system. The problem is that once amyloid starts to accumulate in the brain, sleep cycles are further upset, and the insomnia that occurs with Alzheimer and other dementias further exacerbates the lack of clearance of the brain’s noxious substances.

Although the concept of the glymphatic system is today believed to be related only to amyloid, it is possible that it also plays a role in the disposal of other proteins such as tau and alpha-synuclein that are involved in other neurodegenerative disorders, especially Parkinson disease. Other possible implications of this mechanism are the increase in migraines and seizures in patients who sleep poorly. It is conceivable that, in the future, instead of treating these diseases directly, we could design medications that enhance the functioning of the glymphatic system and radiotracers that could be used in vivo to assess their effects. How CSF gets

into the brain is still unclear, possibly through its external and ventricular surfaces and the perivascular spaces.

PET imaging with the Pittsburgh compound (PiB-PET) has shown that shorter sleep duration is associated with higher amyloid brain burden.⁷ Other studies have shown that unfragmented sleep reduces the risk of Alzheimer disease (and decreases the development of neurofibrillary tangles) and diminishes normal age-related cognitive decline.⁸ Apnea is another factor that prevents adequate sleep consolidation and though it was thought to affect mentation by vascular effects on the brain, the worse cognition associated with it could be caused by interruptions of the lymphatic system function. Of course, one's inability to consolidate sleep is multifactorial and includes comorbidities and genetic and environmental factors among others. Perhaps information gathered by personal fitness devices on the sleep patterns of millions of users will shed more light onto the relationship between sleep and successful aging. Over 60% of all adults report trouble sleeping at night, thus the implications of the relationship between sleep and cognition are staggering.

Regardless of any scientific evidence, sleep is a hot item and even a new, short e-novella by famous (and very good) author Karen Russell deals with the subject.⁹ In this short book, America experiences an epidemic of insomnia and a large corporation decides that sleep is a commodity. Healthy sleepers are urged to "donate" their sleep to those less fortunate. The fact that sleep is indeed a commodity is now being used by industries successfully. Personal fitness and activity tracking devices generated over US \$290 million last year in sales and this is expected to double soon. Today, there are so many brands that manufacture these personal fitness devices that choosing one is difficult, particularly if one did not sleep well the night before.

So, what did I learn about my sleep in the last 2 months of wearing my Up24 band? Well, only good news. I fall asleep faster and sleep longer than I thought and have longer periods of deep sleep than others in my "team" (yes, you cannot only compete for the most activities but also for the most and best sleep). I have also become more aware as to how much people care about how I well sleep: hotels offer me better mattresses, more pillow choices, high-efficiency sheets and pillow covers, mood lightning and soothing sounds, calming pulse-point oils, and some will even call before I go to sleep to remind me to turn my electronic devices off (the blue wavelength light these devices emit affects the secretion of melatonin more powerfully than any other type of light). Airlines lagged behind hotels and now that, at least in business class, the food is improving, they are concentrating on sleep and offering natural-fiber bedding, flat-bed seats, noise-cancellation headphones, and "radio" stations with only white noise. Why the industry is doing all of this is not clear to me and in a recent article in the *New York Times*, the executive director of the Harvard Medical School Division of Sleep Medicine said, "Sleep is the enemy of capitalism, you can't produce or consume when you're asleep."¹⁰ In the same article, Dr. Sanna also says that we need to stop thinking of sleep as a commodity and a lifestyle choice, but rather as the third pillar of health together with diet and exercise. Could it be that living and sleeping better and longer is becoming more important than just accumulating stuff? I do not think so, but to-

night I will go to sleep earlier hoping that it will help me be a smarter and healthier neuroradiologist tomorrow.

REFERENCES

1. Cappuccio FP, Taggart FM, Kandala NB, et al. **Meta-analysis of short sleep duration and obesity in children and adults.** *Sleep* 2008; 31:619–26
2. Brondel L, Romer MA, Nouques PM, et al. **Acute partial sleep deprivation increases food intake in healthy men.** *Am J Clin Nutr* 2010;91:1550–59
3. Markwald RR, Melanson EL, Smith MR, et al. **Impact of insufficient sleep on total daily energy expenditure, food intake, and weight gain.** *Proc Natl Acad Sci U S A* 2013;110:5695–700
4. Greer SM, Goldstein AN, Walker MP. **The impact of sleep deprivation on food desire in the human brain.** *Nat Commun* 2013;4:2259
5. O'Connor A. How sleep loss adds to weight gain. *New York Times*. August 6, 2013. <http://well.blogs.nytimes.com/2013/08/06/how-sleep-loss-adds-to-weight-gain>. Accessed March 27, 2014
6. Xie L, Kang H, Xu Q, et al. **Sleep drives metabolite clearance from the adult brain.** *Science* 2013;342:373–77
7. Malkki M. **Alzheimer disease: sleep alleviates AD-related neuro-pathological processes.** *Nat Rev Neurol* 2013;9:657
8. Lim, AS, Yu L, Kowgier M, et al. **Modification of the relationship of the apolipoprotein E ε4 allele to the risk of Alzheimer disease and neurofibrillary tangle density by sleep.** *JAMA Neurol* 2013;70: 1544–51
9. Russell K. *Sleep Donation*. New York: Atavist; 2014
10. Rosenbloom S. From airlines to hotels, a quest to help you sleep. *New York Times*. March 26, 2014. <http://www.nytimes.com/2014/03/30/travel/from-airlines-to-hotels-a-quest-to-help-you-sleep.html>. Accessed March 27, 2014

EDITORIAL

Point—TAR: A Useful Index to Follow-Up Coiled Intracranial Aneurysms?

L. Pierot, J. Fiehler, and P. White

The Matrix and Platinum Science (MAPS) trial results were recently published showing that Matrix² coils were not inferior (and not superior) to bare metal coils (BMC) in the treatment of ruptured and unruptured intracranial aneurysms.¹ In the trial, 626 patients were enrolled in 43 investigational sites from March 2007 to October 2009. Besides being designed to compare the results of aneurysm treatment with Matrix² and BMC, MAPS was also designed to evaluate a composite clinical outcome measure designated as "target aneurysm recurrence" (TAR) that was defined as occurring when a patient experienced any of the following conditions after his or her initial aneurysm coiling: 1) target aneurysm (re)hemorrhage, 2) target aneurysm retreatment, or 3) death from unknown cause.

As demonstrated by previous studies, there was no significant difference between Matrix² and BMC regarding aneurysm occlusion (evaluated with modified 3-grade Raymond scale) by core lab evaluation at the end of the procedure and at 12 months.^{2,3} There was also no significant difference in the arms with respect to change in aneurysm occlusion evaluated with a 3-grade scale (bet-

<http://dx.doi.org/10.3174/ajnr.A4119>

ter, same, worse). Moreover, no significant difference was detected in the clinical evolution in both groups. In fact, the primary trial end point was TAR and there was no significant difference between groups (Matrix²: 13.3%; BMC: 14.6%; $P = .76$).

Looking in the global population at the TAR events (total: 69), 1 was an unexplained death (1.4% of the events), 4 were rupture/reruptures (5.8%), and 64 were retreatments of aneurysms that had not bled after initial treatment (92.8%). Therefore, the overwhelming majority of TAR events were retreatment not related to a rupture/rerupture. It means that the primary end point of MAPS was in fact more or less retreatment.

There were in the protocol no specific indications or even guidance for aneurysm retreatment; that was entirely at the discretion of the operator. Unfortunately, and irretrievably for TAR as a primary trial end point, indications for aneurysm retreatment are absolutely unclear and no recommendation exists detailing situations in which retreatment has to be performed. It is clear that 2 operators facing the same incompletely occluded aneurysm will frequently not have the same indication for retreatment. In their recent study regarding retreatment decisions of recurrent and residual aneurysms, McDonald et al⁴ have shown that the overall interobserver variability for the decision to retreat was not more than moderate (intraclass correlation coefficient: 0.50). This observation is in line with previous analyses.⁵ As outlined by MAPS investigators themselves, the rate of retreatment is quite heterogeneous from 1 series to another, with a rate as low as 3% in both arms of the HELPS trial.⁶ Similarly, in a CLARITY study, retreatment rate is 3.3% in the BMC group but 9.5% in the Matrix group.³ In the Cerecyte Coil Trial (CCT), retreatment rate was 3.5% in the BMC group and 7.7% in the Cerecyte group.⁷ In MAPS, retreatment rate (not including bleeding/rebleeding cases) is 33 of 315 (10.5%) in the BMC group and 31 of 311 (10.0%) in the Matrix² group. Were BMC less efficacious in MAPS than in HELPS, CCT, and CLARITY, that such a high percentage of retreatment was needed (10.5% compared with 3 to 3.5% in HELPS, CCT, and CLARITY)? Or were indications for retreatment quite different in centers participating in MAPS, many of which did not participate in HELPS, CCT, or CLARITY? Is TAR therefore largely a health economy (ie, geographic) effect?

Aneurysm treatment is dedicated to prevention of rerupture (for ruptured aneurysms) and rupture (for unruptured aneurysms). Indications for treatment of unruptured aneurysms are already a matter of debate and absolutely not clear. In the same way, indications for retreatment of incompletely treated aneurysms are also not clear; retreatment should not be cosmetic (to obtain a nice angiographic result), but again to prevent the risk of rupture/rerupture. Very little is known regarding the risk of rupture/rerupture of incompletely treated aneurysms. From the International Subarachnoid Aneurysm Trial (ISAT), it seems that the risk of rerupture of coiled aneurysms is extremely low and remains so for up to 10 years.⁸ From the Cerebral Aneurysm Rerupture After Treatment trial, it seems that the status for aneurysm occlusion plays a significant role with aneurysm remnant having probably a higher risk of rupture/rerupture than neck remnant.⁹

Thus, indications for aneurysm retreatment are made on a case-by-case basis based on various factors including a patient's

age, initial clinical presentation, potential comorbidities determining the overall prognosis of the patient, aneurysm remnant characteristics, aneurysm dynamics over time, and feasibility and risks of retreatment. These factors will be differently evaluated from one operator to another; an "aggressive" operator (or an operator who is paid on an item of service basis rather than annual salary basis) will probably have wider indications for retreatment compared with a more "conservative" one.

Evaluating an aneurysm treatment means determining its safety and efficacy. The way safety has to be evaluated is relatively clear based on determination of complication rates. This includes rates of thromboembolic events and intraoperative rupture and evaluation of neurologic outcome with mRS or other scales at a given time after the index procedure. Evaluation of efficacy is more complicated. As the goal of the treatment is to prevent aneurysm rupture/rerupture, the best way to evaluate the efficacy of a given aneurysm treatment is certainly to determine the rate of rupture/rerupture after aneurysm treatment. However, as these events are relatively rare, large study populations and/or long follow-up periods are needed to compare the efficacy of 2 different treatments. Accordingly, the tendency has been to evaluate the efficacy through the immediate, mid-term, and long-term anatomic results as well as recanalization rate, with the definitions of recanalization being relatively heterogeneous in the literature.¹⁰ Several scales have been proposed to evaluate aneurysm occlusion; however, the 3-grade Raymond (or Montreal) scale is still the most commonly used in the literature.¹¹ Defining efficacy of aneurysm treatment through the evaluation of aneurysm occlusion is already quite debatable as the link between aneurysm occlusion status and rupture/rerupture is not completely established. However, as the risk of rupture/rerupture of a treated aneurysm is probably at its maximum in cases of aneurysm remnant, evaluation of aneurysm treatment efficacy with angiographic results and recanalization rate is probably acceptable, if not perfect. In fact, the ISAT data, where endovascular anatomic results achieved were often crude by today's standards, rather indicates that the link between occlusion and rupture is limited. The target aneurysm rebleed rate at 10 years was extremely low and in only half of that small number of cases did it lead to a poor clinical outcome.⁸

As shown before, evaluation of aneurysm treatment efficacy with TAR is essentially merely evaluating efficacy through the rate of aneurysm retreatment. As stated by the MAPS investigators, retreatment is a much more important event to the patient compared with an asymptomatic angiographic finding of residual aneurysm.

However, it is possible to evaluate aneurysm occlusion status objectively in a study singularly when an independent core laboratory is used and results have an acceptable reproducibility, whereas aneurysm retreatment decisions cannot be so objectively evaluated.¹² Moreover, volumetric measurement of aneurysm changes over time as an imaging end point can limit the variability of visual assessment.^{13,14} On the contrary, aneurysm retreatment is the result of a completely subjective decision process involving the treating physician and the patient who always has the possibility to refuse the retreatment of the incompletely treated aneurysm. Moreover, as soon as TAR (re-

treatment) is used as the primary end point of a trial, it can certainly modify the indications for retreatment for the patients included in the trial knowing that the treating physician cannot be blind regarding the treatment used. TAR transfers the variability of angiographic evaluation (minimized by blinded dual core lab reading with inter- and intraobserver reproducibility assessments) toward the variability of many therapists who additionally take into consideration far more variables than just anatomy. This transfer adds great interindividual heterogeneity and additional influencing variables. MAPS investigators have identified the drawbacks related to the use of TAR to evaluate aneurysm treatment efficacy, but still their conclusion is that “target aneurysm recurrence is a promising clinical outcome measure that correlates well with established angiographic measurements.” It would have been effectively surprising to learn that TAR was not well correlated with aneurysm occlusion status, which would have meant that completely occluded aneurysm or modest neck remnants have been retreated.

Defining the appropriate way to evaluate the efficacy of intracranial aneurysm treatment is certainly not simple. The best way would be the protection afforded by a given treatment against bleeding/rebleeding as the true clinical end point. However, this parameter is not feasible as bleeding/rebleeding events are exceedingly rare after aneurysm treatment even in previously ruptured aneurysms, let alone unruptured aneurysms. TAR that is overwhelmingly determined by aneurysm retreatment is certainly not a good tool as indications for aneurysm retreatment are unknown and very heterogeneous; including from one country to another, from one center to another, from one physician to another, not to mention from one day to another for the same physician. This additional heterogeneity outbalances the positive effect of the clinical relevance of TAR. Evaluating efficacy with anatomic results as a surrogate end point is certainly not perfect, but it is a relatively simple, clinically meaningful, and a far more reproducible way of doing comparison between different aneurysm treatments.

Disclosures: Laurent Pierot—RELATED: Consulting Fee or Honorarium: Codman, Covidien/ev3, Microvention, Sequent, Stryker. Jens Fiehler—RELATED: Consulting Fee or Honorarium: Acandis, Codman, Microvention, Sequent, Stryker; Support for Travel to Meetings for the Study or Other Purposes/Speaker Beureau Activities: Covidien/ev3, Penumbra; UNRELATED: Travel/Accommodations/Meeting Expenses Unrelated to Activities Listed: Covidien. Phil White—UNRELATED: Consultancy: Codman, Microvention Terumo, Comments: For supporting/running educational activities; Grants/Grants Pending: Microvention Terumo,* Comments: Cofunder grant for RCT-STABILISE; Payment for Lectures (including service on speakers bureaus): Codman, Covidien, Comments: Stroke-related. *Money paid to the institution.

REFERENCES

- McDougall CG, Claiborne Johnston S, Gholkar A, et al. **Bioactive versus bare platinum coils in the treatment of intracranial aneurysms: the MAPS (Matrix and Platinum Science) trial.** *AJNR Am J Neuroradiol* 2014;35:935–42
- Pierot L, Cognard C, Ricolfi F, et al. **Immediate anatomical results after endovascular treatment of ruptured intracranial aneurysms: analysis of the CLARITY series.** *AJNR Am J Neuroradiol* 2010;31:907–11
- Pierot L, Cognard C, Ricolfi F, et al. **Mid-term anatomical results after endovascular treatment of ruptured intracranial aneurysms with Guglielmi detachable coils and Matrix coils: analysis of the CLARITY series.** *AJNR Am J Neuroradiol* 2012;33:469–73
- McDonald JS, Carter RE, Layton KF, et al. **Interobserver variability in retreatment decisions of recurrent and residual aneurysms.** *AJNR Am J Neuroradiol* 2013;34:1035–39
- Daugherty WP, Rad AE, White JB, et al. **Observer agreement regarding the necessity of retreatment of previously coiled recurrent cerebral aneurysms.** *AJNR Am J Neuroradiol* 2011;32:566–69
- White PM, Lewis SC, Gholkar A, et al. **Hydrogel-coated coils versus bare platinum coils for the endovascular treatment of intra-cranial aneurysms (HELPS): a randomised controlled trial.** *Lancet* 2011;377:1655–62
- Molyneux AJ, Clarke A, Sneade M, et al. **Cerecyte coil trial: angiographic outcomes of a prospective randomized trial comparing endovascular coiling of cerebral aneurysms with either Cerecyte or bare platinum coils.** *Stroke* 2012;43:2544–50
- Molyneux AJ, Birks J, Clarke A, et al. **The durability of endovascular coiling versus neurosurgical clipping of ruptured cerebral aneurysms: 18 year follow-up of the UK cohort of the International Subarachnoid Aneurysm Trial (ISAT).** *Lancet* 2014 Oct 28. [Epub ahead of print]
- CARAT Investigators. **Rates of delayed rebleeding from intracranial aneurysms are low after surgical and endovascular treatment.** *Stroke* 2006;37:1437–42
- Benaissa A, Barbe C, Pierot L. **Analysis of recanalization after endovascular treatment of intracranial aneurysm (ARETA trial): presentation of a prospective multicenter study.** *J Neuroradiol* 2014 Jul 7. [Epub ahead of print]
- Raymond J, Guilbert F, Weill A, et al. **Long-term angiographic recurrences after selective endovascular treatment of aneurysms with detachable coils.** *Stroke* 2003;34:1398–403
- Tollard É, Darsaut TE, Bing F, et al. **Outcomes of endovascular treatments of aneurysms: observer variability and implications for interpreting case series and planning randomized trials.** *AJNR Am J Neuroradiol* 2012;33:626–31
- Ries T, Wegscheider K, Wulff A, et al. **Quantification of recurrence volumes after endovascular treatment of cerebral aneurysm as surrogate endpoint for treatment stability.** *Neuroradiology* 2011;53:593–98
- Schönfeld M, Schlotfeldt V, Forkert ND, et al. **Aneurysm recurrence volumetry is more sensitive than visual evaluation of aneurysm recurrences.** *Clin Neuroradiol* 2014 Aug 27. [Epub ahead of print]

EDITORIAL

Counterpoint—Target Aneurysm Recurrence: Measuring What Matters

C.G. McDougall, S.C. Johnston, A. Gholkar, and A.S. Turk

What Is Target Aneurysm Recurrence?

Target aneurysm recurrence (TAR) has been proposed as a measure of clinical effectiveness after aneurysm treatment. It is a composite end point that is meant to capture the clinical events that are most important to patients after aneurysm treatment, specifically aneurysm rupture and retreatment. Because sudden unexplained deaths may also be due to aneurysm rupture, such deaths are conservatively assumed to be due to aneurysmal

<http://dx.doi.org/10.3174/ajnr.A4205>

hemorrhage and are included as one of the components of TAR. Thus, TAR is said to have occurred if ≥ 1 of the following hard end points is experienced by a patient following treatment:

- 1) Target aneurysm rupture
- 2) Sudden unexplained death
- 3) Target aneurysm retreatment.

This effectiveness scale was proposed in the context of the Matrix and Platinum Science (MAPS) trial, a randomized trial that enrolled 626 patients and mandated 5 years of clinical follow-up.¹ It is hoped that TAR events in MAPS can be correlated with the core laboratory adjudicated angiographic treatment results. Thus, it may be possible to better understand how angiographic outcomes predict future clinical recurrences. One-year results have been reported, and the 5-year follow-up, upon which future publications will be based, was completed in October 2014.

TAR Matters Because It Is What Patients Care About

When we treat patients with aneurysms, particularly patients who have recovered after treatment of a ruptured aneurysm, it is striking to see how traumatized many of them are, even years after experiencing an SAH. Like patients with posttraumatic stress disorder, many live with fear hanging over them, even if they are told that the chance of recurrent SAH is exceedingly rare. Recurrent hemorrhage looms in overwhelming importance in the minds of these patients, even if this worry is disproportionate to the frequency with which posttreatment hemorrhage occurs.

Retreatment is a major event for a patient. In addition to being costly, it carries physical risk, and it reminds patients that treatment is imperfect in that it provides only partial protection from future hemorrhage. Once a patient has been treated and the procedural risks are no longer an issue, rehemorrhage and retreatment are far and away the 2 events that concern patients most.

If we, in turn, care about what really matters to our patients, we must track and measure these events and strive to fully understand why they happen. Only then can we systematically address and reduce the rates of rehemorrhage and, consequently, retreatment.

Why “Adequate Occlusion” Is Inadequate

From the inception of aneurysm treatment, the immediate goal of treatment has been complete aneurysm occlusion. Long experience with surgical clipping and infrequent recurrent hemorrhages led to the dogma that surgically obliterated aneurysms rarely rebleed. Despite exceptions being reported,² this assumption has largely carried over to endovascular aneurysm treatment.

Although the definitions of angiographic occlusion after coiling are quite heterogeneous, the most widely used classification scale is the 3-point Raymond (Modified Montreal) scale.³ Recognizing that “complete” aneurysm occlusion after coiling is only achieved half of the time or less,^{1,4-7} we have seen creep into the endovascular literature the concept of “adequate occlusion,” wherein “complete occlusions” and “neck remnants” are lumped together as “adequate occlusions.” This concept is based on the intuitively attractive, but unproven, assumption that rehemorrhage is exceedingly rare in aneurysms that have neck remnants but no residual filling of the aneurysm sac. The implied converse

assumption is that recurrent hemorrhage is only important (if ever) in aneurysms with residual filling.

Unfortunately, other than the Cerebral Aneurysm Rerupture After Treatment (CARAT) Trial,⁸ precious few data exist to support the correlation between completeness of endovascular coiling and the risk of clinical recurrence. As CARAT investigators, we are very much aware that CARAT had major limitations. For example, aneurysm occlusion rates in CARAT were derived retrospectively from angiographic reports dictated by physicians who were self-reporting their treatment results during a period that predated uniform reporting standards such as the Raymond scale. It should be abundantly clear that these results would not be expected to correlate reliably with independent core laboratory readings, and it is unfortunate that, years later, we still lack prospective evidence reliably correlating angiographic end points with clinical outcomes. While the findings of CARAT have been widely referenced, CARAT constitutes level B evidence at best.

In the meantime, this rational-but-unproven assumption of “adequate occlusion” has been coupled with the belief that we cannot measure the clinical events that actually matter. Regardless of how intuitively attractive the angiogram is as an end point, until the evidentiary vacuum is addressed, the assumption that angiographic results correlate with patient outcomes is only a circular argument: “We believe that it matters so we measure it/We measure it so we believe that it matters.” Once this potentially fatal error is accepted, the circular logic seems inescapable. Indeed, the suggestion of Pierot et al⁹ that more accurate volumetric analysis of residual aneurysm filling would be an improvement perpetuates the circular argument. Only through research that shows more precisely how angiographic remnants link to the clinical events that we care about can we resolve this dilemma.

The question is further begged—what do we tell our patients who have Raymond 3 remnants? That their aneurysm occlusion is inadequate? Raymond 3 residual is very common, occurring in roughly 20%–35% of patients in multiple randomized trials.^{1,4,7} Similarly, deterioration in angiographic occlusion between treatment and early angiographic follow-up is in the range of 35%–50%.^{5,10} Are these patients shouldering the bulk of rehemorrhages while we reassure them by quoting low rehemorrhage rates that use the entire population (“adequate” and “inadequately occluded”) as the denominator? We do not and cannot know until we track, measure, and correlate TAR with angiographic end points.

TAR: Imperfect but Fundamental

A fair criticism of TAR is that were TAR to be widely adopted, most TAR events would likely be the result of retreatment—that is, TAR essentially equals retreatment. It is likely that, as with angiographic occlusion scales, retreatment as an end point is more likely to be internally consistent between treatment arms within a trial but less reliable when used to compare one trial with another. Because the indications for retreatment are currently unclear, practice patterns can vary widely, making comparisons between trials problematic if the principal measure is essentially the retreatment rate. Indeed, the MAPS investigators found that in North America, if the treating physician reported residual aneurysm filling (Raymond 3), retreatment was performed within the

first year in 49.2% of patients. For centers outside North America, the comparable retreatment rate was only 19.2%; but with longer follow-up, the retreatment rate for patients with Raymond 3 residual rose to 47.6%, a rate not statistically different from the North American rate (A.S. Turk, DO, unpublished data, 2014). Given that physicians in both locations behaved similarly in re-treating patients with Raymond 3 residual aneurysm filling, it is not clear why retreatment was delayed at centers outside North America, but the need for longer follow-up is clear.

The most recent data from the International Subarachnoid Aneurysm Trial (ISAT), reporting follow-up extending beyond 10 years, suggest that despite older technology with questionable rates of angiographic occlusion, rehemorrhage rates are low but still roughly triple the rate seen after surgical clipping.¹¹ We do not know whether the recurrent hemorrhages happened only in patients with residual aneurysm filling or to what extent hemorrhages occurred in patients with “adequate occlusion.” Moreover, we do not know what role retreatment—or lack of retreatment—played in preventing or permitting recurrent hemorrhage. As reassuring as it is that ISAT rehemorrhage rates are low, we must not accept the belief that rates are low enough. Truly understanding who needs to be retreated is key to driving down the rate of delayed rehemorrhage. For now, we remain in the dark regarding how to manage roughly one-third of our patients—those whom we all seem to believe have “inadequate occlusion.”

It is our belief that the balance between retreatment and rehemorrhage can offset the criticism that TAR equals retreatment and that retreatment is arbitrary. Completely occluded aneurysms and tiny neck remnants are rarely retreated, so it is primarily aneurysms with residual filling (Raymond 3) that are retreated. If residual aneurysm filling is the strongest predictor of rehemorrhage, it is reasonable to expect that for a given rate of residual angiographic filling, lower rates of retreatment will ultimately lead to higher rates of rehemorrhage and vice versa.

For example, if one were to compare the MAPS with the HydroCoil Endovascular Aneurysm Occlusion and Packing Study (HELPS) Trial, one would observe that both trials have similar rates of residual aneurysm filling—approximately one-third of patients—but dramatically different rates of retreatment (roughly 9% for unruptured aneurysms and 14% for ruptured aneurysms in MAPS versus 3% overall in HELPS).^{1,12} If the presumed inverse relationship between retreatment and rehemorrhage holds, then with time, rehemorrhages will eventually comprise a much higher proportion of TAR in centers where few retreatments are done, while centers aggressively retreating residual aneurysm filling may find that their TAR rates are almost entirely driven by retreatments. With a retreatment rate of only 3% as in HELPS, even a few rehemorrhages would result in rehemorrhage becoming a meaningful proportion of the overall TAR rate. Unfortunately, in HELPS as in many other otherwise excellent prospective trials, no attempt was made to capture re-

hemorrhage rates beyond the relatively short-term angiographic end points, in effect burying the impact of delayed hemorrhage.

Conclusions

Studying the balance between retreatment and rehemorrhage, specifically correlating TAR with the angiographic results, is the only viable way to address the issue of retreatment. The question is not TAR versus the angiographic results, it is how the angiographic results predict what we care about—target aneurysm recurrence.

Disclosures: C.G. McDougall—*RELATED: Consultancy*: I am on the Scientific Advisory Board for Covidien and a consultant for MicroVention.

REFERENCES

1. McDougall CG, Johnston SC, Gholkar A, et al. **Bioactive versus bare platinum coils in the treatment of intracranial aneurysms: the MAPS (Matrix and Platinum Science) trial.** *AJNR Am J Neuroradiol* 2014;35:935–42
2. Bendszus M, Hagel C, Maurer M, et al. **Fatal recurrent subarachnoid hemorrhage after complete endovascular aneurysm occlusion.** *AJNR Am J Neuroradiol* 2006;27:2058–60
3. Raymond J, Guilbert F, Weill A, et al. **Long-term angiographic recurrences after selective endovascular treatment of aneurysms with detachable coils.** *Stroke* 2003;34:1398–403
4. Molyneux AJ, Clarke A, Sneade M, et al. **Cerecyte coil trial: angiographic outcomes of a prospective randomized trial comparing endovascular coiling of cerebral aneurysms with either Cerecyte or bare platinum coils.** *Stroke* 2012;43:2544–50
5. Nishido H, Piotin M, Bartolini B, et al. **Analysis of complications and recurrences of aneurysm coiling with special emphasis on the stent-assisted technique.** *AJNR Am J Neuroradiol* 2014;35:339–44
6. Pierot L, Cognard C, Ricolfi F, et al. **Immediate anatomic results after the endovascular treatment of ruptured intracranial aneurysms: analysis in the CLARITY series.** *AJNR Am J Neuroradiol* 2010;31:907–11
7. White PM, Lewis SC, Nahser H, et al. **HydroCoil Endovascular Aneurysm Occlusion and Packing Study (HELPS trial): procedural safety and operator-assessed efficacy results.** *AJNR Am J Neuroradiol* 2008;29:217–23
8. CARAT Investigators. **Rates of delayed rebleeding from intracranial aneurysms are low after surgical and endovascular treatment.** *Stroke* 2006;37:1437–42
9. Pierot L, Fiehler J, White P. **Point—TAR: a useful index to follow-up coiled intracranial aneurysms?** *AJNR Am J Neuroradiol* 2015;36:2–4
10. Pierot L, Cognard C, Ricolfi F, et al. **Mid-term anatomic results after endovascular treatment of ruptured intracranial aneurysms with Guglielmi detachable coils and Matrix coils: analysis of the CLARITY series.** *AJNR Am J Neuroradiol* 2012;33:469–73
11. Molyneux AJ, Birks J, Clarke A, et al. **The durability of endovascular coiling versus neurosurgical clipping of ruptured cerebral aneurysms: 18 year follow-up of the UK cohort of the International Subarachnoid Aneurysm Trial (ISAT).** *Lancet* 2014 Oct 28. [Epub ahead of print]
12. White PM, Lewis SC, Gholkar A, et al. **Hydrogel-coated coils versus bare platinum coils for the endovascular treatment of intracranial aneurysms (HELPS): a randomised controlled trial.** *Lancet* 2011; 377:1655–62

Cerebrovascular Reactivity Mapping: An Evolving Standard for Clinical Functional Imaging

J.J. Pillai and D.J. Mikulis



ABSTRACT

SUMMARY: This review article explains the methodology of breath-hold cerebrovascular reactivity mapping, both in terms of acquisition and analysis, and reviews applications of this method to presurgical mapping, particularly with respect to blood oxygen level–dependent fMRI. Its main application in clinical fMRI is for the assessment of neurovascular uncoupling potential. Neurovascular uncoupling is potentially a major limitation of clinical fMRI, particularly in the setting of mass lesions in the brain such as brain tumors and intracranial vascular malformations that are associated with alterations in regional hemodynamics on either an acquired or congenital basis. As such, breath-hold cerebrovascular reactivity mapping constitutes an essential component of quality control analysis in clinical fMRI, particularly when performed for presurgical mapping of eloquent cortex. Exogenous carbon dioxide challenges used for cerebrovascular reactivity mapping will also be discussed, and their applications to the evaluation of cerebrovascular reserve and cerebrovascular disease will be described.

ABBREVIATIONS: BH = breath-hold; BOLD = blood oxygen level–dependent; CO₂ = carbon dioxide; CVR = cerebrovascular reactivity; NVU = neurovascular uncoupling

Neurovascular coupling is the basis for the blood oxygen level–dependent (BOLD) effect, which refers to the microvascular response to neural activation and the consequent regional decrease in deoxyhemoglobin concentration resulting from greater oxygen delivery to the microvasculature than oxygen consumption by the stimulated adjacent neurons.^{1–3} In reality, the BOLD signal is determined by a complex interaction of changes in CBV, CBF, and the cerebral metabolic rate of oxygen consumption and other factors such as capillary attenuation and diameter and hematocrit.⁴ This neurovascular coupling involves a complex cascade of events at the microstructural, biochemical, and electrophysiologic levels, which includes many components such as astrocytes, neurotransmitters, and chemical mediators in addition to neurons proximally and vascular smooth muscle distally.⁵ Excellent reviews of this topic have been provided by

Koehler et al, 2009,⁵ and Attwell et al, 2010.⁶ In general, it is thought that neurotransmitters such as glutamate that are released at synapses bind to separate receptors on astrocytes and neurons and result in release of various chemical mediators from each that then directly affect arteriolar smooth-muscle tone. For example, nitric oxide released from neurons and prostaglandins released from astrocytes can result in vasodilation.⁶ However, neurovascular coupling is a complex and incompletely understood process that involves multiple signaling pathways, including astrocytic signaling mechanisms involving increases in astrocytic calcium levels.⁵

While in healthy volunteer BOLD fMRI studies and fMRI studies involving patients without regional hemodynamic alterations or abnormalities of arterial or venous vasculature, the neurovascular coupling cascade can be assumed to be intact, the same is not necessarily true for patients with intracranial mass lesions, brain AVMs, cerebral infarctions, or cerebrovascular disease. In these latter cases, the neurovascular coupling cascade may break down at any level from the proximal neuronal end (in the case of nonviable or impaired cortex) to the distal microvascular response. This phenomenon is referred to as neurovascular decoupling or neurovascular uncoupling (NVU). In most cases in which electrical activity is present in viable but nevertheless diseased cortex, the breakdown may occur at the astrocytic, neurotransmitter, or, most often, the vascular “end organ” level. In these cases, evaluation of cerebrovascular reactivity (CVR) can be a use-

From the Division of Neuroradiology (J.J.P.), Russell H. Morgan Department of Radiology and Radiological Science, Johns Hopkins University School of Medicine, Baltimore, Maryland; and Department of Medical Imaging (D.J.M.), The University of Toronto, The University Health Network, The Toronto Western Hospital, Toronto, Ontario, Canada.

This work was supported, in part, by grants from the Canadian Institutes of Health and the Johns Hopkins Brain Science Institute.

Please address correspondence to Jay J. Pillai, MD, Division of Neuroradiology, Russell H. Morgan Department of Radiology and Radiological Science, The Johns Hopkins Hospital, Phipps B-100, 1800 Orleans St, Baltimore, MD 21287; e-mail: jpillai@jhmi.edu

Indicates open access to non-subscribers at www.ajnr.org

<http://dx.doi.org/10.3174/ajnr.A3941>

ful method for detection of NVU potential. NVU is a critical problem in presurgical fMRI because it can manifest as false-negative activation on BOLD fMRI tasks. Unlike in the research setting, where the emphasis typically is on reduction of false-positives (type I statistical errors) by use of stringent statistical thresholds or use of corrections for multiple comparisons, in clinical presurgical fMRI, the emphasis is on the avoidance of false-negatives (type II errors). False-negative activation on clinical fMRI can lead to serious consequences because it may result in inadvertent resection of eloquent cortex that appears BOLD-“silent” or -“invisible” on BOLD activation maps because it may be incapable of displaying a robust or even minimal BOLD response to an appropriate neural stimulus. Similarly, NVU may result, in some cases, in false-positive activation that could result in insufficient resection of a lesion such as a tumor, and this may adversely affect the patient’s overall prognosis. In such a setting, the ability to detect NVU may be critical for patient care because it may necessitate the use of complementary electrophysiologic evaluation (ie, intraoperative cortical stimulation mapping) for the reliable mapping of such eloquent cortex.

It is well-known that in cases of high-grade glioma, tumor angiogenesis is associated with abnormal vasoactivity and permeability of the neovasculature; thus, NVU is a recognized phenomenon in this subset of patients with brain tumor.⁷ However, it has recently been demonstrated that similar NVU can occur with lower grade tumors as well.⁸⁻¹⁰ In the case of low-grade gliomas, the exact mechanism responsible for the NVU is not clear but may be associated with astrocytic dysfunction related to the infiltrative tumors. The prevalence of NVU in brain tumors is quite high according to recent series,⁸⁻¹⁰ though the examples in these series suggest that NVU may not necessarily be an all-or-none (ie, binary) phenomenon, but rather may be present to variable degrees, resulting in variable degrees of reduction of expected ipsilesional BOLD activation in eloquent cortical regions and complete absence of detectable activation only in some cases.¹⁰ Detection of such NVU potential is critical for adequate interpretation of clinical BOLD fMRI activation maps because false-negative activation may be present, depending on the statistical thresholding used. Similar NVU can be seen in AVMs due to regional hemodynamic abnormalities related to the exhaustion of vascular reserve secondary to arteriovenous shunting and loss of perfusion pressure or venous congestion with high outflow resistance.

The Breath-Hold Cerebrovascular Reactivity Mapping Technique

Although hypercapnia challenges have been used in conjunction with BOLD imaging to very effectively evaluate brain CVR, the criterion standard technique for such CVR mapping has been exogenous carbon dioxide (CO₂) gas administration during MR imaging.¹¹⁻¹³ The breath-hold (BH) technique offers a simpler alternative that is easier to implement in the clinical setting and yet can produce similar increases in arterial CO₂ levels and resultant similarly useful BOLD CVR maps as those achieved by using gas-inhalation techniques.¹⁴ This technique involves short-duration BHs, typically in the range of 10–30 seconds, which alternate with periods of normal breathing. Even BHs that are much shorter (eg, as short as 3 seconds) may produce brief states of

hypercapnia that result in measurable BOLD signal changes, but the robustness of the BOLD response and the number of voxels in the brain cortex displaying BOLD signal changes increase with the increasing duration of the BH.^{13,15} In addition, the reproducibility of such BOLD responses is greater and interscan variability is minimized with longer BH periods.^{13,16} While BHs in the range of 20–30 seconds may be feasible for healthy volunteers, in some patients, such as those with brain tumors, a compromise may be necessary between ideal BH duration and patient comfort/tolerance limits. Furthermore, healthy volunteer studies have shown that the use of blocks of paced breathing between successive BH blocks provides a more consistent BOLD baseline from which the breath-hold BOLD signal response can be extracted, resulting in more accurate assessment and reduced interscan variability.^{13,17}

Other studies have suggested that use of end-expiration BHs results in greater reproducibility than end-inspiration BH techniques because end-expiration offers a more natural resting equilibrium state involving the diaphragm, lungs, and chest wall before initiation of a BH challenge.^{13,17} Thomason and Glover¹⁸ have even suggested that the BOLD response resulting from end-expiration BHs is slightly different from that of end-inspiration BHs in that the latter involves more of a biphasic BOLD response, which is less desirable.¹³ One major perceived limitation of BH techniques for CVR mapping is the problem of compliance-related poor repeatability in the setting of neurologically impaired patients. Unlike with exogenous CO₂ administration, where precise quantitative assessment of partial pressure of carbon dioxide and partial pressure of oxygen levels and controlled administration of inhaled CO₂ can be assured, with BH techniques, patient performance can substantially affect these parameters. To allay these concerns, Bright and Murphy¹³ studied 12 healthy volunteers who performed a BH task simulating differing degrees of task compliance with recording of their expired (end-tidal) gas O₂ and CO₂ levels. They noted that while all BH challenges are associated with a mild hypoxia effect in addition to the intended hypercapnia, the effect of the hypoxia is minimal, and by using end-tidal CO₂ as a regressor in their general linear model analysis, repeatable measurements of BOLD signal change as a measure of CVR were possible.¹³ Furthermore, their results are consistent with those of Tancredi and Hoge,¹⁹ who used a similar BH paradigm and reported that the mild hypoxia induced by the BH task did not significantly affect their CVR results.

At Johns Hopkins, we have developed a BH CVR protocol that has been successfully implemented in approximately 95% of patients who have undergone routine clinical BOLD fMRI presurgical mapping examinations during the past 4 years. The technique uses 16-second BH blocks that produce consistently robust BOLD signal changes with minimal patient discomfort. The much longer regular breathing (control) blocks allow equilibration of the BOLD signal following each BH hypercapnia challenge. Unlike the protocol used by Bright and Murphy,¹³ which used end-expiration BHs, at our institution we have adopted end-inspiration BHs because in our experience, it has been easier for neurologically impaired patients to perform end-inspiration BHs. We use a slow, controlled 4-second inspiration before a 16-second BH period, which is then followed by a 40-second block of self-paced normal breathing; this cycle is repeated 4 times, and at the

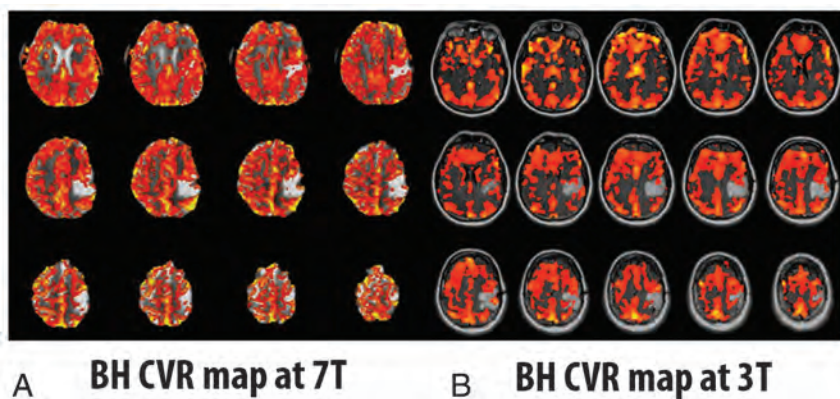


FIG 1. A patient with a left perirolandic low-grade glioma who performed the identical breath-hold protocol at both 7T and 3T. Notice the higher resolution of the 7T imaging due to inherently higher signal-to-noise ratio; the BH CVR map at 7T (A) was thresholded to 0.5% positive BOLD signal change during hypercapnia relative to baseline, whereas the BH CVR map at 3T (B) was thresholded at 0.175% positive BOLD signal change. Comparable results are noted at both field strengths in terms of NVU detection potential.

end of the last BH period, an additional 20-second period of normal breathing is incorporated for a total task duration of 4 minutes 20 seconds.

Analysis of BH BOLD data is easily accomplished by using a general linear model approach; however, the modeling of the hemodynamic response function is based on the hemodynamic response function proposed by Birn et al²⁰ to specifically model the hemodynamic response to a BH task. This modeling takes into account the relatively longer normal breathing blocks that are required for equilibration of BOLD signal following each hypercapnia challenge. At our institution, a standard 2D single-shot gradient-echo EPI T2*-weighted BOLD sequence is used for the BH task on a 3T MR imaging system with the following parameters: TR = 2000 ms, TE = 30 ms, flip angle = 90°, 24-cm FOV, 64 × 64 × 33 acquisition matrix, 4-mm section thickness with 1-mm intersection gap.¹⁰

The advantages of the BH technique in patients with neurologic impairment, compared with exogenous CO₂ administration methods, are that no equipment setup time is needed either outside or within the MR imaging scanner and there is no need for the use of a nasal cannula or facemask. Use of facemasks as part of breathing circuits or gas delivery systems may be uncomfortable for neurologically impaired patients who may be undergoing multiple challenging BOLD functional activation paradigms in the same lengthy MR imaging session, especially with additional physical constraints imposed by the use of a head coil, head padding, headphones and video goggles, or other fMRI stimulus-presentation hardware (eg, screens/mirrors mounted on a head coil when projector systems are used).

Monitoring of patient task performance can be achieved via the use of a standard respiratory belt (provided by most major MR imaging scanner vendors), which is applied by the MR imaging technologist before the start of the scan session. Real-time monitoring of patient task performance can be accomplished via evaluation of the respiratory waveform/bellows; if regular frequency of respirations and consistency of chest wall excursion amplitude are not observed during the initial run, then the task will be repeated, typically with observed improvement in the degree of

task compliance and resultant reduction of physiologic noise on the brain BOLD CVR maps.

Despite concerns in research studies regarding the lack of absolute quantification of CVR by using BH CVR mapping, variable repeatability/reproducibility, and variable patient compliance, as discussed above in detail, we have found such a technique to be perfectly adequate for regional relative CVR assessment in the setting of structural brain lesions such as brain tumors. In such cases, for the detection of NVU potential, we only need to assess relative CVR (ie, ipsilesional regional CVR relative to normal contralateral hemispheric cortical CVR). Furthermore, we stress the need for patient practice in a prescan training session for

the following reasons: 1) Assessment of adequate patient task performance can be made, 2) patient familiarity with the task instructions can ensure excellent task compliance, and 3) patient anxiety can be minimized before scanner bore entry. The MR imaging technologist then repeats the instructions for further reinforcement immediately before actual patient performance of the BH paradigm in the scanner. Such prescan training can be accomplished in approximately 5 minutes for most patients and can be incorporated into a longer prescan training session for clinical fMRI presurgical mapping examinations. We have reported, in several articles, the feasibility of the use of our protocol in patients with brain tumor at 3T.^{8,9,10,21} We have observed similar success at higher field strengths. Figure 1 shows an example of a patient with a left perirolandic low-grade glioma who performed the identical BH protocol at both 7T and 3T.

There are some contraindications, however, to the performance of the BH task. These include patients with dementia or profound language-comprehension difficulties and patients with severe visual impairment who cannot read the visual textual cues that are used as instructions for the task inside the scanner. Furthermore, patients with a large body habitus who are literally too large to fit inside the bore of the MR imaging scanner or who are too large to allow sufficient chest wall excursion within the scanner bore generally cannot perform the BH task. In addition, patients with severe respiratory disorders such as emphysema or chronic bronchitis who may have elevated baseline partial pressure of carbon dioxide levels may not experience the same degree of hypercapnia during performance of a BH task as a person with normal respiratory status; thus, BOLD CVR mapping using a BH task may not be successful in these individuals.

Applications of BH CVR Mapping to Presurgical Mapping

The following clinical case exemplifies the value of BH CVR mapping in clinical presurgical mapping BOLD fMRI examinations.

Figure 2 demonstrates a 41-year-old ambidextrous (but primarily right-handed) male patient with a large infiltrative nonenhancing T2/FLAIR hyperintense left temporal lobe low-grade oligoastrocytoma (World Health Organization grade II) who had

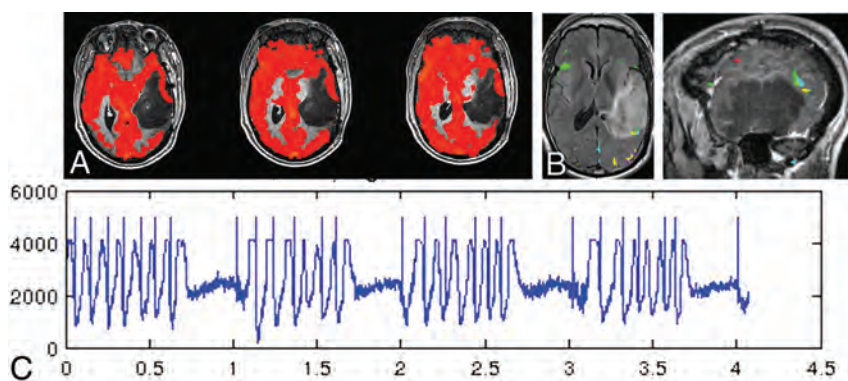


FIG 2. A large left temporal lobe recurrent nonenhancing low-grade oligoastrocytoma in a 41-year-old ambidextrous (but primarily right-handed) male patient. *A*, The prominent regional decrease in CVR on the BH CVR maps (thresholded at a positive 0.35% BOLD signal change during hypercapnia relative to baseline) along the lateral tumor margin as manifested by discontinuity of the cortical “ribbon” of red CVR signal change. Although a mild degree of functional Wernicke area activation is seen along the posterosuperior margin of the mass (*B*), the full extent of Wernicke area activation and inferior parietal lobule activation could not be reliably determined in light of the NVU potential suggested by the abnormally decreased regional CVR. *B*, Activation from 5 different language tasks (silent word generation in red, sentence completion in yellow, rhyming in light blue, sentence reading comprehension in green, and passive story listening in purple), overlaid on both sagittal and axial postcontrast T1-weighted 3D MPRAGE images. Note the relative paucity of activation overall in the left temporal lobe. The respiratory bellows are displayed in the bottom half of the figure (*C*), in which the y-axis represents the amplitude of the respiratory waveform in arbitrary units, while the x-axis represents the timing of the respiratory chest wall movements in minutes. Note the periodic chest wall movements during the breathing blocks of the paradigm and the relatively flat baseline during the breath-hold blocks. Excellent task performance is noted.

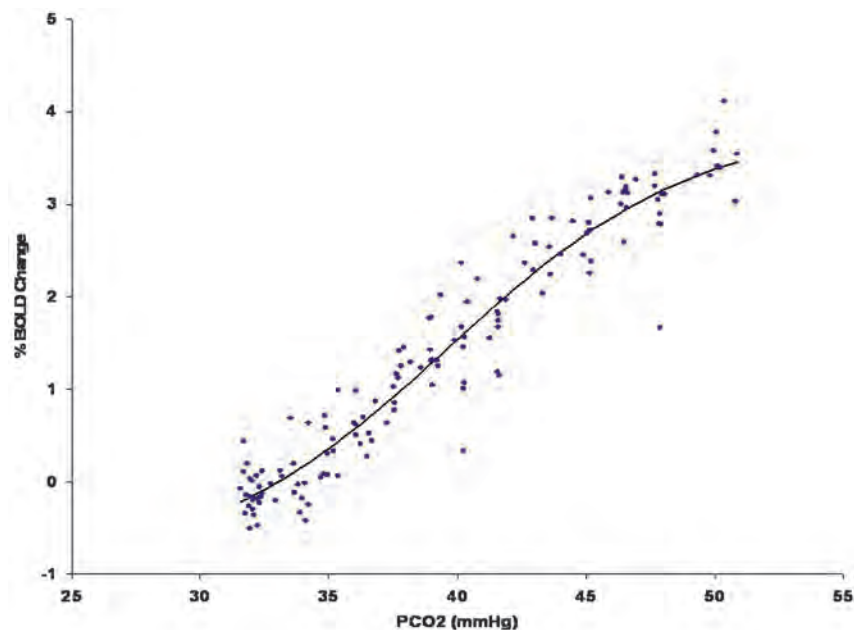


FIG 3. Data from healthy controls showing the relationship between the percentage change in the BOLD signal as a function of increasing arterial partial pressure of carbon dioxide. Note the sigmoidal shape of the curve with maximum slope at approximately 40 mm Hg, which is the typical value of resting arterial CO_2 . This is the point of maximum reactivity and maximum vascular reserve.

undergone previous subtotal resection approximately 2 years before presentation and now presented with prominent tumor progression. Although a mild degree of functional Wernicke area convergent activation was seen along the posterosuperior margin of the mass, the full extent of Wernicke area activation and inferior parietal lobule (receptive language) activation could not be

reliably determined. Prominent regional decrease in CVR on the BH CVR maps in the lateral left temporal lobe cortex in the areas of tumoral infiltration strongly suggested NVU in this clinically asymptomatic patient. Activation from 5 different language tasks (silent word generation, sentence completion, rhyming, reading comprehension, and passive story listening) was displayed in both sagittal and axial anatomic overlays on postcontrast T1-weighted anatomic images. Note the relative paucity of language activation in the left temporal lobe, which is likely to be due to NVU. The respiratory signal/bellows tracing demonstrates excellent task performance. In light of these limitations of fMRI localization, the patient underwent awake craniotomy with intraoperative cortical-stimulation mapping.

CVR Physiology and Cerebrovascular Reserve

As flow resistance increases due to either inflow or outflow obstruction, a vasodilatory response will develop in normal segments of the vasculature to maintain blood flow. Exhaustion of vascular reserve occurs when this compensatory mechanism reaches a maximum. Under these conditions, it is thought that no further vasodilation is possible even to other vasodilatory stimuli, including those of neuronal origin. If neurovascular coupling is exhausted, then blood flow augmentation in response to neural activation will not occur and BOLD signals will not show the expected increase, resulting in type II errors during fMRI experiments. When testing CVR by using a CO_2 stimulus in patients with any of the disease conditions that alter vascular resistance, the manner in which CO_2 is applied is the least critical element in assessing the effect of the disease on tissue reactivity. More critical are the methods used to analyze the relationship between CO_2 changes and blood flow. If the need for reproducibility is important, then knowledge of arterial CO_2 levels is critical. The relationship between CO_2 and blood flow follows a sigmoidal curve (Fig 3). Because

vascular reserve is consumed through compensatory vasodilation in response to increasing vascular stenosis (resistance), no change in reactivity will be observed because the sigmoidal curve is relatively linear over a wide range. However, with additional increases in vascular stenosis, the slope of the curve decreases, indicating a leveling off of reactivity to the same incremental change in CO_2 .

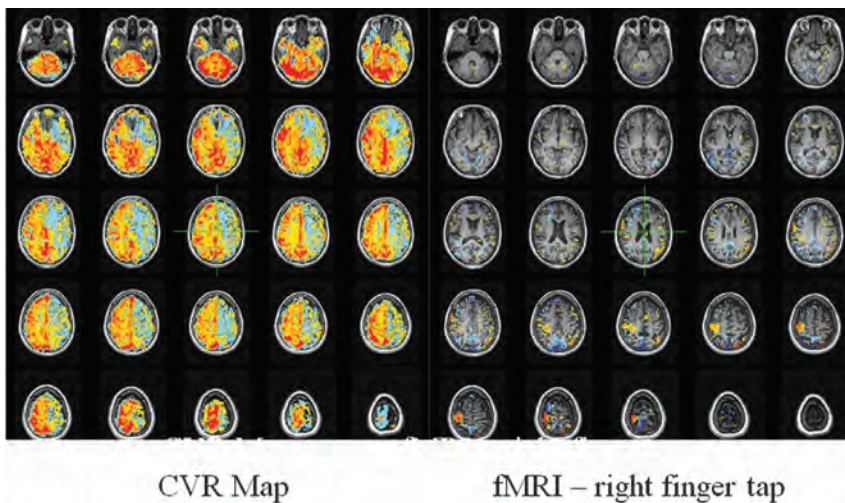


FIG 4. CVR map on the right obtained in a patient with high-grade stenosis of the left internal carotid artery. Red, yellow, and orange indicate degrees of positive BOLD signal during a CO₂ stimulus of 10 mm Hg above resting levels. Blue indicates a decrease in BOLD signal representing steal physiology in the left anterior cerebral artery and MCA territory. This territory would not be expected to show any response to an fMRI experiment that would activate tissue in the regions. A standard right-sided finger-tap motor paradigm shows only right-hemispheric activation. This should not be interpreted to mean that the right hemisphere is controlling right hand movement. It is a type II error caused by neurovascular uncoupling.

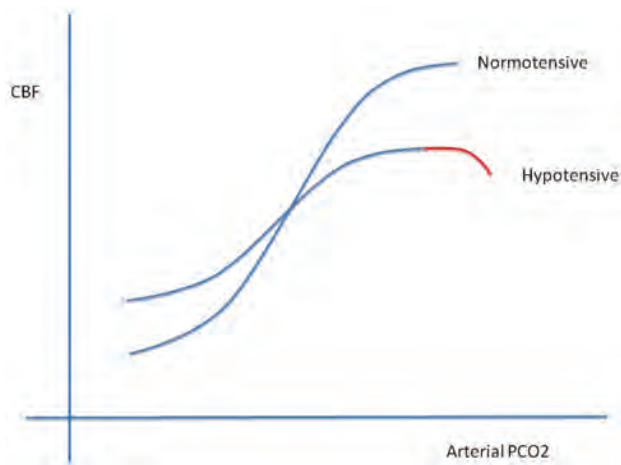


FIG 5. The slope of the sigmoidal curve decreases secondary to hypotension. The vasodilatory response to CO₂ is reduced because some vascular reserve is expended to maintain blood flow at normal levels. Note the red portion of the curve that indicates a drop in flow with high CO₂ stimuli. Although not discussed in the article, we believe that this is a reflection of data points representing steal phenomena. This drop would be expected earlier (smaller elevations in CO₂) in vascular beds exposed to higher proximal resistances as in carotid stenosis. Adapted with permission from BMJ Publishing Group Limited. Harper AM, Glass HI. Effect of alterations in the arterial carbon dioxide tension on the blood flow through the cerebral cortex at normal and low arterial blood pressures. *J Neurol Neurosurg Psychiatry* 1965;28:449–52.

Further increases in stenosis will lead to maximal vasodilation. The vascular bed cannot respond to further elevations in CO₂. At this point, flow resistance has reached an absolute minimum. When this condition is observed clinically, blood flow in the affected vascular territory becomes blood pressure–dependent and hemodynamic transient ischemic attacks or even stroke can occur. If a global vasodilatory stimulus occurs such as hypotension

or hypercapnia, then steal phenomena can develop, in which blood flow is directed away from the territory that is maximally vasodilated. Mapping those areas in the brain that have this physiology is useful for stratifying the risk of ischemic injury (2–5 times higher if steal is present^{22–25}) and for validating the ability of the tissue to respond to an fMRI stimulus (Fig 4).

The issue becomes more complex, however, when reserve in the impaired tissue is not fully exhausted. If the tissue retains some vasodilatory capacity, then a small CO₂ stimulus should elicit a positive BOLD response. A slightly higher CO₂ stimulus, however, may exhaust the tissue's reserve; with normal tissue lowering flow resistance to a greater degree, flow will be directed away from the tissue with lower initial reserve. The presence or absence of steal physiology therefore becomes dependent on the magnitude of the applied CO₂ stimulus and the difference

in vascular reserve between tissue perfusion beds. The importance of this observation is that a perfusion bed with positive reactivity at low CO₂ stimuli may become exhausted and develop negative reactivity (ie, decreased blood flow in response to higher CO₂ levels, ie, steal physiology) (Fig 5).

If a supramaximal stimulus is applied (acetazolamide), then that vascular territory in the brain with the lowest vascular reserve may show steal physiology even if there is only marginal stenocclusive disease affecting this tissue. Even the normally perfused brain would be expected to show this effect under a maximal stimulus because flow resistance (impedance) in gray matter and white matter perfusion beds differs considerably. White matter–penetrating arteries have resistances typically >3–4 times higher than those of penetrating arteries in the cortex.^{26–28} In view of the added complexity rendered by the total of these issues, accurate assessment of the state of CVR deficits requires measurement of the entire vasodilatory portion of the sigmoidal curve (resting partial pressure of carbon dioxide level to 15–20 mm Hg above the resting level). This would require precision control of CO₂, preferably holding arterial O₂ constant while mapping CVR for all increments of CO₂ from resting values to marked hypercapnia. In general, this is impractical without application of CO₂ protocols that incorporate this entire range of stimuli. Reasonable estimates of reactivity can be obtained by using known step changes in CO₂ stimuli, such as resting CO₂ compared with resting CO₂ + 10 mm Hg or even with BH techniques. BH techniques, however, pose unique challenges to CVR analysis to be discussed next.

If follow-up CVR mapping is needed after treatment interventions, then a highly reproducible vasodilatory stimulus is preferred. If the primary clinical goal is to apply fMRI tools for pre-surgical localization of eloquent cortex in relation to brain neoplasms, then reproducibility is not as much of a concern in this single-use setting. The primary concern under these condi-

tions is to adequately interrogate the tissue for evidence of exhausted reserve. If one assumes “ideal” conditions by using “noise-free” BOLD acquisitions, vascular beds that are maximally vasodilated will show blood flow reductions to tiny elevations in CO₂. Therefore, BH techniques that produce small-but-gradual increases in CO₂ would easily detect areas with exhausted reserve. Furthermore, quantitation of BOLD signal change is not necessary because only the presence of BOLD signal decrease, not the magnitude of the decrease, is needed to generate maps of exhausted reserve. The elegance of this construct lies in its independence from any form of thresholding for distinguishing normal-from-abnormal perfusion beds. Simply observing the direction of the change in the BOLD signal in response to the stimulus is all that is required. CVR maps can then be simplified showing areas of positive and negative change. The magnitude of change is not needed.

In real life, the BOLD signal is not perfect and control of CO₂ is not perfect. There is considerable noise in BOLD images requiring repeated application of stimuli during image acquisition to extract signal in a statistically meaningful fashion from the noise. The well-known low-frequency baseline drift of BOLD signals must also be accounted for. The CO₂ stimulus, therefore, must be large enough to lower the BOLD signal sufficiently to survive the statistical requirements for significance. Increasing the duration of image acquisition can also help to improve signal, but there are practical limits in doing so. Most interesting, absolute adherence to BOLD signal decreases in response to vasodilatory stimuli may be too extreme. Small BOLD increases, for example on the order of a 10% threshold or less, may be acceptable for predicting clinically relevant type II fMRI errors. The real threshold for this is not currently known. However, if small positive BOLD responses are considered acceptable, then a greater degree of complexity is introduced into the analysis. If the CO₂ stimulus is small, it may become very difficult to distinguish tissue with vascular impairment from normal tissue because both may show positive responses. If a slightly larger CO₂ stimulus is then provided, previously positive-reacting tissue may then show a negative response when the limit of vasodilation is reached. Because the levels of CO₂ achieved with BH CVR are unknown and because the presence of BOLD signal change in impaired tissue is dependent on CO₂ elevations achieved, the final CVR maps would be expected to have lower prediction accuracy for type II fMRI errors than those in which tight control of CO₂ is applied. Nevertheless, it is foreseeable that population-based BH CVR standardization, including duration of BH, number of repeats, minimum BOLD SNR requirements, and methods of data analysis, should help to alleviate this issue.

The methods used to analyze breath-hold CVR data deserve comment. Compared with controlled CO₂ data in which the stimulus is precisely known, breath-hold CO₂ levels are unknown and there is no reference CO₂ waveform for regression against the BOLD signal. The relationship between the time the individual begins breath-holding and the subsequent rise in brain blood CO₂ is unknown. Clearly some delay needs to be applied to generate the highest correlation between CO₂ and the BOLD signal. We have empirically found this to be approximately 11 seconds (unpublished data). Another method for assessing this correlation is

to use the BOLD signal measured from a large purely venous structure such as the superior sagittal sinus. The temporal pattern of the signal change can then be used as the regressor for the correlation analysis. There is, therefore, no need to use a time delay for compensation because the signal in the brain and the sagittal sinus is virtually identical in time. However, we have observed differences between CVR maps generated by using the 2 analysis methods. More work in this area is clearly needed to establish preferred analytic approaches.

Application of Vasodilatory CO₂ Stimuli

BH results in a gradual increase in arterial CO₂ concentrations, but there is considerable uncertainty about the levels of CO₂ achieved in the blood. Exogenous administration of CO₂ is an attractive alternative because measurement of end-tidal CO₂ levels is enabled (as opposed to BH). This feature should theoretically permit accurate quantitation of CVR. In fact, elevation of arterial CO₂ concentrations by using exogenous administration of CO₂ has been in common use for many years. It is based on the assumption that sampling end-tidal CO₂ under these circumstances is a reasonable approximation of the actual partial pressure of CO₂ in the blood. The problem with this assumption is that end-tidal CO₂ and partial pressure of CO₂ are not equivalent because the method without re-breathing cannot account for the physiologic gradient between end-tidal CO₂ and partial pressure of CO₂. In young healthy individuals, the gradient is generally small but still unknown; therefore, quantitative errors in CVR will be present. The error will increase as a function of age, body position, exercise, and the presence of existing pulmonary disease.²⁹ Furthermore, administration of exogenous CO₂ can stimulate ventilation depending on the CO₂ chemoreflex sensitivity of the individual so that partial pressure of CO₂ may not change at all or may even decrease.²⁸ Therefore, if quantitative CVR is required, simple mask application of CO₂ stimuli is unsuitable. The ability to precisely control arterial blood gasses including CO₂ and O₂ independent of the respiratory rate and tidal volume is desirable for several reasons. Knowledge of arterial CO₂ levels with high temporal resolution enables the application of the CO₂ waveform as the preferred regressor against the BOLD data, yielding more accurate CVR values. Fluctuations in arterial O₂ will also affect the BOLD signal independent of flow-related changes caused by CO₂. Elimination of this confound is also desirable.

Reproducibility is important in assessing disease progression/regression and for determining response to revascularization. These goals can only be achieved with accurate reproducible stimuli. Finally, the ability to precisely control blood gasses opens considerable opportunities for research in brain blood flow and brain blood flow control. For example, generating maps of mean CVR values for a population of controls for each age of life could be used to detect the effects of disease on the brain vasculature in a variety of disorders affecting the central nervous system such as vascular and Alzheimer dementia. There are currently 2 methods available that enable precise control of arterial blood gasses: the dynamic end-tidal forcing method³⁰ and the prospective end-tidal targeting method.³¹

CONCLUSIONS

BH CVR is simple, inexpensive, and easy to implement clinically because all that is necessary from the data-collection standpoint is to confirm that the subject can perform the maneuver as intended before scanning. The information gained can be extremely useful in validating the ability of a perfusion bed to respond to a vasodilatory stimulus, an essential requirement for applying reliable fMRI mapping. Limitations do exist, however, that require additional investigation before widespread use of BH techniques can be recommended for use in settings other than presurgical planning. Methodology that enables precise control of arterial blood gases is preferred, but even though this methodology is available, it is not yet universally implemented. Nevertheless the importance of interrogating blood flow control and the state of vascular reactivity in the brain is expected to increase, gaining relevance in both clinical and research environments.

Disclosures: Jay J. Pillai—OTHER RELATIONSHIPS: unpaid membership in Medical Advisory Board of Prism Clinical Imaging Inc. David J. Mikulis—UNRELATED: Grants/Grants Pending: Canadian Institutes of Health Research (CIHR) grant,* Comments: Agency: CIHR No. 130459, amount and period of support: \$324,598 for January 10, 2013 to January 04, 2017; title: "A Potential Biomarker for Vascular Dementia," Role: Principal Investigator; Patents (planned, pending or issued): US patent filing for "A New Method and Apparatus to Reliably Attain and Maintain Target End Tidal Partial Pressure of Oxygen and Carbon Dioxide," July 22, 2004, provisional No. 60/589,797, applicants: Marat Slessarev, Joseph A. Fisher, Eitan Prisman, David Mikulis, Chris Hudson, Alex Vesely, George Volgyesi, Cliff Ansel; Stock/Stock Options: minor equity positions in Thornhill Research, Inc. *Money paid to the institution.

REFERENCES

- Ogawa S, Tank DW, Menon R, et al. **Intrinsic signal changes accompanying sensory stimulation: functional brain mapping with magnetic resonance imaging.** *Proc Natl Acad Sci U S A* 1992;89:5951–55
- Bandettini PA, Wong EC, Hinks RS, et al. **Time course EPI of human brain function during task activation.** *Magn Reson Med* 1992; 25:390–97
- Kwong KK, Belliveau, JW, Chesler DA, et al. **Dynamic magnetic resonance imaging of human brain activity during primary sensory stimulation.** *Proc Natl Acad Sci U S A* 1992;89:5675–79
- Blockley NP, Griffeth VE, Simon AB, et al. **A review of calibrated blood oxygen level-dependent (BOLD) methods for the measurement of task-induced changes in brain oxygen metabolism.** *NMR Biomed* 2013;26:987–1003
- Koehler RC, Roman RJ, Harder DR. **Astrocytes and the regulation of cerebral blood flow (review).** *Trends Neurosci* 2009;32:160–69
- Attwell D, Buchan AM, Charpak S, et al. **Glia and neuronal control of brain blood flow (review).** *Nature* 2010;468:232–43
- Hou BL, Bradbury M, Peck KK, et al. **Effect of brain tumor neovasculation defined by rCBV on BOLD fMRI activation volume in the primary motor cortex.** *Neuroimage* 2006;32:489–97
- Pillai JJ, Zaca D. **Clinical utility of cerebrovascular reactivity mapping in patients with low grade gliomas.** *World J Clin Oncol* 2011;2:397–403
- Pillai JJ, Zaca D. **Comparison of BOLD cerebrovascular reactivity mapping and DSC MR perfusion imaging for prediction of neurovascular uncoupling potential in brain tumors.** *Technol Cancer Res Treat* 2012;11:361–74
- Zaca D, Jovicich J, Nadar SR, et al. **Cerebrovascular reactivity mapping in patients with low grade gliomas undergoing presurgical sensorimotor mapping with BOLD fMRI.** *J Magn Reson Imaging* 2014;40:383–90
- Shiino A, Morita Y, Tsuji A, et al. **Estimation of cerebral perfusion reserve by blood oxygenation level-dependent imaging: comparison with single-photon emission computed tomography.** *J Cereb Blood Flow Metab* 2003;23:121–35
- Heyn C, Poulblanc J, Crawley A, et al. **Quantification of cerebrovascular reactivity by blood oxygen level-dependent MR imaging and correlation with conventional angiography in patients with Moyamoya disease.** *AJNR Am J Neuroradiol* 2010;31:862–67
- Bright MG, Murphy K. **Reliable quantification of BOLD fMRI cerebrovascular reactivity despite poor breath-hold performance.** *Neuroimage* 2013;83:559–68
- Kastrup A, Krüger G, Neumann-Haefelin T, et al. **Assessment of cerebrovascular reactivity with functional magnetic resonance imaging: comparison of CO(2) and breath holding.** *Magn Reson Imaging* 2001;19:13–20
- Abbott DF, Opdam HI, Briellmann RS, et al. **Brief breath holding may confound functional magnetic resonance imaging studies.** *Hum Brain Mapp* 2005;24:284–90
- Magon S, Basso G, Farace P, et al. **Reproducibility of BOLD signal change induced by breath holding.** *Neuroimage* 2009;45:702–12
- Scouten A, Schwarzbauer C. **Paced respiration with end-expiration technique offers superior BOLD signal repeatability for breath-hold studies.** *Neuroimage* 2008;43:250–57
- Thomason ME, Glover GH. **Controlled inspiration depth reduces variance in breath-holding-induced BOLD signal.** *Neuroimage* 2008;39:206–14
- Tancredi FB, Hoge RD. **Comparison of cerebral vascular reactivity measures obtained using breath-holding and CO2 inhalation.** *J Cereb Blood Flow Metab* 2013;33:1066–74
- Birn RM, Smith MA, Jones TB, et al. **The respiration response function: the temporal dynamics of fMRI signal fluctuations related to changes in respiration.** *Neuroimage* 2008;40:644–54
- Zaca D, Hua J, Pillai JJ. **Cerebrovascular reactivity mapping for brain tumor presurgical planning.** *World J Clin Oncol* 2011; 2:289–98
- Silvestrini M, Vernieri F, Pasqualetti P, et al. **Impaired cerebral vasoreactivity and risk of stroke in patients with asymptomatic carotid artery stenosis.** *JAMA* 2000;283:2122–27
- Markus H, Cullinane M. **Severely impaired cerebrovascular reactivity predicts stroke and TIA risk in patients with carotid artery stenosis and occlusion.** *Brain* 2001;124(pt 3):457–67
- Blaser T, Hofmann K, Buerger T, et al. **Risk of stroke, transient ischemic attack, and vessel occlusion before endarterectomy in patients with symptomatic severe carotid stenosis.** *Stroke* 2002;33:1057–62
- Schoof J, Lubahn W, Baeumer M, et al. **Impaired cerebral autoregulation distal to carotid stenosis/occlusion is associated with increased risk of stroke at cardiac surgery with cardiopulmonary bypass.** *J Thorac Cardiovasc Surg* 2007;134:690–96
- van der Zwan A, Hillen B, Tulleken CA, et al. **A quantitative investigation of the variability of the major cerebral arterial territories.** *Stroke* 1993;24:1951–59
- Mandell DM, Han JS, Poulblanc J, et al. **Selective reduction of blood flow to white matter during hypercapnia corresponds with leukoariosis.** *Stroke* 2008;39:1993–98
- Baddeley H, Brodrick PM, Taylor NJ, et al. **Gas exchange parameters in radiotherapy patients during breathing of 2%, 3.5% and 5% carbogen gas mixtures.** *Br J Radiol* 2000;73:1100–04
- Fierstra J, Sobczyk O, Battisti-Charbonney A, et al. **Measuring cerebrovascular reactivity: what stimulus to use?** *J Physiol* 2013;591(pt 23):5809–21
- Swanson GD, Bellville JW. **Step changes in end-tidal CO2: methods and implications.** *J Appl Physiol* 1975;39:377–85
- Ito S, Mardimae A, Han J, et al. **Non-invasive prospective targeting of arterial PCO2 in subjects at rest.** *J Physiol* 2008;586:3675–82

Are There Differences between Macrocyclic Gadolinium Contrast Agents for Brain Tumor Imaging? Results of a Multicenter Intraindividual Crossover Comparison of Gadobutrol with Gadoteridol (the TRUTH Study)

K.R. Maravilla, M.P. Smith, J. Vymazal, M. Goyal, M. Herman, J.J. Baima, R. Babbel, M. Vaneckova, J. Žižka, C. Colosimo, M. Urbańczyk-Zawadzka, M. Mechl, A.K. Bag, S. Bastianello, E. Bueltmann, T. Hirai, T. Frattini, M.A. Kirchin, and G. Pirovano



ABSTRACT

BACKGROUND AND PURPOSE: Gadobutrol (Gadavist) and gadoteridol (ProHance) have similar macrocyclic molecular structures, but gadobutrol is formulated at a 2-fold higher (1 mol/L versus 0.5 mol/L) concentration. We sought to determine whether this difference impacts morphologic contrast-enhanced MR imaging.

MATERIALS AND METHODS: Two hundred twenty-nine adult patients with suspected or known brain tumors underwent two 1.5T MR imaging examinations with gadoteridol or gadobutrol administered in randomized order at a dose of 0.1 mmol/kg of body weight. Imaging sequences and T1 postinjection timing were identical for both examinations. Three blinded readers evaluated images qualitatively and quantitatively for lesion detection and for accuracy in characterization of histologically confirmed brain tumors. Data were analyzed by using the Wilcoxon signed rank test, the McNemar test, and a mixed model.

RESULTS: Two hundred nine patients successfully completed both examinations. No reader noted a significant qualitative or quantitative difference in lesion enhancement, extent, delineation, or internal morphology (P values = .69–1.00). One hundred thirty-nine patients had at least 1 histologically confirmed brain lesion. Two readers found no difference in the detection of patients with lesions (133/139 versus 135/139, P = .317; 137/139 versus 136/139, P = .564), while 1 reader found minimal differences in favor of gadoteridol (136/139 versus 132/139, P = .046). Similar findings were noted for the number of lesions detected and characterization of tumors (malignant/benign). Three-reader agreement for characterization was similar for gadobutrol (66.4% [κ = 0.43]) versus gadoteridol (70.3% [κ = 0.45]). There were no significant differences in the incidence of adverse events (P = .199).

CONCLUSIONS: Gadoteridol and gadobutrol at 0.1 mmol/kg of body weight provide similar information for visualization and diagnosis of brain lesions. The 2-fold higher gadolinium concentration of gadobutrol provides no benefit for routine morphologic imaging.

ABBREVIATIONS: GBCA = gadolinium-based contrast agent; GRE = gradient recalled-echo; SE = spin-echo

Gadobutrol (Gadavist, Gd-BT-DO3A; Bayer HealthCare, Wayne, New Jersey) and gadoteridol (ProHance, Gd-HP-DO3A; Bracco Diagnostics, Monroe, New Jersey) are nonionic

macrocyclic gadolinium-based contrast agents (GBCAs) approved by the US Food and Drug Administration and other regulatory bodies for MR imaging of the CNS in adults and children older than 2 years of age.^{1,2} The approved routine dose of both agents is 0.1 mmol/kg of body weight. Structurally, the 2 agents differ only in that a hydroxypropyl group on the gadoteridol molecule is replaced by a trihydroxybutyl group on the gadobutrol molecule.³ The published $r1$ relaxivity values at 1.5T are 4.7–5.2

Germany; Department of Diagnostic Radiology (T.H.), Kumamoto University, Honjo, Kumamoto, Japan; Ospedale Valduce (T.F.), Como, Italy; Global Medical and Regulatory Affairs (M.A.K.), Bracco Imaging SpA, Milan, Italy; and Global Medical and Regulatory Affairs (G.P.), Bracco Diagnostics, Monroe, New Jersey.

Please address correspondence to Kenneth R. Maravilla, MD, Radiology and Neurological Surgery, MR Research Laboratory, University of Washington, 1959 NE Pacific, Box 357115, Seattle, WA 98195; e-mail: kmarav@uw.edu

Indicates open access to non-subscribers at www.ajnr.org

Evidence-Based Medicine Level 1.

<http://dx.doi.org/10.3174/ajnr.A4154>

Received August 7, 2014; accepted after revision September 15.

From the MR Research Laboratory (K.R.M.), University of Washington, Seattle, Washington; Department of Radiology (M.P.S.), Beth Israel Deaconess Medical Center, Boston, Massachusetts; Department of Radiology (J.V.), Na Homolce Hospital, Prague, Czech Republic; Seaman Family MR Research Centre (M.G.), University of Calgary, Calgary, Alberta, Canada; Department of Radiology (M.H.), University Hospital Olomouc, Olomouc, Czech Republic; Clinical Radiologists Service Corporation (J.J.B.), Memorial Medical Center, Springfield, Illinois; Good Samaritan Regional Medical Center (R.B.), Corvallis, Oregon; Department of Magnetic Resonance (M.V.), General University Hospital, Prague, Czech Republic; Department of Diagnostic Radiology (J.Ž.), University Hospital Hradec Králové and Faculty of Medicine in Hradec Králové, Charles University, Prague, Czech Republic; Istituto di Radiologia (C.C.), Policlinico “Agostino Gemelli,” Rome, Italy; Department of Radiology (M.U.-Z.), John Paul II Hospital, Krakow, Poland; Department of Radiology (M.M.), University Hospital Brno-Bohunice, Brno, Czech Republic; Department of Radiology (A.K.B.), University of Alabama at Birmingham Medical Center, Birmingham, Alabama; Department of Neuroradiology (S.B.), University of Pavia, Pavia, Italy; Institute for Diagnostic and Interventional Neuroradiology (E.B.), Hannover,

$L \times \text{mmol}^{-1} \times \text{second}^{-1}$ for gadobutrol and $4.1\text{--}4.3 L \times \text{mmol}^{-1} \times \text{second}^{-1}$ for gadoteridol.^{4,5} The presence of human serum albumin has no significant effect on the relaxivity of either agent because neither exhibits protein binding. The only significant difference between the agents is that gadobutrol is formulated at a 1.0-mol/L concentration while gadoteridol, similar to other GBCAs approved for CNS MR imaging, is formulated at a 0.5-mol/L concentration.

A previous single-center comparison of enhancement effectiveness between the 2 agents suggested the superiority of 1.0-mol/L gadobutrol over 0.5-mol/L gadoteridol⁶ in a limited study population (51 patients) with inconsistent, sequence-dependent differences in quantitative enhancement.

The purpose of this multicenter, multinational study was to determine, in a larger patient population by using a rigorous double-blind, randomized, intraindividual, crossover design, whether 1.0-mol/L gadobutrol has benefit over 0.5-mol/L gadoteridol for morphologic brain MR imaging when these agents are administered at identical 0.1-mmol/kg doses in 2 identical MR imaging examinations at 1.5T.

MATERIALS AND METHODS

The study was Health Insurance Portability and Accountability Act-compliant, was conducted according to good clinical practice standards, and was registered at www.clintrials.gov (reference NCT01613417). All patients signed an approved informed consent form before enrollment.

Patients

Two hundred twenty-nine patients referred for contrast-enhanced MR imaging for known or suspected brain tumors were enrolled in a consecutive manner at 19 participating centers between September 2012 and November 2013. The highest number of patients enrolled at any center was 30. Thirteen centers enrolled between 9 and 25 patients. The remaining 5 centers enrolled between 1 and 4 patients. Patients were ineligible if they received any investigational drug within 30 days before study agent administration. Subjects were also excluded if they were to receive any treatment between the 2 examinations that could affect lesion visualization (eg, radiation therapy, steroids, or chemotherapy). Patients were also ineligible if they were pregnant or nursing or had impaired renal function, congestive heart failure, claustrophobia, gadolinium allergy, a cardiac pacemaker, or other contraindications to MR imaging.

The 229 enrolled patients (98 men, 131 women; mean age, 55.3 ± 14.4 years; range, 19–86 years) were prospectively randomized to receive contrast agent according to 1 of 2 administration orders: Gadoteridol was administered first to patients in group A ($n = 113$), while gadobutrol was administered first to patients in group B ($n = 116$).

MR Imaging

MR imaging was performed on 1.5T systems from several vendors (Siemens Avanto [$n = 26$], Sonata [$n = 10$], Aera [$n = 6$], Symphony [$n = 1$], Siemens, Erlangen, Germany; Philips Achieva [$n = 101$], Philips Healthcare, Best, the Netherlands; GE Signa Excite [$n = 24$], HDx [$n = 45$], Optima [$n = 16$], GE Healthcare,

Milwaukee, Wisconsin) using a multichannel head coil. Although higher field strength 3T systems are widely used, especially for their advantages for advanced imaging techniques, this study was performed at 1.5T because these systems are still more commonly used throughout the United States, Europe, and other areas worldwide.

A rigorously controlled imaging protocol comprising T1-weighted spin-echo (SE), T2-weighted fast spin-echo, and T2-weighted FLAIR acquisitions before contrast injection and T1 SE and 3D-T1-weighted high-resolution gradient recalled-echo (GRE) acquisitions after injection ensured protocol uniformity across sites and within individual patients. Sequence parameters varied within predefined ranges necessitated by the use of different imaging systems. However, the same MR imaging scanner, imaging planes, section prescriptions, and sequence parameters were used for both examinations in each patient. Scan parameters were as follows—for the T1 SE sequence: TR = 333–767 ms, TE = 7.7–16 ms, excitations = 1–3, section thickness = 4–5 mm, FOV = $17 \times 22\text{--}28 \times 28$ cm; for the T1 GRE sequence: TR = 5.3–2050 ms, TE = 1.19–7.24 ms, flip angle = $8^\circ\text{--}30^\circ$, excitations = 0.8–1, section thickness = 1–3 mm, FOV = $23 \times 18\text{--}28 \times 28$ cm. Parallel imaging was not used for any patient. Axial scans were all acquired along the inferior callosal plane to ensure image comparability among scans within patient comparisons and across patients.

IV contrast-agent administration was performed identically in both examinations at 0.1 mmol/kg of body weight (0.2 mL/kg for gadoteridol and 0.1 mL/kg for gadobutrol) by using either a manual bolus injection ($n = 207$) or a power injector ($n = 22$). All injections were followed by a saline flush of up to 30 mL. Each agent was administered by an independent drug-dispensing person in the order determined by a randomization list to maintain the study blinding.

Postcontrast image acquisition began at a prespecified time between 3 and 10 minutes after injection but could vary within this range, depending on the site-specific protocol. However, the timing and order of postcontrast sequences were mandated to be identical for both examinations within each patient. The interval between MR imaging examinations was >48 hours to avoid carryover effects but <14 days to minimize the chance of measurable lesion evolution.

Image Evaluation. All images were evaluated by 3 independent neuroradiologists (S.B., E.B., and T.H. with 20, 11, and 24 years of neuroradiology experience, respectively) who were unaffiliated with the study centers and blinded to the contrast agent used, patient clinical and radiologic information, and interpretations by on-site investigators. Each reader evaluated all patient images separately and independently on a multimonitor workstation. The reading consisted of 2 sessions.

Diagnostic Performance. In the first session, each reader evaluated images presented in unpaired, randomized order to determine the extent of anatomic coverage (complete or partial) and to rate the overall quality of visualization (nondiagnostic, poor, fair, good, excellent). Any images rated nondiagnostic would be excluded from subsequent evaluation.

Next, assessments of diagnostic performance were performed

by each offsite reader separately for lesions detected in each of the 2 examinations. For this assessment, each reader assigned a diagnosis to each detected lesion from a list of 99 possible diagnoses ratified by the World Health Organization^{7,8} that covers the range of nontumor diagnoses (white matter disease, vascular lesions, infective/inflammatory disease, infarct, hemorrhage, postoperative or posttreatment changes) and tumor diagnoses (astrocytic tumors, oligodendroglial tumors, ependymal cell tumors, mixed gliomas, neuroepithelial tumors of uncertain origin, tumors of the choroid plexus, neuronal and mixed neuronal-glioma tumors, pineal parenchymal tumors, tumors with neuroblastic or glioblastic elements [embryonal tumors], tumors of the sellar region, hematopoietic tumors, germ cell tumors, tumors of the meninges, nonmeningothelial tumors of the meninges, tumors of cranial and spinal nerves, metastatic tumors, and cysts and tumorlike lesions).

For each lesion, readers assigned either a single diagnosis or could choose to assign differential diagnoses (ie, 2, 3, or > 3 diagnoses). With this approach, a confidence score for correct lesion diagnosis was determined by using a 5-point scale as follows: 5 (single diagnosis, correctly matched with final TRUTH standard diagnosis); 4 (2 differential diagnoses, the first or second correctly matched); 3 (3 differential diagnoses; the first, second, or third correctly matched); 2 (>3 differential diagnoses; the first, second, or third correctly matched) or 1 (no match or nondiagnostic images or lesions confirmed at final diagnosis but not detected at MR imaging).

Subsequent comparisons of diagnostic performance (lesion detection rate, accuracy for tumor characterization—that is, the distinction between benign and malignant tumors based on World Health Organization brain tumor classification) and confidence for lesion characterization were performed for patients with histologically confirmed brain tumors after biopsy or surgical resection. For these evaluations, patients with only follow-up diagnostic data from alternative imaging procedures were excluded. A fourth independent neuroradiologist (T.F. with 20 years of neuroimaging experience), unaffiliated with the study centers and blinded to all clinical and radiologic information, matched the findings of the 3 blinded readers to the final lesion diagnosis for each patient.

Qualitative and Quantitative Assessment of Diagnostic Information. In the second reading session, qualitative and quantitative assessment of images from each patient was performed with images presented in global matched-pairs fashion. For each randomized patient number, all images from examination 1 were displayed simultaneously with the images from examination 2. Each reader could perform all routine interactive image-manipulation functions (eg, window/level, zoom, pan) on both image sets. If the postinjection images from either examination were considered technically inadequate by any of the 3 readers (eg, if artifacts compromised interpretability), no further assessment was performed for that patient by that reader. Once the readers' assessments were recorded and signed off on an electronic Case Report Form, the database for that reading was automatically locked.

Qualitative Assessment. Technically adequate images were evaluated qualitatively for diagnostic information and scored in terms of the following: 1) overall diagnostic preference, 2) lesion border delineation, 3) disease extent, 4) visualization of lesion internal

morphology, and 5) lesion contrast enhancement compared with surrounding normal tissue. All assessments were performed by using 3-point scales from -1 (examination 1 superior) through 0 (examinations equal) to +1 (examination 2 superior). For the various end points, superiority for 1 examination was recorded if it allowed better separation of ≥ 1 lesion from surrounding tissue, structures, or edema; better definition of lesion extent; clearer depiction of intralésion features; better difference in signal intensity between lesions and surrounding normal tissue; or depiction of ≥ 1 lesion seen only on that examination.

Quantitative Assessment. Quantitative evaluation was also performed by each reader, independently by using a simultaneous matched-pairs approach. Signal-intensity (SI) measurements were made by using ROIs positioned on areas of normal brain parenchyma and on up to 3 enhancing lesions per patient identified on postcontrast images from both examinations. Each region of interest placed on the selected postinjection image from one examination appeared simultaneously on the corresponding image from the other examination, to ensure that ROIs of equal size were positioned at identical coordinates on all corresponding image sets. Minor adjustments to ROI position were permitted to allow for slight differences in patient alignment, always taking care to avoid inclusion of vessels. When multiple lesions were present, ROIs were placed on up to 3 of the largest, most conspicuous lesions. A multimonitor imaging workstation (Aquarius, Version 4.4.1.4; TeraRecon, San Mateo, California) was used to determine SI values on a pixel-by-pixel basis and to calculate the percentage enhancement (E%) of lesions and the lesion-to-background ratio (LBR) on T1 SE sequences by using the equations below:

$$E\% = \frac{\text{SI of lesion (postcontrast)} - \text{SI of lesion (precontrast)}}{\text{SI of lesion (precontrast)}} \times 100$$

$$\text{LBR} = \frac{\text{SI of lesion}}{\text{SI of brain}}$$

Safety Assessments

Monitoring for adverse events was performed from the time the patient signed the informed consent form until 24 hours after administration of the first study agent and then from the moment the second study agent was administered until 24 hours after administration of the second agent. Events were classified as serious (death, life-threatening, requiring/prolonging hospitalization) or nonserious (mild [no disability/incapacity; self-resolving], moderate [no disability/incapacity; requiring treatment], or severe [temporary and/or mild disability/incapacity; requiring treatment]). Decisions on event severity and its relationship to the study agent (has reasonable possibility or not) were made by the investigating radiologist.

Statistical Analysis

Power determination was based on the primary efficacy assumption that a 0.1-mmol/kg dose of gadoteridol is noninferior to an equivalent dose of gadobutrol in terms of global diagnostic preference. Sample size was calculated (nQuery, Version 6.01; Statistical Solutions, Cork, Ireland) by using the Newcombe-Wilson

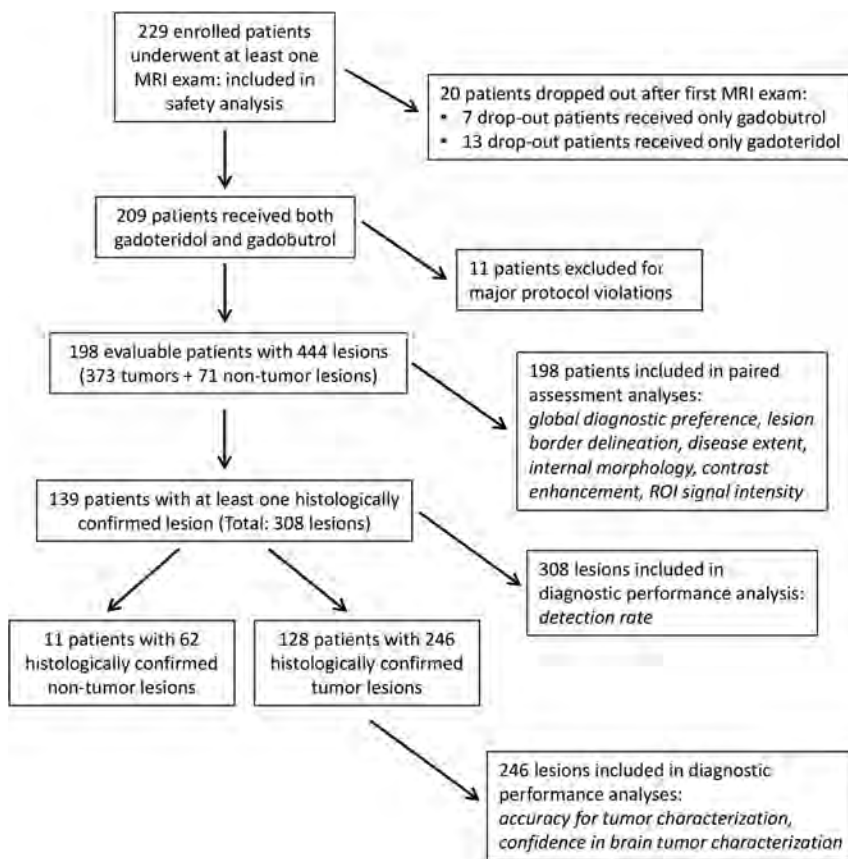


FIG 1. Flow chart outlining patient enrollment, drop-out rates, and lesion study populations.

scoring method, which is based on the lower confidence limit for the difference in paired proportions; an estimated enrollment of 185 subjects was deemed necessary for the lower limit of the observed 2-sided 95% confidence interval for the difference to exceed -5% with 85% power. If one assumed a patient drop-out rate of 10%, a minimum enrollment of 206 subjects was planned.

Analysis of blinded reader evaluations was performed by using the statistical software package SAS, Version 9.2 (SAS Institute, Cary, North Carolina). The distribution of reader preferences for the diagnostic information end points was tested by using the Wilcoxon signed rank test. The Altman general approximate normal method was used to estimate the 2-sided 95% confidence interval for the difference in matched-paired proportions.

Differences in quantitative enhancement between gadoteridol and gadobutrol were analyzed by using a mixed-effects model. The change from predose was the response variable, and factors included in the model were patient, period, sequence, study agent, and predose score. Patient nested within sequence was the random effect.

Determinations of diagnostic performance, including 95% confidence intervals, were performed for patients with histologically confirmed tumors from biopsy or surgery in terms of the lesion-detection rate and accuracy for tumor characterization. Comparison of detection rate and accuracy was performed by using the McNemar test. Interrater agreement was presented as percentage agreement and was assessed by using generalized κ statistics. Agreement was classified as excellent ($\kappa > 0.8$), good ($\kappa = 0.61-0.8$), moderate ($\kappa = 0.41-0.6$), fair ($\kappa = 0.21-0.4$), or

poor ($\kappa \leq 0.2$). An overall mean confidence score \pm SD for lesion characterization was determined from the individual lesion confidence scores assigned to each patient. Comparison of mean confidence scores was performed by using a paired t test. The Fisher exact test was used to compare the incidence of adverse events for the 2 agents and overall quality of visualization. All statistical tests were conducted at a significance level of $P < .05$.

RESULTS

Patients

All 229 enrolled patients underwent at least 1 contrast-enhanced MR imaging examination and were included in the overall safety population. Twenty patients discontinued after the first examination (13/113 [11.5%] after gadoteridol; 7/116 [6.0%] after gadobutrol; $P = .165$). Reasons for discontinuation included withdrawal of consent ($n = 11$), surgical intervention ($n = 3$), mild adverse event ($n = 2$), claustrophobia ($n = 1$), change of hospital ($n = 1$), inability to obtain intravenous access ($n = 1$), and lack of enhancing lesion ($n = 1$). Of the remaining 209 (91.3%) patients, 11 were excluded from the efficacy population because of

protocol violations (study agent doses missing or differing by $>15\%$, $n = 9$; differences of >2 minutes between injection and postdose acquisition start times, $n = 2$). The final efficacy analysis population therefore comprised 198 patients, of which 93 (43 men, 50 women; mean age, 54.4 ± 14.4 years; range, 19–79) were randomized to group A, and 105 (47 men, 58 women; mean age, 55.9 ± 14.3 years; range, 25–82 years), to group B (Fig 1). There were no significant between-group differences in sex ($P = .835$), age ($P = .463$), age groups (18–64 years, ≥ 65 years; $P = .184$), weight ($P = .071$), height ($P = .503$), or race ($P = .150$) distribution.

Anatomic coverage was considered complete for all 198 patients by readers 1 and 3 and for 197/198 patients by reader 2. All images from both agents were considered diagnostic by all readers, and no images were excluded due to motion degradation. Readers 1, 2, and 3 considered the overall quality of visualization to be good or excellent for 91.4%, 89.9%, and 98.5% of patients, respectively, after gadoteridol, and for 92.9%, 90.4%, and 100% of patients after gadobutrol with no significant differences noted ($P = .709$, $P = 1.0$, $P = .248$; readers 1, 2 and 3, respectively). Four hundred forty-four lesions were identified on-site in these 198 patients (Table 1). Of these lesions, 373/444 (84%) in 181 patients were diagnosed as tumors (293 [66%] malignant; 80 [18%] benign), while 71/444 (16%) were nontumors. Among these 198 patients, 139 had at least 1 lesion that was confirmed histologically after biopsy or surgery. In these 139 patients there were 308 lesions (tumors and nontumors), which were included in subsequent analysis of the lesion-detection rate. Among these 139 pa-

Table 1: TRUTH standard lesion diagnoses

Specific Diagnosis	N = 444 (%)
Malignant tumor diagnoses (n = 293) (66%)	
Anaplastic astrocytoma (grade III)	12 (2.7)
Glioblastoma multiforme (grade IV)	55 (12.4)
Anaplastic oligodendroglioma (grade III)	4 (0.9)
Anaplastic oligoastrocytoma (grade III)	8 (1.8)
Ependymoastrocytoma	2 (0.5)
Malignant lymphoma	1 (0.2)
Metastatic tumors	211 (47.5)
Benign tumor diagnoses (n = 80) (18%)	
Astrocytoma (grade II)	2 (0.5)
Pilocytic astrocytoma (noninvasive, grade I)	1 (0.2)
Oligodendroglioma (grade II)	1 (0.2)
Ependymoma (grade II)	1 (0.2)
Mixed oligoastrocytoma (grade II)	1 (0.2)
Pineocytoma (grade I)	1 (0.2)
Pituitary adenoma	5 (1.1)
Craniopharyngioma (grade I)	1 (0.2)
Meningioma (grade I)	38 (8.6)
Atypical meningioma (grade II)	9 (2.0)
Benign mesenchymal tumor	1 (0.2)
Melanocytoma	1 (0.2)
Hemangioblastoma (grade I)	1 (0.2)
Schwannoma (neurinoma, neurilemmoma) (grade I)	16 (3.6)
Cysts and tumorlike lesions (epidermoid)	1 (0.2)
Nontumor diagnoses (n = 71) (16%)	
White matter disease	1 (0.2)
Vascular lesion	10 (2.3)
Infective/inflammatory disease	2 (0.5)
Infarct	1 (0.2)
Hemorrhage	1 (0.2)
Postoperative/posttreatment changes	56 (12.6)

tients, 128 had 246 lesions that were confirmed histologically as tumors, while the remaining 11 patients had lesions confirmed histologically as nontumors. All 246 histologically confirmed tumors were included in assessments of accuracy for tumor characterization (ie, benign-versus-malignant tumors based on World Health Organization brain tumor classification) and for confidence in brain tumor characterization (Fig 1).

Qualitative Image Assessment

Figure 2 graphically displays the results of the 3 blinded readers for global diagnostic preference, lesion-border delineation, disease extent, internal morphology, and qualitative assessment of contrast enhancement, respectively. No significant differences between gadoteridol and gadobutrol were noted by any reader for any parameter. The 95% confidence intervals for all qualitative assessments confirmed that gadoteridol is not inferior to gadobutrol. Agreement among the 3 blinded readers was high for all assessments, ranging from 82.5% of patients for assessment of lesion contrast enhancement to 97.9% of patients for definition of disease extent.

Examples of comparative enhancement between gadoteridol and gadobutrol are shown in Figs 3 and 4.

Quantitative Evaluation

Readers also recorded lesion signal-intensity measurements relative to normal brain parenchyma for up to 3 lesions in each patient. The mean percentage signal enhancement of lesions on T1 SE images was similar for gadoteridol and gadobutrol for all 3

readers (reader 1: 97.3% versus 96.9% [$P = .620$]; reader 2: 95.6% versus 98.8% [$P = .451$]; reader 3: 92.8% versus 95.3% [$P = .772$]).

No significant differences between gadoteridol and gadobutrol were noted by any reader for pre- to postdose changes in lesion-to-background ratio on T1 SE images (Fig 5). Similar findings were noted for assessments of T1 GRE images.

Diagnostic Performance

Lesion Detection. No significant differences between agents were noted by readers 1 and 2 in the number of patients with brain lesions, while only minimal differences were noted by reader 3 (Table 2). Similarly, no significant differences were noted by readers 1 and 2 in the number of lesions detected. On the basis of 308 lesions included in the analysis, all 3 readers agreed for 70.8% ($\kappa = 0.39$) of lesions after gadoteridol administration and for 72.4% ($\kappa = 0.47$) of lesions after gadobutrol administration. At the patient level, on the basis of 139 subjects with histopathologic disease confirmation, all 3 readers agreed in 95.7% ($\kappa = 0.44$) of patients after gadoteridol administration and in 95.0% ($\kappa = 0.48$) of patients after gadobutrol.

Accuracy for Tumor Characterization. Readers 1 and 2 noted no significant differences between gadoteridol and gadobutrol for characterization of detected tumors either at the patient level or at the lesion level (Table 3). Conversely, improved lesion characterization with gadoteridol was noted by reader 3. On the basis of 128 subjects with histologically confirmed brain tumors, all 3 readers agreed in their assessments for 70.3% ($\kappa = 0.45$) of patients after gadoteridol and for 66.4% ($\kappa = 0.43$) of patients after gadobutrol.

Confidence for Brain Tumor Diagnosis. Of 128 patients with histologically confirmed brain tumors, slightly higher mean confidence scores were assigned in the gadoteridol group (reader 1: 3.6 ± 1.8 versus 3.3 ± 1.9 , $P = .016$; reader 2: 3.6 ± 1.5 versus 3.4 ± 1.6 , $P = .011$; reader 3: 3.5 ± 1.6 versus 3.3 ± 1.7 , $P = .119$), indicating more single diagnoses and fewer differential diagnoses with gadoteridol. Similar findings were noted for 246 histologically confirmed tumors (reader 1: 3.5 ± 1.8 versus 3.2 ± 1.9 , $P = .001$; reader 2: 3.7 ± 1.6 versus 3.4 ± 1.7 , $P < .001$; reader 3: 3.3 ± 1.7 versus 3.2 ± 1.8 , $P = .033$).

Safety

Fifteen (6.8%) patients reported adverse events after gadoteridol administration. The most frequent events were dysgeusia ($n = 4$), nausea ($n = 4$), and headache ($n = 2$), followed by "feeling hot," lethargy, cough, dyspnea, pruritus, rash, dizziness, vomiting, migraine, urticaria, and vascular rupture. Two events in 2 patients were local injection site reactions. Eight (3.7%) patients reported adverse events after gadobutrol administration. These included 1 case of injection site reaction plus dizziness, dysgeusia, headache, vomiting, paraesthesia, fatigue, dizziness, convulsion, and oropharyngeal pain. There was no significant difference in the incidence of adverse events between the 2 agents ($P = .199$); no serious adverse events were reported for either agent.

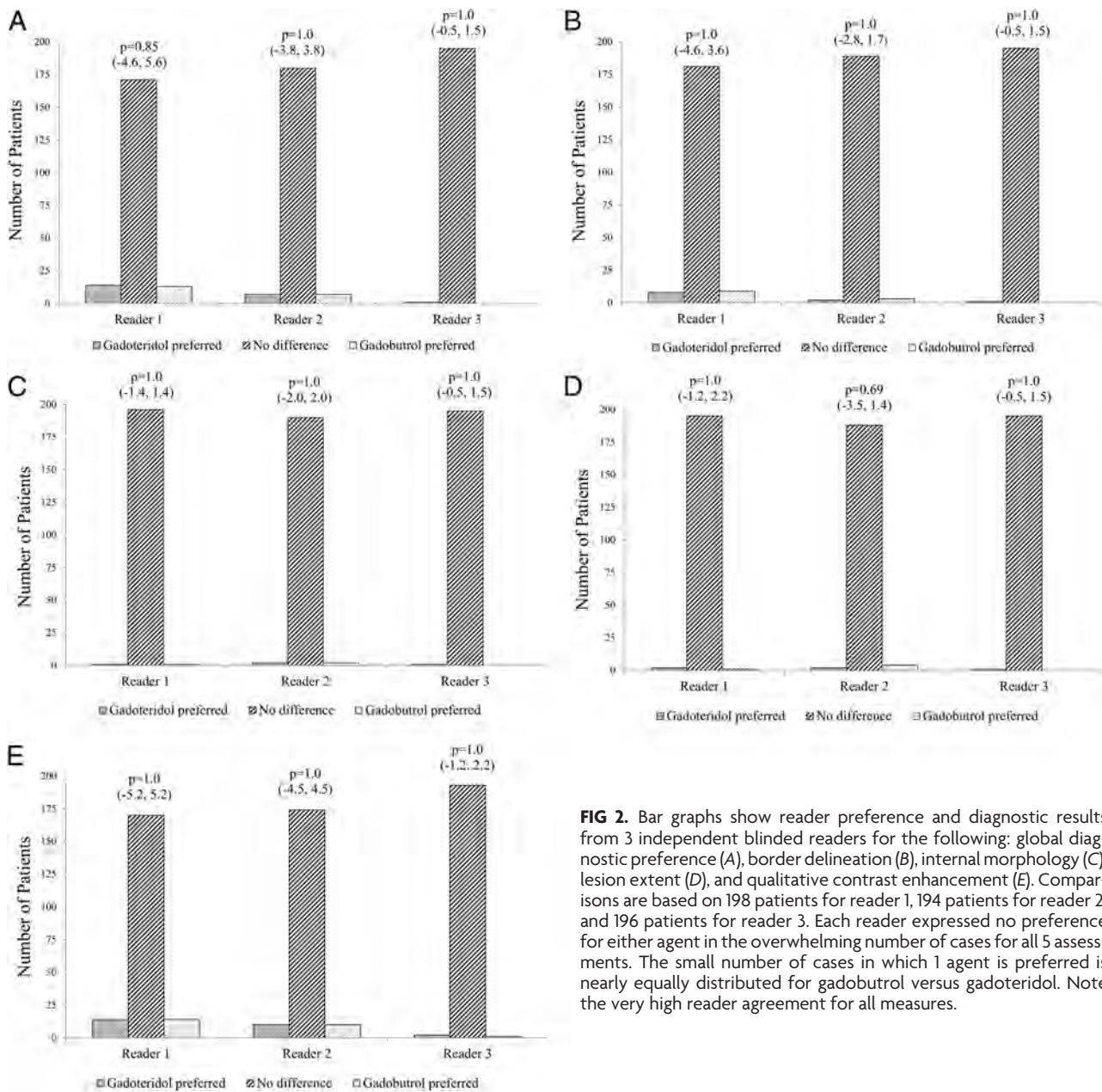


FIG 2. Bar graphs show reader preference and diagnostic results from 3 independent blinded readers for the following: global diagnostic preference (A), border delineation (B), internal morphology (C), lesion extent (D), and qualitative contrast enhancement (E). Comparisons are based on 198 patients for reader 1, 194 patients for reader 2, and 196 patients for reader 3. Each reader expressed no preference for either agent in the overwhelming number of cases for all 5 assessments. The small number of cases in which 1 agent is preferred is nearly equally distributed for gadobutrol versus gadoteridol. Note the very high reader agreement for all measures.

DISCUSSION

A previous small, single-center, intraindividual study compared contrast-enhancement effectiveness of 1.0 mol/L gadobutrol and 0.5 mol/L gadoteridol in 51 patients scheduled for neurosurgery.⁶ Independent injections of gadobutrol and gadoteridol at doses of 0.1-mmol Gd/kg of body weight were administered in randomized order. For the primary efficacy variable “preference in contrast enhancement for one contrast agent or the other,” the rate of “gadobutrol preferred” was significantly higher compared with the rate of “gadoteridol preferred.”⁶

Other studies have been performed as part of clinical trials for marketing approval for 1.0 mol/L gadobutrol in Japan⁹ and the United States.^{10,11} The study in Japan was a multicenter, single-blind, randomized, intraindividual crossover comparison conducted in 175 patients.⁹ Each patient underwent 1 MR imaging examination with gadobutrol and the other with gadoteridol, each at a dose of 0.1 mmol/kg of body weight, administered twice,

for a total dose of 0.2 mmol/kg of body weight. Imaging was performed after the first and second dose of gadobutrol, but only after the second dose of gadoteridol. Noninferiority of gadobutrol (both doses) to gadoteridol at 0.2 mmol/kg of body weight was demonstrated. However, a major limitation of that study is that though a single 0.1-mmol/kg dose of gadoteridol was administered, no images were acquired and the 2 agents were not compared at a single dose. Hence, it is not possible to determine whether a single dose of gadoteridol would have proved noninferior to a single dose of gadobutrol. The second phase III clinical trial, which is unpublished, found no differences between a 0.1-mmol/kg dose of gadobutrol and an equivalent 0.1-mmol/kg dose of gadoteridol for enhanced CNS MR imaging.^{1,10,11} In this study, no differences were noted in qualitative visualization end points (contrast enhancement, lesion border delineation, and visualization of lesion internal morphology), number of lesions detected, or accuracy for lesion

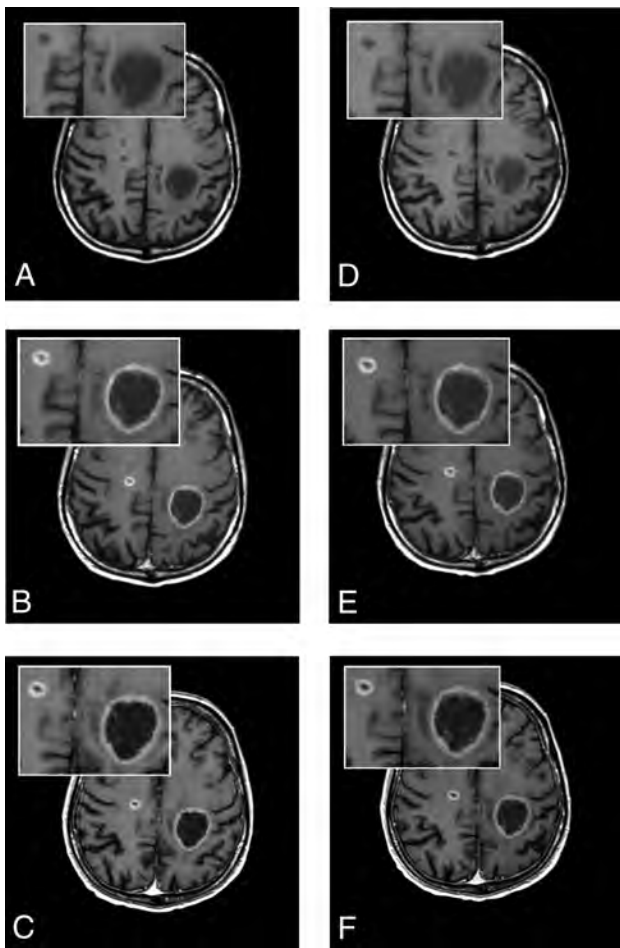


FIG 3. A 61-year-old man with brain metastases from primary lung cancer. Images were acquired before (A, unenhanced T1 SE) and after (B, T1 SE; C, high-resolution T1 GRE) administration of gadoteridol and before (D, unenhanced T1 SE) and after (E, T1 SE; F, high-resolution T1 GRE) administration of gadobutrol. Two lesions clearly seen in both examinations show no differences in contrast enhancement or in the size of lesions.

diagnosis. The results of the study are reflected in the current prescribing information for gadobutrol in the United States.¹

Our findings confirm that no major differences between gadoteridol and gadobutrol are apparent when single 0.1-mmol/kg doses of each agent are administered to patients with confirmed brain lesions. Specifically, evaluating images in matched pairs from ≥ 194 patients for qualitative visualization end points, 3 blinded, expert neuroradiologists expressed no preference for either agent in most cases. In the few cases in which a reader expressed preference, the number of preferences for gadobutrol was approximately equal to the number of preferences for gadoteridol. Similar findings were noted for quantitative enhancement measurements: No significant differences between gadobutrol and gadoteridol were noted either for mean percentage signal enhancement or for pre- to postdose changes in the lesion-to-background ratio. The interreader agreement for assessment of images was high in all cases (complete agreement for 82.5%–97.9% of patients among qualitative end points). For patients with histologically confirmed brain tumors, no significant differences were noted by 2 blinded readers for either lesion detection at

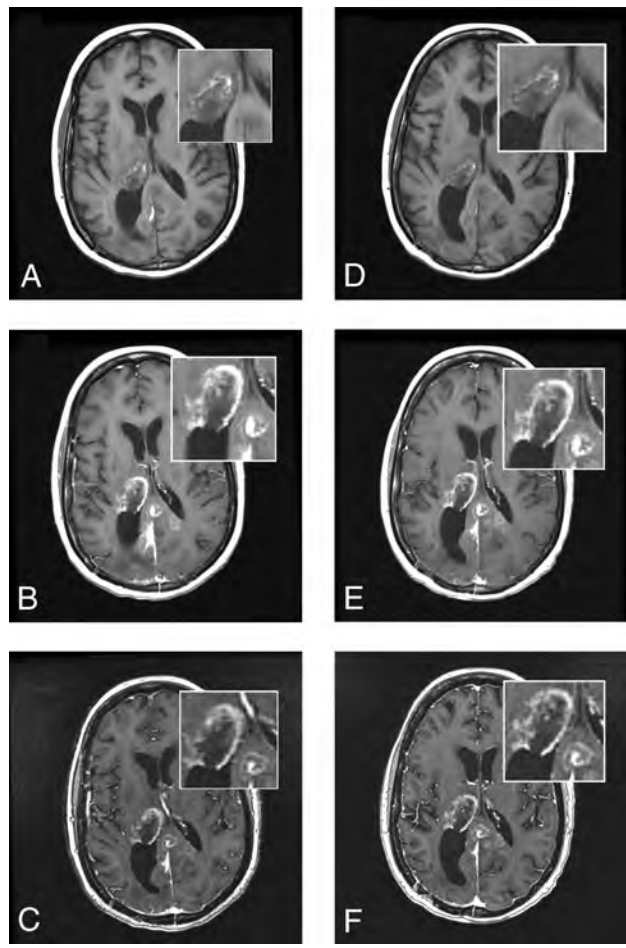


FIG 4. A 51-year-old woman with glioblastoma multiforme. Images were acquired before (A, unenhanced T1 SE) and after (B, T1 SE; C, high-resolution T1 GRE) administration of gadoteridol and before (D, unenhanced T1 SE) and after (E, T1 SE; F, high-resolution T1 GRE) administration of gadobutrol. A rim-enhancing mass in the right thalamus with extension into the posterior interhemispheric region is clearly seen in both examinations. No differences in contrast enhancement or in the size of lesions are apparent.

both patient and lesion levels or for characterization of tumors as malignant or benign. Although 1 blinded reader noted a significant benefit for gadoteridol in patients with brain tumors, the conclusion of our study is that the preference and diagnostic performance of gadobutrol and gadoteridol are similar for imaging of brain tumors when administered at an approved dose of 0.1 mmol/kg of body weight.

Although the interreader agreement for lesion characterization was considered moderate ($\kappa = 0.43$ – 0.45), evaluations were performed in a fully blinded fashion (ie, without access to patient clinical history or the results of other diagnostic tests), and only images acquired by using conventional sequences were evaluated (ie, without the additional information available from advanced imaging techniques such as perfusion, diffusion, or spectroscopic imaging). Moreover, at variance with many literature reports, agreement in this study was determined across 3 readers rather than 2. Hence, if 2 of the 3 readers agreed in their diagnosis but the third disagreed (eg, regarding classification of a detected glioma as grade III [malignant] versus grade II [benign] according to World Health Organization criteria^{7,8}), the overall consensus was dis-

agreement among readers. In this context, overall agreement across 3 readers for 66.4% of patients ($\kappa = 0.43$) after gadobutrol and 70.3% of patients ($\kappa = 0.45$) after gadoteridol was good.

Two conclusions can be derived from this study. First, findings demonstrate that the 2-fold higher concentration of gadobutrol in the commercially available formulation provides no advantage for morphologic imaging of brain lesions. This conclusion is not unexpected, given that image acquisition for morphologic imaging of brain tumors typically begins at least 3–5 minutes following contrast administration, by which time contrast equilibration will have occurred, which would obviate any potential benefits of a higher administered concentration.^{12,13} Second, although *r1* relaxivity is a major factor for contrast efficacy,¹³ the slightly different *r1* relaxivity values for gadobutrol and gadoteridol are insufficient to show any discernable clinical effect, either for qualitative or quantitative lesion enhancement or for diagnostic performance.

These conclusions are supported by other intraindividual crossover studies performed at 1.5T comparing these agents with other GBCAs for brain tumor imaging. Thus, Greco et al¹⁴ com-

pared gadoteridol with gadopentetate dimeglumine (Magnevist [Bayer HealthCare Pharmaceuticals]; *r1*: 3.9–4.1 L × mmol⁻¹ × second⁻¹)^{4,5} in 80 subjects for the presence of disease, degree of enhancement, number of lesions, and additional information gained (lesion-border delineation, improved visualization, distinction of edema, disease classification, and determination of recurrent tumor) and found no significant GBCA preference as determined by 2 blinded readers. More recently, separate prospective multicenter intraindividual crossover studies have compared gadobutrol with gadoterate meglumine (Dotarem [Guerbet, Aulnay-sous-Bois, France]; *r1*: 3.6 L × mmol⁻¹ × second⁻¹)⁴ in 136 patients¹⁵ and gadobenate dimeglumine (MultiHance [Bracco Diagnostics]; *r1*: 6.3–7.9 L × mmol⁻¹ × second⁻¹)^{4,5} in 123 patients.¹⁶ In the former study,¹⁵ significant preference for gadobutrol over gadoterate meglumine was noted by 2 of 3 blinded readers for overall preference. However, none of the 3 readers considered gadobutrol superior to gadoterate meglumine for lesion delineation, while only 1 blinded reader noted minimally significant preference for gadobutrol for the definition of lesion internal structure. Quantitatively, the percentage lesion

enhancement following gadobutrol was approximately 9% higher than that following gadoterate meglumine, but this yielded no significant difference between the 2 agents for measured contrast-to-noise ratio, and no differences in the number of lesions detected with either agent were observed. In comparison, in the latter study,¹⁶ all 3 blinded readers demonstrated a highly significant ($P < .0001$) preference for the higher relaxivity 0.5-mol/L gadobenate dimeglumine over 1.0-mol/L gadobutrol for all qualitative end points (lesion-border delineation, definition of disease extent, visualization of lesion internal morphology, lesion contrast enhancement, and global diagnostic preference) with good interreader agreement for all evaluations. In addition, significant superiority was noted for all quantitative assessments with a mean dif-

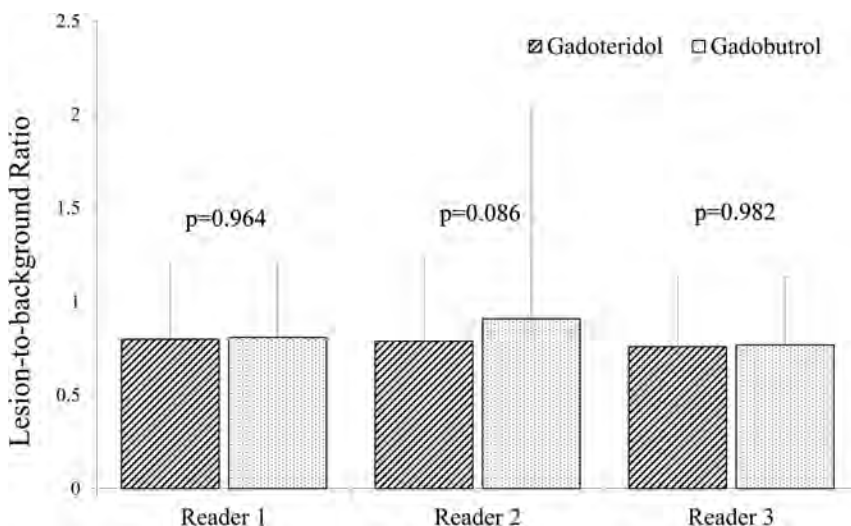


FIG 5. Blinded reader comparison of mean postcontrast-precontrast lesion-to-background ratio on T1 SE sequences after 0.1-mmol/kg doses of gadoteridol and gadobutrol. No significant differences were noted by any reader.

Table 2: Detection of histologically confirmed brain tumors on MR images acquired after administration of 0.1-mmol/kg gadoteridol or 0.1-mmol/kg gadobutrol in 139 patients with 308 brain lesions subsequently confirmed at biopsy or surgery

Lesion Detection	Reader 1		Reader 2		Reader 3	
	Gadoteridol	Gadobutrol	Gadoteridol	Gadobutrol	Gadoteridol	Gadobutrol
No. patients with tumors detected at MRI	133 (95.7%)	135 (97.1%)	137 (98.6%)	136 (97.8%)	136 (97.8%)	132 (95.0%)
<i>P</i> value (95% CI of difference, %)	.317 (-4.2 to 1.4)		.564 (-1.7 to 3.2)		.046 (0.1 to 5.7)	
No. tumors detected at MRI	240 (77.9%)	236 (76.6%)	269 (87.3%)	263 (85.4%)	230 (74.7%)	220 (71.4%)
<i>P</i> value (95% CI of difference, %)	0.480 (-2.3 to 4.9)		0.239 (-1.3 to 5.2)		0.018 (0.6 to 5.9)	

Table 3: Accuracy for brain tumor characterization on MR images acquired after administration of 0.1-mmol/kg gadoteridol or 0.1-mmol/kg gadobutrol in 128 patients with 246 histologically confirmed brain tumors

Lesion Characterization	Reader 1		Reader 2		Reader 3	
	Gadoteridol	Gadobutrol	Gadoteridol	Gadobutrol	Gadoteridol	Gadobutrol
No. patients with tumors correctly characterized at MRI	94 (73.4%)	96 (75.0%)	106 (82.8%)	101 (78.9%)	93 (72.7%)	83 (64.8%)
<i>P</i> value (95% CI of difference, %)	.695 (-9.4 to 6.2)		.132 (-1.1 to 8.9)		.012 (1.8 to 13.8)	
No. tumors correctly characterized at MRI	169 (68.7%)	164 (66.7%)	198 (80.5%)	188 (76.4%)	166 (67.5%)	148 (60.2%)
<i>P</i> value (95% CI of difference, %)	.492 (-3.8 to 7.8)		.059 (-0.1 to 8.3)		.001 (3.0 to 11.6)	

ference of approximately 22% in the percentage lesion enhancement between gadobenate dimeglumine and gadobutrol.

Together with our findings, these studies suggest that only *r1* differences of a certain magnitude are sufficient to elicit discernable clinical differences in GBCA performance. Thus, intraindividual studies that have compared GBCAs with similar *r1* relaxivity have generally demonstrated similar image quality and diagnostic performance,^{10,11,14} while studies that have compared GBCAs with higher *r1* have demonstrated measurable differences in image preference and diagnostic performance.¹⁶

In terms of safety, both gadoteridol and gadobutrol, given at a dose of 0.1 mmol/kg of body weight, were safe and well-tolerated in patients with suspected or confirmed brain pathology, with no serious adverse events reported for either agent. The rates of adverse events were similar for the 2 agents and were similar to rates reported previously for the 2 agents in other comparative studies; in the phase II/III study performed in Japan, 8 adverse events in 7 (4.3%) patients were reported following cumulative doses of 0.2 mmol/kg of body weight of both gadobutrol and gadoteridol,⁹ while in a smaller intraindividual comparative study,⁶ neither agent caused any unexpected or serious adverse events during the study period.

The principal limitations of our study are that although 198 of 229 enrolled patients were included in the per-protocol efficacy population, histologic confirmation of disease was available for only 139 patients, of which only 128 were diagnosed as having brain tumors. On the other hand, this population size and the number of confirmed tumors evaluated ($n = 246$) are comparable with previous intraindividual comparisons of GBCAs for brain tumor imaging¹⁴⁻¹⁶ and should be sufficiently robust to provide a true reflection of the comparable performance of these 2 GBCAs. Additionally, a second limitation is that advanced imaging techniques (eg, perfusion, diffusion, and functional techniques) were not performed. Such techniques are often used to improve the grading and characterization of brain tumors and might have improved both diagnostic performance and interreader agreement in this study had they been used. Although previous studies have compared GBCAs for perfusion imaging,¹³ future studies might benefit from including this technique in the imaging protocol.

In summary, the overriding conclusion of our study is that gadoteridol and gadobutrol confer similar image enhancement and diagnostic performance when administered under identical conditions at an approved dose of 0.1 mmol/kg of body weight. The similar performance of these 2 GBCAs shows that the small difference in *r1* values between the 2 agents does not confer any diagnostic advantage. Furthermore, our study confirms the findings of a previous multicenter study^{10,11} showing that the 2-fold higher gadolinium concentration of the gadobutrol formulation has no significant impact on routine morphologic imaging of brain lesions.

CONCLUSIONS

Gadoteridol and gadobutrol at 0.1 mmol/kg of body weight provide similar qualitative and quantitative imaging results for visualization and diagnosis of brain lesions without any significant differences in safety or tolerability.

ACKNOWLEDGMENTS

The authors thank Sally Friend (University of Washington Medical Center, Seattle, Washington), Tomasz Dróżdź (Świętokrzyskie Centrum Onkologii, Kielce, Poland), Matthew White (Nebraska Medical Center, Omaha, Nebraska), Armando Tartaro (Università degli Studi "G. D'Annunzio," Chieti, Italy), Jacqueline Brunetti (Holy Name Hospital, Teaneck, New Jersey), Barbara Paraniak-Gieszczuk (Helimed Diagnostic Imaging, Katowice, Poland), Linda Anderson (Seaman Family MR Research Centre, University of Calgary, Alberta, Canada), Simona Gaudio (Policlinico "Agostino Gemelli," Rome, Italy), and Daniel S. Gurell (University Diagnostic Medical Imaging PC, Bronx, New York) for enrolling patients into the study, and James R. Fink, MD (University of Washington Medical Center, Seattle, Washington) for assistance with recruiting and image scoring. In addition, the authors are indebted to Ningyan Shen, MD, PhD (Bracco Diagnostics, Monroe, New Jersey) for additional statistical analyses performed for this study.

Disclosures: Kenneth R. Maravilla—RELATED: Grant: Bracco Diagnostics,* Comments: funding support for clinical trial study; Support for Travel to Meetings for the Study or Other Purposes: Bracco Diagnostics, Comments: travel support to attend 1-day Investigator meeting prior to start of trial; Provision of Writing Assistance, Medicines, Equipment, or Administrative Support: Bracco Diagnostics, Comments: no monetary value, only statistical support; UNRELATED: Consulting Fee or Honorarium: Bracco, Guerbet; Grants/Grants Pending: Bayer, Bracco, Guerbet; Payment for Development of Educational Presentations: Bracco. Gianpaolo Pirovano—RELATED: Employment: Bracco Diagnostics, Comments: employee of trial-sponsoring company. Miles A. Kirchin—RELATED: Employment: Bracco Diagnostics, Comments: employee of trial-sponsoring company. Toshinori Hirai—RELATED: Consulting Fee or Honorarium: Bracco Diagnostics; Support for Travel to Meetings for the Study or Other Purposes: Bracco Diagnostics. Martin P. Smith—RELATED: Grant: Bracco Diagnostics,* Comments: My institution was paid by Bracco for each patient recruited into this study in order to screen them, complete the required documents, perform the MRIs, and evaluate the images; UNRELATED: Grants/Grants Pending: Bracco Diagnostics,* Comments: paid for recruiting patients for another gadolinium-based contrast agent study; Other: Bayer Pharmaceuticals, Comments: paid for recruiting patients for a gadolinium-based contrast agent study. Mayank Goyal—UNRELATED: Consulting Fee or Honorarium: Covidien, Comments: for teaching engagements; Grants/Grants Pending: Covidien,* Comments: partial funding of the ESCAPE trial; Payment for Lectures Including Service on Speakers Bureaus: Covidien, Comments: for lecturing on acute stroke. Joseph J. Baima—RELATED: Grant: Bracco Diagnostics,* Comments: Principal Investigator in the Bracco Study PH 107. Robert Babbel—RELATED: Grant: Samaritan Health Services.* Jan Žižka—RELATED: Consulting Fee or Honorarium: University Hospital Hradec Kralove.* Asim K. Bag—UNRELATED: Consulting Fee or Honorarium: Guerbet, Comments: Consultant to Dotarem; Advisory Board. Stefano Bastianello—RELATED: Consulting Fee or Honorarium: Bracco Diagnostics, Comments: for evaluating MR imaging. Eva Bueltmann—RELATED: Consulting Fee or Honorarium: Bracco Diagnostics, Comments: honorarium for blinded reading. Małgorzata Urbańczyk-Zawadzka—UNRELATED: Payment for Manuscript Preparation: PZWL; Grants/Grants Pending: John Paul II Hospital, Kraków, Poland. *Money paid to the institution.

REFERENCES

1. Gadavist product label. http://www.accessdata.fda.gov/drugsatfda_docs/label/2011/201277s000lbl.pdf. Accessed April 11, 2014
2. ProHance product label. http://www.accessdata.fda.gov/drugsatfda_docs/label/2010/020131s024lbl.pdf. Accessed April 11, 2014
3. Hao D, Ai T, Goerner F, et al. MRI contrast agents: basic chemistry and safety. *J Magn Reson Imaging* 2012;36:1060-71
4. Rohrer M, Bauer H, Mintorovitch J, et al. Comparison of magnetic properties of MRI contrast media solutions at different magnetic field strengths. *Invest Radiol* 2005;40:715-24
5. Pintaske J, Martirosian P, Graf H, et al. Relaxivity of gadopentetate dimeglumine (Magnevist), gadobutrol (Gadovist), and gadobenate dimeglumine (MultiHance) in human blood plasma at 0.2, 1.5, and 3 Tesla. *Invest Radiol* 2006;41:213-21

6. Koenig M, Schulte-Altedorneburg G, Piontek M, et al. **Intra-individual, randomised comparison of the MRI contrast agents gadobutrol versus gadoteridol in patients with primary and secondary brain tumours, evaluated in a blinded read.** *Eur Radiol* 2013; 23:3287–95
7. Lopes MB, VandenBerg SR, Scheithauer BW. **The World Health Organization classification of nervous system tumors in experimental neuro-oncology.** In: Levine AJ, Schmidek HH, eds. *Molecular Genetics of Nervous System Tumors*. New York: Wiley-Liss; 1993:1–36
8. Kleihues P, Burger PC, Scheithauer BW. **The new WHO classification of brain tumours.** *Brain Pathol* 1993;3:255–68
9. Katakami N, Inaba Y, Sugata S, et al. **Magnetic resonance evaluation of brain metastases from systemic malignancies with two doses of gadobutrol 1.0M compared with gadoteridol: a multicenter, phase II/III study in patients with known or suspected brain metastases.** *Invest Radiol* 2011;46:411–18
10. Peripheral and Central Nervous System Drugs Advisory Committee. FDA Advisory Committee Briefing Document. New Drug Application 201–277. <http://www.fda.gov/downloads/AdvisoryCommittees/CommitteesMeetingMaterials/Drugs/PeripheralandCentralNervousSystemDrugsAdvisoryCommittee/UCM240354.pdf>. Accessed May 8, 2014
11. Center for Drug Evaluation and Research. Statistical Review and Evaluation. Gadovist. <http://www.fda.gov/downloads/AdvisoryCommittees/CommitteesMeetingMaterials/Drugs/PeripheralandCentralNervousSystemDrugsAdvisoryCommittee/UCM255169.pdf>. Accessed May 8, 2014
12. Heiland S, Erb G, Ziegler S, Krix M. **Where contrast agent concentration really matters: a comparison of CT and MRI.** *Invest Radiol* 2010;45:529–37
13. Kanal E, Maravilla K, Rowley HA. **Gadolinium contrast agents for CNS imaging: current concepts and clinical evidence.** *AJNR Am J Neuroradiol* 2014;35:2215–26
14. Greco A, Parker JR, Ratcliffe CG, et al. **Phase III, randomized, double blind, crossover comparison of gadoteridol and gadopentetate dimeglumine in magnetic resonance imaging of patients with intracranial lesions.** *Australas Radiol* 2001;45:457–63
15. Anzalone N, Scarabino T, Venturi C, et al. **Cerebral neoplastic enhancing lesions: multicenter, randomized, crossover intraindividual comparison between gadobutrol (1.0M) and gadoterate meglumine (0.5M) at 0.1mmolGd/kg body weight in a clinical setting.** *Eur J Radiol* 2013;82:139–45
16. Seidl Z, Vymazal J, Mechl M, et al. **Does higher gadolinium concentration play a role in the morphologic assessment of brain tumors? Results of a multicenter intraindividual crossover comparison of gadobutrol versus gadobenate dimeglumine (the MERIT Study).** *AJNR Am J Neuroradiol* 2012;33:1050–58

Interobserver Agreement in the Interpretation of Outpatient Head CT Scans in an Academic Neuroradiology Practice

G. Guérin, S. Jamali, C.A. Soto, F. Guilbert, and J. Raymond



ABSTRACT

BACKGROUND AND PURPOSE: The repeatability of head CT interpretations may be studied in different contexts: in peer-review quality assurance interventions or in interobserver agreement studies. We assessed the agreement between double-blind reports of outpatient CT scans in a routine academic practice.

MATERIALS AND METHODS: Outpatient head CT scans (119 patients) were randomly selected to be read twice in a blinded fashion by 8 neuroradiologists practicing in an academic institution during 1 year. Nonstandardized reports were analyzed to extract 4 items (answer to the clinical question, major findings, incidental findings, recommendations for further investigations) from each report, to identify agreement or discrepancies (classified as class 2 [mentioned or not mentioned or contradictions between reports], class 1 [mentioned in both reports but diverging in location or severity], 0 [concordant], or not applicable), according to a standardized data-extraction form. Agreement regarding the presence or absence of clinically significant or incidental findings was studied with κ statistics.

RESULTS: The interobserver agreement regarding head CT studies with positive and negative results for clinically pertinent findings was 0.86 (0.77–0.95), but concordance was only 75.6% (67.2%–82.5%). Class 2 discrepancy was found in 15.1%; class 1 discrepancy, in 9.2% of cases. The κ value for reporting incidental findings was 0.59 (0.45–0.74), with class 2 discrepancy in 29.4% of cases. Most discrepancies did not impact the clinical management of patients.

CONCLUSIONS: Discrepancies in double-blind interpretations of head CT examinations were more common than reported in peer-review quality assurance programs.

ABBREVIATION: CHUM = Centre Hospitalier de l'Université de Montréal

The delivery of optimal radiology services may require continuous vigilance and perhaps quality assurance interventions.^{1–3} The content of these interventions may not be evident, however. In addition, the manner in which the error, discrepancy, and disagreement should be handled both in theory and in clinical practice is evolving.⁴

Discrepancies in peer-review approaches have been known for a long time.^{5–7} In 1959, Garland⁸ claimed that radiologists missed approximately 30% of tuberculosis cases in screening chest x-ray examinations.⁹ Garland's report launched a series of investiga-

tions that continue today. However, there is no consensus on a standard method or protocol for evaluating errors and discrepancies in imaging reports, and rates published in the literature differ widely.^{1–3,10–14} Multiple variations in study parameters, including sampling sources, methods, imaging modalities, specialties, categories, interpreter training levels, and degrees of blinding, may have contributed to this wide spectrum.^{2,3,9}

Recently, CT and MR imaging reports of the head, neck, and spine were re-read by staff neuroradiologists, and a 2% clinically significant discrepancy rate was found, an excellent result compared with the 3%–6% radiologic error rates published in general radiology practices.^{3,15,16}

To anyone who has studied reliability or precision of diagnostic imaging tests, such levels of disagreement between interpretations may appear unbelievably low. Peer-review quality assurance “errors and discrepancies” and disagreements in reliability studies of imaging test interpretations may not measure the same things. Discrepancies in the reporting of imaging studies can thus be approached from at least 2 different perspectives.

Received May 9, 2014; accepted after revision June 12.

From the Department of Radiology (G.G., C.A.S., F.G., J.R.), Centre Hospitalier de l'Université de Montréal, Notre-Dame Hospital, Montreal, Quebec, Canada; and Laboratory of Interventional Neuroradiology (S.J., J.R.), Centre Hospitalier de l'Université de Montréal, Notre-Dame Hospital Research Centre, Montreal, Quebec, Canada.

Please address correspondence to Jean Raymond, MD, CHUM–Notre-Dame Hospital, Interventional Neuroradiology, 1560 Sherbrooke East, Pavillon Simard, Room Z12909, Montreal, Quebec, Canada H2L 4M1; e-mail: jean.raymond@umontreal.ca

<http://dx.doi.org/10.3174/ajnr.A4058>

From a quality assurance point of view, optimal radiology services require continuous quality assurance interventions. One report is the true right one, and discrepancies are errors that must be minimized. Performance can be measured; deviations and outliers can be identified, and appropriate measures can then be taken to improve performance.¹⁻³

A different vocabulary is used when discrepancies are examined from a scientific point of view. In the typical absence of a criterion standard of “truth,” the uncertainty is a reality that must be admitted and taken into account when using imaging reports for clinical decisions. Reliability and agreement can be measured by using proper methods, including independent readings; and concordant or diverging verdicts can be tabulated and summarized, though imperfectly, by using marginal sums and appropriate statistical tools (such as κ statistics). No test and certainly no imaging study requiring an element of interpretation will ever be perfectly repeatable.

Reconciliation between these 2 perspectives is desirable. The credibility of quality assurance programs disconnected from scientific methods is shaky. If only errors could be defined, perhaps as discrepancies beyond “normal discrepancies.” Unfortunately attempts to define an acceptable level of radiologic discrepancy are probably futile. Multiple variables are at play, and distinctions, even between acceptable discrepancy and negligence, may remain blurry.¹⁷

To our knowledge, reliability and agreement in the independent interpretation of head CT scans by expert neuroradiologists in a routine academic clinical practice have not been reported. In contrast to a peer-review approach, examining discrepancies after independent interpretations of clinical cases in everyday practice and looking for consensus on discrepant cases may provide a realistic and favorable framework for continuous quality improvement for each and all professionals, rather than the identification of specific deviant individuals. With this end in view, we studied the discrepancy in independent double readings of outpatient head CT scans in an academic practice. We hypothesized that our study would show a discrepancy rate in the range of $\geq 5\%$.

MATERIALS AND METHODS

The present article was written in accordance with the “Guidelines for Reporting Reliability and Agreement Studies” framework.¹⁸ A protocol was initially prepared, including a detailed data-collection form for each interpretation, prespecified plans for comparing pairs of reports, and statistical analyses. The protocol was discussed and accepted by all participating radiologists and by the head of the clinical neuroradiology service. Readers were informed that the identity of the participating radiologists would remain anonymous. As part of a pilot quality-improvement program, the necessity for obtaining informed consent was waived. Nonurgent outpatient head CT scans were interpreted on a double-blind basis within 2 consecutive days. The 2 reports were analyzed by 1 author (G.G.), who filled out the corresponding data-collection forms.

Patients

During 12 months (between July 2012 and July 2013), 119 outpatients (71 women; 48 men; mean age, 60.5 ± 15.4 years) with head CT requests from any outpatient clinic, including a neuro-oncol-

ogy clinic ($n = 35$, 29.4%), were randomly selected from the Centre Hospitalier de l'Université de Montréal (CHUM), Notre-Dame Hospital imaging library on a basis of 2–5 cases per week, on certain weeks only (cases could only be submitted to double reading when the first adjudicator was available to review reports in a timely fashion). No formal sample-size calculations were performed because this pilot project was considered exploratory, but a statistical consultant advised that >100 patients were necessary to provide meaningful confidence intervals.

Cases were blindly and randomly selected and sent back, just as a “new case” would be interpreted within the workflow of the next consecutive day, for an independent re-reading. Cases that, by chance, happened to be read twice by the same reader were excluded from analyses ($n = 5$). CT scans from the emergency department or performed on hospitalized patients were excluded for methodologic and ethical considerations. The first report was automatically erased from the patient file when the second report became available but was saved in a separate file for this study. In this fashion, the second reader never had access to the first report, and head CTs were interpreted twice in a blinded fashion. All examinations were anonymously integrated in the daily workload, and both reports were dictated within 2 consecutive days. The second readings were made available to clinicians and became the permanent official report, unless flagged by G.G. When a finding was mentioned in the first but not in the second report, the second reader was asked to review or discuss the case with the first reader and amend the report if necessary. When the most inclusive or “safest” report was the second official one, no immediate revision was undertaken.

Readers

The readings were performed by 8 certified staff radiologists, fellowship-trained and specialized in neuroradiology with clinical experience ranging from 1 to 37 years (mean, 17.9 ± 7.3 years; median, 17 years). They worked independently, rotating each day within the same tertiary institution. They were aware that a study was ongoing but could not guess which patients were included ($<1\%$ of the patients being examined were part of the study).

Data Extraction and Analyses

Each report was analyzed by 1 author (G.G.) to extract the following 4 items: 1) response to the question raised by the requesting physician, 2) major/clinically pertinent findings (defined as related to the clinical question or requiring immediate management, such as recent ischemic lesions, tumor evolution or recurrence, acute sinusitis, and so forth), 3) incidental findings (defined as not being related to the clinical question and requiring no immediate management, such as chronic sinusitis, cerebral atrophy, old lacunar infarcts), 4) further investigations being proposed.

Pairs of reports were compared, and agreement was assessed regarding the following: 1) detection agreement or agreement on the presence or absence of an abnormal finding, sorting out positive-versus-negative test results; and 2) agreement on the description of the findings regarding the 4 previously mentioned items. For each of the first 3 items (clinical question, major clinically pertinent finding, and incidental finding), concordance was rated according to the content of the reports (and not according to the

Table 1: Agreement among double-blind reports

	Concordant Readings (CI 95%)	Class 2 Discrepancies	Class 1 Discrepancies
Clinically pertinent findings	75.6% (n = 90) (67.2%–82.5%)	15.1% (n = 18)	9.2% (n = 11)
Incidental findings	65.5% (n = 78) (56.6%–73.5%)	29.4% (n = 35)	5% (n = 6)
Answer to the clinician's question	86.7% (n = 85) (78%–92.5%)	12.2% (n = 12)	1% (n = 1)
Further investigations	86.6% (n = 103) (79.2%–91.6%)	13.4% (n = 16)	

Table 2: Class 2 discrepancies in clinically significant findings

	Age (yr)	Sex	NC or CE	Context	Discrepancies
1	66	F	CE	F-up meningioma	Progression vs stable
2	82	F	CE	F-up meningioma	Progression vs stable
3	47	M	NC	F-up subdural hematoma	Complete resolution vs partial regression
4	60	F	NC	F-up hydrocephalus	Stable vs progression
5	47	F	CE	F-up metastasis resection	No recurrence vs recurrence suspicion
6	77	M	CE	Lymphoma	Normal vs clival lesion
7	76	M	NC	F-up pituitary apoplexy	Unchanged vs new hemorrhage
8	63	M	NC	F-up glaucoma	Optic nerve atrophy vs normal
9	66	M	NC	F-up subdural hematoma	Persistence vs complete resolution
10	64	F	NC	Post-op adenoma	Residual mass vs normal
11	75	F	CE	Seizures	Schizencephaly vs no mention
12	74	M	NC	F-up subdural hematoma	Rebleeding vs no rebleeding
13	58	F	CE	F-up metastases	No recurrence vs recurrence
14	37	F	NC	F-up glioblastoma	Herniation vs no mention
15	62	F	CE	Breast CA	Choroidal mets suspicion vs no mention
16	77	F	NC	Dementia	White matter disease vs no mention
17	76	M	CE	Memory loss	Cerebral trophy vs no mention
18	42	M	CE	F-up glioblastoma	Progression vs stable

Note:—NC indicates noncontrast CT; CE, contrast-enhanced CT; CA, cancer; F-up, follow-up; Post-op, postoperative; mets, metastases.

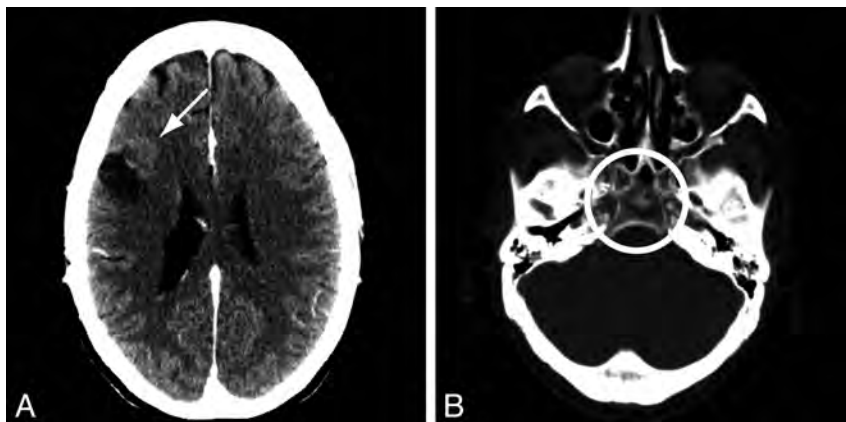


FIG 1. Class 2 discrepancies in pertinent findings. A, A patient followed for recurrence of a resected breast cancer metastasis; one reader reported a recurrence (arrow), whereas the other observer did not mention this finding. B, A lytic lesion of the clivus (circle) was reported by one but not the other reader.

clinical significance of the discordance) as the following: not applicable (in the absence of a clinical question or of any finding); 0, concordant; class 1 discordance, the same findings noted in both reports but in different locations or diverging in severity; class 2 discordance, the finding was not mentioned in one of the reports or opinions diverged on the evolution or recurrence of a lesion.

Subsequently, a senior author (J.R.) who had not previously read any of the examinations reviewed all reports and data-collection forms (unmasked).

Statistical Analyses

The concordance rates for responses to the clinical questions raised by the referring physicians, clinically pertinent findings, incidental findings, and proposed investigations were tabulated to

provide proportions (with 95% confidence intervals). Class 2 discrepancies in reporting pertinent clinical findings from contrast-enhanced and nonenhanced CTs were compared by using the Fisher exact test. The Cohen κ was calculated (with 95% confidence intervals) for the presence/absence of clinically pertinent findings and incidental findings. κ values were interpreted according to Landis and Koch.¹⁹

RESULTS

There were 119 CT examinations; 53 (44.5%) were contrast-enhanced. A clinical question was formulated by the requesting physician in 98 cases (82.4%) and the reader responses were concordant

in 88.1% of cases (95% CI, 80.6%–92.9%). The Cohen κ for positive studies was 0.86 (0.77–0.95) and 0.59 (0.45–0.74) for the presence/absence of any clinically pertinent findings and for incidental findings, respectively.

Readings were in agreement for 75.6% (67.2%–82.5%), 65.5% (56.6%–73.5%), and 86.6% (79.2%–91.6%) of clinically pertinent findings, incidental findings, and recommendations for further investigations, respectively (Table 1). Rates were similar for the 2 subgroups (referred from the neuro-oncology clinic or from all other clinics).

Class 2 discrepancies in reporting clinically pertinent findings were found in 18 cases (15.1%). They are summarized in Table 2. Examples include the presence or absence of a tumor recurrence

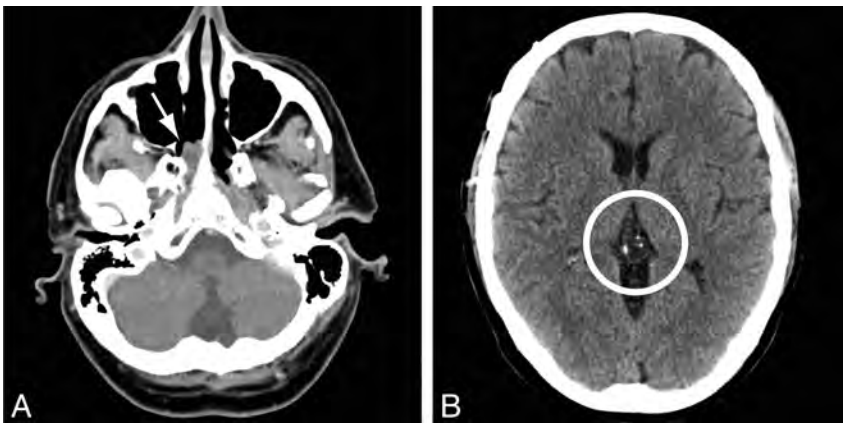


FIG 2. Class 2 discrepancies in incidental findings. *A*, One reader reported a polypoid posterior nasal lesion (arrow), whereas the other observer did not mention this incidental finding. *B*, A pineal cyst (circle) was mentioned in only 1 of the 2 reports.

($n = 4$, Fig 1A), the growth of a meningioma ($n = 2$), the evolution of chronic subdural hematomas ($n = 2$), and the presence of a lytic bone lesion (Fig 1B). These discrepancies were normally distributed between readers ($n = 1, 3, 5, 7, 11, 5, 3, 1$ for 36 discrepant reports). There was no significant difference between contrast-enhanced ($n = 9$ of 53) and nonenhanced studies ($n = 9$ of 66, $P = .62$).

Class 1 discrepancies in clinically pertinent findings were seen in the interpretation of 11 cases. Examples include the location of recent ischemic lesions ($n = 2$), tumor extensions ($n = 2$), or the disconnection of a ventricular shunt ($n = 1$).

Class 2 discrepancies in reporting incidental findings were seen in 35 cases. Examples include the presence or absence of white matter disease ($n = 10$), chronic sinusitis ($n = 6$), old strokes ($n = 5$), atrophy ($n = 4$), a nasal polyp (Fig 2A), or a pineal cyst (Fig 2B). Class 1 discrepancies in calling incidental findings were seen in 6 cases. Examples include the location of lacunar infarcts ($n = 2$) or the extension of chronic sinusitis ($n = 2$).

The senior author confirmed the discrepancies identified by the first adjudicator in all cases, except for 2 minor modifications in the categorization of incidental findings.

DISCUSSION

The salient findings of this study are the following: 1) The interobserver agreement regarding head CT outpatient studies with positive and negative findings measured by the Cohen κ was 0.86 (almost perfect), but 2) class 2 discrepancies in clinically pertinent findings were still found in 15% of cases, above the 5% level we expected from the 3%–6% discrepancy rates reported in previously published neuroradiologic peer-review studies.^{3,15,16}

Different aspects of study design may explain our results. The definitions we used were somewhat arbitrary, though they were inspired from similar studies.^{3,16} Perhaps they were rigorously applied during data extraction. In the absence of standardization of reporting, some variability in the attribution of categoric verdicts to the content of reports of different styles is inevitable.

The levels of disagreement that we observed are not unheard of. Robinson et al²⁰ investigated the concordance among 3

independent observers. Their study showed agreement in 51%, 61%, and 74% of abdominal, chest, and skeletal x-rays, respectively. They also assessed performance by calculating κ statistics of interobserver agreement. Weighted κ values between pairs of observers were higher with skeletal (0.76–0.77) than with chest (0.63–0.68) or abdominal (0.50–0.78) examinations. In a meta-analysis conducted by Wu et al,² the global discrepancy rate was 7.7% (including a major discrepancy rate of 2.4%). The major discrepancy rate varied according to body region: It was lower for head (0.8%) and spine CT (0.7%) than chest (2.8%) and abdominal CT (2.6%). Blinding of the reference

radiologist to the initial report was, however, associated with higher discrepancy rates compared with studies that lacked blinding: Not blinding the initial report yielded a much lower major discrepancy rate (2.0%; 95% CI, 1.4%–2.7%) than with blinding (12.1%; 95% CI, 4.4%–29.4%).

Hence, we believe that the main reason for the difference between our results and those of previous studies on discrepancies in head CT reports is that we used double-blind reporting. A possible explanation is that knowledge of the initial report may lead to a “satisfaction of search” error that reduces discrepancies.²

Most quality assurance studies published in the literature have assessed the discrepancy rates found through a peer-review approach.^{2,3,6,9,21} In that context, the opinion of the second observer is considered the criterion standard, and discrepancies are meant to be errors. However, in many cases, the second radiologist worked in a setting that differs from the normal clinical context. The second interpretation can be biased in many ways, by knowledge of the first interpretation, knowledge of the identity of the first interpreter, or even knowledge of the clinical evolution and outcome of the patient (ie, hindsight bias). Of course, the second interpreter is also aware that he or she is working within an audit process.³ Other studies that have used a double-blind method in a much larger number of patients have found lower discrepancy rates than those reported here.¹ In this case, we suspect that the medical director or quality assurance radiologist knowingly working within an audit process may have biased, according to a principle of charity, the selective identification of the most serious discrepancies only. Our study being done in an anonymous, nonblaming context, with no intent to identify deviant individuals differs from many quality assurance studies and may explain why more frequent disagreements could be identified. Fortunately, most discrepancies had minimal clinical impact in terms of patient management or outcome.

Discrepancies in the present study do not necessarily mean errors. The use of clinical judgment, in assessing the impact of calling a suspicious-but-uncertain finding or the pertinence of reporting an incidental finding, for example, may lead to variations from one individual report to the other.

Some societies have proposed guidelines for peer-review

methods or for holding discrepancy meetings.^{22,23} Many questions remain unanswered, such as which method ought to be followed or which is most efficient.^{22,23} A survey of practices in the United Kingdom has recently shown wide variation in discrepancy meetings.²⁴ Larson and Nance⁶ have emphasized that “peer review can either serve as a coach or a judge, but it cannot do both well.” There is a recent trend to shift away from the identification of deviant individuals to the overall improvement of systems and patient care, to move away from a blame culture to one of continuous feedback, learning from each other’s methods of working and reporting and from each other’s mistakes.

The work presented here was a pilot project. It was not designed to compete with commercially available peer-review systems. The process requires the active participation of a dedicated third physician (in addition to the 2 readers) and is time-consuming. In this particular case, the third physician was a senior resident, who considered the experience informative and enriching. Perhaps this pilot project could shed some light on how we should understand and design methods purported to improve patient care, including systematic quality assurance peer-review systems or discrepancy meetings. Neuroradiologists who participated in this project were initially surprised to see that discrepancies were common. They have started to exchange opinions on the pertinence of incidental findings, for example. The sharing of practices in an open-minded learning context could be a modest but meaningful step, from solo practices to a richer, more stimulating professional experience, perhaps more favorable to better radiology services.

Limitations

There were many limitations to this study: The number of cases was small, the heterogeneity of clinical presentations was modest, and the technique was restricted to head CT. Not all patients were represented, for inpatients and cases from the emergency department were excluded. Participating radiologists were from a single, tertiary referral center. The population we studied had a high prevalence of positive findings. We were careful to explicitly define categories in advance in the research protocol and to make judgments as objective as possible, but such categorization as “incidental finding” remains a judgment that may depend on context, interpretation, local culture, and training. The data were extracted by a single individual, and the review of the data extraction forms by the second rater was not blinded. We had made that decision at the time of study design: A blinded second adjudication could have produced variability in categorization and discrepancies between adjudicators, at the risk of launching an infinite regress. These limitations may have contributed to overestimating agreement between reports. Yet, discrepancies were more frequent than those in previous, nonblinded, peer-review reports, a finding that remains to be confirmed by other double-blind studies.

Comparing reports that widely vary in format and style is fastidious and time-consuming. Some standardization of reporting may be necessary to ease the identification of discrepancies. Adopting a rule of keeping the most inclusive report as the official report, combined with double-blind reading, may increase the number of “overcalls,” compared with a single reading. Finally, no attempt was made to determine the real diagnoses, for the study was focused on agreement and not on diagnostic accuracy.

We did not try to study the causes of discrepancies. The protocol neither included a clinical follow-up period, to monitor what actually happened to study patients, nor tried to evaluate the theoretic impact of any report on clinical decisions.

CONCLUSIONS

Double-blind reading of head CT scans can show class 2 discrepancies in 15% of cases. If duplicated, this finding should be taken into account when planning quality assurance interventions.

ACKNOWLEDGMENTS

The authors acknowledge the participation of the attending neuroradiologists of CHUM and the contribution of the PACS and imaging library staff.

Disclosures: Jean Raymond—UNRELATED: Grants/Grants Pending: Canadian Institutes of Health Research,* Comments: funding for a clinical trial (Canadian UnRuptured aneurysm Endovascular versus Surgery [CURES]).* *Money paid to the institution.

REFERENCES

1. Soffa DJ, Lewis RS, Sunshine JH, et al. **Disagreement in interpretation: a method for the development of benchmarks for quality assurance in imaging.** *J Am Coll Radiol* 2004;1:212–17
2. Wu MZ, McInnes MD, Blair Macdonald D, et al. **CT in adults: systematic review and meta-analysis of interpretation discrepancy rates.** *Radiology* 2014;270:717–35
3. Babiarz LS, Yousem DM. **Quality control in neuroradiology: discrepancies in image interpretation among academic neuroradiologists.** *AJNR Am J Neuroradiol* 2012;33:37–42
4. McCoubrie P, FitzGerald R. **Commentary on discrepancies in discrepancy meetings.** *Clin Radiol* 2014;69:11–12
5. Bender LC, Linnau KF, Meier EN, et al. **Interrater agreement in the evaluation of discrepant imaging findings with the Radpeer system.** *AJR Am J Roentgenol* 2012;199:1320–27
6. Larson DB, Nance JJ. **Rethinking peer review: what aviation can teach radiology about performance improvement.** *Radiology* 2011;259:626–32
7. Mucci B, Murray H, Downie A, et al. **Interrater variation in scoring radiological discrepancies.** *Br J Radiol* 2013;86:20130245
8. Garland LH. **Studies on the accuracy of diagnostic procedures.** *Am J Roentgenol Radium Ther Nucl Med* 1959;82:25–38
9. Berlin L. **Accuracy of diagnostic procedures: has it improved over the past five decades?** *AJR Am J Roentgenol* 2007;188:1173–78
10. Abujudeh HH, Boland GW, Kaewlai R, et al. **Abdominal and pelvic computed tomography (CT) interpretation: discrepancy rates among experienced radiologists.** *Eur Radiol* 2010;20:1952–57
11. Agrawal A, Pandit M, Kalyanpur A. **Systematic survey of discrepancy rates in an international teleradiology service.** *Emerg Radiol* 2011;18:23–29
12. Chung JH, Strigel RM, Chew AR, et al. **Overnight resident interpretation of torso CT at a level 1 trauma center an analysis and review of the literature.** *Acad Radiol* 2009;16:1155–60
13. Goddard P, Leslie A, Jones A, et al. **Error in radiology.** *Br J Radiol* 2001;74:949–51
14. Loevner LA, Sonners AI, Schulman BJ, et al. **Reinterpretation of cross-sectional images in patients with head and neck cancer in the setting of a multidisciplinary cancer center.** *AJNR Am J Neuroradiol* 2002;23:1622–26
15. Borgstede JP, Lewis RS, Bhargavan M, et al. **RADPEER quality assurance program: a multifacility study of interpretive disagreement rates.** *J Am Coll Radiol* 2004;1:59–65
16. Siegle RL, Baram EM, Reuter SR, et al. **Rates of disagreement in imaging interpretation in a group of community hospitals.** *Acad Radiol* 1998;5:148–54

17. Berlin L. **Radiologic errors and malpractice: a blurry distinction.** *AJR Am J Roentgenol* 2007;189:517–22
18. Kottner J, Audige L, Brorson S, et al. **Guidelines for Reporting Reliability and Agreement Studies (GRRAS) were proposed.** *J Clin Epidemiol* 2011;64:96–106
19. Landis JR, Koch GG. **The measurement of observer agreement for categorical data.** *Biometrics* 1977;33:159–74
20. Robinson PJ, Wilson D, Coral A, et al. **Variation between experienced observers in the interpretation of accident and emergency radiographs.** *Br J Radiol* 1999;72:323–30
21. Herman PG, Gerson DE, Hessel SJ, et al. **Disagreements in chest roentgen interpretation.** *Chest* 1975;68:278–82
22. O’Keeffe MM, Piche S, Mason AC. **The Canadian Association of Radiologists (CAR) Guide to Peer Review Systems.** Approved September 10, 2011; Amended July 16, 2012. http://www.car.ca/uploads/standards%20guidelines/20120831_en_peer-review.pdf. Accessed November 21, 2013
23. The Royal College of Radiologists. **Standards for radiology discrepancy meetings.** London ETRCoR, 2007. https://www.rcr.ac.uk/docs/radiology/pdf/Stand_radiol_discrepancy.pdf. Accessed November 21, 2013
24. Prowse SJ, Pinkey B, Etherington R. **Discrepancies in discrepancy meetings: results of the UK national discrepancy meeting survey.** *Clin Radiol* 2014;69:18–22

Social Media and the Neuroradiologist: A Brief Introduction

A. Radmanesh and R.T. Fitzgerald

Use of social media by medical professionals is increasing. Twitter (twitter.com, San Francisco, California) is the social media platform that has attracted the most attention. Recently, radiologists have used Twitter as a “virtual lounge” to engage in professional conversations on topics related to their shared interests or concerns. Twitter has been increasingly used during scientific national and international meetings as an effective means of communication. A recent study by Hawkins (@MattHawkinsMD) et al¹ demonstrated the increasing trend of Twitter use during the Annual Meetings of the Radiological Society of North America. Our personal experience also showed increased and effective use of Twitter during the Annual Meeting and Chapter Leadership Conference of the American College of Radiology.

For this year’s American Society of Neuroradiology (ASNR) Annual Meeting, the hashtag #ASNR14 was registered with Symplur (Upland, California), a healthcare social media analytics organization. Hashtags are words or phrases preceded with the symbol # and serve as tags for following and tracking conversations and groups of messages. Our on-the-scene experience and analysis of the aggregated data by Symplur shows that neuroradiologists have not embraced social media as fast as other radiologists. A total of 404 tweets using the “ASNR14” hashtag were logged from May 15 to May 23, 2014 (Fig 1). These tweets were posted by 51 users, including 11 radiologists attending the meeting, 12 radiologists not attending the meeting, 8 non-radiologists, and 20 institutional accounts. Of the total tweets, 56% (227 of 404) were sent by 3 users, all of whom were radiologists.

Twitter is a microblogging platform that logs almost 340 million tweets (small on-line posts consisting of 140 or fewer characters) each day. Such platforms are not just the domains of teenagers; corporations, politicians, the news media, and social movements have recognized the potential power of these

new methods of communication and networking.² Familiarity with such social media provides neuroradiologists with a powerful tool for communication, which can be used for professional (and personal) purposes.

Common concerns when discussing social media for healthcare are privacy and patient information confidentiality. A simple caveat must always be kept in mind: what is posted remains forever. As such, one should refrain from posting anything that could be offensive to others or embarrassing to the sender. Many platforms provide options to limit others’ access to one’s posts per the user’s discretion. However, it is better to assume that such “firewalls” are not always functional. Another concern regarding social media is the potential infringement of one’s professional life into one’s personal life. Many people use their Twitter account only for professional purposes and do not post private matters. Others create more than one account and use each account for a different purpose.

The value of social media for networking is underestimated. Through the use of hashtags (searchable tags), people from around the world can find ongoing or past conversations on topics of interest. They can join these conversations by including the same hashtag in their posts, thus allowing an unlimited number of people to join the conversation, a true “Conversation Sans Frontières.” Some conversations stay on the Web for potential interested parties who may not be on-line in real time, and participants can join and engage in them at their convenience. An off-line user can be invited into conversations by inclusion of his or her Twitter ID (handle) preceded by “@.” Such networking potentials offer great value for busy neuroradiologists and can open new horizons for professional links and research collaborations. For those exploring the job market, this platform may be used for researching job opportunities.³

Twitter has been used in national and international conferences as a means of communication between individuals regarding particular sessions as well as a platform for organizers to make meeting-related announcements. Twitter allows people from around the world who are not physically present to join the conversation and be part of the “think tank.” For example, the ASNR 2014 debate session on the role of diffusion tensor imaging in traumatic brain injury prompted a stimulating and energetic Twitter conversation between individuals

From the Mallinckrodt Institute of Radiology (A.R.), Washington University School of Medicine, St Louis, Missouri; and Department of Radiology (R.T.F.), University of Arkansas for Medical Sciences, Little Rock, Arkansas.

Please address correspondence to Alireza Radmanesh, MD, Mallinckrodt Institute of Radiology, 510 S Kingshighway Blvd, Campus Box 8131, St Louis, MO 63110; e-mail: radmanasha@mir.wustl.edu; @AliRadmanMD

<http://dx.doi.org/10.3174/ajnr.A4036>

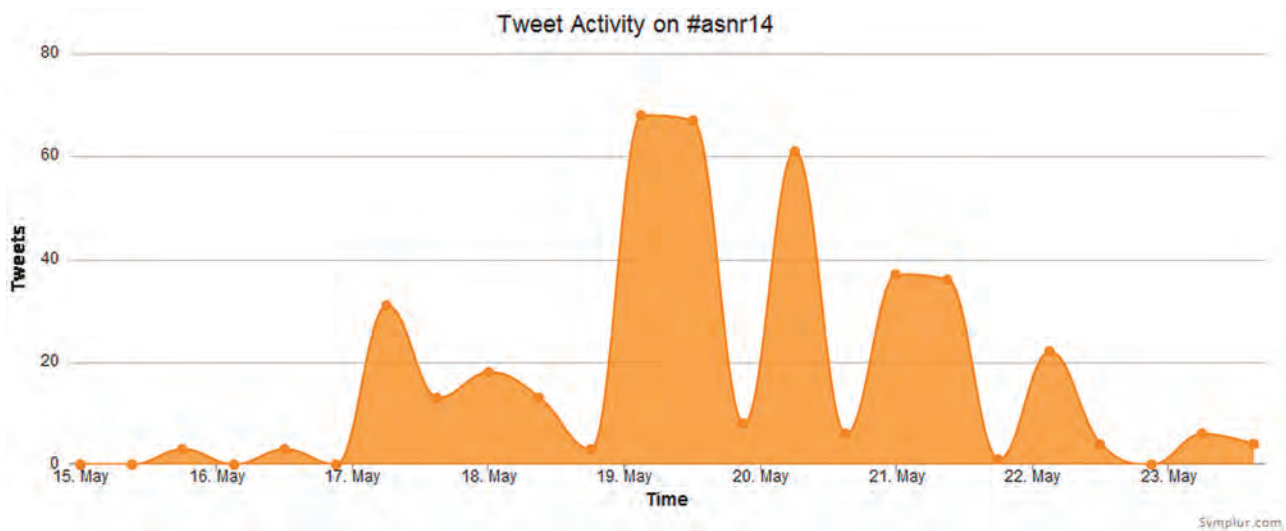


FIG 1. Frequency of posted tweets related to the 2014 Annual Meeting of the American Society of Neuroradiology (ASNR 2014) from May 15–23, 2014.

from around the globe, all thanks to the use of session- and meeting-related hashtags (#TBI, #ASNR14, #debate).

REFERENCES

1. Hawkins CM, Duszak R, Rawson JV. **Social media in radiology: early trends in Twitter microblogging at radiology's largest international meeting.** *J Am Coll Radiol* 2014;11:387–90
2. Dodd GD, III, Naeger DM. **Radiology online: information, education, and networking—a summary of the 2012 Intersociety Committee Summer Conference.** *J Am Coll Radiol* 2013;10:345–48
3. Harolds JA. **Tips for a physician in getting the right job part III: networking and social media, references, and recruiters.** *Clin Nucl Med* 2013;38:805–07

Patient Selection for Stroke Endovascular Therapy— DWI-ASPECTS Thresholds Should Vary among Age Groups: Insights from the RECAST Study

F. Danière, K. Lobotesis, P. Machi, O. Eker, I. Mourand, C. Riquelme, X. Aygnac, J.F. Vendrell, G. Gascou, J. Fendeleur, C. Dargazanli, R. Schaub, H. Brunel, C. Arquizan, A. Bonafé, and V. Costalat



ABSTRACT

BACKGROUND AND PURPOSE: The purpose of this study was to evaluate the benefits of endovascular intervention in large-vessel occlusion strokes, depending on age class.

MATERIALS AND METHODS: A clinical management protocol including intravenous treatment and mechanical thrombectomy was instigated in our center in 2009 (Prognostic Factors Related to Clinical Outcome Following Thrombectomy in Ischemic Stroke [RECAST] study). All patients with acute ischemic stroke with an anterior circulation major-vessel occlusion who presented within 6 hours were evaluated with an initial MR imaging examination and were analyzed according to age subgroups (younger than 50 years, 50–59 years, 60–69 years, 70–79 years; 80 years or older). The mRS score at 3 months was the study end point.

RESULTS: One hundred sixty-five patients were included in the analysis. The mean age was 67.4 years (range, 29–90 years). The mean baseline NIHSS score was 17.24 (range, 3–27). The mean DWI-derived ASPECTS was 6.4. Recanalization of TIC1 2b/3 was achieved in 80%. At 3 months, 41.72% of patients had a good outcome, with a gradation of prognosis depending on the age subgroup and a clear cutoff at 70 years. Only 19% of patients older than 80 years had a good outcome at 3 months (mean ASPECTS = 7.4) with 28% for 70–79 years (mean ASPECTS = 6.8), but 58% for 60–69 years (mean ASPECTS = 6), 52% for 50–59 years (mean ASPECTS = 5.9), and 72% for younger than 50 years (mean ASPECTS = 6.3). In contrast, the mortality rate was 35% for 80 years and older, and 26% for 70–79 versus 5%–9% for younger than 70 years.

CONCLUSIONS: The elderly may benefit from thrombectomy when their ischemic core volume is low in comparison with younger patients who still benefit from acute recanalization despite larger infarcts. Stroke volume thresholds should, therefore, be related and adjusted to the patient's age group.

Ischemic stroke is the third leading cause of death in France (fourth in the United States^{1,2}), leading to significant disability.³ The World Health Organization predicts an increasing number of strokes in Europe during the next 10 years.⁴ Intravenous recombinant tissue plasminogen activator for cerebral arterial occlusion is the established therapy to date for acute ischemic stroke. The odds ratio benefit is 1.28–1.7 for a favorable outcome versus

a placebo^{5,6} within 4.5 hours after stroke onset. Initially, being older than 80 years of age was established as a bad prognostic factor in intravenous treatment^{7–10} and even considered an exclusion criterion.⁵ Today, this statement is seen as controversial, with recent studies having shown that elderly patients would still benefit from IV tPA.^{11,12} In addition, new therapeutic strategies in stroke units are increasingly involving adjunctive endovascular techniques when fibrinolysis is contraindicated or has failed or when large and proximal intracranial vessels are occluded.^{13–17} Previous studies have shown that mechanical thrombectomy by using Stentriever (Trevo; Stryker, Kalamazoo, Michigan), in particular new stent retrievers,¹⁸ was successful in achieving a high rate of arterial recanalization and favorable clinical outcome in large-vessel occlusion.^{19–21} Nevertheless, inclusion and exclusion criteria for these new invasive strategies are still being evaluated and may need to be optimized to avoid futile recanalization, particularly for fragile patients. The purpose of this study was to investigate the benefits and safety of these new recanalization devices according to age subgroups.

Received October 31, 2013; accepted after revision June 23, 2014.

From the Departments of Neuroradiology (F.D., P.M., O.E., C.R., J.F.V., G.G., C.D., A.B., V.C.), Neurology (I.M., X.A., C.A.), and Anesthesiology (J.F.), CHU Montpellier, Montpellier, France; Imaging Department (K.L.), Imperial College Healthcare National Health Service Trust, Charing Cross Hospital, London, United Kingdom; Department of Medical Statistics (R.S.), CHU Montpellier, Arnaud de Villeneuve Hospital, University of Montpellier, Montpellier, France; and Department of Neuroradiology (H.B.), CHU Marseille, Hôpital La Timone, Marseille, France.

Please address correspondence to Vincent Costalat, PhD, CHU Montpellier, Neuroradiology, Avenue Augustin Fliche, Montpellier, France; e-mail: v-costalat@chu-montpellier.fr

Indicates article with supplemental on-line table.

<http://dx.doi.org/10.3174/ajnr.A4104>

MATERIALS AND METHODS

Data Selection

From September 2009 to May 2012, a management protocol including intravenous therapy and mechanical thrombectomy was instigated in our center RECAST study, which followed discussion and consensus agreement among our neurologists, neuroradiologists, and anesthesiologists. Prospective data collection via a specific stroke data base was organized under the supervision of dedicated clinical research assistance. Acceptance by the institutional ethics committee of Montpellier-Centre Hospitalier Universitaire was also obtained. Only anterior circulation strokes were retrieved from this data base to select a more homogeneous stroke population. At the time of the study, 211 patients had been entered and 165 were retrieved for analysis, from which 151 had completed follow-up assessment at 3 months. Patients were divided following age subgroups: younger than 50 years, between 50 and 59 years, between 60 and 69 years, between 70 and 79 years, and older than 80 years.

Initial Neurologic Examination

At first, a stroke neurologist systematically evaluated all patients with the suspicion of an acute ischemic stroke and assessed the severity of the neurologic deficit by using the National Institutes of Health Stroke Scale score.

MR Imaging Protocol

A comprehensive acute brain MR imaging examination with MRA was performed as part of the initial patient work-up. MR imaging examinations were performed by using a 1.5T whole-body MR imaging system (Magnetom Avanto; Siemens, Erlangen, Germany), equipped with a standard 16-channel receive-only head-neck coil. Standardized imaging protocol covering the entire brain included an axial isotropic diffusion-weighted echo-planar spin-echo sequence with $b=0$ and $b=1000$ s/mm² (TR/TE, 4900/90 ms; 25 sections; section thickness, 5 mm; gap, 0 mm; voxel size, $1.9 \times 1.9 \times 5$ mm³; acquisition time, 44 seconds), axial T2*-weighted gradient-echo sequences, fluid-attenuated inversion-recovery sequences, and axial T2. T2 gradient-echo imaging was performed to screen for intracranial hemorrhage. DWI sequences were acquired, as was an apparent diffusion coefficient map to identify the infarct core. The Alberta Stroke Program Early CT Score, calculated on DWI, was used to assess and quantify the infarct core.^{22,23} FLAIR and T2 were also used to corroborate information regarding the time from symptom onset. FLAIR can assess slow flow in the distal territory, showing bright vessels, which are associated with good outcome after recanalization with IV treatment. Parenchymal FLAIR hypersignal was used by the neurologic team to decide on IV treatment but did not interfere with the decision-making for mechanical treatment. When the FLAIR findings were negative, the T2 was cancelled to shorten the examination. When they were positive, the T2 was performed to confirm a physiologic aging of the infarct suspected on the FLAIR. Then, a high-spatial-resolution 3D contrast-enhanced MR angiography with centric k -space ordering was performed just before the perfusion imaging with a fast-spoiled gradient refocused-echo sequence in the coronal plane: (TR/TE, 3.44/1.2 ms; flip angle, 28°; FOV, 300×197 mm; voxel size, $1 \times 0.8 \times 0.7$

mm³). One hundred four sections with a thickness of 0.7 mm in the coronal plane, providing arterial coverage from the aortic arch to the cranial vertex, were obtained during a 22-second acquisition. A phase-contrast solution (0.2 mL/kg, 0.5-mmol/kg Gd-DTPA) was then injected and flushed with 20 mL of saline at 2 mL/s for the contrast-enhanced MRA acquisition. It depicts intracranial and extracranial large-vessel occlusion. If the clinical/radiologic mismatch was not clear, a gradient-echo echo-planar imaging sequence (TR/TE, 1420/25 ms; 25 sections; section thickness, 5 mm; gap, 0 mm; pixel size, $1.8 \times 1.8 \times 5$ mm³; 65 dynamic frames at intervals of 2 seconds) was performed synchronized with an intravenous contrast agent injection (0.5-mmol/kg Gd-DTPA) with a flow rate of 6 mL/s followed by a flush of 20-mL saline. These perfusion-weighted images were used to assess a diffusion/perfusion mismatch. If the clinical/radiologic mismatch appeared to be self-evident (ie, an ASPECTS 8 with an NIHSS score of 18), no perfusion was mandatory because the NIHSS score was considered the main biomarker of impaired brain perfusion.

The mean time between MR imaging door entrance and MR imaging ending was 22 minutes. Furthermore, patients with wake-up stroke are treated routinely in our center on the basis of the FLAIR sequences. Since 2009, the mechanical recanalization in our clinical center follows MR imaging selection. A second neuroradiologist not involved in the initial management reviewed all MR imaging.

Stroke Management Protocol

Inclusion criteria for endovascular therapy were the following: proximal major vessel occlusion (middle cerebral artery: proximal M1, distal M1, M1-M2, M2; intracranial carotid bifurcation; tandem M1 with an ICA occlusion), all patients with stroke with a relevant deficit, and a time window of <6 hours. Exclusion criteria were the following: MR imaging-ASPECTS <5; NIHSS of <8; and spontaneous NIHSS improvement. The FLAIR/T2 images were not considered exclusion criteria for mechanical treatment.

An ASPECTS ≥ 5 on DWI sequences and an NIHSS of ≥ 8 were the only criteria of inclusion written down for the protocol. Nevertheless, the interventionist and neurologist were systematically checking for a clinical/radiologic mismatch between DWI and NIHSS to confirm their decision. If unclear (ie, ASPECTS 5 and NIHSS 9), the PWI/DWI mismatch was studied to confirm the presence of salvageable brain based on the TTP map, with a threshold set at +5 seconds (Fig 1).^{24,25} The volume and the topography of the penumbra were analyzed by the neuroradiologist regarding the volume ratio (PWI/DWI) and the functional importance of the cortical area involved in this expected salvageable brain. The main goal was to avoid any futile recanalization.

For all patients with ischemic stroke presenting with a large-vessel occlusion confirmed on MR imaging, 2 therapeutic options were proposed, depending on the time from symptom onset and contraindications to intravenous thrombolysis. Stand-alone thrombectomy was performed in patients who were outside the IV fibrinolytic therapeutic window (ie, between 4.5 and 6 hours)^{26,27} and in patients with any contraindications to IV fibrinolysis, (eg, warfarin, anticoagulation therapy with international normalized ratio of >1.5, recent surgery, or history of hemorrhage/hematoma). A combined therapy, including IV fibrinolysis

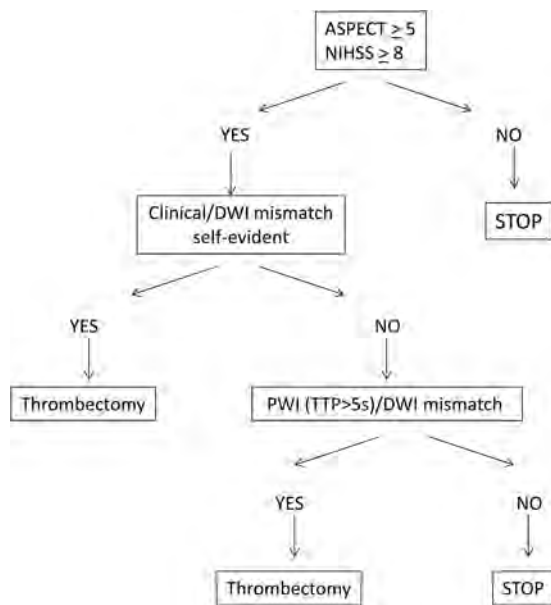


FIG 1. Use of DWI/PWI mismatch in patient selection.

(0.9 mg/kg) and thrombectomy, was chosen in all other cases within 4.5 hours after symptom onset.

Device

Endovascular procedures were performed by using several stent retrievers (Solitaire FR; Covidien, Irvine, California; Revive; Codman Neurovascular, Raynham, Massachusetts; Trevo). These devices are a stent-based thrombectomy system with a closed-cell design and a longitudinal split section. They are delivered through a standard microcatheter (inner lumen diameter of 0.021 inches or 0.027 inches) via a 0.016-inch nitinol push wire.

Mechanical Thrombectomy Protocol

After MR imaging, the anesthesiologist followed the patient with stroke to the angi suite and performed a fast induction while the interventionist was preparing the table. This general anesthesia did not delay the routine management and offered very quick access to the target vessel without patient motion. All procedures were performed via a femoral artery approach. An 8F or 9F Merci balloon guiding catheter (Concentric Medical, Mountain View, California) was introduced through a femoral sheath into the appropriate carotid artery. A 0.21-inch-internal-diameter microcatheter, Prowler Select Plus (Codman & Shurtleff, Raynham, Massachusetts), Vasco 21 (Balt, Montmorency, France), or Headway microcatheter (MicroVention, Tustin, California), was navigated distal to the point of occlusion over a 0.014-inch steerable microwire. The stent retriever was then introduced through the microcatheter, and the device was deployed across the occluding thrombus and maintained in place for a few minutes (3–7 minutes). After this time, the fully deployed stent retriever and the delivery microcatheter were gently pulled back together and recovered through the balloon guiding catheter. Manual aspiration was performed through the hemostatic valve during the retrieval to reverse the flow and to aspirate clot debris eventually present in the lumen of the guide catheter. The integrity of the stent was consistently checked after every pass.

In our protocol, the patient received a full dose of IV fibrinolytics (0.9 mg/kg) when administered as a combined treatment. No additional IA fibrinolytics were allowed in the protocol to decrease the hemorrhagic-transformation risk.²⁸

Recanalization was quantified by the Thrombolysis In Cerebral Infarction scale.²⁹ Successful recanalization was defined as TICI 2b or 3 in all treatable vessels. If the treatable vessel was not opened to at least TICI 2b with a maximum of 5 passes of the thrombectomy device, then the treatment was considered failed. All TICI scores were independently reviewed by a second neuro-radiologist not involved in the procedure.

Postoperative Management

CT was carried out in the angi suite after all procedures were performed, to screen for immediate hemorrhagic transformation, any unforeseen procedural complications, or initial blood-brain barrier disruption, which was defined as an intraparenchymal enhancement on a noncontrast CT, just after the mechanical treatment. A further CT or MR imaging was performed at 24 hours. All 24-hour CT and MR imaging was reviewed by a second neuroradiologist.

Three-Month Follow-Up

All patients were scheduled for a 3-month evaluation with a stroke neurologist. The modified Rankin Scale score at 3 months was recorded^{30,31} and dichotomized as a favorable outcome with a score of 0–2 or an unfavorable outcome with a score of 3–6.

Statistical Analysis

For univariate analysis, a global description of the sample was realized by giving the frequencies for categoric variables. Quantitative variables were described with means and SDs, but also with median, minimum, maximum, and interquartiles (25th and 75th centiles) if the distributions were not normal (tested with the Shapiro-Wilk test). For continuous variables, the comparisons of means between groups (good Rankin versus bad Rankin) were performed by using a parametric test (Student *t* test) or a non-parametric test (Mann-Whitney *U* test) if the distributions were not normal. For categoric variables, the comparisons of percentages between groups (good Rankin versus bad Rankin) were made by using the χ^2 test or the Fisher exact test if the χ^2 was not valid.

For multivariate analysis, the variables included in the logistic model were those that have been shown previously to be associated with studied dependent variables. To determine the relative importance of the predictor variables with regard to the modified Rankin Scale score, we performed multivariate analysis by using logistic regression. A stepwise selection of the variables was used. Age, NIHSS score on arrival, and duration of the obstruction were entered into the model as continuous variables. The categoric variables entered in the model were dichotomous. Odds ratios and their confidence intervals were calculated. The α -to-enter and α -to-exit were set at .05. To assess the predictive ability of the model, we calculated the concordance rate between predicted and observed responses. The goodness of fit of the logistic regression model was assessed by using the likelihood ratio test and the Hosmer-Lemeshow test. All analyses were 2-tailed, with a *P* value < .05 considered statistically significant. Statistical analysis was per-

formed by using SAS statistical software, Version 9 (SAS Institute, Cary, North Carolina).

RESULTS

Patient Characteristics

From September 2009 to May 2012, 211 consecutive patients with large-vessel occlusions were treated by mechanical thrombectomy in the setting of acute ischemic stroke (On-line Table). One hundred sixty-five of 211 patients who had an anterior circulation stroke (47% women and 53% men) were retrieved from the data base. The mean age was 67.4 years (range, 29–90 years). The mean baseline NIHSS was 17.24 (range, 3–27) with higher initial NIHSS in the elderly: 16.39 (younger than 50 years), 15.24 (50–59 years), 16.54 (60–69 years), 17.84 (70–79 years), and 18.83 (80 years and older).

Acute MR Imaging

The mean ASPECTS on DWI was 6.40: 6.39 (younger than 50 years), 6.27 (50–59 years), 5.77 (60–69 years), 6.43 (70–79 years), and 7.25 (80 years and older) (On-line Table). Sixteen patients had an intracranial carotid bifurcation occlusion (9.7%); 49, a tandem occlusion (29.7%); 93, an M1 occlusion (56.36%); and 7, an M2 occlusion (4.24%). MR perfusion was performed in 38 cases and showed a perfusion-diffusion mismatch in 33 cases (87%).

Recanalization Rate

Fifty-five patients (33.0%) received stand-alone thrombectomy, and 110 patients (67.0%) received a combined therapy, less frequent in those 80 years of age and older (On-line Table). Recanalization of TICI 3 was achieved in 59.76% (98 patients); and TICI 2b, in 20.12% (33 patients), with an overall successful recanalization rate of 80% (TICI 3 and TICI 2b) with no differences among age groups. A failure rate was observed in 20%. The mean time between symptom onset and recanalization was 311 minutes (range, 153–574 minutes) with a mean number of stent retriever passes of 2 without differences among age groups.

Peri- and Postprocedural Complications

There were 27 (16.46%) periprocedural complications: 17 distal or collateral emboli, 5 dissections, 2 arterial injuries, and 3 spasms (On-line Table). These were without significant differences among ages: 11% (younger than 50 years), 22% (50–59 years), 22% (60–69 years), 26% (70–79 years), and 19% (80 years and older). Initial blood-brain barrier disruption was found in 87 patients (62.59%). Intracranial hemorrhagic transformation on day 1 on CT or MR imaging was depicted in 41 patients (25.95%) and was symptomatic in only 7.6%, but it was not correlated to the recanalization rate. Ischemic lesion worsening on day 1 on CT or MR imaging was found in 38 patients (25%). There was a significant increase in ischemic lesion worsening for patients who did not experience recanalization (58%) versus those who did (17%), ($P < .05$).

Clinical Follow-Up

At 3 months, 14 patients were lost to follow-up (8.5%), while 41.72% of patients had a good outcome (On-line Table). A clear

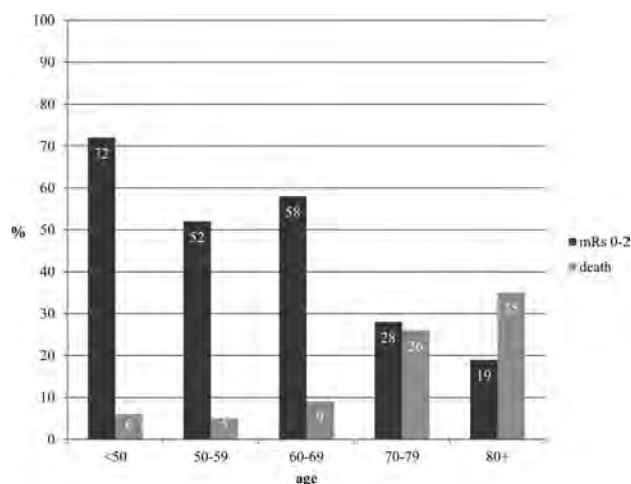


FIG 2. Modified Rankin Scale score and mortality according to the age subgroups.

Table 1: Univariate analysis

Variable (mRS)	No.	Mean	Minimum	Median	Maximum	P Value
Age						
0/1/2	63	61.49	30.00	63.00	88.00	<.001
3/4/5/6	88	71.32	29.00	75.00	90.00	
Initial NIHSS score						
0/1/2	62	15.74	3.00	16.00	27.00	<.001
3/4/5/6	86	18.21	6.00	19.00	27.00	
Initial ASPECTS						
0/1/2	63	6.35	1.00	7.00	9.00	.599
3/4/5/6	84	6.50	0.00	7.00	10.00	
Time						
0/1/2	51	285.67	153.00	282.00	458.00	.013
3/4/5/6	64	335.50	179.00	321.00	855.00	
Passes						
0/1/2	63	1.63	0.00	1.00	5.00	.005
3/4/5/6	87	2.15	0.00	2.00	5.00	

graduation of the prognosis was observed depending on age, with a cutoff at 70 years (Fig 2). The mean age of patients with a good outcome was 61.5 years of age (95% CI, 57.97–65.01) and 71.3 years of age (95% CI, 68.71–73.93) in cases of bad outcome ($P < .001$) (Table 1). Only 19% of patients who were older than 80 years (28% for 70–79 years) had a good outcome at 3 months (mRS 0–2), with a 35% mortality rate (26% for 70–79 years). On the contrary, good outcome was observed between 52% and 78% of patients younger than 70 years; mortality, in <10% of patients (Fig 2). The mean modified Rankin Scale score at 3 months was 2.22 for patients younger than 70 years and 4.1 for those older than 70 years. On multivariate analysis, the odds ratio of bad outcomes was 1.092 (95% CI, 1.046–1.141) for every 5 years' increase in age ($P < .0001$) (Table 2). The NIHSS were higher in those older than 70 years (18.1 versus 16.1; $P = .007$). There were no other statistically significant differences comparing patients older than 70 years with those younger than 70 years in terms of sex, ASPECTS, recanalization rate, site of occlusion, time from onset to recanalization, or complications.

On univariate analysis, criteria significantly related to a good outcome at 3 months were initial NIHSS and rapid recanalization (Tables 1 and 3). The mean initial NIHSS related to good outcome was 15.74 versus 18.21 for bad outcome ($P < .001$). A faster recanalization time was associated with a good outcome

Table 2: Multivariate analysis

Variable	Adjusted Odds Ratio	95% CI	P Value
Age			
Each 5-yr increase	1.092 ^a	1.046–1.141	<.0001
Time			
Each 60-min increase	1.009 ^b	1.002–1.016	.0093

^a For each 5-year increase, risk of bad outcomes at 3 months increased by 1.092.

^b For each 60-minute increase to recanalization time, bad outcomes at 3 months increased by 1.009.

Table 3: Univariate analysis

Variable	mRS 0–2	mRS 3–6	P Value
TICI score			
0/1/2a	13.33%	86.67%	.000329
2b/3	49.58%	50.42%	
BBBD			
No	50.98%	49.02%	.095777
Yes	36.25%	63.75%	
Aggravation of lesions			
No	53.33%	46.67%	.000021
Yes	11.76%	88.24%	
Hemorrhagic or complications at 24 hr			
No	49.06%	50.94%	.002663
Yes	21.05%	78.95%	

Note:—BBBD indicates blood-brain barrier disruption.

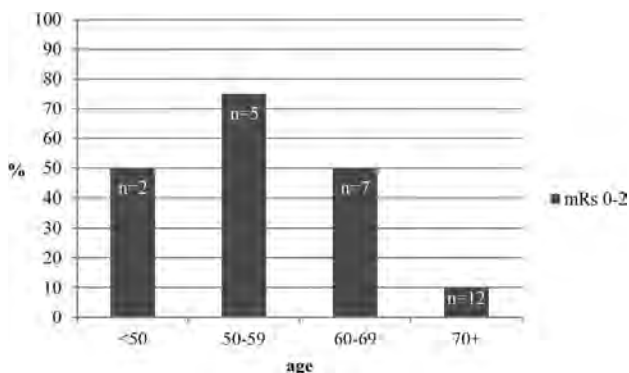


FIG 3. Outcome in protocol deviation (DWI-ASPECTS <5) according to the age subgroups.

(mean time between onset and recanalization, 286 minutes and 7 seconds; $P = .013$). The number of stent retriever passes was also correlated to clinical outcome with 1.63 passes for good outcome and 2.15 for bad outcome ($P = .005$). The final recanalization score of TICI 0/1/2a was a strong predictive factor for a bad outcome with 87% with mRS 3–6 ($P < .0003$) at 3 months. Hemorrhagic transformation and ischemic core extension at 24 hours were correlated to bad outcome: 79% with mRS 3–6 ($P = .002$) and 88% with mRS 3–6 ($P < .001$), respectively. On multivariate analysis, only recanalization time was significant, with an odds ratio of 1.009 (95% CI, 1.002–1.016) for each increase of 60 minutes ($P = .0093$).

Protocol Deviation

We included 26 patients with a DWI-ASPECTS <5: 2 younger than 50 years, five 50–59 years, seven 60–69 years, eleven 70–79 years, and one 80 years or older (Fig 3). Initially, patients with an ASPECTS lower than 5 should not have been considered for mechanical treatment. Nevertheless, the ASPECTS in an emergency has been, in some cases, underestimated by the team on call. Sometimes they decided to try to recanalize the patient to avoid a

malignant infarction; this choice explained a large part of the protocol deviation observed in this series. Each case has been reviewed by 2 neuroradiologists to independently assess the initial ASPECTS and confirm clear protocol deviations. For this population, the mean NIHSS for 70 years and older was 17.24, and the mean time between symptom onset and recanalization was 311 minutes. Stand-alone thrombectomy was received by 58%, and combined procedures, by 42%. The recanalization rate of TICI 2b/3 was achieved in 80%, and no difference existed in terms of complications periprocedurally and symptomatic hemorrhagic transformation. Only 10% of elderly patients (older than 70) who were considered to have protocol deviations regarding the initial DWI-MR imaging (ASPECTS <5) achieved a good outcome, whereas 60% of patients younger than 70 years of age had an mRS 0–2 at 3 months. Ten patients in the subgroup 70–79 years were considered to have protocol deviations and were all rated mRS 3–6 at 3 months. The ASPECTS for good outcomes at 3 months was 7.4 for 80 years and older versus 6.31 for younger than 50 years, 5.91 for 50–59 years, 6 for 60–69 years, and 6.8 for 70–79 years.

Three patients had NIHSS of <8: 1 in the 50–59 year group, 1 in the 60–69 year group, and 1 in the 80 years and older group. These 3 patients presented with a symptomatic large-vessel stroke of the ICA. The practitioners on call should have waited for a clinical worsening of the patients before any treatment. Nevertheless, vertigo and dizziness were reported by 1 patient with an intracranial ICA occlusion with an NIHSS score of 5. Because the high risk of major stroke has been proved in the case of symptomatic large-vessel stroke, they decided to treat by a mechanical approach. In the second patient, a symptomatic intracranial carotid bifurcation occlusion was reported with a fluctuating deficit of 5–8. The patient scored 5 at admission, and despite the threshold of 8 having not been reached, the team decided to proceed with treatment. The 2 patients were fully recanalized with a final mRS 1 at 3 months. In the third case, the NIHSS score was 7 for an MCA occlusion, and the ASPECTS was 10. The team on call considered a clinical/radiologic mismatch present and started a combined strategy despite the initial NIHSS score of 7.

DISCUSSION

This study showed a major difference in patient outcome depending on age (Tables 1 and 2). In our study, 50% of patients were younger than 70 years. In this younger population, thrombectomy efficacy results seemed to be promising, with a good outcome between 58% and 72% at 3 months. These results are encouraging, considering that these patients initially had a severe neurologic deficit and a high NIHSS, secondary to a large-vessel occlusion, which is poorly treatable by IV fibrinolysis alone.³²⁻³⁴ A large prospective multicenter study of large-vessel occlusion in the anterior circulation treated with the Solitaire device (Covidien) recently reported a favorable outcome (mRS 0–2) in 57.9% of patients with a mean age of 68.4 years, underlining the importance of age.³⁵ In our study, there seemed to be an important cutoff at 70 years of age. Only 19% of patients older than 80 years had a good outcome at 3 months and 28% between 70 and 79 years. Loh et al³⁶ also showed that elderly patients were more

likely to die from their stroke than those younger than 80 years, regardless of recanalization success (48% of mortality versus 15%; OR, 5.5).

These differences among age subgroups are not related to a delayed presentation time for the elderly. The time between onset of symptoms and recanalization was, in our study, roughly equivalent among age classes. Moreover, from a technical point of view, the TICI 2b/3 recanalization rate was roughly similar between elderly and younger patients, despite predictably more challenging anatomy in the elderly. The complication rate was in the same range for each age subgroup. Consequently, the huge difference in outcomes between elderly and young patients cannot be solely related to technical issues.

However, physiologic differences may influence this poor outcome in elderly patients. The NIHSS is a well-established initial prognostic factor for intravenous thrombolysis³⁷ and endovascular treatment.^{38,39} The mean initial NIHSS for a good outcome at 3 months was 15.74 versus 18.21 for an unfavorable one. For the same level of occlusion and initial DWI-ASPECTS, the mean initial NIHSS was higher in elderly patients (18.1 for 70 years and older versus 16.1 for younger than 70 years). A higher NIHSS at entrance for the same level of occlusion could be the direct consequence of a physiologically less effective collateral blood supply and therefore larger penumbra in the elderly. The elderly also have less vascular reserve^{40,41}; hence infarct progression may be more rapid and may hence lead to a worse outcome. Furthermore, the elderly have a higher baseline disability before acute stroke and higher rates of in-hospital complications and are more likely to have comorbidities and stroke complications.^{42,43}

Initial ASPECTS is an important prognostic criterion closely related to decision-making. Initial infarct size has proved to be a critical determinant of the 3-month functional outcome.⁴⁴⁻⁴⁶ Nezu et al⁴⁷ showed that an ASPECTS ≤ 5 was related to symptomatic intracerebral hemorrhage and ASPECTS ≥ 7 corresponded to an mRS score of 0–2 at 3 months in patients treated with rtPA. In our stroke-management protocol, an ASPECTS < 5 was therefore initially chosen as an exclusion criterion. Nevertheless, the predictive values of the ASPECTS for a good outcome were very different depending on age subgroups. Our study showed that the 80 years and older group who had good outcomes at 3 months had a mean ASPECTS of 7.4 versus 5.91 for patients 60–69 years. In addition, 90% of elderly patients who were considered to have protocol deviations on initial DWI-MR imaging (high initial necrotic core with ASPECTS < 5) demonstrated a bad outcome at 3 months. On the contrary, we observed a good outcome for DWI-MR imaging protocol deviation (ASPECTS < 5) in patients younger than 70 years of age in 60%, suggesting that younger patients may still benefit from acute recanalization despite more extensive initial necrotic cores. Initial MR imaging selection criteria may need to be refined and adapted, depending on the age class, with probably a lower necrotic core volume (initial ASPECTS-DWI) cutoff for elderly patients and, conversely, a higher volume for patients younger than 70 years. DWI lesion volume was not estimated in our study. Using DWI lesion volume could be an interesting work to purchase and

ameliorate our results on the ASPECTS evaluation to refine the conclusion.⁴⁸

In our protocol, stand-alone thrombectomy and combined therapy were not randomized. Most interesting, we noticed that there was no significant difference in terms of prognosis in individuals treated by endovascular therapy alone versus combined treatment in each age category. Nevertheless, the synergy between thrombolysis and endovascular therapy was more frequent in young patients due to rare IV contraindications in this subgroup compared with the elderly. Because Davalos et al³⁹ demonstrated that combined therapy had better results at 3 months than stand-alone cases (66% of good outcome versus 42%), there is a possibility that this synergistic effect of combined treatment, more often missing in the elderly group, also influenced the final results.

Limitations

One of the major limits of our study is the use of decades to separate our patients, which does not consider physiologic age and baseline health. Comorbidities and life expectancy have to be studied jointly with age in making the decision to treat. Furthermore, thrombectomy has been performed by many different neuroradiologists in our center who all had different rates of learning to manage the procedure. In addition, 14 patients (8.5%) were lost to follow-up and were not analyzed. These results need further confirmation.

CONCLUSIONS

Endovascular techniques promise good results in terms of prognosis in patients with an acute stroke secondary to a major vessel occlusion. Patients younger than 70 years benefit the most from acute mechanical recanalization in anterior circulation stroke (mRS 0–2, 62%; mortality, $< 10\%$). However, in patients older than 70 years, the benefit of mechanical thrombectomy drops (mortality between 26% and 35% with only 19%–26% chance of good outcome). Elderly patients usually benefit if their baseline ischemic volume is low in comparison with young patients who may still benefit from acute recanalization despite larger necrotic cores. Stroke-volume thresholds should, therefore, be related and adjusted to the patient's age class.

Disclosures: Alain Bonafé—UNRELATED: Consultancy: Covidien,* Stryker,* Vincent Costalat—UNRELATED: Consultancy: Covidien, Stryker, MicroVention, Codman, Balt; Payment for Lectures (including service On Speakers Bureaus): Stryker, Balt, MicroVention, Codman; Payment for Development of Educational Presentations: Covidien, MicroVention, Stryker; Travel/Accommodations/Meeting Expenses Unrelated to Activities Listed: MicroVention, Sequent, Stryker, Codman. *Money paid to the institution.

REFERENCES

1. Roger VL, Go AS, Lloyd-Jones DM, et al. **Heart disease and stroke statistics: 2011 update: a report from the American Heart Association.** *Circulation* 2011;123:e18–e209
2. Miniño AM, Murphy SL, Xu J, et al. **Deaths: final data for 2008.** *Natl Vital Stat Rep* 2011;59:1–126
3. Kelly-Hayes M, Beiser A, Kase CS, et al. **The influence of gender and age on disability following ischemic stroke: the Framingham study.** *J Stroke Cerebrovasc Dis* 2003;12:119–26
4. Truelsen T, Piechowski-Jozwiak B, Bonita R, et al. **Stroke incidence**

- and prevalence in Europe: a review of available data. *Eur J Neurol* 2006;13:581–98
5. Hacke W, Kaste M, Bluhmki E, et al. **Thrombolysis with alteplase 3 to 4.5 hours after acute ischemic stroke.** *N Engl J Med* 2008;359:1317–29
 6. **Tissue plasminogen activator for acute ischemic stroke: the National Institute of Neurological Disorders and Stroke rt-PA Stroke Study Group.** *N Engl J Med* 1995;333:1581–87
 7. Longstreth WT Jr, Katz R, Tirschwell DL, et al. **Intravenous tissue plasminogen activator and stroke in the elderly.** *Am J Emerg Med* 2010;28:359–63
 8. Berrouschot J, Rother J, Glahn J, et al. **Outcome and severe hemorrhagic complications of intravenous thrombolysis with tissue plasminogen activator in very old (> or =80 years) stroke patients.** *Stroke* 2005;36:2421–25
 9. Engelter ST, Bonati LH, Lyrer PA. **Intravenous thrombolysis in stroke patients of > or = 80 versus < 80 years of age: a systematic review across cohort studies.** *Age Ageing* 2006;35:572–80
 10. Heuschmann PU, Kolominsky-Rabas PL, Misselwitz B, et al. **Predictors of in-hospital mortality and attributable risks of death after ischemic stroke: the German Stroke Registers Study Group.** *Arch Intern Med* 2004;164:1761–68
 11. Wardlaw JM, Murray V, Berge E, et al. **Recombinant tissue plasminogen activator for acute ischaemic stroke: an updated systematic review and meta-analysis.** *Lancet* 2012;379:2364–72
 12. García-Caldentey J, Alonso de Lecinana M, Simal P, et al. **Intravenous thrombolytic treatment in the oldest old.** *Stroke Res Treat* 2012;2012:923676
 13. Smith WS, Sung G, Saver J, et al. **Mechanical thrombectomy for acute ischemic stroke: final results of the Multi MERCI trial.** *Stroke* 2008;39:1205–12
 14. Rha JH, Saver JL. **The impact of recanalization on ischemic stroke outcome: a meta-analysis.** *Stroke* 2007;38:967–73
 15. Mazighi M, Serfaty JM, Labreuche J, et al. **Comparison of intravenous alteplase with a combined intravenous-endovascular approach in patients with stroke and confirmed arterial occlusion (RECANALISE study): a prospective cohort study.** *Lancet Neurol* 2009;8:802–09
 16. Roth C, Papanagiotou P, Behnke S, et al. **Stent-assisted mechanical recanalization for treatment of acute intracerebral artery occlusions.** *Stroke* 2010;41:2559–67
 17. Penumbra Pivotal Stroke Trial Investigators. **The Penumbra Pivotal Stroke Trial: safety and effectiveness of a new generation of mechanical devices for clot removal in intracranial large vessel occlusive disease.** *Stroke* 2009;40:2761–68
 18. Saver JL, Jahan R, Levy EI, et al. **Solitaire flow restoration device versus the Merci retriever in patients with acute ischaemic stroke (SWIFT): a randomised, parallel-group, non-inferiority trial.** *Lancet* 2012;380:1241–49
 19. Castaño C, Dorado L, Guerrero C, et al. **Mechanical thrombectomy with the Solitaire AB device in large artery occlusions of the anterior circulation: a pilot study.** *Stroke* 2010;41:1836–40
 20. Costalat V, Machi P, Lobotesis K, et al. **Rescue, combined, and stand-alone thrombectomy in the management of large vessel occlusion stroke using the Solitaire device: a prospective 50-patient single-center study: timing, safety, and efficacy.** *Stroke* 2011;42:1929–35
 21. Machi P, Costalat V, Lobotesis K, et al. **Solitaire FR thrombectomy system: immediate results in 56 consecutive acute ischemic stroke patients.** *J Neurointerv Surg* 2012;4:62–66
 22. Pexman JH, Barber PA, Hill MD, et al. **Use of the Alberta Stroke Program Early CT Score (ASPECTS) for assessing CT scans in patients with acute stroke.** *AJNR Am J Neuroradiol* 2001;22:1534–42
 23. Barber PA, Demchuk AM, Zhang J, et al. **Validity and reliability of a quantitative computed tomography score in predicting outcome of hyperacute stroke before thrombolytic therapy: ASPECTS Study Group—Alberta Stroke Programme Early CT Score.** *Lancet* 2000;355:1670–74
 24. Butcher KS, Parsons M, MacGregor L, et al. **Refining the perfusion-diffusion mismatch hypothesis.** *Stroke* 2005;36:1153–59
 25. Wittsack HJ, Ritzl A, Fink GR, et al. **MR imaging in acute stroke: diffusion-weighted and perfusion imaging parameters for predicting infarct size.** *Radiology* 2002;222:397–403
 26. Hacke W, Kaste M, Fieschi C, et al. **Intravenous thrombolysis with recombinant tissue plasminogen activator for acute hemispheric stroke: the European Cooperative Acute Stroke Study (ECASS).** *JAMA* 1995;274:1017–25
 27. Hacke W, Kaste M, Fieschi C, et al. **Randomised double-blind placebo-controlled trial of thrombolytic therapy with intravenous alteplase in acute ischaemic stroke (ECASS II): Second European-Australasian Acute Stroke Study Investigators.** *Lancet* 1998;352:1245–51
 28. Furlan A, Higashida R, Wechsler L, et al. **Intra-arterial prourokinase for acute ischemic stroke: the PROACT II study—a randomized controlled trial. Prolyse in Acute Cerebral Thromboembolism.** *JAMA* 1999;282:2003–11
 29. IMS II Trial Investigators. **The Interventional Management of Stroke (IMS) II study.** *Stroke* 2007;38:2127–35
 30. Rankin J. **Cerebral vascular accidents in patients over the age of 60. II. Prognosis.** *Scott Med J* 1957;2:200–15
 31. van Swieten JC, Koudstaal PJ, Visser MC, et al. **Interobserver agreement for the assessment of handicap in stroke patients.** *Stroke* 1988;19:604–07
 32. Saqqur M, Uchino K, Demchuk AM, et al. **Site of arterial occlusion identified by transcranial Doppler predicts the response to intravenous thrombolysis for stroke.** *Stroke* 2007;38:948–54
 33. Linfante I, Llinas RH, Selim M, et al. **Clinical and vascular outcome in internal carotid artery versus middle cerebral artery occlusions after intravenous tissue plasminogen activator.** *Stroke* 2002;33:2066–71
 34. Molina CA, Alexandrov AV, Demchuk AM, et al. **Improving the predictive accuracy of recanalization on stroke outcome in patients treated with tissue plasminogen activator.** *Stroke* 2004;35:151–56
 35. Pereira VM, Gralla J, Davalos A, et al. **Prospective, multicenter, single-arm study of mechanical thrombectomy using Solitaire flow restoration in acute ischemic stroke.** *Stroke* 2013;44:2802–07
 36. Loh Y, Kim D, Shi ZS, et al. **Higher rates of mortality but not morbidity follow intracranial mechanical thrombectomy in the elderly.** *AJNR Am J Neuroradiol* 2010;31:1181–85
 37. Adams HP Jr, Davis PH, Leira EC, et al. **Baseline NIH Stroke Scale score strongly predicts outcome after stroke: a report of the Trial of Org 10172 in Acute Stroke Treatment (TOAST).** *Neurology* 1999;53:126–31
 38. Costalat V, Lobotesis K, Machi P, et al. **Prognostic factors related to clinical outcome following thrombectomy in ischemic stroke (RECOSt study): 50 patients prospective study.** *Eur J Radiol* 2012;81:4075–82
 39. Dávalos A, Pereira VM, Chapot R, et al. **Retrospective multicenter study of Solitaire FR for revascularization in the treatment of acute ischemic stroke.** *Stroke* 2012;43:2699–705
 40. Epstein SE, Lassance-Soares RM, Faber JE, et al. **Effects of aging on the collateral circulation, and therapeutic implications.** *Circulation* 2012;125:3211–19
 41. Hecht N, He J, Kremenetskaia I, et al. **Cerebral hemodynamic reserve and vascular remodeling in C57/BL6 mice are influenced by age.** *Stroke* 2012;43:3052–62
 42. Di Carlo A, Lamassa M, Pracucci G, et al. **Stroke in the very old: clinical presentation and determinants of 3-month functional outcome: a European perspective—European BIOMED Study of Stroke Care Group.** *Stroke* 1999;30:2313–19
 43. Denti L, Scoditti U, Tonelli C, et al. **The poor outcome of ischemic stroke in very old people: a cohort study of its determinants.** *J Am Geriatr Soc* 2010;58:12–17
 44. Yoo AJ, Chaudhry ZA, Nogueira RG, et al. **Infarct volume is a pivotal**

- biomarker after intra-arterial stroke therapy. *Stroke* 2012;43:1323–30
45. Yoo AJ, Verduzco LA, Schaefer PW, et al. **MRI-based selection for intra-arterial stroke therapy: value of pretreatment diffusion-weighted imaging lesion volume in selecting patients with acute stroke who will benefit from early recanalization.** *Stroke* 2009;40:2046–54
46. Sanák D, Nosal V, Horak D, et al. **Impact of diffusion-weighted MRI-measured initial cerebral infarction volume on clinical outcome in acute stroke patients with middle cerebral artery occlusion treated by thrombolysis.** *Neuroradiology* 2006;48:632–39
47. Nezu T, Koga M, Kimura K, et al. **Pretreatment ASPECTS on DWI predicts 3-month outcome following rt-PA: SAMURAI rt-PA Registry.** *Neurology* 2010;75:555–61
48. de Margerie-Mellon C, Turc G, Tisserand M, et al. **Can DWI-ASPECTS substitute for lesion volume in acute stroke?** *Stroke* 2013;44:3565–67

Percentage Insula Ribbon Infarction of >50% Identifies Patients Likely to Have Poor Clinical Outcome Despite Small DWI Infarct Volume

V.M. Timpone, M.H. Lev, S. Kamalian, L.T. Morais, A.M. Franceschi, L. Souza, and P.W. Schaefer



ABSTRACT

BACKGROUND AND PURPOSE: Large admission DWI infarct volume (>70 mL) is an established marker for poor clinical outcome in acute stroke. Outcome is more variable in patients with small infarcts (<70 mL). Percentage insula ribbon infarct correlates with infarct growth. We hypothesized that percentage insula ribbon infarct can help identify patients with stroke likely to have poor clinical outcome, despite small admission DWI lesion volumes.

MATERIALS AND METHODS: We analyzed the admission NCCT, CTP, and DWI scans of 55 patients with proximal anterior circulation occlusions on CTA. Percentage insula ribbon infarct (>50%, ≤50%) on DWI, NCCT, CT-CBF, and CT-MTT were recorded. DWI infarct volume, percentage DWI motor strip infarct, NCCT-ASPECTS, and CTA collateral score were also recorded. Statistical analyses were performed to determine accuracy in predicting poor outcome (mRS >2 at 90 days).

RESULTS: Admission DWI of >70 mL and DWI–percentage insula ribbon infarct of >50% were among significant univariate imaging markers of poor outcome ($P < .001$). In the multivariate analysis, DWI–percentage insula ribbon infarct of >50% ($P = .045$) and NIHSS score ($P < .001$) were the only independent predictors of poor outcome. In the subgroup with admission DWI infarct of <70 mL ($n = 40$), 90-day mRS was significantly worse in those with DWI–percentage insula ribbon infarct of >50% ($n = 9$, median mRS = 5, interquartile range = 2–5) compared with those with DWI–percentage insula ribbon infarct of ≤50% ($n = 31$, median mRS = 2, interquartile range = 0.25–4, $P = .036$). In patients with admission DWI infarct of >70 mL, DWI–percentage insula ribbon infarct did not have added predictive value for poor outcome ($P = .931$).

CONCLUSIONS: DWI–percentage insula ribbon infarct of >50% independently predicts poor clinical outcome and can help identify patients with stroke likely to have poor outcome despite small admission DWI lesion volumes.

ABBREVIATIONS: IQR = interquartile range; PIRI = percentage insula ribbon infarct

Multimodality imaging is gaining importance as a prognostic tool in the setting of acute stroke; however, finding a reliable and practical imaging marker that can provide additional prognostic information over the National Institutes of Health Stroke Scale alone has been challenging. Current imaging markers that have been shown to be predictive of clinical outcome in acute stroke with proximal anterior circulation occlusions include DWI

infarct volume, Alberta Stroke Program Early CT Score, and “malignant” CTA collateral profile.¹

Large admission DWI infarct volume (>70 mL) is one of the more established imaging markers for poor clinical outcome in acute stroke.^{2,3} DWI lesion volume has been shown to influence response to both intravenous and intra-arterial treatment; specifically, a large pretreatment DWI lesion is recognized as a clinically useful marker for poor treatment response.^{3,4} Clinical outcome is more variable in patients with small infarcts (<70 mL).³ An imaging marker that can more reliably predict clinical outcome in patients with small DWI infarcts has not been established, to our knowledge. Such a marker could be a useful tool for risk-benefit stratification and patient selection for reperfusion therapy.

One potential imaging marker that could help improve prediction of clinical outcome in small infarcts is percentage insular ribbon infarction (PIRI). Prior studies have suggested that prox-

Received April 22, 2014; accepted after revision June 16.

From the Department of Radiology, Massachusetts General Hospital and Harvard Medical School, Boston, Massachusetts.

Abstract previously presented at: Annual Meeting of the Radiological Society of North America, December 1–6, 2013; Chicago, Illinois.

Please address correspondence to Pamela W. Schaefer, MD, Division of Neuroradiology, Department of Radiology, Massachusetts General Hospital, Gray B241H, 55 Fruit St, Boston, MA 02114; e-mail: pschaefer@partners.org

Indicates open access to non-subscribers at www.ajnr.org

<http://dx.doi.org/10.3174/ajnr.A4091>

imal MCA infarcts that involve the insula are associated with infarct growth and unfavorable clinical outcome.⁵⁻⁷ This association is understandable from knowledge of the vascular supply of the insula, which comprises almost exclusively superior and inferior division M2 branches. An infarct from a proximal MCA occlusion that spares the insula may be indicative of good MCA collateral flow, whereas an infarct from a proximal MCA occlusion with insula involvement may be a sign of insufficient MCA collateral flow. Furthermore, the insula is recognized as a functional integration center for autonomic responses, and alterations in blood glucose, blood pressure, myocardial contractility, and body temperature may also contribute to adverse outcome in cerebral ischemia.^{5,8}

The purpose of our study was to determine whether percentage insular ribbon infarct can help identify patients with stroke with proximal vessel occlusions likely to have poor clinical outcome, despite small admission DWI lesion volumes.

MATERIALS AND METHODS

Patient Selection

We retrospectively identified 200 consecutive patients with acute ischemic stroke admitted during a 2-year period. This study was Health Insurance Portability and Accountability Act compliant and was approved by our institutional review board. All patients underwent the standard acute stroke imaging algorithm at our institution. We reviewed the clinical and imaging data of this study cohort. Fifty-five patients met the following inclusion criteria: 1) imaging within 9 hours of symptom onset including NCCT, head and neck CTA, CTP with 8-cm shuttle mode anterior circulation coverage, and MR imaging–DWI within 3 hours of CTP; 2) large-vessel occlusion (ICA terminus and/or proximal MCA [M1 or M2], as per the Boston Acute Stroke Imaging Scale⁹); and 3) modified Rankin Scale score recorded at admission and 3 months after admission. Of the patients excluded, 52 had no proximal occlusion, 41 did not have admission DWI, 21 had a CTP–DWI interval of >3 hours, 13 had posterior circulation strokes, 10 had uninterpretable images, 6 did not have recorded admission and/or 3-month mRS, and 2 had inappropriate location of the CTP acquisition.

Image Acquisition

All imaging was performed in accordance with the standard institutional acute stroke imaging algorithm. CT was performed by using a helical scanner (LightSpeed 64; GE Healthcare, Milwaukee, Wisconsin). Noncontrast head CT was acquired in a helical mode (1.25-mm thickness, 120 kV, 250 mAs) and was reformatted at 5-mm intervals. CTA was performed after administration of 80–90 mL of nonionic contrast (iopamidol, Isovue Multipack-370; Bracco Diagnostics, Princeton, New Jersey) followed by 40 mL of saline, both at 4 mL/s (1.25-mm thickness, 120 kV, auto mA, 0.5–0.7 s/rotation). CTP used 35 mL of nonionic contrast (Isovue Multipack-370; Bracco Diagnostics) at 7 mL/s followed by 40 mL of saline at 4 mL/s (acquisition time, 90 seconds; 80 kV; 500 mAs maximum), providing sixteen 5-mm thick sections (8-cm coverage) through the anterior circulation. All CTP images

were postprocessed with CTP 4D automated software (GE Healthcare). The average total estimated effective radiation dose from the entire CT/CTA/CTP acquisition was approximately 11 mSv.

MR imaging was performed by using a 1.5T Signa scanner (GE Healthcare). Our stroke protocol included a single-shot echo-planar spin-echo DWI sequence with two 180-degree radiofrequency pulses to minimize eddy current warping. Three images per section were acquired at $b=0$ s/mm², followed by 25 at $b=1000$ s/mm², for 28 images per section. Twenty-three to 27 sections covered the entire brain. Imaging parameters were TR/TE, 5000/80–110 ms; FOV, 22 cm; matrix, 128 × 128 zero-filled to 256 × 256; 5-mm section thickness with a 1-mm gap.

Image Analysis

We analyzed, by visual inspection, the following imaging markers on the admission scans of the 55 study patients: 1) percentage insula ribbon infarct (>50%, ≤50%) on NCCT, DWI, CT-CBF, and CT-MTT; 2) percentage DWI motor strip infarct (less than one-third, one-third to two-thirds, more than two-thirds); and 3) CTA collateral score (0 = absent collaterals in >50% of an M2 territory, 1 = diminished collaterals in >50% of an M2 territory, 2 = diminished collaterals in <50% of an M2 territory, 3 = collaterals equal to those of the contralateral side, 4 = increased collaterals).¹ Percentage insula ribbon infarct for each case was determined by visually inspecting the insula on each contiguous imaging section and deciding whether the abnormality as a whole involved more or less than 50% of the total insula. A 50% PIRI binary threshold for total insula was selected because approximately 50% of the insula is supplied by branches from the superior division and 50% is supplied by the inferior division of the MCA. In addition, this was an overall more reproducible and accurate imaging marker in predicting clinical outcome on preliminary analysis, performing better than the 25% PIRI total insula, the 50% PIRI anterior insula, and the two-thirds on 1 section/50% on 2 section techniques used in prior publications.^{6,7} These imaging markers were independently determined by 2 board-certified radiologists with 1 year and 20 years of dedicated neuroradiology experience. Interpreting radiologists were blinded to all clinical and imaging information except for acute neurologic symptoms. Any disagreements were resolved by consensus.

In addition, DWI infarct volumes were manually segmented by a board-certified radiologist with 5 years of general and 2 years of dedicated neuroradiology experience and were corrected by an experienced Certificate of Added Qualification–certified neuroradiologist with 20 years' experience, using semiautomated software (Analyze 8.1; AnalyzeDirect, Overland Park, Kansas). NCCT-ASPECTSs were recorded by the same Certificate of Added Qualification–certified neuroradiologist according to standard methodology, rating 10 distinct brain regions for ischemic hypoattenuation or loss of gray-white matter differentiation. Similarly, the interpreting radiologists were blinded to all clinical and imaging information except for acute neurologic symptoms.

Admission clinical and imaging variables, stratified by good-versus-poor outcome (3-month mRS 0–2 versus 3–6, respectively)

Variable ^a	All Patients	Good Outcome (mRS 0–2)	Poor Outcome (mRS 3–6)	P Value ^b
Patient (No.) (%)	55	23 (42)	32 (58)	–
Female sex (No.) (%)	26 (4)	12 (52)	14 (43)	.731
Age (yr) (mean)	67 ± 15	63 ± 17	70 ± 13	.064
Right hemisphere (No.) (%)	23 (42)	8 (35)	15 (47)	.535
Baseline NIHSS (median) (IQR)	14 (6–18)	6 (4–11)	17 (14–20)	<.001
IV treatment (No.) (%)	18 (33)	9 (39)	9 (28)	.392
IA treatment (No.) (%)	4 (7)	1 (4)	3 (9)	.466
Any treatment (IV or IA) (No.) (%)	10 (18)	3 (13)	7 (22)	.395
No IV or IA treatment (No.) (%)	23 (42)	10 (43)	13 (41)	.628
Ictus to DWI (min) (mean)	286 ± 108	277 ± 134	291 ± 87	.68
Ictus to CT perfusion (min) (mean)	229 ± 107	224 ± 140	232 ± 79	.79
DWI volume >70 mL (No.) (%)	15 (27)	0 (0)	15 (27)	<.001
DWI-PIRI >50% (No.) (%)	22 (40)	3 (5)	19 (35)	<.001
NCCT ASPECTS (median) (IQR)	8 (6–10)	9 (8–10)	7 (5–8)	<.001
Collateral score (median) (IQR)	2 (1–3)	2 (2–3)	1 (1–2)	.002
Malignant collateral pattern (No.) (%)	4 (7)	0 (0)	4 (7)	.131
NCCT-PIRI >50% (No.) (%)	17 (31)	2 (4)	15 (27)	.003
DWI motor strip score, (median) (IQR)	0 (0–0)	0 (0–0)	0 (0–1.5)	.010
CT-CBF-PIRI >50% (No.) (%)	39 (71)	14 (25)	25 (45)	.133
CT-MTT-PIRI >50% (No.) (%)	44 (80)	17 (31)	27 (49)	.294

Note:—IA indicates intra-arterial.

^a Results expressed as absolute numbers (%), mean (±SD), or median (IQR).

^b Continuous, ordinal, and discrete variables compared with the unpaired *t* test, Mann-Whitney *U* test, and Fisher exact test, respectively.

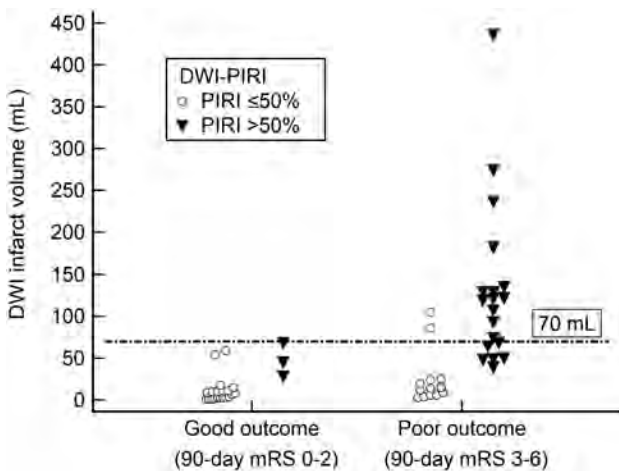


FIG 1. Scatterplot showing clinical outcome for patients stratified by infarct volume and DWI-PIRI. There was a 100% specific admission 70-mL DWI volume cutoff value for poor outcome.

Statistical Analysis

Cases were dichotomized into good (mRS 0–2) versus poor (mRS 3–6) clinical outcome. Univariate binary logistic regression was performed on all imaging markers to determine significance in predicting poor outcome. Adjusting for time-to-imaging and treatment assignment, we performed multivariate binary logistic regression with stepwise selection on significant univariate predictors of poor clinical outcome (baseline NIHSS score, DWI-PIRI, DWI infarct volume, CTA collateral score, NCCT-PIRI, and NCCT-ASPECTS). Two multivariate models with and without DWI imaging predictors were analyzed. We compared continuous, ordinal, and discrete variables using the unpaired *t* test, Mann-Whitney *U* test, and Fisher exact test, respectively. Interrater agreement for imaging markers was determined by

using the κ statistic. MedCalc for Windows software, Version 11.5.1.0 (MedCalc Software, Mariakerke, Belgium) was used to perform statistical analysis. Statistical significance was $P < .05$.

RESULTS

Patient demographics, treatments, and univariate predictors of poor clinical outcome are listed in the Table. Mean time from symptom onset to CT was 3 hours 48 ± 1 minute 43 seconds. Fourteen patients were imaged at 0–3 hours, 36 at 3–6 hours, and 5 at 6–9 hours. The median (interquartile range [IQR]) time between CT and MR imaging studies was 51 minutes (range, 41–65 minutes).

Admission NIHSS score was the only significant clinical predictor of poor outcome ($P < .001$). Admission DWI of >70 mL ($P < .001$), DWI-PIRI of >50% ($P < .001$), NCCT-ASPECTS ($P < .001$), NCCT-PIRI of >50% ($P = .003$), CTA collateral score ($P = .002$), and DWI motor strip ($P = .01$) were significant imaging univariate predictors of poor outcome. PIRI of >50% on CT-CBF and CT-MTT were not significant univariate predictors of poor outcome.

In multivariate analyses, the first binary logistic regression model, with DWI-PIRI of >50%, NIHSS score, DWI of >70-mL threshold, NCCT-ASPECTS, and CTA collateral score as covariates revealed DWI-PIRI of >50% ($P = .045$) and NIHSS score ($P < .001$) to be the only independent predictors of poor outcome. Considering that some centers may have limited access to MR imaging in the emergency department, we performed a second binary logistic model with NCCT-PIRI of >50%, NIHSS score, NCCT-ASPECTS, and CTA collateral score as covariates, which revealed the NIHSS score ($P < .001$) to be the only independent predictor of poor outcome.

The DWI volume threshold of 70 mL was 100% specific and 47% sensitive for poor outcome (Fig 1). Fourteen of 14 patients with DWI lesion volume of >70 mL had mRS 3–6. When DWI volume was <70 mL, clinical outcome was highly variable; 24/41 patients with DWI lesion volume of <70 mL had good outcome with mRS 0–2 and 17/41 patients had poor outcome with mRS 3–6.

In patients with admission DWI infarct of <70 mL ($n = 40$), the 90-day mRS score was significantly worse in those with DWI-PIRI of >50% ($n = 9$, median mRS = 5, IQR = 2–5) compared with those with DWI-PIRI of ≤50% ($n = 31$, median mRS = 2, IQR = 0.25–4, $P = .036$) (Figs 2 and 3). Furthermore, 67% of patients with DWI lesion volume of <70 and DWI-PIRI of >50% had poor outcome. In patients with admission DWI infarct of >70 mL, DWI-PIRI did not have added predictive value for poor outcome ($P = .931$).

Interobserver agreement analyses revealed κ values of 0.81 for DWI-PIRI, 0.82 for NCCT-PIRI, 0.74 for DWI motor strip score,

0.69 for CBF-PIRI, 0.77 for MTT-PIRI, and 0.44 for CTA collateral score.

DISCUSSION

This study demonstrates that DWI-PIRI of >50% independently predicts poor clinical outcome and can help identify patients with stroke likely to have poor outcome despite small admission DWI lesion volumes. Consequently, the DWI-PIRI score may help to more accurately weigh the potential risks versus benefits of advanced stroke treatments than assessment by the NIHSS score and DWI lesion volume alone.

These results are consistent with earlier studies demonstrating that insula infarcts are predictive of penumbral loss and poor clinical outcome compared with infarcts sparing the insula.^{5-7,10,11} Of note, diffusion and perfusion MR imaging have been used to demonstrate that infarctions of the insula are associated with an in-

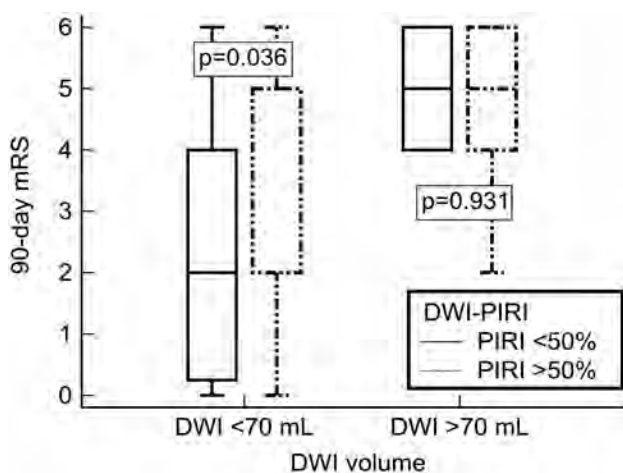


FIG 2. In patients with DWI infarct volumes of <70 mL, 90-day mRS was significantly worse when the DWI-PIRI was >50% compared with a DWI-PIRI of ≤50% ($P = .036$). In patients with DWI infarct volumes of >70 mL, DWI-PIRI did not have added predictive value for poor outcome ($P = .931$).

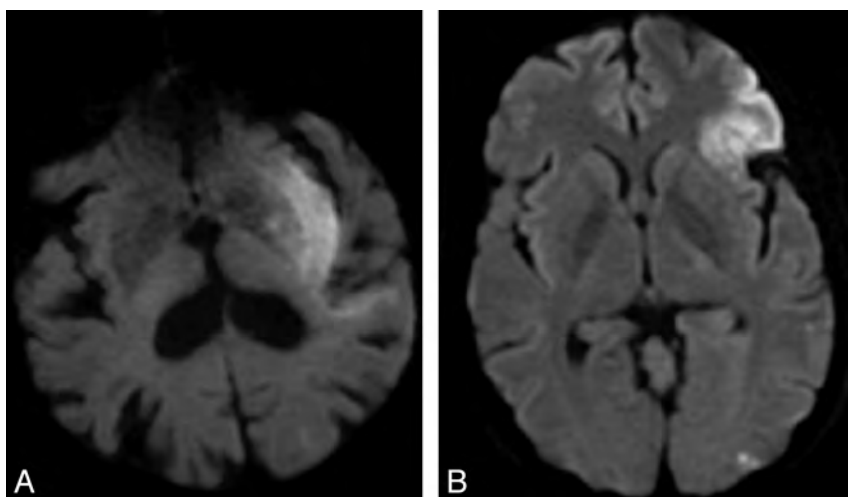


FIG 3. Sample imaging from 2 patients with ICA terminus occlusions. Patients A and B had similar baseline NIHSS scores (11 and 8), similar small volume infarcts on DWI (50 and 59 mL), the same collateral score (2), the same treatment (IV tPA), but differing degrees of insula involvement. The patient with >50% DWI-PIRI (patient A) had a poor clinical outcome (mRS 5 at 90 days), whereas the patient with ≤50% DWI-PIRI (patient B) had a good clinical outcome (mRS 1 at 90 days).

creased percentage of mismatch loss (conversion of potentially viable neighboring penumbra into infarction).^{5,7} Fink et al⁶ dichotomized patients with insula infarcts into “major” (equal to or more than two-thirds on 1 section or >50% on ≥2 sections) versus smaller “minor” insula lesions and found major insula infarct involvement to be associated with larger MCA territory infarcts and higher NIHSS scores, indicating more severe clinical deficits. In another study, Christensen et al¹⁰ showed significantly worse mRS scores at 3 months in patients with right-sided insula infarcts compared with those with left-sided infarcts or no insula involvement.

Our study further expands on these findings by the following means: 1) demonstrating the added prognostic value of DWI-PIRI of >50% in predicting clinical outcome in patients with small DWI lesion volumes, 2) developing a practical and easily reproducible DWI-PIRI scoring system, 3) applying this PIRI scoring method in a patient population with ICA terminus and/or proximal MCA occlusions, and 4) providing direct comparison of our PIRI scoring method with other important imaging and clinical markers of stroke outcome.

Specifically our results show DWI-PIRI of >50%, DWI infarct volume of >70 mL, NCCT ASPECTS, NIHSS score, CTA collateral score, and DWI motor strip score to be univariate predictors of poor clinical outcome, with DWI-PIRI of >50% and NIHSS score being the only independent predictors of poor outcome. The added predictive value of DWI-PIRI to the NIHSS score makes sense if one considers that the NIHSS is a clinical assessment measuring deficits from the infarct and ischemic penumbra. The NIHSS cannot distinguish whether clinical deficits originate from infarcted tissue or tissue at risk for infarction. The DWI-PIRI score provides a unique visual marker that adds value to the NIHSS by partly delineating the amount of clinical deficit due to infarct and by predicting infarct progression. Thus, the addition of DWI-PIRI may be a useful adjunct to the NIHSS and DWI infarct volume in helping to predict clinical outcome, particularly in patients with small DWI infarct volumes who may have a higher potential for infarct growth.

Our threshold of >50% DWI insula infarct involvement for predicting poor clinical outcome adds to the recent work of Kamalian et al,⁷ who demonstrated that >25% DWI insula infarct involvement was the strongest predictor of large mismatch loss (infarct growth) in a cohort of patients with proximal middle cerebral artery occlusions. Our observed larger threshold of >50% insula infarct involvement is likely because we assessed a different outcome measure. While Kamalian et al measured changes in lesion volumes based on follow-up scans, we indirectly assessed loss of insula and other MCA region functions as measured by the 90-day modified Rankin Scale.

The insula has long been an established marker of early MCA stroke^{12,13} and has been shown to be among the

brain regions most vulnerable to ischemia.¹⁴ The association between insula infarct involvement and worsened tissue and clinical outcome may be 2-fold: 1) Insula infarcts may serve as a marker for poor collateral flow throughout the greater MCA territory, and 2) infarcts of the insula may lead to autonomic system alterations that may contribute to adverse tissue outcome.

The insula is supplied almost exclusively by M2 segment MCA branches, with a small contribution from M1 insular branches in some individuals.¹⁵ The superior MCA division gives rise to branches that supply the anterior insula, whereas the inferior MCA division supplies the posterior insula. The insula is vulnerable to ischemia from proximal occlusion of the M1 MCA segment and the superior and inferior division MCA branches because there is limited possibility of recruiting pial collateral supply from the anterior or posterior cerebral arteries. An infarct due to proximal MCA occlusion that spares the insula but involves the more downstream MCA territory might be indicative of good pial collateral circulation, whereas an MCA occlusion with infarct including the insula can be a sign of insufficient collateral circulation and thus infarct growth.⁵

Another link between insula infarct and worsened outcome may be related to the role of the insula in modulation of the autonomic nervous system. Clinical and experimental investigations indicate that there is increased sympathetic nervous system activity, including increased plasma catecholamine levels, in insula infarcts.^{5,16} Some of the effects of sympathetic system activation have been associated with adverse clinical or tissue outcome in cerebral ischemia. For example, an elevated norepinephrine concentration after stroke is a predictor of insula involvement and poor neurologic outcome,¹⁶ and likewise poststroke hyperglycemia occurs more often with insular infarcts and is associated with larger infarct size and poor neurologic outcome.^{5,17} A recent study by Kemmling et al¹⁸ found a significant association between the development of hospital-acquired pneumonia in the setting of right hemispheric peri-insular strokes, an association that is thought to be related to autonomic modulation of the immune system.

The insula is a highly recognizable anatomic structure on cross-sectional imaging due to its distinctive location adjacent to the frontal and temporal operculum, just medial to the Sylvian fissure. Our high interobserver agreement in determining the DWI-PIRI score is in keeping with prior structural MR imaging studies that show high reproducibility for anatomic localization.¹⁹

Limitations of this study include a relatively small sample size, retrospective design, and heterogeneity of treatment. It is noteworthy that the unenhanced CT insula score was not an independent predictor of outcome in the multivariate model, when DWI was excluded and the admission NIHSS score was included. This may be secondary to both shorter time to imaging and lesser sensitivity for infarct detection, compared with DWI. Recanalization status, an established predictor of stroke outcome, was not available for a large number of our patients, thus precluding its entrance into our analysis. Our findings should be validated in a larger prospective study that adjusts for recanalization status.

CONCLUSIONS

DWI percentage insula ribbon infarct of >50% predicts poor clinical outcome in acute ischemic stroke and can help identify patients who are likely to have a poor clinical outcome despite small admission DWI lesion volumes. Because it facilitates direct visual estimation of the likelihood of poor outcome, the DWI-PIRI score may help more accurately weigh the potential risks versus benefits of advanced stroke treatments than clinical assessment by the NIHSS and estimation of DWI lesion volume alone. Consideration of DWI insula infarct involvement may be an additional tool for risk-benefit stratification and patient selection for reperfusion therapy.

Disclosures: Michael H. Lev—RELATED: Grant for Specialized Programs of Translational Research in Acute Stroke, National Institute of Neurological Disorders and Stroke,* for Screening Technology and Outcomes Project in Stroke, National Institute of Neurological Disorders and Stroke*; UNRELATED: Consultancy: GE Healthcare, Grants/Grants Pending: GE Healthcare. Shervin Kamalian—UNRELATED: Grants/Grants Pending: GE Healthcare. *Money paid to the institution.

REFERENCES

1. Souza LC, Yoo AJ, Chaudhry ZA, et al. **Malignant CTA collateral profile is highly specific for large admission DWI infarct core and poor outcome in acute stroke.** *AJNR Am J Neuroradiol* 2012;33:1331–36
2. Yoo AJ, Barak ER, Copen WA, et al. **Combining acute diffusion-weighted imaging and mean transit time lesion volumes with National Institutes of Health Stroke Scale score improves the prediction of acute stroke outcome.** *Stroke* 2010;41:1728–35
3. Yoo AJ, Verduzco LA, Schaefer PW, et al. **MRI-based selection for intra-arterial stroke therapy: value of pretreatment diffusion-weighted imaging lesion volume in selecting patients with acute stroke who will benefit from early recanalization.** *Stroke* 2009;40:2046–54
4. Parsons MW, Christensen S, McElduff P, et al. **Pretreatment diffusion- and perfusion-MR lesion volumes have a crucial influence on clinical response to stroke thrombolysis.** *J Cereb Blood Flow Metab* 2010;30:1214–25
5. Ay H, Arsava EM, Koroshetz WJ, et al. **Middle cerebral artery infarcts encompassing the insula are more prone to growth.** *Stroke* 2008;39:373–78
6. Fink JN, Selim MH, Kumar S, et al. **Insular cortex infarction in acute middle cerebral artery territory stroke: predictor of stroke severity and vascular lesion.** *Arch Neurol* 2005;62:1081–85
7. Kamalian S, Kemmling A, Borgie RC, et al. **Admission insular infarction >25% is the strongest predictor of large mismatch loss in proximal middle cerebral artery stroke.** *Stroke* 2013;44:3084–89
8. Augustine JR. **Circuitry and functional aspects of the insular lobe in primates including humans.** *Brain Res Brain Res Rev* 1996;22:229–44
9. Torres-Mozqueda F, He J, Yeh IB, et al. **An acute ischemic stroke classification instrument that includes CT or MR angiography: the Boston Acute Stroke Imaging Scale.** *AJNR Am J Neuroradiol* 2008;29:1111–17
10. Christensen H, Boysen G, Christensen AF, et al. **Insular lesions, ECG abnormalities, and outcome in acute stroke.** *J Neurol Neurosurg Psychiatry* 2005;76:269–71
11. Laowattana S, Zeger SL, Lima JA, et al. **Left insular stroke is associated with adverse cardiac outcome.** *Neurology* 2006;66:477–83, discussion 483
12. Truwit CL, Barkovich AJ, Gean-Marton A, et al. **Loss of the insular ribbon: another early CT sign of acute middle cerebral artery infarction.** *Radiology* 1990;176:801–06
13. Moulin T, Cattin F, Crepin-Leblond T, et al. **Early CT signs in acute middle cerebral artery infarction: predictive value for subsequent infarct locations and outcome.** *Neurology* 1996;47:366–75

14. Payabvash S, Souza LC, Wang Y, et al. **Regional ischemic vulnerability of the brain to hypoperfusion: the need for location specific computed tomography perfusion thresholds in acute stroke patients.** *Stroke* 2011;42:1255–60
15. Türe U, Yasargil MG, Al-Mefty O, et al. **Arteries of the insula.** *J Neurosurg* 2000;92:676–87
16. Sander D, Winbeck K, Klingelhofer J, et al. **Prognostic relevance of pathological sympathetic activation after acute thromboembolic stroke.** *Neurology* 2001;57:833–38
17. Bruno A, Biller J, Adams HP Jr, et al. **Acute blood glucose level and outcome from ischemic stroke: Trial of ORG 10172 in Acute Stroke Treatment (TOAST) Investigators.** *Neurology* 1999;52:280–84
18. Kemmling A, Lev MH, Payabvash S, et al. **Hospital acquired pneumonia is linked to right hemispheric peri-insular stroke.** *PLoS One* 2013;8:e71141
19. Naidich TP, Kang E, Fatterpekar GM, et al. **The insula: anatomic study and MR imaging display at 1.5 T.** *AJNR Am J Neuroradiol* 2004; 25:222–32

Middle Cerebral Artery Stenosis in Patients with Acute Ischemic Stroke and TIA in Israel

G. Telman, H. Hurani, E. Sprecher, and E. Kouperberg

ABSTRACT

BACKGROUND AND PURPOSE: Middle cerebral artery stenosis is not frequent but a well-established cause of first and recurrent ischemic stroke. Our aim was to investigate middle cerebral artery stenosis in the biethnic (Jewish and Arab) population of patients with acute ischemic stroke and transient ischemic attack in northern Israel.

MATERIALS AND METHODS: The study population included 1344 patients from the stroke data registry who had been hospitalized in the neurologic department because of acute ischemic stroke (1041) or TIA (303) and had undergone transcranial Doppler sonographic examination during the hospitalization.

RESULTS: Of the 1344 patients, 120 (8.9%) were found to have MCA stenosis. The patients with intracranial stenosis were older and had more vascular risk factors (hypertension, diabetes, and hyperlipidemia) and vascular diseases (ischemic heart and peripheral vascular disease) than those without intracranial stenosis. Logistic regression analysis revealed that diabetes ($P = .002$) and peripheral vascular disease ($P = .01$), but not ethnicity, were independent and significant predictors for the presence of MCA stenosis.

CONCLUSIONS: An independent and significant correlation was found between MCA stenosis and vascular risk factors (diabetes mellitus) and vascular diseases, thus emphasizing the similarity of intracranial MCA stenosis and other vascular diseases originating from atherosclerosis. There was no influence of ethnicity on intracranial stenosis in our population.

ABBREVIATION: TCD = transcranial Doppler sonography

Intracranial stenosis is most commonly due to an atherosclerotic lesion of the intracranial vessels, leading to subsequent narrowing or occlusion of these vessels.^{1,2} This condition is being increasingly recognized as an important and underestimated etiology in acute ischemic stroke.³⁻⁵ Differences in the prevalence of intracranial stenosis in various populations have been reported, with the most vulnerable patients seeming to be Asians, Hispanics, and African Americans.⁶⁻¹⁰ Because intracranial stenosis usually represents an atherosclerotic lesion, it is not surprising that there is a clear correlation between intracranial stenosis and vascular diseases and vascular risk factors.¹¹⁻¹⁵

The aim of the present study was to search for possible determinants of potentially symptomatic middle cerebral artery stenosis in patients with stroke and transient ischemic attack in a biethnic (Jewish and Arab) population of northern Israel.

Many studies in the literature suggest different transcranial Doppler sonography (TCD) parameters (peak systolic velocity, mean velocity) and different values as cutoffs for the diagnosis of intracranial stenosis. There are also many different definitions in the literature of intracranial stenosis (eg, “mild, moderate, and severe,” “less and more than 50%,” “50%–69% and more than 70%,” and so forth). There are still no generally accepted criteria for moderate intracranial stenosis. In this study, potentially symptomatic intracranial stenosis was defined as cases in which TCD examination showed a peak velocity in the middle cerebral artery, either left or right, of ≥ 140 cm/s. This value was used by some researchers as a criterion correlating with MCA stenosis of $\geq 50\%$.^{3,16}

MATERIALS AND METHODS

This study was based on the stroke data registry from the vascular laboratory of the Department of Neurology and the Prometheus computerized registry system containing all details of patients hospitalized in the Rambam Health Care Campus, Haifa, Israel, from the end of 1999 to 2010. The 1344 patients included in the study were those consecutively referred from the neurologic department to the vascular laboratory for transcranial Doppler ex-

Received December 1, 2013; accepted after revision May 29, 2014.

From the Department of Neurology, Faculty of Medicine, Rambam Health Care Campus and Technion, Haifa, Israel.

Please address correspondence to G. Telman, MD, Department of Neurology, Rambam Health Care Campus, Haifa, Israel; e-mail: g_telman@rambam.health.gov.il

<http://dx.doi.org/10.3174/ajnr.A4069>

Table 1: Distribution of demographic and vascular risk factors and vascular diseases in the whole group of patients^a

Risk Factor	All Patients (N = 1344)	Patients with Intracranial Stenosis	Patients without Intracranial Stenosis	P Value
Age	65.67 ± 13.2	66.02 ± 12.9	63.85 ± 12.9	<.04
Sex (male)	983 (73.1%)	81 (67.5%)	902 (67.2%)	.14
Ethnicity (Arab)	310 (23.1%)	23 (19.1%)	287 (23.5%)	.28
CVA	1041 (77.5%)	107 (89.2%)	934 (76.3%)	.0005
TIA	303 (22.5%)	13 (10.8%)	290 (23.8%)	.0005
Hypertension	946 (70.4%)	93 (77.5%)	853 (69.8%)	.068
Diabetes	470 (35%)	61 (50.8%)	409 (33.5%)	.0002
Hyperlipidemia	686 (51%)	72 (60%)	614 (50.25%)	.04
Smoking	454 (33.8%)	32 (26.7%)	422 (34.5%)	.07
IHD	398 (29.6%)	42 (35%)	356 (29.1%)	.18
MI	187 (13.9%)	17 (14.2%)	170 (13.9%)	.9
AF	138 (10.3%)	8 (6.7%)	130 (10.6%)	.14
PVD	94 (7%)	17 (14.2%)	77 (6.3%)	.004

Note:—CVA indicates cerebral vascular accident; IHD, ischemic heart disease; AF, paroxysmal or chronic atrial fibrillation; PVD, peripheral vascular disease; MI, myocardial infarction.

^a χ^2 analyses and *t* tests, uncorrected for multiple comparisons, were performed.

amination because of acute ischemic stroke or TIA. TIA was defined clinically as a transient episode of neurologic dysfunction of ischemic origin lasting <24 hours. Of those patients included in the study, 1041 had cerebral vascular accident and 303 had TIA. From those patients with cerebral vascular accident, 117 (11.2%) instances were attributed to the vertebrobasilar territory. Of strokes attributed to the carotid territory, 484 (52.4%) were left-sided. Data for every patient in the study included demographic variables, risk factors, vascular diseases, and results of the TCD examination.

A Pioneer TC 8080 TCD machine (Viasys Nicolet, Madison, Wisconsin), was used. Parameters used for monitoring were the following: depth of insonation of MCA, 51–63 mm; sample volume, 3 mm; power of insonation, 100%; range, 154 cm/s; 256-point fast Fourier transformation. All examinations were performed by a highly experienced TCD operator (E.K). Intra-observer agreement for the TCD examination was estimated by the comparison of MCA peak systolic velocities at 2 consecutive examinations and was very good ($\kappa = 0.84$).

The assignment of ethnicity (Arab or Jewish) was performed by place of birth and residence in addition to first and family names. We examined interobserver agreement among 4 observers for this method of classification of ethnicity in a biethnic northern Israeli population, and agreement was found to be almost perfect, $\kappa = 0.96$, as assessed by the Fleiss κ statistic.¹⁷

Hypertension was defined by either a systolic blood pressure of ≥ 140 mm Hg or a diastolic blood pressure of ≥ 90 mm Hg, by the use of antihypertensive medication, or by a previously established diagnosis of hypertension (in most cases). In those cases in which the hypertension was diagnosed for the first time, the diagnosis was based on repeat measurements throughout the hospitalization. Diabetes mellitus was defined by a recorded random blood glucose level of ≥ 200 mg/dL, by the use of insulin or an oral hypoglycemic agent, or by a previous diagnosis of diabetes mellitus. Hyperlipidemia was defined by the use of lipid-lowering medications; by a fasting serum total cholesterol concentration of > 200 mg/dL, a low-density lipoprotein cholesterol concentration of > 140 mg/dL, a high-density lipoprotein cholesterol concentration of < 40 mg/dL, or a triglyceride concentration of > 150

mg/dL; or by a previous diagnosis of hyperlipidemia. Atrial fibrillation was diagnosed by a physician who reviewed patient electrocardiograms, by following the medical records, or by a previous medical diagnosis. Ischemic heart disease was defined by a history of myocardial infarction, angina pectoris, signs of ischemia on the electrocardiogram, or by the medical records. Peripheral vascular disease was defined by a history of intermittent claudication, peripheral vascular surgery or angioplasty, or by a previous diagnosis. Permission for this study was obtained from the local ethics committee.

Statistical Analysis

Basic comparisons between groups of patients with and without MCA stenosis consisted of *t* tests for normally distributed continuous data and χ^2 tests for categorical data. In cases in which there were > 2 levels in the nonparametric variables tested, additional χ^2 tests were conducted to further examine the distributions. To control for the multiple influences of risk factors in predicting stenosis, we conducted logistic regression analyses. JMP (SAS Institute, Cary, North Carolina) was used for the statistical analyses.

RESULTS

The mean age of the 1344 patients was 64 ± 12.9 years (range, 20–94 years). There were 360 female (26.8%) and 310 Arab (23.1%) patients. Of the 1344 patients, 1041 (77.5%) had acute ischemic stroke and 303 had TIA. Table 1 presents the distribution of vascular diseases and vascular risk factors among the patients included in the study.

TCD data showed that 120 patients (8.9%) had potentially symptomatic MCA stenosis. Seventy-seven of these patients had clinical manifestations related to the side of stenosis, and 34 (28.3%) had bilateral potentially symptomatic intracranial stenosis of the MCA. The patients with intracranial stenosis were older and had more vascular risk factors (hypertension, diabetes, and hyperlipidemia) and vascular diseases (ischemic heart disease and peripheral vascular disease) than those without intracranial stenosis.

Logistic regression analysis revealed that only diabetes mellitus ($P = .002$) and peripheral vascular disease ($P = .01$) were independent and significant predictors for the presence of MCA stenosis (Table 2). No influence of ethnicity on the presence of significant intracranial stenosis was found, either before or after the logistic regression analysis.

DISCUSSION

In this study, we explored the possible predictors of potentially symptomatic MCA stenosis in a large group of patients with stroke and TIA, representing a biethnic population in northern Israel that has not been previously studied. TCD is considered a reliable method for the detection of intracranial stenosis.¹⁸ The prevalence of MCA stenosis in the population of patients with

Table 2: Logistic regression analysis of possible predictors of intracranial stenosis in patients with acute ischemic stroke or TIA^a

Effect	Odds Ratio	95% Confidence Limits	P Value
Ethnicity (Arab vs Jewish)	0.785	0.479–1.284	.33
Age (per yr)	1.009	0.992–1.026	.3
Sex (male vs female)	0.715	0.466–1.097	.124
Hypertension	1.138	0.709–1.826	.59
Diabetes	1.889	1.274–2.801	.002 ^b
Smoking	0.723	0.460–1.137	.16
Hyperlipidemia	1.352	0.899–2.033	.15
IHD	1.243	0.746–2.071	.4
PVD	2.197	1.210–3.987	.01 ^b
MI	0.736	0.381–1.423	.36
AF	0.582	0.272–1.247	.16

Note:—IHD indicates ischemic heart disease; AF, paroxysmal or chronic atrial fibrillation; PVD, peripheral vascular disease; MI, myocardial infarction.

^a Multivariate logistic regression analysis of factors potentially leading to intracranial stenosis. The overall logistic regression model was significant, $P = .0003$.

^b Significant parameters.

stroke and TIA in northern Israel was found to be similar to that in other studies examining white patients.^{19,20} As expected, we found that patients with potentially symptomatic intracranial stenosis were older and had more vascular risk factors. Logistic regression analysis showed that diabetes mellitus and peripheral vascular disease were independent and significant predictors of intracranial stenosis in the studied population. Similar data pointing to the important influence of diabetes in the appearance of intracranial stenosis can be found in the literature.^{21–23}

The other significant finding was a high prevalence of peripheral vascular disease in patients with potentially symptomatic intracranial stenosis. Such data may indicate vulnerability of the peripheral arteries of relatively small diameter in a different location for the development of atherosclerotic lesions in some patients. This finding is supported by other studies that found a correlation between intracranial stenosis and peripheral vascular disease.²⁴ We did not find any differences in the prevalence of intracranial stenosis between the Jewish and the Arab patients, either before or after the logistic regression, contrary to many other populations studied.

Limitations

The main limitation of this study was that although all patients included in the study were consecutively examined by TCD, those patients who were referred for TCD examination were not consecutive. The main reason for not referring patients for TCD was the severity of the stroke or comorbidities. Some other patients were, on the contrary, in good condition and were discharged from the hospital before TCD. Overall, we were able to perform TCD in 61% of patients included in our stroke data base. Because many of those patients had severe stroke due to large-vessel disease, it seems that some underestimation of the prevalence of potentially symptomatic intracranial stenosis may have occurred in our cohort.

Another limitation of our study was that we were not able to evaluate internal carotid artery stenosis in our patients simultaneously with intracranial stenosis. ICA stenosis in the neck is an established important cause of TIA and stroke, and it is important to see MCA stenosis in the perspective of incidence, coexistence, and so forth with ICA stenosis.

CONCLUSIONS

This study dealt mainly with the predictors of potentially symptomatic intracranial stenosis and showed that diabetes and peripheral vascular disease, but not ethnicity, were independent and significant predictors for the presence of MCA stenosis. The screening of patients with stroke and TIA for the presence of potentially symptomatic intracranial stenosis is important because evidence exists that patients with MCA stenosis are prone to severe and devastating first and recurrent strokes and these require more aggressive treatment than any other group of strokes related to large-vessel disease.²⁵ Finally, data about MCA stenosis are relatively limited compared with numerous other sites of atherosclerosis related to stroke. Further exploration of different aspects of MCA stenosis, including genetic and population-based screening studies, is needed for better understanding of stroke mechanisms in this group of patients.

REFERENCES

1. Caplan LR, Gorelick PB, Hier DB. **Race, sex and occlusive cerebrovascular disease: a review.** *Stroke* 1986;17:648–55
2. Korogi Y, Takahashi M, Nakagawa T, et al. **Intracranial vascular stenosis and occlusion: MR angiographic findings.** *AJNR Am J Neuroradiol* 1997;18:135–43
3. Wong KS, Huang YN, Gao S, et al. **Intracranial stenosis in Chinese patients with acute stroke.** *Neurology* 1998;50:812–13
4. Wityk RJ, Lehman D, Klag M, et al. **Race and sex differences in the distribution of cerebral atherosclerosis.** *Stroke* 1996;27:1974–80
5. Weber R, Kraywinkel K, Diener HC, et al. **German Stroke Study Collaboration: symptomatic intracranial atherosclerotic stenoses—prevalence and prognosis in patients with acute cerebral ischemia.** *Cerebrovasc Dis* 2010;30:188–93
6. Gorelick PB, Caplan LR, Hier DB, et al. **Racial differences in the distribution of posterior circulation occlusive disease.** *Stroke* 1985;16:785–90
7. Suh DC, Lee SH, Kim KR, et al. **Pattern of atherosclerotic carotid stenosis in Korean patients with stroke: different involvement of intracranial versus extracranial vessels.** *AJNR Am J Neuroradiol* 2003;24:239–44
8. Jeng JS, Tang SC, Liu HM. **Epidemiology, diagnosis and management of intracranial atherosclerotic disease.** *Expert Rev Cardiovasc Ther* 2010;8:1423–32
9. De Silva DA, Woon FP, Pin LM, et al. **Intracranial large artery disease among OSCP subtypes in ethnic South Asian ischemic stroke patients.** *J Neurol Sci* 2007;260:147–49
10. Suri MF, Johnston SC. **Epidemiology of intracranial stenosis.** *J Neuroimaging* 2009;19:11S–6S
11. Sacco RL, Kargman DE, Zamanillo MC. **Race-ethnic differences in stroke risk factors among hospitalized patients with cerebral infarction: the Northern Manhattan Stroke Study.** *Neurology* 1995;45:659–63
12. Resch JA, Baker AB. **Etiologic mechanisms in cerebral atherosclerosis: preliminary study of 3,839 cases.** *Arch Neurol* 1964;10:617–28
13. Yasaka M, Yamaguchi T, Shichiri M. **Distribution of atherosclerosis and risk factors in atherothrombotic occlusion.** *Stroke* 1993;24:206–11
14. Rincon F, Sacco RL, Kraywinkel G, et al. **Incidence and risk factors of intracranial atherosclerotic stroke: the Northern Manhattan Stroke Study.** *Cerebrovasc Dis* 2009;28:65–71
15. Chaturvedi S, Turan TN, Lynn MJ, et al. **Risk factor status and vascular events in patients with symptomatic intracranial stenosis.** *Neurology* 2007;69:2063–68
16. Boddu DB, Sharma VK, Bandaru VC, et al. **Validation of transcranial Doppler with magnetic resonance angiography in acute cerebral ischemia.** *J Neuroimaging* 2011;21:e34–40
17. Telman G, Kouperberg E, Herscovitz M, et al. **Inter-observer agreement in ethnic assignment in an Arab-Jewish population of northern Israel.** *Health* 2011;3:444–46

18. Felberg RA, Christou I, Demchuk AM, et al. **Screening for intracranial stenosis with transcranial Doppler: the accuracy of mean flow velocity thresholds.** *J Neuroimaging* 2002;12:9–14
19. Sacco RL, Kargman DE, Gu Q. **Race-ethnicity and determinants of intracranial atherosclerotic cerebral infarction: the Northern Manhattan Stroke Study.** *Stroke* 1995;26:14–20
20. White H, Boden-Albala B, Wang C, et al. **Ischemic stroke subtype incidence among whites, blacks, and Hispanics: the Northern Manhattan Study.** *Circulation* 2005;111:1327–31
21. Huang HW, Guo MH, Lin RJ, et al. **Prevalence and risk factors of middle cerebral artery stenosis in asymptomatic residents in Rongqi County, Guangdong.** *Cerebrovasc Dis* 2007;24:111–15
22. Uehara T, Tabuchi M, Mori E. **Risk factors for occlusive lesions of intracranial arteries in stroke-free Japanese.** *Eur J Neurol* 2005;12:218–22
23. Arenillas JF, Molina CA, Chacón P, et al. **High lipoprotein (a), diabetes, and the extent of symptomatic intracranial atherosclerosis.** *Neurology* 2004;63:27–32
24. Ohuchi S, Kawazoe K, Izumoto H, et al. **Head and neck magnetic resonance angiography before coronary artery bypass grafting.** *Surg Today* 2005;35:432–35
25. Chimowitz MI, Lynn MJ, Derdeyn CP, et al, for the SAMMPRIS Trial Investigators. **Stenting versus aggressive medical therapy for intracranial arterial stenosis.** *N Engl J Med* 2011;365:993–1003

Abnormal White Matter Integrity in Chronic Users of Codeine-Containing Cough Syrups: A Tract-Based Spatial Statistics Study

Y.-w. Qiu, H.-h. Su, X.-f. Lv, and G.-h. Jiang



ABSTRACT

BACKGROUND AND PURPOSE: Codeine-containing cough syrups have become one of the most popular drugs of abuse in young people in the world. Chronic codeine-containing cough syrup abuse is related to impairments in a broad range of cognitive functions. However, the potential brain white matter impairment caused by chronic codeine-containing cough syrup abuse has not been reported previously. Our aim was to investigate abnormalities in the microstructure of brain white matter in chronic users of codeine-containing syrups and to determine whether these WM abnormalities are related to the duration of the use these syrups and clinical impulsivity.

MATERIALS AND METHODS: Thirty chronic codeine-containing syrup users and 30 matched controls were evaluated. Diffusion tensor imaging was performed by using a single-shot spin-echo-planar sequence. Whole-brain voxelwise analysis of fractional anisotropy was performed by using tract-based spatial statistics to localize abnormal WM regions. The Barratt Impulsiveness Scale II was surveyed to assess participants' impulsivity. Volume-of-interest analysis was used to detect changes of diffusivity indices in regions with fractional anisotropy abnormalities. Abnormal fractional anisotropy was extracted and correlated with clinical impulsivity and the duration of codeine-containing syrup use.

RESULTS: Chronic codeine-containing syrup users had significantly lower fractional anisotropy in the inferior fronto-occipital fasciculus of the bilateral temporo-occipital regions, right frontal region, and the right corona radiata WM than controls. There were significant negative correlations among fractional anisotropy values of the right frontal region of the inferior fronto-occipital fasciculus and the right superior corona radiata WM and Barratt Impulsiveness Scale total scores, and between the right frontal region of the inferior fronto-occipital fasciculus and nonplan impulsivity scores in chronic codeine-containing syrup users. There was also a significant negative correlation between fractional anisotropy values of the right frontal region of the inferior fronto-occipital fasciculus and the duration of codeine-containing syrup use in chronic users.

CONCLUSIONS: Chronic codeine-containing syrup abuse may be associated with disruptions in brain WM integrity. These WM microstructural deficits may be linked to higher impulsivity in chronic codeine-containing syrup users.

ABBREVIATIONS: BIS = Barratt Impulsiveness Scale; CCS = codeine-containing syrup; FA = fractional anisotropy; IFO = inferior fronto-occipital fasciculus; λ_1 = axial diffusivity; λ_{\perp} = radial diffusivity; TBSS = tract-based spatial statistics

Codeine is by far the most widely used opiate in the world. It has been frequently used as an antitussive agent.¹ It has relatively specific central inhibition of the cough center in the medulla and does not cause respiratory depression. Although codeine is a less addictive

opiate than heroin, continued use can result in physical and psychological dependence.² Codeine-containing cough syrups (CCSs) have become one of the most popular drugs of abuse in young people in the world.³ The exact neurobiologic mechanism underlying CCS addiction is not fully understood. Codeine dependence is different from that of other illicit opioid drugs, and its misuse is associated with a different clinical course.⁴ CCS contains a combination of codeine, a sympathomimetic, and an antihistamine, all of which have central nervous system action, which is not typical of other opioids.⁴

Understanding the mechanism of CCS dependence and developing better therapies to stop CCS abuse are important because of the increasing incidence of dependency. Emerging technologies

Received December 13, 2013; accepted after revision June 15, 2014.

From the Department of Medical Imaging (Y.-w.Q., H.-h.S., G.-h.J.), Guangdong No. 2 Provincial People's Hospital, Guangzhou, China; Department of Medical Imaging (Y.-w.Q.), The First Affiliated Hospital of Gannan Medical University, Ganzhou, China; and Departments of Medical Imaging and Interventional Radiology (X.-f.L.), Cancer Center, Sun Yat-Sen University, Guangzhou, China.

This work was supported by a grant from the Natural Scientific Foundation of China (Grant No. 81201084 for Ying-wei Qiu). The funder had no role in study design, data collection and analysis, decision to publish, or preparation of the manuscript.

Please address correspondence to Ying-wei Qiu, MD, Department of Medical imaging, Guangdong No. 2 Provincial People's Hospital, 510317, Guangzhou, China; e-mail: qiuyl201@gmail.com

Indicates open access to non-subscribers at www.ajnr.org
<http://dx.doi.org/10.3174/ajnr.A4070>

such as neuroimaging have contributed to new insights into the neuropharmacology of CCS addiction.⁵⁻⁷ Hou et al⁵ used single-photon emission CT to demonstrate that the availability of dopamine transporter in the striatum and the volume, weight, and technetium Tc99m-TRODAT-1 corpus striatum/whole-brain uptake ratio were significantly less pronounced in CCS users than in controls. Using high-resolution structural MR imaging and resting-state functional MR imaging, our previous studies reported that the gray matter volume of the ventral medial prefrontal cortex and its functional integrity were deficient in chronic CCS users.^{6,7} However, to the best of our knowledge, the integrity of white matter in CCS users has not been investigated. Knowledge of white matter brain abnormalities and any association between these abnormalities and cognitive function in CCS users might facilitate identification of possible pharmacotherapies that could be used to treat this disorder.

Diffusion tensor imaging is an MR imaging technique used to quantitatively investigate white matter axonal integrity in vivo. DTI is based on the measurement of water molecular motion. Axonal structure restricts water diffusion so that it is greater in the axis parallel to the main axis of axons. Fractional anisotropy (FA) is a measure of the degree to which water diffusion is constrained in the brain, and it is widely used as a general index of axonal integrity.^{8,9} The component measures from which FA is derived, the first (λ_1) and second (λ_2) principal eigenvalues, indicate diffusion axial (parallel) and radial (perpendicular) to the primary axis of the axon. These values provide additional insight into the nature of white matter deficits.^{10,11} The former provides an index of axonal injury, and the latter is sensitive to changes in myelination.^{10,12}

In this study, DTI was used to investigate the white matter integrity of chronic CCS users. An observer-independent tract-based spatial statistics (TBSS) analysis was performed on the DTI data. This method retains the strengths of voxel-based analysis while addressing some of its drawbacks. Drawbacks include aligning images from multiple subjects and the arbitrariness of the choice of spatial smoothing.¹³ The aims of this study were the following: 1) to investigate differences in the topographic distribution of the integrity of white matter between CCS users and healthy controls, 2) to determine whether there was any relationship among abnormalities in the integrity of white matter and the duration of CCS use and a clinical impulsivity trait in CCS users.

MATERIALS AND METHODS

Subjects

This prospective study was approved by the local ethics committee. Written informed consent was obtained from all subjects. Sixty subjects, including 30 control subjects and 30 chronic CCS users, participated in this study. The CCS users were randomly selected from among patients seeking treatment at the Addiction Medicine Division of Guangdong No.2 Provincial People's Hospital. All the CCS users were screened by using the *Diagnostic and Statistical Manual of Mental Disorders-IV* criteria. A urine test and an interview were conducted by a clinical psychologist. All patients were naive for other types of illicit drug use. None of the 60 subjects (30 CCS users and 30 controls) included in present study meet the criteria of *Diagnostic and Statistical Manual of Mental Disorders-IV* for alcohol dependence, and none used alcohol reg-

ularly. Patients regularly used cigarettes and denied any use of psychotropic agents in the month before MR imaging. Inclusion criteria for the control subjects were a lack of a diagnosis of substance abuse or dependence. Exclusion criteria for all participants included neurologic illness, schizophrenia, bipolar disorder, prior significant head trauma, positive HIV status, diabetes, hepatitis C, other major medical illness, and left-handedness.

Behavioral Assessments

The Barratt Impulsiveness Scale (BIS) 11 was surveyed soon after MR imaging to assess participants' impulsivity. The BIS 11 is one of the oldest and most widely used self-reporting measures of impulsive personality traits. This 30-item self-rated scale evaluates 3 factors: attentional/cognitive traits, which refer to tolerance for cognitive complexity and persistence; motor, which refers to the tendency to act on the spur of the moment; and nonplan impulsivity, which refers to the lack of a sense of the future. Items were rated from 1 (rarely/never) to 4 (almost always/always). All items were summed to determine overall impulsiveness scores. Higher scores indicated greater impulsivity.¹⁴ The BIS 11 is a valid and reliable instrument for evaluating healthy and psychiatric Chinese populations.¹⁵

Image Acquisition

MR imaging data were obtained with a 1.5T MR scanner (Achieva Nova-Dual; Philips, Best, the Netherlands). Each subject lay supine with his or her head snugly fixed by a belt and foam pads. Before the DTI scan, a T1-weighted 3D sequence and fluid-attenuated inversion recovery images were captured to exclude subjects with abnormalities. Diffusion imaging data were acquired in 32 diffusion gradient directions ($b=800$ s/mm² along 32 noncollinear directions) plus $b=0$ reference images by using a single-shot spin-echo-planar sequence to collect diffusion-weighted images. Other imaging parameters were as follows: TR = 10,793 ms, TE = 62 ms, FOV = 230 × 230 mm², matrix = 128 × 128, section thickness = 2 mm with no section gap, and voxel size = 2 × 2 × 2 mm³.

Data Preprocessing

All DTI datasets were preprocessed by using the fMRI of the Brain Software Library, Version 4.1.7 (FSL; <http://www.fmrib.ox.ac.uk/fsl>). The raw DTI dataset was corrected for eddy current distortion and head motion by registering the diffusion-weighted images with the null image. This was performed by using affine transformations in the Diffusion Toolbox, Version 2.0, (part of FSL).¹⁶ The DTI datasets were then skull-stripped by using the Brain Extraction Tool, Version 1 (part of FSL) to remove background noise and nontissue components.¹⁷ The diffusion tensor was then calculated by using the DTIFit (from FSL) program for whole-brain volumes to produce FA and axial and radial diffusivities.

TBSS Analysis

Whole-brain voxelwise statistical analysis of the FA data was performed by using TBSS.^{13,16} The TBSS method minimizes potential misalignment problems of other voxel-based whole-brain forms of analysis by identifying a white-matter "skeleton" restricted only to the center of the major white-matter tracts. FA

Table 1: Demographic and clinical characteristics of the chronic codeine-containing cough syrup users and controls^a

Characteristic	CCS Users (n = 30)	Controls (n = 30)	Z Value	P Value
Age (yr) (mean, range)	25.07 (3.084, 20–31)	23.97 (2.470, 20–29)	2.706	.133
Sex (male/female)	28:2	28:2	–	1
Education (yr)	13.03 (2.760)	12.07 (3.423)	1.126	.233
Nicotine (No. cigarette/day)	16.53 (9.609)	13.50 (8.823)	0.036	.208
Cough syrup use (yr) (range)	5.08 (1~8)	N/A	–	–
Age of first use of cough syrup (yr) (range)	19.93 (12~30)	N/A	–	–
Mean dose (mL/day) (range)	487.33 (60~1800)	N/A	–	–
Total BIS scores	71.63 (4.597)	57.13 (5.178)	0.778	.000 ^b
Attentional impulsivity	18.27 (2.947)	15.57 (1.633)	5.341	.000 ^b
Motor impulsivity	30.50 (2.739)	22.13 (3.381)	2.727	.000 ^b
Nonplan impulsivity	22.87 (1.961)	19.63 (2.710)	1.755	.000 ^b

Note:—NA indicates not applicable; –, no value.

^aUnless otherwise indicated, data are means ± SDs.

^b*P* < .05.

values were mapped for each individual onto this standard skeleton for group comparison.

All subjects' FA data were aligned into a common space by using the FSL Nonlinear Registration Tool, FNIRT (<http://fsl.fmrib.ox.ac.uk/fsl/fslwiki/FNIRT>), which uses a b-spline representation of the registration warp field.¹⁸ The cross-subject mean FA image was calculated and used to generate a mean FA skeleton representing the centers of all tracts common to the whole study group. The threshold of the mean FA skeleton was set at 0.2 to exclude voxels that contained gray matter or CSF. Previous studies have also used the same threshold for the FA skeleton.¹⁹ Each individual subject's aligned FA data were projected onto this masked skeleton by filling the skeleton with FA values from the nearest relevant tract center. The skeletonized FA data were fed into the following voxelwise cross-subject statistics, which were based on a nonparametric permutation test (Randomize, part of FSL; <http://fsl.fmrib.ox.ac.uk/fsl/fslwiki/Randomise/UserGuide>).

Nonparametric 2-sample independent *t* tests were used to identify group differences in FA. This comparison was based on a permutation method because of the substantial non-Gaussian distribution of the FA data.^{13,20} Age, years of formal education, and histories of smoking were demeaned and served as nuisance covariates to ensure that any observed difference of FA was independent of these factors. Threshold-free cluster enhancement,²¹ an alternative to conventional cluster-based thresholding, which normally compromises the arbitrary definition of the cluster-forming threshold, was used to identify the significant differences between the 2 groups at *P* < .05. Multiple comparisons were accounted for by controlling for the family-wise error rate. Only clusters still significant after the voxel-level family-wise error (part of FSL) correction were reported. The most probable anatomic localization of each cluster was determined by the FSL Atlases tool (<http://fsl.fmrib.ox.ac.uk/fsl/fslwiki/Atlases>), which incorporates several anatomic templates, including the Talairach atlas, Montreal Neurological Institute structural atlas, Julich histologic atlas, Oxford thalamic connectivity atlas, Harvard-Oxford cortical and subcortical structural atlases, and the Johns Hopkins University DTI-based WM atlases. All reported brain images were acquired by using the "tbss_fill" script from the FSL package.

Volume-of-Interest Analysis of Diffusion Indices

Volume-of-interest analysis was performed to explore the microstructural mechanisms of the observed changes in FA. Changes in

the axial and radial diffusivities (axial, principal longitudinal direction, λ_1 , and radial, transverse diffusion component, $[\lambda_2 + \lambda_3] / 2$) of clusters showing significant FA decrease were calculated. VOI masks were first extracted on the basis of clusters showing significant intergroup FA differences. These VOI masks were then back-projected to the original images of each subject. The mean values of the diffusion indices within the VOIs were then calculated. A 1-sample Kolmogorov-Smirnov test was performed to evaluate the normality of the data. A 1-way analysis of covariance with the group as the independent variable and diffusion indices as the dependent variables was performed after controlling for age, formal years of education, and history of smoking. Statistical significance was set at *P* < .05. A Bonferroni correction was performed for multiple comparisons. A Pearson correlation analysis was used to assess correlations between changes in FA within the VOIs and behavioral measures and the duration of CCS use. *P* < .05 was considered statistically significant.

RESULTS

Demographic and Behavioral Measures

There were no significant differences in age, sex, formal years of education, or number of cigarettes smoked per day between the chronic CCS users and controls. The mean duration of CCS use was 5.05 years. The mean age of the first use of CCS was 19.93 years. The mean dose of CCS used was 487.33 mL/day in CCS users (Table 1).

A comparison of average of BIS 11 scores from the chronic CCS users and control groups is shown in Table 1. CCS users had significantly higher attentional impulsivity, motor impulsivity, nonplan impulsivity, and total scores than the control group (*P* < .05).

TBSS

A value of 0.2 was used to threshold the mean FA skeleton volume so that a total of 140,033 voxels were entered into the voxelwise TBSS analysis. The spatial distribution of the brain regions is presented in Fig 1 and Table 2. Chronic CCS users had lower FA than controls. CCS users had a significantly lower FA (*P* < .05; threshold-free cluster enhancement–corrected) in the inferior fronto-occipital fasciculus (IFO) of the bilateral temporo-occipital regions and the right frontal and the right corona radiata regions than controls. There were no white matter regions in which the controls had significantly lower FA values than the CCS users group.

VOI

Five clusters showed significant differences between the 2 groups, so the 2 left temporo-occipital IFO clusters were combined into 1 cluster. Four parts of the brain that showed significantly low FA values in CCS users were extracted for VOI-based analysis. The results are listed in Table 3. Clusters in CCS users from the bilateral

temporo-occipital regions of the IFO and the right corona radiata had lower FA values, greater radial diffusivity ($P = .000$; $P \leq .001$, and $P \leq .011$, respectively), and a lower axial diffusivity ($P \leq .027$; $P \leq .014$, and $P \leq .018$, respectively) than clusters from controls. The right frontal part of the IFO had a trend-level increase in radial diffusivity ($P \leq .001$) and no difference in longitudinal diffusivity ($P = .097$).

The Pearson correlation analysis demonstrated significant negative correlations between FA values of the right frontal region of the IFO ($r = -0.479$, $P = .007$) and the right superior corona radiata WM ($r = -0.450$, $P = .013$) with the BIS total scores (Fig 2) of chronic CCS users. There was a significant negative correlation between FA values of the right frontal region of the IFO ($r = -0.479$, $P = .007$) and nonplan scores (Fig 2) of chronic CCS users. There was also a significant negative correlation between FA values of the right frontal region of the IFO ($r = -0.561$, $P = .001$) and the duration of CCS use (Fig 3) in chronic CCS users.

DISCUSSION

Here, DTI was used with an observer-independent whole-brain voxelwise TBSS analysis to investigate the integrity of the WM of chronic CCS users. A control group was matched for age, sex, and years of education. Chronic CCS users had significantly lower FA values in the inferior fronto-occipital fasciculus of the right frontal region and the bilateral temporal-occipital regions and the right superior corona radiata WM (Fig 1 and Table 2). These results reflect the deficits in WM integrity and a disruption in the organization of WM tracts in chronic CCS users. This disruption appeared to be related to both myelin pathology and axonal injury, given the increased radial diffusivity and decreased axial diffusivity observed. Most important, the results of correlation analyses showed that FA

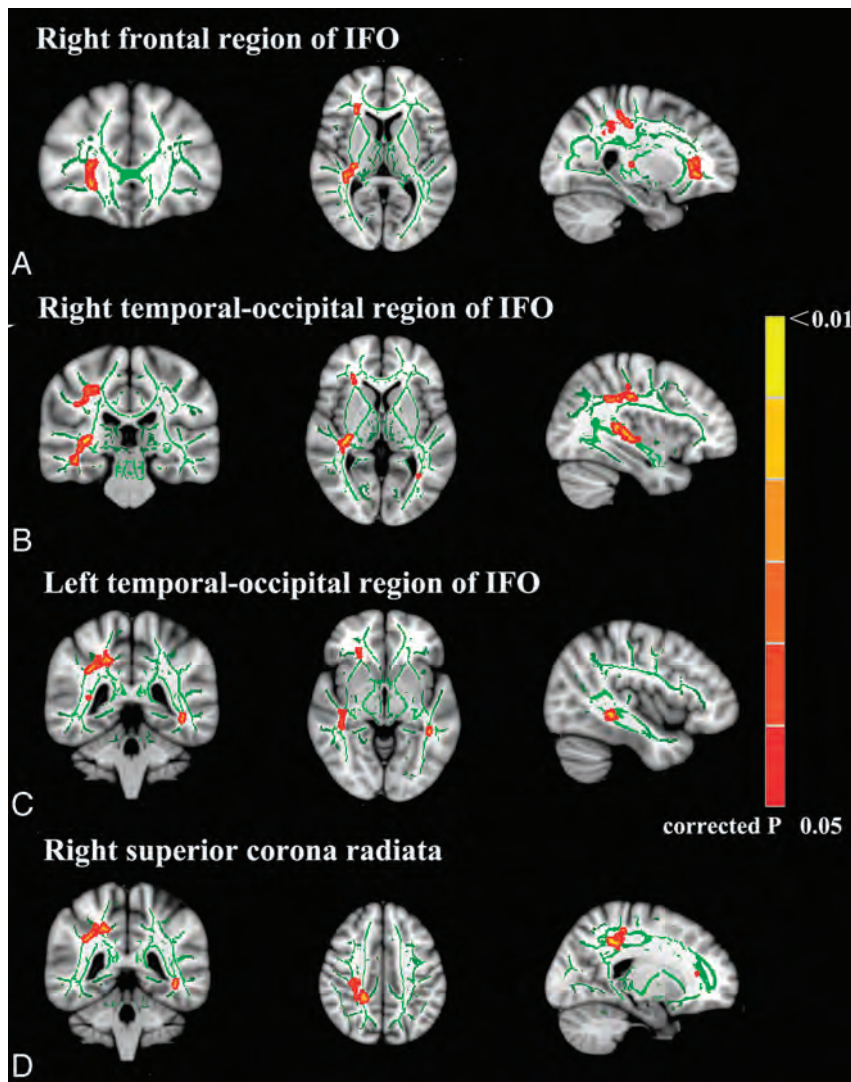


FIG 1. TBSS analysis of FA maps. Maps of the t value ($P < .05$ corrected for multiple comparisons) show, in red, the areas of significantly reduced FA in chronic codeine-containing cough syrup users compared with controls. A, The frontal region of the right IFO. B, The temporo-occipital region of the right IFO. C, The temporo-occipital region of left IFO. D, The right superior corona radiata.

Table 2: Neuroanatomic regions with reduced FA in CCS users relative to healthy controls

Anatomic Regions	Laterality	Talairach Coordinates (x, y, z) ^a	Cluster Size (cm)	Average FA		P Values (Minimum) ^b
				CCS Users	Controls	
Frontal region of the IFO	R	67,154,68	136	0.533	0.564	.048
Temporo-occipital region of IFO	R	54,95,77	389	0.452	0.499	.031
	L	130,84,65	40	0.622	0.661	.042
Superior corona radiata	R	123,66,72	38	0.477	0.549	.046
		71,83,112	586	0.578	0.646	.031

Note:—L indicates left; R, right.

^a All the coordinates are denoted by Montreal Neurological Institute space coordinates.

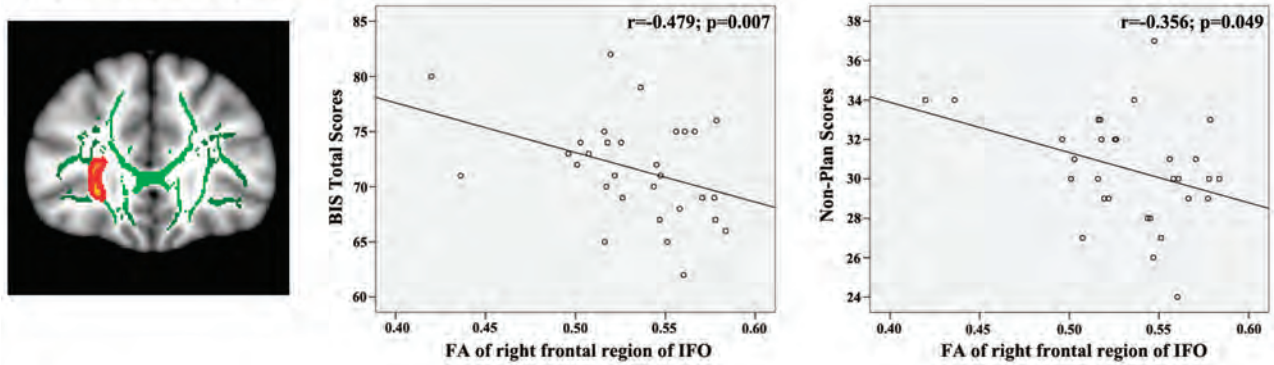
^b $P < .05$, threshold-free cluster enhancement—corrected).

Table 3: Group differences in diffusivity indices from volumes of interest (corrected for age, education, and histories of smoking)

Anatomic Region	λ_1 ($\times 10^{-3}\text{mm}^2/\text{s}$) (Mean)			λ_{\perp} ($\times 10^{-3}\text{mm}^2/\text{s}$) (Mean)		
	Controls	CCS	P Value	Controls	CCS	P Value
Right frontal part of IFO	1.37 \pm 0.05	1.35 \pm 0.05	.097	0.50 \pm 0.05	0.54 \pm 0.03	.001 ^a
Right temporo-occipital part of IFO	1.43 \pm 0.08	1.37 \pm 0.06	.014 ^a	0.40 \pm 0.05	0.45 \pm 0.04	.001 ^a
Left temporo-occipital part of IFO	1.44 \pm 0.07	1.40 \pm 0.07	.027 ^a	0.46 \pm 0.05	0.51 \pm 0.04	.000 ^a
Right superior corona radiata	1.27 \pm 0.07	1.22 \pm 0.07	.018 ^a	0.53 \pm 0.05	0.56 \pm 0.04	.011 ^a

^a $P < .05$.

Right frontal region of IFO



Right superior corona radiata

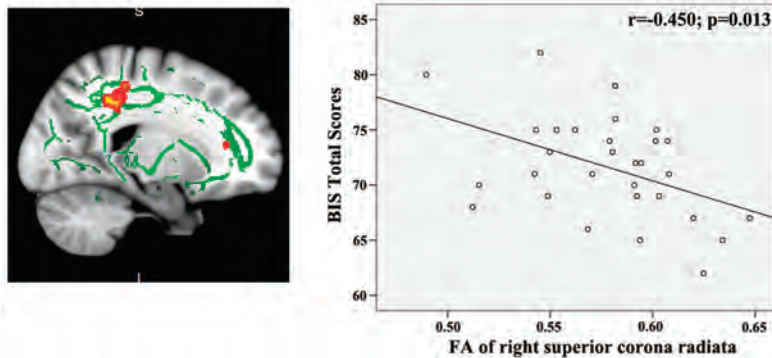


FIG 2. Correlations between mean fractional anisotropy and impulsivity traits in the chronic CCS users.

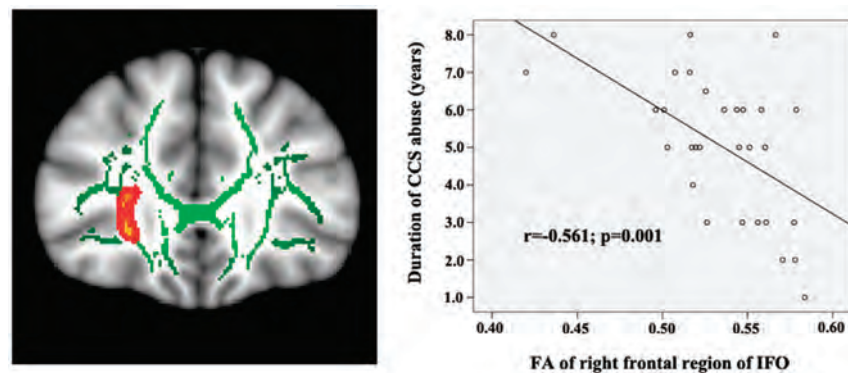


FIG 3. Correlations between mean fractional anisotropy of the right frontal region of the IFO and the duration of CCS use in chronic CCS users.

of the right frontal region of the IFO and the right superior corona radiata WM was negatively correlated with BIS total scores; FA of the right frontal region of the IFO was negatively correlated with nonplan impulsivity and the duration of CCS use in chronic CCS

users (Fig 2). These findings suggest that chronic CCS abuse may cause progressive brain WM integrity impairment. Furthermore, these WM microstructural deficits may be linked to higher impulsivity traits in chronic CCS users.

Abnormal WM Integrity in Chronic CCS Users

A low FA value was found in the bilateral IFO, the right frontal region, and the bilateral temporo-occipital regions of chronic CCS users. The IFO is thought to be part of the dorsal visual stream,²² originating from the dorsal parieto-occipital and medial parietal areas and projecting into the lateral prefrontal areas.²³ The IFO is thought to be involved in processing information that controls action.²⁴ Abnormal WM integrity in the IFO has consistently been observed in other forms of addiction, such as Internet,²⁵

alcohol,²⁶ and heroin.²⁷ The observation of a lower FA value in the bilateral IFO of chronic CCS users is consistent with these previous reports and with the clinical observation that CCS abuse is associated with impaired cognitive control.²⁻⁴ The anterior part of the IFO may be involved in response inhibition. Increased coherence of the anterior part of the IFO might give rise to an increased ability to implement inhibition to overcome the incorrect visuospatial task preparation and hence the incorrect competing response found in invalidly but not validly cued trials.²⁸ The negative correlation among FA values of the right frontal region of the IFO and BIS total scores and nonplan scores supports this hypothesis.

The right superior corona radiata WM also had a lower FA value in CCS users. The corona radiata comprises WM fibers linking the cerebral cortex to the internal capsule and provides important connections among the frontal, parietal, temporal, and occipital lobes.²⁹ Given its anatomic location, the corona radiata WM has been linked to risk-taking, including both cognitive and motor components.^{29,30} The abnormal WM integrity of the right superior corona radiata observed in this study may account for the risk-taking behavior and higher impulsivity found in chronic CCS users. Loss of WM integrity in the corona radiata has been consistently observed in cocaine,³¹ methamphetamine,³² and alcohol dependence.³³ These findings are consistent with those of previous results. The significant negative correlation between the FA value of the right superior corona radiata and the BIS total score supports the conclusions of previous functional studies linking the parietal lobe to impulse control.³⁴

Results also showed the FA values of the right frontal region of the IFO to be negatively correlated to the duration of CCS use. The disruption of white matter integrity in this region may be due to this use. The FA values of the 3 other parts of the brain regions that showed differences between users and controls did not demonstrate any such correlation. Several factors might explain these findings. First, the relatively small sample size could have insufficient power to detect such a difference. Although no significant correlation was found between the FA values of the other 3 parts of the brain and the duration of CCS use, negative trends were observed. Further studies with larger sample sizes are needed. Second, the lower FA values in these regions may not be the result of CCS abuse. They may represent a predisposition to substance abuse.³⁵ Further studies with long-term follow-up are needed to confirm this inference.

Possible Mechanisms Underlying Decreases in FA

The FA value of WM may be affected by many factors, including myelination, axon size, axon attenuation, axonal path geometry, and extracellular water space between fibers.³⁶ Results showed CCS-related WM microstructural damage to be associated with reduced axial diffusivity and increased radial diffusivity in bilateral temporo-occipital regions of the IFO and right superior corona radiata WM. Radial diffusivity mainly reflects the integrity and thickness of myelin sheets covering the axons.¹² Axial diffusivity may reflect the organization of the fibers and axon integrity.¹² The disruption of WM integrity seen in the brain of chronic CCS users is most likely a manifestation of the loss of myelin and axon integrity. Postmortem and DTI studies have also demon-

strated myelin dissolution²⁸ and axon disruption³⁷ in opiate-dependent individuals. Büttner et al³⁷ found β -amyloid precursor protein-immunopositive accumulations to be significantly more pronounced in heroin-predominant polydrug addicts, indicating diffuse axonal damage. Similarly, Bora et al²⁷ demonstrated widespread deficits of white matter integrity in heroin addicts.

Relationship between FA and Behavioral Measures in Chronic CCS Users

Chronic CCS users showed significantly higher BIS total scores, attentional scores, nonplan scores, and motor scores than controls. These findings are consistent with the results of previous neuropsychological studies of heroin and cocaine addicts.³⁸ Results also showed that the BIS total scores were correlated to the FA values of the right frontal region of the IFO and the right superior corona radiata in CCS users. Higher nonplan impulsivity scores were associated with more severe loss of white matter integrity in the right frontal region of the IFO. This association indicates that disruption of the WM integrity in these regions may be responsible for the higher impulsivity found in chronic CCS users. These inferences are supported by a previous study by Lane et al,³⁹ which showed a significant relationship between impaired decision-making (by Iowa gambling task) and DTI-measured white matter integrity in the frontal and parietal regions of cocaine-dependent subjects. In turn, the findings of significant associations among impaired white matter integrity in the right frontal region of the IFO and the right superior corona radiata WM and higher impulsivity in CCS users suggest that white matter integrity may serve as a predictor of abstinence or a potential new treatment target for CCS users.

Limitations of This Study

There were several limitations to the current study. First, the study was cross-sectional in design. The integrity of abnormal white matter was observed in CCS users, and associations with chronic CCS use were inferred. However, we cannot absolutely assert the causation of the CCS dependence and the abnormalities of the white matter integrity. It requires a long-term longitudinal follow-up with detailed experimental and clinical profiling of a cohort of subjects in a future study. The second limitation of this study concerns imaging. The assessment of small fiber tracts was difficult with TBSS because only the major white matter tracts were included in the skeleton.¹³ Because of the nonlinear alignment process, the FA, λ_{\perp} , and λ_1 values that were attributed to a given voxel were not actually measured from that spatial location. Instead, they were derived from a neighborhood, which may disguise the results.¹³ Third, the DTI sequence had only 1 acquisition at $b=0$ s/mm², due to limitations of the imager.⁴⁰ Last, the lifetime quantity of alcohol use was not measured in present study; although none of the subjects included in present study met the *Diagnostic and Statistical Manual of Mental Disorders-IV* criteria for alcohol dependence, binge drinking has been found to be associated with reduced FA in previous studies.⁴¹ Heavier alcohol use without dependence could be related to the present findings.

CONCLUSIONS

DTI was used with TBSS analysis to investigate the microstructure of WM in chronic CCS users. Chronic CCS users are character-

ized by impairment of WM fibers in the bilateral temporo-occipital regions and the right frontal region of the IFO and the right superior corona radiata. In addition, these progressive changes in WM microstructure may be neural and cause greater impulsivity in chronic CCS users.

REFERENCES

- Hutchings HA, Eccles R. The opioid agonist codeine and antagonist naltrexone do not affect voluntary suppression of capsaicin induced cough in healthy subjects. *Eur Respir J* 1994;7:715–19
- Vree TB, van Dongen RT, Koopman-Kimenai PM. Codeine analgesia is due to codeine-6-glucuronide, not morphine. *Int J Clin Pract* 2000;54:395–98
- Shek DT, Lam CM. Adolescent cough medicine abuse in Hong Kong: implications for the design of positive youth development programs in Hong Kong. *Int J Adolesc Med Health* 2006;18:493–503
- Mattoo SK, Basu D, Sharma A, et al. Abuse of codeine-containing cough syrups: a report from India. *Addiction* 1997;92:1783–87
- Hou H, Yin S, Jia S, et al. Decreased striatal dopamine transporters in codeine-containing cough syrup abusers. *Drug Alcohol Depend* 2011;118:148–51
- Qiu Y, Lv X, Su H, et al. Reduced regional homogeneity in bilateral frontostriatal system relates to higher impulsivity behavior in codeine-containing cough syrups dependent individuals. *PLoS One* 2013;8:e78738
- Qiu Y, Lv X, Jiang G, et al. Reduced ventral medial prefrontal cortex (vmPFC) volume and impaired vmPFC-default mode network integration in codeine-containing cough syrups users. *Drug Alcohol Depend* 2014;134:314–21
- Le Bihan D, Mangin JF, Poupon C, et al. Diffusion tensor imaging: concepts and applications. *J Magn Reson Imaging* 2001;13:534–46
- Kubicki M, Westin CF, Maier SE, et al. Diffusion tensor imaging and its application to neuropsychiatric disorders. *Harv Rev Psychiatry* 2002;10:324–36
- Wozniak JR, Lim KO. Advances in white matter imaging: a review of in vivo magnetic resonance methodologies and their applicability to the study of development and aging. *Neurosci Biobehav Rev* 2006;30:762–74
- Seal ML, Yücel M, Fornito A, et al. Abnormal white matter microstructure in schizophrenia: a voxelwise analysis of axial and radial diffusivity. *Schizophr Res* 2008;101:106–10
- Song SK, Yoshino J, Le TQ, et al. Demyelination increases radial diffusivity in corpus callosum of mouse brain. *Neuroimage* 2005;26:132–40
- Smith SM, Jenkinson M, Johansen-Berg H, et al. Tract-based spatial statistics: voxelwise analysis of multi-subject diffusion data. *Neuroimage* 2006;31:1487–505
- Patton JH, Stanford MS, Barratt ES. Factor structure of the Barratt impulsiveness scale. *J Clin Psychol* 1995;51:768–74
- Yao S, Yang H, Zhu X, et al. An examination of the psychometric properties of the Chinese version of the Barratt Impulsiveness Scale, 11th version in a sample of Chinese adolescents. *Percept Mot Skills* 2007;104:1169–82
- Smith S, Jenkinson M, Woolrich M, et al. Advances in functional and structural MR image analysis and implementation as FSL. *Neuroimage* 2004;23:208–19
- Smith S. Fast robust automated brain extraction. *Hum Brain Mapp* 2002;17:143–55
- Rueckert D, Sonoda LI, Hayes C, et al. Nonrigid registration using free-form deformations: application to breast MR images. *IEEE Trans Med Imaging* 1999;18:712–21
- Versace A, Almeida J, Hassel S, et al. Elevated left and reduced right orbitomedial prefrontal fractional anisotropy in adults with bipolar disorder revealed by tract-based spatial statistics. *Arch Gen Psychiatry* 2008;65:1041–52
- Jones DK, Symms MR, Cercignani M, et al. The effect of filter size on VBM analyses of DT-MRI data. *Neuroimage* 2005;26:546–54
- Smith SM. Threshold-free cluster enhancement: addressing problems of smoothing, threshold dependence and localization in cluster inference. *Neuroimage* 2009;44:83–98
- Mishkin M, Ungerleider LG. Contribution of striate inputs to the visuospatial functions of parieto-occipital cortex in monkeys. *Behav Brain Res* 1982;6:57–77
- Schmahmann JD, Pandya DN, Wang R, et al. Association fibre pathways of the brain: parallel observations from diffusion spectrum imaging and autoradiography. *Brain* 2007;130:630–53
- Rizzolatti G, Matelli M. Two different streams form the dorsal visual system: anatomy and functions. *Exp Brain Res* 2003;153:146–57
- Lin F, Zhou Y, Du Y, et al. Abnormal white matter integrity in adolescents with internet addiction disorder: a tract-based spatial statistics study. *PLoS One* 2012;7:e30253
- Herting MM, Schwartz D, Mitchell SH, et al. Delay discounting behavior and white matter microstructure abnormalities in youth with a family history of alcoholism. *Alcohol Clin Exp Res* 2010;34:1590–602
- Bora E, Yücel M, Fornito A, et al. White matter microstructure in opiate addiction. *Addict Biol* 2012;17:141–8
- Forstmann BU, Jahfari S, Scholte HS, et al. Function and structure of the right inferior frontal cortex predict individual differences in response inhibition: a model-based approach. *J Neurosci* 2008;28:9790–96
- Wakana S. Fiber tract-based atlas of human white matter anatomy. *Radiology* 2004;230:77–87
- Berns GS, Moore S, Capra CM. Adolescent engagement in dangerous behaviors is associated with increased white matter maturity of frontal cortex. *PLoS One* 2009;4:e6773
- Bell RP, Foxe JJ, Nierenberg J, et al. Assessing white matter integrity as a function of abstinence duration in former cocaine-dependent individuals. *Drug Alcohol Depend* 2011;114:159–68
- Tobias MC, O'Neill J, Hudkins M, et al. White-matter abnormalities in brain during early abstinence from methamphetamine abuse. *Psychopharmacology* 2010;209:13–24
- Yeh PH, Simpson K, Durazzo TC, et al. Tract-based spatial statistics (TBSS) of diffusion tensor imaging data in alcohol dependence: abnormalities of the motivational neurocircuitry. *Psychiatry Res* 2009;173:22–30
- Hinvest NS, Elliott R, McKie S, et al. Neural correlates of choice behavior related to impulsivity and venturesomeness. *Neuropsychologia* 2011;49:2311–20
- Haney-Caron E, Caprihan A, Stevens MC. DTI-measured white matter abnormalities in adolescents with conduct disorder. *J Psychiatr Res* 2014;48:111–20
- Le Bihan D. Looking into the functional architecture of the brain with diffusion MRI. *Nat Rev Neurosci* 2003;4:469–80
- Büttner A, Rohrmoser K, Mall G, et al. Widespread axonal damage in the brain of drug abusers as evidenced by accumulation of beta-amyloid precursor protein (beta-APP): an immunohistochemical investigation. *Addiction* 2006;101:1339–46
- Verdejo-García AJ, Perales JC, Pérez-García M. Cognitive impulsivity in cocaine and heroin polysubstance abusers. *Addict Behav* 2007;32:950–66
- Lane SD, Steinberg JL, Ma L, et al. Diffusion tensor imaging and decision making in cocaine dependence. *PLoS One* 2010;5:e11591
- Smith S, Johansen-Berg H, Jenkinson M, et al. Acquisition and voxelwise analysis of multi-subject diffusion data with tract-based spatial statistics. *Nat Protoc* 2007;2:499–503
- Kong LM, Zheng WB, Lian GP, et al. Acute effects of alcohol on the human brain: diffusion tensor imaging study. *AJNR Am J Neuroradiol* 2012;33:928–34

Iron and Volume in the Deep Gray Matter: Association with Cognitive Impairment in Multiple Sclerosis

C.M. Modica, R. Zivadinov, M.G. Dwyer, N. Bergsland, A.R. Weeks, and R.H.B. Benedict

ABSTRACT

BACKGROUND AND PURPOSE: There is a well-established correlation between deep gray matter atrophy and cognitive dysfunction in MS. However, the cause of these signs of neurodegeneration is poorly understood. Iron accumulation in the deep gray matter is higher in patients with MS compared with age- and sex-matched healthy controls, and could contribute to disease progression. Our objective was to evaluate the relationship between iron and cognition in several deep gray matter structures while accounting for the influence of volume loss.

MATERIALS AND METHODS: Eighty-five patients with MS and 27 healthy volunteers underwent 3T MR imaging and neuropsychological examination. We used SWI filtered phase to analyze the mean phase of low-phase voxels, indicative of abnormal iron accumulation.

RESULTS: Correlations between mean phase of low-phase voxels and cognitive tests were found in the caudate nucleus ($r = 0.240$ and 0.232), putamen ($r = 0.368$, 0.252 , and 0.238), globus pallidus ($r = 0.235$), and pulvinar nucleus of thalamus ($r = 0.244$, 0.255 , and 0.251) ($P < .05$). However, correlations between structure volume and cognition were more robust. Furthermore, the introduction of structure volume into hierarchical regression analyses after iron metrics significantly improved most models, and mean phase of low-phase voxels did not account for significant variance after volume.

CONCLUSIONS: These findings suggest that iron accumulation plays a significant, if minor, role in MS cognitive decline.

ABBREVIATIONS: BVMT-R = the total learning portion of the Brief Visuospatial Memory Test-Revised; CVLT2 = total learning portion of the California Verbal Learning Test; DGM = deep gray matter; DKEFS-CS = Delis-Kaplan Executive Function System Sorting Test; LPV = low-phase voxel; MP-LPV = mean phase of the low-phase voxels; NP = neuropsychological; PASAT = 3-second Paced Auditory Serial Addition Test; SDMT = Symbol Digit Modalities Test

Investigation of iron accumulation in the central nervous system is an emerging area of research. Iron is elevated in MS at the areas of demyelination¹ and in the CSF,² and could potentially contribute to the understanding of progressive neurodegenerative disease. Iron deposition may adversely impact cellular function, such as enhancing or decreasing production of proteins, or it can cause oxidative stress leading to cell death, directly causing structural damage in the brain.³

SWI is an available method that estimates the degree of iron

deposition, in vivo, using MR imaging.⁴ In a study examining the deep gray matter (DGM) of patients with MS, low-phase voxel (LPV) analysis reflected increased iron accumulation in the caudate nucleus, putamen, globus pallidus, and pulvinar.⁵ Even in clinically isolated syndrome, this representation of increased iron accumulation was found in the putamen and pulvinar.⁶ In a pediatric MS cohort, analysis of LPV reflected increased iron accumulation in both the thalamus and pulvinar while the volume of the LPV was increased in the pulvinar.⁷ LPV volume was also increased in clinically isolated syndrome in the caudate nucleus, putamen, and pulvinar,⁶ and magnetic susceptibility (also indicative of iron level) was increased in the caudate nucleus, putamen, globus pallidus, and pulvinar.⁸

Contemporary research shows that brain atrophy is predictive of cognitive disability in MS, more so than lesion burden.^{9,10} GM atrophy is the subject of intense research because of its correlation with disease progression, neurologic disability,¹¹ cognitive impairment, and neuropsychiatric symptoms.¹² Regional analysis of the DGM in MS revealed that volume is reduced in the thalamus, caudate nucleus, putamen, and globus pallidus.^{13,14} Likewise,

Received November 18, 2013; accepted after revision April 7, 2014.

From the Neuroscience Program (C.M.M.), Buffalo Neuroimaging Analysis Center (C.M.M., R.Z., M.G.D., N.B., R.H.B.B.), MR Imaging Clinical Translational Research Center (R.Z.), and Department of Neurology (R.Z., R.H.B.B.), School of Medicine and Biomedical Sciences, and School of Public Health and Health Professions (A.R.W.), University at Buffalo, State University of New York, Buffalo, New York; and IRCCS (N.B.), "S. Maria Nascente," Don Gnocchi Foundation, Milan, Italy.

This study was supported in part by National MS Society grant #RG4060A3/1 awarded to R.H.B. Benedict.

Please address correspondence to Ralph H.B. Benedict, PhD, SUNY Buffalo Neurology, 100 High St, Suite E2, Buffalo, NY 14203; e-mail: benedict@buffalo.edu

<http://dx.doi.org/10.3174/ajnr.A3998>

Table 1: Demographic characteristics, neuropsychological test scores, and mean phase of the low-phase voxels across subcortical deep gray matter structures

	MS (n = 85)	NC (n = 27)	P Value
Characteristics			
Age	46.0 ± 9.2	41.9 ± 10.7	NS ^a
Education	14.4 ± 2.2	15.3 ± 2.4	NS ^a
Female, n (%)	59 (69.4)	17 (63.0)	NS ^a
Caucasian, n (%)	73 (85.9)	24 (88.9)	NS ^a
Right-handed, n (%)	77 (90.6)	25 (92.6)	NS ^a
Impaired, n (%)	52 (61.2)	1 (3.7)	<.001 ^a
Disease duration	10.9 ± 7.6		
DMT duration ^b	3.8 ± 3.6		
EDSS ^c	3.6 ± 1.9		
T2 lesion volume	18.5 ± 20.3		
T1 lesion volume	3.4 ± 7.1		
NP test scores			
SDMT	50.8 ± 15.8	66.0 ± 10.5	<.001 ^d
PASAT	42.0 ± 15.7	49.8 ± 8.7	.017 ^d
DKEFS-CS	9.5 ± 3.0	11.7 ± 2.4	<.001 ^d
CVLT2	52.1 ± 13.1	64.4 ± 7.4	<.001 ^d
BVMT-R	7.8 ± 2.8	10.4 ± 1.5	<.001 ^d
MP-LPV			
Thalamus	-0.099 ± 0.016	-0.092 ± 0.011	.027 ^a
Caudate nucleus	-0.178 ± 0.021	-0.166 ± 0.011	.007 ^a
Putamen	-0.184 ± 0.033	-0.172 ± 0.028	NS ^a
Globus pallidus	-0.195 ± 0.036	-0.179 ± 0.029	NS ^a
Pulvinar	-0.157 ± 0.036	-0.139 ± 0.012	.014 ^a

Note:—NC indicates healthy control; DMT, disease-modifying therapy; EDSS, Expanded Disability Status Scale; NS, not significant.

^a P value is based on 1-way ANOVA.

^b n = 68 for calculation of DMT duration as only 68 were on therapy.

^c n = 83 for calculation of mean EDSS as 2 patients were not assessed during their clinical visit.

^d P value is based on 1-way ANCOVA, controlling for age and years of education. Age, education, disease duration, and DMT duration data are given as mean years ± SD. Lesion volume is given as mean milliliters ± SD. NP test data for the SDMT, PASAT, DKEFS-CS, CVLT2, and BVMT-R are given as mean test score ± standard deviation. MP-LPV data in the thalamus, caudate nucleus, putamen, globus pallidus, and pulvinar structures are given as radians ± SD.

lower thalamus volume is found in clinically isolated syndrome,¹⁵ and both whole thalamus and pulvinar volume are decreased in patients with pediatric onset.¹⁶ DGM volumes are strongly correlated with fatigue¹⁷ and performance on cognitive tests.^{13,14} Total DGM volume was the strongest predictor of Expanded Disability Status Scale scores in a study utilizing various MR imaging metrics; LPV analysis, reflecting iron accumulation in the DGM, further increased the percentage of variance in the regression model.¹⁸

In sum, the literature shows that DGM atrophy is strongly associated with cognitive dysfunction in MS.¹³ However, the role of iron deposition, as observed with SWI-filtered phase, in explaining cognitive dysfunction is less clear, and potentially interactive effects of iron and volume have not been explored. Here we present findings from an initial investigation of the relationship of iron deposition and cognitive ability in patients with MS.

MATERIALS AND METHODS

Participants

We studied 85 patients with clinically definite MS¹⁹ and 27 healthy, demographically matched controls (Table 1) with approval from the Institutional Review Board. These subjects were a subset from a previously published cohort, and informed consent was obtained.^{12,13} Patients were excluded from the study if they had previous or current substance abuse, current or past major medical, neurologic, or psychiatric disorder outside of MS, or if they had a relapse or steroid pulse treatment within 8 weeks before

evaluation. Patients with depressive disorders that emerged after MS onset were permitted, but those meeting criteria for current major depressive episode were excluded. Participants were free of developmental delay and any medical history that could potentially impact cognitive ability. Of the patients with MS, 57 (67.1%) were in relapsing-remitting, and 28 (32.9%) were in secondary-progressive disease course. Sixty-eight (80.0%) patients with MS were on disease-modifying therapy at the time of the study. Therapy included intramuscular interferon beta-1a, 44 mcg subcutaneous interferon beta-1a, natalizumab, glatiramer acetate, mycophenolate mofetil, intravenous immunoglobulin, interferon beta-1b, mitoxantrone, and the following combinations: intramuscular interferon beta-1a + mycophenolate mofetil, 22 mcg + 44 mcg subcutaneous interferon beta-1a, and glatiramer acetate + mycophenolate mofetil.

MR Imaging Acquisition and Analysis

Participants were examined on a 3T Signa Excite HD 12.0 Twin Speed 8-channel scanner (GE Healthcare, Milwaukee, Wisconsin) with a maximum slew rate of 150 T/m/s and maximum gradient amplitude in each orthogonal plane of 50 mT/m. A multichannel head and neck coil (GE Healthcare) was used to acquire: 2D multiplanar dual FSE proton density and T2WI; FLAIR; 3D high-resolution T1WI using a fast-spoiled gradient echo with magnetization-prepared inversion recovery pulse and spin-echo T1WI; and SWI. Scans were acquired in an axial-oblique orientation, parallel to the subcallosal line. One average was used for all pulse sequences. With the exception of SWI, all sequences were acquired with a 256 × 192 matrix (frequency × phase), FOV of 25.6 cm × 19.2 cm (256 × 256 matrix with phase FOV = 0.75), for an in-plane resolution of 1 mm × 1 mm. For all 2D scans (proton density/T2, FLAIR, spin-echo T1), we collected 48 contiguous, 3-mm-thick sections. For the 3D high-resolution inversion recovery-fast-spoiled gradient echo, we acquired 180 1-mm-thick locations. Other relevant parameters were: for dual FSE proton density/T2, TE1/TE2/TR = 9/98/5300 ms, echo-train length = 14; for FLAIR, TE/TI/TR = 120/2, 100/8, 8500 ms, echo-train length = 24; spin-echo T1WI, TE/TR = 16/600 ms; for 3D high-resolution T1WI, TE/TI/TR = 2.8/900/5.9 ms, flip angle = 10°. SWI was acquired using a 3D flow-compensated gradient-echo sequence with 64 contiguous, 2-mm-thick sections, a 512 × 192 matrix, FOV = 25.6 cm × 19.2 cm (512 × 256 matrix with phase FOV 0.75), for an in-plane resolution of 0.5 mm × 1 mm, flip angle = 12°, and TE/TR = 22/40 ms.

T2 and T1 lesion volume was measured using a semiautomated edge detection contouring technique as previously de-

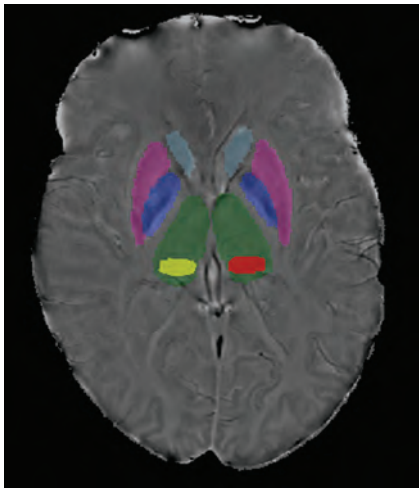


FIG 1. Scan demonstrating deep gray matter structure segmentation. FMRIB's Integrated Registration and Segmentation Tool was applied to the 3D high-resolution T1WI to segment the DGM. Pulvinar (yellow and red) was segmented using a semiautomated contouring technique.

scribed.²⁰ To segment the thalamus, caudate nucleus, putamen, and globus pallidus, FMRIB's Integrated Registration and Segmentation Tool²¹ (<http://www.fmrib.ox.ac.uk/>) was applied to the 3D high-resolution T1WI (Fig 1). As the pulvinar was not identified in this manner, the most representative section was outlined for each patient using a semiautomated contouring technique (Fig 1).²² The SWI-filtered phase image processing method and reproducibility were discussed in a previous study involving reliable scan-rescan analysis in a subset of 6 patients with MS and 6 healthy volunteers.⁵ Voxels having a mean phase value 2 SDs below normal mean phase were identified on a structure-by-structure basis, as previously described, with normal mean phase identified from 330 healthy volunteers aged 8–87 years.²⁰ The thresholded phase voxels, which were identified as abnormally low, were analyzed to calculate their mean phase, yielding mean phase of the low-phase voxels (MP-LPV).²²

Neuropsychological Testing

Neuropsychological testing (NP) was conducted under the supervision of a board-certified neuropsychologist blinded to MR imaging findings. Tests measured processing speed, executive function, and memory in accordance with the recommendations of a consensus panel,²³ and were as follows: oral administration of the Symbol Digit Modalities Test (SDMT)²⁴ for visual information-processing speed; 3.0-second interval Paced Auditory Serial Addition Test (PASAT)²⁵ for auditory information-processing speed; the Correct Sorts component of the Delis-Kaplan Executive Function System Sorting Test (DKEFS-CS)²⁶ for executive function; the Total Learning portion of the second edition of the California Verbal Learning Test (CVLT2)²⁷ for auditory/verbal learning and memory; and the Total Learning portion of the Brief Visuospatial Memory Test-Revised (BVM-T-R)²⁸ for visual learning and memory.

Statistical Analysis

Patients with MS and healthy controls as well as cognitively impaired and nonimpaired patients with MS were compared with

respect to demographic characteristics and MR imaging findings using 1-way ANOVA. Z scores were calculated for each NP test based on healthy controls.²⁹ Impairment was defined as either: a z score < -2 on 1 test with a z score of < -1.5 on at least 1 other test; a z score of < -1.5 on at least 3 tests, as previously defined.³⁰ In patients with MS, age and years of education were correlated with some NP test scores (SDMT, PASAT, DKEFS-CS, CVLT2); therefore, NP tests were compared between patients with MS and healthy controls using 1-way ANCOVA controlling for age and years of education. Partial correlations controlling for age and years of education assessed the association between NP tests and individual DGM structure volumes, disease duration, and duration of disease-modifying therapy. Pearson correlations were examined between MP-LPV and structure volume and LPV volume. Partial correlations controlling for LPV volume, age, and years of education were examined between NP tests and MP-LPV for individual structures of the DGM. Structures that had the strongest relationship of MP-LPV to NP test performance were included in hierarchical linear regression analyses controlling for age and years of education (in Block 1), followed by LPV volume of the structure in Block 2, MP-LPV of the structure in Block 3, and total tissue volume of the structure in Block 4. In this manner, we assessed the association between iron deposition and cognition, and then reassessed the association while controlling for the effects of atrophy. Tests were considered significant at $P < .05$. Analyses were conducted using SPSS for Windows, version 20.0 (IBM, Armonk, New York).

RESULTS

As expected, patients with MS were significantly more cognitively impaired and performed significantly worse on cognitive tests compared with healthy controls (Table 1). MP-LPV was significantly lower in patients with MS in the thalamus, caudate nucleus, and pulvinar, whereas a statistical trend was found for the putamen ($P = .085$) and globus pallidus ($P = .051$) (Table 1). Age, education, and MP-LPV did not significantly differ between cognitively impaired patients with MS and nonimpaired patients with MS, but duration of disease did ($P = .009$). Except for the globus pallidus with CVLT2, all individual structure volumes were significantly correlated to NP test scores (Table 2). Duration of disease and duration of disease-modifying therapy were not related to NP test scores, and were not further investigated.

Next, we assessed whether MP-LPV was linearly related to cognitive performance in patients with MS. To account for the possibility that tissue atrophy results in tissue loss specifically in regions of low-phase value, thereby potentially altering distribution of iron accumulation, we chose to control for the LPV volume. Controlling for LPV volume, MP-LPV of the caudate nucleus, putamen, globus pallidus, and pulvinar, but not the thalamus, correlated with multiple NP test results (Table 2).

MP-LPV was positively correlated with total volume in the same structure in the caudate and pulvinar, and there was a trend with the putamen ($P = .075$), indicating that as iron accumulation increases, the structure decreases in size. MP-LPV was negatively correlated with LPV volume in the same structure in the putamen, globus pallidus, and pulvinar, indicating that as iron accumulation increases, the voxels that contain abnormally high

Table 2: Partial correlation of structure volume and mean phase of the low-phase voxels to neuropsychological tests in patients with multiple sclerosis

	SDMT		PASAT		DKEFS-CS		CVLT2		BVMT-R	
	<i>r</i>	<i>P</i>								
Volume ^a										
Thalamus	0.548	<.001	0.354	.001	0.422	<.001	0.313	.004	0.415	<.001
Caudate nucleus	0.470	<.001	0.357	.001	0.409	<.001	0.257	.019	0.348	.001
Putamen	0.516	<.001	0.405	<.001	0.429	<.001	0.382	<.001	0.518	<.001
Globus pallidus	0.449	<.001	0.296	.007	0.348	.001		NS	0.282	.010
Pulvinar	0.279	.011	0.275	.012	0.309	.005	0.221	.044	0.327	.003
MP-LPV ^b										
Caudate nucleus	0.240	.030	0.232	.036		NS		NS		NS
Putamen	0.368	.001		NS	0.252	.022		NS	0.238	.031
Globus pallidus		NS		NS		NS		NS	0.235	.033
Pulvinar	0.244	.027		NS	0.255	.021		NS	0.251	.023

Note:—NS indicates not significant.

^a Controlling for age and education.

^b Controlling for age, education, and low-phase voxel volume.

Table 3: Mean phase of the low-phase voxels correlated with structure volume and with low-phase voxel volume

	Volume		LPV Volume	
	<i>r</i>	<i>P</i>	<i>r</i>	<i>P</i>
Caudate nucleus	0.268	.013		NS
Putamen		NS	−0.502	<.001
Globus pallidus	−0.452	<.001	−0.483	<.001
Pulvinar	0.266	.014	−0.659	<.001

Note:—NS indicates not significant.

iron accumulation decrease in collective volume in those structures (Table 3).

Finally, we investigated whether iron-sensitive metrics would have a significant bearing on cognitive function relative to age, education, and volumes of the DGM structures showing a significant correlation between MP-LPV and cognition. The R^2 and P values of each regression model are reported in Table 4. With the exception of the caudate nucleus for the PASAT, MP-LPV (controlling for LPV volume) added significant variance in the regression models predicting performance score. However, volume of the structure improved all of the models, except for DKEFS-CS and BVMT-R, as predicted by MP-LPV of the pulvinar. Moreover, when a second series of regression models was conducted with structure volume entered ahead of the iron metrics, MP-LPV was not statistically significant. Furthermore, when a third series of regression models was conducted with T2 lesion volume entered along with age and education, none of the other MR imaging measures remained statistically significant.

DISCUSSION

This study demonstrated a correlation between iron accumulation, as measured by SWI-filtered phase, and cognition in MS. We found that MP-LPV is decreased among patients with MS in the thalamus, caudate nucleus, and pulvinar, and there is a decreasing trend, indicative of higher iron content, in the putamen and globus pallidus. In addition, MP-LPV of the pulvinar, caudate nucleus, putamen, and globus pallidus, but not the thalamus as a whole, is related to cognitive performance. Whereas the correlation between MP-LPV and cognition is statistically significant, the effect size is modest and smaller than the volume/cognition correlation in the DGM. In regression models predicting NP tests, total structural volume significantly increased the R^2 after MP-LPV, whereas entering structure volume first in the models erased

the clinical significance of MP-LPV. We therefore conclude that the association between iron accumulation and cognitive impairment is significant, but considerably smaller than with DGM atrophy or T2 lesion volume.

Previous studies examining cognition in MS have used other methods of investigating iron. An increase in $R2^*$ rate, indicative of iron, in the basal ganglia, but not the thalamus, of patients with MS correlated with a combined standardized score of the SDMT and PASAT.³¹ T2 hypointensity, indicative of iron, in the globus pallidus and caudate nucleus of patients with MS correlated with performance on the SDMT.³² Similar to our findings, these studies showed correlations between iron and cognition in the DGM; however their correlations were stronger, with r values in the 0.3–0.6 range. The effects of $R2^*$, however, may be hidden by local increases in water content,³³ and T2 relaxation times are more variable in older subjects,³⁴ making SWI a preferable measure of iron. Magnetic field correlation, another MR imaging method unaffected by dipolar relaxation which is used for iron imaging, found that iron in the thalamus correlated with CVLT2, and that neither the globus pallidus nor the putamen were correlated to SDMT or CVLT2,³⁵ which contrasts with our findings. Sensitivity to magnetic field inhomogeneities with differing length scales may help explain why these methods yield disparate results.³⁶

While the observation of MR imaging phase value as an interpretation of iron concentration is increasingly common, it does not differentiate between iron that is shielded or unshielded, intracellular or extracellular. If iron accumulation is not properly shielded, oxidative stress could lead to necrosis of the cells within its immediate vicinity.³ As suggested by Kovtunovych et al,³⁷ with macrophages releasing iron into both spleen tissue and circulation, focal iron deposits in the DGM could disperse within the focal area and out into surrounding tissue upon cell death. By definition, MP-LPV is a measurement in the voxels of the highest iron concentration; its value may be attenuated if iron dissipates as a structure atrophies, thereby masking its association with cognitive performance. We controlled for this confound by making use of the LPV volume as a covariate in our analysis.

Table 4: Summary of hierarchical linear regressions predicting neuropsychological test scores

NP Test	Independent Variable (Final Standardized Beta, P Value)	R ²	R ² Change	Model P Value	F Change	F Change P Value
SDMT						
Block 1	Age (-0.115, .238), Ed (0.146, .125)	0.064	0.064	.068	2.780	NS
Block 2	Putamen LPV volume (0.012, .929)	0.082	0.018	.074	1.609	NS
Block 3	Putamen MP-LPV (0.154, .241)	0.206	0.124	.001	12.515	.001
Block 4	Putamen volume (0.468, <.001)	0.333	0.127	<.001	15.028	<.001
PASAT						
Block 1	Age (0.112, .318), Ed (0.175, .096)	0.033	0.033	.255	1.388	NS
Block 2	Caudate n. LPV volume (0.009, .941)	0.042	0.010	.318	0.806	NS
Block 3	Caudate n. MP-LPV (0.120, .304)	0.094	0.052	.092	4.564	.036
Block 4	Caudate n. volume (0.319, .009)	0.169	0.075	.011	7.093	.009
DKEFS-CS						
Block 1	Age (-0.081, .444), Ed (0.191, .078)	0.058	0.058	.085	2.544	NS
Block 2	Pulvinar LPV volume (0.161, .365)	0.072	0.013	.109	1.142	NS
Block 3	Pulvinar MP-LPV (0.160, .373)	0.132	0.061	.022	5.577	.021
Block 4	Pulvinar volume (0.214, .123)	0.158	0.026	.017	2.43	NS
CVLT2						
Block 1	Age (-0.207, .049), Ed (0.158, .122)	0.093	0.093	.018	4.212	.018
Block 2	Putamen LPV volume (0.066, .661)	0.133	0.040	.009	3.710	NS
Block 3	Putamen MP-LPV (0.019, .894)	0.164	0.031	.006	2.942	NS
Block 4	Putamen volume (0.333, .012)	0.228	0.064	.001	6.589	.012
BVMT-R						
Block 1	Age (-0.144, .175), Ed (0.083, .437)	0.042	0.042	.172	1.798	NS
Block 2	Pulvinar LPV volume (0.221, .213)	0.076	0.034	.092	2.981	NS
Block 3	Pulvinar MP-LPV (0.146, .413)	0.134	0.058	.02	5.365	.023
Block 4	Pulvinar volume (0.222, .109)	0.162	0.028	.014	2.625	NS

Note:—Ed indicates education; n, nucleus; NS, not significant.

With the exception of the thalamus, most of the DGM structures examined had MP-LPV values that positively correlated with structure volume and negatively correlated with LPV volume. We would expect MP-LPV to be positively correlated with structure volume if focal deposits of iron accumulation were connected to atrophy. MP-LPV in the globus pallidus, however, negatively correlated with structure volume, which could indicate a curiously different role for iron in that structure. Meanwhile, MP-LPV was conspicuously higher in the thalamus compared with other structures examined, possibly reflective of different functions of the thalamus. The caudate and putamen together make the striatum of the basal ganglia, a region receiving signals from the sensorimotor, premotor, motor, and prefrontal cortices involving voluntary movement.³⁸ Meanwhile, the pulvinar receives signals from the visual cortex involving visual attention.³⁹ Several of the NP tests used manual movement (DKEFS-CS, BVMT-R) and visual perception (SDMT, DKEFS-CS, BVMT-R), likely taxing these structures.

This study is limited by the cross-sectional design, which makes it difficult to characterize the effects of iron in disease course and whether it impacts or is impacted by atrophy. A longitudinal study should help elucidate the temporal and spatial relationships between high iron concentration and tissue atrophy. It also is important to note that the pulvinar structure was analyzed using a single-section method and semiautomated contouring technique, which potentially introduces more variance than analysis using FMRIB's Integrated Registration and Segmentation Tool.

CONCLUSIONS

High iron deposition, as measured by mean phase of the low-phase voxels, in pulvinar, putamen, caudate nucleus, and globus

pallidus is correlated with cognitive performance in patients with MS. However, the contribution of structure volume is more robust. Longitudinal investigation is underway that may tease apart the temporal evolution of iron deposition and atrophy in MS.

Disclosures: Robert Zivadinov—*UNRELATED:* receives personal compensation from Teva Pharmaceuticals, Biogen Idec, EMD Serono, Novartis, Claret, and Sanofi-Genzyme for speaking and consultant fees, and receives financial support for research activities from Biogen Idec, Teva Pharmaceuticals, EMD Serono, Novartis, and Sanofi-Genzyme. Michael Dwyer—*UNRELATED:* received consulting fees from EMD Serono for scientific advisory board activities, and from Claret Medical for image analysis consulting. Ralph H.B. Benedict—*UNRELATED:* receives research support from Accordia, Novartis, Genzyme, Biogen Idec, and Questcor Pharmaceuticals, is on the speakers' bureau for EMD Serono (designing CME courses), and consults for Biogen Idec, Genentech, and Novartis. Dr. Benedict also receives royalties for Psychological Assessment Resources.

REFERENCES

1. Craelius W, Migdal MW, Luessenhop CP, et al. **Iron deposits surrounding multiple sclerosis plaques.** *Arch Pathol Lab Med* 1982;106:397-99
2. LeVine SM, Lynch SG, Ou CN, et al. **Ferritin, transferrin and iron concentrations in the cerebrospinal fluid of multiple sclerosis patients.** *Brain Res* 1999;821:511-15
3. Williams R, Buchheit CL, Berman NE, et al. **Pathogenic implications of iron accumulation in multiple sclerosis.** *J Neurochem* 2012;120:7-25
4. Haacke EM, Xu Y, Cheng YC, et al. **Susceptibility weighted imaging (SWI).** *Magn Reson Med* 2004;52:612-18
5. Zivadinov R, Heininen-Brown M, Schirda CV, et al. **Abnormal subcortical deep-gray matter susceptibility-weighted imaging filtered phase measurements in patients with multiple sclerosis: a case-control study.** *Neuroimage* 2012;59:331-39
6. Hagemeyer J, Weinstock-Guttman B, Bergsland N, et al. **Iron deposition on SWI-filtered phase in the subcortical deep gray matter of patients with clinically isolated syndrome may precede structure-specific atrophy.** *AJNR Am J Neuroradiol* 2012;33:1596-601

7. Hagemeyer J, Yeh EA, Brown MH, et al. **Iron content of the pulvinar nucleus of the thalamus is increased in adolescent multiple sclerosis.** *Mult Scler* 2013;19:567–76
8. Al-Radaideh AM, Wharton SJ, Lim SY, et al. **Increased iron accumulation occurs in the earliest stages of demyelinating disease: an ultra-high field susceptibility mapping study in clinically isolated syndrome.** *Mult Scler* 2013;19:896–903
9. Zivadinov R, Sepcic J, Nasuelli D, et al. **A longitudinal study of brain atrophy and cognitive disturbances in the early phase of relapsing-remitting multiple sclerosis.** *J Neurol Neurosurg Psychiatry* 2001;70:773–80
10. Benedict RH, Weinstock-Guttman B, Fishman I, et al. **Prediction of neuropsychological impairment in multiple sclerosis: comparison of conventional magnetic resonance imaging measures of atrophy and lesion burden.** *Arch Neurol* 2004;61:226–30
11. Fisher E, Lee JC, Nakamura K, et al. **Gray matter atrophy in multiple sclerosis: a longitudinal study.** *Ann Neurol* 2008;64:255–65
12. Benedict RH, Schwartz CE, Duberstein P, et al. **Influence of personality on the relationship between gray matter volume and neuropsychiatric symptoms in multiple sclerosis.** *Psychosom Med* 2013;75:253–61
13. Batista S, Zivadinov R, Hoogs M, et al. **Basal ganglia, thalamus and neocortical atrophy predicting slowed cognitive processing in multiple sclerosis.** *J Neurol* 2012;259:139–46
14. Schoonheim MM, Popescu V, Rueda Lopes FC, et al. **Subcortical atrophy and cognition: sex effects in multiple sclerosis.** *Neurology* 2012;79:1754–61
15. Bergsland N, Horakova D, Dwyer MG, et al. **Subcortical and cortical gray matter atrophy in a large sample of patients with clinically isolated syndrome and early relapsing-remitting multiple sclerosis.** *AJNR Am J Neuroradiol* 2012;33:1573–78
16. Aubert-Broche B, Fonov V, Ghassemi R, et al. **Regional brain atrophy in children with multiple sclerosis.** *NeuroImage* 2011;58:409–15
17. Calabrese M, Rinaldi F, Grossi P, et al. **Basal ganglia and frontal/parietal cortical atrophy is associated with fatigue in relapsing-remitting multiple sclerosis.** *Mult Scler* 2010;16:1220–28
18. Hagemeyer J, Weinstock-Guttman B, Heininen-Brown M, et al. **Gray matter SWI-filtered phase and atrophy are linked to disability in MS.** *Front Biosci (Elite Ed)* 2013;5:525–32
19. Polman CH, Reingold SC, Edan G, et al. **Diagnostic criteria for multiple sclerosis: 2005 revisions to the “McDonald Criteria.”** *Ann Neurol* 2005;58:840–46
20. Zivadinov R, Rudick RA, De Masi R, et al. **Effects of IV methylprednisolone on brain atrophy in relapsing-remitting MS.** *Neurology* 2001;57:1239–47
21. Patenaude B, Smith SM, Kennedy DN, et al. **A Bayesian model of shape and appearance for subcortical brain segmentation.** *Neuroimage* 2011;56:907–22
22. Hagemeyer J, Dwyer MG, Bergsland N, et al. **Effect of age on MRI phase behavior in the subcortical deep gray matter of healthy individuals.** *AJNR Am J Neuroradiol* 2013;34:2144–51
23. Benedict RH, Fischer JS, Archibald CJ, et al. **Minimal neuropsychological assessment of MS patients: a consensus approach.** *Clin Neuropsychol* 2002;16:381–97
24. Smith A. *Symbol Digit Modality Test Manual.* Los Angeles: Western Psychological Services; 1982
25. Gronwall DM. **Paced auditory serial-addition task: a measure of recovery from concussion.** *Percept Mot Skills* 1977;44:367–73
26. Delis DC, Kaplan E, Kramer JH. *Delis-Kaplan Executive Function System (D-KEFS):* New York: Psychological Corporation; 2001
27. Delis DC, Kramer JH, Kaplan E, et al. *California Verbal Learning Test.* 2nd ed. San Antonio: Psychological Corporation; 2000
28. Benedict R. *Brief Visuospatial Memory Test-Revised.* Odessa, Florida: Psychological Assessment Resources; 1997
29. Benedict RH, Cookfair D, Gavett R, et al. **Validity of the minimal assessment of cognitive function in multiple sclerosis (MACFIMS).** *J Int Neuropsychol Soc* 2006;12:549–58
30. Benedict RH, Bruce JM, Dwyer MG, et al. **Neocortical atrophy, third ventricular width, and cognitive dysfunction in multiple sclerosis.** *Arch Neurol* 2006;63:1301–06
31. Khalil M, Langkammer C, Ropele S, et al. **Determinants of brain iron in multiple sclerosis: a quantitative 3T MRI study.** *Neurology* 2011;77:1691–97
32. Brass SD, Benedict RH, Weinstock-Guttman B, et al. **Cognitive impairment is associated with subcortical magnetic resonance imaging grey matter T2 hypointensity in multiple sclerosis.** *Mult Scler* 2006;12:437–44
33. Haacke EM, Miao Y, Liu M, et al. **Correlation of putative iron content as represented by changes in R2* and phase with age in deep gray matter of healthy adults.** *J Magn Reson Imaging* 2010;32:561–76
34. Schenker C, Meier D, Wichmann W, et al. **Age distribution and iron dependency of the T2 relaxation time in the globus pallidus and putamen.** *Neuroradiology* 1993;35:119–24
35. Ge Y, Jensen J, Lu H, et al. **Quantitative assessment of iron accumulation in the deep gray matter of multiple sclerosis by magnetic field correlation imaging.** *AJNR Am J Neuroradiol* 2007;28:1639–44
36. Hu CJ, Jensen H, Williams K, et al. **Comparison of susceptibility-weighted imaging and magnetic field correlation imaging.** *Proc Int Soc Mag Reson Med* 2009;17:4524
37. Kovtunovych G, Eckhaus MA, Ghosh MC, et al. **Dysfunction of the heme recycling system in heme oxygenase 1-deficient mice: effects on macrophage viability and tissue iron distribution.** *Blood* 2010;116:6054–62
38. Arnsten AF, Rubia K. **Neurobiological circuits regulating attention, cognitive control, motivation, and emotion: disruptions in neurodevelopmental psychiatric disorders.** *J Am Acad Child Adolesc Psychiatry* 2012;51:356–67
39. Cotton PL, Smith AT. **Contralateral visual hemifield representations in the human pulvinar nucleus.** *J Neurophysiol* 2007;98:1600–09

Preoperative Prognostic Value of Dynamic Contrast-Enhanced MRI–Derived Contrast Transfer Coefficient and Plasma Volume in Patients with Cerebral Gliomas

T.B. Nguyen, G.O. Cron, J.F. Mercier, C. Foottit, C.H. Torres, S. Chakraborty, J. Woulfe, G.H. Jansen, J.M. Caudrelier, J. Sinclair, M.J. Hogan, R.E. Thornhill, and I.G. Cameron

ABSTRACT

BACKGROUND AND PURPOSE: The prognostic value of dynamic contrast-enhanced MR imaging–derived plasma volume obtained in tumor and the contrast transfer coefficient has not been well-established in patients with gliomas. We determined whether plasma volume and contrast transfer coefficient in tumor correlated with survival in patients with gliomas in addition to other factors such as age, type of surgery, preoperative Karnofsky score, contrast enhancement, and histopathologic grade.

MATERIALS AND METHODS: This prospective study included 46 patients with a new pathologically confirmed diagnosis of glioma. The contrast transfer coefficient and plasma volume obtained in tumor maps were calculated directly from the signal-intensity curve without T1 measurements, and values were obtained from multiple small ROIs placed within tumors. Survival curve analysis was performed by dichotomizing patients into groups of high and low contrast transfer coefficient and plasma volume. Univariate analysis was performed by using dynamic contrast-enhanced parameters and clinical factors. Factors that were significant on univariate analysis were entered into multivariate analysis.

RESULTS: For all patients with gliomas, survival was worse for groups of patients with high contrast transfer coefficient and plasma volume obtained in tumor ($P < .05$). In subgroups of high- and low-grade gliomas, survival was worse for groups of patients with high contrast transfer coefficient and plasma volume obtained in tumor ($P < .05$). Univariate analysis showed that factors associated with lower survival were age older than 50 years, low Karnofsky score, biopsy-only versus resection, marked contrast enhancement versus no/mild enhancement, high contrast transfer coefficient, and high plasma volume obtained in tumor ($P < .05$). In multivariate analysis, a low Karnofsky score, biopsy versus resection in combination with marked contrast enhancement, and a high contrast transfer coefficient were associated with lower survival rates ($P < .05$).

CONCLUSIONS: In patients with glioma, those with a high contrast transfer coefficient have lower survival than those with low parameters.

ABBREVIATIONS: DCE = dynamic contrast-enhanced; HGG = high-grade glioma; HR = hazard ratio; K^{trans} = contrast transfer coefficient; rCBV = relative cerebral blood volume; V_p = plasma volume

In patients presenting with cerebral gliomas, the World Health Organization tumor grade is an important prognostic factor along with clinical and radiologic findings such as age, preoperative Karnofsky performance status, and the presence of contrast enhancement.^{1–4} The extent of tumor resection is another known

factor affecting patient survival.¹ Recently, by using dynamic susceptibility contrast MR imaging, the relative CBV was identified as an important prognostic marker for survival independent of tumor grade.^{5–7} For example, Law et al⁵ have shown that gliomas with high relative cerebral blood volume (rCBV) (>1.75) have a shorter time to progression compared with tumors with similar grades but lower rCBV, regardless of tumor grade.

While dynamic susceptibility contrast-derived rCBV has been shown to predict survival in patients with gliomas in single-center studies, the need for normalization of semiquantitative values with a manually defined reference region can introduce interpatient and interscanner variability and thus limits its use in a multi-institutional clinical trial.⁸ Furthermore, measurements can be biased by T1 effects due to extravascular contrast leakage in tumor vessels.^{9,10} Hemodynamic parameters are more readily quantified

Received December 12, 2013; accepted after revision March 10, 2014.

From the Departments of Diagnostic Imaging (T.B.N., G.O.C., C.H.T., R.E.T., I.G.C., S.C., J.M.C.), Medical Physics (C.F., I.G.C.), Pathology (G.H.J., J.W.), Surgery, Division of Neurosurgery (J.S.), and Medicine, Division of Neurology (M.J.H.), The Ottawa Hospital, University of Ottawa, Ottawa, Ontario, Canada; and Department of Radiology (J.F.M.), Hôpital de Hull, Gatineau, Québec, Canada.

This work was supported by the Brain Tumour Foundation of Canada.

Please address correspondence to Thanh Binh Nguyen, MD, Department of Diagnostic Imaging, The Ottawa Hospital, 1053 Carling Ave, Ottawa, Ontario, K1Y 4E9 Canada; e-mail: thnguyen@toh.on.ca

<http://dx.doi.org/10.3174/ajnr.A4006>

by using a dynamic contrast-enhanced (DCE) MR imaging technique, which allows simultaneous measurement of CBV and the contrast transfer coefficient (K^{trans}). K^{trans} is the volume transfer coefficient of contrast from the vascular compartment to the extravascular compartment. It is influenced by cerebral blood flow and vascular permeability.¹¹ While K^{trans} has been found to increase with glioma grade, its prognostic value remains unclear.^{12,13} A previous study reported that in patients with high-grade gliomas (HGGs), higher values of K^{trans} were associated with longer survival.¹² This finding is unexpected because high K^{trans} implies, in theory, a higher level of angiogenesis, greater biologic aggressiveness, and a shorter survival.

The goal of our study was to determine the prognostic values of K^{trans} and plasma volume (V_p) obtained in tumor by using a simple DCE MR imaging acquisition that relies on the change in signal intensity rather than the T1 relaxation rate.

MATERIALS AND METHODS

Subjects

All examinations were conducted in accordance with the guidelines for human research at our institution, and written informed consent was obtained from all participating subjects. All adult patients presenting at The Ottawa Hospital with a newly diagnosed brain lesion compatible with a glioma between December 2008 and March 2011 were included in this prospective study. We set the following exclusion criteria: prior surgery or biopsy of the presenting brain lesion, pregnancy, renal failure, and a known history of allergy to gadolinium-based MR imaging contrast agent.

We recorded clinical variables such as the following: age, sex, use of steroids before preoperative MR imaging, and the preoperative Karnofsky score. Following MR imaging, patients underwent surgery (biopsy or resection), depending on tumor size, tumor location, and the patient's general condition. The median time interval between the MR imaging examination and surgery was 5.0 days (95% CI, 3.9–7.0 days). Histopathologic diagnosis was provided by an experienced neuropathologist (J.W., with 12 years of experience, or G.H.J., with 23 years of experience) by using the World Health Organization classification. From the operative report, the type of surgery was classified as biopsy or resection. The main outcome measure was overall survival. Follow-up clinical information was obtained primarily from chart review, telephone interview, and archived obituaries. The follow-up period was defined as the interval between the date of surgery and the date of death or the date the patient was last known to be alive. Follow-up was halted on December 12, 2012.

MR Imaging Acquisition

All preoperative and postoperative MR imaging data were acquired by using either a 1.5T (Symphony; Siemens, Erlangen, Germany) or a 3T clinical scanner (Magnetom Trio; Siemens). Preoperative anatomic imaging was performed by using standard sagittal T1-weighted, axial T1-weighted pre- and postcontrast injection, axial FLAIR, axial T2, and coronal T1 postcontrast injection sequences.

DCE MR imaging was performed following the axial T1-weighted precontrast imaging. At 1.5T, DCE MR imaging was

performed by using a 2D FLASH pulse sequence (5 axial sections centered on the tumor, TR = 45 ms, TE = 2.1, 5.5 ms, flip angle = 90°, matrix = 96 × 128, FOV = 17 × 23 cm², section thickness = 5 mm, Δt = 2.2 seconds). 2D FLASH was used for dynamic imaging on the 1.5T scanner due to hardware limitations because the desired temporal resolution (Δt < 3 seconds) could only be achieved with 2D sequences. At 3T, a 3D FLASH sequence was used (18 axial sections, TR = 6.5 ms, TE = 1.7, 3.9 ms, flip angle = 30°, matrix = 96 × 128, FOV = 23 cm², section thickness = 5 mm, Δt = 2.9 seconds).

Gadopentetate dimeglumine (Magnevist; Bayer Pharma, Berlin, Germany) was injected at 0.1 mmol/kg and 4 mL/s, beginning 40 seconds after the start of the scan. The duration of the DCE sequence was 220 seconds.

Pharmacokinetic Modeling

DCE magnitude images were processed directly in nordicICE, Version 2 (NordicNeuroLab, Bergen, Norway) to generate maps of V_p and K^{trans} with the assumption that changes in contrast concentration are proportional to changes in MR imaging signal intensity with the same proportionality constant in tissue and in blood. Kinetic parameters (K^{trans} and V_p) were estimated by using a 2-compartment extended Tofts model implemented in the nordicICE software.¹⁴ The vascular input function was calculated from the superior sagittal sinus.¹⁵

Image Interpretation

A neuroradiologist (C.H.T.) blinded to the histopathologic grade determined the degree of contrast enhancement relative to the choroid plexus: none, mild (less than that of the choroid plexus), or marked (equal to or more than that of the choroid plexus).

A senior radiology resident (J.F.M, third-year radiology resident) traced 4 ROIs (each 25 mm²) in the solid part of the tumor in the areas of visually highest V_p/K^{trans} present on the acquired sections. The maximum value among the 4 region-of-interest values was obtained for K^{trans} and V_p for each patient. All ROIs were verified by a neuroradiologist (T.B.N., with 10 years of experience) to ensure that inadvertent placement on an adjacent vessel was avoided.

Statistical Analysis

All data were analyzed by using MedCalc for Windows, Version 11.5 (MedCalc Software, Mariakerke, Belgium). Patients were divided into 2 groups based on their tumor values of V_p and K^{trans} . Threshold values of 0.05 minutes⁻¹ and 5% for K^{trans} and V_p , respectively, were chosen for simplicity and convenience so that they might be used in clinical practice and for comparison with other related studies. We checked that each group had at least 30% of patients. Kaplan-Meier survival curves were obtained for patients with no or mild enhancement versus marked enhancement and for high tumor V_p/K^{trans} versus low V_p/K^{trans} . Kaplan-Meier survival analysis was also performed for the subgroups of patients with low- and high-grade gliomas. Potential prognostic variables for time-to-death were explored by using Cox proportional hazards modeling. We selected clinical/radiologic/histopathologic variables such as tumor grade, age older than 50 years, Karnofsky performance status score lower than 80, tumor size of >4 cm,

Table 1: Summary of clinical characteristics as univariate predictors of overall survival in 46 patients with gliomas

Characteristics	No.	%	HR (95% CI)	P Value
Age				
50 Years or younger	18	39.1	1	
Older than 50 years	28	60.9	7.62 (2.17–26.71)	.002
Karnofsky performance score				
≥80	25	54.3	1	
<80	21	45.7	2.86 (1.35–6.08)	.007
Maximal tumor diameter				
<4 cm	17	37	1	
≥4 cm	29	63	1.30 (0.61–2.80)	.50
Surgery				
Biopsy only	9	19.6	1	
Resection	37	80.4	4.19 (1.77–9.93)	.001
Histopathologic grade				
Grade 2 (8 pure astrocytomas, 1 oligodendroglioma)	9	19.6	1	
Grade 3 (6 pure astrocytomas, 2 oligoastrocytomas, 1 oligodendroglioma)	9	19.6	0.087 (0.83–9.45)	.87
Grade 4 (26 pure astrocytomas, 2 oligoastrocytomas)	28	40.8	4.14 (1.25–13.8)	.02
Steroid administration				
No	18	39.1	1	
Yes	28	61.9	2.11 (0.96–4.65)	.06

Table 2: Summary of imaging characteristics as univariate predictors of overall survival in 46 patients with gliomas

Characteristics	No.	%	HR (95% CI)	P Value
Sequence				
2D	31	67	1	
3D	15	33	1.00 (0.44 to 2.29)	.99
Contrast enhancement				
None/less than that of choroid plexus	15	33	1	
Equal/more than that of choroid plexus	31	67	8.11 (2.44–26.90)	.0007
K^{trans} (min^{-1})				
<0.05	17	37.0	1	
≥0.05	29	63.0	7.63 (2.63–22.11)	.0002
V_p (mL/100 g)				
<5	20	43.5	1	
≥5	26	56.5	4.17 (1.77–9.80)	.001

biopsy versus resection, and degree of tumor enhancement because these variables have been reported as prognostic factors.^{1–4} Clinical and imaging variables that resulted in a probability < .05 on univariate analysis were entered into multivariate analysis in a forward stepwise regression. Multivariate analysis was performed for 3 models, each model including an imaging variable and clinical variables. For each model, a variable is entered into the model with $P < .05$. Significant variables are entered sequentially; after a variable is entered in the model, variables that became nonsignificant ($P > .1$) are removed. Degree of contrast enhancement, K^{trans} , and V_p were not entered in the same model because they are not independent variables.

RESULTS

Study Population

Forty-six patients with gliomas were included in this study. Seven patients were recruited but were excluded due to lack of a surgical biopsy ($n = 2$) or the presence of metastatic disease on histopathologic examination ($n = 5$). Patient demographics, tumor size, and histopathologic grade are summarized in Table 1, while DCE MR imaging parameters are summarized in Table 2. Among 9 patients with a low-grade glioma, 1 had an oligodendroglioma and 8 had pure astrocytomas. Four of those patients underwent

radiation and chemotherapy. Among 37 patients with HGGs, 1 had an oligodendroglioma, 4 had oligoastrocytomas, and 32 had pure astrocytomas. Thirty-four patients underwent standard chemotherapy and radiation treatment. One patient was enrolled in a clinical trial combining temozolomide with bevacizumab or a placebo. Twenty-eight patients (4 with low-grade gliomas and 24 with HGGs) received steroids before their MR imaging at admission compared with 18 who did not (5 low-grade gliomas and 13 HGGs). In patients with HGGs, no statistically significant difference was found in the median V_p or K^{trans} between patients who received steroids versus those who did not ($P > .64$).

Kaplan-Meier Survival Curve Analysis

Twenty-nine deaths occurred. The median follow-up for those still alive was 836 days. The median survival time for all patients was 597 days with a 1-year survival probability of .62.

Histopathologic Grade

Patients with glioblastoma multiforme had a statistically significant worse survival rate compared with those with grades 3 and 2 ($P < .05$, Fig 1A). There was no statistical difference found in the survival curves for patients with grade 3 versus 2. When we compared those with grade 2 gliomas who had a diagnosis from

a surgical resection (not from a biopsy) with those with grade 3 gliomas, a trend of longer survival for low-grade gliomas was seen, though it was not statistically significant ($P = .2$, Fig 1B).

Degree of Contrast Enhancement

There was a statistical difference in survival between groups with no or mild enhancement versus marked enhancement for all patients ($P = .0001$) and for subgroups of low-grade gliomas ($P = .002$) and HGGs ($P = .01$). For patients with anaplastic astrocytomas, marked enhancement was associated with worse survival ($P = .04$). Among patients with glioblastoma multiforme, 1 had mild enhancement and 1 did not have any enhancement. Their survival rate was not different from those with marked enhancement ($P = .81$).

K^{trans} and V_p

For all gliomas, a statistically significant difference was present in the comparison of survival curves between groups with low and high K^{trans} and V_p ($P < .05$, Figs 2 and 3). Subgroup analysis of patients with HGGs and low-grade gliomas also revealed significant decreases in survival rates in the high K^{trans} and V_p groups compared with their respective “low” counterparts. Further sub-

group analysis of patients with HGGs who underwent resection showed significant decreases in survival rates for patients with high K^{trans} ($P = .007$), but not for patients with high V_p ($P = .08$).

Table 3: Three models combining an imaging parameter with clinical factors as potential prognostic variables of overall survival in patients with gliomas

Factors	HR (95% CI)	P Value
Model 1		
Age older than 50 yr	1.03 (0.99–1.06)	.17
Biopsy vs resection	4.11 (1.68–10.05)	.002
Grade 3 vs 2	1.20 (0.19–7.65)	.85
Grade 4 vs 2	1.21 (0.28–5.33)	.80
Karnofsky score < 80	2.56 (1.19–5.51)	.02
$K^{trans} \geq 0.05 \text{ min}^{-1}$	4.53 (1.22–16.82)	.02
Model 2		
Age older than 50 yr	1.06 (1.03–1.09)	.0002
Biopsy vs resection	3.68 (1.54–8.78)	.004
Grade 3 vs 2	1.06 (0.16–6.89)	.95
Grade 4 vs 2	1.76 (0.35–8.75)	.49
Karnofsky score < 80	3.21 (1.48–6.92)	.003
$V_p \geq 5 \text{ mL}/100 \text{ g}$	1.30 (0.37–4.54)	.68
Model 3		
Age older than 50 yr	1.03 (0.99–1.07)	.087
Biopsy vs resection	4.36 (1.77–10.77)	.002
Grade 3 vs 2	1.28 (0.20–8.25)	.79
Grade 4 vs 2	1.00 (0.22–4.63)	.99
Karnofsky score < 80	2.51 (1.16–5.43)	.02
Marked contrast enhancement	4.79 (1.22–18.87)	.03

In patients with anaplastic astrocytomas, those with high K^{trans} and high V_p had a worse prognosis ($P = .04$). In patients with glioblastoma multiforme, there was a trend toward shorter survival for patients with high K^{trans} /high V_p , but this did not reach statistical significance ($P = .26$ and $P = .50$, respectively).

2D versus 3D Sequence

We did not find any significant differences in survival rates between groups who had 2D versus 3D sequences for all gliomas and for subgroups of low-grade gliomas and HGGs ($P > .5$).

Univariate Predictors of Overall Survival

Univariate predictors of poorer survival were age older than 50 years, preoperative Karnofsky score of <80, biopsy only, grade 4, marked contrast enhancement, and high K^{trans} and V_p values (Table 1). We did not find tumor size a significant prognostic variable ($P = .5$). Patients who were prescribed steroids at admission before their MR imaging examination appear to have a poorer prognosis (hazard ratio [HR] = 2.11, 95% CI 0.96–4.65) than those who were not, but there were more HGGs among them. We found a statistically significant difference in survival between grades 4 and 3 (HR = 4.77, 95% CI, 1.13–20) and grades 4 and 2 (HR = 4.14, 95% CI, 1.25–13.8), but not between grades 3 and 2 (HR = 0.087, 95% CI, 0.83–9.45). When we compared the prognostic value of the 2 DCE

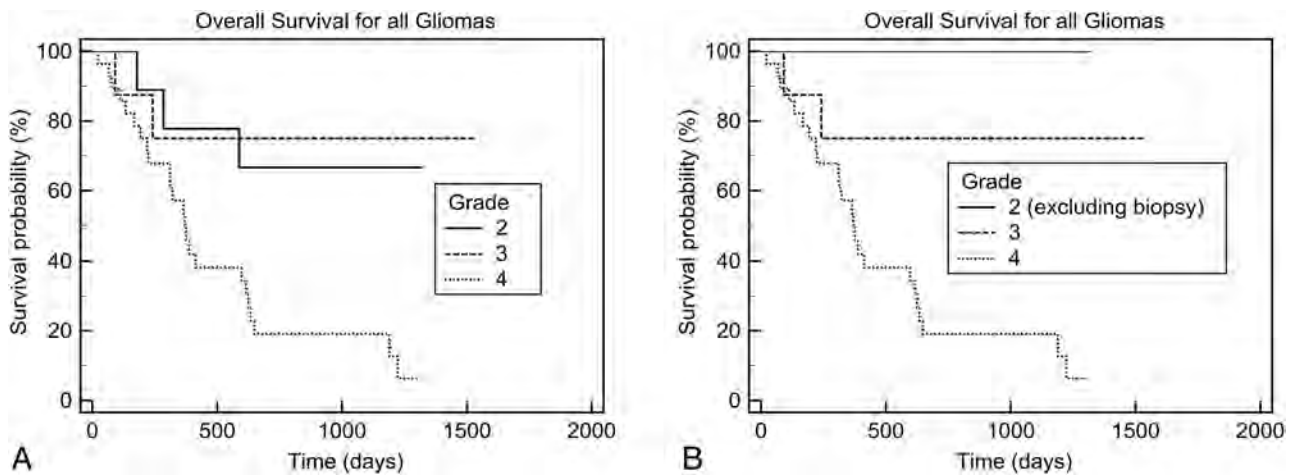


FIG 1. Kaplan-Meier analysis of overall survival according to histopathologic grades. A, All patients (between grades 2 and 3, $P = .8$; and between grades 3 and 4, $P = .02$). B, All patients, excluding those with low-grade gliomas who had a biopsy (between grades 2 and 3, $P = .2$; between grades 3 and 4, $P = .02$).

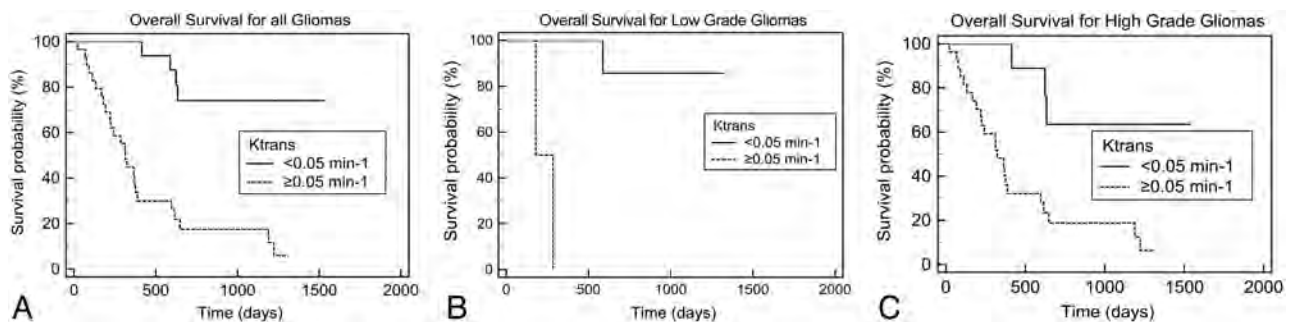


FIG 2. Kaplan-Meier analysis of overall survival according to K^{trans} . A, All patients ($P = .0001$). B, Those with low-grade gliomas ($P = .002$). C, Those with high-grade gliomas ($P = .004$).

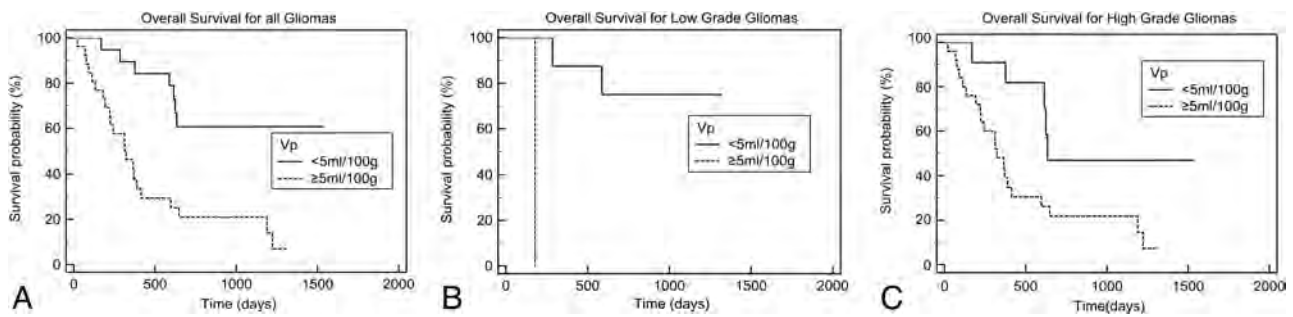


FIG 3. Kaplan-Meier analysis of overall survival according to V_p . A, All patients ($P = .0004$). B, Those with low-grade gliomas ($P = .005$). C, Those with high-grade gliomas ($P = .02$).

parameters, patients with high K^{trans} had a higher hazard of mortality (HR = 7.63, 95% CI, 2.63–22.11) compared with V_p (HR = 4.17, 95% CI, 1.77–9.80). Patients with marked tumor enhancement also had a higher hazard of mortality (HR = 8.11, 95% CI, 2.44–26.90).

Multivariate Predictors of Overall Survival

In multivariate analysis combining clinical and imaging parameters, Karnofsky score of <80 and biopsy were the only significant clinically poor prognostic factors in any model (Table 3). Age older than 50 years was a significant prognostic factor in only 1 of the 3 models. Histopathologic grading and V_p did not remain significant factors in our multivariate analysis. High K^{trans} and contrast enhancement were significant poor prognostic factors, along with biopsy and Karnofsky score of <80.

DISCUSSION

In our study of patients with gliomas, preoperative Karnofsky performance score and the type of surgery were important prognostic factors in both univariate and multivariate analysis, in agreement with the findings in previous studies.^{1–3} Grade IV was found to be a poor prognostic factor compared with grades 3 and 2 in univariate analysis. However, we did not observe a significant difference in survival for grade 3 versus 2. Because some of our patients with grade 2 were diagnosed via biopsy only, sampling error could have led to an improper grading of the tumor, which could explain why we did not observe a statistical difference in survival rates between patients with grade 2 and those with grade 3 gliomas.

With dynamic susceptibility contrast MR imaging, numerous previous articles have recently established rCBV as a prognostic factor in patients with low- and high-grade gliomas.^{5–7} However, use of DSC-derived rCBV as a potential biomarker in a multi-institutional trial is currently limited because it is a semiquantitative measurement, which can be influenced by many postprocessing steps, including the technique of correction for contrast agent extravasation and the choice of the normal contralateral white matter.^{8,9} For patients with gliomas, CBV obtained from the normal contralateral white matter has been shown to have significant interscanner variability.⁸ For DCE, measurement of absolute CBV might be possible because correction of contrast leakage across tumor vessels can be more accurately quantified by using a proper pharmacokinetic model. Furthermore, DCE is not influenced by susceptibility artifacts, which can make measurements

of rCBV by using DSC difficult in gliomas with hemorrhagic components or gliomas located near the skull base.

In patients with gliomas, the use of DCE imaging as a potential biomarker for prognosis has not been well studied. We have found that marked contrast tumoral enhancement and high V_p were negative prognostic factors in all patients with gliomas and in the subgroups of patients with high- and low-grade gliomas. While contrast enhancement remains a significant factor in multivariate analysis, V_p and histopathologic grade did not add any prognostic value when age, type of surgery, and Karnofsky performance status score were also included. Because the hazard ratios for V_p and grade were less than those for age and type of surgery in univariate analysis, we believe that the small sample size in our study did not allow detection of those weaker prognostic factors in multivariate analysis.

High K^{trans} had the same negative prognostic value as marked contrast tumoral enhancement in patients with gliomas and in subgroups of patients with high- and low-grade gliomas. While measurement of K^{trans} requires some postprocessing, K^{trans} might represent a more objective metric in the setting of a multicenter clinical trial because qualitative assessment of the degree of contrast enhancement is subject to interobserver variability. The prognostic value of K^{trans} is similar to that in our findings with CT perfusion.¹⁶ In a different cohort of 20 patients with high-grade gliomas who underwent preoperative CT perfusion, we found that those with a combination of high CBV and permeability surface had an HR of 6.0 (95% CI, 4.2–7.8,) compared with those with lower values. Mathematic modeling based on DCE MR imaging revealed that K^{trans} was correlated with tumor aggressiveness, perhaps due to the increased vessel growth and permeability required for cellular proliferation.¹³ However, Mills et al¹² observed a positive correlation between K^{trans} and prognosis in their group of 19 patients with high-grade gliomas, which led to their hypothesis that tumors with higher baseline K^{trans} might be more responsive to radiation treatment or chemotherapy than those with lower K^{trans} . Another study by Awasthi et al¹⁷ found that high K^{trans} /volume of extravascular space was correlated with a high expression of matrix metalloproteinases and was associated with poorer survival.

These conflicting results on the prognostic value of K^{trans} could be due to the small sample size, different effects of covariate factors (such as the extent of tumor resection, use of radiation treatment or chemotherapy, and molecular/genomic markers),

and/or different DCE MR imaging methods.^{18,19} The method for DCE MR imaging–parameter estimation can influence the magnitude of the hazard ratio. Our method did not use baseline T1 measurements to convert signal intensity to gadolinium concentration as suggested by DCE MR guidelines published by Leach et al.²⁰ This simpler method can yield more useful measurements when the signal intensity–to–noise ratio is low, such as in poorly enhancing tumors.²¹ The method is implemented on commercially available software, and postprocessing time is relatively short.

Our study was limited by the small number of patients, especially those with low-grade gliomas and nonenhancing tumors. A second limitation is that the location of the tumor and the treatment received after surgery were not included as independent variables in our study. For example, 3 patients with glioblastomas did not undergo radiation treatment. This could have explained why we did not find tumor size a statistically significant prognostic factor. We are also aware of potential measurement bias due to methodologic differences between the 2D and 3D techniques used in our study. However, we do not believe that the different pulse sequence and field strengths had a major systematic effect on the pharmacokinetic parameters in our study. Although, in theory, 2D and 3D gradient-echo sequences might have different sensitivities to water exchange and inflow effects, we did not find a statistical difference in the mean and median values of pharmacokinetic parameters in groups of patients scanned with 2D-versus-3D sequences. There was no significant difference in survival for patients with gliomas scanned with 2D-versus-3D sequences. MR imaging signal-intensity curves from the superior sagittal sinus and tumor were not systematically different between patients in the 2 groups.

Because many patients with gliomas received steroids at the time of admission, this treatment might have introduced a measurement bias on the pharmacokinetic parameters. However, in our study, we did not observe a statistical difference in K^{trans} or V_p in patients with grade 3 and 4 gliomas who were given steroids versus those who were not. Corticosteroid treatment has been reported to decrease contrast enhancement in malignant gliomas and to reduce total fractional blood volume.^{22,23} Animal studies have suggested that its antiangiogenic effects are both transient and vessel-size-dependent. In rats with gliomas treated with dexamethasone, rCBV was only significantly reduced on the third day following treatment.²³ While rCBV measured by gradient-echo MR imaging was reduced >50%, an increase in rCBV was observed with spin-echo MR imaging.²⁴ Our study patients usually had started steroid treatment for only a short duration (usually <72 hours) before their MR imaging examination. This duration might explain why we did not see any significant effect on our hemodynamic parameters. This finding is in agreement with that in Bastin et al,²⁵ who did not find a significant change in tumor CBV and CBF before and after 48–72 hours of dexamethasone treatment.

CONCLUSIONS

Preoperative high K^{trans} obtained from DCE MR imaging is associated with poorer outcome in patients with low- and high-grade gliomas. High tumoral K^{trans} has the same prognostic value as the presence of marked tumoral enhancement on postcontrast T1-weighted images.

ACKNOWLEDGMENTS

We thank William Petrcich for his expert statistical advice.

Disclosures: Thanh Binh Nguyen—RELATED: Grant: funding from the Brain Tumour Foundation of Canada,* UNRELATED: Board Membership, Consultancy, Grants/Grants Pending, and Payment for the Development of Educational Presentations: all from Bayer Healthcare. Santanu Chakraborty—UNRELATED: Payment for lectures (including service on Speakers Bureaus): EMD Serono. Matthew J. Hogan—RELATED: Grant: Ottawa Hospital Research Institute and his laboratory have received in-kind support from GE Healthcare of approximately \$11,000 as part of an infrastructure grant from the Canadian Foundation for Innovation in 2011. *Money paid to the institution.

REFERENCES

1. Kalkanis SN, Rosenblum ML. **Malignant gliomas.** In: Bernstein M, Berger MS, eds. *Neuro-oncology: The Essentials.* 2nd ed. New York: Thieme Medical Publishers; 2008:254–65
2. Chaichana K, McGirt M, Niranjan A, et al. **Prognostic significance of contrast-enhancing low-grade gliomas in adults and a review of the literature.** *Neurol Res* 2009;31:931–39
3. Chang EF, Smith JS, Chang SM, et al. **Preoperative prognostic classification system for hemispheric low-grade gliomas in adults.** *J Neurosurg* 2008;109:817–24
4. Pope WB, Sayre J, Perlina A, et al. **MR imaging correlates of survival in patients with high-grade gliomas.** *AJNR Am J Neuroradiol* 26:2466–74
5. Law M, Young RJ, Babb JS, et al. **Gliomas: predicting time to progression or survival with cerebral blood volume measurements at dynamic susceptibility-weighted contrast-enhanced perfusion MR imaging.** *Radiology* 2008;247:490–98
6. Hipp SJ, Steffen-Smith E, Hammoud D, et al. **Predicting outcome of children with diffuse intrinsic pontine gliomas using multiparametric imaging.** *Neuro Oncol* 2011;13:904–09
7. Hirai T, Murakami R, Nakamura H, et al. **Prognostic value of perfusion MR imaging of high-grade astrocytomas: long-term follow-up study.** *AJNR Am J Neuroradiol* 2008;29:1505–10
8. Ellingson B, Zaw T, Cloughesy TF, et al. **Comparison between intensity normalization techniques for dynamic susceptibility contrast (DSC)-MRI estimates of cerebral blood volume (CBV) in human gliomas.** *J Magn Reson Imaging* 2012;25:1472–77
9. Boxerman JL, Schmainda KM, Weisskoff RM. **Relative cerebral blood volume maps corrected for contrast agent extravasation significantly correlate with glioma tumor grade, whereas uncorrected maps do not.** *AJNR Am J Neuroradiol* 2006;27:859–67
10. Boxerman JL, Prah DE, Paulson ES, et al. **The role of preload and leakage correction in gadolinium-based cerebral blood volume estimation determined by comparison with MION as a criterion standard.** *AJNR Am J Neuroradiol* 2012;33:1081–87
11. Henderson E, Sykes J, Drost D, et al. **Simultaneous MRI measurement of blood flow, blood volume, and capillary permeability in mammary tumors using two different contrast agents.** *J Magn Reson Imaging* 2000;12:991–1003
12. Mills SJ, Patankar TA, Haroon HA, et al. **Do cerebral blood volume and contrast transfer coefficient predict prognosis in human glioma?** *AJNR Am J Neuroradiol* 2006;27:853–58
13. Venkatasubramanian R, Arenas RB, Henson MA, et al. **Mechanistic modelling of dynamic MRI data predicts that tumour heterogeneity decreases therapeutic response.** *Br J Cancer* 2010;103:486–97
14. Tofts PS. **Modeling tracer kinetics in dynamic Gd-DTPA MR imaging.** *J Magn Reson Imaging* 1997;7:91–101
15. Nguyen TB, Cron GO, Mercier JF, et al. **Diagnostic accuracy of dynamic contrast-enhanced MR imaging using a phase-derived vascular input function in the preoperative grading of gliomas.** *AJNR Am J Neuroradiol* 2012;33:1539–45
16. Shankar JJ, Nguyen TB, Woulfe J, et al. **Evaluation of CT perfusion in grading and prognostication of high grade gliomas: a pilot study.** *AJR Am J Roentgenol* 2013;200:W504–09
17. Awasthi R, Pandey CM, Sahoo P, et al. **Dynamic contrast-enhanced**

- magnetic resonance imaging-derived k_{ep} as potential biomarker of matrix metalloproteinase 9 expression in patients with glioblastoma multiforme: a pilot study. *J Comput Assist Tomogr* 2012; 36:125–30
18. Jain R, Poisson L, Narang J, et al. **Genomic mapping and survival prediction in glioblastoma: molecular subclassification strengthened by hemodynamic imaging biomarkers.** *Radiology* 2013;267: 212–20
 19. Takahashi Y, Nakamura H, Makino K, et al. **Prognostic value of isocitrate dehydrogenase 1, O⁶-methylguanine-DNA methyltransferase promoter methylation, and 1p19q co-deletion in Japanese malignant glioma patients.** *World J Surg Oncol* 2013;11:284
 20. Leach MO, Brindle KM, Evelhoch JL, et al. **The assessment of antiangiogenic and antivascular therapies in early-stage clinical trials using magnetic resonance imaging: issues and recommendations.** *Br J Cancer* 2005;92:1599–610
 21. Song HK, Xue Y, Yu J, et al. **Comparison of the standard gadolinium concentration and signal difference methodologies for computation of perfusion parameters in DCE-MRI at various SNRs.** In: *Proceedings of the Annual Meeting of the International Society of Magnetic Resonance in Medicine*, Montreal, Quebec, Canada. April 20–26, 2011
 22. Zaki HS, Jenkinson MD, Duplessis DG, et al. **Vanishing contrast enhancement in malignant glioma after corticosteroid treatment.** *Acta Neurochir (Wien)* 2004;146:841–45
 23. Darpolor M, Molthen RC, Schmainda KM. **Multimodality imaging of abnormal vascular perfusion and morphology in preclinical 9L gliosarcoma model.** *PLoS One* 2011;6:e16621
 24. Badruddoja MA, Krouwer HG, Rand SD, et al. **Antiangiogenic effects of dexamethasone in 9L gliosarcoma assessed by MRI cerebral blood volume maps.** *Neuro Oncol* 2003;5:235–43
 25. Bastin ME, Carpenter TK, Armitage PA, et al. **Effects of dexamethasone on cerebral perfusion and water diffusion in patients with high-grade glioma.** *AJNR Am J Neuroradiol* 2006;27:402–08

Mapping p53 Mutations in Low-Grade Glioma: A Voxel-Based Neuroimaging Analysis

Y.Y. Wang, T. Zhang, S.W. Li, T.Y. Qian, X. Fan, X.X. Peng, J. Ma, L. Wang, and T. Jiang



ABSTRACT

BACKGROUND AND PURPOSE: Brain tumor location has proved to be a prognostic factor that may be associated with features of neoplastic origin. Mutation of p53 is an atypical genetic change that occurs during tumorigenesis. Thus, a potential correlation may exist between tumor location and p53 status. The purpose of the current study was to identify anatomic characteristics of mutant p53 expression by using quantitative neuroimaging analyses.

MATERIALS AND METHODS: Preoperative MR images from 182 patients with histologically confirmed low-grade gliomas were retrospectively analyzed. All tumors were manually marked and registered to the standard space. Using a voxel-based lesion-symptom mapping analysis, we located brain regions associated with a high occurrence of p53 mutation and corrected them by using a permutation test. The acquired clusters were further included as a factor in survival analyses.

RESULTS: Statistical analysis demonstrated that the left medial temporal lobe and right anterior temporal lobe were specifically associated with high expression of mutant p53. Kaplan-Meier curves showed that tumors located in these regions were associated with significantly worse progression-free survival compared with tumors occurring elsewhere.

CONCLUSIONS: Our voxel-level imaging analysis provides new evidence that genetic changes during cancer may have anatomic specificity. Additionally, the current study suggests that tumor location identified on structural MR images could potentially be used for customized presurgical outcome prediction.

ABBREVIATIONS: LGG = low-grade glioma; MGMT = O6-methylguanine DNA methyltransferase; MNI = Montreal Neurological Institute; PFS = progression-free survival; VLSM = voxel-based lesion-symptom mapping

Gliomas originate in glial cells in the brain and are the most common type of primary brain tumor.^{1,2} Low-grade gliomas (LGGs) constitute 10%–20% of primary brain tumors and mainly

affect young adults.³ For patients with LGGs, histologic grading remains the most important factor influencing prognosis.⁴ Molecular markers involved in low-grade glioma pathways also play a critical role in determining prognosis.^{5,6}

The *TP53* mutation is an early event in genetic pathogenesis that occurs in all types of cancer. The incidence of *TP53* mutation in LGGs is approximately 53% in diffuse astrocytoma, 44% in oligoastrocytoma, and 13% in oligodendroglioma.^{5,7} Mutant p53 protein is commonly regarded as a surrogate marker for a mutation in *TP53*.⁸ Furthermore, p53 mutations acquire oncogenic properties that enable them to promote proliferation, invasion, metastasis, and cell immortalization.^{9,10} Although it has been widely accepted that the loss of p53 function plays an important role in glioma tumorigenesis,^{11,12} the prognostic role of p53 mutations has remained controversial and no consistent relationship with response to therapy or overall outcome has been reported.^{8,13}

Associations have been made that link tumor location and genetic features in glioma. For example, anatomic characteristics have been demonstrated for several tumor-related molecular bio-

Received April 9, 2014; accepted after revision June 13.

From the Beijing Neurosurgical Institute (Y.Y.W., T.J.) and Department of Epidemiology and Biostatistics (X.X.P.), School of Public Health and Family Medicine, Capital Medical University, Beijing, China; Departments of Neurosurgery (Y.Y.W., T.Z., X.F., L.W., T.J.) and Neuroradiology (S.W.L., J.M.), Beijing Tiantan Hospital, Capital Medical University, Beijing, China; Siemens Healthcare (T.Y.Q.), MR Collaboration NE Asia, Beijing, China; China National Clinical Research Center for Neurological Diseases (L.W.), Beijing, China; and Beijing Institute for Brain Disorders (T.J.), Beijing, China.

Yinyan Y. Wang and Tan Zhang contributed equally to this work.

This work was supported by the National 973 Program No. 2011CB707804 (T.J.) and the National High Technology Research and Development Program No. 2012AA02A508 (T.J.).

Please address correspondence to Tao Jiang, PhD, Beijing Neurosurgical Institute, Capital Medical University, 6, Tiantanxili, Beijing, 100050, China; e-mail: taojiang1964@163.com; and Lei Wang, MD, Department of Neurosurgery, Beijing Tiantan Hospital, Capital Medical University, 6, Tiantanxili, Beijing, 100050, China; e-mail: wangleitiantan@126.com

Indicates open access to non-subscribers at www.ajnr.org

Indicates article with supplemental on-line table.

<http://dx.doi.org/10.3174/ajnr.A4065>

markers, such as 1p and/or 19q,¹⁴ *isocitrate dehydrogenase 1*,¹⁵ O6-methylguanine DNA methyltransferase (MGMT),¹⁶ and TP53.¹⁷ Because location may be related to the genetic profile of the origin of a tumor cell,^{18–20} tumor location is one of the most important characteristics for predicting the development of a glioma and the prognosis of a patient.^{14,15,18,21} However, identifying brain tumor precursor cells and their distinct genetic profiles to increase survival via customized treatment paradigms is a major challenge in neuro-oncologic studies.^{22,23}

Moreover, this issue is far from clear because anatomic characteristics of tumor-related gene expression are rarely investigated. Dichotomous statistics of tumor location based on which lobe is involved have ignored important information such as tumor size. With the goal of providing a more reliable and precise brain atlas to demonstrate the statistical correlation between p53 mutations and tumor intensity, the current study used a voxel-based lesion-symptom mapping (VLSM) approach.²⁴ One hundred eighty-two patients with primarily diagnosed LGG were included in this study. VLSM-defined regions associated with high expression of the p53 mutant were located mainly in the left medial and right anterior temporal lobes. Notably, patients with tumors located in VLSM-defined regions had shorter progression-free survival times (PFSs) compared with those whose tumors occurred elsewhere.

MATERIALS AND METHODS

Patients

One hundred eighty-two patients with newly diagnosed LGGs treated at our institute between September 2006 and December 2011 were enrolled in the current retrospective study. Clinical information of these patients was collected from the Chinese Glioma Genome Atlas data base (<http://www.cgga.org.cn>). Inclusion criteria were the following: 1) histologic confirmation of the LGG with no previous diagnosis of any type of brain tumor, 2) no history of radiation therapy or chemotherapy, 3) no history of biopsy, 4) high-resolution presurgical T2-weighted images, and 5) tissue available for testing p53 expression. Histologic diagnoses were re-evaluated by 2 neuropathologists for all cases according to the new World Health Organization classification of tumors of the nervous system. Surgical resection was used to establish histopathologic diagnoses for all patients. Corresponding frozen tissues were reviewed to ensure a minimum of 80% tumor nuclei and a maximum of 50% necrosis.²⁵ Additional patient characteristics are summarized in the Table. This study was approved by the institutional review board, and written informed consent was obtained from all patients.

MR Imaging and Tumor Registration

MR imaging for most patients ($n = 129$) was performed on a Magnetom Trio 3T (Siemens, Erlangen, Germany) scanner. The T2-weighted image parameters included the following: TR = 5800 ms; TE = 110 ms; flip angle = 150°; FOV = 240 × 188 mm²; and voxel size = 0.6 × 0.6 × 5 mm³. A minority of clinical structural images were acquired on a Magnetom Verio 3T (Siemens) ($n = 32$) or Signa HD 1.5T (GE Healthcare, Milwaukee, Wisconsin) scanner ($n = 21$). Tumors shown on T2-weighted images were delineated by 2 senior neurosurgeons (J.W. and Z. Z., with

Clinical characteristics of patients

Characteristics	Status of p53		P Value
	Mutated (%) (n = 116)	Wild-Type (%) (n = 66)	
Age			
40 yr and older	41 (55)	33 (45)	.028
Younger than 40 yr	75 (69)	33 (31)	
Sex			
Male	70 (65)	37 (35)	.469
Female	46 (61)	29 (39)	
History of seizures			
Yes	70 (62)	42 (38)	.378
No	46 (66)	24 (34)	
Preoperative KPS			
≥80	109 (65)	58 (35)	.499
<80	7 (47)	8 (53)	
Pathology			
Oligodendroglioma	10 (36)	18 (64)	.003
Astrocytoma	48 (76)	15 (24)	
Oligoastrocytoma	58 (64)	33 (36)	

Note:—KPS indicates Karnofsky Performance Status Scale.

16 and 18 years of experience, respectively, in diagnosis by using brain MR imaging) who were blind to patient information. All lesion maps were re-evaluated by a neuroradiologist (S.W.L., with 24 years of experience). Tumor masks were combined as a new tumor mask in the analysis when <5% discrepancy was found. If ≥5% discrepancy was found, the neuroradiologist determined the tumor border. Images of each patient were then registered to a high-resolution (1.0-mm isotropic) brain atlas (Montreal Neurological Institute 152 [MNI152,]) by using a normalizing algorithm provided by SPM8 (<http://www.fil.ion.ucl.ac.uk/spm/software/spm8>).

Voxel-Based Lesion-Symptom Mapping

We first examined the overlap of the normalized tumor masked regions for the entire group and 2 subgroups of patients. Consequently, we performed VLSM analysis²⁴ for the entire cohort of patients to determine brain regions that had a significant expression of the p53 mutant. A regression analysis relating p53 mutation to tumor intensity was fit at each voxel. Patients were then scored by the expression level of p53 mutants in their tumors. With age, sex, and pathology being regressed out, the voxels showing significant correlations of p53 mutants were identified, and the results were further corrected for multiple comparisons by using a permutation test ($n = 500$).^{26,27} The t value of the voxel that was greater than the t value in >95% of permutations was kept in the VLSM results (with an α set at .05; power, >.8).²⁷

p53 Immunohistochemistry

Immunoperoxidase staining for p53 mutants was performed on formalin-fixed, paraffin-embedded tissue sections following the standard procedure introduced in our previous study.²⁸ Briefly, 5-mm tissue sections were deparaffinized, rehydrated, and incubated with 1.0% hydrogen peroxide in tris-buffered saline to block endogenous peroxidase activity. Antigen unmasking was performed by heating samples in sodium citrate buffer (10-mmol/L sodium citrate, pH = 6.0) for 10 minutes at 100°C. Non-specific protein binding was blocked by incubation in 5% horse serum in phosphate-buffered saline, and rabbit polyclonal p53

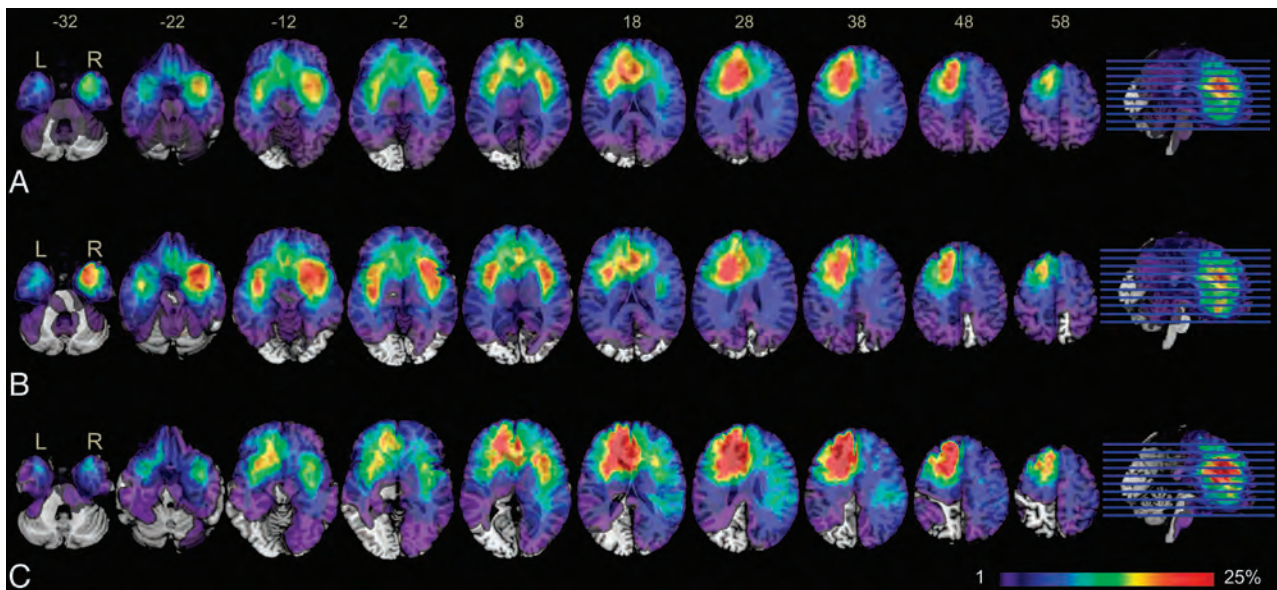


FIG 1. Overlap of tumor lesions. Overlap of all 182 patients with low-grade gliomas included in our study (A), overlap of a subgroup of 116 patients with mutant p53 gliomas (B), and overlap of a subgroup of 66 patients with wild-type p53 gliomas (C). The color range indicates the proportion of overlap of different cohorts, from violet (1 case) to red (>25% of cases overlap). Brain sections are displayed from z-coordinates -32 to $+58$ in the MNI space.

immune globulin G was then applied to the sections for 60 minutes at room temperature. Tumor sections were incubated in secondary antibody for 30 minutes at room temperature following washes in phosphate-buffered saline. Sections were washed and treated with Elite ABC (VECTASTAIN; Vector Laboratories, Burlingame, California), washed again, and then developed with 3,3'-diaminobenzidine tetrahydrochloride (50 mg 3,3'-diaminobenzidine in 100 mL phosphate-buffered saline and 150 mL of 3% hydrogen peroxide). After being rinsed in phosphate-buffered saline, slides were dehydrated in graded alcohols, cleared in xylene, and permanently covered. The immunohistochemical expressions of p53 protein were independently reviewed by 2 experienced pathologists and were then classified as the following: $-$, negative; $+$, isolated positive cells; $++$, clusters of positive cells; and $+++$, mostly positive cells. The scales of positive cells were then used to score mutant p53 expression levels that were documented from 0 ($-$) to 3 ($+++$).

Survival Analysis

Progression-free survival time was considered to be the end point of this study, measured from the date of the first surgical resection to disease progression. After subtotal resection, any volume increase of $\geq 25\%$ in the MR imaging was classified as tumor progression. Any tumor regrowth after gross total resection was classified as tumor recurrence.²⁹ Survival differences between patients with p53 mutations and wild-type p53 were evaluated by using log-rank analysis applied to Kaplan-Meier curves. Consequently, the same analysis was also performed to test the difference in outcome between tumors associated with high-expressing regions of p53 mutations and tumors not associated with these expression patterns. Additional survival analyses in subdivided patient groups, defined by tumor location and p53 status, were performed to further evaluate the effect of p53 mutations on patient outcome. Among patients having p53 mutations, tumors

associated with high-expressing regions of p53 mutations and tumors not associated with these expression patterns were input into a log-rank analysis. For tumors located in VLSM-defined regions, a survival analysis was performed on 2 groups that were determined by their p53 mutation status. Last, a multivariate Cox proportional hazard analysis was performed to determine whether factors including age, sex, history of seizures, preoperative Karnofsky Performance Status score, histopathology, and p53 mutation were predictors for PFS.

RESULTS

Demographic Characteristics

The overlap of all 182 tumors based on T2-weighted hyperintensity demonstrated 3 clusters of tumors that occurred with high frequency. Most interesting, hemispheric asymmetry was present on the overlap map (Fig 1A). Specifically, clusters in the right hemisphere were mainly located in the medial temporal lobe and insula, while most clusters in the left hemisphere were located in the frontal lobe, particularly at the subventricular zone surrounding the left anterior horn of the lateral ventricle. The asymmetric distribution of highly overlapping clusters implies that the occurrence and development of LGGs may have specific anatomic characteristics. LGGs with p53 mutations occurred more frequently in the bilateral temporal lobes and the insula, while LGGs with wild-type p53 demonstrated strong localization in the left frontal lobe (Fig 1B, -C).

Voxel-Based p53 Mutation Mapping

Note that overlaying the lesions yielded the distribution incidence of tumors, instead of truly specific anatomic correlates of the expression of mutant p53. To avoid this, we used VLSM analysis to show the statistically significant regions associated with specific genetic changes. Adequate voxels with high-power values (>0.8) were included in the analysis (Fig 2). Two clusters associated with

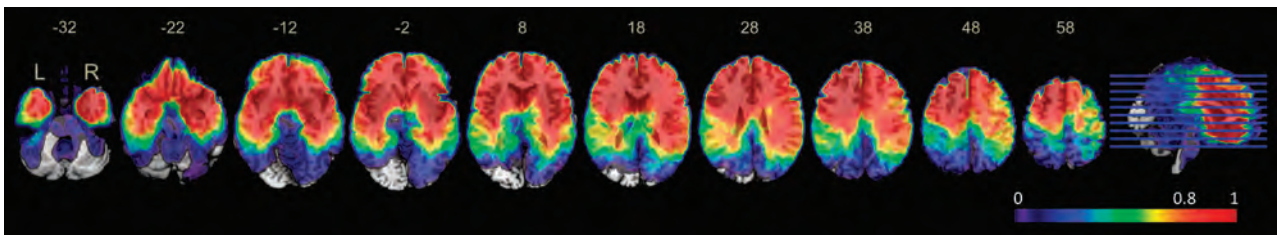


FIG 2. Power map for voxel-based lesion-symptom mapping analysis. The color map on the MNI space shows the distribution of power, ranging from 0 (violet) to 1 (red), with α set to $P < .05$. Only voxels with high-power values (>0.8) were included in the VLSM analysis.

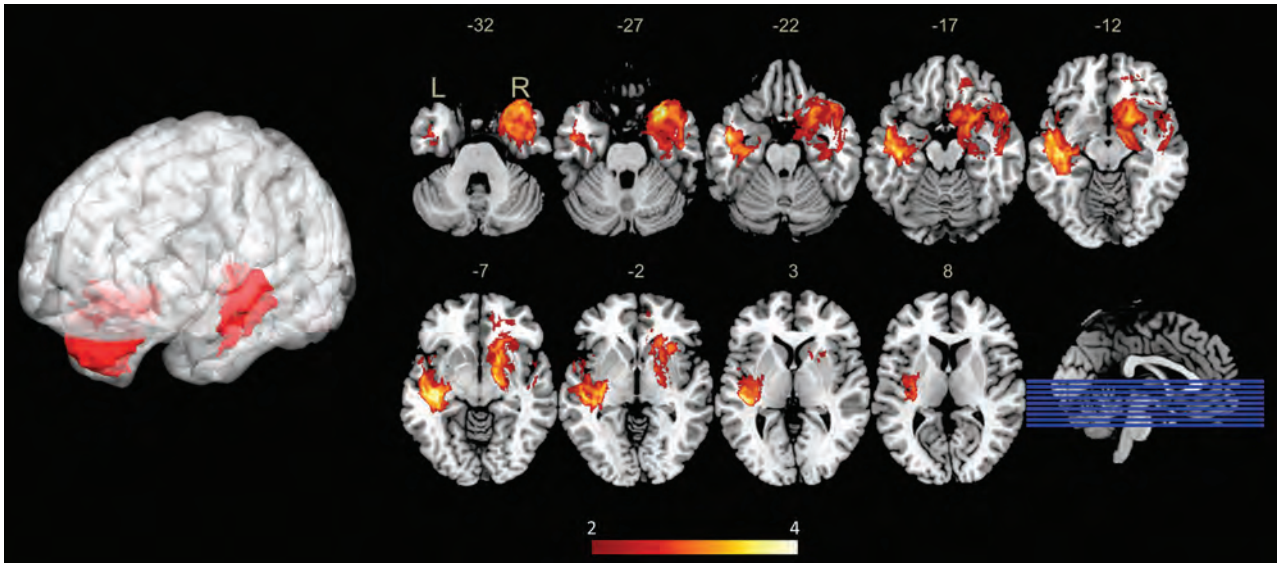


FIG 3. Voxel-based lesion-symptom mapping–defined p53 high-mutant regions. VLSM analysis shows regions associated with high expression of mutant p53 in low-grade gliomas. The left-medial temporal lobe and right-anterior temporal lobes are significantly correlated to high mutant p53 expression. The color range indicates the level of t values from red to yellow (least to most significant). Only significant voxels are rendered on the basis of a critical threshold determined by permutation testing ($n = 500$, $P < .05$).

high expression of mutant p53 were identified in each hemisphere following the permutation-based correction, with major expression being localized to the left medial temporal lobe and the right anterior temporal lobe (Fig 3). Overall, 78.7% (70/89) of cases were detected as having p53 mutations when their tumors involved the VLSM region; furthermore, 49.5% (46/93) of the cases showed expression of wild-type p53 when the tumor did not involve the VLSM region.

Survival Analysis

PFS information was available in 82 patients. PFS-based survival analysis showed no difference in patients with p53-mutated tumors compared with those with p53 wild-type tumors ($P = .2994$) (Fig 4A). In contrast, a significantly worse outcome (PFS) was observed in patients with tumors located in VLSM-defined regions compared with those with tumors outside these regions ($P = .0269$) (Fig 4B). To further investigate the role of p53 mutations in influencing PFS in VLSM-defined regions, we applied a survival analysis to the subdivided cohorts according to tumor location and p53 status. No significant relationship was observed among patients with tumors in VLSM-identified regions; however, a trending difference of PFS was observed among patients with wild-type and mutant p53 tumors ($P = .1032$) (Fig 4C). Most interesting, among p53-mutated cases, a shorter PFS was

observed in patients with tumors located in VLSM-identified regions ($P = .0088$) compared with those with tumors outside these regions (Fig 4D). Finally, a multivariate Cox proportional hazard analysis showed that VLSM-region involvement ($P = .010$, hazard ratio = 3.909), age (40 years or older) ($P = .015$, hazard ratio = 3.400), and preoperative Karnofsky Performance Status < 80 ($P = .024$, hazard ratio = 9.222) were prognostic factors (On-line Table).

DISCUSSION

The current study demonstrated the voxelwise brain risk atlas of LGG occurrence. More important, 2 regions associated with high expression of mutant p53 were identified in each hemisphere by using VLSM analysis. Furthermore, we demonstrated that patients with tumors located in VLSM-identified regions had significantly worse outcomes (PFS) compared with those with tumors occurring elsewhere in the brain.

Anatomic Characteristics of Genetic Changes in Tumors

Previous studies have demonstrated a correlation between genetic changes and tumor location. For instance, tumors with *isocitrate dehydrogenase 1* mutations have frequently been found in the frontal lobe.¹⁵ Additionally, the occurrences of MGMT promoter-methylated glioblastomas have been lateralized to the left

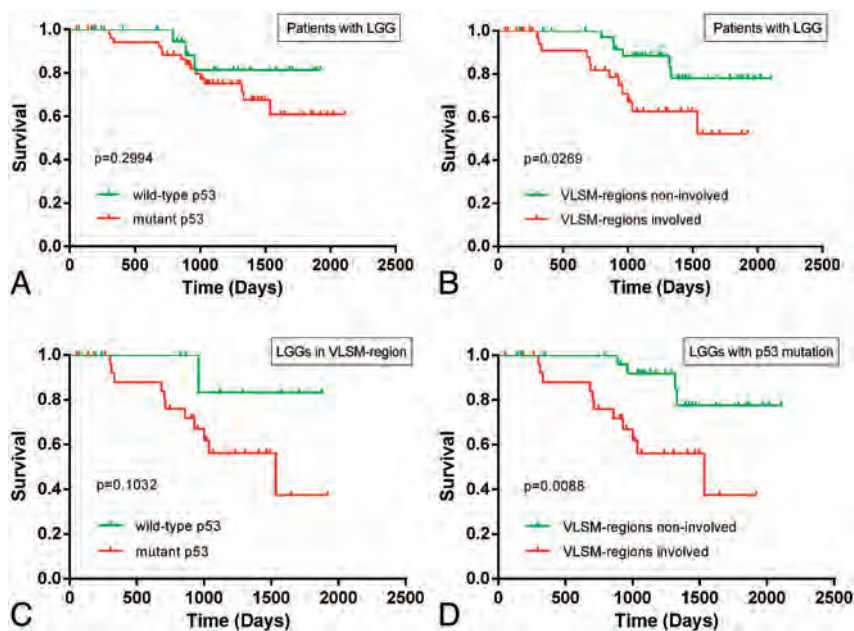


FIG 4. Kaplan-Meier curves showing the PFS for patients with low-grade gliomas. A, No significant difference was observed between patients with wild-type p53 tumors and those with mutant p53 tumors (log-rank, $P = .2994$). B, A statistically significant difference in PFS was observed between patients with tumors in VLSM-identified regions and patients with tumors located outside VLSM-identified regions, a trend toward a difference in PFS was observed between patients with wild-type p53 tumors and those with mutant p53 tumors (log-rank, $P = .1032$). D, Among patients with mutant p53 tumors, a significantly worse PFS was observed in patients with tumors located in VLSM-identified regions compared with patients with tumors outside these regions (log-rank, $P = .0088$).

hemisphere, while MGMT-unmethylated glioblastomas have been lateralized to the right hemisphere.¹⁶ Moreover, it has been shown that phosphatase and tensin homolog loss mostly occurs in the left frontal lobe²³ and that allelic loss of chromosomal arms 1p and/or 19q is more common in the frontal, parietal, and occipital lobes.¹⁴ These molecular biomarkers have been long confirmed as playing an important role in the tumorigenesis of specific regions. In the current study, overlaying a map of tumors demonstrated that LGGs with wild-type p53 mostly occurred in the frontal lobes. In comparison, LGGs with mutant p53 were predominantly located in the bilateral temporal lobes and insula. This finding is consistent with a previous report that *TP53* mutations frequently arise in the temporal lobe.¹⁷

VLSM analyses were then applied to statistically identify the anatomic correlation between tumor incidence and gene expression. In this study, we found that 2 specific brain regions were associated with high-expression levels of mutant p53, which has not been documented in previous LGG studies. Because p53 mutation is an early event in the molecular pathogenesis of LGGs, the strong propensity for p53-mutation gliomas to occur in the temporal lobes and insula indicated that p53 mutations may play a particularly important role in glioma tumorigenesis in these regions.^{11,20} *TP53* mutation and loss of 1p and/or 19q were hypothesized to be mutually exclusive on the basis of previous molecular-epidemiologic evidence.^{4,17} In addition, allelic loss of chromosomal arms 1p and 19q has been shown to be common in most brain regions except for the temporal lobe.¹⁴ On the basis of neuroimaging analysis, the current study showed that LGGs with

mutant p53s were predominantly located in the bilateral temporal lobes. Of note, the inverse localization between brain regions highly associated with p53 mutations and those associated with the loss of 1p and/or 19q provided new radio-epidemiologic insight to the current hypothesis.

Origin of Low-Grade Gliomas

The current hypothesis on tumor origin holds that gliomas may arise from neural stem cells that are mostly isolated from the subventricular zone, which lines the lateral ventricles; the dentate gyrus within the hippocampus; and potentially along deep white matter tracts.^{12,20,30} Our results, in some way, support the neural stem cell hypothesis. This finding is because of the 182 LGGs examined on T2-weighted images, most of the overlay of the tumor areas was located in the subventricular zone surrounding the left lateral ventricle, anterior horn, and hippocampus. Most important, these regions have long been proposed as a possible source of human gliomas, and a number of animal models also support this theory. Specifically, animals exposed to carcinogens and cancer-causing viruses demonstrate tumor formation within the subventricular zone, and these tumors quickly migrate into deep white matter regions, masking their original source.¹⁹

Another model by using the human glial fibrillary acidic protein promoter to undertake *hGFAP-cre*-mediated deletion of p53 and *NF1* showed that early inactivation of p53, in addition to *NF1* loss, induces glioblastoma development with the earliest identifiable area of a tumor being confined to the subventricular zone.³¹ Although neural stem cells are the source of initiation for gliomas, their progression toward a tumorigenic state may be regulated by multiple developmental signaling pathways. Notably, gene expression involved in these pathways is asymmetric.³² For instance, the *SUFU* gene in the sonic hedgehog pathway is overexpressed in the left hemisphere,³³ and the activation of the sonic hedgehog pathway predisposes neural progenitor cells to glioma formation,^{34,35} which may lead to asymmetry in tumorigenesis.

The current study identified the locations associated with high p53 mutation in both hemispheres, but with asymmetric distribution; these findings may serve as a new example of the asymmetric expression associated with genetic changes in brain tumors.

p53 Mutations, Tumor Location, and Survival Outcome

The prognostic or predictive role of p53 mutations has remained controversial. Inconsistent associations have been reported between the overexpression of mutant p53 and patient outcome or tumor response to therapy.^{13,29} A recent meta-analysis suggested that p53 expression is not a significant prognostic marker for hu-

man astrocytomas ($P = .531$, hazard ratio = 1.034).⁸ Most interesting, the same results were demonstrated in this study. There are 2 possible explanations for this. First, it could be that p53 status has no significant impact on survival prognosis. Second, p53 could interact with a multitude of other factors to influence prognosis.

In the current study, the shortest PFS was identified in patients with mutant p53 tumors localized to VLSM-identified regions when cohorts were subdivided according to tumor location and p53 status. This finding suggests that mutant p53 has a significant influence on the prognosis of tumors involving VLSM-identified regions rather than other regions. Survival benefits from region-specific gene expression in tumors have been reported in other molecular biomarkers. As previously discussed, tumors with a methylated MGMT promoter are associated with significantly longer survival periods when located in specific regions in the left hemisphere compared with tumors located in the right hemisphere that have an unmethylated MGMT promoter.¹⁶ Additionally, it has been shown that tumors with mutations in *isocitrate dehydrogenase 1* in the frontal lobe are associated with a favorable prognosis.¹⁵ This study observed a significantly poor prognosis for patients with tumors located in VLSM-identified clusters, which suggests that the impact of p53 status on prognosis may also have regional specificity. We further infer that p53 mutations could play a major role in the tumorigenesis of gliomas arising from the temporal-insula area. Additionally, a multivariate survival analysis revealed that a preoperative Karnofsky Performance Status < 80, VLSM-region involvement, and age older than 40 years are significant prognostic factors for PFS in LGGs. On the basis of these findings, regions associated with a higher incidence of genetic changes (as can be identified by using neuroimaging) could potentially be used for customized molecular therapy and survival prediction.

In the current study, VLSM analysis^{24,36} was used to identify the anatomic specificity of lesion-related characteristics. Although entitled “lesion-symptom mapping,” the principle of this approach allowed us to investigate the anatomic correlates of any characteristic that could be associated with tumors (genetic changes in this case). A related method, entitled “analysis of differential involvement,” has demonstrated the practical role of voxel-based neuroimaging analysis in localizing tumor-associated molecular events. On the basis of a voxelwise Fisher exact test, analysis of differential involvement has been used to identify the anatomic correlates of tumor-specific biomarkers (such as MGMT methylation¹⁶ and *isocitrate dehydrogenase 1*¹⁵) in the brain. The VLSM approach was used in the current study, however, because the regression model is more appropriate than the Fisher exact test when analyzing the graded data of gene expression.

Limitations

Several limitations to the current study should be considered. First, PFS was used as the end point of this study because patients with LGGs have a relatively long survival time; most of our patients are still alive. Nevertheless, patients who were not available for follow-up assessment may have influenced the integrity of our analyses. This may be the reason that no significant difference in

PFS was observed between patients with mutant and wild-type p53 tumors when VLSM regions were involved. Additionally, clinical image registration of anatomically distorted brain structures into a 3D standard space can be challenging. Thus, every tumor mask was determined and manually checked by 2 independent neurosurgeons to minimize inaccuracy.

CONCLUSIONS

This analysis allowed us to identify anatomic correlations among genetic lesions on a voxel basis and levels of mutant p53 expression in a large cohort of patients with LGGs. In addition, we demonstrated that tumor location could be an independent prognostic factor for tumor progression and that tumors located in VLSM-defined regions associated with high expression of mutant p53 have generally worse PFS. Our study provides an example that molecular-related brain regions identified on structural MRI could be used in preoperative surgical planning and clinical survival predictions.

ACKNOWLEDGMENTS

We would like to thank Yuling Yang for tissue-sample collection and clinical data retrieval and Drs J. Wang and Z. Zhang for their effort in tumor segmentation.

Disclosures: Lei Wang—UNRELATED: Grants/Grants Pending: Beijing Committee of Scientific Technology.* Comments: This grant is to support the research on biologic features and clinical treatment of gliomas. Tao Jiang—RELATED: Grants: China Ministry of Science and Technology.* Comments: This study was supported by funds from the National 973 Program (No.2011CB707804), and the National High Technology Research and Development Program (No. 2012AA02A508). *Money paid to the institution.

REFERENCES

1. Yang P, Wang Y, Peng X, et al. **Management and survival rates in patients with glioma in China (2004–2010): a retrospective study from a single-institution.** *J Neurooncol* 2013;113:259–66
2. Yan H, Parsons DW, Jin G, et al. **IDH1 and IDH2 mutations in gliomas.** *N Engl J Med* 2009;360:765–73
3. Youland RS, Brown PD, Giannini C, et al. **Adult low-grade glioma: 19-year experience at a single institution.** *Am J Clin Oncol* 2013;36:612–19
4. Hartmann C, Hentschel B, Tatagiba M, et al. **Molecular markers in low-grade gliomas: predictive or prognostic?** *Clin Cancer Res* 2011;17:4588–99
5. Weiler M, Wick W. **Molecular predictors of outcome in low-grade glioma.** *Curr Opin Neurol* 2012;25:767–73
6. Bourne TD, Schiff D. **Update on molecular findings, management and outcome in low-grade gliomas.** *Nat Rev Neurol* 2010;6:695–701
7. Okamoto Y, Di Patre PL, Burkhard C, et al. **Population-based study on incidence, survival rates, and genetic alterations of low-grade diffuse astrocytomas and oligodendrogliomas.** *Acta Neuropathol* 2004;108:49–56
8. Levidou G, El-Habr E, Saetta AA, et al. **P53 immunopositivity as a prognostic marker for human astrocytomas: a meta-analysis and review of the literature.** *J Neurooncol* 2010;100:363–71
9. Cho Y, Gorina S, Jeffrey PD, et al. **Crystal structure of a p53 tumor suppressor-DNA complex: understanding tumorigenic mutations.** *Science* 1994;265:346–55
10. England B, Huang T, Karsy M. **Current understanding of the role and targeting of tumor suppressor p53 in glioblastoma multiforme.** *Tumour Biol* 2013;34:2063–74
11. Muñoz DM, Tung T, Agnihotri S, et al. **Loss of p53 cooperates with K-ras activation to induce glioma formation in a region-independent manner.** *Glia* 2013;61:1862–72

12. Muñoz DM, Guha A. **Mouse models to interrogate the implications of the differentiation status in the ontogeny of gliomas.** *Oncotarget* 2011;2:590–98
13. Ständer M, Peraud A, Leroch B, et al. **Prognostic impact of TP53 mutation status for adult patients with supratentorial World Health Organization grade II astrocytoma or oligoastrocytoma: a long-term analysis.** *Cancer* 2004;101:1028–35
14. Zlatescu MC, TehraniYazdi A, Sasaki H, et al. **Tumor location and growth pattern correlate with genetic signature in oligodendroglial neoplasms.** *Cancer Res* 2001;61:6713–15
15. Lai A, Kharbanda S, Pope WB, et al. **Evidence for sequenced molecular evolution of IDH1 mutant glioblastoma from a distinct cell of origin.** *J Clin Oncol* 2011;29:4482–90
16. Ellingson BM, Cloughesy TF, Pope WB, et al. **Anatomic localization of O6-methylguanine DNA methyltransferase (MGMT) promoter methylated and unmethylated tumors: a radiographic study in 358 de novo human glioblastomas.** *Neuroimage* 2012;59:908–16
17. Mueller W, Hartmann C, Hoffmann A, et al. **Genetic signature of oligoastrocytomas correlates with tumor location and denotes distinct molecular subsets.** *Am J Pathol* 2002;161:313–19
18. Wechsler-Reya R, Scott MP. **The developmental biology of brain tumors.** *Annu Rev Neurosci* 2001;24:385–428
19. Sanai N, Alvarez-Buylla A, Berger MS. **Neural stem cells and the origin of gliomas.** *N Engl J Med* 2005;353:811–22
20. Jacques TS, Swales A, Brzozowski MJ, et al. **Combinations of genetic mutations in the adult neural stem cell compartment determine brain tumour phenotypes.** *EMBO J* 2010;29:222–35
21. Simpson JR, Horton J, Scott C, et al. **Influence of location and extent of surgical resection on survival of patients with glioblastoma multiforme: results of three consecutive Radiation Therapy Oncology Group (RTOG) clinical trials.** *Int J Radiat Oncol Biol Phys* 1993;26:239–44
22. Barani IJ, Benedict SH, Lin PS. **Neural stem cells: implications for the conventional radiotherapy of central nervous system malignancies.** *Int J Radiat Oncol Biol Phys* 2007;68:324–33
23. Ellingson BM, Lai A, Harris RJ, et al. **Probabilistic radiographic atlas of glioblastoma phenotypes.** *AJNR Am J Neuroradiol* 2013;34:533–40
24. Bates E, Wilson SM, Saygin AP, et al. **Voxel-based lesion-symptom mapping.** *Nat Neurosci* 2003;6:448–50
25. Cancer Genome Atlas Research Network. **Comprehensive genomic characterization defines human glioblastoma genes and core pathways.** *Nature* 2008;455:1061–68
26. Medina J, Kimberg DY, Chatterjee A, et al. **Inappropriate usage of the Brunner-Munzel test in recent voxel-based lesion-symptom mapping studies.** *Neuropsychologia* 2010;48:341–43
27. Kimberg DY, Coslett HB, Schwartz MF. **Power in voxel-based lesion-symptom mapping.** *J Cogn Neurosci* 2007;19:1067–80
28. Li S, Jiang T, Li G, et al. **Impact of p53 status to response of temozolomide in low MGMT expression glioblastomas: preliminary results.** *Neurol Res* 2008;30:567–70
29. Peraud A, Kreth FW, Wiestler OD, et al. **Prognostic impact of TP53 mutations and P53 protein overexpression in supratentorial WHO grade II astrocytomas and oligoastrocytomas.** *Clin Cancer Res* 2002;8:1117–24
30. Li G, Fang L, Fernandez G, et al. **The ventral hippocampus is the embryonic origin for adult neural stem cells in the dentate gyrus.** *Neuron* 2013;78:658–72
31. Zhu Y, Guignard F, Zhao D, et al. **Early inactivation of p53 tumor suppressor gene cooperating with NF1 loss induces malignant astrocytoma.** *Cancer Cell* 2005;8:119–30
32. Sun T, Walsh CA. **Molecular approaches to brain asymmetry and handedness.** *Nat Rev Neurosci* 2006;7:655–62
33. Sun T, Patoine C, Abu-Khalil A, et al. **Early asymmetry of gene transcription in embryonic human left and right cerebral cortex.** *Science* 2005;308:1794–98
34. Pomeroy SL, Tamayo P, Gaasenbeek M, et al. **Prediction of central nervous system embryonal tumour outcome based on gene expression.** *Nature* 2002;415:436–42
35. Hsieh A, Ellsworth R, Hsieh D. **Hedgehog/GLI1 regulates IGF dependent malignant behaviors in glioma stem cells.** *J Cell Physiol* 2011;226:1118–27
36. Nakagawa Y, Matsumura K, Iwasa M, et al. **Single photon emission computed tomography and statistical parametric mapping analysis in cirrhotic patients with and without minimal hepatic encephalopathy.** *Ann Nucl Med* 2004;18:123–29

MRI Grading versus Histology: Predicting Survival of World Health Organization Grade II–IV Astrocytomas

A. Lasocki, A. Tsui, M.A. Tacey, K.J. Drummond, K.M. Field, and F. Gaillard

ABSTRACT

BACKGROUND AND PURPOSE: Histologic grading of intracranial astrocytomas is affected by sampling error and substantial inter- and intraobserver variability. We proposed that incorporating MR imaging into grading will predict patient survival more accurately than histopathology alone.

MATERIALS AND METHODS: Patients with a new diagnosis of World Health Organization grades II–IV astrocytoma or mixed oligoastrocytoma diagnosed between September 2007 and December 2010 were identified. Two hundred forty-five patients met the inclusion criteria. Preoperative MRIs were independently reviewed by 2 readers blinded to the histologic grade, and an MR imaging grade was given. The MR imaging and histopathologic grades were compared with patient survival.

RESULTS: Patients with grade II or III astrocytomas on histology but evidence of necrosis on MR imaging (consistent with a grade IV tumor) had significantly worse survival than patients with the same histology but no evidence of necrosis on MR imaging ($P = .002$ for grade II histology and $P = .029$ for grade III). Their survival was not significantly different from that in patients with grade IV tumors on histology ($P = .164$ and $P = .385$, respectively); this outcome suggests that all or most are likely to have truly been grade IV tumors. MR imaging evidence of necrosis was less frequent in grade II and III oligoastrocytomas, preventing adequate subgroup analysis.

CONCLUSIONS: MR imaging can improve grading of intracranial astrocytomas by identifying patients suspected of being undergraded by histology, with high interobserver agreement. This finding has the potential to optimize patient management, for example, by encouraging more aggressive treatment earlier in the patient's course.

ABBREVIATIONS: ECOG = Eastern Cooperative Oncology Group; HR = hazard ratio; *IDH1* = isocitrate dehydrogenase-1

Management of intracranial astrocytic tumors is heavily influenced by the histologic grade obtained at the time of surgical biopsy or resection. World Health Organization grade IV astrocytomas (glioblastoma) are the most common, and most glioblastomas are considered to arise de novo (primary glioblastomas).^{1,2} Grade II and III astrocytomas (diffuse astrocytoma and

anaplastic astrocytoma, respectively) may also progress to grade IV (glioblastoma) with time. Secondary glioblastomas are associated with a better prognosis and typically demonstrate *isocitrate dehydrogenase-1* (*IDH1*) mutations.² Assigning a specific grade is important for routine patient management and for inclusion into clinical trials. The overall tumor grade depends on the highest grade component within the sample obtained; however, astrocytomas are heterogeneous tumors on both imaging and histology, and different components of the same tumor may exhibit different grades on histopathology. As a result, sampling error sometimes occurs when grading astrocytomas from surgical specimens, in particular when the specimen was obtained by biopsy.^{3–5} It also remains a risk with a resection because the pathologist typically does not receive the entire resected tumor for examination, as generally occurs with visceral tumors. The highest grade component may therefore not be present in the sample available for analysis. This sampling error can lead to undergrading of tumors, which, in turn, can potentially result in undertreatment. In

Received April 28, 2014; accepted after revision June 17.

From the Department of Cancer Imaging (A.L.), Peter MacCallum Cancer Centre, East Melbourne, Victoria, Australia; Departments of Pathology (A.T.), Neurosurgery (K.J.D.), Medical Oncology (K.M.F.), and Radiology (F.G.), The Royal Melbourne Hospital, Parkville, Victoria, Australia; and Melbourne EpiCentre (M.A.T.), Department of Medicine, The University of Melbourne and The Royal Melbourne Hospital, Parkville, Victoria, Australia.

Paper previously presented at: Annual Meeting of the Radiological Society of North America, December 1–6, 2013; Chicago, Illinois; and preliminary pilot data presented at: 14th Congress of the Asian Oceanian Congress of Radiology, August 30 to September 2, 2012; Sydney, Australia.

Please address correspondence to Arian Lasocki, MD, Department of Radiology, Peter MacCallum Cancer Centre, St Andrews Place, East Melbourne, Victoria, Australia 3002; e-mail: arian.lasocki@petermac.org

<http://dx.doi.org/10.3174/ajnr.A4077>

addition, due to varying practices even among pathologists working within the same department, interobserver correlation for histopathology has been shown to be only poor to moderate ($\kappa = 0.06-0.66$).⁶⁻⁸

MR imaging has been shown to correlate with histologic grade⁹⁻¹⁴ but has the important advantage of being able to scan the entire tumor in vivo and is therefore not susceptible to sampling error. When evaluating MR imaging, the literature usually uses histologic grade as the criterion standard; this practice makes it difficult to interpret the results given the aforementioned limitations of histopathology (sampling error and inter- and intraobserver variability) and likely underestimates the accuracy and utility of MR imaging. Using histopathology as the criterion standard also does little to clarify the practical questions of how to proceed when histopathology and MR imaging are disparate and which of the 2 better predicts the patient's outcome in this situation. In particular, it is not clear whether a patient should be presumed to have a higher grade tumor when the MR imaging appearance suggests a higher grade than the histologic assessment.

In this study, we correlated MR imaging appearances with patient survival and compared how well the MR imaging grade predicted biologic behavior compared with the histologic grade. We proposed that incorporating MR imaging into grading could predict patient survival better than the current criterion standard of histopathology alone.

MATERIALS AND METHODS

Patient Selection

Patients with a new diagnosis of a World Health Organization grade II-IV astrocytoma or mixed oligoastrocytoma were identified through the Central Nervous System Tumor Data Base at our hospital, which routinely captures all new patients with astrocytoma treated at our institution. All were adults who had not undergone treatment before surgery. Protoplasmic astrocytomas ($n = 9$) and gemistocytic astrocytomas ($n = 5$), which are known to have atypical imaging appearances, were excluded, as were patients with imaging appearances suggestive of gliomatosis cerebri ($n = 4$). Pure oligodendrogliomas were also not included. We included only patients with MR imaging performed before their first operation for this tumor, including at least a postcontrast sequence, available for review on the PACS. Seventeen patients were excluded due to a lack of preoperative postcontrast MR imaging. The study period was September 2007 to December 2010, to allow adequate time for survival information. Institutional Human Research Ethics Committee approval was obtained.

Patient demographics and baseline Eastern Cooperative Oncology Group (ECOG) performance status were obtained from the data base. The histologic grade of the tumor was taken from the histopathology report available on the clinical information system of the hospital. One patient was excluded because the histopathology had been reported at another institution and was not available for review. Of the histology reports included, all except 1 patient's histology was reported by 1 of 2 experienced neuropathologists. Histology for this single outlying patient and for 6 patients for whom the histopathologic grade was not clearly stated in the hospital report were blindly reviewed and graded by 1 of the 2 neuropathologists for the purposes of the study. *IDH1* mutation test-

ing was subsequently performed for patients with evidence of necrosis on MR imaging but grade II or III histology, to determine if this subset of patients showed an association with *IDH1* mutations, which would be suggestive of secondary glioblastomas. The proliferative index (Ki-67 or topoisomerase) was also determined for these patients, either taken from the formal hospital report ($n = 10$) or calculated on subsequent review if not reported initially ($n = 13$).

MR Imaging Review

Preoperative MRIs were independently reviewed retrospectively on the PACS by 2 readers, blinded to the histologic grade, and an MR imaging grade was given. The readers were an MR imaging fellow and a neuroradiologist with 5 years of subspecialty experience. For this study, the MR imaging grade was determined on the basis of the postcontrast MR imaging, as a surrogate for the histologic grading criteria used at our institution. MR imaging grade IV was assigned when there was evidence of necrosis—a complete enhancing ring on a postcontrast T1-weighted sequence around a central nonenhancing area. If there was enhancement but no convincing necrosis, this finding was designated grade III. Wispy enhancement was not considered sufficient for grade III. MR imaging grade II was assigned when the tumor demonstrated no contrast enhancement or necrosis. Discrepancies in the grade between the 2 MR imaging readers were decided by consensus, with knowledge of their initial MR imaging grade but again blinded to the histopathologic grade.

Most MR imaging studies (236 patients) were performed entirely at our institution, on 1 of 3 scanners (Magnetom Tim Trio; Siemens, Erlangen, Germany, 3T, software VB 17; Signa HDx, 1.5T; GE Healthcare, Milwaukee, Wisconsin, software Version 14; Signa LX, 1.5T; GE Healthcare, software Version 9.1). Most (212 of 245) were standard diagnostic studies. At 1.5T, these generally included at least axial T1WI, T2WI, FLAIR, and DWI sequences; sagittal T1WI; and a susceptibility-sensitive sequence (varying among scanners). Postcontrast T1-weighted sequences were performed in the axial and coronal planes, and usually a volumetric acquisition for the purposes of stereotaxis was performed. At 3T, the only difference was that the pre- and postcontrast T1-weighted sequences were acquired volumetrically, with reconstructions in 3 planes. Overall, MR spectroscopy and dynamic susceptibility contrast perfusion were performed in 63 and 31 patients, respectively. The remainder ($n = 33$) were most commonly limited volumetric postcontrast T1WI studies for stereotaxis. The standard intravenous contrast medium administered was 15 mL of gadopentetate dimeglumine, with the postcontrast sequence generally performed 2-3 minutes after contrast administration.

Surgical Technique

Surgical biopsies and resections were guided stereotactically by targeting the most suspicious areas on MR imaging by using the VectorVision Navigation System (BrainLAB, Feldkirchen, Germany). This usually incorporated a volumetric postcontrast T1WI sequence. Information about whether the operation was a biopsy or resection was obtained from the data base.

Statistical Analysis

Interobserver reliability and agreement between the 2 readers of MR imaging grades were evaluated by using the κ statistic, while

The Spearman correlation coefficient was used to assess the correlation between the histology and MR imaging grades. Both univariate and multivariate Cox logistic regression analyses were used to test for associations between overall survival and age, sex, performance status, and a combination of MR imaging and histologic grades. ECOG performance status was considered in a binary manner, namely 0–1 and 2–4. This grouping was selected because it provided better balance between the 2 groups than the other of the 2 groupings commonly used in the literature: 0–2 and 3–4. Different categoric variables were created that reflected different combinations of MR imaging and histologic grades. For the univariate analysis, the log-rank test was used for associations between survival and categoric variables, while Cox regression was used for continuous variables such as age. Kaplan-Meier curves were estimated to illustrate the association and nonassociations between survival and the categoric variables, with the Cox proportional hazard model used to compare survival between groups, after adjusting for relevant covariates. Results are presented as hazard ratios (HRs) with 95% confidence intervals. A 2-tailed *P* value of .05 was considered statistically significant. STATA statistical analysis software (Version 12.1; StataCorp, College Station, Texas) was used.

RESULTS

Patient Demographics

Two hundred forty-five patients met the inclusion criteria, of 281 patients identified initially. There were 136 men (56%) and 109 women. Patient ages ranged from 19 to 89 years, with a median of 61 years. Patient age was found to be a strong predictor of survival independent of histologic grade; hence, all results provided are corrected for age. Forty patients (16%) had grade II histology, 35 (14%) had grade III, and 170 (69%) had grade IV. Thirty-four patients (14%) had mixed oligoastrocytomas; the remainder had astrocytomas (*n* = 211). All patients underwent MR imaging within 11 days before surgery, and all except 7 patients, within 7 days. ECOG performance status data were available in 91% of patients (223 of 245): Ninety-seven patients were ECOG 0; 60, ECOG 1; 33, ECOG 2; 25, ECOG, 3; and 8, ECOG 4. As for age, performance status was an independent predictor of survival, thus the associations with survival for the MR imaging and histologic grades were also corrected for performance status. These baseline characteristics and the univariate results are presented on Table 1.

MR Imaging Histology Correlation

The MR imaging and histologic grades are compared in Table 2 for astrocytomas and in Table 3 for mixed oligoastrocytomas. Overall agreement between the 2 MR imaging readers was high, occurring in 233 of 245 patients, or 95% (κ = 0.87). Correlation between the MR imaging consensus grade and the histologic grade was moderate at 82% (κ = 0.58).

Astrocytomas

Of the 25 patients with grade II histology, 5 (20%) exhibited MR imaging evidence of necrosis (consistent with a grade IV tumor). Their mean survival was 233 days, significantly worse than the survival of patients with grade II histology but no evidence of necrosis on MR imaging (median survival, >946 days; *P* = .002;

Table 1: Patient baseline characteristics and univariate results

Variable	No. (%), Unless Otherwise Specified	HR	95% CI	<i>P</i> Value
Total	245			
Sex				
Female	109 (44.5%)	1	–	–
Male	136 (55.5%)	1.15	0.86–1.54	.346
Age (yr)				
Continuous				
Median (IQR)	61 (49–71)	1.05	1.04–1.07	<.001
Categorized				
19–53	79 (32.2%)	1	–	–
54–67	80 (32.7%)	2.59	1.75–3.84	<.001
68+	86 (35.1%)	5.05	3.42–7.47	<.001
MRI grade				
II	39 (15.9%)	1	–	–
III	19 (7.8%)	2.28	0.97–5.38	.059
IV	187 (76.3%)	8.39	4.50–15.67	<.001
Histology grade				
II	40 (16.3%)	1	–	–
III	35 (14.3%)	2.55	1.28–5.08	.007
IV	170 (69.4%)	5.88	3.32–10.43	<.001
Histology type				
Astrocytoma	211 (86.1%)	1	–	–
Oligoastrocytoma	34 (13.9%)	0.31	0.18–0.52	<.001
ECOG (continuous)				
Mean ± SD	0.78 ± 1.39	1.47	1.30–1.67	<.001
ECOG (grouped)				
0–1	157 (64.1%)	1	–	–
2–4	66 (26.9%)	2.13	1.54–2.94	<.001

Note.—IQR indicates interquartile range.

Table 2: Number of patients with astrocytoma with each histologic and MRI grade

MRI Grade	Histologic Grade			Total
	II	III	IV	
II	15	5	1	21
III	5	7	4	16
IV	5	16	153	174
Total	25	28	158	211

Table 3: Number of patients with mixed oligoastrocytoma with each histologic and MRI grade

MRI Grade	Histologic Grade			Total
	II	III	IV	
II	13	5	0	18
III	1	1	1	3
IV	1	1	11	13
Total	15	7	12	34

HR = 44.6; 95% CI, 4.0–502.6). These patients with necrosis on MR imaging had statistically equivalent survival (*P* = .164) compared with those with grade IV histology (median survival, 257 days), though with a slight trend toward worse survival (HR = 1.9; 95% CI, 0.8–4.8). The survival of these 3 groups is compared on the Kaplan-Meier curve (Fig 1).

For the grade III histology group, 16 of 28 (59%) had evidence of necrosis on MR imaging, with a median survival of 245 days. Examples are shown in Fig 2. Again, their survival was significantly worse than that for patients without MR imaging evidence of necrosis (median survival, 564 days; *P* = .029; HR = 3.3; 95% CI, 1.1–9.8) and was equivalent to that of the grade IV histology

group ($P = .385$). These survivals are compared on the Kaplan-Meier curve (Fig 3).

IDH1 mutation status was tested on all 21 patients with grade II or III histology but MR imaging evidence of necrosis, and it was negative in all patients. The proliferative index varied widely, from 1% to >75%. Five of the 21 patients had further surgery within 4 months of their initial surgery (after 8, 10, 46, 90, and 109 days, respectively). In each case, histology showed grade IV tumor. Histology was obtained by resection in 9 of 21 patients (43%) with grade II or III histology but MR imaging evidence of necrosis and by biopsy in the other 12. This proportion obtained by resection was slightly higher than that for the patients with grade II or III histology but no evidence of necrosis on MR imaging (11 of 32, 34%). This difference was not statistically significant ($P = .533$).

Of patients with grade II histology, there was no significant difference in survival ($P = .300$) between those with no enhancement (MR imaging grade II) compared with those with enhancement but no evidence of necrosis (MR imaging grade III). Similarly, for patients with grade III histology, there was no significant difference in survival ($P = .119$) between those with MR imaging grades of II and III. Of the patients with grade IV histology, imaging of 4 demonstrated enhancement but not convincing necrosis on MR imaging, and imaging of 1 patient did not exhibit any enhancement. These 5 patients without evidence of necrosis on

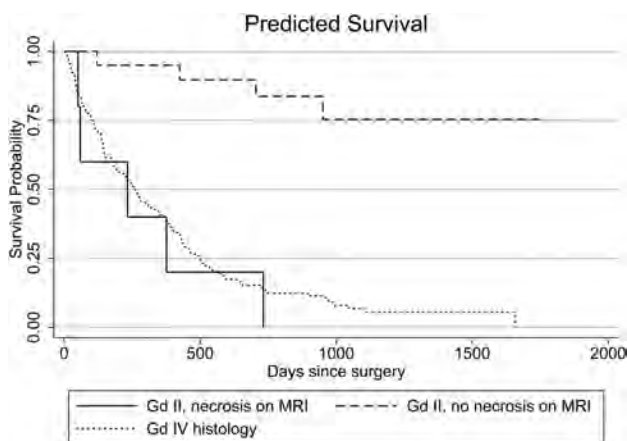


FIG 1. Kaplan-Meier survival curve showing survival of patients with grade II astrocytomas on histology, with and without evidence of necrosis on MR imaging, compared with patients with grade IV histology.

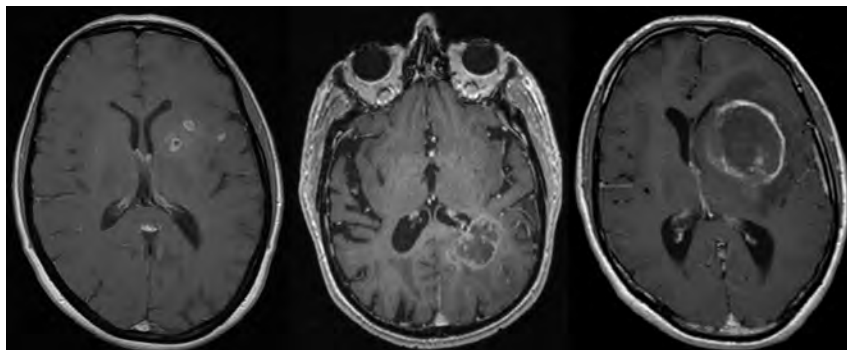


FIG 2. Examples of postcontrast T1-weighted sequences of patients with grade III astrocytomas on histology but MR imaging evidence of necrosis.

MR imaging showed a trend toward longer survival (median survival, 589 days) compared with the remaining patients with grade IV histology (median survival, 252 days; HR = 0.4; 95% CI, 0.1–1.3), though with the small number of patients, this was not statistically significant ($P = .138$).

Mixed Oligoastrocytomas

Fewer grade II and III oligoastrocytomas showed evidence of necrosis on MR imaging (only 1 of each grade); this result precluded adequate subgroup analysis. *IDH1* was positive in 1 of these 2 patients. When corrected for age, ECOG performance status, and histologic grade, patients with mixed oligoastrocytomas had significantly better survival than those with pure astrocytomas ($P = .031$; HR = 0.52; 95% CI, 0.3–0.9).

DISCUSSION

We have described a simple yet robust approach to MR imaging grading of intracranial astrocytomas. MR imaging can accurately identify a significant number of patients undergraded by histology, in particular those suspected of truly having grade IV tumors on the basis of MR imaging evidence of necrosis. The survival data strongly suggest that all or most of the astrocytomas with grade II and III histology but evidence of necrosis on MR imaging were indeed glioblastomas. In addition, they appear to have generally been primary glioblastomas, given *IDH1* mutation negativity, rather than secondary glioblastomas (which are associated with *IDH1* mutations and typically have a better prognosis).² Undergrading occurred with both stereotactic biopsies and definitive resections. We have shown that MR imaging has excellent interobserver agreement, better than the inter- and intraobserver agreement reported for pathologic grading of astrocytomas ($\kappa = 0.06–0.66$).^{6–8} In addition, combining MR imaging studies from different scanners indicates that these results using standard sequences should be achievable in most institutions, rather than being vendor- or model-specific. Finally, the high correlation between a relatively inexperienced reader and a more experienced reader shows that the grading system can be easily used by radiologists of varying experience.

We consider grade IV the most important histologic grade to determine accurately at diagnosis because the management is usually more aggressive than for grade III and, in particular, grade II tumors,^{15–17} and patients can deteriorate rapidly. Correct identification of grade IV tumors allows appropriate intensification of treatment to a multimodality regimen at diagnosis. Patients with grade IV tumors are also those who are potential candidates for the greatest number of clinical trials and novel therapies. Clinical trial participation has been shown to be an independent predictor of longer survival in glioblastoma¹⁸; hence, being ineligible for a trial due to undergrading has the potential to adversely affect a patient's outcome.

Our results build on work by authors at least as far back as Dean et al,⁹ who, in

1990, aimed to grade astrocytic tumors on the basis of a variety of MR imaging features. Already >2 decades ago, they postulated that “MR imaging may serve as an adjunct in case management when the clinical course and MR findings appear to be at odds with the neuropathologic diagnosis.”⁹ Our results are similar to a much more recent study of 151 patients by Pope et al,¹⁹ in which patients with grade III histology but MR imaging evidence of necrosis (8 of 43 grade III tumors, 19%) had survival similar to that in patients with grade IV tumors, and 105 of 110 histologically proved grade IV tumors had MR imaging evidence of necrosis. In our study, the number of patients with grade III histology but MR imaging evidence of necrosis was greater (16 of 28, 57%). We have also shown a similar difference in survival for patients with histologic grade II tumors and evidence of necrosis on MR imaging (5 of 25, 20%), which was not examined by Pope et al.

Previous articles have shown overall moderate correlation between an MR imaging grade by using conventional sequences and the histopathologic grade,^{9-14,20} which improves when adding advanced imaging sequences such as perfusion (in particular relative cerebral blood volume) or spectroscopy.^{10,11,13,14,21-24} The results for DWI have been conflicting,^{13,21} as they have for the presence

of magnetic susceptibility suggestive of hemorrhage.^{25,26} A practical difficulty with the advanced sequences is that they are generally continuous variables, with at least some overlap between tumors of different grades. It is likely that the degree of overlap between tumor grades would substantially increase once those tumors with MR imaging evidence of necrosis are excluded; this change would decrease the specificity and thus the utility of these sequences. A further difficulty with many of the studies of MR imaging grading of astrocytic tumors is that grade III and IV tumors have been considered together as “high-grade gliomas.”^{11,13,14,21-23,25,27,28} In general, distinction between grade III and IV tumors was inaccurate^{11,27} or was not assessed, yet this distinction can be very important for determining both management options and clinical trial inclusion. Not unexpectedly, our simple grading system was less helpful in differentiating grade II and III tumors on the basis of the presence or absence of enhancement, and this is likely to be a setting in which the advanced sequences will have particular value.

We acknowledge that management may have varied substantially among patients. Age and performance status are both important factors in the decision-making process, and we think that correcting for these variables addresses this variation in management between patients, especially given that ours is a single-institution study in the post-Stupp era.¹⁷ During the study period, our postsurgery standard therapy for patients with grade IV tumors was combination temozolomide and radiation therapy followed by adjuvant temozolomide; patients with grade III tumors were initially treated with surgery and postoperative radiation therapy, followed by the introduction of temozolomide when there was evidence of recurrence, while patients with grade II tumors were generally managed with surgery alone, followed by active surveillance until evidence of dedifferentiation was seen. Molecular and genetic markers such as *IDH1* mutation status, proliferative index, and O6-methylguanine DNA methyltransferase methylation were not typically obtained during the study period and were not used to guide treatment. A further potential criticism of this study is that advanced imaging sequences were underused in determining the MR imaging grade. Although advanced sequences can be beneficial in grading, our aim was to develop a fairly direct MR

imaging correlate for the WHO classification, which was simple and reproducible by all institutions. Additionally, given that we have shown that the presence of necrosis on MR imaging (as a surrogate for necrosis on histopathology) is sufficient to identify most grade IV tumors, including those suspected of being undergraded due to sampling error, it is not clear from the literature how useful the advanced sequences are for assessing tumors that do not have evidence of necrosis on the postcontrast T1-weighted sequence.

Our patient group consisted of those with a higher proportion of grade IV tumors than some other studies. This may partly relate to our exclusion of patients with protoplasmic and gemistocytic

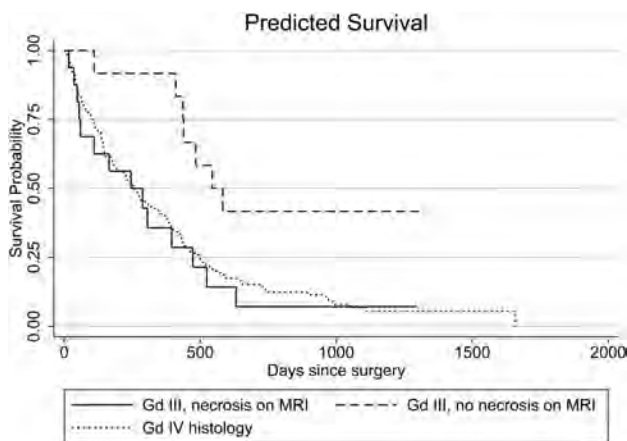


FIG 3. Kaplan-Meier survival curve showing survival of patients with grade III astrocytomas on histology, with and without evidence of necrosis on MR imaging, compared with patients with grade IV histology.

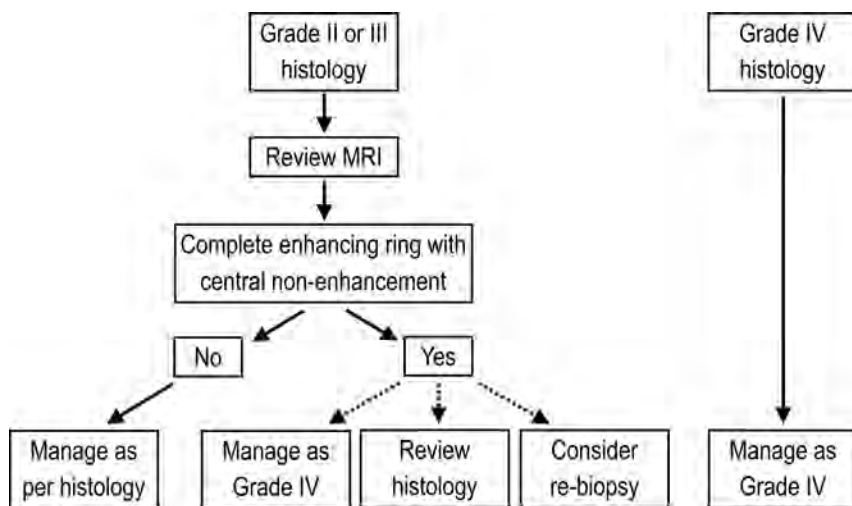


FIG 4. Suggested management algorithm for a combined histologic/MR imaging grading system.

variants and those suspected on MR imaging of having gliomatosis cerebri. It is not clear whether these patients were included in other studies. We considered it important to exclude these histologic variants from our study because they have imaging appearances that vary significantly from the more common diffuse fibrillary variety (contrast enhancement and cystic change being far more common), and in the case of gemistocytic astrocytomas, the prognosis is worse.^{1,29,30} The patients suspected of having gliomatosis cerebri were also excluded for this same reason of having a worse prognosis because including them could have unfairly biased against histology. Nevertheless, due to the size of our study, the absolute number of grade II and III tumors was large compared with that in the existing literature.

The management of astrocytomas has progressed beyond just histologic assessment, with molecular and genetic markers being able to provide information on prognosis and expected treatment outcomes.³¹ The interpretation and implications of the genetic analysis are affected by the histologic grade, however; hence, it remains important to optimize the accuracy of grading. Accurate grading becomes even more important when these markers are not available (for example, due to cost). In either case, using MR imaging to improve the accuracy of grading can help optimize management and prognostication with little or no added cost because an MR imaging has generally already been performed.

The algorithm we suggest for incorporating an MR imaging grade into the overall management (Fig 4) hinges on all patients with grade II and grade III astrocytoma having their preoperative MR imaging reviewed for grading, with the radiologist aware of the histology but potentially blinded to the histologic grade. If the MR imaging does show evidence of necrosis, our results suggest that the tumor can simply be treated as grade IV, with the appropriate multimodality therapy. If histologic confirmation of grade IV tumor is necessary, we suggest reviewing the histology in the first instance, specifically looking for evidence of necrosis to verify the MR imaging appearances. If no necrosis is revealed on review, repeat surgery could also be considered, though in practice, it would be a last resort. The results for astrocytomas were not reproduced for oligoastrocytomas due to the smaller numbers and less frequent upgrading of tumors based on MR imaging.

CONCLUSIONS

Using MR imaging in tandem with conventional histologic grading can significantly enhance the accuracy of grading of intracranial astrocytomas, with high interobserver agreement. Detection of necrosis on MR imaging in a histologic grade II or III astrocytoma suggests that the patient has been undergraded by histology. This result has the potential to optimize patient management, for example, by encouraging a more aggressive treatment strategy earlier in the patient's course.

Disclosures: Arian Lasocki—RELATED: Support for Travel to Meetings for the Study or Other Purposes: Radiology Resources (prize awarded by the Royal Australian and New Zealand College of Radiologists); Kathryn M. Field—UNRELATED: Payment for Lectures (including service on Speakers Bureaus): Roche; Travel/Accommodations/Meeting Expenses Unrelated to Activities Listed: Merck Sharp and Dohme; Frank Gaillard—UNRELATED: Consultancy: Medtronic; Comments: educational talks about MRI in the context of MRI-safe pacemakers and neurostimulators; Employment: Radiopaedia.org; Comments: Founder, Editor, CEO of Radiopaedia.org, an online collaborative radiology resource, www.radiopaedia.org.

REFERENCES

- Louis DN, ed. *WHO Classification of Tumours of the Central Nervous System*. 4th ed. Lyon: International Agency for Research on Cancer; 2007
- Ohgaki H, Kleihues P. **The definition of primary and secondary glioblastoma.** *Clinical Cancer Research* 2013;19:764–72
- Chandrasoma PT, Smith MM, Apuzzo ML. **Stereotactic biopsy in the diagnosis of brain masses: comparison of results of biopsy and resected surgical specimen.** *Neurosurgery* 1989;24:160–65
- Glantz MJ, Burger PC, Herndon JE, et al. **Influence of the type of surgery on the histologic diagnosis in patients with anaplastic gliomas.** *Neurology* 1991;41:1741–44
- Jackson RJ, Fuller GN, Abi-Said D, et al. **Limitations of stereotactic biopsy in the initial management of gliomas.** *Neuro Oncol* 2001;3:193–200
- Coons SW, Johnson PC, Scheithauer BW, et al. **Improving diagnostic accuracy and interobserver concordance in the classification and grading of primary gliomas.** *Cancer* 1997;79:1381–93
- Mittler MA, Walters BC, Stopa EG. **Observer reliability in histological grading of astrocytoma stereotactic biopsies.** *J Neurosurg* 1996;85:1091–94
- Prayson RA, Agamanolis DP, Cohen ML, et al. **Interobserver reproducibility among neuropathologists and surgical pathologists in fibrillary astrocytoma grading.** *J Neurol Sci* 2000;175:33–39
- Dean BL, Drayer BP, Bird CR, et al. **Gliomas: classification with MR imaging.** *Radiology* 1990;174:411–15
- Knopp EA, Cha S, Johnson G, et al. **Glial neoplasms: dynamic contrast-enhanced T2*-weighted MR imaging.** *Radiology* 1999;211:791–98
- Law M, Yang S, Wang H, et al. **Glioma grading: sensitivity, specificity, and predictive values of perfusion MR imaging and proton MR spectroscopic imaging compared with conventional MR imaging.** *AJNR Am J Neuroradiol* 2003;24:1989–98
- Möller-Hartmann W, Herminghaus S, Krings T, et al. **Clinical application of proton magnetic resonance spectroscopy in the diagnosis of intracranial mass lesions.** *Neuroradiology* 2002;44:371–81
- Arvinda HR, Kesavadas C, Sarma PS, et al. **Glioma grading: sensitivity, specificity, positive and negative predictive values of diffusion and perfusion imaging.** *J Neurooncol* 2009;94:87–96
- Kim HS, Kim SY. **A prospective study on the added value of pulsed arterial spin-labeling and apparent diffusion coefficients in the grading of gliomas.** *AJNR Am J Neuroradiol* 2007;28:1693–99
- Brown PD. **Low-grade gliomas: the debate continues.** *Curr Oncol Rep* 2006;8:71–77
- DeAngelis LM. **Anaplastic glioma: how to prognosticate outcome and choose a treatment strategy.** *J Clin Oncol* 2009;27:5861–62
- Stupp R, Mason WP, van den Bent MJ, et al. **Radiotherapy plus concomitant and adjuvant temozolomide for glioblastoma.** *N Engl J Med* 2005;352:987–96
- Field KM, Drummond KJ, Yilmaz M, et al. **Clinical trial participation and outcome for patients with glioblastoma: multivariate analysis from a comprehensive dataset.** *J Clin Neurosci* 2013;20:783–89
- Pope WB, Sayre J, Perlina A, et al. **MR imaging correlates of survival in patients with high-grade gliomas.** *AJNR Am J Neuroradiol* 2005;26:2466–74
- Chishty IA, Rafique MZ, Hussain M, et al. **MRI characterization and histopathological correlation of primary intra-axial brain glioma.** *Journal of the Liaquat University of Medical and Health Sciences* 2010;9:64–69
- Zonari P, Baraldi P, Crisi G. **Multimodal MRI in the characterization of glial neoplasms: the combined role of single-voxel MR spectroscopy, diffusion imaging and echo-planar perfusion imaging.** *Neuroradiology* 2007;49:795–803
- Chawla S, Wang S, Wolf RL, et al. **Arterial spin-labeling and MR spectroscopy in the differentiation of gliomas.** *AJNR Am J Neuroradiol* 2007;28:1683–89
- Bisdas S, Kirkpatrick M, Giglio P, et al. **Cerebral blood volume mea-**

- surements by perfusion-weighted MR imaging in gliomas: ready for prime time in predicting short-term outcome and recurrent disease? *AJNR Am J Neuroradiol* 2009;30:681–88
24. Meyerand ME, Pipas JM, Mamourian A, et al. **Classification of biopsy-confirmed brain tumors using single-voxel MR spectroscopy.** *AJNR Am J Neuroradiol* 1999;20:117–23
 25. Pinker K, Noebauer-Huhmann IM, Stavrou I, et al. **High-resolution contrast-enhanced, susceptibility-weighted MR imaging at 3T in patients with brain tumors: correlation with positron-emission tomography and histopathologic findings.** *AJNR Am J Neuroradiol* 2007;28:1280–86
 26. Asari S, Makabe T, Katayama S, et al. **Assessment of the pathological grade of astrocytic gliomas using an MRI score.** *Neuroradiology* 1994;36:308–10
 27. Bulakbasi N, Kocaoglu M, Örs F, et al. **Combination of single-voxel proton MR spectroscopy and apparent diffusion coefficient calculation in the evaluation of common brain tumors.** *AJNR Am J Neuroradiol* 2003;24:225–33
 28. Bulakbasi N, Kocaoglu M, Farzaliyev A, et al. **Assessment of diagnostic accuracy of perfusion MR imaging in primary and metastatic solitary malignant brain tumors.** *AJNR Am J Neuroradiol* 2005;26:2187–99
 29. Krouwer HG, Davis RL, Silver P, et al. **Gemistocytic astrocytomas: a reappraisal.** *J Neurosurg* 1991;74:399–406
 30. Avninder S, Sharma M, Deb P, et al. **Gemistocytic astrocytomas: histomorphology, proliferative potential and genetic alterations: a study of 32 cases.** *J Neurooncology* 2006;78:123–27
 31. Thomas La, Di Stefano AL, Ducray F. **Predictive biomarkers in adult gliomas: the present and the future.** *Curr Opin Oncol* 2013;25:689–94

Macro- and Microstructural Changes in Patients with Spinocerebellar Ataxia Type 6: Assessment of Phylogenetic Subdivisions of the Cerebellum and the Brain Stem

K. Sato, K. Ishigame, S.H. Ying, K. Oishi, M.I. Miller, and S. Mori



ABSTRACT

BACKGROUND AND PURPOSE: Site-specific degeneration patterns of the infratentorial brain in relation to phylogenetic origins may relate to symptoms in patients with spinocerebellar degeneration, but the patterns are still unclear. We investigated macro- and microstructural changes of the infratentorial brain based on phylogenetic origins and their correlation with symptoms in patients with spinocerebellar ataxia type 6.

MATERIALS AND METHODS: MR images of 9 patients with spinocerebellar ataxia type 6 and 9 age- and sex-matched controls were obtained. We divided the infratentorial brain on the basis of phylogenetic origins and performed an atlas-based analysis. Comparisons of the 2 groups and a correlation analysis assessed with the International Cooperative Ataxia Rating Scale excluding age effects were performed.

RESULTS: A significant decrease of fractional volume and an increase of mean diffusivity were seen in all subdivisions of the cerebellum and in all the cerebellar peduncles except mean diffusivity in the inferior cerebellar peduncle in patients compared with controls ($P < .0001$ to $< .05$). The bilateral anterior lobes showed the strongest atrophy. Fractional volume decreased mainly in old regions, whereas mean diffusivity increased mainly in new regions of the cerebellum. Reflecting this tendency, the International Cooperative Ataxia Rating Scale total score showed strong correlations in fractional volume in the right flocculonodular lobe and the bilateral deep structures and in mean diffusivity in the bilateral posterior lobes ($r = 0.73$ to ± 0.87).

CONCLUSIONS: We found characteristic macro- and microstructural changes, depending on phylogenetic regions of the infratentorial brain, that strongly correlated with clinical symptoms in patients with spinocerebellar ataxia type 6.

ABBREVIATIONS: FA = fractional anisotropy; ICARS = International Cooperative Ataxia Rating Scale; ICP = inferior cerebellar peduncle; LDDMM = large deformation diffeomorphic metric mapping; MCP = middle cerebellar peduncle; MD = mean diffusivity; SCA6 = spinocerebellar ataxia type 6; SCP = superior cerebellar peduncle

Spinocerebellar ataxia type six (SCA6) is a rare, late-onset, autosomal dominant disease. SCA6 is associated with a genetic defect (CAG repeat expansion) in the gene encoding for a subunit of a voltage-gated calcium channel, which is associated with neuronal loss mainly in Purkinje cells in the cerebellar cor-

tex.¹ SCA6 is not fatal, but the accompanying cerebellar dysfunction is permanent and progressive.² Cerebellar atrophy is a characteristic imaging feature, and mild atrophy of the brain stem and subtle atrophy of the thalamus or the cerebral cortex can occur.^{3,4}

Although the definite diagnosis of SCA6 is made by genetic examination, MR imaging can narrow the differential diagnosis of neurodegenerative diseases that can cause ataxia. MR imaging helps select the candidates for genetic examination.⁵ Degeneration patterns of the infratentorial brain are the key to differentiating SCA6 from other neurodegenerative diseases presenting with ataxia, and cerebellar degeneration is a characteristic imaging feature in patients with SCA6. However, few studies^{6,7} have investigated site-specific degeneration patterns of the infratentorial brain, and their segmentations were not easy to assess clinically. Moreover, correlations between site-specific degeneration patterns and clinical symptoms require further characterization.

The cerebellum has 3 regions derived from different phyloge-

Received May 8, 2014; accepted after revision July 14.

From the Russell H. Morgan Department of Radiology and Radiological Science (K.S., K.I., K.O., S.M.), Departments of Radiology (S.H.Y.), Neurology (S.H.Y.), and Ophthalmology (S.H.Y.), and Center for Imaging Science (M.I.M.), Johns Hopkins University School of Medicine, Baltimore, Maryland; Department of Radiology (K.S.), Juntendo University School of Medicine, Tokyo, Japan; Department of Radiology (K.I.), University of Yamanashi, Yamanashi, Japan; and F.M. Kirby Research Center for Functional Brain Imaging (S.M.), Kennedy Krieger Institute, Baltimore, Maryland.

K. Sato and K. Ishigame contributed equally to this work.

Please address correspondence to Kanako Sato, MD, PhD, Department of Radiology, Juntendo University School of Medicine, 2-1-1 Hongo, Bunkyo-ku, Tokyo, Japan 113-8421; e-mail: satokana.tky@gmail.com

Indicates open access to non-subscribers at www.ajnr.org

<http://dx.doi.org/10.3174/ajnr.A4085>

netic origins (the archicerebellum, the paleocerebellum, and the neocerebellum)⁸⁻¹⁰ that form distinct neural pathways between the cerebellum and other regions of the brain. These 3 regions are believed to have different functions.^{9,11,12} It is of great interest to know how the cerebellar macro- and microstructural changes in each phylogenetic region manifest as symptoms in patients with SCA6.

Thus, in the present study, we investigated changes of both volume and diffusion metrics: mean diffusivity (MD) and fractional anisotropy (FA) obtained with DTI. Changes of diffusion metrics have been reported in other types of spinocerebellar ataxia and in multiple system atrophy.^{13,14} There are few DTI studies of patients with SCA6,^{15,16} and they investigated only part of the cerebellum or the cerebellar peduncles with manual methods.

We hypothesized that clinical symptoms in patients with SCA6 are correlated with macro- and microstructural changes depending on the phylogenetic origins of the cerebellum. The purposes of this study were to investigate these correlations and to identify the site-specific degeneration patterns of the infratentorial brain that are also clinically assessable in patients with SCA6. To our knowledge, this is the first MR imaging study combining volumetric and DTI analyses based on phylogenetic regions.

MATERIALS AND METHODS

Subjects

This study was approved by our institutional review board and complied with the Health Insurance Portability and Accountability Act. Written informed consent was obtained from all participants. We acquired MR images of the brain in 9 patients with SCA6 (5 women and 4 men; mean age, 57.9 ± 7.25 years) and 9 age-matched healthy controls (5 women and 4 men; mean age, 58.8 ± 7.51 years) obtained between August 2005 and September 2009 from the Johns Hopkins University School of Medicine, and the images were retrospectively analyzed.

Clinical Evaluation

All participants completed a medical questionnaire, and the possibility of secondary ataxia was excluded. Symptoms were assessed with the International Cooperative Ataxia Rating Scale (ICARS).¹⁷ ICARS scores have a maximum of 100 points as the total of 4 subscores: the static score, limb score, dysarthria score, and oculomotor score.

The neurologic examinations of all of patients and controls were performed by a neurologist (S.H.Y.) at the departments of radiology, neurology, and ophthalmology at the Johns Hopkins University School of Medicine. The neurologist had >10 years of experience in the design and measurement of quantitative neurologic assessments and was blinded to the MR imaging results.

Data Acquisition

Brain imaging was performed with a 3T MR imaging scanner (Intera; Philips Healthcare, Best, the Netherlands). An axial single-shot spin-echo echo-planar imaging sequence was used for the DTI. The parameters used were as follows: TR/TE, 6491/69 ms; b-value, 700 s/mm²; diffusion-encoding gradients, 30 directions;¹⁸ number of signals acquired, 2; FOV, 212 × 212 mm; matrix size, 256 × 256 mm; intersection gap, 0 mm; section thick-

ness, 2.2 mm; section number, 65. EPI with no diffusion weighting ($b=0$ s/mm²) was performed for use in spatial normalization.

3D-magnetization prepared rapid acquisition of gradient echo images and T2WI were acquired. T2WI was used to exclude other brain diseases. The MPRAGE parameters were as follows: TR/TE, 10.33/6 ms; FOV, 212 × 212 mm; matrix size, 256 × 256 mm; intersection gap, 0 mm; section thickness, 1.1 mm; section number, 65. The T2WI parameters were the same as those for MPRAGE except for the following: TR/TE1/TE2, 3465/28.2/80.0 ms; section thickness, 1.5 mm.

Registration and Normalization

We used a single-subject template, the Johns Hopkins University–Montreal Neurological Institute template, which was normalized to Montreal Neurological Institute space.^{19,20} Each participant's MPRAGE and DTI (FA, trace) images were skull-stripped by using statistical parametric mapping followed by manual delineation and were normalized to the templates by using a 9-parameter linear algorithm²¹ and large deformation diffeomorphic metric mapping (LDDMM) (<http://www.birncommunity.org/tools-catalog/large-deformation-diffeomorphic-metric-mapping-lddmm/>).^{22,23} Using the deformation fields from LDDMM and the inverse linear matrix, we then warped our parcellation map (ie, Johns Hopkins University–Montreal Neurological Institute–based parcellation map) from the template to each subject's space. The details of the LDDMM operation are described elsewhere.^{20,24} All image transformation was achieved with the software DiffeoMap (<https://www.mristudio.org/>).

Creation of the Infratentorial Parcellation Map

We modified the Johns Hopkins University–Montreal Neurological Institute–based parcellation map in which the original left and right cerebellum were manually parcellated, and we divided the cerebellum into 12 subdivisions to create the infratentorial parcellation map as shown in Fig 1. The vermis was separated from the hemispheres by its elevated edge and was subdivided into the anterior and the posterior vermis by the primary fissure. The left and right hemispheres were subdivided into the anterior and posterior lobes by the primary fissure. The tonsils were separated from the hemispheres by the secondary fissure.

The flocculonodular lobes were separated from the hemispheres and the tonsils by the posterolateral fissure. The deep structures were separated on the basis of the T1-weighted contrast of the Johns Hopkins University–Montreal Neurological Institute atlas. These included the white matter and the 3 nuclei (dentate, interpositus, and fastigial) of the corpus medullare with the exclusion of the middle cerebellar peduncle (MCP). We divided the brain stem into 6 subdivisions; the midbrain, the pons, the medulla, the superior cerebellar peduncle (SCP), the MCP, and the inferior cerebellar peduncle (ICP) following the original Johns Hopkins University–Montreal Neurological Institute–based parcellation map. In total, the infratentorial parcellation map had 18 subdivisions.

Atlas-Based Analysis

We conducted an atlas-based analysis by using the infratentorial parcellation map. We measured the volume, MD, and FA of each

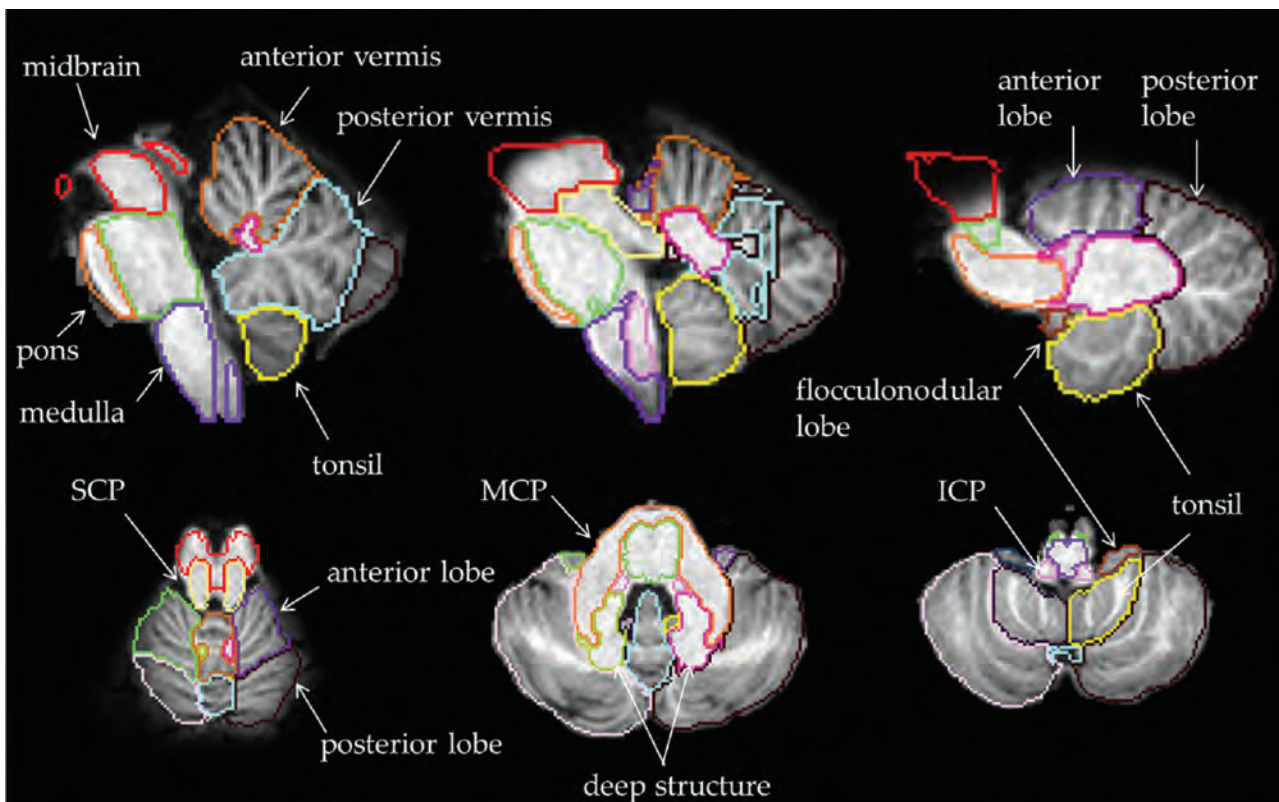


FIG 1. Infratentorial parcellation map. The cerebellum is divided into 12 subdivisions, and the brain stem, into 6 subdivisions.

subdivision and determined the correlation of each with the ICARS in each subdivision. Volume was evaluated as fractional volume (ie, the volume in each subdivision divided by the intracranial volume of each subject). We also calculated the percentage changes in the fractional volume, MD, and FA compared with controls by dividing each patient's data by the average of the controls' data in each subdivision.

CSF spaces were excluded by a signal-intensity threshold at 25 on MPRAGE images and by an MD threshold at $0.0023 \text{ mm}^2/\text{s}$ on DTI ($0.007 \text{ mm}^2/\text{s}$ on trace images). We investigated the correlation of fractional volume and MD in each subdivision to determine the partial volume effects of CSF due to atrophy on the results of MD.

Statistics

Statistical analyses were performed with the software SPSS, Version 13.0 (IBM, Armonk, New York). Comparisons of the patient and control groups were performed by using an independent-samples *t* test after confirming normal distribution of the data by Kolmogorov-Smirnov testing. The Mann-Whitney *U* test was used for the subdivisions in which the values were not normally distributed. Correlations between the data and the ICARS scores were assessed by using a Spearman correlation analysis. We conducted a multiple linear regression analysis with age effects as a covariant in the subdivisions in which the data were significantly correlated with age. A Bonferroni correction was adopted when the number of groups was <5 , and the false discovery rate correction was adopted when the number of groups was >5 .

RESULTS

Whole Brain and the ICARS

We first analyzed the data in 3 regions of the brain: the cerebrum, the cerebellum, and the brain stem. Among these, only the cerebellum showed a significant decrease in fractional volume and a significant increase in MD in the patients with SCA6 compared with the controls ($P < .0001$). The FA did not show any significant differences. The fractional volume in both the cerebellum and the brain stem showed significant correlations with the ICARS total score ($P < .05$, $r = -0.80, -0.77$). FA showed neither significant changes nor significant correlations.

Infratentorial Subdivisions and the ICARS

We next investigated changes of the data in the infratentorial subdivisions (Fig 2) and the correlations with the ICARS scores (Table). In the cerebellum, all subdivisions showed significant decreases of fractional volume ($P < .0001$ to $<.01$) and increases of MD ($P < .0001$ to $<.001$) in patients with SCA6 compared with controls. FA showed significant decreases only in the bilateral posterior lobes and the right tonsil ($P < .01$ to $<.05$). The strongest correlation with the ICARS total score was seen in the fractional volume in the right deep structure ($P < .01$, $r = -0.87$) and the MD in the left posterior lobe ($P < .01$, $r = 0.87$).

Among the ICARS subscores, the static and dysarthria scores showed significant correlations mainly in old regions, including the archicerebellum and the spinocerebellum ($P < .001$ to $<.05$, $r = -.92$ to 0.85). The limb score showed significant correlations mainly in the neocerebellum and the right deep structure ($P < .05$, $r = -0.74$ to 0.73). The strongest correlation with ICARS

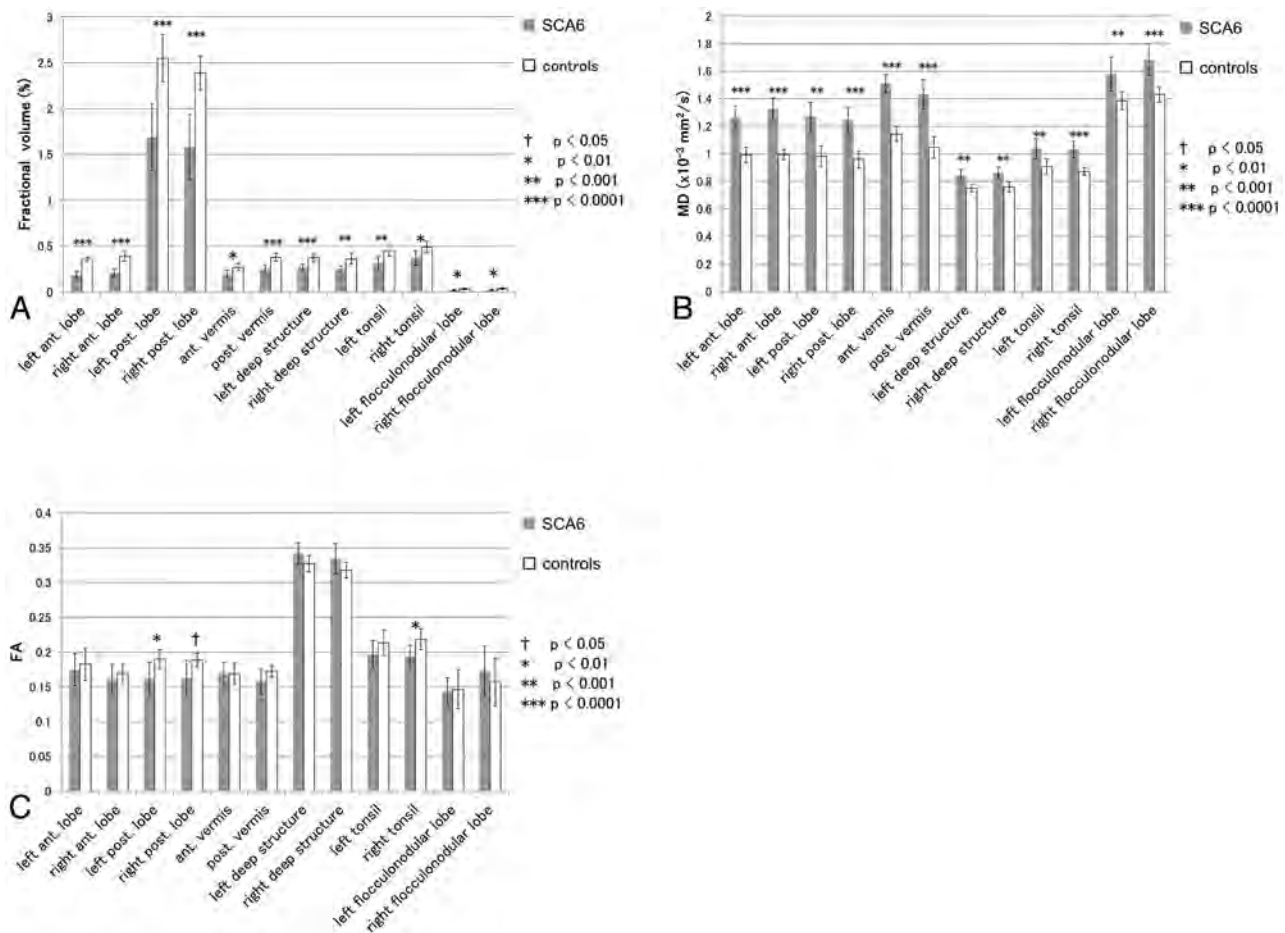


FIG 2. Comparison of the data in each cerebellar subdivision between patients with SCA6 and controls. Independent samples *t* tests were performed with false discovery rate correction applied to $P < .05$. Ant. indicates anterior; post., posterior.

Correlations between the data and ICARS scores in the infratentorial brain^a

SCA6	Fractional Volume (%)	MD ($\times 10^{-3}$ mm ² /s)	FA
Left anterior lobe	Static ^b ($r = -0.82$), Dysarthria ^c ($r = -0.73$)	NS	NS
Right anterior lobe	NS	NS	NS
Left posterior lobe	NS	Total ^d ($r = 0.87$), Dysarthria ^c ($r = 0.77$)	Limb ^c ($r = -0.73$)
Right posterior lobe	Static ^c ($r = -0.66$)	Total ^d ($r = 0.83$), Limb ^c ($r = 0.73$)	NS
Anterior vermis	NS	NS	NS
Posterior vermis	NS	NS	Limb ^c ($r = -0.73$)
Left deep structure	Total ^c ($r = -0.75$)	NS	NS
Right deep structure	Total ^d ($r = -0.87$), Limb ^c ($r = -0.74$)	NS	NS
Left tonsil	NS	NS	NS
Right tonsil	NS	Total ^c ($r = 0.73$), Static ^d ($r = 0.82$), Dysarthria ^d ($r = 0.85$)	NS
Left flocculonodular lobe	Static ^c ($r = -0.74$)	NS	NS
Right flocculonodular lobe	Total ^d ($r = -0.77$), Static ^d ($r = -0.92$), Dysarthria ^d ($r = -0.80$)	NS	NS
Midbrain	Total ^c ($r = -0.77$)	NS	NS
Pons	NS	NS	NS
Medulla	NS	NS	NS
SCP	Static ^c ($r = -0.71$)	NS	NS
MCP	NS	NS	NS
ICP	NS	NS	NS

Note:—NS indicates not significant.

^a ICARS scores that significantly correlated with the data are shown. “Static,” “Dysarthria,” and “Limb” are subscores of ICARS. A Spearman correlation analysis with false discovery rate correction applied to $P < .05$ was performed. A multiple linear regression analysis excluding age effects was performed in the subdivisions in which the data significantly correlated with age.

^b $P < .001$.

^c $P < .05$.

^d $P < .01$.

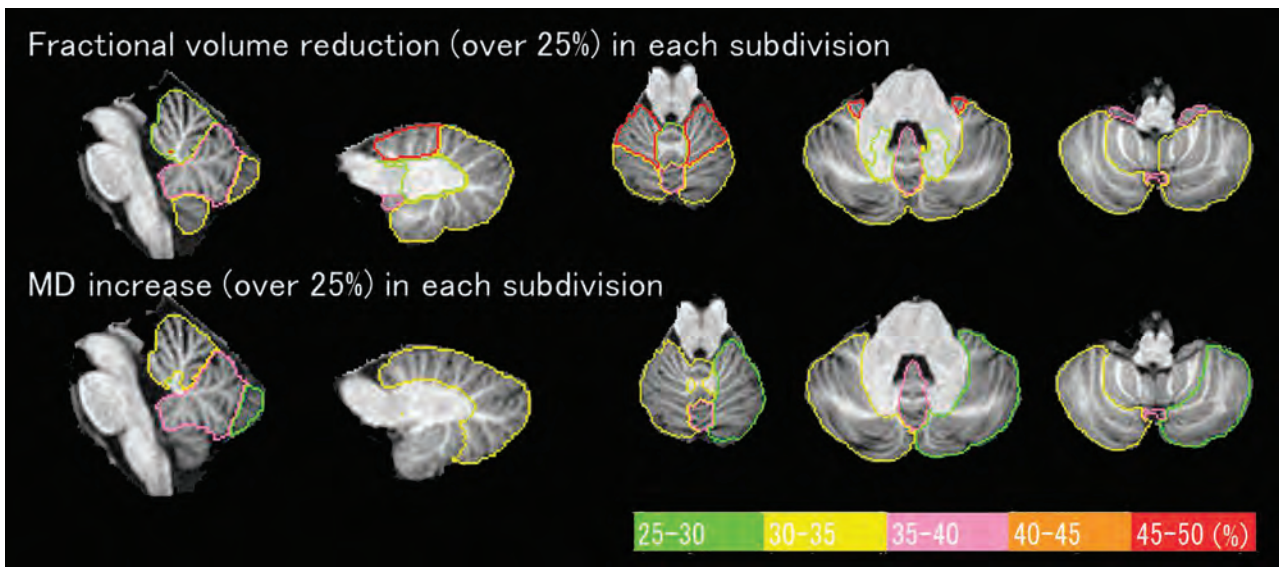


FIG 3. Percentage changes of fractional volume and MD in patients with SCA6 compared with controls (changes of >25% are shown). The degrees of percentage change are presented in different colors. The changes of FA are <25% and are not shown.

subscores was the static score and the fractional volume in the right flocculonodular lobe ($P < .01$, $r = -0.92$). FA showed a significant correlation only with the limb score in the left posterior lobe and in the posterior vermis ($P < .05$, $r = -0.73$). In the brain stem, the fractional volume was significantly decreased in all of the cerebellar peduncles ($P < .01$ to $<.05$). MD was significantly increased in the SCP and the MCP ($P < .0001$ to $<.05$). A significant increase of FA was seen in the MCP ($P < .05$). The ICARS total score was significantly correlated with the fractional volume in the midbrain ($P < .05$, $r = -0.77$), and the ICARS static score was significantly correlated with the SCP ($P < .05$, $r = -0.71$).

Percentage Changes of the Data

Percentage changes of the data in the patients with SCA6 compared with the controls are shown in Fig 3. This procedure clarified the difference in the results that depended on subdivisions by excluding the effects of the volume difference of each subdivision on the results of fractional volume.

Atrophy of the bilateral anterior lobes was the most prominent, followed by atrophy of the flocculonodular lobes and the posterior vermis. MD showed the largest increase in the posterior vermis. In terms of phylogenetic origins, atrophy was seen mainly in old regions, and increased MD was seen mainly in new regions. FA decreased or increased depending on the subdivisions, and these changes were <25%. The correlations between the percentage changes and ICARS scores were indistinguishable from the correlations between the raw data and ICARS scores.

Correlations between Fractional Volume and MD

To examine the partial volume effects, we investigated the correlations between the fractional volume and MD of each infratentorial subdivision. No significant correlation was seen except in the left posterior lobe in the controls ($P < .05$, $r = -0.74$).

DISCUSSION

The localization of cerebellar functions has been under debate for more than a century.²⁵ Although much of the cerebellar topography is still unmapped, it is known that phylogenetically, the cerebellum has 3 origins: the archicerebellum, the paleocerebellum, and the neocerebellum.^{8,9,12} The archicerebellum corresponds to the flocculonodular lobes and may include the tonsils as well. The archicerebellum is also referred to as the “vestibulocerebellum” because it is connected to the vestibular nuclei, which maintain equilibrium and eye-movement control. The paleocerebellum includes the vermis and the hemispheres near the midline or anterior region, and it is also called the “spinocerebellum” because of its spinal connections, which receive somatosensory information and control posture/gait and muscle tone. The neocerebellum is the lateral part of the hemispheres, with principally corticopontocerebellar connections. It is also called the “cerebrocerebellum” and is related to the planning of movements and speech.

The LDDMM used in this study enabled us to transform subject images to template images with high accuracy by using a single normalized subject (Johns Hopkins University–Montreal Neurological Institute template).^{20,22,23} With LDDMM, we analyzed the subjects’ brain images on the basis of anatomic units, and automated segmentation was possible on all subjects’ images (atlas-based analysis).^{24,26}

Our results confirmed the significant correlation of fractional volume in both the cerebellum and the brain stem with the symptoms of patients with SCA6 (Table). MD was recognized as another parameter to detect cerebellar degeneration. Although it has been reported that cerebral degeneration can occur in patients with SCA6,^{11,27} this finding was not demonstrated in our study.

Our detailed investigation of the cerebellum revealed a significant decrease of fractional volume and a significant increase of MD in all subdivisions in the cerebellum in the patients with SCA6 (Fig 2). Further analysis of the percentage changes excluded the effects of volume differences among the subdivisions, and in

turn, the atrophy of small subdivisions became apparent (Fig 3). This procedure excluded unknown factors that could affect the correlation between the ICARS scores and the data, as well as age. The fractional volume was decreased mainly in phylogenetically older regions of the cerebellum, including the archicerebellum and the paleocerebellum. The largest atrophy was seen in the bilateral anterior lobes of the paleocerebellum, followed by atrophy of the posterior vermis and the bilateral flocculonodular lobes. These new findings have not been made clear in previous studies. Pathologically, the most prominent degeneration was reported in the archicerebellum, and the resultant vertigo is a characteristic feature in patients with SCA6.¹¹

Contrary to fractional volume, a large increase of MD was seen mainly in new regions of the cerebellum, including the paleocerebellum and the neocerebellum (Fig 3). These regions include the cerebellar cortex. MD represents the degree of diffusion independent of the orientation of the tissue.^{28,29} The increase of MD in new regions may thus be related to degeneration of the cerebellar cortex, but the correct interpretation of the results has not yet been established. MD often increases due to partial volume effects—that is, the contamination of CSF.³⁰ However, we observed no significant correlation between fractional volume and MD in most subdivisions. In addition, the MD was increased in the deep structures in which partial volume effects should be absent or subtle. These findings suggest that MD reflects other phenomena, not only partial volume effects.

In the brain stem, all the cerebellar peduncles showed significant decreases of fractional volume. MD was significantly increased in the SCP and the MCP. FA was also increased in the MCP. The percentage changes were similar.

Several studies have investigated changes of volume in the brain stem,^{3,6} but they did not separate the cerebellar peduncles from the brain stem, or they investigated only the cerebellar peduncles by using manually placed regions of interest.¹⁵ The cerebellar peduncles are neural pathways connecting the cerebellum and the brain stem or the cerebrum, which in turn make the circuits in the cerebellum to control movement.^{8,9} DTI enabled us to separate the cerebellar peduncles from the brain stem, and it was revealed that the reported atrophy of the brain stem in patients with SCA6 may be due to atrophy of the cerebellar peduncles.

When Purkinje cells are damaged, inhibitory effects by their efferent fibers would be affected.³¹ This result explains the decrease of fractional volume and increased MD in the SCP in patients with SCA6 in the present study because the SCP is the main efferent pathway from the cerebellum. The cerebellar cortex receives afferent fibers mainly from the midbrain and the medulla via the MCP and the ICP. Afferent fibers might be also affected because atrophy or increased MD were seen in the MCP and the ICP.

A decrease in FA was seen only in limited subdivisions (Fig 2C). Increased FA was seen in the MCP. FA was increased in the brain stem and in the deep structures, too. In patients with SCA6, the main affected region is the cerebellar cortex.^{32,33} The utility of FA as a parameter is unclear without direct white matter damage, though subsequent white matter degeneration can occur. Takahashi et al³⁴ reported that folial white matter degeneration sec-

ondary to cortical degeneration was observed in patients with SCA6, but deep white matter was preserved. In general, it is difficult to detect the changes of FA in the cortex due to its isotropic feature.^{35,36}

The cerebellum has a complex network,⁸ which indicates that it has isotropic features. As a certain fiber in a subdivision in the cerebellum degenerates, FA in the subdivision can increase because of more unified fiber orientations. Changes of FA are likely to be subtle in chronic lesions compared with acute lesions due to the recovery of FA.^{37,38} These reasons might explain the unexpected changes of FA in our results.

Similar to the percentage changes, some ICARS scores were well-correlated with the fractional volume mainly in older regions and with MD mainly in newer regions (Table). Reflecting this tendency, the ICARS total score showed strong correlations in fractional volume in the bilateral deep structures and the right flocculonodular lobe and in MD in the bilateral posterior lobes ($r = 0.73$ to ± 0.87). Strong correlations in fractional volume in the bilateral deep structures are understandable because most infratentorial fibers pass through the corpus medullare. Atrophy of the deep structures has not been well-studied, but in the present study, it was nearly 30% compared with that in controls. Analogously, in the brain stem, the midbrain showed a significant correlation with the ICARS total score.

The ICARS static score showed significant correlations in the archicerebellum and paleocerebellum. The right flocculonodular lobe in particular showed a very strong correlation with fractional volume ($r = -0.92$). The flocculonodular lobes receive fibers from the vestibular nuclei and play an important role in balance.^{10,11} Our results were consistent with this feature. A correlation between the ICARS static score and fractional volume was also seen in the SCP. The SCP is the main path of the efferent fibers from the cerebellum, and our results confirmed its importance.

The ICARS limb score showed significant correlations in the neocerebellum and the right deep structure because both are related to limb function.⁹ It is known that the cerebellar nuclei in the deep structures are also related to limb movement.

The ICARS dysarthria score showed significant correlations in the archicerebellum and in the left cerebellar hemisphere. It is known that development of language in the brain is asymmetric and that lesions of the superior paravermal region are commonly associated with dysarthria,⁹ and our results are consistent with this description. The correlation that we observed between the dysarthria score and the archicerebellum is a new finding.

There were some limitations in this study. First, the number of subjects was small. SCA6 is rare, but studies of larger numbers of subjects would add credibility to the present findings. Characteristic site-specific degeneration patterns in patients with SCA6 could be useful for differential diagnoses, but comparisons with patients with multiple system atrophy, other types of SCA, or secondary ataxia are necessary.

CONCLUSIONS

We found characteristic macro- and microstructural changes depending on phylogenetic regions of the infratentorial brain that strongly correlated with clinical symptoms in patients with SCA6.

ACKNOWLEDGMENTS

We give special thanks to Shigeki Aoki for his assistance with the interpretation of the data.

Disclosures: Kanako Sato—*RELATED: Grant:* Japan Society for the Promotion of Science, *Comments:* My stay at Johns Hopkins University School of Medicine for this study was supported by the International Training program provided by Japan Society for the Promotion of Science; *UNRELATED: Payment for Manuscript Preparation:* University research institute for diseases of old age, Juntendo University, *Comments:* Assistance for writing the manuscript in English was supported. Sarah H. Ying—*RELATED: Grant:* National Institutes of Health*; *UNRELATED: Employment:* Johns Hopkins University; *Grants/Grants Pending:* National Institutes of Health.* Kenichi Oishi—*UNRELATED: Grants/Grants Pending:* National Institutes of Health/Eunice Kennedy Shriver National Institute of Child Health and Human Development (R01HD065955)* Michael I. Miller—*RELATED: Grant:* supported by standard grants from the National Institutes of Health; *Board Membership:* AnatomyWorks, *Comments:* Susumu Mori is the president; I hold equity in this company. Susumu Mori—*RELATED: Grant:* National Institutes of Health,* *Comments:* ROIAG020012, R01NS084957, P41EB015909; *UNRELATED: Patents (planned, pending or issued):* There are issued and pending patents that are not related to the presented work*; *Other:* CEO of AnatomyWorks, a startup company. *Money paid to the institution.

REFERENCES

1. Taroni F, DiDonato S. Pathways to motor incoordination: the inherited ataxias. *Nat Rev Neurosci* 2004;5:641–55
2. Nagaoka U, Suzuki Y, Kawanami, T, et al. Regional differences in genetic subgroup frequency in hereditary cerebellar ataxia, and a morphometrical study of brain MR images in SCA1, MJD and SCA6. *J Neurol Sci* 1999;164:187–94
3. Eichler L, Bellenberg B, Hahn HK, et al. Quantitative assessment of brain stem and cerebellar atrophy in spinocerebellar ataxia types 3 and 6: impact on clinical status. *AJNR Am J Neuroradiol* 2011;32:890–97
4. Jacobi H, Hauser TK, Giunti P, et al. Spinocerebellar ataxia types 1, 2, 3 and 6: the clinical spectrum of ataxia and morphometric brain-stem and cerebellar findings. *Cerebellum* 2012;11:155–66
5. Yagishita A. *Imaging Diagnosis of Neurological Diseases* [in Japanese]. Tokyo, Japan: Shujunsysa; 2011:42
6. Schulz JB, Borkert J, Wolf S, et al. Visualization, quantification and correlation of brain atrophy with clinical symptoms in spinocerebellar ataxia types 1, 3 and 6. *Neuroimage* 2010;49:158–68
7. Jung BC, Choi SI, Du AX, et al. Principal component analysis of high resolution MRI defines disease-specific mode of cerebellar neurodegeneration in SCA types 2 and 6. *Cerebellum* 2012;11:887–95
8. Eccles JC. Circuits in the cerebellar control of movement. *Proc Natl Acad Sci U S A* 1967;58:336–43
9. Grimaldi G, Manto M. Topography of cerebellar deficits in humans. *Cerebellum* 2012;11:336–51
10. Fulton JF, Dow RS. The cerebellum: a summary of functional localization. *Yale J Biol Med* 1937;10:89–119
11. Wang X, Wang H, Xia Y, et al. Spinocerebellar ataxia type 6: systematic patho-anatomical study reveals different phylogenetically defined regions of the cerebellum and neural pathways undergo different evolutions of the degenerative process. *Neuropathology* 2010;30:501–14
12. Dietrichs E. Clinical manifestation of focal cerebellar disease as related to the organization of neural pathways. *Acta Neurol Scand* 2008;117:6–11
13. Mandelli ML, De Simone T, Minati L, et al. Diffusion tensor imaging of spinocerebellar ataxias types 1 and 2. *AJNR Am J Neuroradiol* 2007;28:1996–2000
14. Prakash N, Hageman N, Hua X, et al. Patterns of fractional anisotropy changes in white matter of cerebellar peduncles distinguish spinocerebellar ataxia-1 from multiple system atrophy and other ataxia syndromes. *Neuroimage* 2009;47(suppl 2):T72–81
15. Ying SH, Landman BA, Chowdhury S, et al. Orthogonal diffusion-weighted MRI measures distinguish region-specific degeneration in cerebellar ataxia subtypes. *J Neurol* 2009;256:1939–42
16. Du AX, Cuzzocreo JL, Landman BA, et al. Diffusion tensor imaging reveals disease-specific deep cerebellar nuclear changes in cerebellar degeneration. *J Neurol* 2010;257:1406–08
17. Trouillas P, Takayanagi T, Hallett M, et al. International Cooperative Ataxia Rating Scale for pharmacological assessment of the cerebellar syndrome: the Ataxia Neuropharmacology Committee of the World Federation of Neurology. *J Neurol Sci* 1997;145:205–11
18. Jones DK, Horsfield MA, Simmons A. Optimal strategies for measuring diffusion in anisotropic systems by magnetic resonance imaging. *Magn Reson Med* 1999;42:515–25
19. Mori S, Oishi K, Jiang H, et al. Stereotaxic white matter atlas based on diffusion tensor imaging in an ICBM template. *Neuroimage* 2008;40:570–82
20. Oishi K. Atlas-based whole brain analysis using large deformation diffeomorphic metric mapping: application to normal elderly and Alzheimer's disease participants. *Neuroimage* 2009;46:486–99
21. Woods RP, Grafton ST, Watson JD, et al. Automated image registration. II. Intersubject validation of linear and nonlinear models. *J Comput Assist Tomogr* 1998;22:153–65
22. Beg MF, Miller MI, Troune A, et al. Computing large deformation metric mappings via geodesic flows of diffeomorphisms. *Int J Comput Vis* 2005;61:139–57
23. Miller MI, Troune A, Younes L. On the metrics and Euler-Lagrange equations of computational anatomy. *Annu Rev Biomed Eng* 2002;4:375–405
24. Miller MI, Beg MF, Ceritoglu C, et al. Increasing the power of functional maps of the medial temporal lobe by using large deformation diffeomorphic metric mapping. *Proc Natl Acad Sci U S A* 2005;102:9685–90
25. Buckner RL, Krienen FM, Castellanos A, et al. The organization of the human cerebellum estimated by intrinsic functional connectivity. *J Neurophysiol* 2011;106:2322–45
26. Faria AV, Zhang J, Oishi K, et al. Atlas-based analysis of neurodevelopment from infancy to adulthood using diffusion tensor imaging and applications for automated abnormality detection. *Neuroimage* 2010;52:415–28
27. Seidel K, Siswanto S, Brunt ER, et al. Brain pathology of spinocerebellar ataxias. *Acta Neuropathol* 2012;124:1–21
28. Bassar PJ, Jones DK. Diffusion-tensor MRI: theory, experimental design and data analysis—a technical review. *NMR Biomed* 2002;15:456–67
29. Le Bihan D, Turner R, Douek P, et al. Diffusion MR imaging: clinical applications. *AJR Am J Roentgenol* 1992;159:591–99
30. Kang XJ, Herron TJ, Turken U, et al. Diffusion properties of cortical and pericortical tissue: regional variations, reliability and methodological issues. *Magn Reson Imaging* 2012;30:1111–22
31. Iwata NK, Ugawa Y. The effects of cerebellar stimulation on the motor cortical excitability in neurological disorders: a review. *Cerebellum* 2005;4:218–23
32. Sasaki H, Kojima H, Yabe I, et al. Neuropathological and molecular studies of spinocerebellar ataxia type 6 (SCA6). *Acta Neuropathol* 1998;95:199–204
33. Yang Q, Hashizume Y, Yoshida M, et al. Morphological Purkinje cell changes in spinocerebellar ataxia type 6. *Acta Neuropathol* 2000;100:371–76
34. Takahashi H, Ikeuchi T, Honma Y, et al. Autosomal dominant cerebellar ataxia (SCA6): clinical, genetic and neuropathological study in a family. *Acta Neuropathol* 1998;95:333–37
35. Le Bihan D, van Zijl P. From the diffusion coefficient to the diffusion tensor. *NMR Biomed* 2002;15:431–34
36. Mori S, Zhang J. Principles of diffusion tensor imaging and its applications to basic neuroscience research. *Neuron* 2006;51:527–39
37. Tievsky AL, Ptak T, Farkas J. Investigation of apparent diffusion coefficient and diffusion tensor anisotropy in acute and chronic multiple sclerosis lesions. *AJNR Am J Neuroradiol* 1999;20:1491–99
38. Takagi T, Nakamura M, Yamada M, et al. Visualization of peripheral nerve degeneration and regeneration: monitoring with diffusion tensor tractography. *Neuroimage* 2009;44:884–92

3T MRI Reveals Extra- and Intracranial Involvement in Giant Cell Arteritis

S. Siemonsen, C. Brekenfeld, B. Holst, A.-K. Kaufmann-Buehler, J. Fiehler, and T.A. Bley



ABSTRACT

BACKGROUND AND PURPOSE: The frequency and amount of intracranial, intradural inflammatory vessel wall enhancement in giant cell arteritis remain unclear. The purpose of this work was to prospectively assess the intracranial extent of vasculitic changes in patients with giant cell arteritis using a dedicated MR imaging protocol optimized for assessment of mural changes of intracranial arteries.

MATERIALS AND METHODS: Twenty-eight patients with suspected giant cell arteritis underwent 3T MR imaging. Imaging included a fat-saturated T1WI pre- and postcontrast application optimized for assessment of intradural vessel wall enhancement and high-resolution fat-saturated T1WI to evaluate superficial extracranial vessels. Temporal artery biopsies were available in 11 cases. Vessel wall enhancement of intradural and extracranial vessels was evaluated by 2 observers independently.

RESULTS: Twenty patients had giant cell arteritis; 9 cases were biopsy-proved. Clear vessel wall enhancement of superficial extracranial and intradural internal carotid arteries was detected in 16 and 10 patients, respectively. Slight vessel wall enhancement of the vertebral arteries was seen. Of 9 patients with giant cell arteritis with vessel occlusion or stenosis, 2 presented with cerebral ischemic infarcts. Vessel occlusion or stenosis site coincided with the location of vessel wall enhancement of the vertebral arteries in 4 patients and of the intradural ICA in 1 patient.

CONCLUSIONS: Vessel wall enhancement of intradural arteries, mainly the ICA, can be regularly found in patients with giant cell arteritis. Mural inflammatory changes of the intradural ICA detected on MR imaging may identify a subgroup of patients with giant cell arteritis and should be further evaluated in clinical studies.

ABBREVIATIONS: fsT1WI = fat-saturated T1WI; GCA = giant cell arteritis; TAB = temporal artery biopsy; VWE = vessel wall enhancement

Giant cell arteritis (GCA) commonly affects large- and medium-sized arteries with predominance in the aorta and the supra-aortic vessels such as the subclavian, carotid, and axillary arteries and the superficial cranial arteries, among others.^{1,2} Recent imaging studies have shown inflammatory involvement of the aorta in up to 65% and of the subclavian arteries in up to 35% of patients.^{3,4}

The extent of vasculitic changes to the intracranial vasculature

is discussed controversially and is currently not fully understood. Not a single intracranial artery was involved in a postmortem study of patients who died during the phase of active GCA when the extracranial superficial temporal and ophthalmic arteries were severely inflamed. The different composition of the intracranial arteries with less elastic tissue in the media compared with the extracranial arteries may correlate with the inflammatory activity in GCA.⁵ However, a more recent article indicated that intracranial involvement in GCA does occur, presumably less frequently.⁶

High-resolution MR imaging studies have been proved to reliably detect mural inflammation such as mural thickening and increased mural contrast enhancement of the superficial temporal and occipital arteries in biopsy-proved GCA.^{7,8} Diagnostic criteria for detecting intracranial vasculitis are intramural contrast uptake, in most cases combined with wall thickening.⁹ These criteria are valid for patients presenting with primary angiitis of the central nervous system, childhood primary angiitis of the central nervous system or GCA, and other causes of central nervous system vasculitis.¹⁰

Received May 12, 2014; accepted after revision July 13.

From the Department of Diagnostic and Interventional Neuroradiology (S.S., T.A.B.), University Medical Center Hamburg-Eppendorf, Hamburg, Germany; and Department of Diagnostic and Interventional Radiology (C.B., B.H., A.-K.K.-B., J.F.), University Hospital of Würzburg, Würzburg, Germany.

This work was supported by Deutsche Forschungsgemeinschaft, DFG: BL 1132/1-1.

Please address correspondence to Susanne Siemonsen, MD, Department of Diagnostic and Interventional Neuroradiology, University Medical Center Hamburg-Eppendorf, Martinistr 52, 20246 Hamburg, Germany; e-mail: s.siemonsen@uke.uni-hamburg.de

Indicates open access to non-subscribers at www.ajnr.org

<http://dx.doi.org/10.3174/ajnr.A4086>

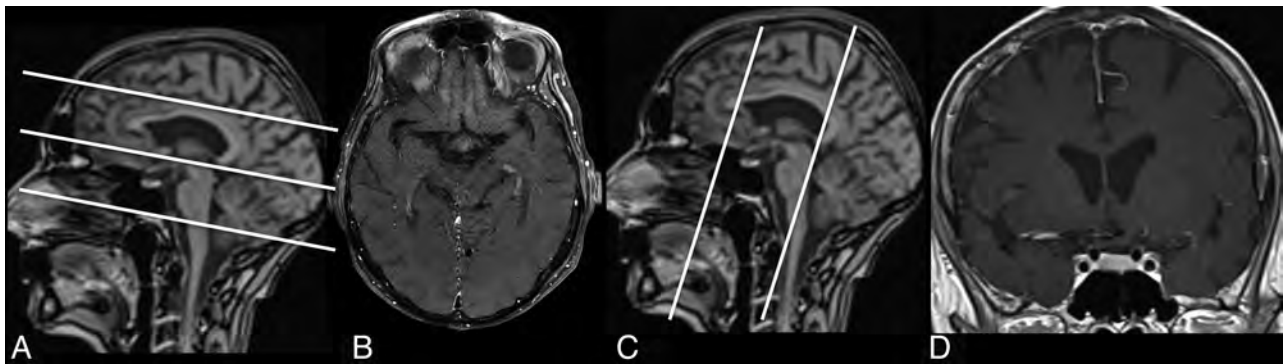


FIG 1. Fat-saturated T1WI scans post-contrast medium application and corresponding scouts optimized for assessment of intradural VWE (C and D), and high-resolution fsT1WI scans to evaluate superficial extracranial vessels (A and B).

A retrospective analysis of high-resolution MR imaging of the superficial cranial arteries of 50 patients with GCA did not reveal any inflammatory mural changes of the intracranial arteries of the circle of Willis.¹¹ However, the MR imaging protocol in that particular study was optimized to depict mural inflammation of the superficial cranial arteries and was not specifically adjusted for visualization of the intradural arteries. The purpose of this work was to prospectively assess the intracranial extent of vasculitic changes in patients with GCA using a dedicated MR imaging protocol optimized for assessment of mural changes of intracranial arteries.

MATERIALS AND METHODS

Patients

Twenty-eight consecutive patients (21 women, 7 men; 62–91 years of age; mean, 74 years) with clinically suspected GCA were referred to our institution between 2012 and 2013 and were prospectively included in our study. The study was approved by the local ethics review committee and is in accordance with the Declaration of Helsinki. Written informed consent was obtained from all subjects. Patients were referred for MR imaging by rheumatologists, ophthalmologists, and neurologists experienced in diagnosing and treating patients with GCA. All patients underwent an MR imaging examination of the brain, including dedicated sequences optimized for assessment of mural changes of the extracranial and intracranial arterial vessel walls.

Temporal artery biopsy (TAB) was performed in 11 of the 28 patients. Biopsy specimens were obtained from the frontal branch of the superficial temporal artery that was clinically most prominently affected. MR imaging was performed before TAB in all except 1 patient. Twenty patients were found to be positive for GCA (GCA-positive) according to the clinician's final diagnosis. In 11 of these patients positive for GCA, diagnosis was validated only by fulfillment of the American College of Rheumatology clinical criteria for GCA,¹² and in 9, by positive histopathologic findings of multinucleated giant cells or mononuclear cells infiltrating the wall of the frontal branch of the superficial temporal artery. In 1 patient positive for GCA, histology yielded false-negative results.

Five patients were found negative for GCA (GCA-negative) according to the clinician's final diagnosis. In 3 patients, the definite diagnosis remained unclear; these patients were excluded from further analysis.

Of the 20 patients positive for GCA, 18 began corticosteroid treatment 1–8 days (median, 3.5 days) before MR imaging, while 2 had not received any corticosteroid treatment.

C-reactive protein level and erythrocyte sedimentation rate were available at admission in all 20 and 19 patients positive for GCA, respectively. C-reactive protein level was available in all patients negative for GCA; erythrocyte sedimentation rate, in 4 of 5 patients. In 1 patient, the exact erythrocyte sedimentation rate was not documented, but a clear elevation was noted.

MR Imaging Examination and Protocol

All MR imaging was performed on a 3T system (Magnetom Skyra; Siemens, Erlangen, Germany) with a 20-channel head coil. The MR imaging protocol included diffusion-weighted imaging; TOF angiography; fluid-attenuated inversion recovery; fat-saturated T1WI (fsT1WI) scans before and after gadolinium administration, optimized for the assessment of intradural vessel wall enhancement (VWE); and high-resolution fsT1WI scans to evaluate mural changes of superficial extracranial vessels. In 16 patients, contrast-enhanced MR angiography of the cervical arteries was performed. All patients received 16 mL of a gadolinium-based contrast agent (gadopentetate dimeglumine, 0.5 mmol/mL, Mag-nograp; Marotrust, Jena, Germany).

For DWI, a single-shot, spin-echo, echo-planar imaging sequence was used, and images were collected with $b=0$ and 1000 s/mm^2 . TOF angiography was performed by using 3D fast imaging with a steady-state precession sequence with venous saturation, a magnetization transfer saturation pulse, and a tilted optimized nonsaturation excitation-up pulse. Coronal oriented multisection fsT1WI spin-echo sequences were acquired before and 3 minutes after venous injection of a gadolinium-based contrast agent. The image localizer was positioned perpendicular to the orientation of the vessel. Postcontrast, multisection fsT1WI spin-echo images were acquired with an in-plane resolution of 0.2×0.2 mm. Two consecutive acquisitions were performed covering 10.8 cm in a craniocaudal direction with the lowest section leveling with the earlobes (Fig 1). Details on sequence parameters are shown in Table 1.

MR Imaging Evaluation

The extracranial vessels (ie, the frontal and parietal branches of the superficial temporal and the occipital arteries) were evaluated by 2 experienced neuro-/radiologists (S.S. and T.A.B.) on fsT1WI

Table 1: MRI sequence parameters

Sequence	TE (ms)	TR (ms)	TI (ms)	FOV (mm)	Matrix	Sections	Section			
							Thickness (mm)	Flip Angle	Orientation	Gap
FLAIR	90	9000	2500	230	270 × 320	25	5		Axial	10%
DWI	90	7900		230	256 × 256	25	5		Axial	10%
TOF	3.43	21		200	384 × 331	136	5	18°	Axial	
fsTIWI pre- and post-GD	11	549		200	320 × 320	20	2	150°	Coronal	
2 × fsTIWI post-GD	22	500		200	1024 × 768	18	3		Axial	

Note:—GD indicates gadolinium injection.

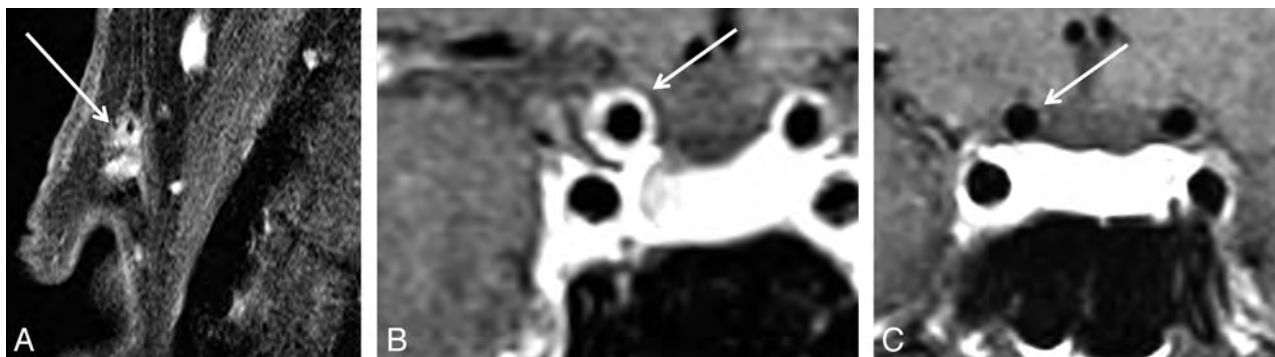


FIG 2. A patient with GCA with vessel wall enhancement of extracranial (A) and intracranial intradural internal carotid arteries (B). In contrast, patient with GCA without VWE of intracranial intradural arteries (C).

high-resolution MR images. Both readers were blinded to the clinical, biopsy, and laboratory findings. As previously proposed, mural thickening and prominent contrast enhancement of the vessel wall were considered signs of mural inflammation.⁷ MRI signs of extracranial vessel wall inflammation and thickening were documented by each rater separately for all 3 locations bilaterally. In case of differing results, a consensus rating was established. Depending on the consensus, we dichotomized patients in the following manner: Patients with signs of inflammation of any of the evaluated branches of the superficial temporal artery or occipital artery were grouped into MR-GCA-positive, and patients with negative ratings, into MR-GCA-negative.

Intradural vessels of patients were evaluated on fsTIWI before and after contrast agent administration independently for signs of vessel wall enhancement and/or thickening indicating mural inflammation by 2 experienced neuroradiologists (S.S. and C.B.) who were blinded to the patient's clinical information and diagnosis during the rating. The wall of the internal carotid artery was rated as positive contrast-enhancing (MR-ICA-positive) in cases where a circular enhancement was clearly visible distant from the cavernous sinus (ie, at least 2 sections distant from the last section including a part of the cavernous ICA; Fig 2). Otherwise patients were rated as MR-ICA-negative. The vertebral arteries were evaluated at least 0.5 cm distant from entering the spinal canal, close to the confluents to avoid misjudging the accompanying venous vessels at the site of dural penetration. Similarly, the anterior cerebral artery, posterior cerebral artery, and middle cerebral artery were evaluated for VWE. Any sign of clear enhancement in comparison with corresponding native scans was rated as positive. In case of differing results, a consensus rating was established by a third experienced neuroradiologist (B.H.).

The V4 segment of the vertebral artery was not assessable in 6 patients due to positioning of the localizer but was included in the analysis in all other cases. Similarly, the basilar artery was prone to

pulsation artifacts and was not assessable in 3 patients. In addition, cerebral MR images and angiographies were evaluated by 1 experienced neuroradiologist (S.S.) for acute ischemic infarction visible on DWI, signs of previous infarction, or other pathologies on FLAIR images. TOF angiography of intracranial vessels and contrast-enhanced angiography of cervical vessels if available were evaluated for stenosis or vessel occlusion. These ratings were performed independent from intracranial and extracranial ratings, and evaluators were blinded to the results of ratings of extra- or intracranial VWE.

Statistical Analysis

The interobserver agreement for extracranial and intracranial vessel involvement was evaluated with the Cohen κ test and magnitude guidelines applied according to Landis and Koch.¹³ The median values and SD for age, C-reactive protein level, and erythrocyte sedimentation rate were calculated for the patient groups (GCA-positive and GCA-negative). The diagnosis of GCA by MR imaging was compared with the clinical diagnosis. In addition, association of extracranial and intracranial mural inflammation with the GCA diagnosis was evaluated by using the χ^2 test. The sensitivity, specificity, and positive and negative predictive values were calculated and reported with corresponding confidence intervals and *P* values (Fisher exact test). Statistical analysis was conducted by using R statistical computing software, Version 3.0.0 (<http://www.r-project.org/>).

RESULTS

Clinical Findings of Patients

The mean \pm SD level of C-reactive protein at admission was 80.5 ± 71.6 mg/dL in patients positive for GCA and 36.6 ± 65.7 mg/dL in patients negative for GCA. The mean \pm SD erythrocyte sedimentation rate at admission, if available, was 70.58 ± 31.57 mm/h in patients positive for GCA and 45.50 ± 38.79 mm/h in

Table 2: Patient details on clinical and MRI findings

Patient No.	Age (yr)	Sex	GCA-Diagnosis	MR-GCA	MR-ICA	TAB	Initial Presentation to MRI (days)	ROIDS to MRI (days)
1	77	F	Positive	Positive	R+L	Positive	3	2
2	72	M	Positive	Positive	R+L	Positive	2	1
3	81	F	Positive	Negative	Negative	NA	2	2
4	74	M	Positive	Positive	L	NA	5	4
5	71	F	Positive	Positive	R+L	Positive	8	8
6	70	F	Positive	Positive	L	NA	4	4
7	66	F	Positive	Positive	Negative	Positive	1	1
8	75	F	Positive	Positive	L	NA	2	2
9	71	M	Positive	Negative	Negative	NA	6	5
10	73	F	Positive	Negative	Negative	Positive	1	1
11	91	M	Positive	Positive	Negative	NA	6	6
12	72	F	Negative	Negative	Negative	NA	4	0
13	73	M	Positive	Positive	R+L	Positive	2	0
14	78	F	Negative	Negative	Negative	Negative	1	1
15	63	F	Positive	Positive	Negative	NA	2	0
16	86	F	Positive	Positive	Negative	Positive	4	4
17	64	M	Positive	Positive	Negative	NA	4	3
18	68	M	Positive	Positive	L	Positive	3	3
19	75	F	Positive	Positive	R+L	NA	2	1
20	62	F	Positive	Positive	L	NA	7	7
21	70	F	Negative	Negative	Negative	NA	4	NA
22	83	F	Negative	Negative	Negative	NA	9	NA
23	87	F	Positive	Negative	Negative	Negative	8	8
24	78	F	Positive	Positive	Negative	Positive	4	4
25	79	F	Negative	Positive	Negative	NA	6	1

Note:—R indicates right; L, left; ROIDS, corticosteroids; NA, not applicable.

patients negative for GCA. There was no significant difference between the groups ($P > .05$). On admission, 3 of the patients positive for GCA presented with temporal artery tenderness to palpation; 4, with visual impairment and new headache; 7, with temporal artery tenderness to palpation in combination with visual impairment; 3, with recent weight loss and new headache; and 3, with new headache and weight loss in combination with dizziness and gait abnormalities.

Evaluation of Extracranial Arteries

The MR images had good diagnostic quality in 25 cases; only 1 patient terminated the scan before the second slab of the fsT1WI for evaluation of extracranial vessels was finished; therefore, in this patient, only the lower slab was available for evaluation. In 1 case, assessment of the extracranial arteries was slightly impaired due to motion artifacts. Nevertheless, the superficial occipital artery, the frontal branch of the superficial temporal artery, and the parietal branch of the superficial temporal artery could be clearly depicted in all scans.

In 1 patient (patient 23) with false-negative biopsy results, the biopsy specimen was extracted from the left temporal artery 5 days before MR imaging, and this sample was found to be negative for GCA. The diagnosis of GCA in this patient was validated by the American College of Rheumatology clinical criteria. MR imaging also revealed no signs of mural inflammation, only slight diffuse contrast enhancement adjacent to the left temporal artery where the sample was harvested, consistent with granulation tissue. Nevertheless, in this patient, treatment with corticosteroids was initiated 3 days before biopsy and 8 days before MR imaging.

The Cohen κ for interrater reliability for assessment of MR-GCA-positive and MR-GCA-negative was almost perfect with

0.905 ($P < .001$). Nevertheless, κ values for ratings of 1-sided or bilateral involvement of the frontal branches of the superficial temporal artery were substantial at 0.662 ($P < .01$); for the parietal branches, moderate at 0.51 ($P < .01$); and for involvement of the occipital artery, moderate at 0.603 ($P < .01$).

Among the 150 extracranial arteries examined, 85 (56.7%) were considered inflamed and 65 (43.3%), to be unaffected.

Of the 20 patients positive for GCA, 16 were rated as MR-GCA-positive, while 4 were rated MR-GCA-negative and were therefore false-negatives. Three of these patients negative for MR-GCA did not show any clear VWE in any of the evaluated arteries. One of the patients positive for GCA showed solitary VWE of only the frontal branch of the left superficial temporal artery. In all other patients MR-GCA-positive, at least 2 extracranial arteries were involved. Bilateral involvement was found in all true-positive cases. One patient negative for GCA was rated as MR-GCA-positive and therefore false-positive. The frontal branches of the superficial temporal artery were involved in 16 of 20 patients positive for GCA; the parietal branches, in 11; and the occipital artery, in 13, respectively. Details for each patient are presented in Table 2.

Sensitivity and specificity of MR-GCA ratings for the detection of GCA diagnosis were 0.80 (95% CI, 0.56–0.94) and 0.80 (95% CI, 0.28–0.99), respectively. The positive predictive value was 0.94 (95% CI, 0.71–0.99), and the negative predictive value was 0.50 (95% CI, 0.15–0.84) with $P < .05$.

Patients with false-negative findings (patients 3, 9, 10, and 23) were treated with corticosteroids between 1 and 8 days (mean, 4 days) before MR imaging.

In the subgroup of the 9 patients with biopsy-proved GCA, 8 were MR-GCA-positive and 1 was rated MR-GCA-negative. In

the subgroup of patients with a clinical diagnosis of GCA, 8 patients were rated as MR-GCA-positive, while 3 were rated as MR-GCA-negative.

Evaluation of Intradural Arteries

The Cohen κ for evaluation of intradural ICA VWE was almost perfect with 0.839. Bilateral enhancement was detected in 5 of 25 patients, and unilateral enhancement, in 5 patients, whereas in 15 patients, there was no enhancement (MR-ICA-negative). Therefore 10 patients displayed signs of uni- or bilateral VWE of the intradural ICA (MR-ICA-positive). In 9 of these patients, VWE was accompanied by vessel wall thickening. Of the 10 patients positive for MR-ICA, all were positive for GCA. Of the 15 patients negative for MR-ICA, 5 were negative for GCA and 10 were positive for GCA. There was no significant difference in C-reactive protein and erythrocyte sedimentation rate between the 2 groups ($P > .05$).

Sensitivity and specificity of MR-ICA ratings for the prediction of GCA diagnosis were 0.50 (95% CI, 0.25–0.70) and 0.99 (95% CI, 0.40–0.99), respectively. The positive predictive value was 0.99 (95% CI, 0.63–0.99), and the negative predictive value was 0.34 (95% CI, 0.11–0.59) with $P > .05$.

There was a significant association of MR-GCA-positive and MR-ICA-positive findings ($P < .05$) when including all 25 pa-

tients. Within the patients positive for GCA, there was no significant association between MR-GCA-positive and MR-ICA-positive findings (Table 3).

In the subgroup of the 9 patients with biopsy-proved GCA, 5 were MR-ICA-positive and 4 were MR-GCA-negative. In the subgroup of patients with a clinical diagnosis of GCA, 5 patients were rated as MR-ICA-positive, while 6 were rated as MR-GCA-negative.

In addition, 5 patients presented with bilateral VWE of the vertebral arteries (all GCA-positive); 4, with VWE of the left (3 of 4 GCA-positive) vertebral arteries, adding to 8 venous vessels at the site of dural penetration ratings (7 positive for GCA, 1 negative for GCA). Therefore, 11 cases were rated as MR-vertebral artery-negative (3 negative for GCA, 8 positive for GCA). VWE of the basilar artery was detected in none of our patients. One GCA-positive patient displayed VWE of the left M1 segment (MR-MCA-positive).

Vessel Stenosis or Occlusion

In total, 13 patients did not present with any site of vessel occlusion or stenosis (2 GCA-negative and 11 GCA-positive). Of the remaining 12 patients, 9 were positive for GCA and 3, negative for GCA. Of these, 6 patients showed V4 stenosis (3 right, 1 left, 2 bilateral), while 2 patients presented with V4 occlusion. ICA siphon stenosis was observed in 4 (1 right, 1 left, 2 bilateral); right ICA occlusion, in 1 patient. Vessel occlusion or stenosis site coincided with the VWE location of the vertebral arteries in 4 (Fig 3) and of the intradural ICA in 1 patient, with right intracavernous ICA occlusion sparing the distal carotid-T.

Brain Parenchymal Findings

Of the 25 included patients, 2 presented with pathologic brain parenchymal findings on MR imaging. Both patients were GCA-

Table 3: Ratings of extra- and intracranial vessel wall inflammation and grouping according to GCA diagnosis

	MR-ICA-Positive	MR-ICA-Negative	Total
GCA-Positive			20
MR-GCA-Positive	10	6	16
MR-GCA-Negative	0	4	4
GCA-Negative			5
MR-GCA-Positive	1	0	1
MR-GCA-Negative	0	4	4

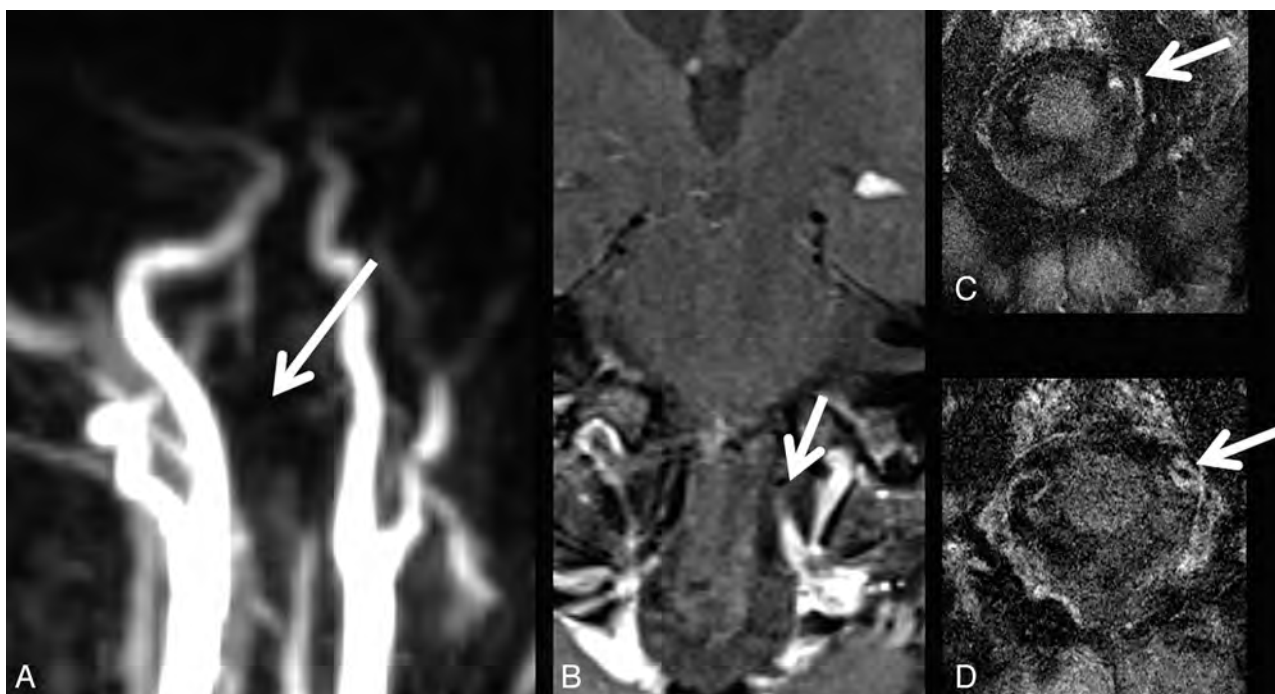


FIG 3. A patient with GCA with occlusion of the left vertebral artery (A) and corresponding vessel wall enhancement (B–D).

positive. One patient (patient 5) presented with subacute ischemic infarcts of the cerebellum and the right head of the caudate nucleus and cortical watershed infarction caused by right ICA occlusion. Another patient presented with a history of cerebellar ischemic infarction combined with right V4 segment occlusion and left V3/V4 stenosis. Additionally, 11 patients had imaging signs indicative of degenerative cerebral microangiopathy.

DISCUSSION

In our study, most patients positive for GCA were characterized through clear signs of mural inflammation of at least 2 affected extracranial arteries. These observations are in line with previous studies reporting mural inflammation of the temporal artery in patients with GCA depicted by high-resolution MR imaging.^{8,14-16} Even patients who received corticosteroids for >2 days before MR imaging displayed signs of mural inflammation. A sensitivity of 0.80 and a specificity of 0.80 for the detection of GCA by using this imaging protocol were comparable with recent studies with reported values of sensitivities between 0.80% and 0.85% and specificities ranging from 0.71% to 0.95%.^{7,17} This result might be accounted for by the differing number of days that patients received corticosteroids before MR imaging examination.

Irrespective of extracranial VWE, we observed clear VWE of the intradural ICA in at least 50% of patients positive for GCA, while none of the patients negative for GCA presented with this finding. Additionally, signs of mural inflammation of the vertebral arteries were observed in 4 patients positive for GCA and of the proximal MCA in 1 patient. Involvement of intracranial and intradural arteries has so far been reported by only a small number of case reports.¹⁸⁻²⁰ A review of several published GCA cases with intracranial and intradural involvement concluded that these might only represent a subset of patients with GCA and they seem to occur rarely. Likewise, cerebral infarcts have been reported in only 3%–4% of patients with GCA.^{21,22} In comparison, we observed pathologic brain parenchymal findings with a higher incidence (15%), a rate similar to that in another study reporting an incidence of 14.3%. Nevertheless ischemic infarcts still seem to be a rare finding in GCA. Several studies suggest that ischemic infarctions in cases of GCA are caused by stenosis or occlusion mainly of extradural vertebral and carotid arteries rather than intracranial or intradural vasculitis.^{5,23-28}

Accordingly, in our study, VWE of the brain-supplying arteries coincided more frequently with corresponding arterial occlusion or stenosis in cases in which the vertebral arteries were affected rather than in cases of involvement of the intradural ICA. VWE of the intradural ICA was observed in a number of patients positive for GCA, but only 1 case corresponding to local vessel occlusion was detected. Correspondingly, cerebrovascular ischemic events in our patient group were only observed in patients with concomitant pathology of the extradural or extracranial vessels. Therefore, unlike in other forms of primary or secondary cerebral vasculitis,¹⁰ in patients positive for GCA, VWE of the intracranial ICA was not regularly associated with corresponding stenosis or occlusion.

So far, larger studies focusing on GCA have not reported involvement of any intradural arteries.^{7,8,10,11,14} This discrepancy might be caused by the differing study designs and MR imaging

protocols that are typically based on the focus of the study. In general, deferring sequence parameters optimized for visualization of mural inflammation of intra- and extracranial vessels are mandatory. While the MR imaging sequence used for the evaluation of extracranial vessels is technically focused on high-resolution and contrast of the skull and scalp region, T1WI for the evaluation of intracranial vessels is focused on reduction of pulsation artifacts, a high signal-to-noise ratio, and contrast within the FOV center (Fig 1).^{9,10}

In patients positive for GCA, involvement of intradural vessels coincided rarely with stenosis or occlusion and the occurrence of associated ischemic infarctions. Therefore, former studies might not have recognized mural inflammation of the intradural arteries in patients with GCA because in most studies, patients were only included and examined extensively provided they presented with ischemic stroke.^{18,19,23,29} Nevertheless, most of these patients did not undergo an MR imaging examination including sequences adapted for evaluation of intracranial VWE.^{6,11}

Moreover, postmortem examination can only be performed in patients with GCA with lethal complications (eg, cerebrovascular ischemic events) but not systematically. In addition, postmortem analysis in patients with GCA cannot guarantee an acute state of inflammation of the analyzed tissue. Still, at least intradural involvement of the vertebral arteries was reported in single postmortem cases.^{5,6} Another postmortem study reported 1 of 4 patients with GCA with generalized vasculitis in large and small cerebral vessels.¹⁹ Accordingly, studies focused on primary or secondary vasculitis with cerebral involvement generally do not include patients with a GCA diagnosis. Nevertheless, at least 1 study reported a case of biopsy-proved GCA with VWE of the right carotid-T with co-localized vessel stenosis or occlusion and acute ischemic infarction.¹⁰ Another group reported a case of a GCA-induced aneurysm of the MCA.³⁰

However, none of these studies systematically evaluated prospectively recruited patients with GCA. In comparison with the high sensitivity and specificity of mural inflammation of extracranial vessels for a GCA diagnosis, the sensitivity for ICA involvement was very low, while specificity was high. Therefore, signs of inflammation of the intradural arteries are not potentially a diagnostic criterion. Nevertheless, this imaging sign seems to be highly specific and might therefore identify a subgroup of patients with GCA.

A limitation of our study was that most of our patients had already received corticosteroids for numerous days before MR imaging. Initially, there might have been more cases with VWE than we were able to detect in our study setting.

Another limitation might be that we also included patients as GCA-positive who were diagnosed clinically by fulfillment of the American College of Rheumatology criteria but not through TAB. However, TAB is a very invasive technique; therefore, we consider this approach reasonable. Also, there was no significant difference found in patients diagnosed clinically and patients diagnosed through TAB. In addition, sections of the intracavernous ICA were not evaluated for mural inflammation, even though these have been reported more frequently in postmortem cases.⁵ Nevertheless, in our opinion, this ICA section is not reliably assessable, given that it is accompanied by venous structures yielding

hyperintense signal in postcontrast T1WI, indistinguishable from VWE. Additionally, ratings for extra- and intracranial VWE were performed by different raters, and in case of extracranial VWE evaluation, consensus rating was achieved by concomitant re-evaluation, while in cases of intracranial VWE ratings, the consensus was established by a third rater. Nevertheless, inter-rater agreement for extracranial VWE was in line with that in previous studies; therefore, we consider our ratings valid. In addition, we did not perform quantitative measurements of the amount of enhancement before and after contrast enhancement. Nevertheless, visual evaluation of contrast enhancement of the extra- or intracranial vessel wall is a standard procedure in clinical routine and is performed as standard in many published studies. Therefore, we consider this approach reasonable. Another limitation might be that in theory, contrast enhancement of arterial vessel walls can also be caused by atherosclerotic plaques. However, these tend to enhance only on 1 side of the vessel wall in comparison with the circular enhancement we observed. Nevertheless, some of the observed changes might also, at least in part, be induced by atherosclerotic plaques.

CONCLUSIONS

VWE as a sign of mural inflammation of extracranial vessels is a frequent finding in GCA. Additionally, VWE of intradural arteries, mainly the ICA, can be regularly found in patients with GCA. VWE of intradural arteries observed in patients with GCA does not seem to be associated with vessel occlusion or stenosis and cerebral infarction. Mural inflammation of the intradural ICA detected in MR imaging might therefore identify a subgroup of patients with GCA. Therefore, clinical significance (eg, the prognostic value of VWE of the intradural ICA) should be evaluated further in clinical studies.

Disclosures: Caspar Brekenfeld—UNRELATED: Payment for Lectures (including service on Speakers Bureaus); Codman, Comments: preparation and performance of lecture. Jens Fiehler—UNRELATED: Consultancy: Stryker, Codman, MicroVention; Grants/Grants Pending: MicroVention; Payment for Lectures (including service on Speakers Bureaus); Stryker, Codman, MicroVention, Penumbra, Philips Healthcare, Covidien; Travel/Accommodations/Meeting Expenses Unrelated to Activities Listed: Covidien. Thorsten A. Bley—RELATED: Grant: Deutsche Forschungsgesellschaft grant: BL 1132/1-1; UNRELATED: Payment for Lectures (including service on Speakers Bureaus); Bracco, Siemens, Guerbet, Bayer, GE Healthcare.

REFERENCES

- Salvarani C, Cantini F, Hunder GG. **Polymyalgia rheumatica and giant-cell arteritis.** *Lancet* 2008;372:234–45
- Weyand CM, Goronzy JJ. **Medium- and large-vessel vasculitis.** *N Engl J Med* 2003;349:160–69
- Maksimowicz-McKinnon K, Clark TM, Hoffman GS. **Takayasu arteritis and giant cell arteritis: a spectrum within the same disease?** *Medicine* 2009;88:221–26
- Blockmans D. **Diagnosis and extension of giant cell arteritis: contribution of imaging techniques.** *Presse Med* 2012;41:948–54
- Wilkinson IM, Russell RW. **Arteries of the head and neck in giant cell arteritis: a pathological study to show the pattern of arterial involvement.** *Arch Neurol* 1972;27:378–91
- Salvarani C, Giannini C, Miller DV, et al. **Giant cell arteritis: involvement of intracranial arteries.** *Arthritis Rheum* 2006;55:985–89
- Bley TA, Uhl M, Carew J, et al. **Diagnostic value of high-resolution**

- MR imaging in giant cell arteritis.** *AJNR Am J Neuroradiol* 2007;28:1722–27
- Bley TA, Weiben O, Uhl M, et al. **Assessment of the cranial involvement pattern of giant cell arteritis with 3T magnetic resonance imaging.** *Arthritis Rheum* 2005;52:2470–77
- Küker W. **Cerebral vasculitis: imaging signs revisited.** *Neuroradiology* 2007;49:471–79
- Küker W, Gaertner S, Nagele T, et al. **Vessel wall contrast enhancement: a diagnostic sign of cerebral vasculitis.** *Cerebrovasc Dis* 2008;26:23–29
- Bley TA, Geiger J, Jacobsen S, et al. **High-resolution MRI for assessment of middle meningeal artery involvement in giant cell arteritis.** *Ann Rheum Dis* 2009;68:1369–70
- Hunder GG, Bloch DA, Michel BA, et al. **The American College of Rheumatology 1990 criteria for the classification of giant cell arteritis.** *Arthritis Rheum* 1990;33:1122–28
- Landis JR, Koch GG. **The measurement of observer agreement for categorical data.** *Biometrics* 1977;33:159–74
- Bley TA, Uhl M, Venhoff N, et al. **3-T MRI reveals cranial and thoracic inflammatory changes in giant cell arteritis.** *Clin Rheumatol* 2007;26:448–50
- Bley TA, Wieben O, Vaith P, et al. **Magnetic resonance imaging depicts mural inflammation of the temporal artery in giant cell arteritis.** *Arthritis Rheum* 2004;51:1062–63, author reply 1064
- Markl M, Uhl M, Wieben O, et al. **High resolution 3T MRI for the assessment of cervical and superficial cranial arteries in giant cell arteritis.** *J Magn Reson Imaging* 2006;24:423–27
- Bley TA, Reinhard M, Hauenstein C, et al. **Comparison of duplex sonography and high-resolution magnetic resonance imaging in the diagnosis of giant cell (temporal) arteritis.** *Arthritis Rheum* 2008;58:2574–78
- Browne L, Hardiman O, O'Dwyer H, et al. **Intracranial giant cell arteritis with fatal middle cerebral artery territory infarct.** *Clin Neuropathol* 2003;22:199–203
- Büttner T, Heye N, Przuntek H. **Temporal arteritis with cerebral complications: report of four cases.** *Eur Neurol* 1994;34:162–67
- McLean CA, Gonzales MF, Dowling JP. **Systemic giant cell arteritis and cerebellar infarction.** *Stroke* 1993;24:899–902
- Caselli RJ, Hunder GG, Whisnant JP. **Neurologic disease in biopsy-proven giant cell (temporal) arteritis.** *Neurology* 1988;38:352–59
- González-Gay MA, Blanco R, Rodríguez-Valverde V, et al. **Permanent visual loss and cerebrovascular accidents in giant cell arteritis: predictors and response to treatment.** *Arthritis Rheum* 1998;41:1497–504
- Bogousslavsky J, Deruaz JP, Regli F. **Bilateral obstruction of internal carotid artery from giant-cell arteritis and massive infarction limited to the vertebrobasilar area.** *Eur Neurol* 1985;24:57–61
- Butt Z, Cullen JF, Mutlukan E. **Pattern of arterial involvement of the head, neck, and eyes in giant cell arteritis: three case reports.** *Br J Ophthalmol* 1991;75:368–71
- Cardell BS, Hanley T. **A fatal case of giant-cell or temporal arteritis.** *J Pathol Bacteriol* 1951;63:587–97
- Cull RE. **Internal carotid artery occlusion caused by giant cell arteritis.** *J Neurol Neurosurg Psychiatry* 1979;42:1066–67
- Sheehan MM, Keohane C, Twomey C. **Fatal vertebral giant cell arteritis.** *J Clin Pathol* 1993;46:1129–31
- Thielen KR, Wijdicks EF, Nichols DA. **Giant cell (temporal) arteritis: involvement of the vertebral and internal carotid arteries.** *Mayo Clin Proc* 1998;73:444–46
- Ahdab R, Thabuy F, Menager de Froberville E, et al. **Reversible vertebral artery stenosis following corticotherapy in giant cell arteritis.** *Eur Neurol* 2008;59:331–31
- Kozuka S, Iguchi I, Furuse M, et al. **Cerebral aneurysm induced by giant cell arteritis: a case report.** *Angiology* 1979;30:131–37

Surpass Flow Diverter in the Treatment of Intracranial Aneurysms: A Prospective Multicenter Study

A.K. Wakhloo, P. Lylyk, J. de Vries, C. Taschner, J. Lundquist, A. Biondi, M. Hartmann, I. Szikora, L. Pierot, N. Sakai, H. Imamura, N. Sourour, I. Rennie, M. Skalej, O. Beuing, A. Bonafé, F. Mery, F. Turjman, P. Brouwer, E. Boccardi, L. Valvassori, S. Derakhshani, M.W. Litzenberg, and M.J. Gounis, for the Surpass Study Group

EBM
2

ABSTRACT

BACKGROUND AND PURPOSE: Incomplete occlusion and recanalization of large and wide-neck brain aneurysms treated by endovascular therapy remains a challenge. We present preliminary clinical and angiographic results of an experimentally optimized Surpass flow diverter for treatment of intracranial aneurysms in a prospective, multicenter, nonrandomized, single-arm study.

MATERIALS AND METHODS: At 24 centers, 165 patients with 190 intracranial aneurysms of the anterior and posterior circulations were enrolled. The primary efficacy end point was the percentage of intracranial aneurysms with 100% occlusion on 6-month DSA. The primary safety end point was neurologic death and any stroke through a minimum follow-up of 6 months.

RESULTS: Successful flow-diverter delivery was achieved in 161 patients with 186 aneurysms (98%); the mean number of devices used per aneurysm was 1.05. Clinical follow-up (median, 6 months) of 150 patients (93.2%), showed that the primary safety end point occurred in 18 subjects. Permanent neurologic morbidity and mortality were 6% and 2.7%, respectively. Morbidity occurred in 4% and 7.4% of patients treated for aneurysms of the anterior and posterior circulation, respectively. Neurologic death during follow-up was observed in 1.6% and 7.4% of patients with treated intracranial aneurysms of the anterior and posterior circulation, respectively. Ischemic stroke at ≤ 30 days, SAH at ≤ 7 days, and intraparenchymal hemorrhage at ≤ 7 days were encountered in 3.7%, 2.5%, and 2.5% of subjects, respectively. No disabling ischemic strokes at > 30 days or SAH at > 7 days occurred. New or worsening cranial nerve deficit was observed in 2.7%. Follow-up angiography available in 158 (86.8%) intracranial aneurysms showed 100% occlusion in 75%.

CONCLUSIONS: Clinical outcomes of the Surpass flow diverter in the treatment of intracranial aneurysms show a safety profile that is comparable with that of stent-assisted coil embolization. Angiographic results showed a high rate of intracranial aneurysm occlusion.

ABBREVIATIONS: EVT = endovascular treatment; FD = flow diverter; PUFs = Pipeline Embolization Device for Uncoilable or Failed Aneurysms

Previous *in vivo* and *in vitro* hemodynamic experimental studies showed that optimization is required to balance the porosity (metal-free/metal area) and pore or mesh density (number of

pores/mm²) of flow diverters (FDs) to optimize the effect on flow reduction within the aneurysm sac while keeping the side branches (perforators) patent.¹⁻⁶ We evaluated, in a multicenter, prospective, nonrandomized study, our hypothesis that a single optimized FD would suffice to obliterate a variety of aneurysms located in the anterior and posterior circulation without occluding perforators.

MATERIALS AND METHODS

Patients and Study Design

Patients with intracranial aneurysms undergoing attempted endovascular treatment (EVT) with the FD (Surpass FD; Stryker

University Medical Center, Rotterdam, the Netherlands; Department of Neuroradiology (E.B., L.V.), Niguarda Ca' Granda Hospital, Milan, Italy; Department of Neuroradiology (S.D.), Essex Center for Neurological Sciences, Queen's University Hospital, London, United Kingdom; and Stryker Neurovascular (M.W.L.), Fremont, California.

Please address correspondence to Ajay K. Wakhloo, MD, PhD, FAHA, Division of Neuroimaging and Intervention HI-144, Departments of Radiology, Neurology, and Neurosurgery, 55 Lake Ave North, University of Massachusetts Medical School, Worcester, MA 01655; e-mail: ajay.wakhloo@umassmemorial.org

EBM
2 Evidence-Based Medicine Level 2.

<http://dx.doi.org/10.3174/ajnr.A4078>

Received April 9, 2014; accepted after revision June 25.

From the Division of Neuroimaging and Intervention (A.K.W.), Departments of Radiology, Neurology, and Neurosurgery, and New England Center for Stroke Research (M.J.G.), University of Massachusetts Medical School, Worcester, Massachusetts; Department of Neurosurgery (P.L., J.L.), ENERI, Buenos Aires, Argentina; Department of Neurosurgery (J.d.V.), Radboud University Nijmegen Medical Center, Nijmegen, the Netherlands; Department of Neuroradiology (C.T.), University of Freiburg, Freiburg, Germany; Department of Neuroradiology and Endovascular Therapy (A. Biondi), University of Besançon, Besançon, France; Department of Neuroradiology (M.H.), Helios Hospital, Berlin, Germany; National Institute of Neurosciences (I.S.), Budapest, Hungary; Department of Neuroradiology (L.P.), Hôpital Maison Blanche, University Hospital of Reims, Reims, France; Department of Neurosurgery (N. Sakai, H.I.), Kobe City Medical Center General Hospital, Kobe, Japan; Department of Neuroradiology (N. Sourour), Hôpital Pitié-Salpêtrière, Paris, France; Department of Neuroradiology (I.R.), The Royal Hospitals, Belfast, Ireland; Department of Neuroradiology (M.S., O.B.), Universitätsklinikum Magdeburg, Magdeburg, Germany; Department of Neuroradiology (A. Bonafé), Hôpital Guy de Chauliac, Montpellier, France; Department of Neurosurgery (F.M.), Pontificia Universidad Católica de Chile, Santiago, Chile; Department of Neuroradiology (F.T.), Hôpital Neurologique, Lyon, France; Department of Neuroradiology (P.B.), Erasmus

Neurovascular, Fremont, California) were enrolled consecutively in a multicenter, prospective data base that included 24 centers in Europe, South America, and Japan. In Europe and Chile, patients were treated with the FD after it received approval for distribution by the Notified Body (CE Mark); outside Europe, patients were treated under a compassionate use protocol. All procedures and the sharing of data recorded in the data base were approved by the institutional review board or ethics committee at each participating site; written informed consent was obtained from all patients or their proxy before the procedure.

Patients were considered for enrollment if they had aneurysms of any size located in the anterior or posterior circulation deemed difficult to treat with currently available surgical or endovascular techniques or expected to have a high recanalization rate with standard EVT (wide-neck defined as >4 mm or dome-to-neck ratio of ≤ 2). Patients were not eligible for enrollment if they had experienced a subarachnoid hemorrhage associated with a ruptured intracranial aneurysm within 30 days, had contraindications for dual antiplatelet therapy or were nonresponders to acetylsalicylic acid and clopidogrel, or had a nontreated brain arteriovenous malformation in the territory of the target aneurysm. Inhibition of platelet function was assessed (VerifyNow P2Y12 assay; Accumetrics, San Diego, California), and inhibition between 30% and 90% was considered therapeutic. Patients were given acetylsalicylic acid (81 mg) and clopidogrel (75 mg) for a minimum of 3 days before the procedure. Dual antiplatelet therapy was continued for a minimum of 3 months, followed by lifelong continuation of acetylsalicylic acid. A loading dose of 350 mg of acetylsalicylic acid and 150 mg of clopidogrel was given 6–24 hours before EVT if patients were acutely treated. The goal, whenever feasible, was to treat the target vessel with a single device.

Follow-up digital subtraction angiography was typically scheduled at 1–3, 6, and 12 months and, in a few patients, at a later time point, performed on an outpatient basis. All angiograms were evaluated by 2 independent reviewers not involved in patient care. The efficacy end point was the percentage of subjects with 100% occlusion of the aneurysm.

The safety end point was the percentage of patients experiencing death and any stroke through the minimum follow-up of 6 months. Functional outcome by using the modified Rankin Scale score and cranial nerve II–VI examination was assessed at baseline, at discharge, and at follow-up.

Technology and Endovascular Procedure

The FD is made of a cobalt-chromium alloy with a low porosity (metal surface area coverage, 30%); a high mesh density (20–32 pores/mm²); and a self-expanding, single-layer braided, tubular structure. The device comes in various diameters, ≤ 5.3 mm, and lengths, ≤ 50 mm. The 2-mm device has 48 wires; the 3- and 4-mm devices have 72 wires, and the 5-mm device has 96 wires, to provide a constant high mesh density over various diameters of the device, as supported by previous *in vitro*⁵ and *in vivo* studies.⁶ The filament diameter ranges from 25 to 36 μm , depending on the device diameter, to maintain the mechanical stability of the implant and the square shape of the mesh and the mesh attenuation at the implantation site. The braid angle is designed to avoid changes of mesh density in curved arterial segments and in vary-

ing arterial diameters. It also helps to reduce foreshortening of the FD (29%–42% depending on implant diameter) from constraint stage to nominal diameter once implanted. To improve radiopacity, the device has 12 platinum wires (92% platinum, 8% tungsten) integrated in the mesh with the same wire diameter as the remaining cobalt-chromium wires.

The delivery system of the FD is composed of an inner catheter (the pusher) and an outer catheter (the delivery catheter) compatible with any 0.014-inch microwire. The outer diameter of the distal part measures 3.7F, and of the proximal part, 3.9F. The FD comes premounted at the very distal end of its delivery system. Two different generations of FD delivery systems were used in this study. The system used in the first 45 subjects was stiffer, while the second generation of delivery system had an improved trackability.

Except in 4 patients, the implantation was performed with the patient under general anesthesia. Following access, the patients were administered heparin to maintain an activated clotting time of >250 seconds. Typically, a bi- or triaxial approach was used. A long sheath was placed in either the common carotid or subclavian artery. A guide (intermediate) catheter was navigated through the sheath over either the FD delivery system and a 0.014-inch microwire or a standard microcatheter. If a microcatheter was used, an exchange-length 0.014-inch microwire was introduced and the microcatheter was replaced by the FD delivery catheter. The delivery system has markers indicating the location of the constrained implant and was positioned at the desired site across the aneurysm neck. If satisfactory initial wall apposition was not obtained, postdilation of the FD with a compliant balloon was permitted. Postdilation was performed with compliant balloons, either Scepter C (Microvention, Tustin, California) or HyperForm (Covidien, Irvine, California). Technical success was defined as the proportion of patients in whom the FD was delivered to cover the aneurysm neck.

RESULTS

From April 2010 to January 2013, EVT with the FD was attempted in 165 patients with 190 intracranial aneurysms. Single-center results from a small subset of these patients ($n = 26$) have previously been reported.⁷ Patient demographics, clinical presentation at treatment, and indication for EVT are presented in Table 1. Patients with ruptured aneurysms (3.9%) were treated after initial partial coiling and in a subacute stage at least 30 days following the SAH. Most aneurysms were discovered incidentally or after work-up for chronic headaches (31.8%). A common reason for the use of the FD was recanalization or regrowth of previously coiled (with or without stent assistance) aneurysms, necessitating re-intervention (21.7%). In nearly one-fifth of the aneurysms, mass effect was present with cranial nerve deficits.

Aneurysm characteristics are provided in Table 1. In the anterior circulation, 118 aneurysms (63.4%) originated below the internal carotid artery terminus (Fig 1), and 41 (22%), distal to the circle of Willis (including the middle cerebral artery bifurcation, Fig 2); 27 (14.5%) originated at various locations in the posterior circulation, including 4 fusiform aneurysms of the entire basilar trunk (Fig 3). The mean aneurysm and neck diameters were 10.4 ± 0.7 and 6.0 ± 0.4 mm, respectively; the dome-to-neck ratio

Table 1: Patient information and characteristics of aneurysms treated with the FD

Patients	161
Aneurysms	186
Women (%)	72.4
Mean age (yr) (range)	57.1 (28–82)
Presentation/indications for treatment (%)	
Incidental finding/headaches	31.8
Recurrent after coiling/coiling and stenting	21.7
Cranial nerve deficit/mass effect	18.6
Associated second ruptured aneurysm	13.1
Stroke/transient ischemic attack	7.8
Subarachnoid hemorrhage (not acute)	3.9
Recurrent after clipping/failed clipping	2.3
Seizures	0.8
Total No. of aneurysms treated	186
<5 mm	53
5–9.9 mm	64
10–20 mm	47
>20 mm	22
Measurements (mean ± SEM)	
Aneurysm dome size (mm)	10.4 ± 0.7
Aneurysm neck size (mm)	6 ± 0.4
Dome: neck ratio	1.6 ± 0.08
Proximal parent artery diameter (mm)	3.8 ± 0.1
Distal parent artery diameter (mm)	3.0 ± 0.1
Anterior circulation ICA (%)	118 (63.4)
Petrocavernous	5 (2.7)
Cavernous	20 (10.7)
Carotid cave	3 (1.6)
Superior hypophyseal	5 (2.7)
Paraophthalmic	34 (18.2)
Paraclinoid ICA	4 (2.2)
Supraclinoid ICA	6 (3.2)
Posterior communicating artery	36 (19.4)
Anterior choroidal artery	5 (2.7)
Anterior circulation distal to circle of Willis (%)	41 (22)
ICA terminus	5 (2.7)
Anterior cerebral artery (including AcomA and pericallosal)	12 (6.4)
Middle cerebral artery	24 (12.9)
Posterior circulation (%)	27 (14.5)
Vertebral artery (VA and VB junction)	8 (4.3)
Posterior inferior cerebellar artery	6 (3.2)
Basilar trunk	9 (4.8)
Posterior cerebral artery	3 (1.6)
Superior cerebellar artery	1 (0.5)
Morphology (%)	
Wide-neck saccular	125 (67.2)
Fusiform/dissecting	54 (29.0)
Blister	7 (3.8)
Focal disease	100 (53.8)
Dysplastic artery	86 (46.2)

Note:—AcomA indicates anterior communicating artery; VA, vertebral artery; VB, vertebralbasilar; SEM, standard error of the mean.

was $1.6 \pm 0.08\%$. Eighty-six aneurysms (46.2%) were associated with dysplastic parent arteries, 54 (29%) were either fusiform or dissecting, and 7 (3.8%) were blood blister-type. The mean proximal artery diameter was 3.8 ± 0.1 mm, and the distal parent artery diameter, 3.0 ± 0.1 mm.

Technical Complications

Of 190 intracranial aneurysms in which treatment was attempted in 165 patients, access to the target site failed in 4 subjects due to the stiffer first generation of the FD delivery system and the tor-

tuosity of the parent artery. Thus, FD placement was achieved in 186 aneurysms (device success of 98%) or 161 patients (Table 2). The average number of FDs used was 1.05 per aneurysm and 1.2 per patient. Most aneurysms were treated with a single FD (1 device, 127 aneurysms). In 23 and 2 aneurysms, 2 and 3 devices, respectively, were deployed. In 14 and 2 patients with 2 and 3 adjacent aneurysms, respectively, a single FD was used. Additional coils were present from previous treatment or placed in 36 aneurysms (19.3%). During treatment, imprecise FD placement resulted in incomplete neck coverage in 4 (2.1%) aneurysms (technical success of 97%) and a guidewire perforation in 5 patients (3.1%). Guidewire perforation led to SAH and intraparenchymal hemorrhage in 3 and 2 patients, respectively (Table 2). Postdilation of the FD because of a malapposition was performed with compliant balloons in 36 aneurysms (19.4%). Clot formation on the implant surface was observed in 6 patients (3.7%), all of which were successfully treated with intra-arterial administration of abciximab (5–18 mg) in 4 patients or eptifibatid in 2 subjects. Vasospasm due to catheter manipulation was reported at the tip of or around the long sheath of the guide catheter in 6 patients but promptly resolved with local intra-arterial administration of nicardipine ($n = 5$, 2–15 mg) or verapamil ($n = 1$, 10 mg). Periprocedural ICA dissections were reported in 2 patients and led to complete vessel occlusion that remained asymptomatic due to existing collateral blood supply.

Safety and Clinical Outcome

During the clinical follow-up (median, 6 months; range, 1–38 months) available in 150 (93.2%) patients, a primary end point occurred in 18 subjects (12%). Of these patients, 5 (3.3%) returned to baseline during follow-up, 5 (3.3%) continued to experience a minor neurologic deficit ($mRS \leq 2$), 4 (2.7%) have permanent major neurologic disabilities ($mRS > 2$), and 4 (2.7%) died. Of the patients with a primary end point, hemorrhage was seen in 10 patients (6.2%) and was related to the following: 1) a periprocedural wire perforation in 5 (3.1%) patients, 2) a subdural hematoma that developed within 24 hours in 1 patient who was kept on therapeutic heparin and required surgical decompression, 3) a subarachnoid hemorrhage 5 days after implant in 1 subject, and 4) intraparenchymal hemorrhage seen in 3 patients following FD implantation and up to 14 days following EVT. No further aneurysmal ruptures were encountered during the follow-up period. New or worsening of pre-existing cranial nerve deficits following treatment were observed in 4 (2.7%) subjects. There were an additional 3 deaths during the follow-up period from nonvascular causes: One patient was diagnosed with lung cancer 1 year following aneurysm treatment and died 1 year thereafter, 1 was lost to follow-up and was subsequently discovered to have died from complications of a brain tumor, and 1 patient died from pneumonia 1 year after FD implantation. Changes in the mRS score are reported in Fig 4.

Anterior Circulation. In the subgroup analysis, 5 patients with anterior circulation aneurysms experienced permanent neurologic deficits and 2 patients died. Complications were related to thromboembolic events in 3 patients, including 1 patient with a 16-mm ophthalmic artery aneurysm who had a delayed anterior choroidal artery occlusion and a stroke following the procedure.

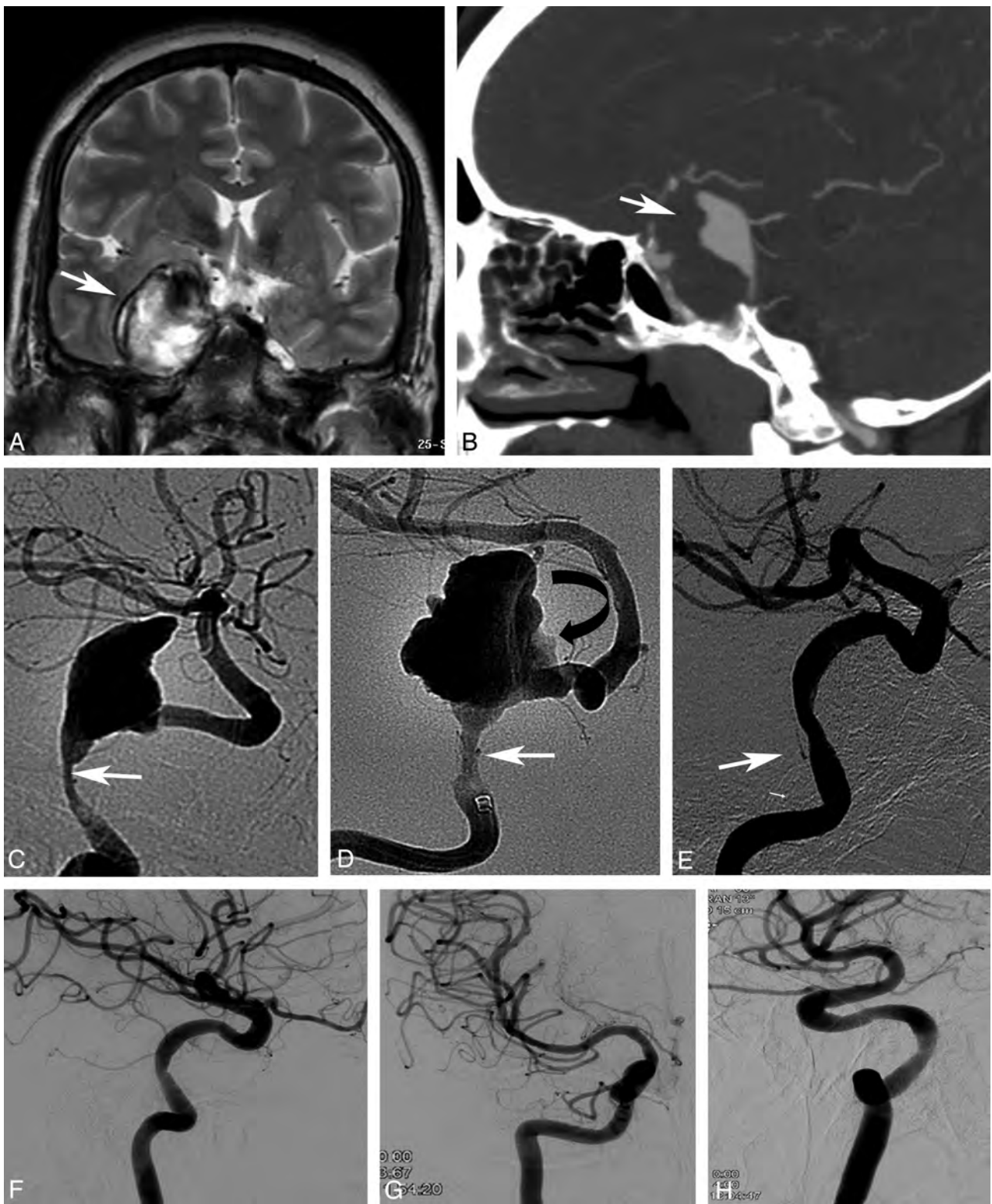


FIG 1. Coronal T2-weighted MRI (A) and sagittal contrast CT (B), in a young female with a giant, partially thrombosed dissecting aneurysm of the right internal carotid artery (arrows). Lateral (C) and frontal DSA images (D) show the site of dissection (arrow) and irregular aneurysmal lumen corresponding to intra-aneurysmal clot (curved arrow). Seven-month follow-up angiography after placement of a Surpass FD (E) shows complete aneurysm occlusion with mild narrowing at the level of dissection (arrow). Twelve-month follow-up in lateral, frontal, and oblique views (F–H) shows stable aneurysm occlusion with no major remaining stenosis. Note the nearly isolated right hemisphere due to a small right A1 artery.

Wire perforation was encountered in 2 patients, including 1 patient with a large dissecting fusiform aneurysm of the pericallosal artery. All 5 patients showed various degrees of improvement of

their neurologic deficits and functional status (mRS) at their latest clinical follow-up.

Of the patients with anterior circulation aneurysms who had

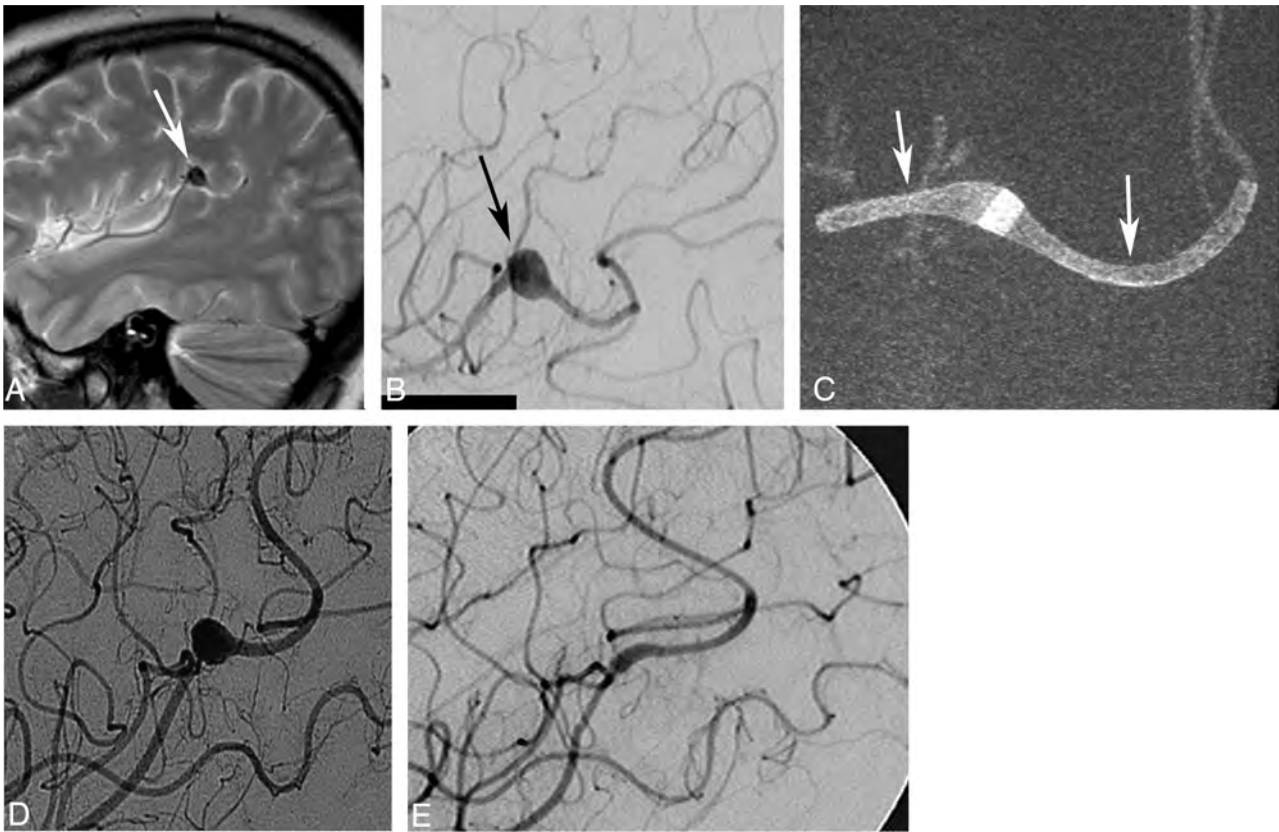


FIG 2. A, A young female patient with a mycotic aneurysm (*arrow*) of the left middle cerebral artery intractable to antibiotic treatment. B, The fusiform aneurysm (*arrow*) measures 8×7 mm and originates from the angular artery. The patient failed a balloon-test occlusion of the angular artery and was considered for flow-diverter treatment. Conebeam CT (C) shows the aneurysm treated with 2 overlapping Surpass FDs (2×15 and 2×10 mm, *arrows*). Follow-up angiogram (D) shows excellent parent artery flow and filling of the aneurysm. Six-month follow-up angiogram (E) shows a complete aneurysm occlusion. Note that a second FD device had to be implanted because the first one did not cover the entire lesion. This was related to poor visibility of the first generation of the FD, which did not have platinum markers, which were added to the second generation of the implant.



FIG 3. A, A male patient with a 20×30 mm symptomatic fusiform basilar trunk aneurysm involving both anterior inferior cerebellar arteries (*arrows*) and the vertebrobasilar junction. Coil occlusion (B) of the left vertebral artery to prevent "endoleak" (*curved arrow*) and placement of a single 5×50 mm Surpass FD with patency of anterior inferior cerebellar arteries (conebeam angio-CT; insert, *small arrows*). C and D, Progressive thrombosis of the aneurysm with remodeling of the basilar trunk and preservation of both anterior inferior cerebellar arteries (*small arrows*) at 3- and 14-month follow-up angiography. Note the previously occluded left internal carotid artery with a secondary enlarged left posterior communicating artery feeding the middle cerebral artery. The distal basilar trunk and left P1 segment not covered by the FD remain enlarged.

transient neurologic deficits during the clinical follow-up period, 1 experienced parenchymal bleeding ipsilateral to the treated area. The patient presented with a frontal lobe hematoma 1 day after treatment of a giant carotid cavernous aneurysm that required decompressive surgery; after initial headache, the patient remains asymptomatic following surgery.

Posterior Circulation. During the clinical follow-up period, 2 of 27 patients (7.4%) treated for posterior circulation aneurysms died, both of whom presented with symptomatic fusiform aneurysms affecting the entire basilar trunk and proximal segment of the posterior cerebral arteries.

Procedure-related morbidity was encountered in 2 patients

Table 2: FD implantation, technical complications, primary safety end point, and other major adverse events at a median 6-month clinical follow-up (range 1–38 months)

FD implantation	
Attempted treatment (patients/aneurysms)	165/190
FD implantation at target site (patients/aneurysms)	161 (97.5%)/186 (98%)
Average No. of devices used per patient	1.2
Average No. of devices used per aneurysm	1.05
Average procedure length (min)	79.8
Technical complications	
Incorrect placement with partial aneurysm coverage	4 (2.1%)
Guidewire perforation	5 (3.1%)
Intraoperative thrombus formation (asymptomatic/symptomatic)	6 (3.7%)/0
Vasospasm	6 (3.7%)
Serious adverse events	
Any death during the follow-up	7 (4.3%)
Patients available for follow-up	150 (93.2%)
Patients lost to or refusing follow-up	11 (6.8%)
Primary end point (any stroke and neurologic death)	18 (12%)
Permanent morbidity	9 (6.0%)
Procedure-related mortality	4 (2.7%)

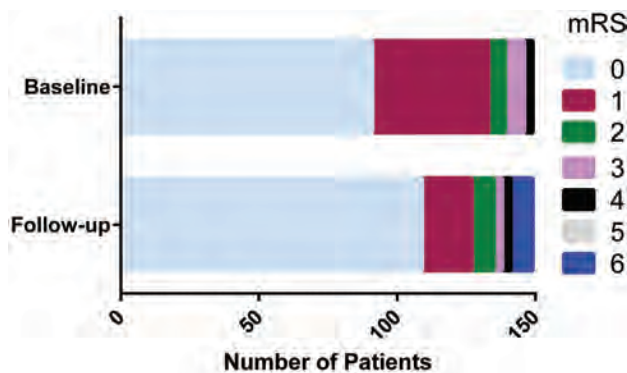


FIG 4. Modified Rankin Scale score at presentation and follow-up in 150 patients. A Wilcoxon matched-pairs signed rank test ($P = .55$) indicates no significant change in patient neurologic outcomes.

(7.4%). One patient was treated for a 19-mm symptomatic basilar apex–superior cerebellar artery aneurysm. After initially having an excellent recovery, 3 weeks following the EVT, the patient had a midbrain and brain stem stroke from a suspected perforator occlusion, resulting in right-sided hemiplegia. The other patient, who was treated for a large basilar trunk aneurysm, had pre-existing severe intracranial atherosclerotic disease and a history of posterior circulation stroke. Five months following the EVT and discontinuation of dual antiplatelet therapy, the patient presented with basilar thrombosis that was treated with IV thrombolysis. Despite successful revascularization, the patient retained homonymous hemianopia and diplopia at left lateral gaze.

The only confirmed perianeurysmal bleed was in a posterior circulation aneurysm observed several weeks after the EVT in a patient with a growing large symptomatic (occipital pain and ataxia) dissecting vertebral artery–posterior inferior cerebellar artery aneurysm that, at follow-up angiography, was completely obliterated. The patient’s preprocedural symptoms have resolved completely, and the patient remains asymptom-

atic 24 months following the procedure. In the posterior circulation, 1 patient presented with a parenchymal superior vermian bleed 6 days after placement of the FD for a dissecting intracranial segment of the vertebral artery. The patient presented with mild dizziness and returned to baseline at 30-day follow-up.

Efficacy

Of 186 aneurysms that received an FD, 158 (86.8%) were available for a DSA follow-up (median, 6 months; range, 1–38 months). Additionally, 2 patients had a 6-month follow-up MRA that was not assessed because the protocol required DSA. Complete occlusion (100%) was seen in 118 (75%) aneurysms of all locations (Table 3). Near-complete or complete occlusion (95%–100%) was observed in 127 (80%) aneurysms. A subgroup analysis showed complete occlusion in 78.6% of anterior circulation aneurysms below the ICA terminus, while 65.8% and 72.7% of aneurysms located in the anterior circulation distal to the circle of Willis and the posterior circulation, respectively, were occluded (Table 3). Starting at 3-month follow-up, a progressive thrombosis of the aneurysm was seen, with most of the aneurysms obliterated between 6 and 12 months after FD placement (Fig 5). Of the 5 aneurysms that were previously treated with stent-assisted coil embolization, 3 did not show complete occlusion at 6-month follow-up angiography and were successfully re-treated with a second FD. Of the 4 aneurysms with incomplete neck coverage at EVT, 2 showed incomplete occlusion at follow-up.

At follow-up, significant stenosis ($\geq 50\%$) within the FD was seen in 8 patients (5%), who remained asymptomatic. The area of stenosis was associated with device malapposition that had not been addressed with balloon postdilatation at the time of placement in all 8 patients. Another patient ceased dual antiplatelet therapy 4 months following treatment due to head trauma, and subsequently the implant was occluded with worsening of pre-existing aphasia.

DISCUSSION

Specific Features of the FD

The single-layer braided FD used in this clinical study was engineered on the basis of previous extensive experimental hydrodynamic studies.^{5,6,8,9} In vitro and computational fluid dynamic research showed that FDs create impedance to the flow at the neck of the aneurysm and reduce the hydrodynamic circulation inside the aneurysm pouch.¹⁰ This outcome is achieved by the attenuation of the peak and mean kinetic energy of the blood entering the aneurysm with each pulse cycle. Subsequent in vivo experiments confirmed that the flow reduction led to progressive aneurysm thrombosis and, ultimately, endothelialization of the FD surface and the aneurysm neck.⁶ As detailed previously, this result required an FD porosity of optimally 70%, which was sufficient for an intra-aneurysmal flow reduction while maintaining flow through vital perforators.^{5,8–11} With the increase in diameter and to maintain biomechanical stability within the parent artery, the number of wires of an FD had to be increased. Ensuring the desired porosity required a reduction of FD wire thickness. These changes resulted in a consistent mesh density and

Table 3: Primary efficacy end point at a median of 6 months (range, 1–38 months)^a

Aneurysm Location	Aneurysm Occlusion				Total
	Occlusion Rate ^b (%)			100	
	<50	50–95	>95		
Anterior circulation (ICA)	6 (6.1%)	11 (11.2%)	4 (4.1%)	77 (78.6%)	98
Petrocavernous		1		3	4
Cavernous		2	2	12	16
Carotid cave	1			3	4
Superior hypophyseal	1			3	4
Paraophthalmic	2	2		24	28
Paraclinoid				3	3
Supraclinoid	1	1		3	5
Posterior communicating artery	1	4	2	24	31
Anterior choroidal artery		1		2	3
Anterior circulation distal to circle of Willis	2 (5.3%)	9 (23.7%)	2 (5.3%)	25 (65.8%)	38
ICA terminus	1	1	1	2	5
Anterior cerebral artery (including AcomA)		1	1	7	9
Middle cerebral artery	1	7		16	24
Posterior circulation	1 (4.5%)	2 (9.1%)	3 (13.6%)	16 (72.7%)	22
VA and VB junction		1		7	8
Posterior inferior cerebellar artery		1	2	2	5
Basilar trunk	1		1	4	6
Posterior cerebral artery				3	3
Total	9 (6%)	22 (13%)	9 (6%)	118 (75%)	158

Note:—AcomA indicates anterior communicating artery; VA, vertebral artery; VB, vertebralis.

^a Digital subtraction angiography follow-up was available in 158 aneurysms (86.8%).

^b Occlusion rates at the latest follow-up are based on aneurysm volume calculated on pre-and posttreatment digital subtraction angiograms.

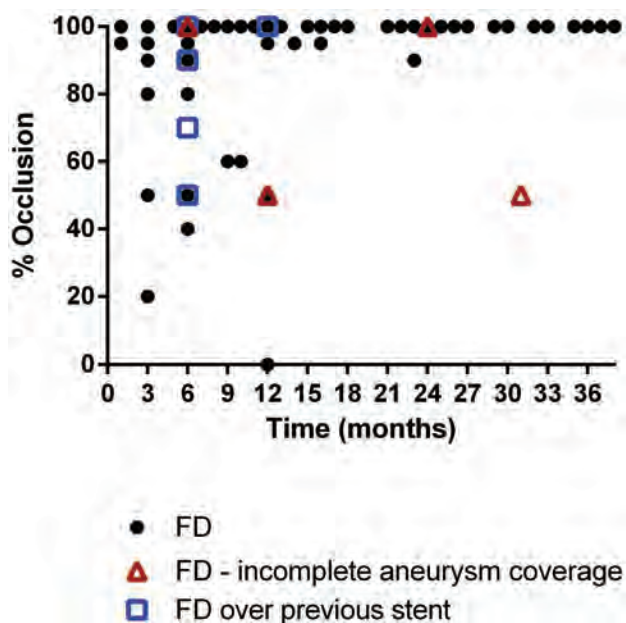


FIG 5. Percentage of occlusion of the aneurysm as a function of time from implant. Incomplete coverage of the aneurysm by the FD and FD implantation over a prior stent are noted by red triangles and blue squares, respectively.

cell shape of the implant, enabling an effective flow reduction at various parent vessel diameters. The resulting braid angle also reduced the foreshortening of the device and enhanced a precise placement.

“Herniation” of the FD into the aneurysm alters the ultrastructure of the device (cell shape and porosity) and changes the effect on flow diversion, as recently reported with other nitinol-based implants.¹² The braid angle also eliminates the potential risk of creating pockets of large openings between the struts, es-

pecially in aneurysms located in tight bends. Changes of FD configuration and mesh porosity once implanted into the artery may create an inconsistent pattern of intra-aneurysmal flow and insufficient resistance to the flow at the aneurysm neck that necessitates the use of multiple FDs. The central goal of the aforementioned engineering studies was to create a single optimized FD for efficacious treatment across a broad range of intracranial aneurysms. Preliminary data of the Surpass FD at a single center reinforced these experimental results, demonstrating an occlusion rate of 94% at 6 months in 31 aneurysms.⁷ The reported occlusion rate in this multicenter study is lower; however, this was anticipated because the prior report was from a single center at a high-volume site that has extensive experience with this device.

The clinical data presented herein reinforce the experimental findings.⁶ The use of a single device (compared with a median of 3 used in the Pipeline Embolization Device for Uncoilable or Failed Aneurysms [PUFS] trial¹³) led to a comparable high rate of progressive aneurysm occlusion. Moreover, the average procedural time in this study was 79.8 minutes compared with 124 minutes in the PUFS trial.¹³ Similar to our observations, the PUFS study confirmed the progressive nature of aneurysm occlusion: At 6 months, 73.6% of aneurysms were obliterated, and at 12 months, 86.8% were thrombosed. As in our series, a high complete occlusion rate was observed in large or giant aneurysms. Specifically, there were 22 aneurysms of >10 mm located in the ICA below the circle of Willis having no underlying prior stent, with follow-up at a minimum of 6 months. In this small cohort, 18 (81.8%) were completely occluded at 6-month follow-up and 3 (13.6%) had a small neck remnant (>95% occluded). One aneurysm (4.5%) was >90% occluded at 6-month follow-up angiography. Several recently published meta-analyses of EVT in >1000 intracranial aneurysms with FDs showed a complete

occlusion rate as high as 76%.^{14,15} A retrospective analysis of the Italian multicenter experience with flow-diverter devices for intracranial aneurysms that included the Pipeline Embolization Device (Covidien) and Silk stent (Balt Extrusion, Montmorency, France) showed an 85% aneurysm occlusion at 3 months.¹⁶

Patient Selection and Angiographic Occlusion

Caution should be exercised when comparing occlusion rates between different FDs because patient selection and trial design may affect outcome. In our series, only 14% of the patients presented with extradural aneurysms, whereas in the PUFs trial, a large subgroup had petrous and cavernous aneurysms (44.4%).¹³ Thus, the risk of spontaneous aneurysm rupture before complete aneurysm thrombosis during the observation period differs. These preliminary data are encouraging, and the FD achieved a complete (100%) or near-complete (>95%) occlusion at follow-up in 81% of the treated aneurysms. To render a true assessment of the FD, we enrolled patients with aneurysms originating at all locations in the intracranial circulation, including more challenging aneurysms such as those found at the MCA bifurcation and anterior communicating artery. Like other studies, a variety of aneurysms with complex angiographic appearances (multiple adjacent aneurysms with dysplastic arteries, dissecting and blister aneurysms) was captured in our series and most likely does not reflect the same underlying disease or disease stage. Lanzino et al¹⁷ showed, in a matched-pair analysis, that FD treatment in 22 paraclinoid aneurysms achieved a 77.3% complete occlusion versus 45.4% with standard EVT, including stent-assisted coiling with fewer intra- and postoperative complications for the FD arm.

Bleeding and Thromboembolic Complications

Previously published studies and case series have reported morbidity and mortality as high as 9% and 6%, respectively.^{13,18-22} Morbidity and mortality with the Silk device (Balt Extrusion) are reported to be slightly higher, with $\leq 15\%$ and 8%, respectively.²³⁻²⁵ Two recently published meta-analyses on FD treatment in up to 1451 patients with 1654 aneurysms showed a not-negligible procedure-related morbidity and mortality of 5%–10% and 4%, respectively.^{14,15} The authors found an occurrence of postoperative SAH, intraparenchymal hemorrhage, and perforator infarctions of 3% in each category. The rates of SAH, intraparenchymal hemorrhage, and ischemic stroke at ≤ 30 days were 3%, 3%, and 5%, respectively. SAH, intraparenchymal hemorrhage, and ischemic stroke at >30 days occurred in 2%, 2%, and 3% of the patients, respectively. Perforator occlusions were significantly higher in the posterior circulation compared with aneurysms located in the anterior circulation. Ischemic stroke was encountered in 6% of patients.¹⁴ Our results are comparable with those in other studies; any permanent neurologic morbidity and mortality were seen in 6% and 2.7%, respectively. In our series, we did not encounter SAH after 7 days following FD placement. In a preliminary study of this FD in 39 patients, there was a lower permanent morbidity rate of 4% and no mortality.⁷ This larger, multicenter study showed a slight increase in morbidity. The increase in mortality is likely attribut-

able to the study design and the inclusion of complex aneurysms, particularly in the posterior circulation.

Our experience with the FD in the posterior circulation has been comparable with that in the anterior circulation with the exception of fusiform dolichoectatic aneurysms of the entire basilar trunk. Two of 4 patients treated for an entire basilar trunk aneurysm died from FD treatment. Siddiqui et al²⁶ reported 7 patients with large or giant fusiform vertebrobasilar aneurysms treated with the Silk or Pipeline Embolization Device, 4 of whom died; 3 were left with severe disability following the procedure. The use of a single, long implant, compared with the need for telescoping the Pipeline Embolization Device with the potential risk of perforator occlusion, may mitigate periprocedural morbidity.

Although stent-assisted coil embolization has not been the subject of randomized clinical trials, this technology has been available for cerebrovascular aneurysm treatment for more than a decade. Consequently, numerous studies have been published regarding the safety and efficacy of the technique. In a comprehensive review by Shapiro et al,²⁷ stent-assisted coil-embolization complications and mortality were seen in 19% and 2.1%, respectively. Although most aneurysms included in this analysis were unruptured, acutely ruptured aneurysms were also included. As with all new technology, there was a documented learning curve, with complication rates being higher in the first 10 patients treated. Most complications (10%) were thromboembolic. If we restricted the analysis to unruptured or nonacutely ruptured aneurysms, the rates of morbidity and mortality varied between 3.8%–8.3% and 0%–3.9%, respectively.²⁸⁻³⁴ The data presented in our study show a safety profile comparable with that of stent-assisted coil embolization.

Study Limitations

Assessment at clinical follow-up and serious adverse events were self-adjudicated by physicians' participating sites. Another major limitation of the data collected is the nonrandomized nature of the study and lack of a control arm. Patients with ruptured aneurysms were not included in the acute stage but were treated electively if other treatments were not an option. Finally, most aneurysms included in this trial are <10 mm. Presently, the FD studied herein is undergoing the Surpass intraCranial aneurysm Embolization system Trial (SCENT), which is a multicenter, prospective single-arm trial designed to assess the safety and efficacy of the device for the treatment of large or giant wide-neck aneurysms. On completion of this trial, more data will be available on the ability of the device to treat large and giant aneurysms.

CONCLUSIONS

Clinical data demonstrate an acceptable safety profile compared with other FD technology and stent-assisted coil embolization. High occlusion rates were observed for a wide range of intracranial aneurysms of the anterior and posterior circulation without the need for coiling and with the use of a single FD implant. The observed progressive occlusion requires long-term follow-up studies. The treatment of a subset of fusiform aneurysms affecting the entire basilar artery remains challenging.

Disclosures: Ajay K. Wakhloo—UNRELATED: Consultancy: Stryker Neurovascular; Employment: Surpass Medical; Grants/Grants Pending: Philips Healthcare*; Payment for Lectures (including service on Speakers Bureaus): Harvard Medical School, Miami Baptist Health; Stock/Stock Options: Surpass Medical. Pedro Lylyk—UNRELATED: Board Membership: Covidien, Comments: no monetary compensation; Consultancy: Covidien, Surpass, Cardiatis, MicroVention, Phoenix; Payment for Lectures (including service on Speakers Bureaus): Covidien; Stock/Stock Options: Surpass; Travel/Accommodations/Meeting Expenses Unrelated to Activities Listed: Covidien, Cardiatis, Sequent, MicroVention. Joost de Vries—UNRELATED: Consultancy: Stryker Neurovascular; Grants/Grants Pending: Stryker Neurovascular,* Covidien,* Johnson & Johnson*; Stock/Stock Options: Stryker Neurovascular; Travel/Accommodations/Meeting Expenses Unrelated to Activities Listed: Stryker Neurovascular. Christian Taschner—UNRELATED: Consultancy: Stryker Neurovascular; Grants/Grants Pending: MicroVention,* Acandis.* Istvan Szikora—UNRELATED: Consultancy: Stryker Neurovascular, Covidien; Payment for Lectures (including service on Speakers Bureaus): Stryker Neurovascular, Covidien. Laurent Pierot—UNRELATED: Consultancy: Stryker. Nobuyuki Sakai—UNRELATED: Consultancy: Stryker, Terumo/MicroVention, Codman, Covidien; Payment for Lectures (including service on Speakers Bureaus): Stryker, Terumo/MicroVention, Codman, Covidien, Asahi INTECC, Medtronic. Nader Sourour—UNRELATED: Consultancy: Covidien, Penumbra, Stryker; Travel/Accommodations/Meeting Expenses Unrelated to Activities Listed: Surpass, Stryker, Comments: training. Ian Rennie—UNRELATED: Employment: proctoring agreement with Stryker Neurovascular, Comments: agreement in place recently (no work done as yet and no payments made). Matthew J. Gounis—UNRELATED: Consultancy: Codman Neurovascular, Surpass (Contract Research Organization), Surpass Medical, Stryker Neurovascular, Comments: fee-per-hour consulting; Grants/Grants Pending: Philips Healthcare,* National Institutes of Health,* Covidien/ev3,* Silk Road,* Lazarus Effect,* Wyss Institute,* Fraunhofer Institute,* Stryker Neurovascular.* Marc W. Litzzenberg—UNRELATED: Employment: Stryker Neurovascular. Francis Turjman—UNRELATED: Consultancy: Covidien, Codman, Balt; Grants/Grants Pending: Covidien; Payment for Lectures (including service on Speakers Bureaus): Codman, Covidien; Payment for Development of Educational Presentations: Codman; Travel/Accommodations/Meeting Expenses Unrelated to Activities Listed: Stryker, Covidien, Codman. Patrick Brouwer—UNRELATED: Board Membership: Netherlands Neurovascular Association (nonpaid membership); Consultancy: Codman, DePuy Synthes*; Payment for Lectures (including service on Speakers Bureaus): Balt Extrusion,* Toshiba.* Alain Bonafé—UNRELATED: Consultancy: Stryker. Edoardo Boccardi—UNRELATED: Board Membership: Stryker, Covidien, MicroVention; Consultancy: Stryker, Covidien, MicroVention; Payment for Lectures (including service on Speakers Bureaus): MicroVention; Travel/Accommodations/Meeting Expenses Unrelated to Activities Listed: Stryker. *Money paid to the institution.

REFERENCES

- Wakhloo AK, Schellhammer F, de Vries J, et al. Coated and non-coated stents for vessel reconstruction and treatment of aneurysms and AV fistulas: an experimental study (abstract). *Neuroradiology* 1992;34(suppl):24
- Wakhloo AK, Schellhammer F, Vries JD, et al. Self-expanding and balloon-expandable stents in the treatment of carotid aneurysms: an experimental study in a canine model. *AJNR Am J Neuroradiol* 1994;15:493–502
- Turjman F, Acevedo G, Moll T, et al. Treatment of experimental carotid aneurysms by endoprosthesis implantation: preliminary report. *Neurol Res* 1993;15:181–84
- Geremia G, Haklin M, Brennecke L. Embolization of experimentally created aneurysms with intravascular stent devices. *AJNR Am J Neuroradiol* 1994;15:1223–31
- Seong J, Wakhloo AK, Lieber BB. In vitro evaluation of flow diverters in an elastase-induced saccular aneurysm model in rabbit. *J Biomech Eng* 2007;129:863–72
- Sadasivan C, Cesar L, Seong J, et al. An original flow diversion device for the treatment of intracranial aneurysms: evaluation in the rabbit elastase-induced model. *Stroke* 2009;40:952–58
- De Vries J, Boogaarts J, Van Norden A, et al. New generation of flow diverter (Surpass) for unruptured intracranial aneurysms: a prospective single-center study in 37 patients. *Stroke* 2013;44:1567–77
- Lieber BB, Gounis MJ. The physics of endoluminal stenting in the treatment of cerebrovascular aneurysms. *Neurol Res* 2002;24(suppl 1):S33–42
- Lieber BB, Sadasivan C. Endoluminal scaffolds for vascular reconstruction and exclusion of aneurysms from the cerebral circulation. *Stroke* 2010;41:S21–25
- Aenis M, Stancampiano AP, Wakhloo AK, et al. Modeling of flow in a straight stented and non-stented sidewall aneurysm model. *J Biomech Eng* 1997;119:206–12
- Kallmes DF, Ding YH, Dai D, et al. A new endoluminal, flow-disrupting device for treatment of saccular aneurysms. *Stroke* 2007;38:2346–52
- Raymond J, Darsaut TE, Makoyeva A, et al. Endovascular treatment with flow diverters may fail to occlude experimental bifurcation aneurysms. *Neuroradiology* 2013;55:1355–63
- Becks T, Kallmes DF, Saatci I, et al. Pipeline for uncoilable or failed aneurysms: results from a multicenter clinical trial. *Radiology* 2013;267:858–68
- Brinjikji W, Murad MH, Lanzino G, et al. Endovascular treatment of intracranial aneurysms with flow diverters: a meta-analysis. *Stroke* 2013;44:442–47
- Arrese I, Sarabia R, Pintado R, et al. Flow-diverter devices for intracranial aneurysms: systematic review and meta-analysis. *Neurosurgery* 2013;73:193–99, discussion 199–200
- Briganti F, Napoli M, Tortora F, et al. Italian multicenter experience with flow-diverter devices for intracranial unruptured aneurysm treatment with periprocedural complications: a retrospective data analysis. *Neuroradiology* 2012;54:1145–52
- Lanzino G, Crobeddu E, Cloft HJ, et al. Efficacy and safety of flow diversion for paraclinoid aneurysms: a matched-pair analysis compared with standard endovascular approaches. *AJNR Am J Neuroradiol* 2012;33:2158–61
- Lylyk P, Miranda C, Ceratto R, et al. Curative endovascular reconstruction of cerebral aneurysms with the Pipeline embolization device: the Buenos Aires experience. *Neurosurgery* 2009;64:632–42
- Fischer S, Vajda Z, Aguilar Perez M, et al. Pipeline embolization device (PED) for neurovascular reconstruction: initial experience in the treatment of 101 intracranial aneurysms and dissections. *Neuroradiology* 2012;54:369–82
- Szikora I, Berentei Z, Kulcsar Z, et al. Treatment of intracranial aneurysms by functional reconstruction of the parent artery: the Budapest experience with the Pipeline embolization device. *AJNR Am J Neuroradiol* 2010;31:1139–47
- McAuliffe W, Wycoco V, Rice H, et al. Immediate and midterm results following treatment of unruptured intracranial aneurysms with the Pipeline embolization device. *AJNR Am J Neuroradiol* 2012;33:164–70
- O'Kelly CJ, Spears J, Chow M, et al. Canadian experience with the Pipeline embolization device for repair of unruptured intracranial aneurysms. *AJNR Am J Neuroradiol* 2013;34:381–87
- Byrne JV, Beltechi R, Yarnold JA, et al. Early experience in the treatment of intracranial aneurysms by endovascular flow diversion: a multicentre prospective study. *PLoS One* 2010;5:e12492
- Velioglu M, Kizilkilic O, Selcuk H, et al. Early and midterm results of complex cerebral aneurysms treated with Silk stent. *Neuroradiology* 2012;54:1355–65
- Lubicz B, Collignon L, Raphaeli G, et al. Flow-diverter stent for the endovascular treatment of intracranial aneurysms: a prospective study in 29 patients with 34 aneurysms. *Stroke* 2010;41:2247–53
- Siddiqui AH, Abla AA, Kan P, et al. Panacea or problem: flow diverters in the treatment of symptomatic large or giant fusiform vertebral basilar aneurysms. *J Neurosurg* 2012;116:1258–66
- Shapiro M, Becks T, Sahlein D, et al. Stent-supported aneurysm coiling: a literature survey of treatment and follow-up. *AJNR Am J Neuroradiol* 2012;33:159–63
- Standhardt H, Boecher-Schwarz H, Gruber A, et al. Endovascular treatment of unruptured intracranial aneurysms with Guglielmi detachable coils: short- and long-term results of a single-centre series. *Stroke* 2008;39:899–904
- Santillan A, Greenberg E, Patsalides A, et al. Long-term clinical and angiographic results of Neuroform stent-assisted coil embolization

- in wide-necked intracranial aneurysms. *Neurosurgery* 2012;70:1232–37, discussion 1237
30. Wakhloo AK, Linfante I, Silva CF, et al. **Closed-cell stent for coil embolization of intracranial aneurysms: clinical and angiographic results.** *AJNR Am J Neuroradiol* 2012;33:1651–56
 31. Starke RM, Durst CR, Evans A, et al. **Endovascular treatment of unruptured wide-necked intracranial aneurysms: comparison of dual microcatheter technique and stent-assisted coil embolization.** *J Neurointerv Surg* 2014 Mar 25. [Epub ahead of print]
 32. Wang K, Sun Y, Li AM. **Peri-procedural morbidity and mortality associated with stent-assisted coiling for intracranial aneurysms.** *Interv Neuroradiol* 2013;19:43–48
 33. Hwang SK, Hwang G, Bang JS, et al. **Endovascular Enterprise stent-assisted coil embolization for wide-necked unruptured intracranial aneurysms.** *J Clin Neurosci* 2013;20:1276–79
 34. Kim SR, Vora N, Jovin TG, et al. **Anatomic results and complications of stent-assisted coil embolization of intracranial aneurysms.** *Interv Neuroradiol* 2008;14:267–84

International Retrospective Study of the Pipeline Embolization Device: A Multicenter Aneurysm Treatment Study

D.F. Kallmes, R. Hanel, D. Lopes, E. Boccardi, A. Bonafé, S. Cekirge, D. Fiorella, P. Jabbour, E. Levy, C. McDougall, A. Siddiqui, I. Szikora, H. Woo, F. Albuquerque, H. Bozorgchami, S.R. Dashti, J.E. Delgado Almandoz, M.E. Kelly, R. Turner IV, B.K. Woodward, W. Brinjikji, G. Lanzino, and P. Lylyk



ABSTRACT

BACKGROUND AND PURPOSE: Flow diverters are increasingly used in the endovascular treatment of intracranial aneurysms. Our aim was to determine neurologic complication rates following Pipeline Embolization Device placement for intracranial aneurysm treatment in a real-world setting.

MATERIALS AND METHODS: We retrospectively evaluated all patients with intracranial aneurysms treated with the Pipeline Embolization Device between July 2008 and February 2013 in 17 centers worldwide. We defined 4 subgroups: internal carotid artery aneurysms of ≥ 10 mm, ICA aneurysms of < 10 mm, other anterior circulation aneurysms, and posterior circulation aneurysms. Neurologic complications included spontaneous rupture, intracranial hemorrhage, ischemic stroke, permanent cranial neuropathy, and mortality. Comparisons were made with *t* tests or ANOVAs for continuous variables and the Pearson χ^2 or Fisher exact test for categorical variables.

RESULTS: In total, 793 patients with 906 aneurysms were included. The neurologic morbidity and mortality rate was 8.4% (67/793), highest in the posterior circulation group (16.4%, 9/55) and lowest in the ICA < 10 -mm group (4.8%, 14/294) ($P = .01$). The spontaneous rupture rate was 0.6% (5/793). The intracranial hemorrhage rate was 2.4% (19/793). Ischemic stroke rates were 4.7% (37/793), highest in patients with posterior circulation aneurysms (7.3%, 4/55) and lowest in the ICA < 10 -mm group (2.7%, 8/294) ($P = .16$). Neurologic mortality was 3.8% (30/793), highest in the posterior circulation group (10.9%, 6/55) and lowest in the anterior circulation ICA < 10 -mm group (1.4%, 4/294) ($P < .01$).

CONCLUSIONS: Aneurysm treatment with the Pipeline Embolization Device is associated with the lowest complication rates when used to treat small ICA aneurysms. Procedure-related morbidity and mortality are higher in the treatment of posterior circulation and giant aneurysms.

ABBREVIATIONS: IntrePED = International Retrospective Study of Pipeline Embolization Device; IPH = intraparenchymal hemorrhage; PED = Pipeline Embolization Device

Endoluminal flow-diverter therapy has gained widespread acceptance for the treatment of intracranial aneurysms.¹⁻⁴ High rates of complete aneurysm occlusion have been reported, even in

large and giant aneurysms, with the use of endoluminal flow diverters.¹⁻⁷ The Pipeline Embolization Device (PED; Covidien, Irvine, California) received CE mark approval in 2008 for the embolization of cerebral aneurysms and received US FDA approval in 2011 (PMA P100018) for the treatment of large and giant wide-neck aneurysms in the internal carotid artery, from the petrous to the superior hypophyseal segments. While numerous previous studies have reported overall rates of adverse events similar to

Received March 27, 2014; accepted after revision June 23.

From the Department of Radiology (D.F.K., W.B., G.L.), Mayo Clinic, Rochester, Minnesota; Department of Neurosurgery (R.H.), Mayo Clinic, Jacksonville, Florida; Department of Neurological Surgery (D.L.), Rush University Medical Center, Chicago, Illinois; Department of Neuroradiology (E.B.), Niguarda CA' Granda Hospital, Milan, Italy; Department of Neuroradiology (A.B.), Hôpital Gui de Chauliac, Montpellier, France; Department of Radiology (S.C.), Hacettepe University Hospitals, Ankara, Turkey; Department of Neurological Surgery (D.F., H.W.), Stony Brook University Medical Center, Stony Brook, New York; Department of Neurosurgery (P.J.), Thomas Jefferson University, Philadelphia, Pennsylvania; Department of Neurosurgery (E.L., A.S.), University at Buffalo, State University of New York, Buffalo, New York; Department of Neurosurgery (C.M., F.A.), Barrow Neurological Associates, Phoenix, Arizona; National Institute of Neurosciences (I.S.), Budapest, Hungary; Department of Neurology (H.B.), Oregon Health and Science University, Portland, Oregon; Norton Neuroscience Institute (S.R.D.), Louisville, Kentucky; Department of Radiology (J.E.D.A.), Neuroscience Institute, Abbott Northwestern Hospital, Minneapolis, Minnesota; Division of Neurosurgery, Department of Surgery (M.E.K.), University of Saskatchewan, Saskatoon, Saskatchewan, Canada;

Department of Neurosciences (R.T.), Medical University of South Carolina, Charleston, South Carolina; Vista Radiology PC (B.K.W.), Knoxville, Tennessee; and Department of Neuroscience (P.L.), Equipo de Neurocirugía Endovascular Radiología Intervencionista, Buenos Aires, Argentina.

Preliminary results of this study previously presented at: Annual Meeting of the Society of NeuroInterventional Surgery, July 29–August 1, 2013; Miami, Florida.

Please address correspondence to David Kallmes, MD, Mayo Clinic, 200 First St SW, OLI-112 SMH, Rochester, MN 55905; e-mail: Kallmes.david@mayo.edu

Indicates article with supplemental on-line appendix.

<http://dx.doi.org/10.3174/ajnr.A4111>

those in other endovascular procedures, case reports and small case series documenting severe and “unexpected” complications have raised questions about the safety of these devices.^{1,3,8,9} Severe and unexpected adverse events include spontaneous rupture of treated aneurysms and intraparenchymal intracranial hemorrhage unrelated to aneurysm rupture.^{8,10-12} These reports led to policies in some regions mandating concomitant coil embolization with flow-diverter therapy to mitigate the risk of spontaneous aneurysm rupture.¹³

Most previous literature on flow-diversion therapy comprised single-center case series, either retrospective or prospective, and has substantial selection bias, which may affect the rates of severe and unexpected adverse events. These biases may be diminished through pooling of consecutive patients treated at multiple centers in a “real-world” setting, with homogeneous end points and methods of data analysis. The International Retrospective Study of Pipeline Embolization Device (IntrePED) registry was designed for this purpose and to determine rates of important neurologic safety events following PED placement for intracranial aneurysm treatment.

MATERIALS AND METHODS

Study Design and Participants

We retrospectively evaluated all patients with intracranial aneurysms treated with the Pipeline Embolization Device between July 2008 and February 2013 in 6 countries in 17 centers experienced in PED use. Local institutional review boards or ethics committees approved the study and use of patients’ retrospective data. An institutional review board/ethics committee waiver of informed consent (and Health Insurance Portability and Accountability Act Waiver of Authorization for US sites) or a sponsor institutional review board/ethics committee–approved informed consent form was obtained from each participating site. Written informed consent was obtained from each patient, if required. This observational registry was funded and supported by Covidien, with scientific oversight of the study steering committee members. Physicians who contributed data for this study were endovascular-trained neurointerventionalists. Each site that participated was required to have at least 1 physician who had treated a minimum of 10 PED cases before the time of institutional review board/ethics committee approval for the study. Unless an investigator had been a participant in a clinical study before commercialization of the PED, this study captures the investigators’ experience as new users of the device. A majority of the 26 IntrePED physicians were new users, and their early cases were included in the registry.

Data were collected from the time of the first commercial use of PED at a site until the time of institutional review board/ethics committee approval of the study protocol for that site. Investigational centers were required to provide data on all consecutive patients to eliminate selection bias, provided that the patients fulfilled the following conditions: 1) received PED treatment for an intracranial aneurysm after the date of regulatory approval in that region or country, and 2) had a clinical evaluation following treatment during the window of time before institutional review board/ethics committee approval. Because this was a retrospective study, there were no patients lost to follow-up.

Seven hundred ninety-three patients treated for 906 aneurysms were enrolled. Many patients (38%) had been previously reported in the literature.¹⁴⁻²⁹ We defined 4 primary anatomic/size subgroups: internal carotid artery aneurysms ≥ 10 mm (“large ICA”), ICA aneurysms of <10 mm (“small ICA”), other anterior circulation aneurysms (“other anterior”), and posterior circulation aneurysms.

Procedures

Because this was a retrospective study, procedural details and periprocedural patient management varied across centers. All centers used a common study protocol that specified the data to be collected, study end points, events of interest, and statistical analyses. The Steering Committee defined neurologic “clinical safety events of interest” a priori, including spontaneous rupture of the target aneurysm causing subarachnoid hemorrhage or cavernous carotid fistula, intraparenchymal hemorrhage (IPH) (both ipsilateral and contralateral), ischemic stroke, parent artery stenosis, and permanent cranial neuropathy. Site investigators identified events of interest according to the study protocol through retrospective review of the patient’s record. All events of interest were reviewed in detail by an Adverse Events Review Committee, comprising of 3 members of the Steering Committee, including the overall study principal investigator. The committee determined the category of event and whether the event was major or minor. A “major” adverse event was defined as an ongoing clinical deficit at 7 days following the event. “Minor” adverse events were defined as events that resolved within 7 days with no clinical sequelae. All major adverse events are included in the neurologic morbidity and mortality rates. Long-term neurologic morbidity and mortality rates included morbidity and mortality due to adverse events occurring any time in the postoperative period (<30 days and ≥ 30 days). Information collected during the study was standardized across centers and included baseline characteristics of patients and aneurysms, procedural information, prespecified clinical safety events of interest, and follow-up clinic visits or telephone calls. A list of data collected for each patient/aneurysm is provided in the On-line Appendix. Because this was a retrospective study, the timing of the patient follow-up evaluations was conducted per institution standard of care.

Statistical Analysis

Statistical analyses were performed by using SAS, Version 9.1 or higher (SAS Institute, Cary, North Carolina). Summary statistics are presented for all data available by using means and SDs for continuous variables and frequency tabulations for categorical variables. Comparisons between groups for continuous variables were evaluated by using *t* tests or ANOVAs and the Fisher exact test or Pearson χ^2 for binary categorical variables. Most statistical analyses were performed across patient groups—that is, on a per-patient basis. Because some patients had >1 aneurysm treated with a PED, however, each patient’s first aneurysm was used to classify patients into the 4 anatomic/size subgroups, and the largest aneurysm was used to classify patients into the 3 aneurysm size categories. Some analyses, including aneurysm characteristics and spontaneous ruptures across aneurysm-size groups, were performed across all aneurysms rather than across patients.

Table 1: Aneurysm characteristics

Aneurysm Characteristics	Anterior ICA ≥10 mm (n = 311)	Anterior <10 mm (n = 349)	Posterior (n = 59)	Other Anterior ≥10 mm (n = 178)	Total (n = 896) ^a	P Value
Aneurysm size (mm)						
Mean ± SD	16.8 ± 6.2	5.2 ± 2.2	14.5 ± 9.0	9.8 ± 7.9	10.7 ± 7.7	<.001
Median, range	15.0, 10.0–42.0	5.0, 1.0–9.9	11.8, 1.7–45.0	7.2, 1.0–55.0	9.0, 1.0–55.0	
Aneurysm type						
Small	0	349/349 (100%)	19/58 (32.8%)	105/178 (59.0%)	473/897 (52.8%)	
Large	268/311 (86.2%)	0	29/58 (50.0%)	60/178 (33.7%)	357/897 (39.8%)	
Giant	43/311 (13.8%)	0	10/58 (17.2%)	13/178 (7.3%)	66/897 (7.3%)	
Aneurysm neck (mm)						
Mean ± SD	8.5 ± 5.1	4.1 ± 2.2	9.3 ± 8.4	5.3 ± 5.1	6.2 ± 4.9	<.001
Median, range	7.6, 0.9–50.0	4.0, 0.8–22.0	8.0, 1.7–53.0	4.0, 1.0–50.0	5.0, 0.8–53.0	
Aneurysm shape						
Fusiform	49/311 (15.8%)	17/349 (4.9%)	17/59 (28.8%)	29/178 (16.3%)	112/897 (12.5%)	<.001
Saccular	239/311 (76.9%)	305/349 (87.4%)	25/59 (42.4%)	118/178 (66.3%)	686/897 (76.5%)	
Dissecting	10/311 (3.2%)	8/349 (2.3%)	13/59 (22.0%)	22/178 (12.4%)	53/897 (5.9%)	
Other	13/311 (4.2%)	19/349 (5.4%)	4/59 (6.8%)	9/178 (5.1%)	46/897 (5.1%)	
Aneurysm location						
Internal carotid artery	311/311 (100%)	349/349 (100%)	0	0	660/897 (73.6%)	<.001
Middle cerebral artery	0	0	0	43/178 (24.2%)	43/897 (4.8%)	
Posterior cerebral artery	0	0	15/59 (25.4%)	0	15/897 (1.7%)	
Basilar artery	0	0	44/59 (74.6%)	0	44/897 (4.9%)	
Other	0	0	0	135/178 (75.8%)	135/897 (15.1%)	
Presented with ruptured aneurysm	12/311 (3.9%)	24/345 (7.0%)	4/59 (6.8%)	34/176 (19.3%)	74/891 (8.2%)	<.001
Multiple PEDs used	143/311 (46.0%)	97/347 (28.0%)	19/59 (32.2%)	47/178 (26.4%)	306/895 (34.2%)	<.001

Note:—n indicates the number of aneurysms.

^a Aneurysm size was not reported for 10 aneurysms.

Role of the Funding Source

An academic principal investigator and an academic steering committee supervised the trial design and operations. The steering committee interpreted the results, and the principal investigator wrote the report. The study sponsor was responsible for site management, data management, statistical analysis, and safety reporting. The corresponding author was the academic principal investigator for the study and had full access to all study data and the final responsibility for the decision to submit for publication.

RESULTS

Seven hundred ninety-three patients with 906 aneurysms (76 [8.4%] ruptured, 824 [91%] unruptured, and 6 [0.7%] unknown) were included. Three hundred eleven aneurysms (34.3%) were ICA ≥10 mm, 349 aneurysms (38.5%) were ICA <10 mm, 59 aneurysms (6.5%) were in the posterior circulation, and 178 aneurysms (19.6%) were ≥10 mm and located in anterior circulation locations other than the ICA. Combined location/size information was not available for 9 aneurysms. Posterior circulation aneurysms were generally large, with an average size of 14.5 ± 9.0 mm. Patients with non-ICA anterior circulation aneurysms presented with aneurysm rupture in 19.3% of cases (34/176), a significantly higher rate than that in the other groups (*P* < .001). Four hundred seventy-three aneurysms (52.8%) were small, 357 aneurysms (39.8%) were large, and 66 aneurysms (7.3%) were giant. Median follow-up was 19.3 months with 706 (89%) patients having follow-up of >12 months. Size information was not available for 10 aneurysms.

Multiple PEDs were used in 308 cases (34.2%). Patients with ICA aneurysms ≥10 mm had the highest rate of multiple PED use (46.0%, 143/311) and were significantly more likely to receive treatment with multiple PEDs compared with the other groups (*P* < .001). Mean procedure time was 101 minutes 30 seconds ±

50 minutes 30 seconds and was highest in the ICA aneurysms ≥10-mm group (111 minutes 24 seconds ± 56 minutes 36 seconds) (*P* < .01). Aneurysm data are summarized in Table 1.

The 30-day morbidity and mortality rate was 6.3% (50/793) with a 30-day neurologic morbidity rate of 5.7% (44/793) and a 30-day neurologic mortality rate of 2.6% (21/793). The long-term neurologic morbidity and mortality rate was 8.4% (67/793) with a neurologic morbidity rate of 7.4% (59/793) and a neurologic mortality rate of 3.8% (30/793). Individual morbidity and mortality rates did not add up to the total combined morbidity and mortality rate because some patients had >1 neurologic morbidity. The morbidity and mortality rates were highest in the posterior circulation group (16.4%, 9/55) and lowest in the ICA <10 mm group (4.8%, 14/294). The morbidity and mortality rates were higher in patients with giant aneurysms compared with those with large and small aneurysms (25.8% versus 8.8% versus 5.4%, *P* < .01). When patients with ruptured, dissecting, or fusiform aneurysms were excluded, the overall morbidity and mortality rate was 5.7%.

The spontaneous rupture rate was 0.6% (5/793), with 2 of the 5 events being cavernous carotid fistulas with clinical sequelae. Four of the 5 cases occurred within 30 days. There was no difference in the spontaneous rupture rate among the 4 groups (*P* = .17). Spontaneous rupture was higher in giant aneurysms (4.5%, 3/66) compared with large (0.6%, 2/357) and small aneurysms (0.0%, 0/473) (*P* < .001). Overall the intraparenchymal hemorrhage rate was 2.4% (19/793). There was no difference in the hemorrhage rate among the primary patient subgroups (*P* = .73) or among aneurysm sizes (*P* = .24). Fifteen (79%) of the 19 hemorrhages occurred within 30 days of the procedure.

The ischemic stroke rate was 4.7% (37/793). A majority of strokes occurred within 30 days of treatment (26/793, 3.3%). The

Table 2: Complications by aneurysm location and size subgroups

Complications	Anterior ICA ≥10 mm (n = 275)	Anterior ICA <10 mm (n = 294)	Posterior (n = 55)	Other Anterior (n = 165)	Total (n = 793) ^a	95% CI; P Value
Mean aneurysm size (mm)	16.8 ± 6.2	5.2 ± 2.2	14.5 ± 9.0	9.8 ± 7.9	10.7 ± 7.7	(10.2–11.2); <.001
Spontaneous rupture	4 (0.7%)	0 (0.0%)	0 (0.0%)	1 (0.6%)	5 (0.6%)	(0.2%–1.5%); .17
Intraparenchymal hemorrhage	6 (2.2%)	6 (2.0%)	1 (1.8%)	6 (3.6%)	19 (2.4%)	(1.3%–3.4%); .73
Ischemic stroke	15 (5.5%)	8 (2.7%)	4 (7.3%)	10 (6.1%)	37 (4.7%)	(3.2%–6.2%); .16
Parent artery stenosis	1 (0.4%)	1 (0.4%)	0 (0.0%)	0 (0.0%)	2 (0.3%)	(0%–0.7%); 1.0
Cranial neuropathy	2 (0.7%)	0 (0.0%)	0 (0.0%)	0 (0.0%)	2 (0.3%)	(0%–0.7%); .30
Neurologic morbidity	24 (8.7%)	14 (4.5%)	5 (9.1%)	16 (9.7%)	59 (7.4%)	(5.6%–9.2%); .16
Neurologic mortality	11 (4.0%)	4 (1.4%)	6 (10.9%)	9 (5.5%)	30 (3.8%)	(2.5%–5.1%); <.01
Neurologic morbidity and mortality (all patients)	26 (9.5%)	14 (4.8%)	9 (16.4%)	18 (10.9%)	67 (8.4%)	(6.5%–10.3%); .01
Neurologic morbidity and mortality (patients with unruptured aneurysms)	24/263 (9.2%)	11/270 (4.1%)	7/51 (13.7%)	11/131 (8.4%)	53/717 (7.4%)	(5.5%–9.3%); .03
Neurologic morbidity and mortality (patients with ruptured aneurysms)	2/12 (16.7%)	3/24 (12.5%)	2/4 (50.0%)	7/34 (20.6%)	14/76 (18.4%)	(10.0%–27.1%); .35
Neurologic morbidity and mortality (excluding ruptured, dissecting, or fusiform aneurysms)	15 (7.0%)	9 (3.6%)	3 (12.0%)	6 (6.8%)	33 (5.7%)	(4.1%–7.3%); .19

Note:—*n* indicates the number of patients.

^a Numbers do not sum across categories and subcategories because some patients experienced >1 event.

Table 3: Occurrence of complications by time

Complications	<72 Hours		72 Hours–30 Days		>30 Days		Total (n = 793) ^a	P Value
	Anterior (n = 738)	Posterior (n = 55)	Anterior (n = 738)	Posterior (n = 55)	Anterior (n = 738)	Posterior (n = 55)		
Spontaneous rupture	1 (0.1%)	0 (0%)	3 (0.4%)	0 (0%)	1 (0.1%)	0 (0%)	5 (0.6%)	.51
Intraparenchymal hemorrhage	3 (0.4%)	1 (1.8%)	11 (1.5%)	0 (0%)	4 (0.5%)	0 (0%)	19 (2.4%)	.83
Ischemic stroke	17 (2.3%)	2 (3.6%)	7 (0.9%)	0 (0%)	9 (1.2%)	2 (3.6%)	37 (4.7%)	.58
Parent artery stenosis	0 (0%)	0 (0%)	1 (0.1%)	0 (0%)	1 (0.1%)	0 (0%)	2 (0.3%)	.63
Cranial neuropathy	0 (0%)	0 (0%)	2 (0.3%)	0 (0%)	0 (0%)	0 (0%)	2 (0.3%)	.58
Neurologic morbidity	20 (2.7%)	3 (5.5%)	21 (2.8%)	0 (0%)	13 (1.8%)	2 (3.6%)	59 (7.4%)	.56
Neurologic mortality	4 (0.5%)	1 (1.8%)	13 (1.8%)	2 (3.6%)	7 (0.9%)	3 (5.5%)	30 (3.8%)	<.01
Neurologic morbidity and mortality (all patients)	23 (3.1%)	3 (5.5%)	22 (3.0%)	2 (3.6%)	13 (1.8%)	4 (7.3%)	67 (8.4%)	<.01
Neurologic morbidity and mortality (patients with unruptured aneurysms)	19/664 (2.9%)	3/51 (5.9%)	16/664 (2.4%)	1/51 (2.0%)	11/664 (1.7%)	3/51 (5.9%)	53/717 (7.4%)	.08
Neurologic morbidity and mortality (patients with ruptured aneurysms)	4/70 (5.7%)	0/4 (0%)	6/70 (8.6%)	1/4 (25.0%)	2/70 (2.9%)	1/4 (25.0%)	14/76 (18.4%)	.17
Neurologic morbidity and mortality (excluding ruptured, dissecting, or fusiform aneurysms)	13/549 (2.4%)	1/25 (4.0%)	12/549 (2.2%)	0/25 (0%)	5/549 (0.9%)	2/25 (8.0%)	33/575 (5.7%)	.41

Note:—*n* indicates the number of patients.

^a Numbers do not sum across categories and subcategories because some patients experienced >1 event.

highest stroke rates were seen in patients with posterior circulation aneurysms (7.3%, 4/55) and the “other anterior circulation” group (6.1%, 10/165). The anterior circulation ICA <10-mm group had the lowest stroke rates (2.7%, 8/294) (*P* = .16). When studying differences based on aneurysm size, patients with giant aneurysms had the highest stroke rates (14.5%, 9/62) compared with patients with large (5.0%, 17/339) and small aneurysms (2.8%, 11/386) (*P* < .01).

In-stent stenosis occurred in 0.3% (2/793) with no significant differences among groups (*P* = 1.0). Permanent cranial neuropathy occurred in 0.3% (2/793) of patients with no significant differences among groups (*P* = .30). These data are summarized in Tables 2–4.

Neurologic mortality was 3.8% (30/793) and was significantly different among the 4 primary patient subgroups (*P* < .01). The 30-day mortality rate was 2.5% (20/793), which represented nearly two-thirds of all mortality observed in the average 19.3 months of follow-up. Patients with posterior circulation aneurysms had the highest rate of neurologic mortality (10.9%, 6/55), and patients with anterior ICA <10-mm aneurysms had the low-

est neurologic mortality (1.4%, 4/294). The mortality rate was significantly higher in patients with giant aneurysms compared with those with large and small aneurysms, respectively (9.6% versus 5.0% versus 1.8%, *P* < .01). The overall mortality rate in patients who presented with ruptured aneurysms was 10.5% (8/76), with no significant differences among groups (*P* = .11). These data are summarized in Tables 2–4.

In addition to the above-listed major events, 5 cases of intracranial hemorrhage, 15 cases of ischemic strokes, and 5 cases of parent artery stenosis were also observed as minor events in which the patient’s symptoms resolved within 7 days of the event occurrence with no clinical sequelae. Three additional deaths were reported due to non-neurologic reasons.

DISCUSSION

This large multicenter study of flow-diversion therapy demonstrated a neurologic morbidity and mortality rate of 8.4%. Most adverse events were ischemic strokes from thromboembolic complications and were substantially more common in large, anterior circulation aneurysms and posterior circulation aneurysms com-

Table 4: Complications by aneurysm size

Complications	Small (n = 386) (N = 473)		Large (n = 339) (N = 357)		Giant (n = 62) (N = 66)		Total (n = 793) ^{a,b} (N = 906)	P Value
	Anterior (n = 372)	Posterior (n = 14)	Anterior (n = 309)	Posterior (n = 30)	Anterior (n = 52)	Posterior (n = 10)		
Mean aneurysm size (mm)	5.1 ± 2.2	6.0 ± 2.6	14.8 ± 4.0	15.0 ± 4.3	28.8 ± 5.3	29.1 ± 7.2	10.7 ± 7.7	<.001
Spontaneous rupture	0 (0%)	0 (0%)	2 (0.5%)	0 (0%)	3 (5.8%)	0 (0%)	5 (0.6%)	<.01
Intraparenchymal hemorrhage	7 (1.9%)	0 (0%)	8 (2.6%)	0 (0%)	3 (5.8%)	1 (10.0%)	19 (2.4%)	.24
Ischemic stroke	10 (2.7%)	1 (7.1%)	16 (5.2%)	1 (3.3%)	7 (13.5%)	2 (20.0%)	37 (4.7%)	<.01
Parent artery stenosis	1 (0.3%)	0 (0%)	1 (0.3%)	0 (0%)	0 (0%)	0 (0%)	2 (0.3%)	1.0
Cranial neuropathy	0 (0%)	0 (0%)	2 (0.6%)	0 (0%)	0 (0%)	0 (0%)	2 (0.3%)	.41
Neurologic morbidity	18 (4.8%)	1 (7.1%)	24 (7.8%)	1 (3.3%)	12 (23.1%)	3 (30.0%)	59 (7.4%)	<.01
Neurologic mortality	6 (1.6%)	1 (7.1%)	15 (4.9%)	2 (6.7%)	3 (5.8%)	3 (30.0%)	30 (3.8%)	<.01
Neurologic morbidity and mortality ^a (all patients)	19 (5.1%)	2 (14.3%)	27 (8.7%)	3 (10.0%)	12 (23.1%)	4 (40.0%)	67 (8.4%)	<.01
Neurologic morbidity and mortality (patients with unruptured aneurysms)	11/321 (3.4%)	1/12 (8.3%)	23/291 (7.9%)	3/29 (10.3%)	12/51 (23.5%)	3/9 (33.3%)	53/717 (7.4%)	<.01
Neurologic morbidity and mortality (patients with ruptured aneurysms)	8/51 (15.7%)	1/2 (50.0%)	4/18 (22.2%)	0/1 (0%)	0/1 (0%)	1/1 (100%)	14/76 (18.4%)	.23
Neurologic morbidity and mortality (excluding ruptured, dissecting, or fusiform aneurysms)	11/294 (3.7%)	0/7 (0%)	12/217 (5.5%)	2/13 (15.4%)	7/37 (18.9%)	1/5 (20.0%)	33/574 (5.7%)	<.01

Note:—n indicates the number of patients; N, number of aneurysms.

^a Six patients did not have aneurysm size reported.

^b Numbers do not sum across categories because some patients experienced >1 event.

pared with small, anterior circulation aneurysms. Spontaneous aneurysm rupture was rare, occurring in 0.6% of patients, with 3/5 events occurring within giant aneurysms. Intraparenchymal hemorrhage, unrelated to rupture of the target aneurysm but resulting in major neurologic deficit, was noted in 2.4% of patients. These results are important because they provide clarity regarding the previously noted severe and unexpected adverse events associated with flow-diversion therapy in a real-world setting. Our data suggest strongly that spontaneous aneurysm rupture is not of clinical concern in non-giant aneurysms. Parenchymal hemorrhage remains of concern, especially because its etiology is unclear.

Our findings corroborate those of numerous previously published smaller studies and meta-analyses. Previously published studies have demonstrated morbidity and mortality rates ranging from 0%–12% and 0%–7%, respectively.^{30–32} Two large meta-analyses of flow-diverter treatment demonstrated morbidity rates of 5.0%–7.3% and mortality rates of 2.8%–4.0%.^{1,3} Our study, which is the largest clinical study of PED to date to our knowledge, demonstrated a 30-day morbidity rate of 5.5% (44/793) and a 30-day mortality rate of 2.5% (20/793).

Posttreatment aneurysm rupture is a serious concern of flow-diverter therapy. Concerns for postoperative aneurysm rupture with flow diverters are so serious that Balt Extrusion issued a medical device alert instructing practitioners not to use the Silk flow diverter (Balt Extrusion, Montmorency, France) without coils due to the “potential for patient death.”¹³ In their meta-analysis of flow-diverter treatment, which included the PED and Silk flow-diverter devices, Brinjikji et al³ found an overall postoperative rupture rate of 4%, with an early rupture rate of 3% with a significantly higher rupture rate in large and giant aneurysms. Our study demonstrated a posttreatment rupture rate of <1%, 3/5 occurring among patients with giant aneurysms. While postoperative rupture rates are minimal in patients with small and large aneurysms, postoperative rupture remains a real and significant complication of Pipeline treatment in patients with giant aneurysms.

Spontaneous IPH is a poorly understood complication of

flow-diverter treatment. Hemorrhagic transformation of ischemic stroke, hemodynamic alteration from flow-diverter placement, dual antiplatelet therapy, potential association with intraprocedural foreign body emboli, and the significant role of P2Y12 receptor overinhibition are proposed mechanisms.^{8,14,15,33} Prior studies have reported rates ranging from 0% to 10% for this complication.^{8,30,34,35} In their meta-analysis, Brinjikji et al³ found an IPH rate of 3.0%. Arrese et al¹ found a postoperative hemorrhage rate of 1.8%, not stratifying by SAH and IPH. Our study found an IPH rate of 2.4%. Similar to prior studies, our study found no difference in IPH rates by aneurysm size or location.³

Ischemic strokes due to thromboembolism and perforator infarctions are well-described complications of flow-diverter treatment. Ischemic stroke may result from stent wall thrombus formation and occlusion, parent artery occlusion, or distal thromboembolic events. Our study found an ischemic stroke rate of 4.7%, with higher rates in posterior circulation aneurysms compared with the ICA aneurysm <10-mm group (7.3% versus 2.7%).^{1,3,9,36} Similar to Brinjikji et al,³ we also found that the stroke rate increased with aneurysm size as patients with large and giant aneurysms had higher stroke rates than those with small aneurysms. Intraoperatively, acute thrombus formation can be mitigated by prompt injection of glycoprotein IIb/IIIa platelet inhibitors; however, it is difficult to reduce the long-term risk of thromboembolic events associated with flow-diverter treatment.³⁷

Endosaccular coiling (with or without stent assistance) is an alternative to flow-diverter therapy. A systematic review of stent-assisted coiling by McLaughlin et al³⁸ found an intraprocedural complication rate of 4.0%, a postprocedural thromboembolic event rate of 4.3%, and a delayed in-stent stenosis rate of 5.3%. These complication rates are similar to the findings of our study on the PED. In a study of stent-assisted coiling in patients with subarachnoid hemorrhage, Bodily et al³⁹ found a clinically significant thromboembolic event rate of 6%. A meta-analysis by Shapiro et al⁴⁰ found that the overall procedural complication rate associated with stent coiling was 19%, the thromboembolic complication rate was 10%, and the periprocedural mortality was

2.1%. In the Neuroform stent (Stryker Neurovascular, Kalamazoo, Michigan) experience in 284 patients, Fiorella et al⁴¹ reported a cumulative ischemic stroke rate of 8.8% and a 2.8% neurovascular death rate. They also reported that 15.1% of the cases had major recanalization requiring retreatment. Piotin et al⁴² reported results on the treatment of aneurysms with coils, with and without stents, in 1137 patients. The rate of permanent neurologic procedure-related complications was 7.4% of the procedures with stents versus 3.8% in the procedures without stents ($P = .64$). Procedure-induced mortality occurred in 4.6% of the procedures with stents versus 1.2% in the procedures without stents ($P = .006$). The rate of thrombotic complications in the stent group was 14.8%, accounting for 11.1% of mortalities.⁴² Retrospective studies comparing flow diversion with the PED with coiling (with and without stent assistance) have demonstrated that the PED provides higher aneurysm occlusion rates with similar morbidity and mortality rates.^{23,43} In our study, anterior circulation aneurysms measuring <10 mm had the lowest neurologic morbidity and mortality rates (4.8%). These findings corroborate those of a previous study comparing the PED with stent-assisted coiling of patients with small, unruptured anterior circulation aneurysms, which demonstrated a complication rate of 5% in the PED group and 3% in the stent-assisted coiling group.⁴³ Given the wide range of treatment options available for the endovascular treatment of intracranial aneurysms, careful study and stratification of outcomes by aneurysm location and size are recommended to determine the best treatment for each patient. Ultimately, further comparative studies, especially in the case of small ICA aneurysms, are needed to determine which subsets of intracranial aneurysms would benefit most from PED placement compared with endosaccular coiling.

Limitations

Our study has limitations. It was a retrospective study in which sites followed their standard of practice for treating aneurysms with PED, and there was a wide range of treatment regimens (eg, antiplatelet therapy) among centers. However, all study adverse events collected were prespecified in the study protocol and were adjudicated by the Adverse Events Review Committee to maintain consistency in the study results. Patients who underwent failed embolization or who did not have follow-up were excluded per the study design. There was no systematic imaging of patients required in this study because sites were required to follow their standard procedures. There was no protocol regarding the minimum duration of follow-up, and follow-up timing was per standard of care for the treating physician and institution. Another limitation of the study is that the reporting of major and minor complications was based on the duration of symptoms, not their severity or degree of disability. Information regarding management of the major and minor complications was not collected. A broad range of aneurysm types and sizes was included in this registry (ie, saccular/blister/ruptured/fusiform/dissecting), and subgroup analyses were not performed for the subset of blister/fusiform/dissecting aneurysms in this study. Last, 38% of these patients had been included in prior publications.

CONCLUSIONS

Our study suggests that the treatment of intracranial aneurysms with PED is associated with the lowest complication rates when used to treat small aneurysms of the ICA. The rates of procedural-related morbidity and mortality are not negligible. Patients with posterior circulation aneurysms and giant aneurysms are at higher risk of ischemic stroke. Patients with large or giant aneurysms are at higher risk of ischemic stroke and SAH compared with small aneurysms. The neurologic morbidity and mortality rate drops when patients with difficult-to-treat aneurysms (ruptured, dissecting, or fusiform) are excluded. The complication rates with PED are comparable with those of other endovascular treatment options such as stent-assisted coiling. These findings should be considered when selecting the best therapeutic option for intracranial aneurysms.

Disclosures: David F. Kallmes—*RELATED: Grant: ev3/Covidien,* Comments: funding for enrollment in clinical trial; Consulting Fee or Honorarium: ev3/Covidien,* Comments: funding for Principal Investigator duties, Steering Committee and Adverse Event Adjudication Committee; Grants/Grants Pending: MicroVention,* ev3/Covidien,* SurModics,* Codman,* Sequent Medical,* Benvenue Medical,* National Institutes of Health,* Comments: funding for preclinical research and clinical trials; Royalties: University of Virginia Patent Foundation, Comments: spinal fusion; Other: Radiological Society of North America. Comments: editorial support money to institution. Demetrius Lopes—*RELATED: Board Membership: Covidien (advisory board); Consultancy: Covidien; Grant: Covidien; Payment for Lectures (including service on Speakers Bureaus, papers, and teaching): Covidien; Other: Covidien (proctorship, advisory board). Edoardo Boccardi—RELATED: Consulting Fee or Honorarium: Covidien; Support for Travel to Meetings for the Study or Other Purposes: Covidien; UNRELATED: Consultancy: Covidien, Comments: consultation and proctoring. Saruhan Cekirge—RELATED: Consulting Fee or Honorarium: Covidien; UNRELATED: Consultancy: MicroVention, Covidien, Sequent. Pascal Jabbour—UNRELATED: Consultancy: Covidien. Cameron McDougall—RELATED: Consulting Fee or Honorarium: ev3/Covidien; Fees for Participation in Review Activities such as Data Monitoring Boards, Statistical Analysis, Endpoint Committees, and the Like: ev3/Covidien (steering committee, medical advisory board); UNRELATED: Board Membership: ev3/Covidien; Consultancy: MicroVention/Terumo, Codman/Johnson and Johnson; Personal Fees: MicroVention (principal investigator, FRED). Adnan Siddiqui—UNRELATED: Board Membership: Codman & Shurtleff, Covidien, Comments: advisory board; Consultancy: Codman & Shurtleff, Concentric Medical, ev3/Covidien, GuidePoint Global, Penumbra, Stryker, Pulsar Vascular, MicroVention, Lazarus Effect, Blockade Medical, Comments: no consulting salary arrangements; all consulting is per project and/or per hour; Grants/Grants Pending: National Institutes of Health (coinvestigator: National Institute of Neurological Disorders and Stroke 1R01NS064592-01A1, hemodynamic induction of pathologic remodeling leading to intracranial aneurysms)* University at Buffalo (Research Development Award)* National Institutes of Health (coinvestigator: National Institute of Biomedical Imaging and Bioengineering 5 R01 EB002873-07, Micro-Radiographic Image for Neurovascular Interventions)*; National Steering Committees: Penumbra (3D Separator Trial), Covidien (SWIFT PRIME Trial), MicroVention (FRED Trial); Payment for Lectures (including service on speakers bureaus): Codman & Shurtleff; Stock/Stock Options: Hotspur, Intratech Medical, StimSox, Valor Medical, Blockade Medical, Lazarus Effect; Other: Abbott Vascular, Penumbra, Abbott Vascular, and Codman & Shurtleff (for training other neurointerventionists in carotid stenting and for training physicians in endovascular stenting for aneurysms), Comments: honoraria. Henry Woo—RELATED: Other: Covidien,* Comments: startup costs for institutional review board submission and payment for enrolled patients; UNRELATED: Grants/Grants Pending: Siemens,* Comments: grants for clinical and academic research; Royalties: Codman & Shurtleff, Comments: royalties for development of intellectual property; Other: shareholder in Vascular Simulators. Britton K. Woodward—UNRELATED: Personal Fees: Covidien, Comments: consultant for proctoring of cases. Shervin R. Dashti—UNRELATED: Other: proctoring fees from Covidien, MicroVention. Jossier E. Delgado Almandoz—RELATED: Personal Fees: Covidien/ev3; UNRELATED: Personal Fee: Terumo/MicroVention. Istvan Szikora—RELATED: Grant: Covidien; Personal Fees: Covidien. Elad Levy—UNRELATED: Shareholder/Ownership Interest: Intratech Medical Ltd, Mynx Access Closure, Blockade Medical LLC. Alain Bonafé—UNRELATED: Personal Fees: Covidien (proctoring for PED). Michael E. Kelly—RELATED: Other: Covidien sponsored the IntrePED study, and all funds were paid to University of Saskatchewan. Raymond Turner—RELATED: Grants: Covidien, MicroVention, Codman, Blockade Medical, Reverse Medical; Personal Fees: Covidien, MicroVention, Codman, Blockade Medical, Pulsar Vascular. David Fiorella—UNRELATED: Grants: Siemens, MicroVention; Personal**

Fees: Covidien/ev3, Cordis, Nfocus Neuromedical, Micrus Endovascular, Comments: Consultant; Royalties: Codman & Shurtleff (Revive); Ownership Interests: Vascular Simulators LLC, TDC Technologies, CVSL. Giuseppe Lanzino—UNRELATED: Consultancy: Edge Therapeutics, Covidien/ev3, Codman, Pedro Lylyk—UNRELATED: Consultancy: ev3, MicroVention, Covidien, Codman; Payment for Lectures (including service on Speakers Bureaus): Covidien, MicroVention, Codman, Ricardo Hanel—RELATED: Grant: MicroVention; UNRELATED: Consultancy: Covidien, Codman, Stryker; Other: Blockade (shareholder). *Money paid to the institution.

REFERENCES

- Arrese I, Sarabia R, Pintado R, et al. **Flow-diverter devices for intracranial aneurysms: systematic review and meta-analysis.** *Neurosurgery* 2013;73:193–99; discussion 199–200
- Briganti F, Napoli M, Tortora F, et al. **Italian multicenter experience with flow-diverter devices for intracranial unruptured aneurysm treatment with periprocedural complications: a retrospective data analysis.** *Neuroradiology* 2012;54:1145–52
- Brinjikji W, Murad MH, Lanzino G, et al. **Endovascular treatment of intracranial aneurysms with flow diverters: a meta-analysis.** *Stroke* 2013;44:442–47
- Yu SC, Kwok CK, Cheng PW, et al. **Intracranial aneurysms: mid-term outcome of Pipeline embolization device: a prospective study in 143 patients with 178 aneurysms.** *Radiology* 2012;265:893–901
- Chan TT, Chan KY, Pang PK, et al. **Pipeline embolisation device for wide-necked internal carotid artery aneurysms in a hospital in Hong Kong: preliminary experience.** *Hong Kong Med J* 2011;17:398–404
- Cirillo L, Dall’Olio M, Princiotta C, et al. **The use of flow-diverting stents in the treatment of giant cerebral aneurysms: preliminary results.** *Neuroradiol J* 2010;23:220–24
- Siddiqui AH, Kan P, Abla AA, et al. **Complications after treatment with Pipeline embolization for giant distal intracranial aneurysms with or without coil embolization.** *Neurosurgery* 2012;71:E509–13; discussion E513
- Cruz JP, Chow M, O’Kelly C, et al. **Delayed ipsilateral parenchymal hemorrhage following flow diversion for the treatment of anterior circulation aneurysms.** *AJNR Am J Neuroradiol* 2012;33:603–08
- Pierot L. **Flow diverter stents in the treatment of intracranial aneurysms: where are we?** *J Neuroradiol* 2011;38:40–46
- Darsaut TE, Rayner-Hartley E, Makoyeva A, et al. **Aneurysm rupture after endovascular flow diversion: the possible role of persistent flows through the transition zone associated with device deformation.** *Interv Neuroradiol* 2013;19:180–85
- Kuzmik GA, Williamson T, Ediriwickrema A, et al. **Flow diverters and a tale of two aneurysms.** *J Neurointerv Surg* 2013;5:e23
- Turowski B, Macht S, Kulcsar Z, et al. **Early fatal hemorrhage after endovascular cerebral aneurysm treatment with a flow diverter (SILK-Stent): do we need to rethink our concepts?** *Neuroradiology* 2011;53:37–41
- Lubicz B, Collignon L, Raphaeli G, et al. **Flow-diverter stent for the endovascular treatment of intracranial aneurysms: a prospective study in 29 patients with 34 aneurysms.** *Stroke* 2010;41:2247–53
- Piano M, Valvassori L, Quilici L, et al. **Midterm and long-term follow-up of cerebral aneurysms treated with flow diverter devices: a single-center experience.** *J Neurosurg* 2013;118:408–16
- Delgado Almandoz JE, Crandall BM, Scholz JM, et al. **Pre-procedure P2Y12 reaction units value predicts perioperative thromboembolic and hemorrhagic complications in patients with cerebral aneurysms treated with the Pipeline embolization device.** *J Neurointerv Surg* 2013;5(suppl 3):iii3–10
- Delgado Almandoz JE, Crandall BM, Scholz JM, et al. **Last-recorded P2Y12 reaction units value is strongly associated with thromboembolic and hemorrhagic complications occurring up to 6 months after treatment in patients with cerebral aneurysms treated with the Pipeline embolization device.** *AJNR Am J Neuroradiol* 2014;35:128–35
- Hanel RA, Taussky P, Dixon T, et al. **Safety and efficacy of ticagrelor for neuroendovascular procedures: a single center initial experience.** *J Neurointerv Surg* 2014;6:320–22
- el-Chalouhi N, Jabbour PM, Tjoumakaris SI, et al. **Treatment of large and giant intracranial aneurysms: cost comparison of flow diversion and traditional embolization strategies.** *World Neurosurg* 2014;82:696–701
- Chalouhi N, McMahon JF, Moukartzel LA, et al. **Flow diversion versus traditional aneurysm embolization strategies: analysis of fluoroscopy and procedure times.** *J Neurointerv Surg* 2014;6:291–95
- Chalouhi N, Tjoumakaris S, Dumont AS, et al. **Treatment of posterior circulation aneurysms with the Pipeline embolization device.** *Neurosurgery* 2013;72:883–89
- Jabbour P, Chalouhi N, Tjoumakaris S, et al. **The Pipeline embolization device: learning curve and predictors of complications and aneurysm obliteration.** *Neurosurgery* 2013;73:113–20
- Chitale R, Gonzalez LF, Randazzo C, et al. **Single center experience with Pipeline stent: feasibility, technique, and complications.** *Neurosurgery* 2012;71:679–91
- Chalouhi N, Tjoumakaris S, Starke RM, et al. **Comparison of flow diversion and coiling in large unruptured intracranial saccular aneurysms.** *Stroke* 2013;44:2150–54
- O’Kelly CJ, Spears J, Chow M, et al. **Canadian experience with the Pipeline embolization device for repair of unruptured intracranial aneurysms.** *AJNR Am J Neuroradiol* 2013;34:381–87
- Cruz JP, O’Kelly C, Kelly M, et al. **Pipeline embolization device in aneurysmal subarachnoid hemorrhage.** *AJNR Am J Neuroradiol* 2013;34:271–76
- Kan P, Siddiqui AH, Veznedaroglu E, et al. **Early postmarket results after treatment of intracranial aneurysms with the Pipeline embolization device: A US multicenter experience.** *Neurosurgery* 2012;71:1080–87
- Siddiqui AH, Abla AA, Kan P, et al. **Panacea or problem: flow diverters in the treatment of symptomatic large or giant fusiform vertebrobasilar aneurysms—clinical article.** *J Neurosurg* 2012;116:1258–66
- de Barros Faria M, Castro RN, Lundquist J, et al. **The role of the Pipeline embolization device for the treatment of dissecting intracranial aneurysms.** *AJNR Am J Neuroradiol* 2011;32:2192–95
- Brinjikji W, Lanzino G, Cloft HJ, et al. **Patency of the posterior communicating artery after flow diversion treatment of internal carotid artery aneurysms.** *Clin Neurol Neurosurg* 2014;120:84–88
- Berge J, Biondi A, Machi P, et al. **Flow-diverter Silk stent for the treatment of intracranial aneurysms: 1-year follow-up in a multicenter study.** *AJNR Am J Neuroradiol* 2012;33:1150–55
- Leonardi M, Cirillo L, Toni F, et al. **Treatment of intracranial aneurysms using flow-diverting Silk stents (BALT): a single centre experience.** *Interv Neuroradiol* 2011;17:306–15
- Velioglu M, Kizilkilic O, Selcuk H, et al. **Early and midterm results of complex cerebral aneurysms treated with Silk stent.** *Neuroradiology* 2012;54:1355–65
- Hu YC, Deshmukh VR, Albuquerque FC, et al. **Histopathological assessment of fatal ipsilateral intraparenchymal hemorrhages after the treatment of supraclinoid aneurysms with the Pipeline embolization device.** *J Neurosurg* 2014;120:365–74
- Byrne JV, Beltechi R, Yarnold JA, et al. **Early experience in the treatment of intra-cranial aneurysms by endovascular flow diversion: a multicentre prospective study.** *PLoS One* 2010;5:pii: e12492
- McAuliffe W, Wycoco V, Rice H, et al. **Immediate and midterm results following treatment of unruptured intracranial aneurysms with the Pipeline embolization device.** *AJNR Am J Neuroradiol* 2012;33:164–70
- Wong GK, Kwan MC, Ng RY, et al. **Flow diverters for treatment of intracranial aneurysms: current status and ongoing clinical trials.** *J Clin Neurosci* 2011;18:737–40
- Tahtinen OI, Manninen HI, Vanninen RL, et al. **The Silk flow-diverting stent in the endovascular treatment of complex intracranial aneurysms: technical aspects and midterm results in 24 consecutive patients.** *Neurosurgery* 2012;70:617–23; discussion 623–24
- McLaughlin N, McArthur DL, Martin NA. **Use of stent-assisted coil**

- embolization for the treatment of wide-necked aneurysms: a systematic review. *Surg Neurol Int* 2013;4:43
39. Bodily KD, Cloft HJ, Lanzino G, et al. **Stent-assisted coiling in acutely ruptured intracranial aneurysms: a qualitative, systematic review of the literature.** *AJNR Am J Neuroradiol* 2011;32:1232–36
40. Shapiro M, Becske T, Sahlein D, et al. **Stent-supported aneurysm coiling: a literature survey of treatment and follow-up.** *AJNR Am J Neuroradiol* 2012;33:159–63
41. Fiorella D, Albuquerque FC, Woo H, et al. **Neuroform stent assisted aneurysm treatment: evolving treatment strategies, complications and results of long term follow-up.** *J Neurointerv Surg* 2010;2:16–22
42. Piotin M, Blanc R, Spelle L, et al. **Stent-assisted coiling of intracranial aneurysms: clinical and angiographic results in 216 consecutive aneurysms.** *Stroke* 2010;41:110–15
43. Chalouhi N, Starke RM, Yang S, et al. **Extending the indications of flow diversion to small, unruptured, saccular aneurysms of the anterior circulation.** *Stroke* 2014;45:54–58

Treatment of Poor-Grade Subarachnoid Hemorrhage Trial

D. Mitra, B. Gregson, V. Jayakrishnan, A. Gholkar, A. Vincent, P. White, and P. Mitchell



ABSTRACT

BACKGROUND AND PURPOSE: Management of poor-grade subarachnoid hemorrhage is based on limited evidence from small single-center retrospective observational studies. The purpose of this study was to undertake a single-center randomized controlled feasibility trial comparing a strategy of early endovascular aneurysm treatment with treatment after neurologic recovery in this group of patients.

MATERIALS AND METHODS: Patients with poor-grade SAH were randomized within 24 hours of admission to early treatment or treatment after neurologic recovery. If a patient was randomized to early treatment, the aneurysm was treated endovascularly within 24 hours of randomization. Recruitment rate, safety profile, and functional outcome at the time of discharge and at 6 months were assessed.

RESULTS: Fourteen of 51 patients screened were eligible for the trial. Of these 14, 8 patients were randomized (57%). All patients in the early coiling arm received treatment within 24 hours of randomization. There was no treatment-related complication. Overall, good outcome occurred in 25% of patients; the mortality rate was 75%. Patients in the early treatment arm ($n = 5$) had a good outcome rate of 20%, while those in treatment after neurologic recovery arm ($n = 3$) had a good outcome rate of 33.3%.

CONCLUSIONS: This was a feasibility study that demonstrated that recruitment and randomization for comparing management strategies in poor-grade SAH are feasible. The recruitment rate among eligible patients was encouraging (57%), though a number of patients had to be excluded due to ineligibility. A multicenter study is necessary to recruit the numbers required to compare the clinical outcomes of these management strategies.

ABBREVIATIONS: ISAT = International Subarachnoid Aneurysm Trial; WFNS = World Federation of Neurosurgical Societies

Intracranial aneurysms are being treated with increasing frequency by endovascular coiling. The International Subarachnoid Aneurysm Trial (ISAT),¹ an international, multicenter, randomized controlled trial comparing coiling with surgical clipping, demonstrated that there was a 6.9% reduction of absolute risk and a 22.6% reduction of relative risk of death or dependency at the end of 1 year in the coiling arm. On the basis of this finding, early aneurysm coiling of patients with good-grade subarachnoid hemorrhage has become an established practice. Poor-grade SAHs (World Federation of Neurosurgical Societies [WFNS] grades IV

and V) were significantly under-represented in ISAT because these patients are usually not considered for clipping unless they have made substantial clinical improvement.^{2,3} Although they were not under-represented in the Barrow Ruptured Aneurysm trial, this study did not assess treatment timing.⁴ ISAT re-raised the question of the balance of risks of aneurysm treatment in the early days after poor-grade SAH but did not provide the data to determine the answer.¹ Early coiling could potentially have the advantage of reducing the rebleeding rate without the increased treatment risks incurred by early surgical clipping in poor-grade SAH patients.² The benefit of such a strategy, however, cannot be extrapolated from ISAT and should be supported by robust (randomized controlled trial) data before being adopted as standard practice. We have undertaken a single-center randomized parallel-group feasibility trial between patients with poor-grade SAH who were treated early with endovascular coiling and those who were managed by the traditional method (ie, treated [coiled or clipped] after clinical neurologic improvement) as a first step toward answering this important question. The outcome measures were the following: 1) recruitment rate, 2) trial safety assessed by

Received February 21, 2014; accepted after revision May 19.

From the Departments of Neuroradiology (D.M., V.J., A.G.), Neurosurgery (P.M.), and Anesthesiology and Intensive Care (A.V.), Royal Victoria Infirmary, Newcastle upon Tyne, United Kingdom; and Institutes of Aging and Health (P.W.) and Neurosciences (B.G.), Newcastle University, Newcastle upon Tyne, United Kingdom.

Please address correspondence to Dipayan Mitra, MD, Department of Neuroradiology, Level Five New Victoria Wing, Royal Victoria Infirmary, Newcastle upon Tyne, NE1 4LP, United Kingdom; e-mail: Dipayan.Mitra@nuth.nhs.uk

Evidence-Based Medicine Level 2.

<http://dx.doi.org/10.3174/ajnr.A4061>

mortality and adverse event rates, and 3) distribution of 6-month functional outcome measured by the modified Rankin Scale score. This pilot study is expected to inform the design of a future multicenter randomized controlled trial.

MATERIALS AND METHODS

Full approvals from the institutional ethics committee and hospital research and development department were obtained for the trial.

Inclusion and Exclusion Criteria

The trial included patients older than 18 years admitted to the neurosciences intensive therapy unit with WFNS grade IV or V SAH who were hemodynamically stable and whose next of kin provided assent for inclusion.

Exclusion criteria were the following: 1) age older than 75 years, 2) signs of brain stem death not promptly reversed by antiepileptic treatment, 3) pure intraventricular hemorrhage, 4) large intracerebral hematoma requiring immediate clot evacuation, 5) lack of clinical equipoise (ie, the treating clinician believed that there was a much greater benefit to be gained for that patient by one or the other of the treatment arms), and 6) pregnancy.

Trial Design and Randomization

Patients admitted to the intensive therapy unit were stabilized from neurologic and cardiorespiratory points of view as per established protocol. If the patient was initially admitted to a different hospital, confirmation of the Glasgow Coma Scale score before intubation/ventilation was sought from the referral letter. Once SAH was confirmed by imaging and the patient was stable, the admitting neurosurgical/anesthetic team assessed them for eligibility for the trial.

If the patient fulfilled the eligibility criteria, an appropriate clinician (intensive therapy unit consultant/registrar or neurosurgical consultant/registrar or neuroradiology consultant/registrar) discussed the trial and provided written information to the next of kin. The clinician returned after an interval to allow adequate time for reflection and obtained informed assent for the trial from the next of kin.

If assent was not obtained from the next of kin, the reason was documented.

A screening log was completed, recording the number of patients assessed, the number meeting the inclusion criteria, and the number excluded because of the presence of ≥ 1 exclusion criteria (and if excluded, the reason for it).

After obtaining assent, we performed randomization within 24 hours of admission to the intensive therapy unit. A randomized block design (with variable block sizes of 2, 4, and 6) was used with 2 strata (hydrocephalus and no hydrocephalus) to ensure that patients with significant hydrocephalus (as determined by a requirement for CSF drainage) were equally distributed between the 2 trial arms.

The 2 Trial Arms

Early Treatment Arm. If the patient was randomized to the early treatment arm, the result of randomization was communicated to

the interventional neuroradiology team. Appropriate assent for the coiling procedure was then obtained. If amenable to endovascular treatment, the aneurysm was treated within 24 hours of randomization.

Treatment after Clinical Improvement Arm. If the patient was randomized to the treatment after clinical improvement arm, the result was communicated to the intensive therapy unit and neurosurgical team who continued managing the patient as per local established protocol. If and when the patient's neurologic status improved to WFNS grade III or better, the aneurysm was treated appropriately. There was no specific time-delay criterion for aneurysm treatment in this arm.

Aneurysm Treatment

Standard local procedures for aneurysm treatment were followed. Endovascular treatment of the aneurysms was performed with biplane angiography equipment (Integris Allura; Philips Healthcare, Best, the Netherlands). All patients were treated under general anesthetic and received a standard regimen of anticoagulation with heparin. Balloon assistance was used as required. None of the patients required a stent-assisted technique.

Follow-Up

Angiographic Follow-Up. Angiographic follow-up was performed as per the local established protocol (5 and 24 months following the coiling procedure).

Clinical Follow-Up. Patients were assessed for their functional status at the time of discharge and at 6 months following ictus. Assessment was performed by members of the endovascular team blinded to the results of randomization on the basis of the modified Rankin Scale.

RESULTS

Screening and Recruitment

The study was performed in a single United Kingdom neurosciences center. Fifty-one patients admitted to the intensive therapy unit with poor-grade SAH were screened over 29 months (August 2008 to January 2011). Fourteen patients were found to be eligible for the trial. Eight of 14 eligible were randomized for the study. The other 6 could not be included because assent from the next of kin could not be obtained. The recruitment rate among patients eligible for the trial was therefore 57%, while the recruitment rate of patients screened was 16%.

Thirty-seven patients were excluded from the study because they did not meet the inclusion criteria. A number of factors were responsible for patients being ineligible for the trial, which are summarized in Table 1.

Five patients were randomized to the early treatment arm, and 3 patients were randomized to the treatment after recovery arm.

Demographics

Of the 8 patients included in the study, 4 were men and 4 were women. The age of patients ranged between 26 and 64 years, with an average age of 53 years. Of the 5 patients (3 women and 2 men) randomized to early treatment, the age range was 26–64 years with an average age of 53 years. Of the 3 patients (2 men and 1

Table 1: Reason for ineligibility for randomization among the patients screened for the trial

Reason for Ineligibility	No.	%
Improvement of neurologic status before randomization	8	23
Expiry of time window for randomization	5	13
Emergency clot evacuation	5	13
Hemodynamic instability	5	13
Beyond age range	4	11
Pure intraventricular hemorrhage	3	8
Signs of coning	3	8
Lack of equipoise	3	8
No aneurysm on CT angiogram (AVM found)	1	3

Table 2: Treatment-unrelated adverse events

Treatment-Unrelated Adverse Event	No.
Aneurysm rebleeding	1
Hydrocephalus (early)	5
Hydrocephalus (late)	1
Intracerebral hematoma	2
Intraventricular hemorrhage	2
Diffuse cerebral edema	1

woman) randomized to treatment after recovery, the age range was 51–54 years, with an average age of 52 years.

Prerandomization Assessment

Five patients in the study had an admission WFNS grade of V, while 3 patients had an admission WFNS grade of IV. Of patients in the early treatment arm, 3 had a WFNS grade of V and 2 had a WFNS grade of IV. Of patients in the treatment after recovery arm, 2 patients had a WFNS grade of V, while 1 had a WFNS grade of IV.

All patients included in the trial had a CT head study before randomization. The Fisher grade of the admission CT was available in 7 of the 8 patients in the trial. All these CT studies demonstrated Fisher grade 4 SAH.

Randomization

Patients were randomized within 5–24 hours of admission to the intensive therapy unit (average, 11 hours). The mean time interval between randomization and aneurysm treatment in patients randomized to the early treatment arm was 9 hours 30 minutes (range, 2 hours 15 minutes to 22 hours). Only 1 of the 3 patients randomized to the treatment after recovery arm received aneurysm treatment. The time interval between randomization and aneurysm treatment in this patient was 21 hours.

Aneurysm Treatment and Adverse Events

Six of 8 patients in the study received endovascular treatment of their aneurysms. Two patients (both in the treatment after neurologic recovery arm) died before the aneurysm was treated. None of the patients in the study received surgical clipping.

Of the patients who had endovascular aneurysm treatment, there were no treatment-related adverse events. Adverse events not related to treatment are summarized in Table 2. At the time of randomization, 5 patients (3 in the early treatment arm and 2 in the conventional arm) had hydrocephalus requiring surgical

Table 3: Summary of outcomes between early treatment and treatment after recovery arms

	Early Treatment Arm	Treatment after Recovery Arm
No. of patients	5	3
WFNS score on admission	WFNS IV-II WFNS V-III	WFNS IV-I WFNS V-II
Good outcome	1 (MRS 1)	1 (MRS 0)
Poor outcome	4 (all MRS 6)	2 (all MRS 6)

drainage. Delayed hydrocephalus occurred in 1 patient (early treatment arm).

Outcomes

Functional outcomes were assessed at the time of discharge and at 6 months following ictus with the modified Rankin Scale questionnaire. At the time of discharge, 1 patient had an mRS score of 2 and 1 had an mRS score of 3. The other 6 patients died (mRS 6). At 6 months, 1 patient improved from mRS 2 to mRS 0 and the other patient improved from mRS 3 to mRS 1. Therefore, the overall good outcome (mRS 0–2) rate at 6 months was 25%, and the poor outcome rate (mRS 3–6) at the same time was 75%. The overall mortality rate was also 75%. The good outcome rate in the early treatment arm was 20%, while the good outcome rate in the treatment after recovery arm was 33% (Table 3).

DISCUSSION

Endovascular treatment is relatively less invasive than clipping and has been demonstrated to improve outcome in patients with good-grade SAH.¹ As a result, a number of centers are now also treating patients with poor-grade SAH with early endovascular coiling. Several single-center, retrospective, nonrandomized studies on early endovascular treatment of patients with poor-grade SAH have been published,^{5–12} as summarized in Table 4. While these studies provide important data in understanding outcomes in this group of patients, there are a number of difficulties in interpreting their results. First, sizes of the studies are mostly rather modest and vary widely, from 11⁶ to 111 subjects.¹⁰ Second, the inclusion criteria are also extremely variable. For example, while 1 study considers WFNS grade IV and V to be poor-grade,¹² another study has only included WFNS grade V,⁶ and some have included patients on the basis of Hunt and Hess grades 4 and 5.^{5,7,8,10} Significant heterogeneity also exists in outcome measures and follow-up. A small majority of studies have used the Glasgow Outcome Scale over the modified Rankin Scale. The follow-up also varied between 6 months¹² to up to 2 years.¹⁰ There are also differences in the definition of good and poor outcomes.^{5–12}

With regard to neurosurgical studies, the International Cooperative Study² reported a good recovery rate in patients with poor-grade SAH ranging from 10% to 33% in the various subgroups based on the timing of surgery. Some smaller scale single-center studies suggested that early surgical clipping may lead to better results, but mostly in selected groups.^{3,13,14} A study that included patients with poor-grade SAH who did not receive aneurysm treatment (ie, neither clipping nor coiling) reported a mortality rate of 71%.¹⁵

Specifically lacking from the endovascular studies are data

Table 4: Summary of studies of patients with poor-grade subarachnoid hemorrhage treated with early endovascular coiling

Study (yr)	No. of Patients	Methodology	Good Outcome (%)	Mortality Rate (%)
Bracard et al ⁵ (2002)	80	Included HH grades 4 and 5, good outcome GOS 1 or 2, up to 1 year follow-up	52.5 (GOS 1–2) 8.75 GOS 3	37.5
van Loon et al ⁶ (2002)	11	WFNS grade V, outcome measure GOS, mean follow-up 12 months	36	18
Weir et al ⁷ (2003)	27	HH grades 4 and 5, outcome assessed by mRS, mean follow-up 23 months	30	59
Jain et al ⁸ (2004)	13	Older than 70 yr, poor HH grades 4 and 5, outcome measure GOS	15	47
Bergui and Bradac ⁹ (2004)	45		48	44
Suzuki et al ¹⁰ (2006)	111	HH grades 4/5, outcome by mRS, follow-up ≤24 mo	35.1	32.4
Pereira et al ¹¹ (2007)	51	Outcome by GOS at 12 mo, GOS 1–3 considered good; 4–5, poor	57	35
Taylor et al ¹² (2011)	47	WFNS grades IV/V, 6-month GOS for outcome	53	27

Note:—GOS indicates Glasgow Outcome Scale; HH, Hunt and Hess.

analogous to the evidence base for early clipping, which compares coiling with conservative treatment; and the argument largely depends on the extrapolated assumption that coiling is a benign intervention. While the studies mentioned inform clinical practice in poor-grade SAH to a limited extent, significant uncertainties still exist, and robust evidence in the form of a randomized controlled trial is lacking.

The present study demonstrates that recruitment to such a randomized controlled trial is feasible. The recruitment rate among patients eligible for the study was encouraging (57%). The recruitment rate among the total number of patients screened for the study was much more modest at 16%. Screening and recruitment in the current study were largely performed during normal working hours, thus excluding a number of patients outside these hours. As shown in Table 1, the most frequent reasons for ineligibility (36%) were the following: 1) expiry of the time window for randomization, and 2) improvement of neurologic status before the patient could be randomized. If patient screening and recruitment are supported by the research staff 7 days a week, a higher recruitment rate would be realistic.

The study set out to assess the safety of conducting a randomized controlled trial in this group of patients. Six of 8 patients in the study underwent endovascular aneurysm treatment, while the other 2 died before aneurysm treatment. None of the patients undergoing endovascular treatment had any treatment-related complication; this finding suggests that a trial such as the present one is safe to conduct. As expected, a proportionately high number of disease-related adverse events did occur (Table 2). With regard to the feasibility of performing early coiling within the stipulated timeframe, the average time from randomization to treatment in patients in the early treatment arm was 9 hours 30 minutes, which suggests that the trial requirement of a maximum of 24 hours between randomization and treatment is achievable. No patient in this study had to be excluded because of noncompliance to this requirement.

Hydrocephalus is often thought to be the cause of incorrect WFNS grading and, therefore, incorrect classification as poor-grade SAH. To identify “true” poor-grade SAH, some centers advocate sedation-reversal followed by formal neurologic assessment.³ However sedation-reversal increases the risk of aneurysm rebleed, and postreversal neurologic assessment introduces delay into the process of randomization and treatment, making it diffi-

cult to study the benefits of early treatment. In this study, the decision regarding sedation-reversal has been left to the intensive therapy unit team. If a patient’s postreversal neurologic status improved rapidly to the extent that he or she no longer had a poor-grade SAH, then the patient was not randomized. If a patient was randomized, then he or she remained in the allocated trial arm regardless of the speed of recovery. Hydrocephalus was used as a stratification criterion to ensure that an equal proportion of patients with hydrocephalus were included in the 2 arms and that the outcomes were not skewed by this factor.

The overall mortality rate in this study was 75%, which is higher than that in many reported series. This is most probably due to the small size of this study and possible bias toward randomizing more patients with grade V than with grade IV. Most patients in this study had admission WFNS grades V; and 5 of 6 patients who died had an admission WFNS grade of V.

Although the numbers are small, our experience suggests that the benefit of early endovascular treatment in a poor-grade SAH population should not be assumed unless there are robust multicenter randomized controlled trial data to support it. In this study, the good outcome rate in the treatment after recovery arm (33%) was better than that in the early coiling arm (20%).

CONCLUSIONS

This study suggests that a randomized controlled trial to evaluate the best management strategy in patients with poor-grade SAH is safe and feasible. While the recruitment rate among eligible patients was encouraging, a significant number of patients could not be randomized due to expiry of the time window for randomization and lack of assent. A fully resourced multicenter study should be able to address these issues and recruit sufficient numbers to achieve robust outcome data.

ACKNOWLEDGMENTS

We acknowledge the contribution of Elaine McColl, Director of Newcastle Clinical Trials Unit, and Nicola Hind, Consultant Neuroradiographer, Royal Victoria Infirmary, Newcastle upon Tyne, for their exceptional help in design and recruitment of this trial.

Disclosures: Anil Gholkar—UNRELATED: Consultancy: Stryker Neurovascular, Codman Neurovascular, MicroVention, Comments: I organize and participate in training

courses organized by these entities; *Travel/Accommodations/Meeting Expenses Unrelated to Activities Listed*: Stryker Neurovascular, MicroVention, *Comments*: These entities have contributed to my expenses towards travel and accommodation to participate in Society of Neuro-Interventional Surgery meeting in 2013 and World Federation of Interventional and Therapeutic Neuroradiology meeting in 2011. Vijay Jayakrishnan—*UNRELATED: Payment for Lectures (including service on Speakers Bureaus)*: Codman Depuy, *Comments*: for providing teaching to health care professionals. Philip White—*UNRELATED: Consultancy*: Codman, MicroVention, *Comments*: organizing educational meetings; *Grants/Grants Pending*: Codman,* Covidien,* *Comments*: paid to the University of Glasgow but Co-Chief Investigator on grant part industry-funded; *Payment for Lectures (including service on Speakers Bureaus)*: Covidien; *Travel/Accommodations/Meeting Expenses Unrelated to Activities Listed*: MicroVention, *Comments*: support to attend Society of Neuro-Interventional Surgery 2013 meeting in Miami; *OTHER RELATIONSHIPS*: A grant for a multicenter trial has been developed and submitted to UK National Institutes of Health Research based on a feasibility pilot described in this work. Patrick Mitchell—*UNRELATED: Grants/Grants Pending*: UK National Institute for Health Research,* *Comments*: We are applying for a grant from National Institute for Health Research UK to run a larger version of the trial (Treatment of Poor-Grade Subarachnoid Hemorrhage Trial 2). *Money paid to the institution.

REFERENCES

- Molyneux AJ, Kerr RS, Yu LM, et al, for the International Subarachnoid Aneurysm Trial (ISAT) Collaborative Group. **International subarachnoid aneurysm trial (ISAT) of neurosurgical clipping versus endovascular coiling in 2143 patients with ruptured intracranial aneurysms: a randomised comparison of effects on survival, dependency, seizures, rebleeding, subgroups, and aneurysm occlusion.** *Lancet* 2005;366:809–17
- Kassell NF, Torner JC, Haley EC, et al. **The international cooperative study on the timing of aneurysm surgery. Part 2. Surgical results.** *J Neurosurg* 1990;73:37–47
- Hutchinson PJ, Power DM, Tripathi P, et al. **Outcome from poor grade aneurysmal subarachnoid haemorrhage: which poor grade subarachnoid haemorrhage patients benefit from aneurysm clipping?** *Br J Neurosurg* 2000;14:105–09
- McDougall CG, Spetzler RF, Zabramski JM, et al. **The Barrow ruptured aneurysm trial.** *J Neurosurg* 2012;116:135–44
- Bracard S, Lebedinsky A, Anxionnat R, et al. **Endovascular treatment of Hunt and Hess grade IV and V aneurysms.** *AJNR Am J Neuroradiol* 2002;23:953–57
- van Loon J, Waerzeggers Y, Wilms G, et al. **Early endovascular treatment of ruptured cerebral aneurysms in patients in very poor neurological condition.** *Neurosurgery* 2002;50:457–64
- Weir RU, Marcellus ML, Do HM, et al. **Aneurysmal subarachnoid hemorrhage in patients with Hunt and Hess grade 4 or 5: treatment using the Guglielmi detachable coil system.** *AJNR Am J Neuroradiol* 2003;24:585–90
- Jain R, Deveikis J, Thompson B. **Endovascular management of poor-grade aneurysmal subarachnoid hemorrhage in geriatric population.** *AJNR Am J Neuroradiol* 2004;25:596–600
- Bergui M, Bradac G. **Acute endovascular treatment of ruptured aneurysms in poor-grade patients.** *Neuroradiology* 2004;46:161–164
- Suzuki S, Jahan R, Duckwiler GR, et al. **Contribution of endovascular therapy to the management of poor-grade aneurysmal subarachnoid hemorrhage: clinical and angiographic outcomes.** *J Neurosurg* 2006;105:664–70
- Pereira A, Sanchez-Peña P, Biondi A, et al. **Predictors of 1 year outcome after coiling for poor-grade subarachnoid hemorrhage.** *Neurocrit Care* 2007;7:18–26
- Taylor C, Robertson F, Brealey D, et al. **Outcome in poor grade subarachnoid hemorrhage patients treated with acute endovascular coiling of aneurysms and aggressive intensive care.** *Neurocrit Care* 2011;14:341–47
- Laidlaw JD, Siu KH. **Poor-grade aneurysmal subarachnoid hemorrhage: outcome after treatment with urgent surgery.** *Neurosurgery* 2003;53:1275–80
- Bailes JE, Spetzler RF, Hadley MN, et al. **Management morbidity and mortality of poor-grade aneurysm patients.** *J Neurosurg* 1990;72:559–66
- Hijdra A, van Gijn J, Nagelkerke NJ, et al. **Prediction of delayed cerebral ischemia, rebleeding, and outcome after aneurysmal subarachnoid hemorrhage.** *Stroke* 1988;19:1250–56

Rescue Treatment of Thromboembolic Complications during Endovascular Treatment of Cerebral Aneurysms: A Meta-Analysis

W. Brinjikji, S.F. Morales-Valero, M.H. Murad, H.J. Cloft, and D.F. Kallmes



ABSTRACT

BACKGROUND AND PURPOSE: Intraprocedural thrombus formation during endovascular treatment of intracranial aneurysms is often treated with glycoprotein IIb/IIIa inhibitors and, in some instances, fibrinolytic therapy. We performed a meta-analysis evaluating the safety and efficacy of GP IIb/IIIa inhibitors compared with fibrinolysis. We also evaluated the safety and efficacy of abciximab, an irreversible inhibitor, compared with tirofiban and eptifibatide, reversible inhibitors of platelet function.

MATERIALS AND METHODS: We performed a comprehensive literature search for studies on rescue therapy for intraprocedural thromboembolic complications with glycoprotein IIb/IIIa inhibitors or fibrinolysis during endovascular treatment of intracranial aneurysms. We studied rates of periprocedural stroke/hemorrhage, procedure-related morbidity and mortality, immediate arterial recanalization, and long-term good clinical outcome. Event rates were pooled across studies by using random-effects meta-analysis.

RESULTS: Twenty-three studies with 516 patients were included. Patients receiving GP IIb/IIIa inhibitors had significantly lower perioperative morbidity from stroke/hemorrhage compared with those treated with fibrinolytics (11.0%; 95% CI, 7.0%–16.0% versus 29.0%; 95% CI, 13.0%–55.0%; $P = .04$) and were significantly less likely to have long-term morbidity (16.0%; 95% CI, 11.0%–21.0% versus 35.0%; 95% CI, 17.0%–58.0%; $P = .04$). There was a trend toward higher recanalization rates among patients treated with glycoprotein IIb/IIIa inhibitors compared with those treated with fibrinolytics (72.0%; 95% CI, 64.0%–78.0% versus 50.0%; 95% CI, 28.0%–73.0%; $P = .08$). Patients receiving tirofiban or eptifibatide had significantly higher recanalization rates compared with those treated with abciximab (83.0%; 95% CI, 68.0%–91.0% versus 66.0%; 95% CI, 58.0%–74.0%; $P = .05$). No difference in recanalization was seen in patients receiving intra-arterial (77.0%; 95% CI, 66.0%–85.0%) or intravenous GP IIb/IIIa inhibitors (70.0%; 95% CI, 57.0%–80.0%, $P = .36$).

CONCLUSIONS: Rescue therapy with thrombolytic agents resulted in significantly more morbidity than rescue therapy with glycoprotein IIb/IIIa inhibitors. Tirofiban/eptifibatide resulted in significantly higher recanalization rates compared with abciximab.

ABBREVIATIONS: GP IIb/IIIa = glycoprotein IIb/IIIa; IA = intra-arterial; TIMI = Thrombolysis in Myocardial Infarction

Periprocedural thromboembolic complications from endovascular treatment of intracranial aneurysms occur in 2%–15% of patients.¹ Intraprocedural thrombus formation is often treated with pharmacologic rescue, by using intra-arterial or intravenous administration of glycoprotein IIb/IIIa (GP IIb/IIIa) inhibitors or fibrinolytics. The primary goal of rescue therapy is to recanalize

the artery to avoid permanent neurologic deficits. Many studies have described intraprocedural administration of GP IIb/IIIa inhibitors and thrombolytic agents during endovascular treatment of intracranial aneurysms. Some studies have suggested that patients receiving GP IIb/IIIa inhibitors have better outcomes than those treated with fibrinolytic therapy. Studies have also examined the comparative efficacy of irreversible GP IIb/IIIa inhibitor agents (abciximab) and reversible agents (tirofiban/eptifibatide) and the comparative efficacy of intra-arterial and intravenous administration of GP IIb/IIIa inhibitors, but they have not demonstrated any significant differences in recanalization rates and outcomes.^{2,3} Overall however, the evidence is limited to small case series. We performed a meta-analysis of the literature examining angiographic and clinical outcomes in patients treated with GP IIb/IIIa inhibitors and fibrinolytic therapy for intraprocedural

Received April 17, 2014; accepted after revision June 23.

From the Departments of Radiology (W.B., H.J.C., D.F.K.) and Neurosurgery (S.F.M.-V., H.J.C., D.F.K.) and Center for Science of Healthcare Delivery (M.H.M.), Mayo Clinic, Rochester, Minnesota.

Please address correspondence to Waleed Brinjikji, MD, Department of Radiology, Mayo Clinic, 200 SW First St, Rochester, MN 55905; e-mail: brinjikji.waleed@mayo.edu

 Indicates article with supplemental on-line table.

<http://dx.doi.org/10.3174/ajnr.A4066>

Table 1: Rescue therapy outcomes with GP IIb/IIIa inhibitors versus fibrinolytics

Outcome	GP IIb/IIIa Inhibitor % (95% CI)	I ²	Fibrinolytic % (95% CI)	I ²	P Value
Postoperative clinical stroke	14.0 (8.0–23.0)	65	27.0 (11.0–51.0)	53	.20
Postoperative infarct on imaging	28.0 (19.0–39.0)	56	39.0 (19.0–63.0)	0	.42
Postoperative hemorrhage	7.0 (4.0–10.0)	0	14.0 (6.0–31.0)	26	.12
Perioperative morbidity from stroke/hemorrhage	11.0 (7.0–16.0)	10	29.0 (13.0–55.0)	55	.04
Perioperative mortality from stroke/hemorrhage	6.0 (4.0–9.0)	0	12.0 (5.0–25.0)	0	.16
Long-term good neurologic outcome	82.0 (78.0–86.0)	0	65.0 (42.0–83.0)	43	.07
Long-term morbidity	16.0 (11.0–21.0)	13	35.0 (17.0–58.0)	43	.04
Recanalization rate	72.0 (64.0–78.0)	49	50.0 (28.0–73.0)	37	.08

thrombus formation during intracranial aneurysm treatment.⁴ We also performed subgroup analyses to compare outcomes of patients treated with abciximab versus tirofiban/eptifibatide and those treated with intra-arterial (IA) and intravenous GP IIb/IIIa rescue therapy.

MATERIALS AND METHODS

A comprehensive literature search of the data bases PubMed, Ovid MEDLINE, and Ovid EMBASE was designed and conducted by an experienced librarian with input from the authors. The key words “intracranial aneurysm,” “endovascular therapy,” “fibrinolytic,” “tPA,” “glycoprotein IIb/IIIa,” “abciximab,” “coil,” “thromboembolic,” and “rescue” were used in both “AND” and “OR” combinations. The search was limited to articles published from 1990 to January 2014 in the English language only. All studies reporting patients treated with GP IIb/IIIa inhibitors or fibrinolysis during endovascular treatment of intracranial aneurysms were selected. The inclusion criteria were the following: a series of >5 patients, with available data on periprocedural complications and angiographic outcomes. Studies performed by using administrative/insurance data bases were excluded. Two reviewers independently selected the included studies. For each study, we independently extracted the following information: recanalization rate, perioperative clinical stroke, perioperative infarct on imaging, perioperative hemorrhage, perioperative morbidity and mortality from stroke/hemorrhage, long-term good neurologic outcome, and long-term morbidity. Perioperative complications were identified as those that occurred within 30 days of the procedure. The recanalization rate was defined as a Thrombolysis in Cerebral Infarction score of ≥ 2 or a Thrombolysis in Myocardial Infarction (TIMI) score of ≥ 2 . In cases in which patients underwent rescue therapy for a TIMI/TICI score of 2, recanalization was defined as a 1-point improvement in the recanalization rate. In series in which TIMI/TICI scores were not provided, recanalization was defined by using the words “near-complete or complete recanalization.” Patients included in the long-term outcome analysis required a minimum of 3 months of follow-up. Good clinical outcome was defined as an mRS score of ≤ 2 .

The primary objective of this study was to compare outcomes among patients treated with GP IIb/IIIa inhibitors and those treated with fibrinolytics. For this comparison, we did not control for the method of administration (IV or IA) or the drug used (ie, abciximab, tirofiban, eptifibatide, recombinant tissue plasminogen activator, streptokinase, and so forth). We performed 2 subgroup analyses: 1) comparing outcomes of patients treated with large-molecule/irreversible GP IIb/IIIa inhibitors (abciximab) with those treated with small-molecule/reversible GP IIb/IIIa in-

hibitors (tirofiban/eptifibatide), and 2) comparing outcomes of patients receiving IA GP IIb/IIIa inhibitors versus IV GP IIb/IIIa inhibitors.

Statistical Analysis

Most of the included studies were noncomparative. Therefore, we estimated from each cohort the cumulative incidence (event rate) and 95% confidence interval for each outcome. Event rates for each intervention were pooled in a meta-analysis across studies by using the random-effects model.⁵ In this model, studies are weighted by the inverse of their variance (ie, larger studies will have larger weight). The incidence rates of the different outcomes were compared between GP IIb/IIIa cohorts and fibrinolytic treatment cohorts by using an interaction test as described by Altman and Bland.⁶ Additional comparisons were made between abciximab and tirofiban/eptifibatide and between IA versus IV GP IIb/IIIa inhibitors. Heterogeneity of the treatment effect across studies was evaluated by using the I² statistic.⁷

RESULTS

Literature Review

Studies included in our literature review are summarized in the On-line Table. Our literature search yielded 623 articles; 562 articles were excluded after reading the abstract alone. Twenty-one studies were excluded for not meeting our minimum size criterion of ≥ 5 patients. Seventeen studies were excluded because they reported rescue therapy during endovascular procedures other than aneurysm treatment. Twenty-three studies met our inclusion criteria. In total, 533 patients were included in this study. Four hundred eighty patients received GP IIb/IIIa inhibitors (90.0%), and 63 patients (11.8%) received fibrinolytic therapy. Eighteen studies provided the proportion of patients during the study time period receiving rescue therapy for thromboembolic complications. From these studies, 444/7276 (6.1%) received rescue therapy. Among patients receiving GP IIb/IIIa inhibitors, 322 patients received abciximab and 145 patients received either tirofiban or eptifibatide. One hundred forty-nine patients received IV GP IIb/IIIa inhibitors, and 284 patients received IA GP IIb/IIIa inhibitors.

GP IIb/IIIa versus Fibrinolytics

Outcomes for GP IIb/IIIa inhibitors versus fibrinolytic therapy for rescue treatment are summarized in Table 1. The postoperative clinical stroke rate was 14.0% (95% CI, 8.0–23.0) for patients treated with GP IIb/IIIa inhibitor compared with 27.0% (95% CI, 11.0–51.0) for those treated with fibrinolytics ($P = .20$). The postoperative hemorrhage rate was 7.0% (95%

Table 2: Rescue therapy outcomes with GP IIb/IIIa inhibitors: abciximab versus tirofiban/eptifibatide

Outcome	Abciximab % (95% CI)	I ²	Tirofiban/Eptifibatide % (95% CI)	I ²	P Value
Postoperative clinical stroke	14.0 (8.0–25.0)	50	13.0 (4.0–33.0)	77	.86
Postoperative infarct on imaging	28.0 (19.0–39.0)	44	37.0 (9.0–76.0)	81	.67
Postoperative hemorrhage	7.0 (4.0–10.0)	0	14.0 (6.0–31.0)	26	.12
Perioperative morbidity from stroke/hemorrhage	12.0 (8.0–18.0)	4	8.0 (4.0–16.0)	3	.30
Perioperative mortality from stroke/hemorrhage	6.0 (4.0–10.0)	0	6.0 (3.0–12.0)	0	.16
Long-term good neurologic outcome	85.0 (79.0–89.0)	0	78.0 (69.0–85.0)	0	.15
Long-term morbidity	14.0 (9.0–21.0)	15	18.0 (11.0–29.0)	19	.37
Recanalization rate	66.0 (58.0–74.0)	32	83.0 (68.0–91.0)	60	.05

Table 3: Rescue therapy outcomes with GP IIb/IIIa inhibitors: IA versus IV administration

Outcome	IA GP IIb/IIIa % (95% CI)	I ²	IV GP IIb/IIIa % (95% CI)	I ²	P Value
Postoperative clinical stroke	14.0 (7.0–26.0)	70	14.0 (8.0–26.0)	0	.94
Postoperative infarct on imaging	33.0 (20.0–50.0)	58	23.0 (13.0–36.0)	28	.30
Postoperative hemorrhage	5.0 (3.0–9.0)	0	7.0 (3.0–15.0)	18	.66
Perioperative morbidity from stroke/hemorrhage	10.0 (7.0–15.0)	0	13.0 (6.0–27.0)	34	.57
Perioperative mortality from stroke/hemorrhage	6.0 (4.0–10.0)	0	8.0 (4.0–14.0)	0	.53
Long-term good neurologic outcome	83.0 (76.0–88.0)	0	78.0 (69.0–85.0)	10	.37
Long-term morbidity	14.0 (10.0–21.0)	0	17.0 (11.0–25.0)	2	.56
Recanalization rate	77.0 (66.0–85.0)	58	70.0 (57.0–80.0)	33	.36

CI, 4.0–10.0) for patients treated with GP IIb/IIIa inhibitors compared with 14.0% (95% CI, 6.0–31.0) for those treated with thrombolytics ($P = .12$). Perioperative morbidity from stroke/hemorrhage was significantly higher in the fibrinolytics group (29.0%; 95% CI, 13.0–55.0) compared with the GP IIb/IIIa group (11.0%; 95% CI, 7.0–16.0; $P = .04$). Long-term morbidity was significantly higher in the fibrinolytics group (35.0%; 95% CI, 17.0–58.0) compared with the GP IIb/IIIa group (16.0%; 95% CI, 11.0–21.0; $P = .04$). There was a trend toward significantly higher recanalization rates with GP IIb/IIIa inhibitors (72.0%; 95% CI, 64.0–78.0) compared with fibrinolytics (50.0%; 95% CI, 28.0–73.0; $P = .08$).

Abciximab versus Tirofiban/Eptifibatide

Comparison of outcomes of patients receiving abciximab and tirofiban/eptifibatide are summarized in Table 2. Patients receiving tirofiban/eptifibatide had significantly higher recanalization rates (83.0%; 95% CI, 68.0–91.0) compared with those receiving abciximab (66.0%; 95% CI, 58.0–74.0; $P = .05$). Patients treated with tirofiban/eptifibatide had a non-statistically significant higher rate of postoperative hemorrhage (14.0%; 95% CI, 6.0–31.0) compared with those treated with abciximab (7.0%; 95% CI, 4.0–10.0; $P = .12$). No difference was seen in perioperative morbidity and mortality or long-term morbidity.

Intra-Arterial versus Intravenous GP IIb/IIIa Inhibitors

Comparison of outcomes of IA versus IV GP IIb/IIIa inhibitors is summarized in Table 3. No difference in the recanalization rate was seen on the basis of the method of administration of GP IIb/IIIa inhibitors because patients treated with IA therapy had a recanalization rate of 77.0% (95% CI, 66.0–85.0) and those treated with IV therapy had a recanalization rate of 70.0% (95% CI, 57.0–80.0; $P = .36$). Clinical outcomes and complication rates did not differ by method of GP IIb/IIIa inhibitor administration.

DISCUSSION

Our systematic review of rescue therapy for the treatment of intraoperative thromboembolic complications in the setting of aneurysm coiling demonstrated higher rates of short- and long-term morbidity among patients treated with fibrinolysis relative to those receiving GP IIb/IIIa inhibitors. In addition, we found a trend toward improved recanalization rates with GP IIb/IIIa inhibitors compared with thrombolytics. Patients receiving tirofiban/eptifibatide had significantly higher recanalization rates compared with those receiving abciximab; however, no difference was seen in clinical outcomes. No difference in outcome was seen among patients receiving intra-arterial and intravenous rescue therapy with GP IIb/IIIa inhibitors. These data should prompt practitioners to avoid fibrinolytics in place of GP IIb/IIIa agents for rescue therapy during coil embolization.

In most case series, the rate of rescue therapy for thromboembolic complications ranged between 5% and 10%.^{1,3,8-19} Our systematic review found that approximately 6% of patients received rescue therapy during the treatment of intracranial aneurysms. Clinical outcomes of patients receiving GP IIb/IIIa inhibitors and fibrinolytics are variable. In a study of 592 patients undergoing rescue therapy in a large administrative data base, Brinjikji et al⁴ found that patients with unruptured aneurysms receiving fibrinolytics had significantly higher rates of discharge to institutions other than home (37.5% versus 7.4%). Patients with ruptured aneurysms receiving fibrinolytics had significantly higher rates of in-hospital mortality (26.0% versus 14.5%) and discharge to institutions other than home (59.4% versus 36.5%). Our study found significantly higher rates of short- and long-term morbidity among patients receiving fibrinolytic therapy for rescue treatment. Furthermore, there was a trend toward improved recanalization rates among patients treated with GP IIb/IIIa inhibitors.

The infarction rate among patients receiving rescue therapy ranges between 10% and 40%, with higher rates generally seen in studies with postoperative MR imaging.^{1,3,8-19} In a series of 477 patients with 515 intracranial aneurysms, Ries et al¹ reported that

48 patients (10%) had thromboembolic events, 42 of these patients received rescue therapy with GP IIb/IIIa inhibitors, and 1 patient received rescue therapy with rtPA. Of the patients who did not receive rescue therapy, 3/5 had infarcts, while 31% of patients receiving GP IIb/IIIa inhibitor rescue therapy had infarctions on CT. Linfante et al¹⁵ found that approximately 10% of patients undergoing endovascular embolization of intracranial aneurysms required intra-arterial GP IIb/IIIa inhibitor rescue therapy, with an infarct and hemorrhage rate of 0%. Many prior studies that have demonstrated high infarct rates on postoperative imaging also show that many of these infarcts are clinically silent.^{1,8,14} In our study, there was no significant difference in the rate of clinical stroke and infarction on imaging between patients treated with GP IIb/IIIa inhibitor and those receiving thrombolytics.

The efficacy of small-molecule/reversible GP IIb/IIIa inhibitors (tirofiban/efitibatide) relative to the large-molecule/irreversible inhibitor (abciximab) has not been well-established. One might assume that reversible, competitive inhibitory agents such as tirofiban/efitibatide may lose potency, thus leading to decreased recanalization rates. In a meta-analysis of abciximab versus small-molecule GP IIb/IIIa inhibitors among patients receiving percutaneous coronary interventions, Gurm et al²⁰ found no difference in clinical and angiographic outcomes between these 2 agents. In a large randomized controlled trial of abciximab versus eptifibatide for coronary revascularization, Zeymer et al²¹ found similar safety and efficacy rates between the 2 drugs. We found significantly higher recanalization rates, with no difference in clinical outcome, when comparing small-molecule GP IIb/IIIa inhibitors and abciximab.

The efficacy of intravenous-versus-intra-arterial administration of GP IIb/IIIa inhibitors for rescue therapy is also not well-established. One might assume that local intra-arterial administration of GP IIb/IIIa inhibitors at the site of thrombus formation would yield higher recanalization rates and thus improved clinical outcomes due to increased local concentrations of the therapeutic agent. A number of studies in the cardiology literature, in which GP IIb/IIIa inhibitors are routinely used in percutaneous coronary intervention, have examined the safety and efficacy of both the route and type of GP IIb/IIIa inhibitor administration. In a meta-analysis of randomized controlled trials of intracoronary versus intravenous administration of glycoprotein IIb/IIIa inhibitors during percutaneous coronary intervention for acute coronary syndrome, Friedland et al²² found that intracoronary administration resulted in higher recanalization rates and short-term mortality after intervention. Fu et al²³ found that intracoronary administration increased coronary flow and myocardial reperfusion but did not improve outcomes compared with intravenous administration. While intra-arterial administration of GP IIb/IIIa inhibitors may lead to higher concentrations of the agent at the site of the thrombus, an intravenous bolus of GP IIb/IIIa inhibitors has been found to reduce platelet aggregation to <20% within 10 minutes of administration.²⁴ It may be that intra-arterial administration is beneficial only in the short term, which may not be sufficient to provide clinical benefit. Our study found no differences in recanalization or clinical outcomes between patients receiving IA or IV GP IIb/IIIa inhibitors.

Limitations

Our study has limitations. The data on which this meta-analysis is based are affected by publication bias. Studies with favorable results are more likely to be published. Moreover, the limitations of single-center experiences for selection bias and potential complication under-reporting are well-known. Many details were lacking from the studies included in our analysis. For example, many studies did not provide TICI/TIMI grading for vessel recanalization. We did not stratify outcomes on the basis of aneurysm rupture status. Reporting of long-term neurologic outcomes was inconsistent across studies. In addition, many of the series analyzed and included in our analysis were cases collected during several years, and it is possible that complication rates have improved as a result of increased operator experience and skill and improved devices and technology. Regarding the method of GP IIb/IIIa administration, there was variation in how intravenous doses were administered (loading dose alone, loading dose plus drip, or drip alone). The comparisons reported in this meta-analysis are made across studies, not within studies; this difference greatly weakens inference. Most of the studies in our analysis were noncomparative, and groups were not randomized. An ideal meta-analysis comparing variable pharmacologic therapies would include only comparative studies with randomized groups. Overall, the quality of the studies included in this analysis was low. If one used the Grading of Recommendations, Assessment, Development, and Evaluation framework, the quality of evidence (confidence in estimates) is very low because of imprecision, heterogeneity, and methodologic limitations of the included studies.²⁵⁻²⁷

CONCLUSIONS

In this study, rescue therapy with GP IIb/IIIa inhibitors is associated with less long- and short-term morbidity compared with fibrinolytics for rescue therapy during intracranial aneurysm coiling. Our meta-analysis suggests that eptifibatide/tirofiban treatment results in significantly higher recanalization rates than treatment with abciximab. No difference in outcome was seen on the basis of the method of administration of GP IIb/IIIa inhibitors. Further clinical trials might study the relative safety and efficacy of various GP IIb/IIIa inhibitors and methods of administration to help determine the best treatment for intraprocedural thromboembolic complications during intracranial aneurysm treatment.

Disclosures: Harry J. Cloft—UNRELATED: Grants/Grants Pending: Cordis Endovascular,* Comments: site Principal Investigator at enrolling site for Stenting and Angioplasty with Protection in Patients and High Risk for Endarterectomy registry sponsored by Cordis Endovascular. David Kallmes—UNRELATED: Consultancy: GE Healthcare,* ev3,* Comments: planning and implementation of clinical trials; Grants/Grants Pending: MicroVention,* ev3,* Codman,* Sequent,* SurModics,* Benvenue Medical,* Comments: planning and implementation of clinical trials, pre-clinical research; Royalties: University of Virginia Patent Foundation, Comments: Spine Fusion. *Money paid to the institution.

REFERENCES

1. Ries T, Siemonsen S, Grzyska U, et al. **Abciximab is a safe rescue therapy in thromboembolic events complicating cerebral aneurysm coil embolization: single center experience in 42 cases and review of the literature.** *Stroke* 2009;40:1750–57
2. Jeong HW, Jin SC. **Intra-arterial infusion of a glycoprotein IIb/IIIa antagonist for the treatment of thromboembolism during coil em-**

- bolization of intracranial aneurysm: a comparison of abciximab and tirofiban.** *AJNR Am J Neuroradiol* 2013;34:1621–25
3. Jones RG, Davagnanam I, Colley S, et al. **Abciximab for treatment of thromboembolic complications during endovascular coiling of intracranial aneurysms.** *AJNR Am J Neuroradiol* 2008;29:1925–29
 4. Brinjikji W, McDonald JS, Kallmes DF, et al. **Rescue treatment of thromboembolic complications during endovascular treatment of cerebral aneurysms.** *Stroke* 2013;44:1343–47
 5. DerSimonian R, Laird N. **Meta-analysis in clinical trials.** *Control Clin Trials* 1986;7:177–88
 6. Altman DG, Bland JM. **Interaction revisited: the difference between two estimates.** *BMJ* 2003;326:219
 7. Higgins JP, Thompson SG, Deeks JJ, et al. **Measuring inconsistency in meta-analyses.** *BMJ* 2003;327:557–60
 8. Aggour M, Pierot L, Kadziolka K, et al. **Abciximab treatment modalities for thromboembolic events related to aneurysm coiling.** *Neurosurgery* 2010;67:503–08
 9. Aviv RI, O'Neill R, Patel MC, et al. **Abciximab in patients with ruptured intracranial aneurysms.** *AJNR Am J Neuroradiol* 2005;26:1744–50
 10. Brooks NP, Turk AS, Niemann DB, et al. **Frequency of thromboembolic events associated with endovascular aneurysm treatment: retrospective case series.** *J Neurosurg* 2008;108:1095–100
 11. Bruening R, Mueller-Schunk S, Morhard D, et al. **Intraprocedural thrombus formation during coil placement in ruptured intracranial aneurysms: treatment with systemic application of the glycoprotein IIb/IIIa antagonist tirofiban.** *AJNR Am J Neuroradiol* 2006;27:1326–31
 12. Fiorella D, Albuquerque FC, Han P, et al. **Strategies for the management of intraprocedural thromboembolic complications with abciximab (ReoPro).** *Neurosurgery* 2004;54:1089–97, discussion 1097–98
 13. Gralla J, Rennie AT, Corkill RA, et al. **Abciximab for thrombolysis during intracranial aneurysm coiling.** *Neuroradiology* 2008;50:1041–47
 14. Kang HS, Kwon BJ, Roh HG, et al. **Intra-arterial tirofiban infusion for thromboembolism during endovascular treatment of intracranial aneurysms.** *Neurosurgery* 2008;63:230–37, discussion 237–38
 15. Linfante I, Etezadi V, Andreone V, et al. **Intra-arterial abciximab for the treatment of thrombus formation during coil embolization of intracranial aneurysms.** *J Neurointerv Surg* 2010;2:135–38
 16. Mounayer C, Piotin M, Baldi S, et al. **Intraarterial administration of abciximab for thromboembolic events occurring during aneurysm coil placement.** *AJNR Am J Neuroradiol* 2003;24:2039–43
 17. Park JH, Kim JE, Sheen SH, et al. **Intraarterial abciximab for treatment of thromboembolism during coil embolization of intracranial aneurysms: outcome and fatal hemorrhagic complications.** *J Neurosurg* 2008;108:450–57
 18. Song JK, Niimi Y, Fernandez PM, et al. **Thrombus formation during intracranial aneurysm coil placement: treatment with intra-arterial abciximab.** *AJNR Am J Neuroradiol* 2004;25:1147–53
 19. Velat GJ, Burry MV, Eskioğlu E, et al. **The use of abciximab in the treatment of acute cerebral thromboembolic events during neuroendovascular procedures.** *Surg Neurol* 2006;65:352–58, discussion 358–59
 20. Gurm HS, Tamhane U, Meier P, et al. **A comparison of abciximab and small-molecule glycoprotein IIb/IIIa inhibitors in patients undergoing primary percutaneous coronary intervention: a meta-analysis of contemporary randomized controlled trials.** *Circ Cardiovasc Interv* 2009;2:230–36
 21. Zeymer U, Margenet A, Haude M, et al. **Randomized comparison of eptifibatid versus abciximab in primary percutaneous coronary intervention in patients with acute ST-segment elevation myocardial infarction: results of the EVA-AMI Trial.** *J Am Coll Cardiol* 2010;56:463–69
 22. Friedland S, Eisenberg MJ, Shimony A. **Meta-analysis of randomized controlled trials of intracoronary versus intravenous administration of glycoprotein IIb/IIIa inhibitors during percutaneous coronary intervention for acute coronary syndrome.** *Am J Cardiol* 2011;108:1244–51
 23. Fu G, Jia L, Zhao X, et al. **A comparison of intracoronary with intravenous glycoprotein IIb/IIIa inhibitors during percutaneous coronary intervention in patients with acute coronary syndrome: a meta-analysis of randomized controlled trials.** *J Interv Cardiol* 2012;25:223–34
 24. Thiele H, Wahrle J, Hambrecht R, et al. **Intracoronary versus intravenous bolus abciximab during primary percutaneous coronary intervention in patients with acute ST-elevation myocardial infarction: a randomised trial.** *Lancet* 2012;379:923–31
 25. Balshem H, Helfand M, Schünemann HJ, et al. **GRADE guidelines. 3. Rating the quality of evidence.** *J Clin Epidemiol* 2011;64:401–06
 26. Guyatt GH, Oxman AD, Kunz R, et al. **GRADE guidelines. 6. Rating the quality of evidence-imprecision.** *J Clin Epidemiol* 2011;64:1283–93
 27. Murad MH, Swiglo BA, Sidawy AN, et al. **Methodology for clinical practice guidelines for the management of arteriovenous access.** *J Vasc Surg* 2008;48:26S–30S
 28. Cognard C, Weill A, Castaings L, et al. **Intracranial berry aneurysms: angiographic and clinical results after endovascular treatment.** *Radiology* 1998;206:499–510
 29. Cronqvist M, Pierot L, Boulin A, et al. **Local intraarterial fibrinolysis of thromboemboli occurring during endovascular treatment of intracerebral aneurysm: a comparison of anatomic results and clinical outcome.** *AJNR Am J Neuroradiol* 1998;19:157–65
 30. Cho YD, Lee JY, Seo JH, et al. **Intra-arterial tirofiban infusion for thromboembolic complication during coil embolization of ruptured intracranial aneurysms.** *Eur J Radiol* 2012;81:2833–38
 31. Hähnel S, Schellinger PD, Gutschalk A, et al. **Local intra-arterial fibrinolysis of thromboemboli occurring during neuroendovascular procedures with recombinant tissue plasminogen activator.** *Stroke* 2003;34:1723–28
 32. Jeon JS, Sheen SH, Hwang G, et al. **Intraarterial tirofiban thrombolysis for thromboembolisms during coil embolization for ruptured intracranial aneurysms.** *J Cerebrovasc Endovasc Neurosurg* 2012;14:5–10
 33. Koebbe CJ, Horowitz MB, Levy EI, et al. **Intraarterial thrombolysis for thromboemboli associated with endovascular aneurysm coiling: report of five cases.** *Interv Neuroradiol* 2002;8:151–58
 34. Sedat J, Chau Y, Mondot L, et al. **Is eptifibatid a safe and effective rescue therapy in thromboembolic events complicating cerebral aneurysm coil embolization? Single-center experience in 42 cases and review of the literature.** *Neuroradiology* 2014;56:145–53
 35. Walsh RD, Barrett KM, Aguilar MI, et al. **Intracranial hemorrhage following neuroendovascular procedures with abciximab is associated with high mortality: a multicenter series.** *Neurocrit Care* 2011;15:85–95

One-Year MR Angiographic and Clinical Follow-Up after Intracranial Mechanical Thrombectomy Using a Stent Retriever Device

F. Eugène, J.-Y. Gauvrit, J.-C. Ferré, J.-C. Gentric, A. Besseghir, T. Ronzière, and H. Raoult



ABSTRACT

BACKGROUND AND PURPOSE: Little is known about the consequences of arterial wall damage that may be due to mechanical endovascular thrombectomy. Our aim was to perform 1-year MR angiographic and clinical follow-up of patients treated with mechanical endovascular thrombectomy using the Solitaire device.

MATERIALS AND METHODS: Patients with stroke treated between August 2010 and July 2012 were prospectively evaluated with a minimum follow-up of 1 year after mechanical endovascular thrombectomy. Angiographic follow-up was performed on a 3T MR imaging scanner and included intracranial artery TOF MRA and supra-aortic artery gadolinium-enhanced MRA. Images were assessed to detect arterial abnormalities (stenosis, occlusion, dilation) and were compared with the final post-mechanical endovascular thrombectomy run to differentiate delayed and pre-existing abnormalities. Clinical evaluation was performed with the mRS and the 36-Item Short-Form Health Survey questionnaire quality-of-life scale.

RESULTS: Thirty-nine patients were angiographically assessed at the mean term of 19 ± 4 months. MRA showed intracranial artery abnormalities in 10 patients, including 5 delayed intracranial artery abnormalities in 4 patients (4 stenoses and 1 dilation), 4 cases of pre-existing intracranial artery stenosis, and 2 occlusions. Pre-existing etiologic cervical artery stenosis or occlusion was observed in 2 patients. All these patients remained asymptomatic during the follow-up period. A significant clinical improvement was observed at 1-year follow-up in comparison with 3-month follow-up ($P < .0001$), with a good outcome achieved in 62.5% of patients and an acceptable quality of life restored.

CONCLUSIONS: One-year follow-up identifies delayed asymptomatic arterial abnormalities in patients treated with the Solitaire device.

ABBREVIATIONS: FU = follow-up; MET = mechanical endovascular thrombectomy; SF-36 = 36-Item Short-Form Health Survey Questionnaire; TOAST = Trial of Org 10172 in Acute Stroke Treatment

Stent-based devices have proved particularly efficient for achieving fast, safe, and successful recanalization in proximal artery occlusion,¹ with recanalization rates of approximately 80%–90% by using the Solitaire device (Covidien, Irvine, California).^{1–5} Until now, evaluation of mechanical endovascular thrombectomy (MET) safety and efficacy has mainly relied on short-term 3-month clinical follow-up, but no data have been available about angiographic arterial changes related to MET procedures or

stroke etiology and their possible correlation with clinical changes on long-term follow-up (FU).

In animal models, MET was shown to be responsible for vascular damage,^{6,7} depending on the device type, proving less frequent with wall-contact devices such as stent retrievers than with aspiration ones.⁶ The only published short-term angiographic follow-up study after MET by using various devices reported 0.9% arterial occlusion and 3.4% de novo stenosis. All cases were asymptomatic and identified as a consequence of arterial wall damage likely due to MET.⁸ Yet arterial stenosis may evolve with time and lead to clinical decline. It, therefore, seems relevant to assess angiographic vascular status and changes and to correlate any changes with clinical outcomes in patients treated with stent retrievers.

The purpose of this study was to perform 1-year 3T MR angiographic FU of patients treated with a Solitaire device to identify potential wall damage. Angiographic data were correlated with

Received February 8, 2014; accepted after revision April 21.

From the Departments of Neuroradiology (F.E., J.-Y.G., J.-C.F., H.R.), Clinical Pharmacology (A.B.), and Neurology (T.R.), Centre Hospitalier Universitaire, Rennes, France; and Department of Neuroradiology (J.-C.G.), Centre Hospitalier Universitaire, Brest, France.

Please address correspondence to H el ene Raoult, MD, 2 Rue Henri Le Guilloux, 35000 Rennes, France; e-mail: helene.raoult@chu-rennes.fr

Indicates article with supplemental on-line table.

<http://dx.doi.org/10.3174/ajnr.A4071>

clinical FU data on the basis of both functional and quality-of-life evaluation criteria.

MATERIALS AND METHODS

Patient Identification

Ethics approval for this study was granted by the institutional review board after review of the stroke protocol. Informed consent was obtained from all patients before the FU MR imaging. Consecutive patients treated with MET by using a Solitaire stent between August 2010 and July 2012 were included. Angiographic and clinical FU was systematically performed with a minimum follow-up of 1 year after MET.

Patients were eligible for an endovascular procedure according to the institutional stroke protocol if they met the following inclusion criteria: feasibility of thrombectomy within 6 hours of symptom onset for anterior circulation occlusion or within 24 hours for posterior circulation occlusion, proximal thrombus on MR imaging or angio-CT, with no limit in terms of age, initial NIHSS score, or the size of the infarct on imaging.

The exclusion criteria were as follows: comorbidity with poor prognosis (neoplasia, cardiac or respiratory failure) or hemorrhagic event as shown on initial imaging.

Within 4.5 hours of symptom onset, all eligible patients received an intravenous thrombolysis bolus according to the generally accepted inclusion and exclusion criteria. MET was performed either immediately after intravenous thrombolysis (“combined therapy”), 1 hour after initiation of intravenous thrombolysis if no clinical improvement was observed (“rescue therapy”), or otherwise as “stand-alone” therapy when the patient was not eligible for intravenous thrombolysis.³ Combined or rescue therapy was performed according to the time from symptom onset and the location of the occlusion, as in the REscue, COmbined and Stand-alone Thrombectomy (RECOST) study,³ or the terms of the protocol if the patient was enrolled in a randomized trial.

Treatment Protocol

All procedures were performed by a neurointerventionalist on a biplanar system (Allura; Philips Healthcare, Best, Netherlands) with the patient under general anesthesia, with a target systolic blood pressure of above 140 mm Hg,⁹ and by using a femoral artery approach. For anterior circulation occlusions, a 6F or 8F guide catheter (Envoy; Codman & Shurtleff, Raynham, Massachusetts) was inserted into the target carotid artery. We preferred 8F guide catheters to achieve fast and effective recanalization when the procedure was performed by a lone practitioner. For posterior circulation occlusions, a 6F guide catheter was inserted into the dominant, or navigable, vertebral artery. The guide catheter was injected with nimodipine (15-mL nimodipine [Nimotop]/L of sodium chloride). A 0.021-inch inner lumen Rebar-18 microcatheter (Covidien) was carefully navigated through the thromboembolic occlusion over a 0.014-inch steerable Transend microwire (Stryker, Kalamazoo, Michigan) under fluoroscopic control. A microcatheter angiographic run was subsequently performed to confirm the correct position of the microcatheter distal

to the thrombus. The microwire was replaced by the Solitaire FR (Covidien) mechanical thrombectomy retrievable stent (4 × 15 mm or 4 × 20 mm). The Solitaire FR was fully deployed, and angiographic runs were performed to check for correct placement and expansion of the device and flow restoration. The fully deployed Solitaire FR was maintained in place for 5–7 minutes, and the stent and microcatheter were then removed. During retrieval, manual aspiration was performed with a 60-mL syringe to reverse the flow and remove any clot debris in the guide catheter lumen. If necessary, up to 5 Solitaire passes were performed.

Neither intra-arterial rtPA nor any device other than Solitaire was used.

In the case of underlying arterial stenosis at the cerebral occlusion site or in the involved cervical artery, additional angioplasty by using a balloon and possibly permanent stent placement was performed at the discretion of the operator.

All patients were admitted to the intensive stroke care unit for at least 24 hours, where neurologic deficits were monitored and care followed the European Guidelines (<http://www.eso-stroke.org>) on acute stroke care. Secondary preventive treatments were administered according to the applicable European Guidelines.

Baseline Neuroradiologic Evaluation and Follow-Up

The baseline neuroradiologic data retrieved included the following: infarct extension on pretreatment imaging (lesions were considered severe if the DWI-ASPECTS was <5 for anterior circulation occlusion³ or >3 according to the scale of Renard et al¹⁰ for posterior circulation occlusion), details of the recanalization procedure (number of passes; occurrence of dissection, vasospasm, or extravasation; and procedural time defined as the interval between femoral puncture and the last angiographic run), and time to recanalization (between symptom onset and the first Solitaire deployment⁴). Good recanalization after MET was defined with a Thrombolysis in Cerebral Infarction score of 2b or 3.¹¹

A CT scan was obtained immediately after the procedure in the angiography suite to screen for immediate hemorrhagic transformation or any unforeseen procedural complications and after 24 hours to detect intracranial hemorrhage.¹²

One-year FU MR imaging was prospectively performed from July 2012 to January 2013 on a 3T system (Magnetom Verio; Siemens, Erlangen, Germany) including DWI, axial FLAIR, high-resolution arterial wall axial TSE T2WI (TE/TR = 80/3000 ms, FOV = 180, voxel = 0.4 × 0.5 × 1.7, time of acquisition = 4 minutes 48 seconds), axial gradient-recalled echo T2 sequences, 3D TOF (TE/TR = 3.5/25 ms, FOV = 200, voxel = 0.4 × 0.6 × 0.5, time of acquisition = 3 minutes 46 seconds), and 3D BolusTrak gadolinium-enhanced supra-aortic artery MR angiography (FOV = 320, voxel = 0.7 × 0.7 × 0.7, time of acquisition = 0 minutes 44 seconds).^{13,14}

Indeed, MRA is a noninvasive imaging tool and, at 3T, has proved reliable for detecting intracranial stenosis in comparison with DSA.¹⁵ MR images were analyzed in consensus by 2 experienced neuroradiologists (J.-Y.G., H.R.) to detect stroke recurrence or hemorrhagic lesions in comparison with pretreatment MR imaging. MRA images (gadolinium-enhanced supra-aortic artery and 3D TOF) were analyzed together to

Table 1: Baseline characteristics of patients (40 survivors at 1-year follow-up) and recanalization therapy

	Population (n = 40)	ACO (n = 30)	PCO (n = 10)
Basic data			
Age (yr), mean (SD; range)	57.4 (15.2; 27–79)	60 (14.9; 35–79)	49.6 (14.1; 27–71)
Female sex (%)	12 (30%)	10	2
Pretreatment NIHSS score, mean (SD)	15.9 (5.5)	16.1 (4.9)	15.5 (7.3)
Premorbid status			
Charlson Index ≥ 3 (%)	4 (10)	3	1
Etiology			
TOAST I—large-artery atherosclerosis	10	5	5
TOAST II—cardiac embolism	16	14	2
TOAST IV—other determined etiology	4	3	1
TOAST V—undetermined etiology	9	7	2
Initial imaging			
CT	8	8	3
MRI	32	25	7
DWI-ASPECTS < 5	5	5	
Target-vessel territories			
M1 segment of the MCA	29	29	
M2 segment of the MCA	1	1	
Basilar artery	10		10
Recanalization strategy			
Stand-alone	21	14	7
Bridging	10	8	2
Rescue	9	8	1
Endovascular therapy			
Solitaire passes, mean (range)	2.0 (1–7)	1.9 (1–4)	2.4 (1–7)
Procedural time (min), mean (SD, range)	75 (40, 30–189)	69 (30, 30–150)	96 (54, 30–189)
Time to recanalization (min), mean (SD, range)	322 (127, 127–793)	288 (90, 67–430)	421 (170, 150–793)

Note:—ACO indicates anterior circulation occlusion; PCO, posterior circulation occlusion.

detect arterial abnormalities,⁸ including stenosis, occlusions, and dilation at the original site of cerebral occlusion and in the involved cervical artery. Images were compared with the final post-MET run to differentiate delayed and pre-existing abnormalities.

Baseline Clinical Evaluation and Follow-Up

The following data were retrieved from the medical files: age, sex, pre-existing comorbidity (considered high if the Charlson Comorbidity Index was ≥ 3), vascular risk factors, clinical presentation, stroke etiology according to Trial of Org 10172 in Acute Stroke Treatment (TOAST) criteria, and recanalization strategy. One-year clinical FU was performed by a vascular neurologist (T.R.) on the same day as MR imaging, by using the mRS score, and it was compared with the outcome of the 3-month clinical FU previously performed by the same vascular neurologist. Good outcome was defined as an mRS score of ≤ 2 , and improvement or decline of at least 1 point on the mRS score defined a change in clinical outcome.¹⁶ A patient was considered symptomatic during FU if he or she presented with clinical TIA or stroke recurrence with a permanent deficit.

The previously completed mailed 36-Item Short Form Health Survey Questionnaire (SF-36) was retrieved during the visit. This questionnaire assesses 8 domains on physical, emotional, and mental functioning; is widely used to measure health-related quality of life; and has been validated for patients following a stroke.¹⁷

Statistical Analysis

Statistical analysis was performed by using MedCalc for Windows (MedCalc Software, Mariakerke, Belgium). The change in the

mRS score between 3-month and 1-year FU was compared by a χ^2 test,¹⁶ according to 4 categories (mRS 0–1; mRS 2, 3, and 4–6).¹⁶ To identify independent predictors of angiographic and clinical outcome at 1-year FU, we performed a backward stepwise logistic regression analysis, including all variables, with $P < .2$ (Fisher exact test) in univariate analysis (age, sex, initial NIHSS score, Charlson Index, TOAST criteria, diabetes, hypertension, smoking, use of intravenous thrombolysis, DWI lesion severity, time to recanalization, procedure time, number of stent passes).

RESULTS

Baseline Characteristics of Patients and Recanalization Therapy

Of the 52 patients treated with endovascular therapy by using a Solitaire device between August 2010 and July 2012, 8 died, 4 were lost to follow-up, and 40 were finally available for angiographic assessment at 1-year FU (Table 1). Good recanalization (TICI 2b–3) was achieved in 39/40 patients. Three symptomatic hemorrhages¹² occurred (5.8%) as shown on the 24-hour CT. These were not visible on the CT scan obtained in the angiography suite and therefore were presumed not to be directly related to the procedure itself.

MR Angiographic Follow-Up

One-year angiographic FU was available for 39 of the 40 survivors because 1 patient refused the MR imaging. The mean time from stroke to angiographic FU was 19 ± 4 months. The 1-year FU was delayed for a few months for some patients due to their unavailability. On morphologic sequences, in 32 patients investigated with MR imaging before MET, the comparison between pretreat-

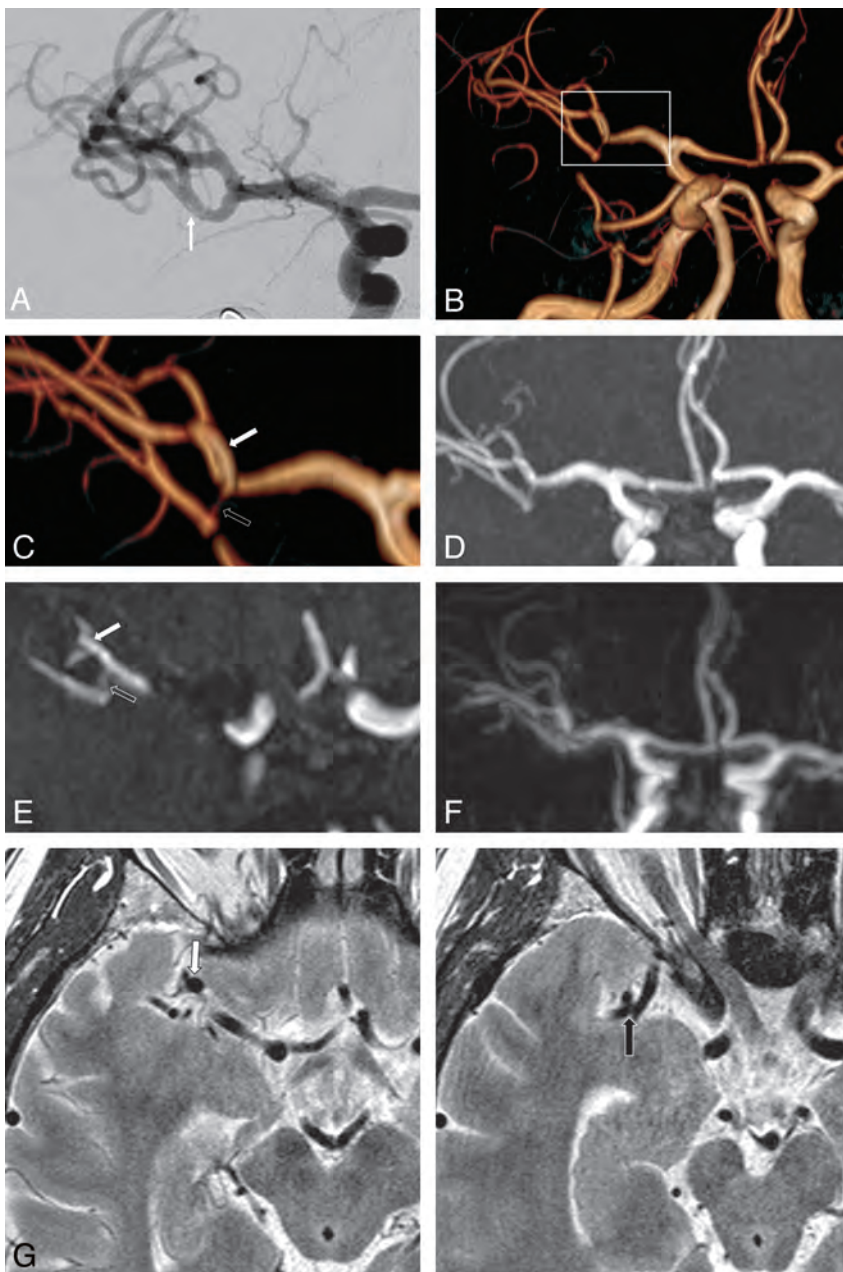


FIG 1. Eighteen-month MR imaging follow-up of de novo arterial stenosis and dilation (patient 2). Final post-MET angiographic run (A) of a 53-year-old patient treated for a right MI middle cerebral artery occlusion, with 5 Solitaire passes in the superior and inferior M2 MCA branches, shows a flap in the inferior stenosis suggestive of dissection (arrow). TOF volume-rendering (B and C), MIP (D), native image (E), gadolinium-enhanced MRA (F), and high-resolution T2 (G) reveal an asymptomatic dilation (white arrow) of the superior M2 MCA branch and $>50\%$ stenosis (black arrow) of the inferior M2 MCA branch of the target vessel. Wall analysis at the stenosis is difficult on high-resolution T2 due to the vertical orientation and the size of the stenosed arterial segment.

ment DWI and long-term FLAIR showed lesion extension for 7 patients (21.9%) without any stigmata of a new infarct in other territories, lesion reduction for 4 patients (12.5%), and lesion stability for 21 patients (65.6%).

MRA showed 10/39 patients (25.6%) presenting with intracranial artery lumen abnormalities, which are summarized in the On-line Table. Four patients (10.3%) (patients 1–4) had delayed de novo stenosis of a target vessel, which appeared normal on the final post-MET run. The number of stent passes was 1 for 2 pa-

tients and 4 for 2 patients. For 1 of these patients, de novo $>50\%$ stenosis of the inferior M2 branch coexisted with dilation of the superior M2 branch, compared with the final post-MET run, which showed no stenosis but a suggestive dissection flap on the inferior M2 branch (Fig 1). Four patients (10.3%) had stenosis of a target vessel, which pre-existed the final post-MET run (patients 5–8). For 3 of these patients, intracranial stenosis was considered as the stroke etiology and stenosis was stable. For 1 of these patients (patient 5), the final post-MET run and long-term FU showed stable $>50\%$ stenosis, whereas atrial fibrillation was considered the stroke etiology (Fig 2). Last, 2 patients had occlusions (patients 9 and 10) of a target vessel, which were due to recanalization failure. Cervical artery abnormalities were seen for 1 patient (patient 11) with vertebral stenosis and in another (patient 12) with occlusion of the carotid dissection site, regarded as the etiology of the stroke.

Medical secondary prevention drugs for these 12 patients were the following: 7/12 (58.3%) on statins, 5/12 (22.7%) on oral anticoagulation, 9/12 (75.0%) on platelet inhibitors, and 4/12 (33.3%) on antihypertensive medication.

Correlation with Clinical Follow-Up

One-year clinical FU was obtained for 40 survivors. All angiographic lesions were clinically asymptomatic. One patient experienced a recurrent TIA (2%) without associated arterial MRA abnormalities. The comparison of 3-month and 1-year outcomes showed significant clinical improvement ($P < .001$), with good clinical outcomes achieved in 50.9% of patients at short-term FU, rising to 62.5% at 1-year FU.

Detailed mRS scores are presented in Fig 3, and SF-36 scores, obtained for 38 of the 40 one-year survivors, are provided in Table 2.

Predictors of MR Angiographic and Clinical Long-Term Outcomes

No independent factor was identified as predicting arterial abnormality occurrence or mRS at 1-year FU. The number of stent retriever passes did not emerge as a relevant predictor ($P = .22$). However, 2 independent predictors were associated with a higher SF-36 score after backward stepwise logistic regression: age younger than 65 years ($P = .005$; 95% CI, -28.634 to -5.454) and time to recanalization ≤ 4.5 hours ($P = .006$; 95% CI, -28.509 to -5.329).

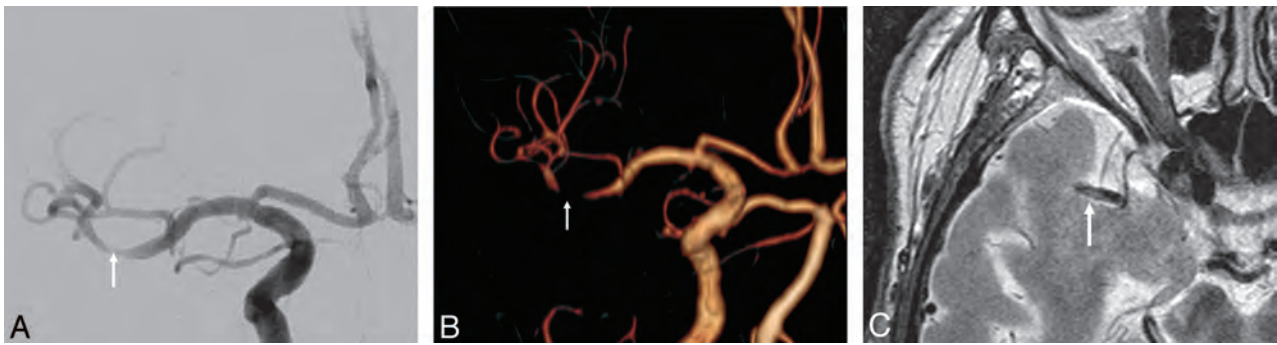


FIG 2. Seventeen-month MR imaging follow-up of pre-existing arterial stenosis (patient 5). Final post-MET angiographic run (A) of a 77-year-old patient treated for a right M1 middle cerebral artery occlusion with 2 Solitaire passes, 1 in the superior and 1 in the inferior M2 MCA branch, shows >50% stenosis in the inferior M2 MCA division (arrow). TOF volume-rendering (B) shows persistent stenosis (worsening aspect was considered due to TOF stenosis overestimation). High-resolution T2 MRA (C) shows M2 posterior wall thickening. Atrial fibrillation was established as the etiology of the stroke.

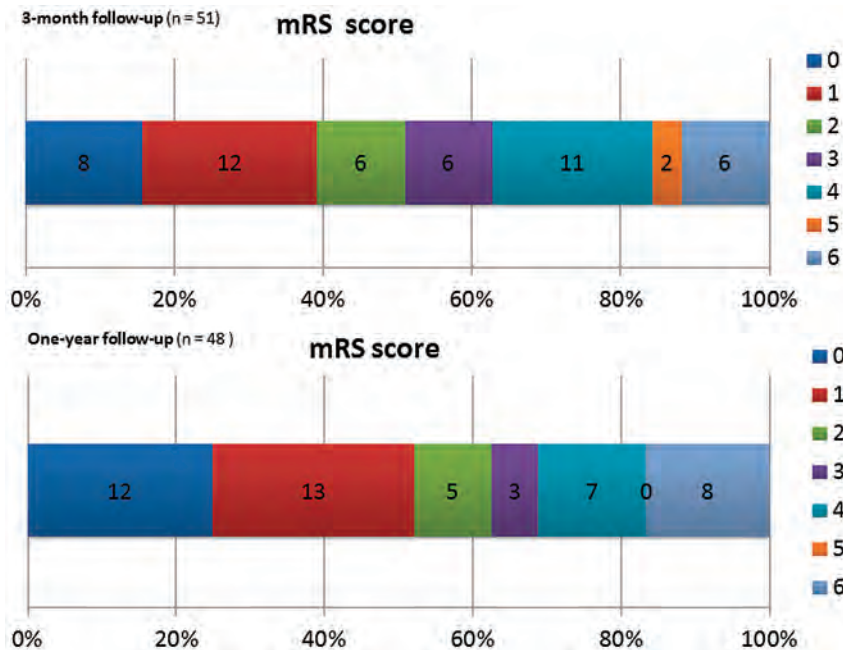


FIG 3. Clinical follow-up. Distribution of 3-month and 1-year mRS (0–6). Values on the bar graphs indicate the number of patients.

Table 2: Clinical outcomes at 1-year follow-up

	Population (n = 48)	ACO	PCO
mRS 0–1 (%)	25 (52.1)	17/34 (50.0)	8/14 (57.1)
mRS 0–2 (%)	30 (62.5)	22/34 (64.7)	8/14 (57.1)
mRS 3 (%)	3 (6.2)	2/34 (5.9)	1/14 (7.1)
mRS 4–5 (%)	7 (14.6)	6/34 (17.6)	1/14 (7.1)
mRS 6 (mortality) (%)	8/48 (16.7)	4/34 (11.8)	4/14 (28.6)
SF-36 PCS (mean) (median, range)	51.2 (52.8, 5.6–100)	49.9 (51.9, 5.6–100)	56.3 (60.6, 32.9–71.0)
SF-36 MCS (mean) (median, range)	51.4 (47.1, 4.0–98.8)	50.4 (47.1, 4.0–98.8)	53.9 (48.6, 32.3–81.1)

DISCUSSION

Our study shows that 1-year MR angiographic FU could identify delayed arterial stenosis or dilation in 10.3% of patients. These delayed arterial abnormalities are of unknown pathophysiologic etiology but may illustrate device-related arterial wall damage, which, up to now, was mainly reported in histopathologic animal

studies.^{18,6} Pre-existing stenosis did not appear to have worsened at 1-year FU or to be likely after MET. All arterial abnormalities remained asymptomatic during the FU period, and no independent predictor of arterial abnormality was identified. Moreover, considering the patients in this study as a whole, we observed further significant clinical improvement between 3-month and 1-year FU, whereas natural stroke history without treatment suggests stable clinical outcome over time.¹⁹ This suggests that clinical evaluation would be more appropriate at 1 or 2 years rather than at 3 months.

MR imaging performed for 1-year FU benefits from the accuracy of TOF-MRA sequences at 3T,²⁰ with high-resolution T2 sequences allowing vessel wall analysis.¹⁴ One-year MR imaging showed intracranial artery abnormalities, stenosis, or dilation in 8 patients (4 with stenosis pre-existing on the final post-MET run, 3 with isolated de novo stenosis, 1 with delayed de novo stenosis associated with arterial dilation), all asymptomatic, as described below.

Three patients had stenosis that pre-existed on the final post-MET run and was established as the stroke etiology (patients 6 to 8). This low rate of post-MET vasospasm that occurred in our study would suggest the efficacy of subsequent optimal medical treatment alone, at least at this FU point between 1 and 2 years.

Three patients had delayed isolated stenosis, and 1 patient had delayed stenosis associated with additional delayed arterial dilation (patients 1–4). Three patients had a known stroke etiology other than atherosclerosis suggestive of device-related arterial wall damage or unknown physiologic causes.

One patient (patient 5) had pre-existing stenosis on the final post-MET run, though the established stroke etiology was cardiac embolism. One theory might be a post-MET vasospasm followed by stenosis due to device-related wall damage, but other physiopathologic causes should not be excluded. This was the only case of vasospasm on the final post-MET run, though some studies have reported immediate post-MET vasospasm^{8,21,22} and even indicated that it may predict subsequent stenosis.⁸ This low rate of post-MET vasospasm in our study may be explained by the continuous infusion of nimodipine through the catheter throughout the procedure. All these patients received appropriate medical secondary prevention.

In summary of our angiographic results, among the 39 patients investigated with MRA 1 year after MET by using Solitaire, for 5 patients (13%) arterial abnormalities (intracranial artery occlusive disease, stenosis, or dilation) might be related to the stent retriever device but ischemic injury of the vessel itself or unknown pathophysiologic causes may also be advanced. Several animal studies have already observed intima and medial layer damage after MET.^{6,18} Endothelial damage caused by stent trauma is likely to be one of the underlying mechanisms of delayed stenosis observed in patient studies, though no stenosis was reported for animal models, probably due to the lack of available FU data. Our results corroborate the recent single study on angiographic short-term follow-up after MET in patients, which showed 3.4% de novo stenosis on digital subtraction angiography⁸ at a median of 3-month FU after MET by using various stent retrievers. The higher stenosis rate in our study may be explained by a possible stenosis overestimation due to TOF imaging. Thus <50% of stenosis cases on MRA may have been insignificant on digital subtraction angiography. Moreover, our FU period was longer than that in the previous study (median of 19 months versus 3 months), yet de novo stenosis may occur late. No predictor for delayed stenosis was identified by the logistic regression. Considering that arterial stenosis may evolve with time and lead to clinical decline, though asymptomatic at 1-year FU, our study suggests that clinical FU after MET should be extended beyond 2 years and associated with noninvasive MR angiographic FU to detect and monitor arterial abnormalities and subsequently gain a greater understanding of their physiopathologic involvement.

Our study has some limitations. First, the small sample size warrants caution, and the stroke protocol applied during the inclusion period did not include certain limitations, such as age or size of the infarct, which are actually considered poor prognostic factors.^{4,23} It is also possible that infarct extension could not be revealed as a predictor of outcome on DWI because pretreatment imaging was a CT scan and not MR imaging for 20% of patients. Second, TOF MRA may overestimate stenosis. Third, the result of <50% stenosis was not shown, and stenosis quantification was not confirmed on digital subtraction angiography (the standard of reference). However being noninvasive, MRA allows repeat scans and, at 3T, proved reliable for detecting stenosis in comparison with DSA, with a sensitivity

and specificity of 85% and 95%, respectively, in patients with stenosis of >50%.¹⁵

Last, high-resolution arterial wall TSE T2 sequences are limited because acquisition is performed in only the axial plane. 3D high-resolution T1 vessel wall imaging should, therefore, be preferred in future imaging FU. Further long-term FU studies (3–5 years) are required to detect clinical symptoms related to arterial stenosis and, therefore, determine whether MR angiographic FU should be recommended in routine practice. Moreover, further studies including larger cohorts with higher statistical power should help to highlight predictors of arterial abnormality occurrence.

CONCLUSIONS

One-year FU of patients treated with Solitaire identified delayed asymptomatic arterial abnormalities, some of which may be due to stent retriever–related wall damage. No predicting factor for their occurrence was identified.

Disclosures: François Eugène—UNRELATED: Travel/Accommodations/Meeting Expenses Unrelated to Activities Listed: Covidien, Comments: 2012 Congress of European Federation of Neurological Societies. Thomas Ronzière—UNRELATED: Payment for Lectures (including service on Speakers Bureaus): Boehringer Ingelheim; Travel/Accommodations/Meeting Expenses Unrelated to Activities Listed: Boehringer Ingelheim, Genzyme.

REFERENCES

1. Dávalos A, Pereira VM, Chapot R, et al. **Retrospective multicenter study of Solitaire FR for revascularization in the treatment of acute ischemic stroke.** *Stroke* 2012;43:2699–705
2. Dorn F, Stehle S, Lockau H, et al. **Endovascular treatment of acute intracerebral artery occlusions with the Solitaire stent: single-center experience with 108 recanalization procedures.** *Cerebrovasc Dis* 2012;34:70–77
3. Costalat V, Machi P, Lobotesis K, et al. **Rescue, combined, and stand-alone thrombectomy in the management of large vessel occlusion stroke using the Solitaire device: a prospective 50-patient single-center study: timing, safety, and efficacy.** *Stroke* 2011;42:1929–35
4. Raouf H, Eugene F, Ferre JC, et al. **Prognostic factors for outcomes after mechanical thrombectomy with Solitaire stent.** *J Neuroradiol* 2013;40:252–59
5. Pereira VM, Gralla J, Dávalos A, et al. **Prospective, multicenter, single-arm study of mechanical thrombectomy using Solitaire flow restoration in acute ischemic stroke.** *Stroke* 2013;44:2802–07
6. Gory B, Bresson D, Kessler I, et al. **Histopathologic evaluation of arterial wall response to 5 neurovascular mechanical thrombectomy devices in a swine model.** *AJNR Am J Neuroradiol* 2013; 34:2192–98
7. Park S, Hwang SM, Song JS, et al. **Evaluation of the Solitaire system in a canine arterial thromboembolic occlusion model: is it safe for the endothelium?** *Interv Neuroradiol* 2013;19:417–24
8. Kurre W, Perez MA, Horvath D, et al. **Does mechanical thrombectomy in acute embolic stroke have long-term side effects on intracranial vessels? An angiographic follow-up study.** *Cardiovasc Intervent Radiol* 2013;36:629–36
9. Davis MJ, Menon BK, Baghirzada LB, et al. **Anesthetic management and outcome in patients during endovascular therapy for acute stroke.** *Anesthesiology* 2012;116:396–405
10. Renard D, Landragin N, Robinson A, et al. **MRI-based score for acute basilar artery thrombosis.** *Cerebrovasc Dis* 2008;25:511–16
11. Higashida RT, Furlan AJ, Roberts H, et al. **Trial design and reporting standards for intra-arterial cerebral thrombolysis for acute ischemic stroke.** *Stroke* 2003;34:e109–37
12. Hacke W, Kaste M, Fieschi C, et al. **Randomised double-blind placebo-controlled trial of thrombolytic therapy with intravenous al-**

- teplase in acute ischaemic stroke (ECASS II): Second European-Australasian Acute Stroke Study Investigators. *Lancet* 1998;352:1245–51
13. Mühlenbruch G, Das M, Mommertz G, et al. **Comparison of dual-source CT angiography and MR angiography in preoperative evaluation of intra- and extracranial vessels: a pilot study.** *Eur Radiol* 2010;20:469–76
 14. Li ML, Xu WH, Song L, et al. **Atherosclerosis of middle cerebral artery: evaluation with high-resolution MR imaging at 3T.** *Atherosclerosis* 2009;204:447–52
 15. Choi CG, Lee DH, Lee JH, et al. **Detection of intracranial atherosclerotic stenosis with 3D time-of-flight magnetic resonance angiography with sensitivity encoding at 3T.** *AJNR Am J Neuroradiol* 2007;28:439–46
 16. Jung S, Mono ML, Fischer U, et al. **Three-month and long-term outcomes and their predictors in acute basilar artery occlusion treated with intra-arterial thrombolysis.** *Stroke* 2011;42:1946–51
 17. Anderson C, Laubscher S, Burns R. **Validation of the Short Form 36 (SF-36) health survey questionnaire among stroke patients.** *Stroke* 1996;27:1812–16
 18. Nogueira RG, Levy EI, Gounis M, et al. **The Trevo device: preclinical data of a novel stroke thrombectomy device in two different animal models of arterial thrombo-occlusive disease.** *J Neurointerv Surg* 2012;4:295–300
 19. Fischer U, Mono ML, Zwahlen M, et al. **Impact of thrombolysis on stroke outcome at 12 months in a population: the Bern stroke project.** *Stroke* 2012;43:1039–45
 20. Pierot L, Portefaix C, Gauvrit JY, et al. **Follow-up of coiled intracranial aneurysms: comparison of 3D time-of-flight MR angiography at 3T and 1.5T in a large prospective series.** *AJNR Am J Neuroradiol* 2012;33:2162–66
 21. Jahan R. **Solitaire flow-restoration device for treatment of acute ischemic stroke: safety and recanalization efficacy study in a swine vessel occlusion model.** *AJNR Am J Neuroradiol* 2010;31:1938–43
 22. Machi P, Costalat V, Lobotesis K, et al. **Solitaire FR thrombectomy system: immediate results in 56 consecutive acute ischemic stroke patients.** *J Neurointerv Surg* 2012;4:62–66
 23. Costalat V, Lobotesis K, Machi P, et al. **Prognostic factors related to clinical outcome following thrombectomy in ischemic stroke (RECAST study): 50 patients prospective study.** *Eur J Radiol* 2012;81:4075–82

Preclinical Evaluation of the Thrombogenicity and Endothelialization of Bare Metal and Surface-Coated Neurovascular Stents

S. Krajewski, B. Neumann, J. Kurz, N. Perle, M. Avci-Adali, G. Cattaneo, and H.P. Wendel



ABSTRACT

BACKGROUND AND PURPOSE: Stent-assisted coiling is routinely used for the endovascular treatment of complex or wide-neck intracranial aneurysms. However, in-stent thrombosis, thromboembolic events, and ischemic complications remain a major concern associated with stent implants. Therefore, a novel low-profile neurovascular stent with a bare metal surface was investigated with regard to thrombogenicity and endothelialization and compared with the same stent coated with albumin or heparin.

MATERIALS AND METHODS: The bare metal and heparin- or albumin-coated stents were loaded in heparin-coated tubing, which was then filled with heparinized human blood ($n = 5$) and circulated at 150 mL/min and 37°C for 60 minutes. Before and after circulation, measurement of various inflammation and coagulation markers and scanning electron microscopy were performed. Endothelialization of the stents was investigated in an in vitro model including human umbilical vascular endothelial cells.

RESULTS: Our results showed that platelet loss and platelet activation and activation of the coagulation cascade, which are induced by the bare metal stents, were significantly reduced by heparin or albumin coating. Adverse effects on erythrocytes, leukocytes, and the complement cascade were not induced by the bare metal or coated stents. Moreover, the bare metal and albumin-coated stents showed good endothelialization properties.

CONCLUSIONS: Albumin and heparin coatings clearly improve the thrombogenicity of the stents and thus may represent fundamental progress in the treatment of intracranial aneurysms. Moreover, preclinical evaluation of neurovascular stents under physiologic conditions supports and accelerates the development of more biocompatible neurovascular stents.

ABBREVIATIONS: HUVECs = human umbilical vascular endothelial cells; SEM = scanning electron microscopy; TAT = thrombin-antithrombin III

Endovascular treatment of complex or wide-neck intracranial aneurysms has been proved feasible by using the stent-assisted coiling technique, which was primarily described in 1997.¹ In this procedure, self-expandable, nitinol-made stents, braided or laser cut, are delivered into the parent vessel by using microcatheters with an inner lumen between 0.0165 and 0.027 inches to retain coils within the aneurysm.^{1,2}

Thus, the implanted stent prevents coil protrusion within the

parent vessel, reduces coil compaction and hence recanalization, and provides a scaffold for endothelialization.²⁻⁵

However, the endoluminal presence of the implant can lead to activation of platelets and leukocytes following adverse effects like thromboembolic complications, hemorrhage, or proinflammatory reactions. Platelet activation is associated with the release of granules containing a plethora of molecules mainly promoting platelet activation and blood coagulation. Therefore, antiplatelet therapy is required, which can prevent intra-aneurysmal thrombosis and thus aneurysm occlusion but also increases the risk of hemorrhagic complications.⁶ Moreover and despite antiplatelet therapy, ischemic complications remain a major concern associated with stent implants. A retrospective review of stent-assisted coiling procedures in 624 patients between 2000 and 2011 revealed intra- and postprocedural in-stent thrombosis and thromboembolic events in 9.0% of the patients, whereas low or no response to antiplatelet agents and early interruption of therapy are possible causes for ischemic events.²

A retrospective study of 36 patients treated with stent-assisted

Received March 6, 2014; accepted after revision June 23.

From the Department of Thoracic, Cardiac and Vascular Surgery (S.K., B.N., J.K., N.P., M.A.-A., H.P.W.), Clinical Research Laboratory, University Hospital Tuebingen, Tuebingen, Germany; and Acandis GmbH & Co KG (G.C.), Pforzheim, Germany.

The study was funded by the German Federal Ministry of Economic Affairs (Economics and Energy).

Please address correspondence to Stefanie Krajewski, PhD, Department of Thoracic, Cardiac and Vascular Surgery, University Hospital Tuebingen, Clinical Research Laboratory, Tuebingen University, Calwerstr 7/1, 72076 Tuebingen, Germany; e-mail: stefanie.krajewski@uni-tuebingen.de

Indicates open access to non-subscribers at www.ajnr.org

<http://dx.doi.org/10.3174/ajnr.A4109>

coiling after aneurysm rupture showed that in 17%, stent-related thromboembolic complications occurred. Intra- and postprocedural clopidogrel administration was related to an incidence of thrombotic events of 20% and 29%, respectively. Even pretreatment with clopidogrel could not prevent thrombotic events, which were shown in 6% of cases.⁷

Therefore, preventing or strongly decreasing activation of platelets and the coagulation cascade, while enhancing or at least not impairing endothelialization, is a primary objective in the treatment of endovascular diseases. Stent design, influence on fluid dynamics, and particularly surface modifications are current options to decrease activation of platelets and the coagulation cascade, and they also address hemorrhagic stroke, because the necessity for antiplatelet therapy can be reduced. Previous studies show that surface coatings with the antithrombotic molecules heparin and albumin, which is the most abundant protein in blood, increase the biocompatibility of different biomaterials.⁸⁻¹⁰

In our study, an in vitro model was established, which allows investigation of neurovascular stents with regard to thrombogenicity and coagulation activation.

Small-diameter tubing and low flow rates simulating intracranial vessel conditions were used to investigate novel low-profile neurovascular stents with bare metal surfaces or 2 coatings, including albumin and heparin, with regard to thrombogenicity. Furthermore, a predisposition toward endothelialization was investigated in an in vitro rotation model including human umbilical vascular endothelial cells (HUVECs).

MATERIALS AND METHODS

For this study, the neurovascular stent Acclino ($n = 24$; Acanadis, Pforzheim, Germany) was used. Acclino is a low-profile, laser-cut stent with an electropolished surface and strut dimensions ranging between $\sim 55 \mu\text{m}$ (wall thickness) and $\sim 35 \mu\text{m}$ (strut width).

The stent is deliverable within the 1.9F microcatheter NeuroSlider 17 (Acandis) with a lumen of 0.0165 inches ($\sim 0.42 \text{ mm}$). The small catheter lumen and the size of the stent (3.5 and 4.5 mm in expanded configurations) allow the application in distal intracranial vessels with diameters between 2 and 4 mm, whereas the closed-cell structure allows retrieval and repositioning up to 90% of its deployment.

For the current study, specific Acclino stent samples with a wall thickness of $\sim 75 \mu\text{m}$ were manufactured to reproduce a worst-case scenario with regard to blood flow interruption caused by the stent structure.

Blood Sampling

Blood-sampling procedures were approved by the ethics committee of the University of Tuebingen, Tuebingen, Germany. Blood was collected from healthy volunteers ($n = 5$), who gave signed informed consent, and was anticoagulated with 1.5 IU/mL Heparin-Natrium (Rathiofarm, Ulm, Germany). Exclusion criteria for the blood donors were the following: smokers; drug intake in the last 2 weeks before blood sampling, especially hemostasis-affecting agents like acetylsalicylic acid; oral contraceptives; non-steroidal antiplatelet drugs; and others, to guarantee optimal hemostatic function.

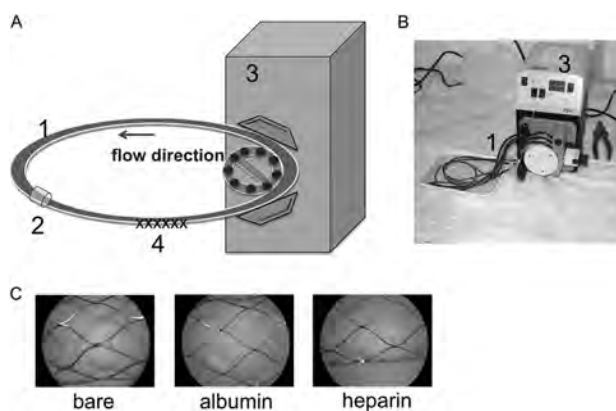


FIG 1. Closed-loop in vitro circulation model for neurovascular stent testing by using fresh human whole blood. Schematic overview (A) and photograph (B) of the in vitro circulation model consisting of the following: 1) heparin-coated tubing (inner diameter = 3.2 mm, length = 75 cm), 2) connection tubing, 3) peristaltic pump (flow rate = 150 mL/min), 4) test device. C, Representative macroscopic images of uncoated and albumin- and heparin-coated stents after circulation for 60 minutes at 37°C ($\times 20$ magnification).

Neurovascular Stent Coating

For albumin coating, 8 neurovascular stents were first incubated for 2 hours at room temperature in 1% human serum albumin (HSA; CSL Behring, Marburg, Germany), followed by a washing step in saline and a 30-minute incubation in a suspension containing 0.5-mg of 1-ethyl-3-(3-dimethylaminopropyl)carbodiimide hydrochloride (Thermo Scientific, Karlsruhe, Germany) for albumin cross-linking. Afterward, the stents were incubated again in 1% HSA for 2 hours at room temperature followed by another washing step in saline. After being coated, the stents were air-dried and stored at 4°C until analysis in the in vitro thrombogenicity model. The heparin coating of the stents ($n = 8$) for the thrombogenicity and endothelialization experiments was performed according to standard methods.¹¹ To guarantee sterile conditions in the endothelialization model, we sterilized the stents by using ethylene oxide.

In Vitro Thrombogenicity Model

This novel model was established to investigate the effect of neurovascular stents on various cascade reactions of the human hemostatic system (coagulation cascade, cell alteration, complement system, and inflammation) during blood circulation (Fig 1A, -B).

For each blood donor ($n = 5$), 4 polyvinyl chloride tubes (inner diameter = 3.2 mm, length = 75 cm; Tygon; Saint-Gobain Performance Plastics, Chamy, France) were coated with heparin by Enson (Enson, Cape Coral, Florida) and left empty or loaded with either 1 bare metal, 1 albumin-, or 1 heparin-coated stent. Subsequently, each tubing was filled with a total of 6-mL heparinized human blood, closed by silicone connection tubing, and circulated at 150 mL/min in a water bath at 37°C for 60 minutes. For each donor, 6 mL of heparinized blood served for the measurement of baseline values before circulation. Before and after circulation, the blood was directly transferred to the corresponding terminating media and was further processed for enzyme-linked immunosorbent assays and whole blood analysis.

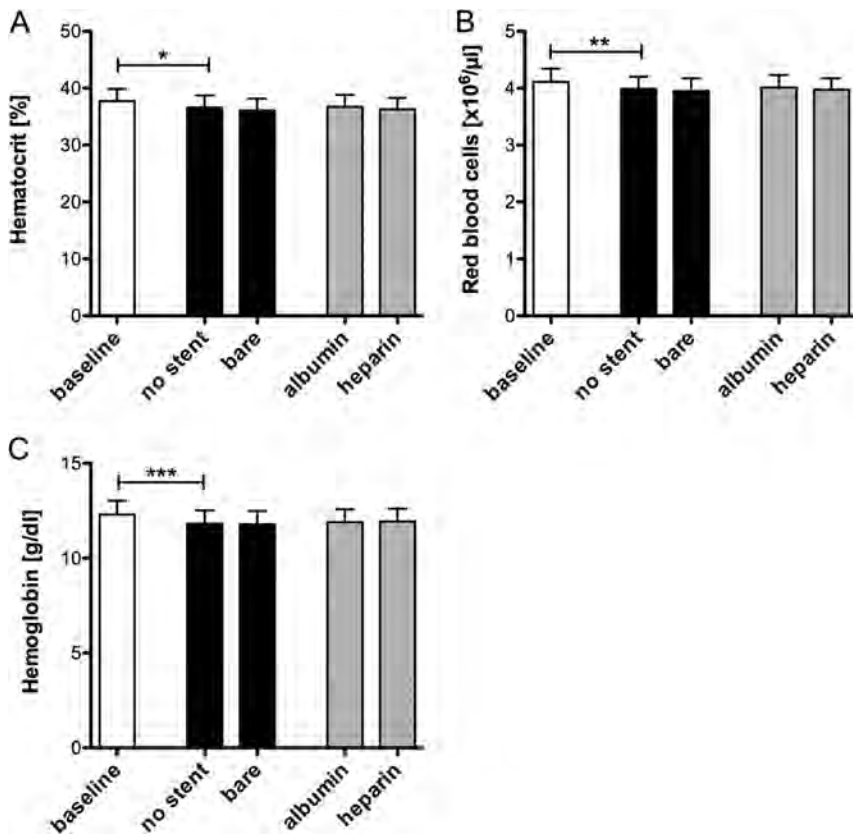


FIG 2. Neurovascular stents do not change hematocrit levels, erythrocyte number, or hemoglobin concentration. Heparin-coated tubing was loaded with bare metal, albumin-, or heparin-coated neurovascular stents and filled with 6 mL of fresh heparinized human blood. Tubing without a stent served as a negative control. Hematocrit level (A), erythrocyte numbers (B), and hemoglobin concentrations (C) were analyzed before and after 60 minutes of circulation at 150 mL/min. Data are given as means and standard error of the mean ($n = 5$) and were analyzed by using repeated-measures ANOVA with the Bonferroni multiple-comparison test. One asterisk indicates $P < .05$; two asterisks, $P < .01$; three asterisks, $P < .001$.

Endothelialization Model

The endothelialization experiments ($n = 3$) were performed as previously described.¹² Briefly, 2-mL bioreactor chambers were loaded with either a sterilized bare metal, an albumin-, or a heparin-coated stent. Isolation of HUVECs was adapted from a previously described method for the isolation of endothelial cells from residual saphenous vein biopsies.¹² For each sample, 2.5×10^6 cells were resuspended in 2.5-mL VasuLife EnGS medium (CellSystems, Troisdorf, Germany) containing a VasuLife EnGS LifeFactors Kit, 50- $\mu\text{g}/\text{mL}$ gentamicin, and 0.05- $\mu\text{g}/\text{mL}$ amphotericin B (PAA Laboratories, Cölbe, Germany).

Following the addition of the cell suspension, the bioreactor chambers were assembled in the rotation device and rotated at 37°C and 5% CO_2 . After 72 hours of incubation, the stents were washed in phosphate buffered saline and subsequently prepared for scanning electron microscopy analysis.

Measurement of Hemostatic Markers

The analysis of markers indicating activation of platelets and leukocytes and the coagulation cascade and complement system was performed in plasma by enzyme-linked immunosorbent assays, according to the manufacturer's instructions. To investigate released, plasmatic markers indicating platelet and leukocyte activation, we analyzed PF-4 (Abcam,

Cambridge, United Kingdom) and polymorphonuclear neutrophil elastase (Demeditec Diagnostics, Kiel-Wellsee, Germany) levels. As a marker for coagulation, we determined thrombin-antithrombin III (TAT) complexes (Siemens Healthcare, Marburg, Germany). Moreover, we analyzed SC5b-9 (TECOMedical, Bünde, Germany) to detect activation of the complement system.

Whole Blood Count Analysis

The number of erythrocytes, leukocytes, and platelets and hematocrit and hemoglobin values were measured by a cell counter system (ABX Micros 60; Axon Lab AG, Baden, Switzerland) in baseline samples and after circulation in all groups.

Scanning Electron Microscopy

Scanning electron microscopy (SEM) was performed to investigate the thrombogenicity and the endothelialization rate of the different stent surfaces after contact with human whole blood and HUVECs, respectively. After each experiment, the stents were rinsed in phosphate buffered saline and fixed in glutaraldehyde solution (2% in phosphate buffered saline, pH 7.4) overnight at 4°C. After another washing step with phosphate buffered saline, the stents were dehydrated by using ascending concentrations of ethanol

(Emsure; Merck, Darmstadt, Germany) and critical point dried. After sputtering with gold palladium, we performed SEM analysis by using the EVO LS 10 scanning electron microscope (Carl Zeiss, Jena, Germany).

Statistics

Data are depicted as means with standard error of the mean. Data were analyzed by using repeated-measures ANOVA with the Bonferroni multiple comparison test to analyze differences among groups. All analyses were performed by using the statistical software package GraphPad Prism (Version 5; GraphPad Software, San Diego, California). Statistical significance was defined as $P < .05$.

RESULTS

Hemocompatibility Testing of Neurovascular Stents

Contact of whole blood with artificial surfaces like stents, catheters, implants, and so forth is associated with various alterations of the hemostatic system. To evaluate the hemocompatibility of the bare metal ($n = 5$), albumin- ($n = 5$), or heparin-coated ($n = 5$) stents for neurovascular application, we developed an in vitro model to guarantee a defined and continuous blood flow mimicking blood circulation in the brain (Fig 1A, -B). Directly after

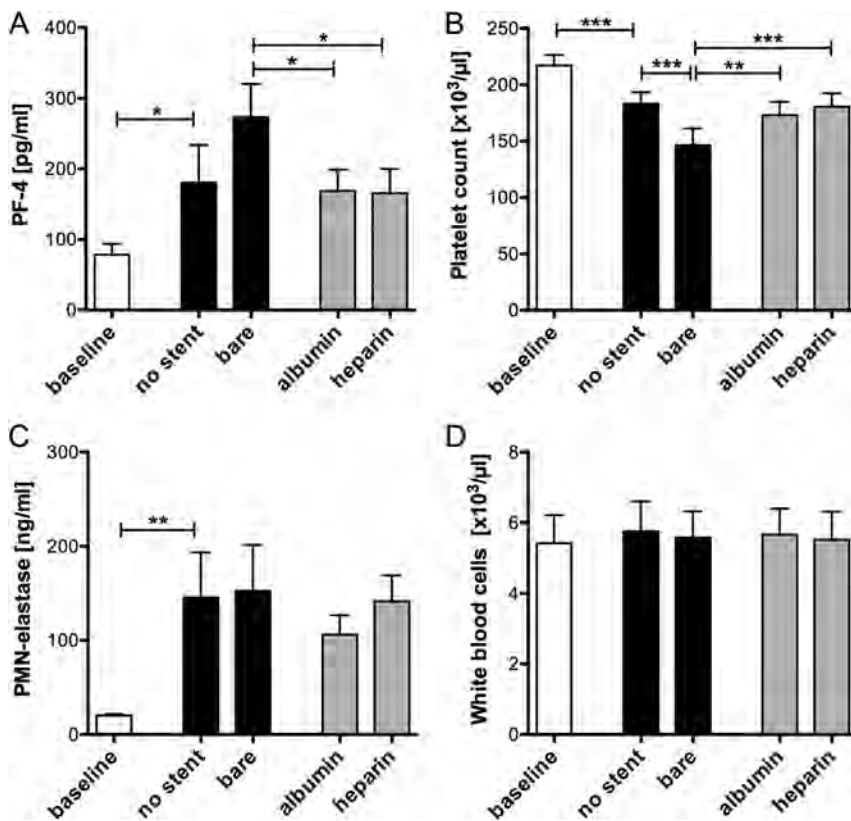


FIG 3. Platelet activation is significantly reduced due to albumin and heparin coating. Bare metal, albumin-, or heparin-coated neurovascular stents were circulated in the in vitro model for 60 minutes at 150 mL/min. Before and after circulation, PF-4 plasma levels (A), platelet counts (B), polymorphonuclear neutrophil-elastase concentrations (C), and white blood cell numbers (D) were analyzed in all groups. Data are given as mean and standard error of the mean ($n = 5$); groups were compared by using repeated-measures ANOVA with the Bonferroni multiple comparison test. One asterisk indicates $P < .05$; two asterisks, $P < .01$; three asterisks, $P < .001$.

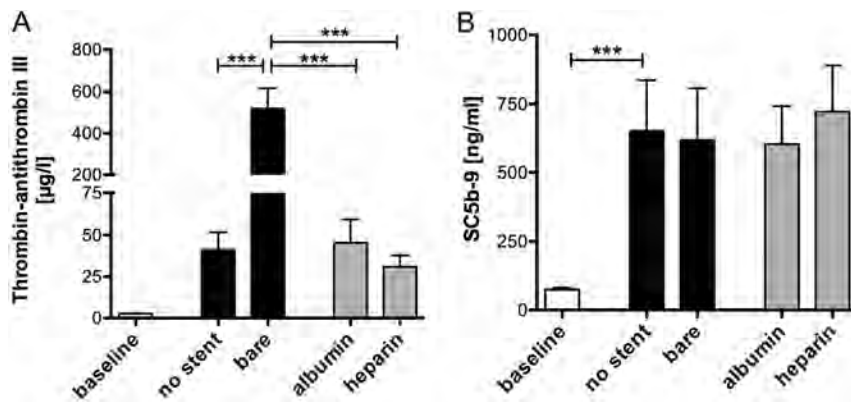


FIG 4. Albumin and heparin coating of neurovascular stents profoundly reduces activation of the coagulation cascade. TAT levels (A) and Sc5b-9 concentrations (B) were measured in human whole blood before and after circulation in the bare metal, albumin-, or heparin-coated stent groups. Blood circulated without a stent served as a negative control. Data are given as mean and standard error of the mean ($n = 5$), and groups were compared by using repeated-measures ANOVA with the Bonferroni multiple comparison test. Three asterisks indicate $P < .001$.

circulation, macroscopic images, which are exemplarily shown in Fig 1C from 1 blood donor, were obtained of each stent.

Whole Blood Count Analysis. Before and after circulation in the in vitro model, the whole blood was analyzed in all groups. Circulation induced a significant decrease of hematocrit ($P < .05$, Fig

2A), red blood cell counts ($P < .01$, Fig 2B), and hemoglobin levels ($P < .001$, Fig 2C) in the control group containing no stent. No significant changes were observed in the bare metal and albumin- and heparin-coated stent groups compared with the control group.

Platelet and Leukocyte Activation. The concentration of PF-4, a small chemokine released from platelet α granules, is significantly increased during circulation in both control groups containing no stent and a bare metal stent, respectively ($P < .05$, Fig 3A). In the groups containing albumin- or heparin-coated stents, the release of PF-4 was significantly reduced ($P < .05$). Platelet activation was also estimated by the analysis of platelet counts. Compared with a platelet count of $217.200 \pm 9.300 \mu\text{L}$ before circulation, a significant loss of platelets in the control group containing no stent ($P < .001$) was observed, which was further increased in the bare metal stent group ($P < .001$, Fig 3B). Again, the decrease in platelet numbers was less severe in the coated stent groups ($P < .01$).

Despite platelet activation, leukocyte activation based on granule release and leukocyte counts was investigated. The plasma concentration of polymorphonuclear neutrophil-elastase released from granulocytes significantly increased because of circulation in the in vitro model ($P < .01$, Fig 3C). In the stent groups, no significant differences compared with the control group were detected. Similar results were obtained for the leukocyte counts (Fig 3D), in which no significant differences were detected among the groups after circulation.

Effects on the Coagulation Cascade and the Complement System. Activation of the coagulation cascade was estimated by the formation of the TAT complex indicating thrombin generation before and after circulation in all groups (Fig 4A). Compared with a TAT concentration of $41.1 \pm 10.6 \mu\text{g/L}$ in the group containing no stent, a significant increase in TAT concentration was found in the bare

metal stent group ($518.3 \pm 98.9 \mu\text{g/L}$, $P < .001$). Stents coated with albumin or heparin induced a significantly lower activation of the coagulation cascade ($P < .001$), reaching values comparable with the group containing no stent.

The formation of Sc5b-9, the final complex of the complement

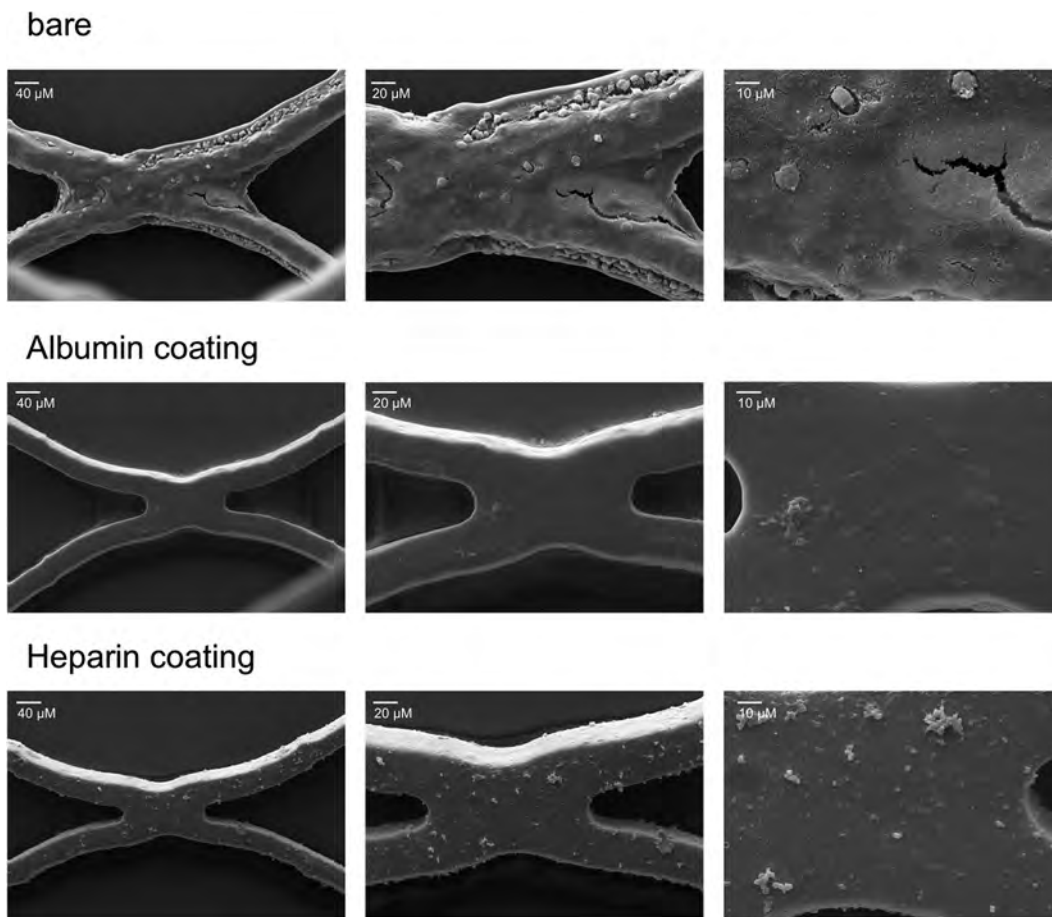


FIG 5. Thrombogenicity is reduced by albumin and heparin coating of neurovascular stents. Representative SEM images of the inner lumen of a bare metal stent or stents coated with albumin and heparin after circulation for 60 minutes at 150 mL/min (magnification $\times 500$, $\times 1000$, and $\times 2500$).

Classification of the bare metal, albumin-coated, and heparin-coated neurovascular stents based on results gained from the thrombogenicity and endothelialization models^a

Neurovascular Stent	Thrombogenicity ^b	No. of Experiments	Endothelialization ^c	No. of Experiments
Bare metal	1.87 \pm 0.4	5	3 \pm 0	3
Albumin-coated	0.4 \pm 0.5	5	2.8 \pm 0.3	3
Heparin-coated	0.2 \pm 0.2	5	1.3 \pm 0.6	3

^a Data are mean values \pm SD.

^b Thrombogenicity: 0 = no thrombogenicity, 1 = very minor thrombogenicity, 2 = minor thrombogenicity, 3 = moderate thrombogenicity, and 4 = serious thrombogenicity.

^c Endothelialization performance: 0 = no endothelialization, 1 = very little endothelialization, 2 = little endothelialization, 3 = good endothelialization, and 4 = complete endothelialization.

system, significantly increased on circulation ($P < .001$, Fig 4B). No significant differences in Sc5b-9 generation were observed between the control and the stent-containing groups.

Blood Cell Adhesion on Stents. After circulation, each stent was analyzed by using scanning electron microscopy, whereby a clear difference in thrombogenicity was observed. SEM images of each stent are exemplarily shown from 1 donor at magnifications of $\times 500$, $\times 1000$, and $\times 2500$ (Fig 5). The bare metal stents showed a profound adhesion of blood cells, particularly platelets, and the formation of an attenuated fibrin network for all blood donors. In contrast, no or only a few platelets were detected on the surface of the albumin- and heparin-coated stents.

Overall, the albumin- and heparin-coated stents exhibited

very little thrombogenicity compared with the bare metal stents, which also did not induce strong thrombogenic reactions (Table).

Endothelialization Properties of Neurovascular Stents

Next to hemocompatibility, the rate of endothelialization is another factor in characterizing the performance of a stent. Adhesion of HUVECs on the surface of the bare metal ($n = 3$), albumin- ($n = 3$), and heparin-coated ($n = 3$) stents was thus investigated after 72 hours of dynamic incubation in a specific model. SEM images showed that the bare metal stents and the albumin-coated stents displayed good endothelialization performance. Most interesting, the adhesion of HUVECs on the surface of the heparin-coated stents was decreased compared with the bare metal and albumin-coated stents (Fig 6 and Table).

DISCUSSION

The findings of our study indicate that surface coating of neurovascular stents with albumin or heparin significantly reduces platelet loss, platelet activation, and activation of the coagulation cascade. Other blood cell counts, activation of leukocytes, and the

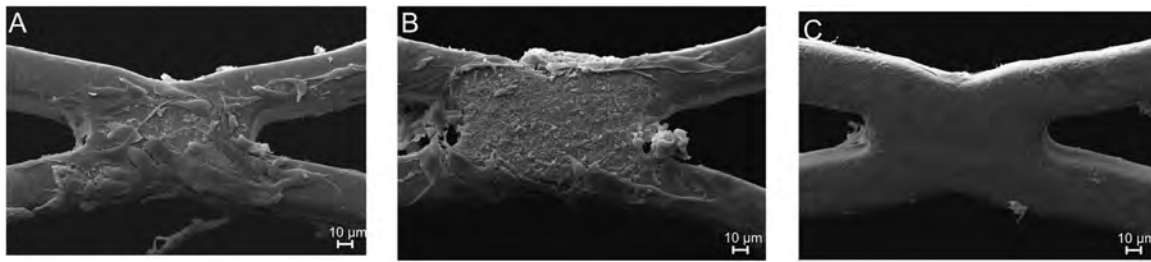


FIG 6. Endothelialization of neurovascular stents. Representative SEM images of the inner lumen of a bare metal stent (A) or stents coated with albumin (B) and heparin (C) after incubation with human umbilical vascular endothelial cells in a rotating bioreactor for 72 hours (magnification $\times 1000$).

complement system were not altered by the bare metal or coated stents.

To investigate the hemostatic performance of a low-profile neurovascular stent and different surface coatings, we established a dynamic in vitro model with focus on cerebral-like flow conditions and lumen size. A flow rate of $150 \text{ mL}/\text{min}^{-1}$ was set according to blood flow in the middle cerebral artery, resulting from measurement in 92 patients.¹³ A tubing diameter of 3.2 mm was chosen, which is an appropriate size for distal intracranial vessels like the middle cerebral artery.

In our study, platelet counts and SEM analysis showed that a high number of platelets adhere to the surface of the bare metal stents. Platelet adhesion and aggregation were seen in particular at junctions between stent struts, thus indicating the role of flow dynamic phenomena like fluid stagnation or turbulence.

Previous studies investigating biomaterials showed that heparin coating is most frequently used to increase the hemocompatibility and decrease the thrombogenicity of various biomaterials.^{14–16} Furthermore, albumin coating of arterial prostheses decreased activation of the coagulation cascade and platelet and leukocyte adhesion.¹⁷

In our study, both coatings showed excellent performance in preventing platelet adhesion, resulting in platelet counts similar to those in the control group without stents. Platelet activation investigated by measuring platelet granule release was also decreased by both coatings, indicating good antithrombotic surface properties.

The amount of TAT complex was also extremely reduced by the coatings; this finding shows the important role of surface material in the (intrinsic) coagulation cascade.

With regard to endothelialization, various studies have investigated the effect of heparin- or albumin-coated biomaterials in different in vitro and in vivo models.^{8,18–21}

In our in vitro study, endothelial cell adhesion was shown on the surface of the bare metal and albumin-coated stents, whereas the heparin coating seems not to promote cell adhesion. Compared with the in vivo situation, our endothelialization experiments were performed in an isolated system containing endothelial cells and cell culture media with 2% fetal calf serum. Under physiologic conditions, the adsorption of blood plasma proteins, such as albumin and fibrinogen, occurs immediately after implantation of the biomaterial. Hence, the low amount of plasma proteins in our cell culture experiments might have influenced

the endothelialization performance of the different stents; thus, further in vivo investigations are warranted.

CONCLUSIONS

Although the application of low-profile stents has greatly expanded the possibilities in treating intracranial aneurysms, improving the performance of stents with regard to biocompatibility is still necessary and can be achieved by implant surface modifications. In this in vitro study, albumin and heparin coatings reduced the thrombogenicity of the stents in comparison with the bare metal stent. Therefore, a surface that decreases platelet and coagulation activation can represent crucial progress in the treatment of intracranial aneurysms.

REFERENCES

- Higashida RT, Smith W, Gress D, et al. **Intravascular stent and endovascular coil placement for a ruptured fusiform aneurysm of the basilar artery: case report and review of the literature.** *J Neurosurg* 1997;87:944–49
- McLaughlin N, McArthur DL, Martin NA. **Use of stent-assisted coil embolization for the treatment of wide-necked aneurysms: a systematic review.** *Surg Neurol Int* 2013;4:43
- O’Kelly CJ. **Should stents be used in the treatment of ruptured intracranial aneurysms?** *J Neurosurg Sci* 2011;55:27–33
- Wanke I, Forsting M. **Stents for intracranial wide-necked aneurysms: more than mechanical protection.** *Neuroradiology* 2008;50:991–98
- Mocco J, Fargen KM, Albuquerque FC, et al. **Delayed thrombosis or stenosis following Enterprise-assisted stent-coiling: is it safe? Mid-term results of the interstate collaboration of Enterprise stent coiling.** *Neurosurgery* 2011;69:908–13, discussion 913–14
- Ries T, Buhk JH, Kucinski T, et al. **Intravenous administration of acetylsalicylic acid during endovascular treatment of cerebral aneurysms reduces the rate of thromboembolic events.** *Stroke* 2006;37:1816–21
- Golshani K, Ferrel A, Lessne M, et al. **Stent-assisted coil embolization of ruptured intracranial aneurysms: a retrospective multi-center review.** *Surg Neurol Int* 2012;3:84
- Marois Y, Chakfe N, Guidoin R, et al. **An albumin-coated polyester arterial graft: in vivo assessment of biocompatibility and healing characteristics.** *Biomaterials* 1996;17:3–14
- Mulvihill JN, Faradji A, Oberling F, et al. **Surface passivation by human albumin of plasmapheresis circuits reduces platelet accumulation and thrombus formation: experimental and clinical studies.** *J Biomed Mater Res* 1990;24:155–63
- Chen J, Chen C, Chen Z, et al. **Collagen/heparin coating on titanium surface improves the biocompatibility of titanium applied as a blood-contacting biomaterial.** *J Biomed Mater Res A* 2010;95:341–49
- Johnson I, Perchy D, Liu H. **In vitro evaluation of the surface effects on magnesium-yttrium alloy degradation and mesenchymal stem cell adhesion.** *J Biomed Mater Res A* 2012;100:477–85

12. Avci-Adali M, Kobba J, Neumann B, et al. **Application of a rotating bioreactor consisting of low-cost and ready-to-use medical disposables for in vitro evaluation of the endothelialization efficiency of small-caliber vascular prostheses.** *J Biomed Mater Res B Appl Biomater* 2013;101:1061–68
13. Zhao M, Amin-Hanjani S, Ruland S, et al. **Regional cerebral blood flow using quantitative MR angiography.** *AJNR Am J Neuroradiol* 2007;28:1470–73
14. Hirsh J, Siragusa S, Cosmi B, et al. **Low-molecular-weight heparins (LMWH) in the treatment of patients with acute venous thromboembolism.** *Thromb Haemost* 1995;74:360–63
15. Blezer R, Fouache B, Willems GM, et al. **Activation of blood coagulation at heparin-coated surfaces.** *J Biomed Mater Res* 1997;37:108–13
16. Klement P, Du YJ, Berry L, et al. **Blood-compatible biomaterials by surface coating with a novel antithrombin-heparin covalent complex.** *Biomaterials* 2002;23:527–35
17. Kottke-Marchant K, Anderson JM, Umemura Y, et al. **Effect of albumin coating on the in vitro blood compatibility of Dacron arterial prostheses.** *Biomaterials* 1989;10:147–55
18. Bae IH, Park IK, Park DS, et al. **Thromboresistant and endothelialization effects of dopamine-mediated heparin coating on a stent material surface.** *J Mater Sci Mater Med* 2012;23:1259–69
19. Moer R, Myreng Y, Mølstad P, et al. **Stenting in small coronary arteries (SISCA) trial: a randomized comparison between balloon angioplasty and the heparin-coated beStent.** *J Am Coll Cardiol* 2001;38:1598–603
20. Serruys PW, Emanuelsson H, van der Giessen W, et al. **Heparin-coated Palmaz-Schatz stents in human coronary arteries: early outcome of the Benestent-II Pilot Study.** *Circulation* 1996;93:412–22
21. Blindt R, Vogt F, Astafieva I, et al. **A novel drug-eluting stent coated with an integrin-binding cyclic Arg-Gly-Asp peptide inhibits neointimal hyperplasia by recruiting endothelial progenitor cells.** *J Am Coll Cardiol* 2006;47:1786–95

Parent Artery Occlusion in Large, Giant, or Fusiform Aneurysms of the Carotid Siphon: Clinical and Imaging Results

M.-A. Labeyrie, S. Lenck, D. Bresson, J.-P. Desilles, A. Bisdorff, J.-P. Saint-Maurice, and E. Houdart

ABSTRACT

BACKGROUND AND PURPOSE: Parent artery occlusion has long been considered the reference treatment for large/giant or fusiform aneurysms of the carotid siphon. However, meager recent data exist on this technique, which tends to be replaced by stent-assisted reconstructive techniques. In our department since 2004, we have assessed the safety, efficacy, and complication risk factors of parent artery occlusion by using coils for trapping these aneurysms.

MATERIALS AND METHODS: We determined retrospectively the complication rate, factors associated with the occurrence of an ischemic event, changes in symptoms of mass effect, evolution of the aneurysmal size, and the growth of an additional aneurysm after treatment.

RESULTS: Fifty-six consecutive patients were included, with a median age of 54 years (range, 25–85 years; 92% women), 48% with giant aneurysms and 75% with infraclinoid aneurysms. There was a permanent morbidity rate of 5% exclusively due to ischemia, a zero mortality rate, an aneurysmal retraction rate of 91%, and an improvement rate for pain of 98% and for cranial nerve palsy of 72%, with a median follow-up of >3 years. Para-/supraclinoid topography of the aneurysm ($P = .043$) and the presence of cardiovascular risk factors ($P = .024$) were associated with an excessive risk of an ischemic event, whereas the presence of a mural thrombus had a protective role ($P = .033$).

CONCLUSIONS: In this study, parent artery occlusion by using coils to treat large/giant or fusiform aneurysms of the carotid siphon was safe and effective, especially for giant infraclinoid aneurysms. According to recent meta-analyses, these results suggest that the validation of stent-assisted reconstructive treatments for these aneurysms requires controlled studies with parent occlusion artery.

ABBREVIATIONS: BOT = balloon occlusion test; IE = ischemic event; PAO = parent artery occlusion; Q1–Q3 = interquartile range

There is a high risk of severe bleeding, debilitating pain, or progressive cranial nerve palsy with symptomatic, intradural, or some extradural, large, giant, or fusiform aneurysms of the carotid siphon.^{1–3} The selective endovascular coiling of this type of aneurysm is not usually adopted due to the low rate of recovery and technical difficulties when the neck of the aneurysm is large.^{4–6} The surgical treatment (selective or deconstructive by trapping) is technically challenging and is rarely performed, in our experience, for large supracavernous aneurysms with a well-tolerated occlusion test, and it is usually not performed for large intracavernous aneurysms because of the risk of cranial nerve injury. Proximal occlusion without trapping (surgical or endovascular) has a lower rate of aneurysmal retraction and should not be performed for carotid aneurysms.

Endovascular parent artery occlusion (PAO) with trapping of the aneurysm has long been considered the reference treatment for large, giant, or fusiform aneurysms of the carotid siphon. However, data from the literature assessing this technique focus on small or old series using mainly detachable balloons, which are no longer available in most departments of neuroradiology.^{7–11} Besides, developing new reconstructive stent-assisted embolization techniques, including flow diversion, offer a therapeutic possibility for this type of aneurysm that could be preferred to deconstructive techniques.^{12–14} Assessing carotid occlusion for treating this type of aneurysm remains relevant today.

The main objective of this study was to assess the safety and efficacy of PAO by using coils to treat large, giant, or fusiform aneurysms of the carotid siphon. The secondary objective was to determine the factors associated with the occurrence of an ischemic event (IE) in the outcomes.

MATERIALS AND METHODS

Patients

From a prospective registry, we retrospectively included consecutive patients treated in our center between January 2004 and

Received March 24, 2014; accepted after revision June 23.

From the Departments of Interventional Neuroradiology (M.-A.L., S.L., J.-P.D., A.B., J.-P.S.-M., E.H.) and Neurosurgery (D.B.), Université Paris Diderot, Pôle Neurosensoriel, Lariboisière Hospital, Paris, France.

Please address correspondence to Marc-Antoine Labeyrie, MD, Service de Neuro-radiologie, Hôpital Lariboisière, 2 Rue Ambroise Paré, 75010, Paris, France; e-mail: marc-antoine.labeyrie@lrh.aphp.fr

<http://dx.doi.org/10.3174/ajnr.A4064>

December 2013 by PAO for a saccular aneurysm with a diameter of ≥ 15 mm or a fusiform aneurysm (regardless of its diameter) on the carotid siphon. Indications for PAO for these kinds of aneurysms were limited, in our center, to intradural aneurysms and/or symptomatic aneurysms and/or aneurysms with sphenoid sinus erosion. Proximal carotid occlusions without trapping were excluded from the analysis. For each patient, we collected the following data: 1) age and sex, 2) the presence of at least 1 cardiovascular risk factor, 3) the administration of antiplatelet therapy during the procedure, and 4) the symptoms at presentation (asymptomatic, pain [including headache, hemifacial pain, or retro-orbital pain], cranial nerve palsy, subarachnoid hemorrhage, or cavernous carotid fistula). Cerebral imaging before the procedure was reviewed to determine the characteristics of the aneurysm: 1) its topography (intraclinoid versus para-/supraclinoid), 2) its morphology (giant saccular aneurysms [≥ 25 mm], large saccular aneurysms [≥ 15 mm and < 25 mm], and fusiform aneurysms), 3) the presence of a mural thrombus, 4) the presence of additional aneurysms, and 5) a delay of ≥ 2 seconds on the venous filling during the balloon occlusion test (BOT).

Parent Artery Occlusion

PAO was performed in a local standardized way after a 70-IU/kg bolus of heparin. No systematic heparin was maintained afterwards. No systematic antiplatelet therapy was introduced before, during, or after the procedure. Dual antiplatelet therapy (aspirin, 75 mg/day, and clopidogrel, 75 mg/day) was introduced 7 days before the treatment when a reconstructive treatment was initially planned. In these cases, an antiplatelet assay was systematically performed, and the antiplatelet therapy was adjusted when necessary.

A preliminary BOT was performed by using an inflated non-detachable balloon (Magic B1; Balt, Montmorency, France; or HyperForm, 4–15 mm; Covidien, Irvine, California) in the intrapetrous segment of the internal carotid artery. The occlusion was considered well-tolerated if the relative delay of venous filling was ≤ 1 second (Fig 1B, -C) or if it was ≤ 4 seconds with a perfect clinical tolerance for 20 minutes, even after a hypotension test with intravenous injection of a 1- to 2-mg bolus of nifedipine to decrease the mean arterial pressure > 20 mm Hg compared with baseline. As in other series, a delay of > 4 seconds was considered a contraindication to permanent occlusion of the internal carotid artery.¹⁵ The definitive occlusion of the artery was performed by trapping the aneurysm by using detachable platinum coils (Fig 1A). The objective was to completely stop the blood flow at the neck of the aneurysm. Ideally, an upstream and downstream occlusion of the aneurysm with loose packing in the aneurysm was performed. When the upstream segment was too short to set up coils, an occlusion of the aneurysm and of the parent artery was performed in opposition and downstream. The occlusion was considered satisfying if there was absolutely no progression of the contrast agent downstream of the occlusion. Occlusion was performed with soft, detachable platinum 0.014-inch-diameter coils and 30- to 50-cm length (Soft Detach-18S Embolization Coil system; Cook Medical, Bjaeverskov, Denmark). Relying on our experience, we noticed that at least 3 meters of coils were needed to occlude a carotid artery. Conventional intracranial detachable

3D-shaped 0.010-inch-diameter platinum coils were used as a first coil to occlude short downstream segments. All the procedures, including BOT and definitive occlusion, were performed as first-line with the patient under local anesthesia. They were performed with the patient under general anesthesia in noncompliant patients or when a reconstructive treatment was initially planned. After permanent occlusion, the patients were kept in the intensive care unit for at least 48 hours for monitoring, according to previously described protocol in the literature.¹⁵

Before the procedure, informed written consent was obtained from all the patients. This study was approved by the ethics committee “Ile-de-France 4.”

Clinical and Imaging Follow-Up

Clinical and imaging data were retrospectively analyzed from the medical file and prospectively analyzed with a systematic phone call to patients by an interventional neuroradiologist independent of the procedures (M.-A.L.). We distinguished early (≤ 30 days) or late (> 30 days until the last follow-up) follow-up. Patients for whom no clinical or imaging data were available for > 30 days after the procedure were considered lost to follow-up and were excluded from the analysis of the late follow-up period.

We determined the occurrence of the following variables: 1) a hemorrhagic stroke, 2) a symptomatic cerebral or retinal IE (with resolved or persistent symptoms at discharge), 3) death regardless of its cause, 4) changes in the cranial nerve palsy intensity felt according to a qualitative scale (resolved/improved, unchanged, worsened/appearing), 5) changes in the treated aneurysm on CT or MR imaging (retracted, unchanged, or grown) (retraction of the sac was arbitrarily defined as a decrease of $> 10\%$ of the diameter of the aneurysm), and 6) the growth of an additional aneurysm (de novo or pre-existing aneurysm). Given the good correlation between BOT timing and quantitative cerebral perfusion,^{16,17} IEs occurring in patients with a phlebogram delay of < 2 seconds during the occlusion test were considered embolic. We also determined the modified Rankin Scale score at the last follow-up for all included patients, whatever the follow-up time.

Statistical Analysis

Statistical analysis was performed by using SPSS, Version 15.0, software (IBM, Armonk, New York). Continuous variables were described as medians and interquartile ranges (Q1–Q3), and were compared with a Mann-Whitney-Wilcoxon test. Variables by category were compared by using a χ^2 or Fisher exact test.

The factors associated with the occurrence of cerebral/retinal IEs after treatment were analyzed with a univariate analysis and then with an exploratory binary logistic regression (for variables with $P < .1$ in univariate analysis).

RESULTS

Population

Fifty-six consecutive patients treated by PAO for large, giant, or fusiform aneurysms of the carotid siphon were included in the study. Clinical and imaging data before the procedure were available for every patient. The patients had all been treated by using coils according to the protocol and indications previously defined. All patients had a well-tolerated BOT with a relative delay of

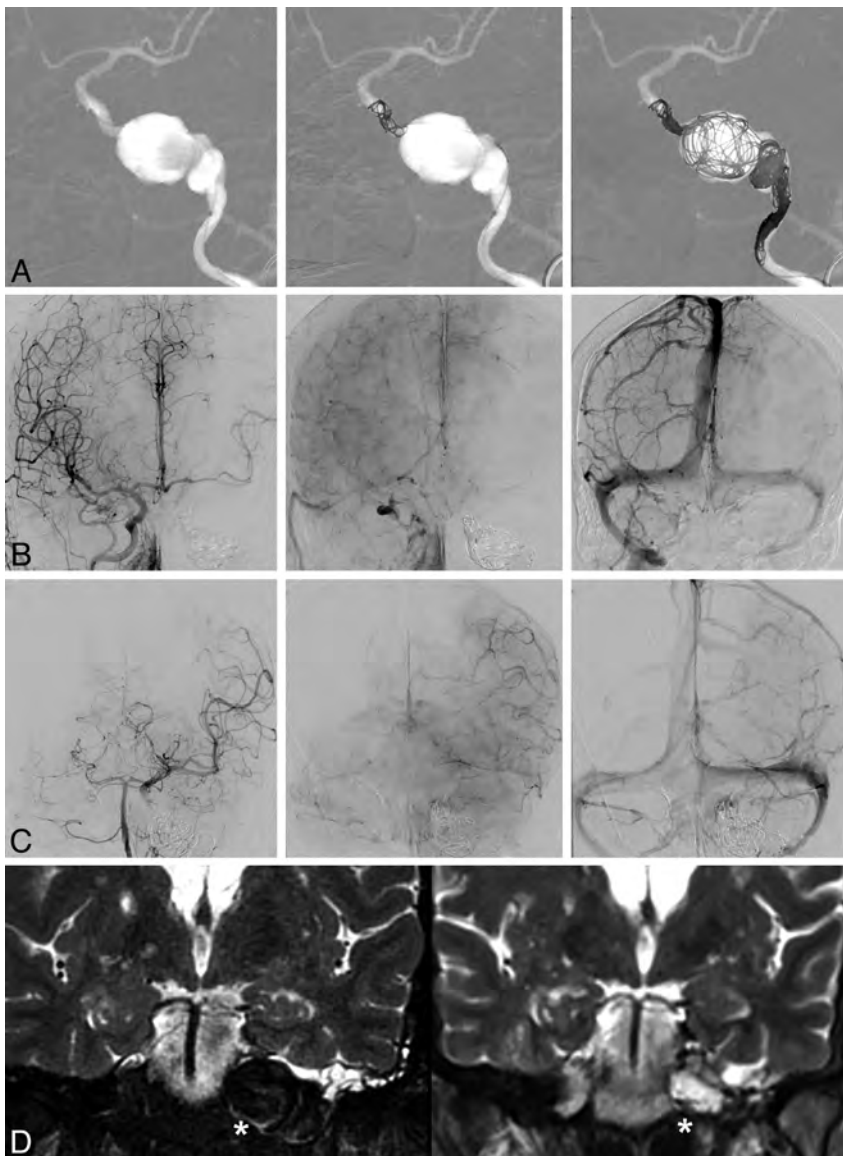


FIG 1. Parent artery occlusion in a 51-year-old woman with a left giant intrapetrous carotid aneurysm revealed by a hearing loss. Front projection of angiography before and during the occlusion (A), final angiography through the right carotid artery (B), final angiography through the left vertebra (C), and T2 coronal MR imaging before and 2 years after treatment (D). A, Coils were set upstream and downstream of the aneurysm, thus trapping the aneurysm and stopping the flow at its neck, and were set loosely in the aneurysm itself to maintain the thrombus. The final control (B) shows that the left middle cerebral artery is partially supplied by the right carotid artery via the anterior communicating artery, but is well supplied by the vertebrobasilar axis (C) via the left posterior communicating artery, with a venous return almost synchronous between the left external temporal veins and cerebellar veins. D, MR imaging shows a significant retraction of the aneurysm (white asterisk) after occlusion.

venous filling of <4 seconds. One patient who failed a first BOT underwent bypass surgery and had a PAO after a second BOT. A trapping with complete occlusion of the aneurysm was obtained in all patients. The patients' initial characteristics are presented in Table 1. Early clinical follow-up (≤ 30 days) was available for every patient. Thirteen patients (23%) were lost to follow-up after being discharged. Most of them (12/13) were sent and followed by hospital centers from abroad. There was no significant difference between the patients lost to follow-up and the remainder of the study population regarding the variables before treatment and the rate of early cerebral/retinal IEs

in early follow-up after treatment (data not shown). For the remainder of the population, the median clinical and radiologic follow-up (Q1–Q3) was, respectively, 45 months (range, 25–90 months) and 27 months (range, 13–55 months). Among these patients, all had a clinical and MR imaging follow-up of ≥ 3 months.

Follow-Up after Carotid Occlusion

At the last follow-up, the increase of the mRS score after the procedure was <2 (excellent outcome) in 53/56 (95%) patients, equal to 2 in 2/56 (3.5%) patients (moderate aphasia and facial palsy, moderate limb paresis), and equal to 3 in 1/56 (1.5%) patients (severe dominant arm paresis). In patients with infraclinoid aneurysms, it was <2 in 41/42 (97.5%) patients and equal to 2 in 1/42 (2.5%) patients. Permanent morbidity was due exclusively to postprocedure early IEs. No intracranial hemorrhagic event or death was observed throughout the follow-up period. The outcome and the complications after treatment are presented in Table 2.

Occurrence of Cerebral/Retinal IEs

During the early follow-up, an IE was reported in 15/56 (27%) patients and was completely resolved without sequelae at discharge in 10/15 (67%). A good Willisian substitute (suggested by a BOT timing of <2 seconds) was observed in 12/15 (80%) patients with an early IE. During the late follow-up, an IE was reported in 4/43 (9%) patients, with a time lapse between 3 months and 2.5 years after the treatment. For all patients with a late IE, the symptoms were completely resolved at discharge. They occurred in the context of low blood pressure in 3/4 and after interruption of aspirin in 1 patient who had already had an IE during the early period. All patients with IEs were managed in a stroke unit. All had antiplatelets or heparin for the early period. Among them, 2/15 also received an intravenous bolus of abciximab (ReoPro, 10 mg) in the very acute phase. Patients with recurrent IEs had long-term antithrombotic therapy. The univariate analysis of the factors associated with the occurrence of an IE after treatment (whatever the delay) is presented in Table 3. The exploratory multivariate analysis (entry for $P < .1$) found that the existence of at least 1 cardiovascular risk factor (OR = 7; CI 95%, 1.3–37; $P = .024$) and the para-/supraclinoid topography of the treated aneurysms (OR = 6; CI 95%, 1.1–40; $P = .043$) were significantly associated with the occurrence of an IE after treatment. The presence of a mural thrombus

Table 1: Baseline characteristics of the 56 patients of the study

Characteristics	Value
Age (yr) (median) (Q1–Q3)	54 (46–66)
Female (No.) (%)	51 (92)
Vascular risk factor (No.) (%)	31 (55)
Antiaggregation platelet therapy (No.) (%)	15 (27)
Asymptomatic (No.) (%)	4 (7)
Pain (No.) (%)	43 (77)
Cranial nerve palsy (No.) (%)	40 (72)
SAH or CCF (No.) (%)	4 (7)
Giant saccular aneurysms (≥ 25 mm) (No.) (%)	27 (48)
Large saccular aneurysms (≥ 15 mm, < 25) (No.) (%)	24 (43)
Fusiform aneurysms (No.) (%)	5 (9)
Infraclinoid aneurysms (No.) (%)	42 (75)
Mural thrombus (No.) (%)	15 (27)
Multiple aneurysms (No.) (%)	11 (20)
Timing of BOT ≥ 2 sec (No.) (%)	7 (13)
General anesthesia (No.) (%)	16 (28)

Note:—CCF indicates carotid cavernous fistula.

Table 2: Outcome and complications in 56 patients after carotid occlusion with coils for large, giant, or fusiform aneurysms of the carotid siphon

Characteristics	Early FU (≤ 30 days) (n = 56)	Late FU (> 30 days) (n = 43)
Death (No.) (%)	0	0
Intracranial hemorrhage (No.) (%)	0	0
Ischemic event		
Resolved symptoms (No.) (%)	10 (18)	4 (9)
Minor persistent symptoms ^a (No.) (%)	2 (3.5)	0
Major persistent symptoms ^b (No.) (%)	3 (5.5)	0
Pain		
Resolved or improved (No.) (%)	NA	42 (98)
Unchanged (No.) (%)	NA	0
Worsened (No.) (%)	NA	1 (2)
Cranial nerve palsy		
Resolved or improved (No.) (%)	NA	23 ^c (72)
Unchanged (No.) (%)	NA	9 ^c (28)
Worsened (No.) (%)	NA	0
Embolized aneurysm		
Retracted (No.) (%)	NA	39 (91)
Unchanged (No.) (%)	NA	4 (9)
Grown (No.) (%)	NA	0
De novo/additional growing aneurysm (No.) (%)	NA	1 (2)

Note:—NA indicates not assessed.

^a Modified Rankin Scale score ≤ 1 .

^b Modified Rankin Scale score > 1 .

^c n = 32.

decreased this occurrence significantly (OR = 0.1; CI 95%, 0.01–0.8; $P = .033$). The other variables were not significantly associated with the occurrence of an IE: age, fusiform nature of the aneurysm, aneurysm size of ≥ 25 mm, and the administration of antiplatelet therapy during the procedure. In the univariate analysis, patients with early or late transient IEs presented more often with a relative delay of venous filling during the BOT of ≥ 2 seconds ($P = .043$). This association persisted in the group of patients with late IEs ($P = .072$).

Symptoms of Mass Effect

Pain partially or completely improved in 42/43 (98%) patients. The cranial nerve palsy partially or completely improved in 27/32 (84%) patients. Among these patients, 4/32 (12%) presented with

an initial improvement of the cranial nerve palsy, followed by an unexplained late recurrence with a time lapse ranging from 4 months to 4 years, whereas the volume of the aneurysmal sac was retracted or stable on MR imaging. The occurrence or worsening of cranial nerve palsy was observed in 2/56 (3.5%) patients in the early follow-up after carotid occlusion. For both of these patients, it was transient in the days following the treatment and then partially or completely improved. Two other patients who did not present with any improvement of the palsy developed a corneal ulceration in the months following the carotid occlusion, related to a sensitive deficiency in the V1 trigeminal branch area already present before the procedure.

Aneurysm Follow-Up

An aneurysmal retraction was observed on MR imaging in 39/43 (91%) patients (Fig 1D). The 4 patients without significant retraction presented with an aneurysm still circulating in a retrograde manner on the angiographic control, supplied in 3 patients by the ophthalmic artery. The absence of significant retraction was associated with a more frequent para-/supraclinoid topography of the aneurysm (3/12 [25%] versus 1/31 [4%], $P = 0.059$). One patient of 43 (2%) presented with growth of a contralateral carotid aneurysm 2 years after the carotid occlusion, requiring selective embolization with no clinical consequences.

DISCUSSION

Our study showed that in a retrospective series of 56 consecutive patients, PAO by using coils for large/giant or fusiform aneurysms of the carotid siphon presents a morbidity risk of 5% (2.5% in patients with infraclinoid aneurysm), a zero mortality risk, an aneurysmal retraction rate of 91%, an improvement in pain of 98%, and an improvement rate for cranial nerve palsy of 72% for a median follow-up of > 3 years. Factors favoring a postprocedural ischemic complication are the para-/supraclinoid topography of the aneurysm and the presence of at least 1 acquired cardiovascular risk factor. On the contrary, the presence of a mural thrombus is associated with a decreasing ischemic risk. This is the largest published series of carotid occlusion by using coils for this type of indication, to our knowledge.

Our study shows a zero mortality rate and morbidity exclusively due to cerebral infarction immediately after the procedure without hemorrhage, supporting the results of previous series of PAO.^{3,9,11}

The ischemic events after treatment in our series were most often due to embolism, because a majority (78%) occurred in patients with a very good circle of Willis. The greater proportion of IEs in the group of patients presenting with a para-/supraclinoid aneurysm could be explained by residual intracarotid flow phenomena coming from the ophthalmic artery or from external carotid emboli. Unlike in the study of Clarençon et al,⁹ the presence of a mural thrombus was associated with a decreasing ischemic risk. A hypothesis could be that the flow is already slowed down in thrombosed aneurysms and the occlusion is, therefore, more rapidly effective with a lower risk of embolus. However, no protective effect of the antiplatelet therapy during the procedure was demonstrated in our study.

The IEs occurring in the hemodynamic context and/or in pa-

Table 3: Comparison of main baseline characteristics in patients with and without ischemic events after carotid occlusion (n = 56)

Characteristics	Ischemic Events (n = 18)	No Ischemic Events (n = 38)	P Value
Age (yr) median (Q1–Q3)	55 (50–64)	52 (43–67)	.477
Female (No.) (%)	18 (100)	33 (86)	.131
Vascular risk factor (No.) (%)	14 (78)	17 (44)	.032
Antiplatelet therapy (No.) (%)	5 (28)	10 (36)	.856
Giant aneurysms (≥ 25 mm) (No.) (%)	7 (39)	20 (53)	.336
Fusiform aneurysms (No.) (%)	1 (6)	4 (10)	.479
Infraclinoid aneurysms (No.) (%)	11 (61)	31 (82)	.099
Mural thrombus (No.) (%)	1 (6)	14 (37)	.011
Delay of phlebogram ≥ 2 sec (No.) (%)	4 (22)	3 (8)	.140

tients with a longer relative delay of venous filling during BOT are most often transient and have a good prognosis. Because they can occur a long time after the PAO, they encourage preventing low flow or low blood pressure, especially during general anesthesia in patients treated despite a nonoptimal circle of Willis

The rate of IEs in our study was higher than the rate reported in most of the studies of PAO in the literature, which varies from 4.5% to 14%.^{8–11} The systematic inclusion of consecutive patients obtained from a prospective registry and the consideration of even early and late transient cerebral or retinal IEs in our study may explain a part of this difference. Besides, we cannot exclude the effect of the embolization technique performed exclusively by using coils in our series and exclusively or mostly by using detachable balloons in other series. We could hypothesize that the slower occlusion of the carotid artery (in approximately 10 minutes) obtained by using coils compared with the immediate occlusion obtained with a balloon could promote the migration of emboli. A possible improvement of PAO by using coils would be to perform a transitory occlusion with a balloon of the cervical carotid artery during the coiling. Even if most of the IEs had a good prognosis at the last follow-up—especially for the infraclinoid aneurysms—their relatively high rate of occurrence requires restricting the indications for PAO to patients with debilitating pain, cranial nerve palsy, and/or intradural aneurysms.¹⁰

PAO in our study had an excellent efficacy for pain, a partial efficacy for cranial nerve palsy, and an excellent rate of aneurysm occlusion. These results are comparable with those in other series of PAO by using predominantly detachable balloons.^{3,9,11} We report 4 cases of late recurrence of oculomotor disorders despite an initial regression and a significant retraction of the aneurysm on MR imaging. This phenomenon has already been described for carotid siphon aneurysms treated by a reconstructive method by using coils.¹⁸ It has never been reported, to our knowledge, after PAO and remains unexplained.

We also report a case of a growing contralateral carotid aneurysm 2 years after PAO, which required coil embolization. A recent meta-analysis showed that the development of a new aneurysm or the growth of a pre-existing aneurysm after carotid occlusion has a 4.3% frequency and occurs within an average of 9.1 years after the occlusion.¹⁹ This phenomenon would be promoted by the high compensatory flow of the substitute pathways of the occluded carotid artery. This risk is low but higher than the risk reported for reconstructive treatments.²⁰ Given the expected

longer timeframe in which a de novo aneurysm develops after PAO, compared with the mean follow-up in our study, we cannot establish the long-term safety of PAO concerning this variable. This timeframe should probably justify life-long MR imaging surveillance for patients treated by PAO.

Whereas selective techniques with coils plus or minus non-flow-diverter stents are considered the criterion standard for the treatment of most saccular aneurysms of <10–15 mm, they are associated with a high rate of recanalization

in larger aneurysms.^{4,5,11} Endovascular PAO with trapping has long been considered the first-line treatment of large aneurysms. New reconstructive stent-assisted treatments with flow diverters are increasingly being developed because they have been shown to be effective in several cases series. A recent prospective noncomparative study including 107 patients treated with Pipeline flow diverters (Covidien) for large or giant aneurysms of the carotid siphon showed a complete aneurysmal occlusion rate of 73.6% at 180 days and a rate of major ipsilateral stroke or neurologic death at 180 days of 5.6%. The safety after 180 days and changes in the symptoms of mass effect were not available.¹⁴ One other noncomparative study, including 27 patients, reported excellent flow-diverter stenting of aneurysms with symptoms of mass effect, with a 100% rate of improvement of the symptoms of mass effect and of aneurysm retraction.¹² Because they preserve the parent vessel, flow-diverter stents might prevent the occurrence of an early or late hemodynamic ischemic event and de novo aneurysms. Nevertheless, the superiority of this technique has not yet been proved by comparative studies with PAO and is still debated.²¹ Furthermore, recent meta-analyses concerning flow-diverter stents show that the mortality rate is close to 4%, regardless of the type of aneurysm.^{22,23} It was 4% in the study of Briganti et al²³ for 76 patients treated for intracavernous aneurysms. The reported fatal complications with stent-assisted techniques are due to major hemorrhagic or ischemic complications, which are completely absent from carotid occlusion series.

Almost one-fifth patients in our study were lost to follow-up. They were almost exclusively patients living abroad for whom the follow-up could not be performed in our hospital or in a reference center in their country and whose phone numbers were unavailable or incorrect. It is very unlikely that taking these into account would have modified the morbidity and mortality rates because serious complications were observed only during the early follow-up, which could be analyzed for each patient. Furthermore, baseline characteristics were similar in patients with and without a late follow-up. Given the exploratory nature of this study, blind analysis by an independent review board has not been performed, introducing potential interpretation biases.

CONCLUSIONS

In this study, PAO to treat large, giant, or fusiform aneurysms of the carotid siphon is safe and effective, especially for giant infraclinoid aneurysms. Because of the ischemic event risk, this treatment should be limited to symptomatic patients or aneurysms

with a high risk of severe bleeding. According to recent meta-analyses, our results suggest that the validation of stent-assisted reconstructive treatments for these aneurysms requires controlled studies with PAO.

ACKNOWLEDGMENTS

The authors would like to thank the Head and Neck Department at the Lariboisière Hospital for their direct or indirect intervention in the management of our study patients.

REFERENCES

1. Goldenberg-Cohen N, Curry C, Miller NR, et al. **Long term visual and neurological prognosis in patients with treated and untreated cavernous sinus aneurysms.** *J Neurol Neurosurg Psychiatry* 2004;75:863–67
2. Barrow DL, Alleyne C. **Natural history of giant intracranial aneurysms and indications for intervention.** *Clin Neurosurg* 1995;42:214–44
3. Zhang Z, Lv X, Wu Z, et al. **Clinical and angiographic outcome of endovascular and conservative treatment for giant cavernous carotid artery aneurysms.** *Interv Neuroradiol* 2014;20:29–36
4. Gao X, Liang G, Li Z, et al. **A single-centre experience and follow-up of patients with endovascular coiling of large and giant intracranial aneurysms with parent artery preservation.** *J Clin Neurosci* 2012;19:364–69
5. van Rooij WJ, Sluzewski M. **Unruptured large and giant carotid artery aneurysms presenting with cranial nerve palsy: comparison of clinical recovery after selective aneurysm coiling and therapeutic carotid artery occlusion.** *AJNR Am J Neuroradiol* 2008;29:997–1002
6. Chalouhi N, Tjoumakaris S, Gonzalez LF, et al. **Coiling of large and giant aneurysms: complications and long-term results of 334 cases.** *AJNR Am J Neuroradiol* 2014;35:546–52
7. Larson JJ, Tew JM Jr, Tomsick TA, et al. **Treatment of aneurysms of the internal carotid artery by intravascular balloon occlusion: long-term follow-up of 58 patients.** *Neurosurgery* 1995;36:26–30; discussion 30
8. van Rooij WJ. **Endovascular treatment of cavernous sinus aneurysms.** *AJNR Am J Neuroradiol* 2012;33:323–26
9. Clarençon F, Bonneville F, Boch AL, et al. **Parent artery occlusion is not obsolete in giant aneurysms of the ICA: experience with very-long-term follow-up.** *Neuroradiology* 2011;53:973–82
10. Stiebel-Kalish H, Kalish Y, Bar-On RH, et al. **Presentation, natural history, and management of carotid cavernous aneurysms.** *Neurosurgery* 2005;57:850–57; discussion 850–57
11. van der Schaaf IC, Brilstra EH, Buskens E, et al. **Endovascular treatment of aneurysms in the cavernous sinus: a systematic review on balloon occlusion of the parent vessel and embolization with coils.** *Stroke* 2002;33:313–18
12. Szikora I, Marosfoi M, Salomvary B, et al. **Resolution of mass effect and compression symptoms following endoluminal flow diversion for the treatment of intracranial aneurysms.** *AJNR Am J Neuroradiol* 2013;34:935–39
13. Chalouhi N, Tjoumakaris S, Starke RM, et al. **Comparison of flow diversion and coiling in large unruptured intracranial saccular aneurysms.** *Stroke* 2013;44:2150–54
14. Becske T, Kallmes DF, Saatci I, et al. **Pipeline for uncoilable or failed aneurysms: results from a multicenter clinical trial.** *Radiology* 2013;267:858–68
15. Abud DG, Spelle L, Piotin M, et al. **Venous phase timing during balloon test occlusion as a criterion for permanent internal carotid artery sacrifice.** *AJNR Am J Neuroradiol* 2005;26:2602–09
16. Struffert T, Deuerling-Zheng Y, Engelhorn T, et al. **Monitoring of balloon test occlusion of the internal carotid artery by parametric color coding and perfusion imaging within the angio suite: first results.** *Clin Neuroradiol* 2013;23:285–92
17. Gevers S, Heijtel D, Ferns SP, et al. **Cerebral perfusion long term after therapeutic occlusion of the internal carotid artery in patients who tolerated angiographic balloon test occlusion.** *AJNR Am J Neuroradiol* 2012;33:329–35
18. Dagain A, Nataf F, Page P, et al. **Endovascular coil transfixing a cranial nerve five years after embolisation.** *Acta Neurochir (Wien)* 2008;150:705–07; discussion 707
19. Arambepola PK, McEvoy SD, Bulsara KR. **De novo aneurysm formation after carotid artery occlusion for cerebral aneurysms.** *Skull Base* 2010;20:405–08
20. Ferns SP, Sprengers ME, van Rooij WJ, et al. **De novo aneurysm formation and growth of untreated aneurysms: a 5-year MRA follow-up in a large cohort of patients with coiled aneurysms and review of the literature.** *Stroke* 2011;42:313–18
21. van Rooij WJ, Sluzewski M. **Unruptured carotid artery aneurysms presenting with symptoms of mass effect: outcome after selective coiling, parent vessel occlusion, and flow diversion.** *AJNR Am J Neuroradiol* 2013;34:940–41
22. Brinjikji W, Murad MH, Lanzino G, et al. **Endovascular treatment of intracranial aneurysms with flow diverters: a meta-analysis.** *Stroke* 2013;44:442–47
23. Briganti F, Napoli M, Tortora F, et al. **Italian multicenter experience with flow-diverter devices for intracranial unruptured aneurysm treatment with periprocedural complications: a retrospective data analysis.** *Neuroradiology* 2012;54:1145–52

MR Imaging of Myeloperoxidase Activity in a Model of the Inflamed Aneurysm Wall

M.J. Gounis, I.M.J. van der Bom, A.K. Wakhloo, S. Zheng, J.-Y. Chueh, A.L. Kühn, and A.A. Bogdanov Jr



ABSTRACT

BACKGROUND AND PURPOSE: Although myeloperoxidase activity in vivo can be visualized by using noninvasive imaging, successful clinical translation requires further optimization of the imaging approach. We report a motion-sensitized driven-equilibrium MR imaging approach for the detection of a myeloperoxidase activity-specific gadolinium-containing imaging agent in experimental aneurysm models, which compensates for irregular blood flow, enabling vascular wall imaging in the aneurysm.

MATERIALS AND METHODS: A phantom was built from rotational angiography of a rabbit elastase aneurysm model and was connected to a cardiac pulse duplicator mimicking rabbit-specific flow conditions. A T1-weighted turbo spin-echo-based motion-sensitized driven-equilibrium pulse sequence was optimized in vitro, including the addition of fat suppression and the selection of the velocity-encoding gradient parameter. The optimized sequence was applied in vivo to rabbit aneurysm models with and without inflammation in the aneurysmal wall. Under each condition, the aneurysms were imaged before and after intravenous administration of the imaging agent. The signal-to-noise ratio of each MR imaging section through the aneurysm was calculated.

RESULTS: The motion-sensitized driven-equilibrium sequence was optimized to reduce flow signal, enabling detection of the myeloperoxidase imaging agent in the phantom. The optimized imaging protocol in the rabbit model of saccular aneurysms revealed a significant increase in the change of SNR from pre- to post-contrast MR imaging in the inflamed aneurysms compared with naive aneurysms and the adjacent carotid artery ($P < .0001$).

CONCLUSIONS: A diagnostic MR imaging protocol was optimized for molecular imaging of a myeloperoxidase-specific molecular imaging agent in an animal model of inflamed brain aneurysms.

ABBREVIATIONS: LPS = lipopolysaccharide; MPO = myeloperoxidase; MSDE = motion-sensitized driven-equilibrium; PHASES = Population, Hypertension, Age, Size of Aneurysm, Earlier Subarachnoid Hemorrhage from Another Aneurysm, and Site of Aneurysm; SPIR = spectral presaturation inversion recovery; UIA = unruptured intracranial aneurysms; VENC = velocity-encoding gradient parameter

Due to the continuing improvements to the safety of unruptured intracranial aneurysm (UIA) treatment, there has been a steady increase in procedure numbers. Between 2001 and 2006, there was a 22-fold increase in UIAs treated by endovascular coil embolization,¹ and in 2008, approximately 57,000 UIAs were ei-

ther surgically clipped or coiled in the United States alone.² While the annual risk of rupture of an UIA is estimated to be between 0% and 33% depending on size, morphology, anatomic location, and history of subarachnoid hemorrhage,^{3,4} the combined rate of morbidity and mortality resulting from coil embolization and surgical clipping is approximately 5% and 14%, respectively.² Thus, the risk-benefit analysis does not support interventional treatment of all unruptured aneurysms but dictates, rather, that UIAs be carefully selected on the basis of their relative risk of rupture. Currently, it is not possible to accurately assess the UIA risk of rupture. The challenge therefore lies in the ability to positively identify UIAs that are progressing to rupture. Accordingly, new methods for improving this capability will be critical for im-

Received April 10, 2014; accepted after revision June 30.

From the Department of Radiology (M.J.G., I.M.J.v.d.B., A.K.W., S.Z., J.-Y.C., A.L.K., A.A.B.), New England Center for Stroke Research; and Departments of Neurosurgery and Neurology (A.K.W.) and Radiology (A.A.B.), Laboratory of Molecular Imaging Probes, University of Massachusetts Medical School, Worcester, Massachusetts.

This work was funded by the National Institute on Aging grant 5R01AG034901-02.

Paper previously presented at: Annual Meeting of the International Society for Magnetic Resonance in Medicine, April 20–26 2013; Salt Lake City, Utah; American Society of Mechanical Engineering Summer Bioengineering Conference, June 26–29, 2013; Sunriver, Oregon; and Society of NeuroInterventional Surgery Conference, July 29 to August 1, 2013; Miami, Florida.

Please address correspondence to Matthew J. Gounis, PhD, Department of Radiology, New England Center for Stroke Research, University of Massachusetts

Medical School, 5 Lake Ave N, SA-107R, Worcester, MA 01655; e-mail: Matthew.Gounis@umassmed.edu

Indicates open access to non-subscribers at www.ajnr.org

<http://dx.doi.org/10.3174/ajnr.A4135>

proving clinical decision-making in managing individual cases. Toward this end, a diagnostic method has been recently devised to enable imaging of UIA wall inflammation by using iron oxide nanoparticles.^{5,6}

The recent focus on inflammation-induced events and markers is primarily due to their role as a potential contributor to aneurysm rupture (reviewed in Tulamo et al⁷). Inflammation is likely associated with vascular remodeling which, with time, exposes the aneurysm to increased risk of rupture. One of the major inflammation-associated tissue markers, myeloperoxidase (MPO), is a secretable heme-containing oxidoreductase of azurophilic granules of polymorphonuclear cells. Secreted MPO produces chlorinating bactericidal species (eg, hypochlorous acid) from hydrogen peroxide during neutrophilic respiratory burst and chloride anions. In addition to a well-known role in the host defense system against microorganisms, MPO has been implicated in the initiation and destabilization of atherosclerotic plaques (reviewed in Nicholls and Hazen⁸). Recently, MPO presence in human brain aneurysm specimens was shown to correlate with the Population, Hypertension, Age, Size of Aneurysm, Earlier Subarachnoid Hemorrhage from Another Aneurysm, and Site of Aneurysm (PHASES) model⁹ of aneurysm risk of rupture.¹⁰ Enzymatic activity of neutrophilic myeloperoxidase can be used as a highly selective and sensitive target for detecting inflammation by using clinical imaging modalities (MR imaging, SPECT).¹¹⁻¹⁵ A gadolinium (III) chelate MPO activity-sensing MR imaging probe has also been investigated in an animal model of inflamed saccular aneurysms.¹⁶ With a 3D T1-weighted fast-field echo pulse sequence, local accumulation of the probe as determined by enhancement correlated with MPO activity at the site of *Escherichia coli* lipopolysaccharide (LPS) injection. Signal changes measured on MR imaging were possible at the clinical field strength (3T) and gadolinium (III) dose.

Although these results are promising, the MR imaging protocols (specifically for axial black-blood imaging) have to be optimized to detect the presence of MPO within an aneurysm, especially given the complexity of intra-aneurysmal flow and the resultant attenuation of the MR imaging signal. At this juncture, the MPO activity-specific imaging agent is experimental and is not approved for human use. Therefore, we optimized the MR imaging protocol for detecting MPO activity in both in vitro and in vivo aneurysm models.

MATERIALS AND METHODS

In Vitro MR Imaging Sequence Optimization

All MR imaging studies were conducted on a 3T Achieva scanner (Philips Healthcare, Best, the Netherlands) by using an 8-element, receive-only knee coil (Philips Healthcare). Radiofrequency was transmitted with the built-in quadrature body coil. To optimize MR imaging sequences that are insensitive to the complex intra-aneurysmal flow patterns, we first conducted an in vitro phantom study. A silicone vascular replica was built from 3D rotational angiography of a rabbit elastase aneurysm by using a rapid prototyping technique previously described.¹⁷ The phantom was connected to a flow-loop-driven programmable pulsatile pump simulating the aortic waveform of the rabbit¹⁸ by using a blood

analog working fluid that matched the T1 and viscosity of blood. We applied a turbo spin-echo pulse sequence combined with the following components to suppress blood flow signal: black-blood double inversion recovery,¹⁹ small FOV quadrature inversion recovery,²⁰ and motion-sensitized driven-equilibrium (MSDE).²¹ All images were acquired with 2-mm sections along the long axis of the aneurysm in a 100-mm FOV with an acquired in-plane resolution of 0.4×0.4 mm. The TSE-based double inversion recovery, small FOV quadrature inversion recovery, and MSDE scan parameters included TR/TE of 456/10 ms, 750/11 ms, and 698/9 ms; and flip angles of 90°, 90°, and 70°, respectively. The number of signal averages for all sequences was 2. The flow velocity-encoding gradient parameter (VENC) had values between 1 and 8 cm/s.

Once the flow was adequately suppressed, the phantom aneurysm was embedded in solid coconut oil to account for extravascular fat. Images were also acquired using a spectral presaturation inversion recovery (SPIR) fat-suppression method. Finally, a small capsule containing 150 $\mu\text{mol/L}$ of Gd-DTPA in a volume of ~ 30 μL was included in the aneurysm replica to determine whether sufficient flow suppression was achieved to enable detection of a representative amount of retained Gd-containing imaging agent.

Additional sequences included the following: a 3D time-of-flight sequence (voxel size, $0.208 \times 0.208 \times 1$ mm³; gap, -0.5 mm; TR/TE, 20.1/3.6 ms; flip angle, 20°; number of signal averages, 2), and a coronal and axial T1-weighted fast-field echo sequence (voxel size, $0.625 \times 0.625 \times 2$ mm³; gap, -1.0 mm; TR/TE, 17.9/2.3 ms; flip angle, 25°).

In Vivo MR Imaging of a Rabbit Model

All in vivo procedures were first approved by our Institutional Animal Care and Use Committee. A saccular aneurysm model in New Zealand White rabbits ($n = 8$) was created as previously described.²² Three weeks after the aneurysms were created, the animals were re-anesthetized and imaged by using the MR imaging protocol established from our in vitro phantom study. Due to the location of the aneurysm, respiratory gating was used. The naïve aneurysms were imaged before and 3 hours after IV administration of the MPO activity-specific paramagnetic imaging agent (DTPA[Gd] bis-hydroxytryptamide, bis-5HT-DTPA[Gd]) at a dose of 0.1 mmol Gd/kg in 15 mL of 5% meglumine, pH 7.¹⁶ The synthesis, purification, and in vitro testing of bis-5HT-DTPA(Gd) were essentially performed as previously reported.¹⁴

One week after the baseline MR imaging study was performed, 7 animals were returned to the surgical suite for LPS-induced inflammation of the aneurysm wall, as previously described.¹⁶ Briefly, with the animal under general anesthesia, a 6F guide catheter was positioned at the root of the brachiocephalic artery by using a standard transfemoral approach. Thereafter, a standard microcatheter (0.016-inch inner diameter) was navigated into the aneurysm sac over a 0.014-inch guidewire. With the microcatheter placed deep into the dome, a 0.014-inch stainless steel hypotube with a ground distal tip was advanced through the microcatheter and inserted carefully into the aneurysm wall. LPS (1-mg, 200- μL total volume) was injected through the hypotube for approximately 10 minutes. The remaining animal served as a nega-

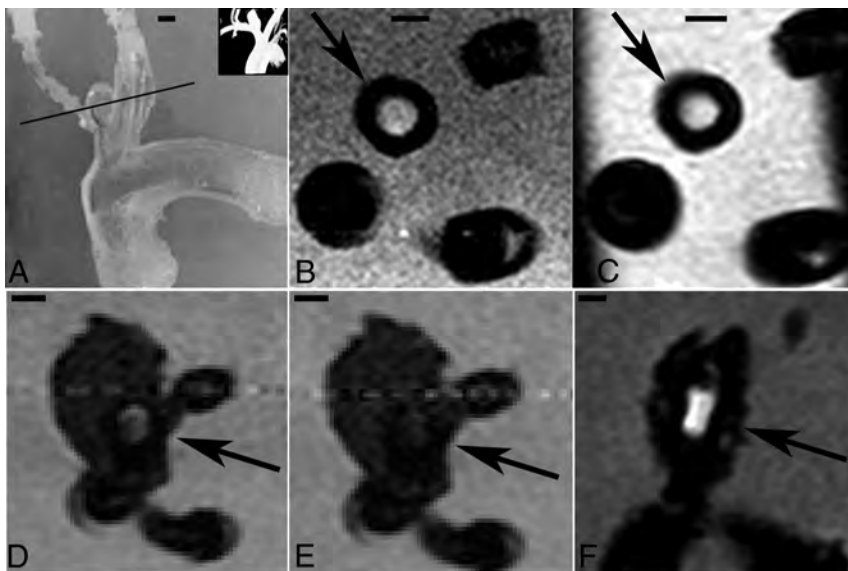


FIG 1. A, A silicone replica of a rabbit elastase-induced aneurysm of the right common carotid artery (arrows) was built and subjected to MR imaging (axial projections along a line in A; the inset is rotational angiography data on which the model was built). Double inversion recovery black-blood (B) and small FOV quadrature recovery (C) suppressed the flow signal in the adjacent arteries but not within the aneurysm dome (arrows). The MSDE sequence combined with SPIR to suppress the surrounding fat with a VENC of 2 cm/s had persistent flow signal in the aneurysm dome (D, arrow), which was eliminated with a VENC of 1 cm/s (E). With a VENC of 1 cm/s and SPIR for fat suppression, we were able to image a realistic Gd-DTPA contrast agent concentration (150 $\mu\text{mol/L}$) contained within a capsule implanted in the aneurysm (F, frontal projection). Horizontal scale bars represent 3 mm.

tive control. Two days after the LPS administration, the MR imaging study was repeated before and after intravenous infusion of the MPO activity-specific imaging agent. After the final imaging study, the animals were euthanized and the aneurysms were surgically explanted for histologic analysis. The aneurysm tissue was embedded in tissue-freezing medium, snap-frozen in liquid nitrogen, and stored at -80°C until processing.

Rabbit tissues were carefully divided in half along the long axis of the aneurysm. The first section was processed by using an alkaline phosphatase immunohistochemistry approach due to the high autofluorescence of rabbit sections. The rabbit aneurysm and contralateral carotid artery sample sections were incubated for 90 minutes in 50-mmol/L tris, 100-mmol/L NaCl (tris-buffered saline), containing 1-mmol/L ethylenediaminetetraacetic acid, pH 7, to block endogenous phosphatase activity, and were blocked in 5% bovine serum, 10-mg/mL bovine serum albumin, tris-buffered saline, pH 7.5, for 2 hours. The primary antibodies (cross-reacting with rabbit antigens) were the corresponding mouse anti-human monoclonal antibodies (2C7, dilution: 1:100; Abcam, Cambridge, Massachusetts). The secondary antibody (anti-mouse rabbit-alkaline phosphatase conjugate; Roche, Basel, Switzerland) was used at 1:1000 dilution.

The remaining aneurysm tissue was subjected to an analysis of MPO activity performed by using a commercially available MPO kit (Fluoro MPO; Cell Technology, Mountain View, California). A typical assay included homogenization of 1–10 mg of saline-rinsed, rapidly defrosted tissue in a vial containing a slurry of 300-mg sterile glass beads (1-mm diameter) suspended in 0.5 mL of 0.5% solution of hexadecyltrimethylammonium bromide, 10-mmol/L *N*-ethylmaleimide in 0.1-mol/L potassium phosphate,

pH 6.5. The homogenization was performed by using a mini-BeadBeater (Bio-Spec Products, Bartlesville, Oklahoma) for 12 cycles (30 seconds each) with 1-minute cooling on ice between the cycles. The final disruption was performed by using 3 freeze-thaw cycles. The samples were cleared by centrifugation (8000 \times g, 5 minutes), and the activity of MPO was determined in the supernatant by using a fluorescent analog of MPO substrate in the presence of hydrogen peroxide. The rates of fluorescence increase were determined by using a kinetic assay ($\lambda_{\text{ex}} = 550$ nm, $\lambda_{\text{em}} = 600$ nm) with an MPO standard solution (Cell Technology) to generate calibration curves. The protein content in the homogenized samples was determined by using a bicinchoninic acid kit (Bio-Rad Laboratories, Berkeley, California). The total MPO activity was expressed in international units per milligram wet sample and international units per milligram extractable protein.

MR Image and Statistical Analysis

Images from the phantom study were qualitatively reviewed by the entire investigative team (all authors) for flow and fat suppression and sufficient contrast-to-noise to distinguish the Gd-DTPA capsule from the background. Selection of the optimized sequence in vitro was reached by consensus of the team. In the rabbit study, 2 experienced observers (M.J.G., 10 years; A.L.K., 2 years) created elliptical regions of interest around the aneurysm and left common carotid artery. Region-of-interest selection was reviewed by a neuroradiologist with >20 years of experience in cerebrovascular imaging (A.K.W.). The signal-to-noise ratio was calculated by dividing the mean intensity within the region of interest by the SD of the image background. The SNR pre-contrast was subtracted from the post-contrast value, and the change in SNR was compared between the naïve and inflamed aneurysms and the left common carotid artery.

The results are expressed as mean \pm standard error of the mean. A repeated-measures ANOVA with a Tukey multiple comparisons posttest was used to make comparisons of the SNR changes. $P < .05$ was statistically significant.

RESULTS

In Vitro MR Imaging Sequence Optimization

The vascular replica used for sequence optimization is shown in Fig 1A. Although excellent flow suppression was achieved with the double inversion recovery and small FOV quadrature inversion recovery techniques in the adjacent arteries, substantial flow signal within the aneurysm persisted (Fig 1B, -C). The MSDE technique by using a VENC of 1 cm/s was shown to provide excellent flow suppression compared with larger VENC values (Fig 1D, -E). We confirmed that the MSDE sequence with a VENC of 1 cm/s and the addition of SPIR eliminated the signal from blood flow

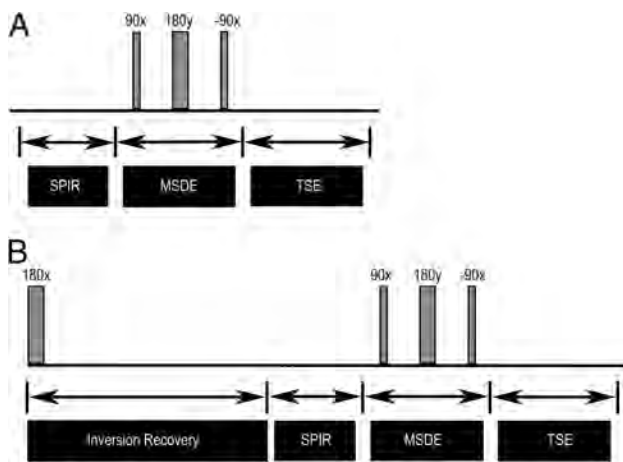


FIG 2. Schematic of the TSE-based MSDE pulse sequence optimized in the in vitro study (A), subsequently modified for in vivo rabbit aneurysm imaging (B).

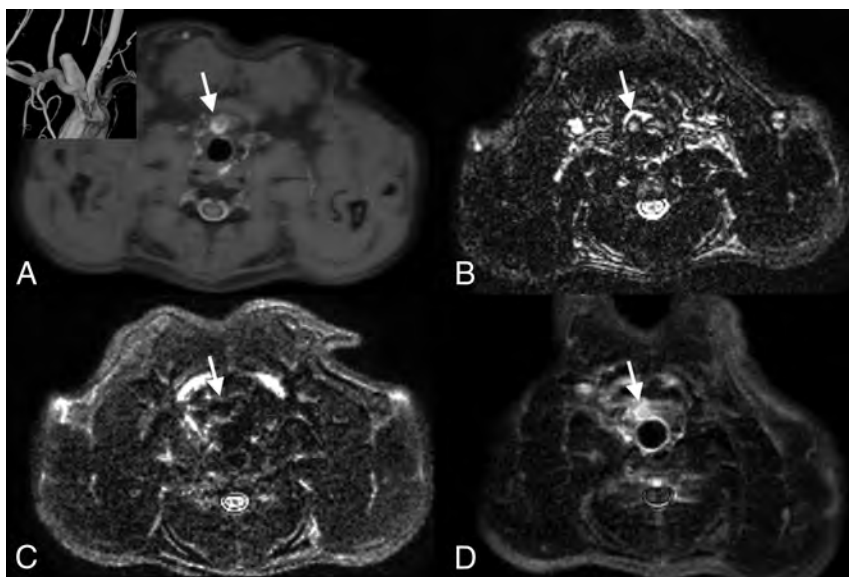


FIG 3. Model of a sacular aneurysm (arrows) in the rabbit (A, axial projection, turbo spin-echo with SPIR, inset rotational angiogram in frontal oblique projection). MSDE images before receiving the MPO-specific contrast agent (B) and after IV administration of bis-5HT-DTPA(Gd) in the naïve (C) and inflamed (D) aneurysms (0.1-mmol Gd/kg).

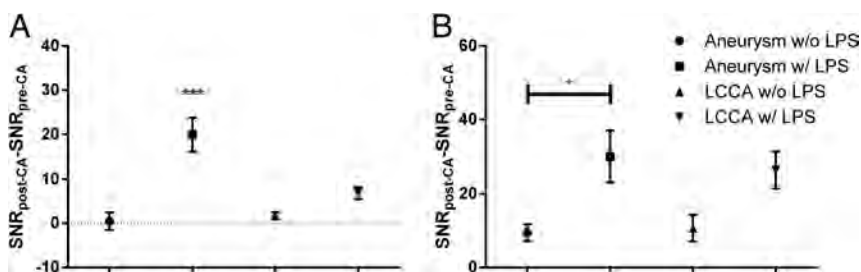


FIG 4. A, Signal-to-noise ratio change of the inflamed aneurysm was highly significant by using the MSDE sequence and was negligible in the naïve aneurysm as well as the left common carotid artery, suggesting adequate flow suppression. B, SNR change calculated from the T1-fast-field echo axial sections shows a significant increase between the inflamed and naïve aneurysm model, but no differences between the inflamed aneurysm and the left common carotid artery either before or after LPS administration, suggesting flow dependence. The asterisk indicates $P < .05$; triple asterisks, $P < .0001$, contrast agent: bis-5HT-DTPA(Gd).

and adjacent fat, respectively, yet provided sufficient T1-weighted contrast to image the capsule containing 0.1-mmol/L Gd-DTPA inserted and affixed in the aneurysm dome (Fig 1F). The optimal sequence was the fat-suppressed T1-weighted TSE-based MSDE pulse sequence (Fig 2A), including the following parameters: TR/TE 698/9 ms; flip angle, 70°; TSE factor, 4 with low-high profile order; VENC, 1 cm/s; and number of signal averages, 2.

In Vivo MR Imaging of a Rabbit Model

We transferred the optimized MSDE sequence to the rabbit aneurysm model. However, due to the location of the aneurysm, significant motion artifacts due to respiration were observed. Therefore, MR imaging was performed with respiratory triggering. Data acquisition was performed during the expiration phase by using a multi-2D method that required TR = 5000 ms as determined by the length of the respiratory cycle. Consequently, T1-weighting for contrast enhancement was lost. To overcome this loss, we added an inversion pulse to

the sequence to gain T1 sensitivity by inversion recovery (Fig 2B). The inversion recovery delay time (800 ms) was determined by minimizing the signal generated by the aneurysm wall in an effort to maximize the signal difference with respect to post-5HT-DTPA(Gd) imaging (Fig 3). A TSE method with a TSE factor of 16 was used for imaging, and a low-to-high profile was used to achieve a small TE value of 8.6 ms.

Compared with the naïve aneurysm, on average, a 40-fold increase in the SNR change from pre- to post-contrast MSDE imaging in the inflamed aneurysm model was found (Fig 4A). The mean SNR change in the naïve left common carotid artery and the left common carotid artery following injection of LPS into the aneurysm wall was 1.7 and 6.8, respectively. The model of the inflamed aneurysm had a significant increase in the SNR change compared with all controls ($P < .0001$). Similar trends in the SNR change were observed by using the 3D T1-weighted fast-field echo sequence; however, significant differences between the inflamed aneurysm versus the control left common carotid artery were not found (Fig 4B). The aneurysm model including the LPS modification had 19.4 ± 10.8 U MPO per milligram, whereas the negative control animal had 0.45 U MPO per milligram. Similar to that in our previous study,¹⁶ the LPS-induced inflammation demonstrated a large infiltration of MPO and macrophages within the aneurysm wall compared with the naïve control (Fig 5).

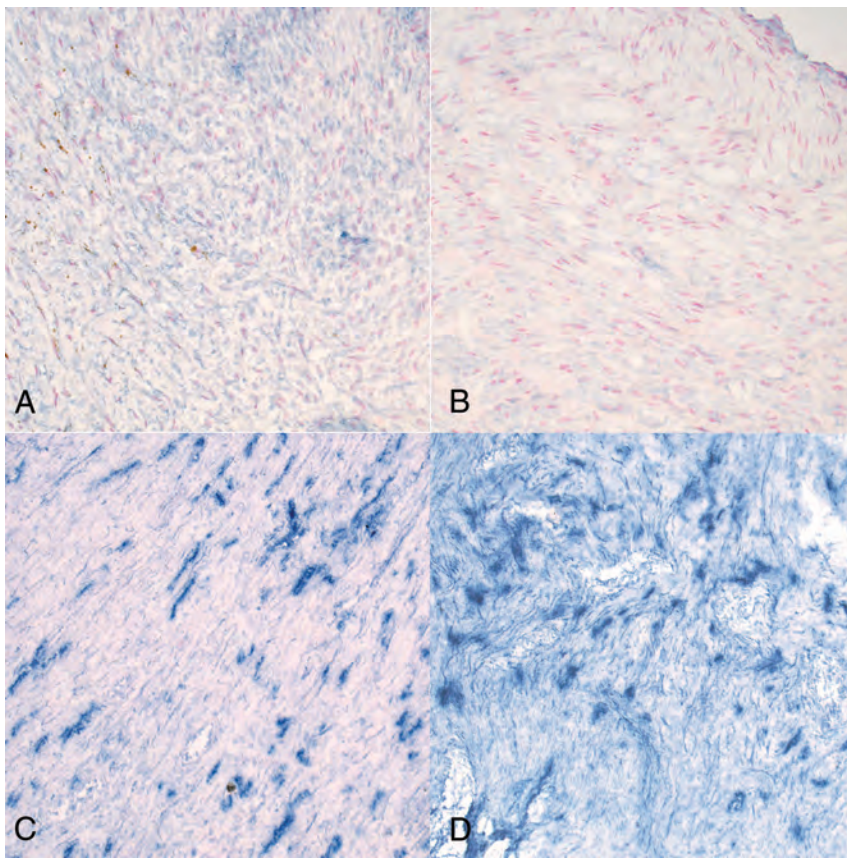


FIG 5. Histology of the aneurysm wall in the animal model without (A and B) and with (C and D) perivascular injection with LPS. The naïve aneurysm has limited macrophage infiltration (A) and no MPO (B). The modification with LPS induces significant macrophage (C) infiltration and has prominent distribution of MPO (D). All images are at $\times 20$ magnification.

DISCUSSION

With advances in noninvasive neuroimaging, aneurysms are being detected incidentally with increasing frequency.^{23,24} The patients diagnosed with UIA and facing the potentially dismal outcome of aneurysmal SAH (associated with a 50% mortality rate) experience a significant decrease in quality of life.²⁵ An objective test to assess rupture risk could potentially impact the decision to treat UIAs. To achieve this goal in clinical practice, thorough evaluation of multiple sequences may lead to a unified MR imaging protocol for risk stratification of intracranial aneurysms.

We have proposed to exploit the relationship between inflammation and aneurysm progression to rupture (reviewed in Tullamo et al⁷) as a means of assessing rupture risk through MR imaging. The exact time course of aneurysm progression to rupture has not been determined in humans. Most of our understanding of factors that may contribute to aneurysm progression and rupture has been gained through studies using animal models. The consensus from these studies is that aneurysm growth is strongly influenced by mediators of inflammation such as interleukin-1- β ,²⁶ nuclear factor κ B,²⁷ and monocyte chemoattractant protein-1.²⁸ The presence of these molecules in the vessel wall is most likely due to leukocyte infiltration, which has recently been shown to have a direct link to aneurysm development.²⁹ Neutrophils are the most abundant leukocytes capable of trafficking into the vessel wall. They secrete an array of signaling molecules such

as cytokines, as well as MPO and elastase,³⁰ which reduce wall strength and thus allow the aneurysm to expand.

The direct role of neutrophil-derived MPO in UIA rupture has not been extensively studied, but a confluence of evidence from research aimed at determining the risk of acute cardiovascular events identified MPO as a key player (reviewed in Schindhelm et al³¹). More recently, MPO presence has been correlated with the PHASES model of the annual rupture risk of aneurysms.¹⁰ In addition to its role in inflammation, MPO mediates oxidative cell stress due to the production of reactive oxygen species contributing to vessel wall damage. Building on previous work with human aneurysm tissue,^{32,33} a rat model was developed in which an allogeneic arterial graft was decellularized before its anastomosis to the aorta of the experimental animal.³⁴ Nearly 50% of these decellularized aneurysms progressed to rupture, whereas control aneurysms remained stable. Histologic analysis demonstrated that thrombus formation within the decellularized aneurysm could not organize; this feature led to recanalization, inflammation, wall degeneration, and ultimate rupture. Similar conclusions regarding the role of incomplete thrombosis and subsequent inflammatory cell infiltration into the aneurysm wall with

marked degeneration were confirmed in a swine venous pouch aneurysm model.³⁵

To enable molecular imaging of MPO activity with high resolution, we selected the realistic rabbit elastase model of saccular aneurysms due to the complex intra-aneurysmal hemodynamics, which are similar to that of human intracranial aneurysms.³⁶ The TSE-based MSDE sequence in a phantom model allowed suppression of the signal from intra-aneurysmal blood flow to a degree that was not achievable by using double inversion recovery³⁷ or small FOV quadrature inversion recovery²⁰ black-blood imaging. The optimized sequence demonstrated a 40-fold increase in SNR in the inflamed aneurysm model compared with the naïve aneurysm following 5HT-DTPA(Gd) administration. This is a dramatic improvement from the previously used T1-fast-field echo protocol.¹⁶ Contrast retention within the aneurysm wall has been observed for up to 6 hours,¹⁶ and in other models, clearance of the contrast has been documented at 24 hours.¹⁵ Further study of contrast dynamics as these apply to aneurysms is needed.

The MPO activity of the aneurysm model after being treated with LPS was similar to that measured in unruptured human aneurysms; however, the negative control naïve rabbit aneurysm had >40 -fold reduction in MPO activity.¹⁰ A limitation of our approach is that direct comparisons of the enzymatic MPO activity measurements in human specimens and the rabbit model are

not possible due to the well-known interspecies variability.³⁸ Qualitatively, the alkaline phosphatase staining showed an abundance of MPO in the inflamed rabbit aneurysm (Fig 4). Another limitation of this model is the artificial induction of inflammatory changes that do not involve hemodynamic activation of the endothelium and subsequent aneurysm wall remodeling, which is suspected in aneurysm pathogenesis. Thoughtful research has focused on characterizing intra-aneurysmal hemodynamics associated with rupture,³⁹⁻⁴¹ and correlating local hemodynamics with noninvasive imaging of MPO activity presents an exciting experimental paradigm. Although the animal model of inflamed intracranial aneurysm presented herein may not be relevant to achieve this goal, it may be possible to link intra-aneurysmal hemodynamics with MPO activity in clinical aneurysm specimens obtained during clipping.¹⁰

CONCLUSIONS

A diagnostic MR imaging protocol has been optimized for detection of an MPO-specific paramagnetic imaging agent in an animal model of inflamed intracranial aneurysms.

Disclosures: Matthew J. Gounis—RELATED: Grant: Philips Healthcare,* Comments: Research instrumentation and science keys were provided by Philips Healthcare; UNRELATED: Consultancy: Stryker Neurovascular, Surpass Inc (contract research organization), Surpass Medical, Codman Neurovascular, Comments: fee-per-hour consulting; Grants/Grants Pending: National Institutes of Health,* Stryker Neurovascular,* Codman Neurovascular,* Lazarus Effect,* Covidien, ev3,* Fraunhofer Institute,* Philips Healthcare,* Silk Road,* Tay Sachs Foundation,* Lundbeck,* Imrarnsjah Martijn John van der Bom—UNRELATED: Employment: Philips Healthcare. Ajay K. Wakhloo—UNRELATED: Consultancy: Stryker Neurovascular; Employment: Surpass Medical; Grants/Grants Pending: Philips Healthcare*; Payment for Lectures (including service on Speakers Bureaus): Harvard Medical School, Miami Baptist Health; Stock/Stock Options: Surpass Medical. Alexei A. Bogdanov Jr—RELATED: Grant: National Institute on Aging, 5R01AG034901-02. *Money paid to the institution.

REFERENCES

- Alshekhlee A, Mehta S, Edgell RC, et al. **Hospital mortality and complications of electively clipped or coiled unruptured intracranial aneurysm.** *Stroke* 2010;41:1471-76
- Brinjikji W, Rabinstein AA, Nasr DM, et al. **Better outcomes with treatment by coiling relative to clipping of unruptured intracranial aneurysms in the United States, 2001-2008.** *AJNR Am J Neuroradiol* 2011;32:1071-75
- Morita A, Kirino T, Hashi K, for the UCAS Japan Investigators. **The natural course of unruptured cerebral aneurysms in a Japanese cohort.** *N Engl J Med* 2012;366:2474-82
- Wiebers DO, Whisnand JP, Huston J, 3rd, et al. **Unruptured intracranial aneurysms: natural history, clinical outcome, and risks of surgical and endovascular treatment.** *Lancet* 2003;362:103-10
- Hasan DM, Mahaney KB, Magnotta VA, et al. **Macrophage imaging within human cerebral aneurysms wall using ferumoxytol-enhanced MRI: a pilot study.** *Arterioscler Thromb Vasc Biol* 2012;32:1032-38
- Hasan D, Chalouhi N, Jabour P, et al. **Early change in ferumoxytol-enhanced magnetic resonance imaging signal suggests unstable human cerebral aneurysm: a pilot study.** *Stroke* 2012;43:3258-65
- Tulamo R, Frösen J, Hemesniemi J, et al. **Inflammatory changes in the aneurysm wall: a review.** *J Neurointervent Surg* 2010;2:120-30
- Nicholls SJ, Hazen SL. **Myeloperoxidase and cardiovascular disease.** *Arterioscler Thromb Vasc Biol* 2005;25:1102-11
- Greving JP, Wermer MJ, Brown RD Jr, et al. **Development of the PHASES score for prediction of risk of rupture of intracranial aneurysms: a pooled analysis of six prospective cohort studies.** *Lancet Neurol* 2014;13:59-66
- Gounis MJ, Vedantham S, Weaver JP, et al. **Myeloperoxidase in human intracranial aneurysms: preliminary evidence.** *Stroke* 2014;45:1474-77
- Chen JW, Pham W, Weissleder R, et al. **Human myeloperoxidase: a potential target for molecular MR imaging in atherosclerosis.** *Magn Reson Med* 2004;52:1021-28
- Chen JW, Querol Sans M, Bogdanov A Jr, et al. **Imaging of myeloperoxidase in mice by using novel amplifiable paramagnetic substrates.** *Radiology* 2006;240:473-81
- Querol M, Chen JW, Weissleder R, et al. **DTPA-bisamide-based MR sensor agents for peroxidase imaging.** *Org Lett* 2005;7:1719-22
- Querol M, Chen JW, Bogdanov AA Jr. **A paramagnetic contrast agent with myeloperoxidase-sensing properties.** *Org Biomol Chem* 2006;4:1887-95
- Ronald JA, Chen JW, Chen Y, et al. **Enzyme-sensitive magnetic resonance imaging targeting myeloperoxidase identifies active inflammation in experimental rabbit atherosclerotic plaques.** *Circulation* 2009;120:592-99
- DeLeo MJ 3rd, Gounis MJ, Hong B, et al. **Carotid artery brain aneurysm model: in vivo molecular enzyme-specific MR imaging of active inflammation in a pilot study.** *Radiology* 2009;252:696-703
- Chueh JY, Wakhloo AK, Gounis MJ. **Neurovascular modeling: small-batch manufacturing of silicone vascular replicas.** *AJNR Am J Neuroradiol* 2009;30:1159-64
- Seong J, Sadasivan C, Onizuka M, et al. **Morphology of elastase-induced cerebral aneurysm model in rabbit and rapid prototyping of elastomeric transparent replicas.** *Biorheology* 2005;42:345-61
- Park JK, Lee CS, Sim KB, et al. **Imaging of the walls of saccular cerebral aneurysms with double inversion recovery black-blood sequence.** *J Magn Reson Imaging* 2009;30:1179-83
- Yarnykh VL, Yuan C. **T1-insensitive flow suppression using quadruple inversion-recovery.** *Magn Reson Med* 2002;48:899-905
- Wang J, Yarnykh VL, Yuan C. **Enhanced image quality in black-blood MRI using the improved motion-sensitized driven-equilibrium (iMSDE) sequence.** *J Magn Reson Imaging* 2010;31:1256-63
- Altes TA, Cloft HJ, Short JG, et al. **1999 ARRS Executive Council Award: creation of saccular aneurysms in the rabbit—a model suitable for testing endovascular devices.** *AJR Am J Roentgenol* 2000;174:349-54
- Tummala RP, Baskaya MK, Heros RC. **Contemporary management of incidental intracranial aneurysms.** *Neurosurg Focus* 2005;18:E9-18
- Vernooij MW, Ikram MA, Tanghe HL, et al. **Incidental findings on brain MRI in the general population.** *N Engl J Med* 2007;357:1821-28
- Buijs JE, Greebe P, Rinkel GJE. **Quality of life, anxiety and depression in patients with an unruptured intracranial aneurysm with or without aneurysm occlusion.** *Neurosurgery* 2012;70:868-72
- Moriwaki T, Takagi Y, Sadamasu N, et al. **Impaired progression of cerebral aneurysms in interleukin-1-β-deficient mice.** *Stroke* 2006;37:900-05
- Aoki T, Kataoka H, Shimamura M, et al. **NF-κB is a key mediator of cerebral aneurysm formation.** *Circulation* 2007;116:2830-40
- Aoki T, Kataoka H, Ishibashi R, et al. **Impact of monocyte chemoattractant protein-1 deficiency on cerebral aneurysm formation.** *Stroke* 2009;40:942-51
- Kanematsu Y, Kanematsu M, Kurihara C, et al. **Critical roles of macrophages in the formation of intracranial aneurysm.** *Stroke* 2011;42:173-78
- Topham MK, Carveth HJ, McIntyre TM, et al. **Human endothelial cells regulate polymorphonuclear leukocyte degranulation.** *FASEB J* 1998;12:733-46
- Schindhelm RK, van der Zwan LP, Teerlink T, et al. **Myeloperoxidase: a useful biomarker for cardiovascular disease risk stratification?** *Clin Chem* 2009;55:1462-70
- Frösen J, Tulamo R, Heikura T, et al. **Lipid accumulation, lipid oxidation, and low plasma levels of acquired antibodies against oxidized lipids associate with degeneration and rupture of the intracranial aneurysm wall.** *Acta Neuropathol Commun* 2013;1:71

33. Laaksamo E, Tulamo R, Liiman A, et al. **Oxidative stress is associated with cell death, wall degradation, and increased risk of rupture of the intracranial aneurysm wall.** *Neurosurgery* 2013;72:109–17
34. Marbacher S, Marjamaa J, Bradacova K, et al. **Loss of mural cells leads to wall degeneration, aneurysm growth, and eventual rupture in a rat aneurysm model.** *Stroke* 2014;45:248–54
35. Raymond J, Darsaut TE, Kotowski M, et al. **Thrombosis heralding aneurysmal rupture: an exploration of potential mechanisms in a novel giant swine aneurysm model.** *AJNR Am J Neuroradiol* 2013;34:346–53
36. Zeng Z, Kallmes DF, Durka MJ, et al. **Hemodynamics and anatomy of elastase-induced rabbit aneurysm models: similarity to human cerebral aneurysms?** *AJNR Am J Neuroradiol* 2011;32:595–601
37. Krings T, Mandell DM, Kiehl TR, et al. **Intracranial aneurysms: from vessel wall pathology to therapeutic approach.** *Nat Rev Neurol* 2011;7:547–59
38. Rausch PG, Moore TG. **Granule enzymes of polymorphonuclear neutrophils: a phylogenetic comparison.** *Blood* 1975;46:913–19
39. Cebal JR, Mut F, Weir J, et al. **Quantitative characterization of the hemodynamic environment in ruptured and unruptured brain aneurysms.** *AJNR Am J Neuroradiol* 2011;32:145–51
40. Valen-Sendstad K, Steinman DA. **Mind the gap: impact of computational fluid dynamics solution strategy on prediction of intracranial aneurysm hemodynamics and rupture status indicators.** *AJNR Am J Neuroradiol* 2014;35:536–43
41. Pereira VM, Brina O, Bijlenga P, et al. **Wall shear stress distribution of small aneurysms prone to rupture: a case-control study.** *Stroke* 2014;45:261–64

Establishing a Rabbit Spinal Tumor Model for Nonvascular Interventional Therapy through CT-Guided Percutaneous Puncture Inoculation

L. Chen, J. Xiao, I.-C. Su, Y.-W. Wu, B. Zhang, K.-Y. Ge, Y.-C. Chang, C. Yang, and C.-F. Ni



ABSTRACT

BACKGROUND AND PURPOSE: An animal spinal tumor model is needed to better simulate the clinical situation and to allow percutaneous puncture, which may provide an experimental platform for the new nonvascular interventional therapies. We established a rabbit spinal tumor model through a CT-guided percutaneous puncture inoculation technique for nonvascular interventional therapy.

MATERIALS AND METHODS: VX2 tumor cells were inoculated into the lumbar vertebrae of 32 rabbits through a CT-guided percutaneous puncture technique; then, the development of hind limb paraparesis was observed in the rabbits twice a day. MR imaging and CT were performed on days 14, 21, and 28 postinoculation and at the development of hind limb paraparesis. On days 21 and 28 postinoculation, 2 rabbits, whose imaging suggested successful modeling without hind limb paraparesis, were chosen on each day. The lumbar vertebrae were sampled from 1 rabbit for histopathologic examination, and the other rabbit underwent PET-CT examination before percutaneous vertebroplasty. Finally the lesion vertebrae were sampled for histopathologic examination.

RESULTS: The success rate of modeling was 90.6% (29/32) in our study. On day 21 postinoculation, successful modeling was achieved in 21 rabbits, with 19 having no hind limb paraparesis. On day 28 postinoculation, another 7 achieved successful modeling, and only 1 developed hind limb paraparesis. Percutaneous vertebroplasty treatment was successful for the 2 rabbit models.

CONCLUSIONS: Establishment of a rabbit spinal tumor model through a CT-guided percutaneous puncture technique and inoculation of VX2 tumor is easy and has a high success rate. The established model can be used to study nonvascular interventional therapies for spinal tumor, including percutaneous vertebroplasty.

ABBREVIATIONS: HLP = hind limb paraparesis; PVP = percutaneous vertebroplasty

Approximately 5%–10% of all patients with cancer have metastases to the spinal column.^{1,2} Vertebral metastasis has major clinical significance and can acutely impact patient quality of life. It is not only an indicator of bad prognosis but also produces severe pain, spinal instability, and neurologic compression following pathologic vertebral fracture. Despite multimodality

treatment of spinal diseases, which includes a combination of surgery, radiation therapy, and chemotherapy, the median life expectancy for these patients is <1 year.^{3,4} Recently various interventional mini-invasive therapies, such as percutaneous vertebroplasty (PVP) and radiofrequency ablation through percutaneous puncture, have yielded encouraging preliminary clinical outcomes in the local treatment of spinal tumor.^{5–7} However, the treatment mechanism of these therapies remains unclear,^{8–10} and some have a higher rate of complications.^{11,12} In addition, more basic and preclinical research is needed to improve the curative efficacy of the newly developed treatment instruments and to reduce their complications. Due to lack of a live spinal tumor model for percutaneous puncture, previous research was mainly conducted with healthy animals, cadavers, or computer-simulated systems.^{13–15} A live animal spinal tumor model is urgently needed to better simulate the clinical situation and to allow percutaneous puncture, which may provide an experimental platform for the newly emerging mini-invasive interventional therapies. The present study, using CT-guided percutaneous puncture inoculation of VX2 tumor cells, created a rabbit spinal tumor model that allows

Received December 20, 2013; accepted after revision March 11, 2014.

From the Departments of Interventional Radiology (L.C., K.-Y.G., Y.-C.C., C.Y., C.-F.N.) and Nuclear Medicine (Y.-W.W., B.Z.), The First Affiliated Hospital of Soochow University, Suzhou, China; Department of Orthopedic Surgery (J.X.), Zhongshan Hospital, Fudan University, Shanghai, China; Division of Neurosurgery (I.-C.S.), Department of Surgery, Taipei Cathay General Hospital, Taipei, Taiwan; and School of Medicine (I.-C.S.), Fu-Jen Catholic University, New Taipei City, Taiwan.

This work was supported by a grant from the National Natural Science Foundation of China (grant No. 81101136); a grant from the Shanghai Municipal Natural Science Foundation, China (grant No. 11ZR1448300); a grant from Jiangsu Provincial Special Program of Medical Science, China (BL2012004); and a grant from the International Exchange Health Program of Jiangsu Province, China (grant No. 2012020).

Please address correspondence to Cai-Fang Ni, MD, PhD, The First Affiliated Hospital of Soochow University, 188 Shizi St. 215006 Suzhou, China; e-mail: cfnisz@163.com

Indicates open access to non-subscribers at www.ajnr.org

<http://dx.doi.org/10.3174/ajnr.A3956>

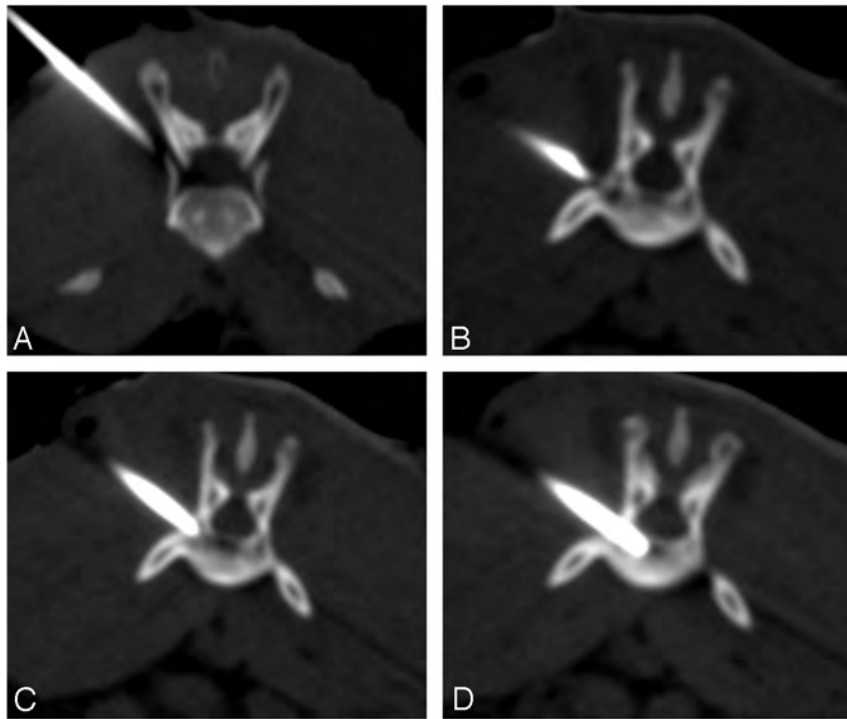


FIG 1. CT-guided percutaneous puncture inoculation of a VX2 tumor mass. *A*, Incorrect positioning of puncture needle and the adjustment of needle position and direction. *B*, Correct positioning of puncture needle, just at the junction of the vertebral body and left vertebral pedicle. *C*, Puncture needle breaking the vertebral cortical bone and reconfirming that the needle positioning is not deep enough. *D*, Slow advancement of the puncture needle to the middle of vertebral body.

mini-invasive therapies through a percutaneous puncture approach and observed the development and pathologic manifestation of hind limb paraparesis (HLP) in an animal model.

MATERIALS AND METHODS

The protocol of this experiment was approved by the animal research committee of our institution and was conducted in accordance with the guidelines of the International Council on Animal Care. Healthy New Zealand white rabbits ($n = 32$), weighing 3–3.5 kg, were purchased from the Laboratory Animal Center of our university. Fasting was prescribed from the night before the inoculation in 32 rabbits, and 3% pentobarbital was used for general anesthesia via a rabbit ear vein at a dose of 30 mg/kg before inoculation, imaging examination, and PVP treatment.

Preparation of VX2 Tumor Mass

Rabbit VX2 carcinoma preparation was performed as previously described.^{16,17} Successful inoculation of the VX2 mass into the thigh muscles of the New Zealand rabbit could lead to a palpable tumor mass at the inoculation site 3 weeks later. At 30 minutes before inoculation, tumor was surgically obtained from the thigh of tumor-bearing rabbits; then, the fresh tumor tissues around the border of the tumor were harvested after removing the hemorrhage and necrotic tissues. The tumor tissues were cut into small blocks (approximately 1.0 mm^3 , 2×10^5 tumor cells), which were soaked in saline until use.

Percutaneous Puncture Inoculation Technique

The experimental rabbits were anesthetized and fixed in a prone position, and the skin on the left low back was prepared. CT localization set the junction of the head side of the L4 or L5 vertebral body and the left pedicle as the puncture point. A 17-ga coaxial introducer needle (Angiotech, Gainesville, Florida) was used to puncture the target vertebra under CT guidance, and the needle advancement was stopped when it reached the middle area of the punctured vertebral body (Figs 1 and 2); then, the inner core of the trocar was used to coaxially push the 2 tumor blocks into the vertebrae body through the sheathed needle, and finally a piece of Gelfoam (0.5 cm; Jinling Pharmaceutical Company, Nanjing, China) was used to seal the needle tract.

Observation of the Postinoculation Procedure

Animals were examined twice daily for signs of HLP after transplantation. On days 14, 21, and 28 postinoculation, MR imaging and CT were performed. On days 21 and 28 postinoculation, 2 rabbits, whose imaging examination suggested tumor growth but with no signs of paralysis, were chosen each day. One animal was used to harvest lesion vertebrae for pathologic examination, the other underwent an ^{18}F -FDG PET-CT examination before using polymethylmethacrylate bone cement (Cranio-plastic; Codman, Raynham, Massachusetts) to conduct PVP treatment, and finally the lesion vertebrae samples were harvested for histopathology. For the rest of the experimental rabbits, both MR imaging and CT were performed immediately after development of HLP; then, lesion vertebrae samples were harvested for pathologic examination. Animals with no HLP at 3 months postinoculation and no tumor growth on imaging examination were sacrificed, and the spines were processed for histopathology.

Imaging Examination and PVP Technique

An MX 8000 4-channel CT scanner (Marconi Medical Systems, Cleveland, Ohio) was used. The scanning parameters were the following: tube voltage, 120 kV(peak); tube current, 200 mA; section thickness, 2 mm; reconstruction interval, 2 mm; and rotation time, 1 second.

MR imaging was performed with a 1.5T imaging unit (Eclipse; Philips Healthcare, Best, the Netherlands) and a spine coil. Sagittal T1-weighted (TR/TE, 500/12 ms) and sagittal and axial T2-weighted (TR/TE, 4500/112 ms) images were obtained, and sagittal T1-weighted images were obtained after intravenous administration of 0.1-mmol/kg gadopentetate dimeglumine (Magnevist; Schering, Berlin, Germany).

Fasting was prescribed for 4 hours before PET-CT, and ^{18}F -

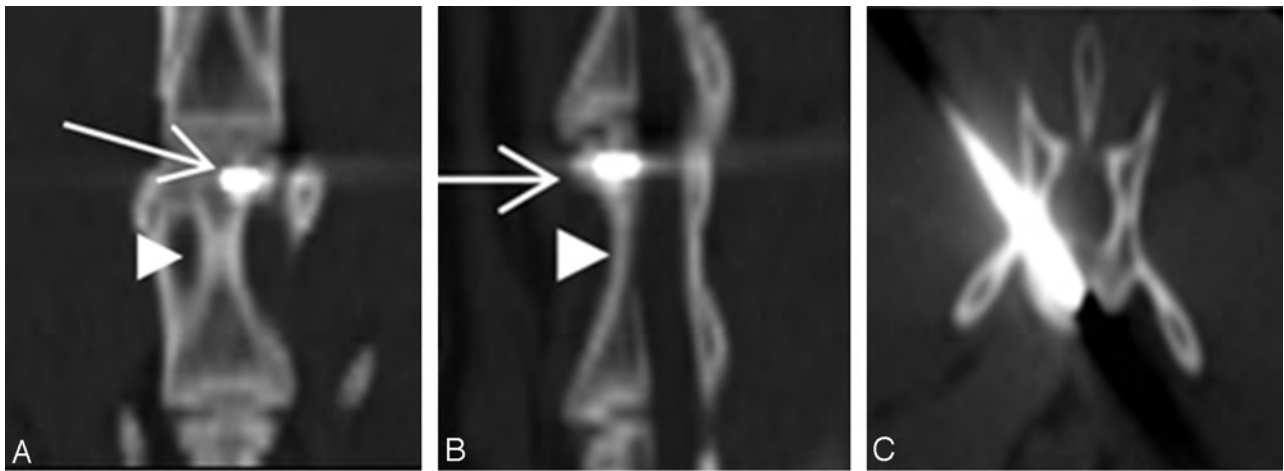


FIG 2. CT scan reconstruction after successful puncture: coronal section (A), sagittal section (B), and axial section (C). The rabbit vertebra is narrow and long, with the central part being thin and small (arrowhead). The cross-section of the vertebral head is relatively thicker, and the puncture needle tip (arrow) is positioned at the relatively thicker side of vertebra head after successful puncture.

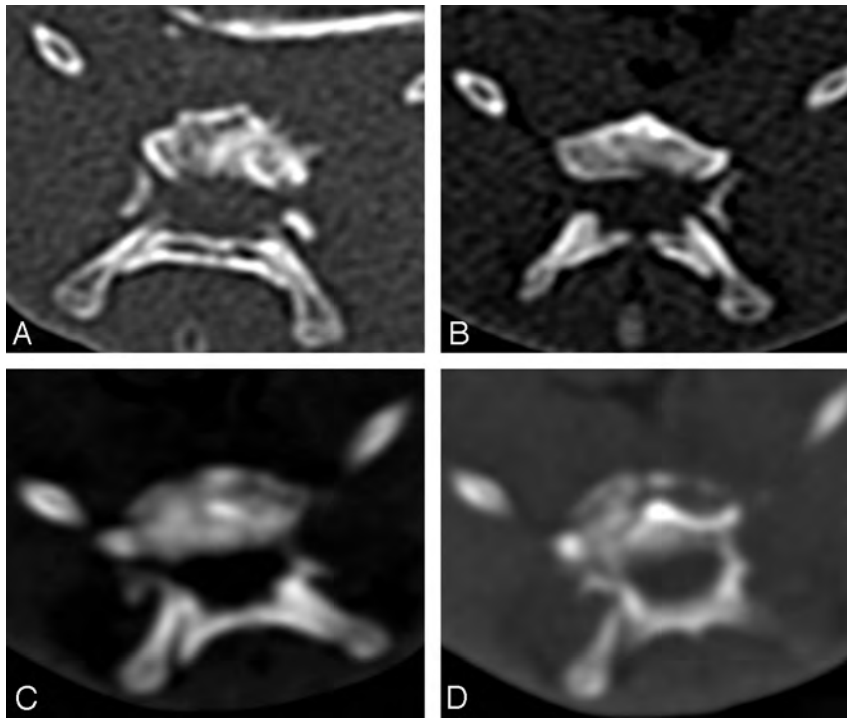


FIG 3. CT of a successful model of a spinal tumor. A and B, Irregular bone destruction inside the lumbar vertebrae and cortical bone destruction at the vertebra posterior border. C and D, Another experimental animal with vertebral bone destruction. The vertebral cortical bone broke at the vertebra border, with a small amount of high-attenuation osteogenesis inside.

FDG was injected via a rabbit ear vein (27.8 MBq/Kg); 45 minutes later the rabbits were fixed in a prone position for PET-CT scanning (Discovery LS; GE Healthcare, Milwaukee, Wisconsin). The parameters for CT were as follows: An initial scout view was obtained with 10 mAs and 120 kVp, followed by spiral CT at a table speed of 17.5 mm/s and a pitch of 1.75 with 120 mAs, 140 kV. PET images were obtained with a weight-based protocol and 4–6 minutes of acquisition time per bed position. All PET images were reconstructed by using an iterative algorithm, with CT-based attenuation correction applied. Metabolic images from PET and anatomic images from CT were fused in a postprocessing workstation (Xeleris 1.1; GE Healthcare).

PVP was performed under CT guidance. An 18-ga vascular access needle punctured the spinal tumor to deliver approximately 0.5-mL polymethylmethacrylate bone cement (Corinplast 3; Corin, Gloucester, UK) for PVP therapy.

RESULTS

Successful Modeling Rate

All 32 rabbits underwent successful puncture with no acute paralysis, and successful modeling was achieved in 29, with a success rate of 90.6% (29/32), which was confirmed by histopathologic results. Among the 3 failed cases, 1 had no tumor growth inside the vertebra, but inside paravertebral soft tissues; and 2 had no spinal tumor growth after inoculation or paralysis 3 months later and reimaging examination still found no tumor growth. The 2 rabbits were sacrificed and pathologic examination of the lumbar vertebrae undergoing tumor inoculation found no tumor cells, indicating inoculation failure.

Hind Limb Paralysis Time

On day 14 postinoculation, only 1 rabbit had spinal tumor growth as shown by MR imaging, and HLP occurred on day 19 postinoculation. On day 21 postinoculation, 21 rabbits had spinal tumor growth as shown by both MR imaging and CT and 2 had HLP. On day 28 postinoculation, spinal tumor growth was observed in another 7 rabbits as shown by MR imaging and CT and 1 had HLP. Among the 29 rabbits that achieved successful modeling, 25 developed HLP on average 26.4 ± 4.2 days after inoculation (range, 19–36 days). On days 19, 28, 33, 34, 35, and 36 postinoculation, 1 paralysis occurred each day. On days 21, 23, and 24, two cases of paralysis occurred each day; on days 25 and 26, four cases of paralysis occurred each day, and on day 27, five cases of paralysis occurred; so the peak time for successful

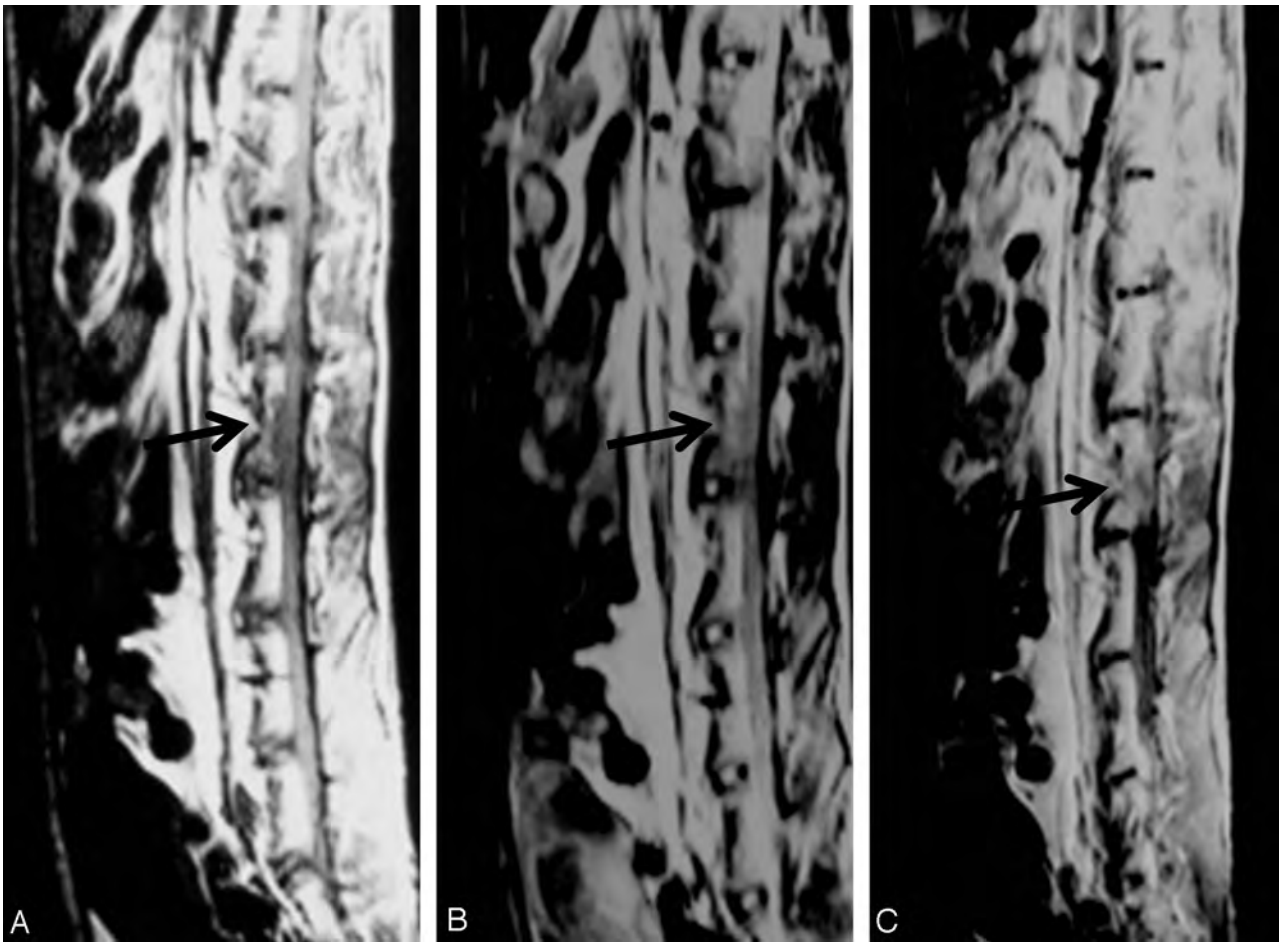


FIG 4. MR images of the vertebra of a paralyzed rabbit with abnormal signal (*arrow*) from the L4 vertebra. *A*, Low signal on T1WI. *B*, High signal on T2WI. *C*, Enhanced scan shows significantly enhanced lesions and spinal cord compression.

modeling animals to show signs of HLP was on days 25–27 postinoculation. For the 4 rabbits achieving successful modeling but with no HLP, pathologic samples were still harvested on days 21 and 28, or vertebra samples were obtained for pathologic examination after PET-CT and PVP treatment.

Imaging Manifestation of the Spinal Tumor Model

CT of the lumbar vertebrae showed irregular osteolytic bone destruction inside, with high-attenuation osteogenesis also observed in some spinal tumors, and vertebral posterior border bone destruction observed at the late stage (Fig 3). MR imaging revealed that L4 or L5 vertebrae showed low signal on T1WI and high signal on T2WI, with uneven signal attenuation. Enhanced scanning showed heterogeneous enhancement. For cases with a larger tumor, the border with the spinal cord was unclear, and the latter was compressed locally (Fig 4). CT images of the PET-CT results were the same as those described above, but the fused images revealed increased uptake of radionuclide in the tumor inoculation area (Fig 5), with the standardized uptake value increased notably. For the 2 rabbits receiving PVP treatment, the puncture of the spinal tumor model was smooth, and the sedimentation of bone cement inside the vertebral body was satisfactory (Fig 6).

Pathology of the Spinal Tumor Model

Pathologic samples of the lesion vertebrae showed tumor growth inside the vertebral body. For the rabbits without paralysis, cortical bone on the posterior border was intact; for the rabbits with paralysis, tumor mass intruded into and compressed the spinal cord (Fig 7). Hematoxylin-eosin staining showed extensive osteolytic activity induced by tumor cells inside the vertebrae, complicated by mild osteogenic activity. The tumor cell was large, with well-demarcated borders, cellular atypia, and a visible pathologic mitotic count. Tumor cells had a nest arrangement, with regional invasive growth destroying the cortical bone (Fig 7).

DISCUSSION

The previous rat- or mice-based spinal tumor models were mainly used for studying tumor metastasis mechanisms, radiation therapy, and drug screening.^{18,19} However, the rat vertebra is small, making it difficult to accommodate a thick needle in various non-vascular interventional treatments (such as PVP, radiofrequency ablation) by using a percutaneous puncture technique. Recent rabbit models of spinal tumors created by different surgical methods requiring more experimental techniques and more advanced equipment also sustained even greater trauma, which is not helpful for conducting the ensuing experiments.^{16,17} More important,

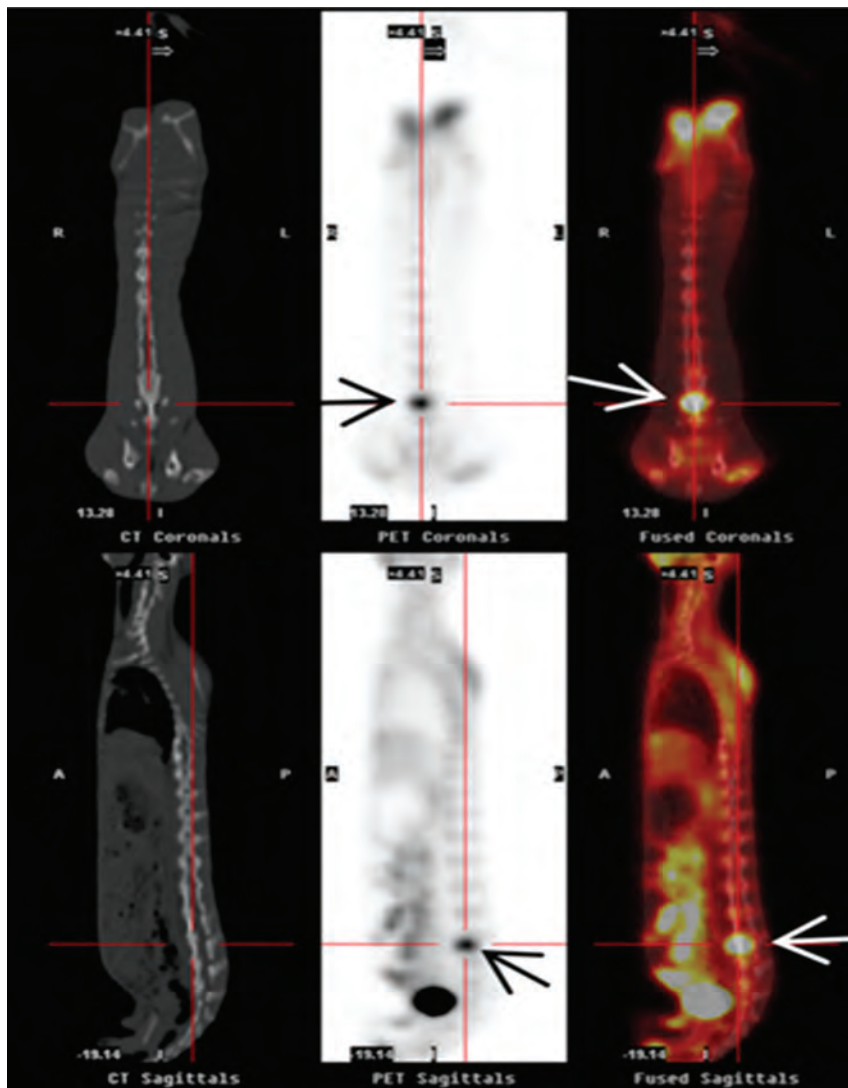


FIG 5. PET-CT images of a spinal tumor in a successful rabbit model with increased uptake of radionuclide at L5 vertebra (*arrow*). The left column shows a reconstructed image at CT coronal and sagittal positions, the middle column shows PET image, and the right column shows PET-CT fused image.

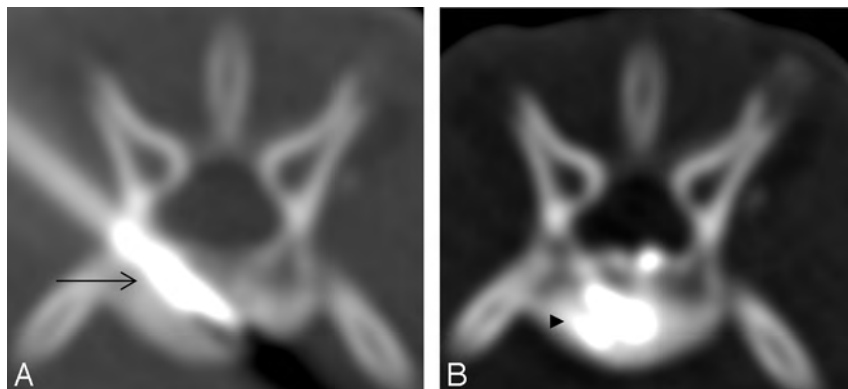


FIG 6. CT-guided PVP treatment of a rabbit spinal tumor. *A*, High-attenuation metallic puncture needle (*arrow*) into the vertebral body during PVP. *B*, Satisfactory sedimentation of high-attenuation bone cement (*arrowhead*) in the vertebral body after PVP.

those tumor models were through direct-inoculation surgery. The inoculation approach of the model of Amundson et al¹⁶ was through the posterior pedicle, breaching the vertebral lamina

some heat; at the same time, differences exist in specific heat and thermal conductivity between bone tissue and soft tissue, which could all directly affect the actual temperature inside the spinal

directly into the spinal canal, then into the posterior vertebral edge, so that the tumors were mainly located on the posterior vertebral edge. Meanwhile, the same approach is also needed when the model is used for research on nonvascular interventional therapy; this will make puncturing very difficult because it entails breaching the spinal canal, which may easily cause nerve damage and is disadvantageous for observing the efficacy of ensuing treatments. So Amundson et al's model is mainly used for studying surgical procedures.²⁰ Our model is prepared through a lateral pedicle approach, particularly for percutaneous puncture of the vertebrae, through which the ensuing experiments could also be performed for nonvascular interventional therapy, which makes our model more suitable for research on this therapy.

In 2010, Sciubba et al²¹ reported a successful rabbit vertebral tumor model constructed through a percutaneous puncture technique, which was used for studying ultrasonic ablation treatment of spinal tumor. This model had a grossly apparent spinal and paraspinal tissue mass. We noticed that Sciubba et al mainly focused on how to treat the model; they did not give sufficient description on the details of establishment procedure, including the specific sites for puncture, images of the model at different time points, and the development of paralysis. We also noticed that some radiofrequency electrodes used in Sciubba et al's research for tumor treatment actually punctured the paravertebral soft-tissue tumor, instead of vertebral tumor. Differences exist between paravertebral tumor and vertebral tumor. According to the literature, factors like bone cement polymerization temperature during PVP and temperature changes inside the vertebral body and spinal canal during radiofrequency ablation treatment may be directly associated with the treatment efficacy and complications.^{5,12}

The vertebral body has its special anatomic structure. CSF adjacent to the back of the vertebral body can take away

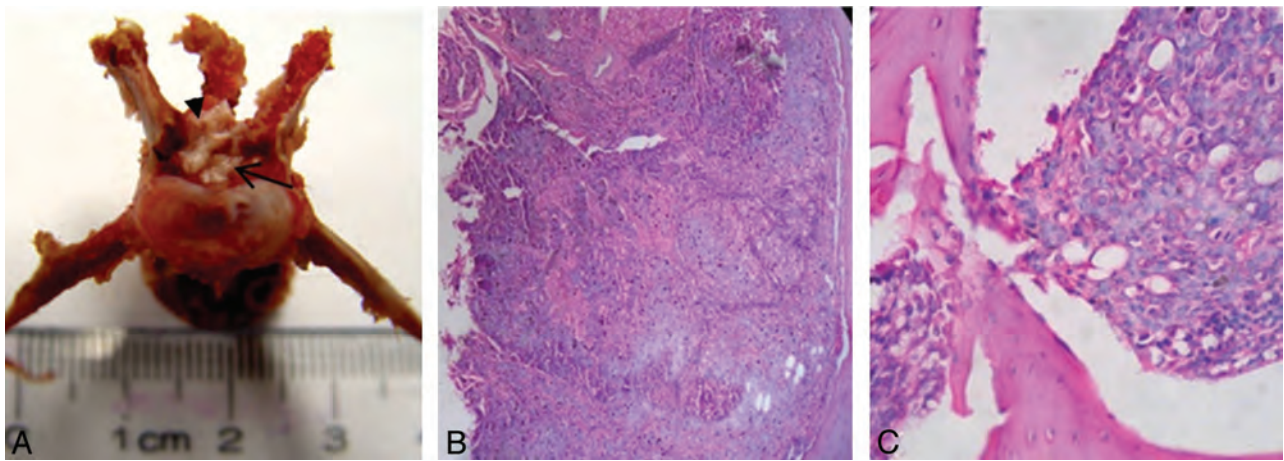


FIG 7. General pathology and hematoxylin-eosin staining of a successful animal model. *A*, Bone destruction at the posterior border of the vertebra, with the spinal cord (*arrowhead*) being compressed by the back side of the tumor (*arrow*). *B*, Magnification $\times 40$. *C*, Hematoxylin-eosin staining. Tumor cells have a nest arrangement under the microscope, and the cells are bulky, with clear boundaries, a high level of cell atypia, an increased nuclear cytoplasm ratio, visible pathologic mitotic count, and a staggered arrangement of tumor cells and bone. Magnification $\times 400$.

tumor and spinal canal during treatment.^{13,22} The above pathophysiologic traits of vertebral tumor are not easily found in paravertebral tumor. Therefore, establishment of a real vertebral tumor model for the percutaneous puncture technique will contribute greatly to the emerging nonvascular interventional therapies for vertebral tumors.

In this study, the rabbit VX2 spinal tumor model was established through percutaneous puncture inoculation under CT guidance. All the rabbits in our study successfully underwent percutaneous puncture for inoculating VX2 tumor mass; posttransplantation imaging and pathologic examination confirmed the high success rate of tumor inoculation. Meanwhile, we noticed that PET-CT has been increasingly used to evaluate the treatment efficacy in malignant bone tumors. In the present article, the PET-CT results of 2 animal models both clearly displayed the spinal tumor, suggesting that PET-CT could also evaluate the efficacy of all types of newly emerging interventional therapies for the tumor model.²³

PVP treatment based on the rabbit model also achieved preliminary success, indicating its potential in studying mini-invasive interventional treatments through percutaneous puncture. In addition, in another study, we are using our model to study PVP treatment for spinal tumor and to develop a new type of PVP bone cement. For example, detecting the polymerization temperature of bone cement inside the spinal tumor model can better reflect the temperature change during polymerization of bone cement in the clinical setting. To sum up, our model can be used for further exploration of the mechanism of various nonvascular interventional therapies for spinal tumor; the efficacy and safety of some newly developed interventional equipment and materials could also be tested with this model. Eventually, we hope our model can serve as a better platform for studying various emerging mini-invasive interventional treatments for vertebral tumors.

To make it easier to puncture the target vertebra, one should target the larger lumbar vertebrae of the rabbit for modeling. However, because the sixth lumbar vertebra is usually obscured by the ilium, which may affect the puncture approach, the L4 or L5 vertebra is a more suitable target. The rabbit vertebra is narrow and long, with a thin middle part, making it difficult to accommodate the puncture

needle.²⁴ However, the size of the vertebral head side is larger, with a triangular cross-section and a maximum oblique diameter of approximately 1.0 cm, where the pedicle is located; thus, the area suitable for tumor inoculation should be the narrow area 0.5 cm from the endplate of the vertebral head side (Fig 2). Conventional clinical practice is to puncture the lumbar vertebra through a pedicle approach; however, the rabbit pedicle is thin and is difficult to puncture. Puncture through the lateral pedicle route is relatively easy and can avoid damage to the spinal canal structures. The rabbit was in a prone position when undergoing puncture, and the junction of the vertebral body and the left pedicle was chosen as the optimal approach for the convenience of the right-handed laboratory personnel. All 32 rabbits underwent such an approach for puncture without postoperative acute HLP, indicating that the transpedicular lateral approach is feasible and safe.

CT-guided puncture technology is the key to successful modeling. The advancement of the puncture needle should be stopped promptly when the needle tip reaches the cortical bone of the lumbar vertebra; then CT should be used to guide the puncture needle angle until the needle tip is positioned just at the left lateral margin of the vertebra head side and to penetrate the needle into vertebral body along the adjusted direction (Fig 1). The penetration depth of the puncture needle was approximately 0.5 cm. Caution should be exercised during the process to prevent the needle from penetrating too deep and damaging the cortical bone of the contralateral vertebra, avoiding the tumor mass being pushed into contralateral paraspinal soft tissue. To ensure that the tumor mass is pushed into the vertebral body, one should push the inner core of the puncture trocar 3–4 times inside the needle sheath. Finally, Gelfoam should be pushed along the sheath to embolize the needle tract to avoid paraspinal tumor mass implantation caused by the shedding of the tumor mass.

For various surgical techniques used to establish a rabbit model of vertebral tumors, the average time for the experiment animal to develop signs of HLP was 18–30 days.^{16,17} The average time in the present study was 26.4 ± 4.2 days, consistent with other experiments, and paralysis occurred mostly on days 25–27 postinoculation. Amundson et al¹⁶ reported that imaging could not find vertebral

tumors in the experiment animals within 14 days postinoculation. In this study, MR imaging revealed that on day 14 postinoculation, there was only 1 case of vertebral tumor growth, accounting for 3.5% (1/29) of the total successful models, suggesting that rabbit VX2 spinal tumor growth was hard to detect by imaging examination within 2 weeks postinoculation. For the total 29 successful modeling animals in this study, 72.4% (21/29) of the vertebral lesions could be confirmed by MR imaging and CT examination 21 days postinoculation. Meanwhile, the peak time for successful modeling animals to show signs of HLP was on days 25–27 postinoculation. Therefore, it is recommended that when using this model, the treatment should begin on day 21 postinoculation, when successful modeling can be found and confirmed by imaging examinations in most cases, while HLP has not yet developed.

Despite of the above effort, we admit that heterogeneity in the amount and location of placement of the tumor cells may exist in this study. The left side of the rabbit L4 or L5 vertebral body and the lateral pedicle approach were chosen for puncture in all the animals, and the vertebral head side with a larger triangular cross-section was chosen for tumor inoculation to keep the utmost consistency in the inoculation location. Most of the animals reached the experimental end point of HLP within a relatively tight range. There were 3 cases of failed animal modeling in this experiment, with 1 case having paraspinal soft-tissue tumor growth, which might be caused by tumor cell leakage, while the reason for the other 2 failed cases was not clear and should be addressed in further experiments. Also, this study aimed to investigate the feasibility of establishing a rabbit model of vertebral tumors through percutaneous puncture and the associated imaging manifestations, so the mechanism of paralysis was not discussed, which may also need to be addressed in future studies.

CONCLUSIONS

Our method in the present study is easy to perform and less invasive with a low animal mortality rate and a high successful modeling rate. Our model, which was established in the rabbit by using an interventional method, may provide a better platform for studying various mini-invasive interventional therapies for vertebral tumor via percutaneous puncture and other treatments, including radiation therapy and surgery.

Disclosures: Long Chen, Yi-Wei Wu, Kun-Yuan Ge, Yong-Chuang Chang, Chao Yang, Cai-Fang Ni—RELATED: Grant: a grant from the National Natural Science Foundation of China (grant No. 81101136),* a grant from Jiangsu Provincial Special Program of Medical Science, China (BL2012004);* and a grant from the International Exchange Health Program of Jiangsu Province, China (grant No. 2012020).* Jian Xiao—RELATED: Grant: a grant from the Shanghai Municipal Natural Science Foundation, China (grant No. 11ZR1448300).* *Money paid to the institution.

REFERENCES

- Barron KD, Hirano A, Araki S, et al. Experiences with metastatic neoplasms involving the spinal cord. *Neurology* 1959;9:91–106
- Geldof AA, Rao BR. Prostatic tumor (R3327) skeletal metastasis. *Prostate* 1990;16:279–90
- Fourney DR, Abi-Said D, Rhines LD, et al. Simultaneous anterior-posterior approach to the thoracic and lumbar spine for the radical resection of tumors followed by reconstruction and stabilization. *J Neurosurg* 2001;94(2 suppl):232–44
- Cooper PR, Errico TJ, Martin R, et al. A systematic approach to spinal reconstruction after anterior decompression for neoplas-

- tic disease of the thoracic and lumbar spine. *Neurosurgery* 1993;32:1–8
- Nakatsuka A, Yamakado K, Takaki H, et al. Percutaneous radiofrequency ablation of painful spinal tumors adjacent to the spinal cord with real-time monitoring of spinal canal temperature: a prospective study. *Cardiovasc Intervent Radiol* 2009;32:70–75
- Lee B, Franklin I, Lewis JS, et al. The efficacy of percutaneous vertebroplasty for vertebral metastases associated with solid malignancies. *Eur J Cancer* 2009;45:1597–602
- Itagaki MW, Talenfeld AD, Kwan SW, et al. Percutaneous vertebroplasty and kyphoplasty for pathologic vertebral fractures in the Medicare population: safer and less expensive than open surgery. *J Vasc Interv Radiol* 2012;23:1423–29
- Anselmetti GC, Manca A, Kanika K, et al. Temperature measurement during polymerization of bone cement in percutaneous vertebroplasty: an in vivo study in humans. *Cardiovasc Intervent Radiol* 2009;32:491–98
- Paul L, Santonja C, Izquierdo E. Complete necrosis of a spinal giant cell tumor after vertebroplasty. *J Vasc Interv Radiol* 2006;17:727–31
- Chen L, Ni RF, Liu SY, et al. Percutaneous vertebroplasty as a treatment for painful osteoblastic metastatic spinal lesions. *J Vasc Interv Radiol* 2011;22:525–28
- Nakatsuka A, Yamakado K, Maeda M, et al. Radiofrequency ablation combined with bone cement injection for the treatment of bone malignancies. *J Vasc Interv Radiol* 2004;15:707–12
- Munk PL, Murphy KJ, Gangi A, et al. Fire and ice: percutaneous ablative therapies and cement injection in management of metastatic disease of the spine. *Semin Musculoskelet Radiol* 2011;15:125–34
- Wegener B, Zolyniak N, Gulecyuz MF, et al. Heat distribution of polymerisation temperature of bone cement on the spinal canal during vertebroplasty. *Int Orthop* 2012;36:1025–30
- Tschirhart CE, Finkelstein JA, Whyne CM. Optimization of tumor volume reduction and cement augmentation in percutaneous vertebroplasty for prophylactic treatment of spinal metastases. *J Spinal Disord Tech* 2006;19:584–90
- Lu J, Deng J, Zhao H, et al. Safety and feasibility of percutaneous vertebroplasty with radioactive (153)Sm PMMA in an animal model. *Eur J Radiol* 2011;78:296–301
- Amundson E, Pradilla G, Brastianos P, et al. A novel intravertebral tumor model in rabbits. *Neurosurgery* 2005;57:341–46; discussion 341–46
- Takahashi M, Ogawa J, Kinoshita Y, et al. Experimental study of paraplegia caused by spinal tumors: an animal model of spinal tumors created by transplantation of VX2 carcinoma. *Spine J* 2004;4:675–80
- Ushio Y, Posner R, Kim JH, et al. Treatment of experimental spinal cord compression caused by extradural neoplasms. *J Neurosurg* 1977;47:380–90
- Arguella F, Baggs RB, Duerst RE, et al. Pathogenesis of vertebral metastasis and epidural spinal cord compression. *Cancer* 1990;65:98–106
- Yamada K, Terai H, Matsumoto T, et al. Effect of spinal fixation in rabbits with metastatic tumor using a novel spinal fusion model. *J Spinal Disord Tech* 2012 Jul 19. [Epub ahead of print]
- Sciubba DM, Burdette EC, Cheng JJ, et al. Percutaneous computed tomography fluoroscopy-guided conformal ultrasonic ablation of vertebral tumors in a rabbit tumor model. Laboratory investigation. *J Neurosurg Spine* 2010;13:773–79
- Aebli N, Goss BG, Thorpe P, et al. In vivo temperature profile of intervertebral discs and vertebral endplates during vertebroplasty: an experimental study in sheep. *Spine (Phila Pa 1976)* 2006;31:1674–78; discussion 1679
- Peller PJ. Role of positron emission tomography/computed tomography in bone malignancies. *Radiol Clin North Am* 2013;51:845–64
- Knipe MF. Principles of neurological imaging of exotic animal species. *Vet Clin North Am Exot Anim Pract* 2007;10:893–907, vii

Degeneration and Plasticity of the Optic Pathway in Alström Syndrome

R. Manara, V. Citton, P. Maffei, J.D. Marshall, J.K. Naggert, G. Milan, R. Vettor, A. Baglione, A. Vitale, C. Briani, F. Di Salle, and A. Favaro



ABSTRACT

BACKGROUND AND PURPOSE: Alström syndrome is a rare inherited ciliopathy in which early progressive cone-rod dystrophy leads to childhood blindness. We investigated functional and structural changes of the optic pathway in Alström syndrome by using MR imaging to provide insight into the underlying pathogenic mechanisms.

MATERIALS AND METHODS: Eleven patients with genetically proved Alström syndrome (mean age, 23 years; range, 6–45 years; 5 females) and 19 age- and sex-matched controls underwent brain MR imaging. The study protocol included conventional sequences, resting-state functional MR imaging, and diffusion tensor imaging.

RESULTS: In patients with Alström syndrome, the evaluation of the occipital regions showed the following: 1) diffuse white matter volume decrease while gray matter volume decrease spared the occipital poles (voxel-based morphometry), 2) diffuse fractional anisotropy decrease and radial diffusivity increase while mean and axial diffusivities were normal (tract-based spatial statistics), and 3) reduced connectivity in the medial visual network strikingly sparing the occipital poles (independent component analysis). After we placed seeds in both occipital poles, the seed-based analysis revealed significantly increased connectivity in patients with Alström syndrome toward the left frontal operculum, inferior and middle frontal gyri, and the medial portion of both thalami (left seed) and toward the anterior portion of the left insula (right and left seeds).

CONCLUSIONS: The protean occipital brain changes in patients with Alström syndrome likely reflect the coexistence of diffuse primary myelin derangement, anterograde trans-synaptic degeneration, and complex cortical reorganization affecting the anterior and posterior visual cortex to different degrees.

ABBREVIATIONS: AS = Alström syndrome; MNI = Montreal Neurological Institute; TFCE = threshold-free cluster enhancement

Alström syndrome (AS) is a rare (<1:100,000) autosomal recessive monogenic ciliopathy with severe multisystem involvement. Besides childhood truncal obesity, type 2 diabetes, hypertriglyceridemia, cardiomyopathy, and progressive pulmo-

nary, hepatic, and renal dysfunction, patients with AS have cone-rod dystrophy presenting early in infancy and leading to complete blindness in the second decade. Unlike other ciliopathies (eg, Bardet-Biedl syndrome), patients with AS do not present with cognitive impairment.¹ However, a recent MR imaging study² showed that most patients with AS older than 30 years have brain atrophy, periventricular white matter abnormalities, or lacune-like lesions. Additionally, voxel-based morphometry revealed white and gray matter volume decreases more evident in the posterior regions, while diffusion tensor imaging showed diffuse supratentorial myelin abnormalities also involving regions that appeared normal at conventional imaging. The pathogenesis of these changes is not clear and might be due to genetically determined primary myelin derangement, progressive neurodegenerative processes, early profound sensorineural deprivation, or a combination of all these mechanisms. The impact of these changes on brain function has not yet been investigated. Studies on early blindness in subjects without Alström syndrome have shown that the (visual) occipital

Received May 28, 2014; accepted after revision July 4.

From the Department of Medicine and Surgery (R.M., A.V., F.D.S.), Neuroradiology, University of Salerno, Salerno, Italy; Department of Radiology (V.C.), Neuroradiology Unit, IRCCS San Camillo Hospital, Venezia, Italy; Department of Internal Medicine (P.M., G.M., R.V.), University Hospital of Padova, Padova, Italy; Jackson Laboratory (J.D.M., J.K.N.), Bar Harbor, Maine; and Department of Neurosciences (A.B., C.B., A.F.), University of Padua, Padova, Italy.

This research was supported by National Institutes of Health research grant 036878.

Please address correspondence to Valentina Citton, MD, Department of Radiology, Neuroradiology Unit, IRCCS San Camillo Hospital Venezia, Italy; e-mail: valentinacitton@gmail.com

Indicates open access to non-subscribers at www.ajnr.org

Indicates article with supplemental on-line photo.

Evidence-Based Medicine Level 2.

<http://dx.doi.org/10.3174/ajnr.A4115>

Epidemiologic, genetic, and clinical findings of patients with AS in the present study

No.	Genotype (Axon)	Vision		Hearing		Heart Ejection			Psychiatric Disorders
		Deficit ^a	Deficit ^b	Overweight ^c	Hypertension ^d	Fraction ^e	Dyslipidemia	DM2 ^f	
1	Heterozygosis 8 and 16	+	—	++	—	Normal	—	+	—
2	Heterozygosis 8 and 16	+	+	++	—	Normal	—	+	—
3	Heterozygosis 8 and un	+	+	+	—	Normal	—	+	—
4	Heterozygosis 8 and 10	+	+	+	—	Normal	—	+	—
5	Heterozygosis 8 and un	++	+	+	+	Normal	+	++	—
6	Heterozygosis 10 and 12	+	+	—	—	Normal	—	+	—
7	Heterozygosis 8 and 16	+	+	+	+	25% ^g	+	++	—
8	Heterozygosis 8 and 8	++	+	++	+	47%	—	++	Depression
9	Heterozygosis 8 and 8	++	+	+	—	Normal	+	+	Depression
10	Homozygosis 10 and 10	++	+	+	+	Normal	+	—	Anxiety, depression, bulimia ^h
11	Homozygosis 16 and un	++	+	+	+	Normal	+	—	Paranoid personality disorder ⁱ
12	Homozygosis 10	++	+	—	+	Normal	+	++	—

Note:—un indicates unknown mutation; DM2, diabetes mellitus type 2.

^a Vision Deficit: + indicates severe vision deficit (<1/20); ++, blindness.

^b Hearing Deficit: — indicates normal hearing; +, hearing deficit >20 dB.

^c Overweight: — indicates normal weight (body mass index, 18.5–25); +, overweight (body mass index, 25–30); ++, obesity (body mass index, >30).

^d Hypertension: — indicates normotensive; +, under antihypertensive treatment.

^e Heart Ejection Fraction: normal value, >55%.

^f DM2: ++ indicates diabetes mellitus type 2; +, insulin resistance or hyperinsulinemia or impaired glucose tolerance; —, no disorders in glucidic metabolism.

^g Dilated cardiomyopathy.

^h Under therapy with valproic acid, bromazepam, and olanzapine.

ⁱ Under therapy with valproic acid, quetiapine, risperidone, and paroxetine.

cortex remodulates its function and undergoes structural changes likely related to abnormal selective pruning of exuberant connections and/or sensory deprivation-dependent effects on normal cortex maturation.³ Recently, resting-state fMRI has proved to be a powerful tool for investigating functional connectivity, even in situations in which the task execution is difficult (eg, visual tasks in blind subjects). Resting-state fMRI might provide functional data complementary to the information obtained from the structural MR imaging-based analyses developed for the evaluation of white matter integrity (tract-based spatial statistics) and cortical development (sulcation, curvature, cortical thickness analyses).

This multimodality MR imaging study on a cohort of patients with AS aims to provide an integrated account of functional and structural changes of the regions devoted to the visual function in this rare disease and new insights into the pathogenic mechanisms leading to brain changes in early blindness.

MATERIALS AND METHODS

Participants

Eleven patients (mean age, 23 years; range, 6–45 years; 5 females) with Alström syndrome were recruited from our Department of Internal Medicine. All patients met the diagnostic criteria for AS based on genetic analysis and clinical observations¹ and had a normal intelligence quotient.

Nineteen age- and sex-matched unrelated healthy subjects or patients referred to neuroimaging for headache with no history of prematurity, head trauma, neurologic or psychiatric disease, and neurosurgery represented our control group (mean age, 23 years; range, 6–43; 10 females).

Two patients with AS and 1 control were left-handed according to the Edinburgh Handedness Inventory.⁴ The exclusion criteria were the presence of contraindications to MR imaging and age younger than 6 years to avoid sedation. Our University Hos-

pital Ethics Committee approved the study. Written informed consent was obtained from patients or their parents.

All subjects underwent a complete physical and neurologic examination including neurosensory analysis (retinopathy and hearing loss) and were investigated for cardiovascular risk factors (obesity, diabetes mellitus type 2, cardiomyopathy, and hyperlipidemia). Clinical findings are summarized in the Table.

MR Imaging Acquisition

MR images were obtained at 1.5T (Achieva; Philips Medical Systems, Best, the Netherlands) with a standard quadrature head coil.

The MR imaging study protocol included the following:

- 1) 3D T1-weighted imaging (TR/TE, 20/3.8 ms; flip angle, 20°; section thickness, 1 mm; acquired voxel size, 1 × 1 mm; reconstructed voxel size, 0.66 × 0.66 mm; acquisition matrix, 212 × 210; reconstructed matrix, 320 × 320; acquisition time, approximately 7 minutes);
- 2) Fluid-attenuated inversion-recovery (TR/TE/TI, 10,000/140/2800 ms; echo-train length, 53; flip-angle, 90°; section thickness, 5 mm; acquisition voxel, 0.90 × 1.15 mm; reconstructed voxel, 0.9 × 0.9 mm; acquisition time, 3 minutes 20 seconds);
- 3) Diffusion tensor images acquired with single-shot echo-planar diffusion-weighted imaging (TR/TE, 11,114/80 ms; acquisition matrix, 112 × 110; echo-train length, 59; reconstructed matrix, 128 × 128; acquisition voxel, 2 × 2 mm; reconstructed voxel, 1.75 × 1.75 × 2 mm; sensitivity encoding p reduction, 2; section-thickness, 2 mm without gap; NEX, 2; acquisition time, 12 minutes 24 seconds). The axial sections covered the whole brain including the cerebellum. The diffusion-sensitizing gradients were applied along 32 noncollinear gradient-encoding directions with maximum $b=800$ s/mm². One additional image without diffusion gradients ($b=0$ s/mm²) was also acquired.

4) Resting-state fMRI data with 250 continuous functional volumes (TR/TE, 2216/50 ms; flip angle, 90°; 21 axial sections; acquisition matrix, 96×96 ; reconstructed matrix, 128×128 ; acquisition voxel, 2.4×2.4 mm; reconstructed voxel, 1.8×1.8 mm; section thickness, 5.5 mm; gap between sections, 0.5 mm; acquisition time; 8 minutes 27 seconds). For the core dataset, subjects were instructed to remain still, stay awake, and keep their eyes open.

Image Processing

Data Processing of Volumetric Images. We used the optimized voxel-based morphometry protocol available in the statistical parametric mapping software (SPM8, www.fil.ion.ucl.ac.uk/spm/software/spm8).⁵ The protocol consisted of the following: A study-specific gray and white matter template was built from the 30 segmented native images affine-registered to the International Consortium for Brain Mapping-152 gray matter template. The native segmented images were then nonlinearly normalized onto this template, introducing a “modulation” for distortions due to the nonlinear component of the transformation by dividing each voxel of each registered gray matter volume image by the Jacobian of the warp field. The modulated normalized gray matter volume images were then smoothed with an isotropic Gaussian kernel with a σ of 3 mm.

For statistical analyses, we used a parametric *t* test as implemented by SPM8, by using age as a covariate of no interest. Results for gray matter were considered significant for $P < .05$, after correction for multiple comparisons by using an initial cluster-threshold at $P < .001$ uncorrected (minimum size = 20 voxels). Region-of-interest analyses for hippocampal regions were performed by using WFU-PickAtlas 3.0.3 (<http://fmri.wfubmc.edu/software/PickAtlas>), while contrasts were analyzed by using SPM8.⁶

Data Processing of DTI. The whole-brain DTI analysis method is reported in a previous publication.² We used probabilistic maps of the optic pathways in the Juelich histologic atlas (<http://neuro.debian.net/pkg/fsl-juelich-histological-atlas.html>), thresholded at 50% to create masks to be applied to the study-specific skeleton restricted to optic radiations. The threshold-free cluster enhancement (TFCE) approach was used to obtain the significant differences between the 2 groups at $P \leq .05$, after accounting for multiple comparisons by controlling for the family-wise error rate.

Data Processing of Functional Images. Resting-state scans were preprocessed by using both Analysis of Functional Neuro-Images (version AFNI_2010_10_19_1028; <http://afni.nimh.nih.gov/afni>) and fMRI of the Brain Software Library (FSL, Version 4.1.6; <http://www.fmrib.ox.ac.uk/fsl>). Preprocessing was performed as described in Biswal et al⁷ and Neuroimaging Informatics Tools and Resources Clearinghouse (www.nitrc.org/projects/fcon_1000). The first 5 volumes of every scan were discarded to remove possible stabilization effects. Preprocessing consisted of motion correction by using Fourier interpolation (volume registration by using least-squares alignment of 3 translational and 3 rotational parameters); spatial smoothing by using a 6-mm full width at half maximum Gaussian kernel; mean-based intensity normalization of all volumes; linear and quadratic detrending; and spatial normalization via estimation of a linear transforma-

tion from the individual functional space to Montreal Neurological Institute-152 (MNI152) standard brain space according to each individual’s high-resolution anatomic image. A high-pass-filter setting of 200 seconds (<0.005 Hz) was used to reduce very low-frequency artifacts such as scanner drift. During scanning acquisition, 2 patients with Alström syndrome and 1 control subject displayed a single brief movement of head displacement of >3 mm or 3° . Given the type of networks in which we were interested, we decided to remove the interested volumes (20–30 volumes) before preprocessing (these subjects were then excluded from independent component analysis, [http://en.pudn.com/downloads226/sourcecode/math/detail1062122_e] but not from dual regression analyses). No major scanner artifacts were detected.

Temporal-concatenation group independent component analysis was used in the whole group of patients and controls to generate group-level components of the dataset by MELODIC (FSL).⁸ Before statistical inference, the networks of interest (medial, lateral, and ventral visual networks) were identified on visual inspection and by comparison with available maps in the literature.⁹ The dual-regression approach was used to obtain a connectivity map for each of the 3 components and for each subject. The standardized maps obtained by dual regression were used to perform group comparisons and correlations with age, education, and hand lateralization as nuisance variable covariates of interest.

Nonparametric permutation testing (5000 permutations) was used for statistical analysis of spatial maps, by the TFCE method for multiple comparisons and thresholding at $P < .05$. To control for the effects of brain atrophy on functional connectivity, we used the segmented anatomic images of all subjects to obtain voxelwise probability maps of gray matter, for use as a nuisance variable in statistical analyses.^{10,11} Additionally, a seed-based analysis was performed. We selected 2 symmetric seeds in the occipital pole (MNI coordinates: MNI 9, -96, 9 and MNI -9, -96, 9). Regions of interest were drawn in the occipital pole (1 on the left and 1 on the right occipital pole) to unveil eventual connections with other regions of the brain.

To perform the seed-based analysis, we removed nuisance signals by multiple regression. Each individual’s 4D time-series was regressed on 9 predictors, consisting of white matter, CSF, the global signal, and 6 motion parameters (3 cardinal directions and rotational movement around 3 axes). The time-series of the nuisance signals were extracted by the following methods:

- Averaging all voxels in the brain (global signal) across the time-series
- Segmenting each individual’s high-resolution structural image, applying a threshold at 80% tissue type probability, and averaging all voxels within the thresholded mask (white matter and CSF) across each time-series and
- Using the residuals obtained from motion correction by the FMRIB Linear Image Registration Tool (<http://www.fmrib.ox.ac.uk/>).

Each participant’s residual 4D time-series was transformed into Montreal Neurological Institute space by a linear affine transformation implemented in FSL, and the time-series was extracted for each seed. Time-series were averaged across all voxels in the seed region of interest; then, for each participant, the correlations between the time-series of the seed region of interest and

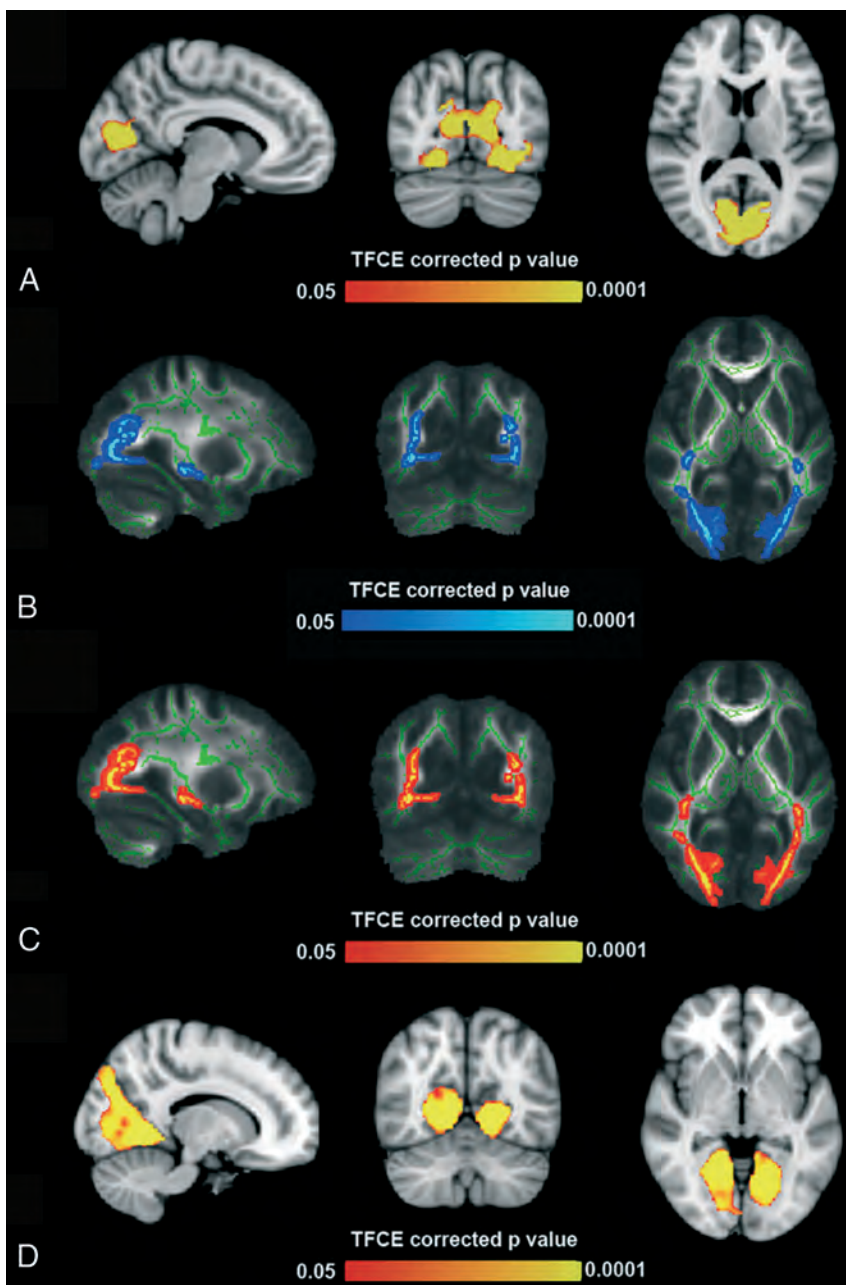


FIG 1. A, Gray matter voxel-based morphometry analysis: areas of significant difference (TFCE-corrected $P < .05$) between subjects with AS and healthy controls within the occipital pole (5386 voxels; peak, $-16, -68, 6$). Analysis was conducted with age as a covariate. B and C, Tract-based spatial statistics analysis: areas of significant difference (TFCE-corrected $P < .05$) between subjects with AS and healthy controls. Analyses were conducted with age as a covariate and showed diffuse decrease of fractional anisotropy (peaks, $33, -65, -2$ and $28, -60, -1$) and diffuse increase of radial diffusivity (peaks, $31, -65, 11$ and $-25, -68, 0$). D, Resting-state fMRI analysis: areas of significant differences (TFCE-corrected $P < .05$) between subjects with AS and healthy controls within the medial visual networks (2189 voxels; peak, $21, -51, -3$). Analysis was conducted with age as a covariate.

of each voxel in the brain were determined. Last, correlation maps were converted to Z-value maps. The resulting standardized maps were then used to perform group comparisons and correlations by using age and hand lateralization as nuisance variables.

RESULTS

Conventional MR Imaging

Conventional MR imaging findings have been reported in a previous study on the same study group.² In particular, mild enlarge-

ment of the atria and the posterior horns of the lateral ventricles was observed in 3 patients bilaterally and in 1 patient on the left side. Images of the 3 patients older than 30 years with AS showed periventricular white matter hyperintensity also involving the optic radiations. None of images of the patients with AS showed signal abnormalities at the level of the lateral geniculate bodies.

Voxel-Based Morphometry of the Occipital Regions

Patients with AS showed significantly lower gray and white matter volume compared with controls in the occipital region (Fig 1A and On-line Fig 1). The analysis revealed the symmetric decrease of gray matter, more evident in the anterior part of the calcarine cortex and the fusiform gyri, with relative sparing of the occipital poles.

On the other hand, the decrease of white matter involved the optic radiation entirely, including the most posterior portion.

DTI Analysis of the Occipital Regions

Tract-based spatial statistics analysis showed significant reduction of fractional anisotropy and increased radial diffusivity in the optic radiations of patients with AS compared with controls (Fig 1B, -C). Axial diffusivity and mean diffusivity analysis did not reveal any differences between patients with AS and controls.

Resting-State fMRI: The Visual Networks

All the resting-state functional networks were detected in both patients and controls. After including gray matter probability maps as a nuisance variable to control for brain atrophy, among the visual networks (medial, lateral, and ventral), we found reduced connectivity in patients with AS in the medial visual network (2189 voxels; peak, $21, -54, -3$) and in the lateral visual network (53 voxels; peak, $33, -87, 18$). The large cluster of reduced connectivity in the medial visual network

involved the anterior portion of the calcarine region with sparing of the occipital poles (Fig 1D). If we set a seed in each occipital pole (On-line Fig 2A), the seed-based analysis revealed significantly increased connectivity in patients with AS toward a small region in the anterior portion of the left insula (right seed, On-line Fig 2B) and toward large cortical regions of the left anterior insula, frontal operculum, inferior and middle frontal gyri, and with the medial portion of both thalami (left seed, On-line Fig 2C).

DISCUSSION

This multimodality MR imaging study of patients with Alström syndrome disclosed a diffuse occipital ultrastructural white matter derangement and atrophy and an inhomogeneous visual cortex involvement that spared the occipital pole in terms of both atrophy and connectivity. These findings are relatively unexpected in a condition in which the main mechanism of blindness resides in a precocious cone-rod dystrophy,¹² which should affect primarily the retinal neurons projecting to the occipital poles. Among the several pathogenic mechanisms that might affect the optic pathway in AS, the following may play a role in determining the observed parenchymal structural and functional changes: 1) anterograde trans-synaptic degeneration following cone-rod dystrophy, 2) primary myelin derangement, 3) neural occipital reorganization due to chronic visual deafferentation.

Anterograde Trans-Synaptic Degeneration

Neural injury might induce axonal degeneration in the direction of its terminal (anterograde degeneration) and toward the cell body (retrograde degeneration). In addition, neural injury might also lead to trans-synaptic degeneration of neurons that are downstream or upstream connected with the injured neuron.¹³

Trans-synaptic degeneration of the visual pathway has been well-documented in pathologic studies. Cellular death of the lateral geniculate bodies has been observed in patients with lesions occurring from the retina to the optic tract (eg, eye enucleation).¹⁴ Trans-synaptic degeneration may also occur in a retrograde fashion because lesions of the optic radiation or calcarine cortex might cause degeneration of retinal ganglion cells.¹⁵ Retinal thinning at the optical coherence tomograph¹⁶ and optic tract atrophy at MR imaging have been demonstrated following acquired unilateral occipital damage in humans.¹⁷ Lesions along the optic pathway can lead to lateral geniculate body T2 hyperintensity,¹⁷ and optic radiation abnormalities have been documented in patients affected with glaucoma by DTI.¹⁸ In these cases, a decreased fractional anisotropy concomitant to increased radial diffusivity and mean diffusivity was consistent with axonal loss due to retrograde trans-synaptic degeneration of the lateral geniculate bodies. In patients with AS, the lateral geniculate bodies did not present with signal abnormalities on conventional imaging. Furthermore, the pattern of DTI changes observed in the optic radiation of patients with AS was not consistent with axonal loss because the mean diffusivity and the first eigenvalue were not significantly increased.

Primary Myelin Derangement

Previously, whole-brain tract-based spatial statistics analysis showed that patients with AS present with diffuse myelin derangement characterized by decreased fractional anisotropy and increased radial diffusivity.² The same pattern was detected in the occipital white matter including the optic radiation. This DTI pattern has been reported in other diseases characterized mostly by myelin derangement such as relapsing-remitting multiple sclerosis and in animal models of dysmyelination. Primary myelin issues have already been reported in both the central and peripheral nervous system of patients with AS. The primary cilia of Schwann cells seem to be the regulators of their hedgehog signal-

ing-mediated myelination,¹⁹ while genetic studies have shown that sonic hedgehog signaling at the level of primary cilia is essential for patterning the embryonic stem cells into oligodendrocytes. Delamination of the myelin sheaths was detected by transmission electron microscopy at the level of the gingiva in AS.²⁰ Notably, by voxel-based morphometry and functional analyses, only the anterior part of the calcarine cortex presented with significant volume and functional impairment. On the contrary, the occipital poles did not present with significant atrophy, suggesting that the diffuse myelin derangement does not lead to uniform structural and functional cortical changes.

Neural Occipital Reorganization due to Chronic Visual Deafferentation

The most striking finding in this study was the preserved connectivity and gray matter volume of the occipital pole despite its role in the foveal binocular vision, while the remaining calcarine cortex showed both atrophy and impaired connectivity.

Most intriguing, the functional connectivity between the posterior occipital poles and the inferior frontal triangular areas (part of Brodmann Areas 44, 45, 47) was increased in patients with AS compared with controls. The inferior frontal triangular area is classically considered as a motor speech-production area and is involved in action understanding and imitation.²¹ In blind individuals, the occipital visual and frontal language areas are simultaneously activated when performing a Braille-reading task.²² In patients with AS, the early degeneration of the retinal cones, projecting to the occipital poles, might reduce the visual input before the stage of synaptic revision (which occurs during the first 8 months of postnatal life and is critically dependent on the activity of visual afferent inputs),²³ likely redirecting the process of connectivity maturation. The subsequent degeneration of the rods might occur at a stage of decreased cortical plasticity, leading to atrophy and reduction of connectivity. In patients with AS, the timing of retinal degeneration might therefore influence differently the stimuli-driven development of the tuning visual cortex.²⁴

CONCLUSIONS

Several pathogenic mechanisms such as anterograde trans-synaptic degeneration, primary myelin derangement, and differential cortical reorganization seem to contribute to the optic pathway derangement in AS. Increased understanding of these mechanisms might help identify targeted therapies aimed at slowing or reversing the neurodegenerative phenomena that are part of Alström syndrome.

Disclosures: Renzo Manara—UNRELATED: Payment for Lectures (including service on Speakers Bureaus); BioMarin, Comments: symposium on mucopolysaccharidosis type 6 at a congress. Jan D. Marshall—RELATED: Grant: National Institutes of Health 036878,* Comments: supports all work on Alström Syndrome. Jürgen K. Naggert—RELATED: Grant: National Institutes of Health*; Consulting Fee or Honorarium: National Institutes of Health (grant review); Support for Travel to Meetings for the Study or Other Purposes: National Institutes of Health (grant review); UNRELATED: Grants/Grants Pending: National Institutes of Health,* Comments: DK085441. *Money paid to the institution.

REFERENCES

1. Marshall JD, Beck S, Maffei P, et al. Alström syndrome. *Eur J Hum Genet* 2007;15:1193–202

2. Citton V, Favaro A, Bettini V, et al. **Brain involvement in Alström syndrome.** *Orphanet J Rare Dis* 2013;8:24
3. Anurova I, Renier LA, De Volder AG, et al. **Relationship between cortical thickness and functional activation in the early blind.** *Cereb Cortex* 2014 Feb 10. [Epub ahead of print]
4. Oldfield RC. **The assessment and analysis of handedness: the Edinburgh inventory.** *Neuropsychologia* 1971;9:97–113
5. Ashburner J, Friston KJ. **Voxel-based morphometry: the methods.** *Neuroimage* 2000;11:805–21
6. Maldjian JA, Laurienti PJ, Kraft RA, et al. **An automated method for neuroanatomic and cytoarchitectonic atlas-based interrogation of fMRI data sets.** *Neuroimage* 2003;19:1233–39
7. Biswal BB, Mennes M, Zuo XN, et al. **Toward discovery science of human brain function.** *Proc Natl Acad Sci U S A* 2010;107:4734–39
8. Zuo XN, Kelly C, Adelstein JS, et al. **Reliable intrinsic connectivity networks: test-retest evaluation using ICA and dual regression approach.** *Neuroimage* 2010;49:2163–77
9. Oakes TR, Fox AS, Johnstone T, et al. **Integrating VBM into the general linear model with voxelwise anatomical covariates.** *Neuroimage* 2007;34:500–08
10. Smith SM, Nichols TE. **Threshold-free cluster enhancement: addressing problems of smoothing, threshold dependence and localization in cluster inference.** *Neuroimage* 2009;44:83–98
11. Filippini N, Nickerson LD, Beckmann CF, et al. **Age-related adaptations of brain function during a memory task are also present at rest.** *Neuroimage* 2012;59:3821–28
12. Marshall JD, Maffei P, Collin GB, et al. **Alstrom syndrome: genetics and clinical overview.** *Cur Genomics* 2011;12:225–35
13. Saxena S, Caroni P. **Mechanisms of axon degeneration: from development to disease.** *Prog Neurobiol* 2007;83:174–91
14. Beatty RM, Sadun AA, Smith L, et al. **Direct demonstration of trans-synaptic degeneration in the human visual system: a comparison of retrograde and anterograde changes.** *J Neurol Neurosurg Psychiatry* 1982;45:143–46
15. Bridge H, Jindahra P, Barbur J, et al. **Imaging reveals optic tract degeneration in hemianopia.** *Invest Ophthalmol Vis Sci* 2011;52:382–88
16. Cowey A, Alexander I, Stoerig P. **Transneuronal retrograde degeneration of retinal ganglion cells and optic tract in hemianopic monkeys and humans.** *Brain* 2011;134:2149–57
17. Uggetti C, Egitto MG, Fazzi E, et al. **Trans-synaptic degeneration of lateral geniculate bodies in blind children: in vivo MR demonstration.** *AJNR Am J Neuroradiol* 1997;18:233–38
18. Song SK, Sun SW, Ramsbottom MJ, et al. **Dysmyelination revealed through MRI as increased radial (but unchanged axial) diffusion of water.** *Neuroimage* 2002;17:1429–36
19. Ruat M, Roudaut H, Ferent J, et al. **Hedgehog trafficking, cilia and brain functions.** *Differentiation* 2012;83:S97–104
20. Yoshimura K, Takeda S. **Hedgehog signaling regulates myelination in the peripheral nervous system through primary cilia.** *Differentiation* 2012;83:S78–85
21. Nishitani N, Schürmann M, Amunts K, et al. **Broca's region: from action to language.** *Physiology (Bethesda)* 2005;20:60–69
22. Burton H, Snyder AZ, Conturo TE, et al. **Adaptive changes in early and late blind: a fMRI study of Braille reading.** *J Neurophysiol* 2002;87:589–607
23. Bienenstock EL, Cooper LN, Munro PW. **Theory for the development of neuron selectivity: orientation specificity and binocular interaction in visual cortex.** *J Neurosci* 1982;2:32–48
24. Lewis TL, Maurer D. **Multiple sensitive periods in human visual development: evidence from visually deprived children.** *Dev Psychobiol* 2005;46:163–83

MRI Texture Analysis Predicts p53 Status in Head and Neck Squamous Cell Carcinoma

M. Dang, J.T. Lysack, T. Wu, T.W. Matthews, S.P. Chandarana, N.T. Brockton, P. Bose, G. Bansal, H. Cheng, J.R. Mitchell, and J.C. Dort



ABSTRACT

BACKGROUND AND PURPOSE: Head and neck cancer is common, and understanding the prognosis is an important part of patient management. In addition to the Tumor, Node, Metastasis staging system, tumor biomarkers are becoming more useful in understanding prognosis and directing treatment. We assessed whether MR imaging texture analysis would correctly classify oropharyngeal squamous cell carcinoma according to p53 status.

MATERIALS AND METHODS: A cohort of 16 patients with oropharyngeal squamous cell carcinoma was prospectively evaluated by using standard clinical, histopathologic, and imaging techniques. Tumors were stained for p53 and scored by an anatomic pathologist. Regions of interest on MR imaging were selected by a neuroradiologist and then analyzed by using our 2D fast time-frequency transform tool. The quantified textures were assessed by using the subset-size forward-selection algorithm in the Waikato Environment for Knowledge Analysis. Features found to be significant were used to create a statistical model to predict p53 status. The model was tested by using a Bayesian network classifier with 10-fold stratified cross-validation.

RESULTS: Feature selection identified 7 significant texture variables that were used in a predictive model. The resulting model predicted p53 status with 81.3% accuracy ($P < .05$). Cross-validation showed a moderate level of agreement ($\kappa = 0.625$).

CONCLUSIONS: This study shows that MR imaging texture analysis correctly predicts p53 status in oropharyngeal squamous cell carcinoma with ~80% accuracy. As our knowledge of and dependence on tumor biomarkers expand, MR imaging texture analysis warrants further study in oropharyngeal squamous cell carcinoma and other head and neck tumors.

ABBREVIATIONS: HNSCC = head and neck squamous cell carcinoma; FTFT-2D = 2D fast time-frequency transform tool; Post-Gad T1WI = T1WI with gadolinium; ST = Stockwell transform; TP53 = mutation in the gene encoding the p53 protein; Weka = Waikato Environment for Knowledge Analysis

Head and neck cancer is the sixth most common cancer worldwide,¹ with squamous cell carcinoma accounting for approximately 90% of all cases. Most head and neck squamous cell carcinoma (HNSCC) occurs in the oral cavity, oropharynx, and larynx. Alcohol and tobacco consumption and prior infection with human papillomavirus are the major risk factors associated with the development of head and neck squamous cell carcinoma.

Oropharyngeal squamous cell carcinoma is of particular interest because its incidence is increasing, particularly among younger, nonsmoking patients.²

Accurate staging of HNSCC is essential for treatment planning and prognostication, and a standard tool used for staging is the American Joint Committee on Cancer Tumor, Node, Metastasis staging system, currently in its seventh revision.³ As we learn more about tumor biology, however, it is clear that this staging system does not fully predict clinical behavior and prognosis. Our knowledge of head and neck cancer pathogenesis has rapidly increased, and better understanding of molecular mechanisms holds the promise of discovering predictive and prognostic biomarkers that might be helpful in the management of HNSCC.⁴ The tumor suppressor p53 plays an important role in conserving genomic stability.⁵ p53 facilitates DNA repair by regulating the cell cycle and has a role in preventing cancer emergence.^{6,7} Mutations in the gene encoding the p53 protein, *TP53*, occur in almost 50% of all cancers.^{8,9} In most of HNSCC, mutation and inactivation of p53 is an essential and early event in neoplastic

Received March 16, 2014; accepted after revision June 15.

From the Section of Otolaryngology–Head and Neck Surgery (T.W.M., S.P.C., P.B., J.C.D.) and Department of Radiology (M.D., J.T.L.), University of Calgary, Calgary, Alberta, Canada; Department of Radiology (H.C., J.R.M.), Mayo Clinic College of Medicine, Scottsdale, Arizona; Department of Population Health Research (N.T.B.), Alberta Health Services, Calgary, Alberta, Canada; and School of Computing, Informatics, Decision Systems Engineering (G.B., T.W.), Arizona State University, Tempe, Arizona.

Drs Mitchell and Dort are co-senior authors on this project.

Please address correspondence to Joseph C. Dort, MD, Section of Otolaryngology–Head and Neck Surgery, University of Calgary, HRIC 2A02, 3280 Hospital Dr NW, Calgary, Alberta, Canada, T2N 4Z6; e-mail: jdort@ucalgary.ca

Indicates open access to non-subscribers at www.ajnr.org

<http://dx.doi.org/10.3174/ajnr.A4110>

transformation, and *TP53* mutations are associated with poor prognosis in HNSCC.¹⁰⁻¹² A landmark prospective study classified *TP53* gene mutations on the basis of their effect on p53 protein structure.¹³ Broadly, disruptive mutations disturb the formation of p53-DNA complexes, while nondisruptive mutations have little effect on the association between p53 and DNA. The study reported a significant association between the presence of *TP53* disruptive mutations and worse overall survival in surgically treated HNSCC compared with both nondisruptive *TP53* mutations and wild-type *TP53*.¹³ A recent study has also implicated disruptive mutations in *TP53* leading to radiation-treatment failure.¹⁴

Medical imaging plays a critical role in the assessment of many head and neck tumors, and both CT and MR imaging have important roles in the anatomic evaluation of HNSCC.¹⁵⁻¹⁸ In addition to anatomic details, the analysis of MR images provides additional metabolic and biologic information in tumors.¹⁹ Mathematic techniques that quantify image characteristics have been applied to a vast array of pathologies, from multiple sclerosis,²⁰ attention deficit/hyperactivity disorder,²¹ and Alzheimer disease²² to breast cancer,²³ cervical cancer,²⁴ and brain tumors.²⁵ Studies in glioblastoma have shown that there is a correlation between the methylation of O6-methylguanine-DNA methyltransferase and MR imaging features.²⁶ Levner et al²⁷ extracted texture features from MR images by using spatial frequency analysis and the Stockwell transform (ST) representation²⁸ and fed these characteristics into a neural network to predict the methylation status with an average accuracy of 87.7%.²⁷ Brown et al²⁵ also extracted ST texture features from brain MR images to find that codeletion of chromosomes 1p and 19q, a marker of good prognosis in oligodendroglioma brain cancer, could be predicted with 94% accuracy. These studies suggest that differences in tumor-tissue composition react with MR imaging signals differently, thus affecting texture features.

Yu et al²⁹ looked at differentiating tissues by using texture characterization on FDG-PET/CT images in head and neck cancers. We explored the use of ST texture features on MR images with a machine-learning technique to objectively differentiate head and neck tumors by p53 status. We hypothesized that MR image analysis could successfully discriminate p53-positive and -negative tumors.

MATERIALS AND METHODS

Patients

This prospective study was approved by the University of Calgary Conjoint Health Research Ethics Board. Patients older than 18 years of age with biopsy-proved HNSCC of the oropharynx or hypopharynx presenting to the University of Calgary Head and Neck Tumor Clinic between October 2010 and September 2011 were eligible for inclusion. Patients were excluded under the following conditions: 1) They had already been treated for the index cancer, 2) were undergoing palliative treatment only, 3) had already been treated for another head and neck primary cancer, or 4) had a tumor with a greatest axial extent of <2 cm. The last criterion ensured that the lesions were large enough for accurate MR imaging texture analysis. Twenty-one patients were eligible for inclusion in the study; however, in 1 patient, p53 immunohistochemistry was not performed and another 4 patients did not have MR imaging performed before treatment. Therefore, the fi-

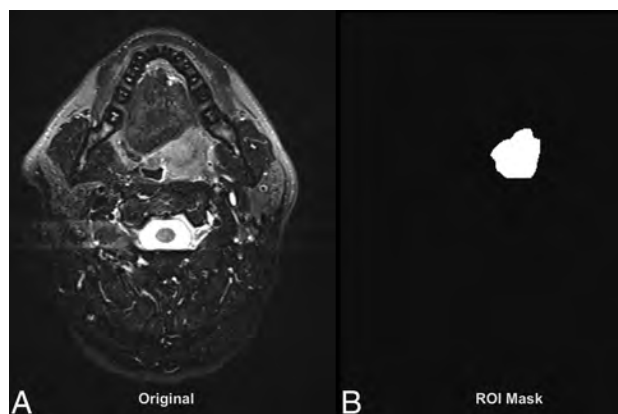


FIG 1. Sample of the FTFT-2D input data for texture analysis. A, Original DICOM MR image (T2WI). B, Region-of-interest mask of the tumor.

nal study cohort included 16 patients. Patient image data were anonymized by using DICOM Anonymizer Pro (<http://www.neologica.it/eng/DICOMAnonymPro.php>).³⁰

Interventions

All subjects underwent a standard pretreatment work-up that included a complete clinical head and neck examination, fiberoptic endoscopy, contrast-enhanced CT, MR imaging, and an examination under anesthesia with appropriate biopsies. No additional procedures or interventions were imposed on the subjects, and no delays in treatment resulted from their participation in this study.

Histopathology and p53 Immunohistochemistry

Tumor biopsies or surgically resected specimens or both were reviewed by an anatomic pathologist by using hematoxylin-eosin light microscopy. Immunohistochemistry staining for p53 was performed in 20 of 21 specimens, our standard protocol for oropharyngeal and hypopharyngeal cancers. The intensity of immunohistochemistry staining was graded by the pathologist by using a 4-category scoring system ranging from 0 for no visible stain to 3+ for diffusely positive staining. According to standard practice, cases that were graded as 3+ were considered positive for p53.

Imaging

Imaging focused on the oropharynx and hypopharynx was performed on MR imaging systems operating at 1.5T with 3-mm sections and 1-mm in-plane resolution. Standard clinical MR images were used, including the following that were subsequently used for texture analysis: axial fast spin-echo T2-weighted imaging with fat saturation, axial fast spin-echo T1WI with gadolinium (Post-Gad T1WI), and axial diffusion-weighted imaging with an apparent diffusion coefficient map.

Image Processing and Texture Analysis

Each patient's MR images were analyzed by an experienced neuroradiologist (J.T.L.), who then outlined the tumor region of interest by using OsiriX Imaging Software (<http://www.osirix-viewer.com>). Both OsiriX and DICOM Anonymizer Pro were run on an iMac 3.2-GHz Intel Core i7, Mac OS X Snow Leopard (Apple, Cupertino, California). We then used OsiriX to create masks

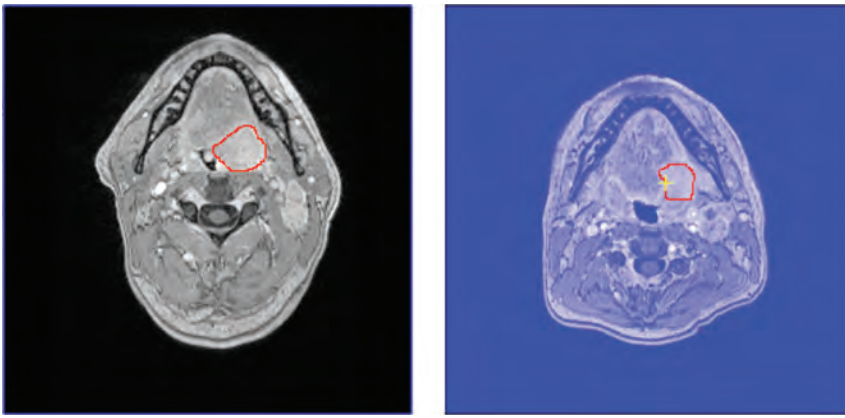


FIG 2. Tumors outlined on source MR images (Post-Gad T1WI) of 256×256 image size. The tumor in the left image is p53-negative. The tumor in the right image is p53-positive.

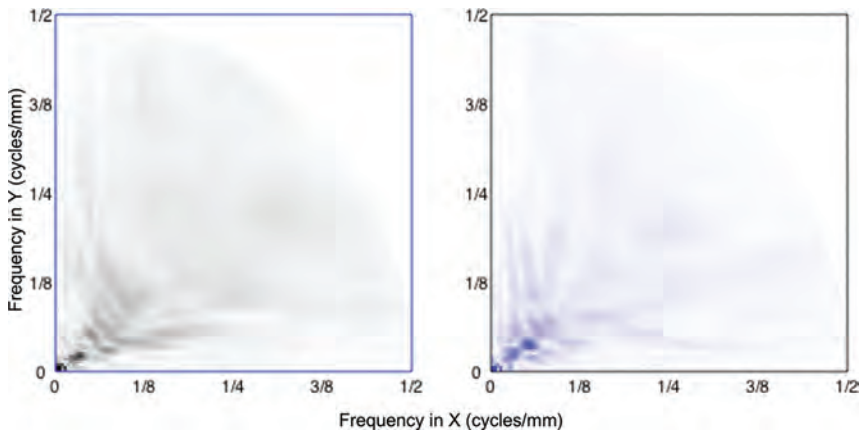


FIG 3. Graphic display of the average local spectrum for a p53-negative tumor (left image, black shades) and for a p53-positive tumor (right image, blue shades). The average amplitudes of ST at individual pixels were obtained by using FTFT-2D by using the same intensity range and scale for the 2 plots. Darker shades indicate higher ST amplitudes.

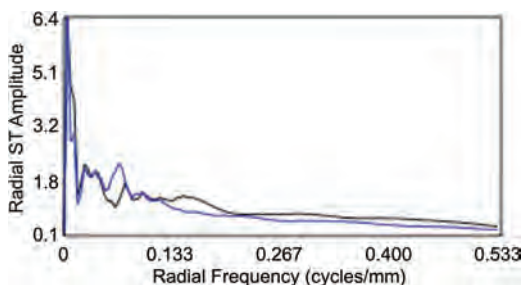


FIG 4. Radial ST amplitude plots for a p53-negative (black line) tumor and a p53-positive (blue line) tumor (the same tumor as in Fig 3).

of the tumor outlines (Fig 1). The masks and MR images of all cases were then fed into the 2D fast time-frequency transform tool (FTFT-2D) (Medical Imaging Informatics; Mayo Clinic, Scottsdale, Arizona), which processes the Stockwell transform of local spectra for a 2D image and its statistics and quantifies the texture features.³¹ This tool requires an input of the mask and its respective original MR image in DICOM file format. The images need to be $\leq 512 \times 512$ pixels. The pixels inside and outside the region of interest were set to 65,535 and 0, respectively, and were exported as a DICOM file. The FOV and matrix size of the

scans were preprocessed to 240 mm and 256×256 pixels, respectively, with a trilinear interpolation algorithm by using MeVisLab (MeVis Medical Solutions, Bremen, Germany).

To illustrate the quantified texture analysis procedure by using the FTFT-2D tool, we present a comparison of 2 HNSCC cases; 1 p53-negative and the other p53-positive (Fig 2). The corresponding local spectrum and radial ST amplitude plots are seen in Figs 3 and 4, respectively. The radial frequencies, 0.067–0.533 cycles/mm, were divided into 12 bands from the output of FTFT-2D. We used 3 texture values: the average, SD, and maximum values of the local spectrum. One hundred eight tumor MR imaging features were used for texture analysis (3 MR images \times 12 frequency bands \times 3 texture values). These tumor characteristics were fed into Waikato Environment for Knowledge Analysis (Weka, <http://www.cs.waikato.ac.nz/ml/weka/packageMetaData/>), a tool with a collection of machine-learning algorithms for data preprocessing, classification, and visualization.³² The dataset dimension reduction was performed by using the subset-size forward-selection algorithm in Weka. This algorithm is a commonly used feature-selection method³³ to identify useful features. It starts with empty feature subsets and adds 1 subset of features at each step until the model prediction result does not improve any further.

By doing so, important features are selected while redundant features are eliminated. The Bayesian network classifier³⁴ was then used with the 10-fold stratified cross-validation in Weka to assess how well this predictive model would perform with the subset of the features being selected. The Bayesian network is a graphic model that learns the conditional probabilities among the features and applies the Bayes rule to calculate the posterior class probability for classification. Because the Bayesian network models the dependencies among all the features, it has proved to be effective in handling missing values in the dataset.^{35,36} Bayesian statistical methods can smooth the model so that all available data can be used for training; thus, this process efficiently addresses the overfitting issue.^{35,36}

RESULTS

Of the 16 eligible patients with evaluable data, 8 tumors were p53-positive and 8 were p53-negative. The 2 groups (p53+ and p53-) had similar clinical characteristics (Table 1).

After the texture quantification and machine-learning process, we found that 15 of the 108 independent variables were the most significant on the basis of the selected attributes by using the subset-size forward-selection algorithm. The 15 independent vari-

Table 1: Clinical characteristics^a

Characteristic	p53-Positive	p53-Negative
Female	1	1
Male	7	7
Age (yr) (mean)	56 ± 13	56 ± 11
T2	1	3
T3	2	1
T4	5	4
N1	1	1
N2	7	7

^a All *P* values are not significant.

Table 2: Discriminatory texture features

Texture Attribute	MRI Sequence	Radial Frequency Band (cycles/mm)
Average value of the local spectrum	ADC map	0.189–0.231
		0.269–0.307
		0.307–0.344
		0.344–0.382
SD of the local spectrum	Post-Gad T1WI	0.382–0.420
		0.307–0.344
	ADC map	0.496–0.533
		0.420–0.458
Maximum value of the local spectrum	ADC map	0.458–0.496
		0.496–0.533
	Post-Gad T1WI	0.231–0.269
		T2WI

Note:—SD indicates standard deviation.

Table 3: BN classification of p53 status

	TP Rate	FP Rate	Precision	Recall	F-Measure	ROC Area
p53-Positive	0.625	0.375	0.625	0.625	0.625	0.680
p53-Negative	0.625	0.375	0.625	0.625	0.625	0.680
Weighted average	0.625	0.375	0.625	0.625	0.625	0.680

Note:—BN indicates Bayesian network; FP, false-positive; TP, true-positive; ROC, receiver operating characteristic.

Table 4: Discriminatory texture features

Texture Attribute	MRI Sequence	Radial Frequency Band (cycles/mm)
Average value of the local spectrum	ADC map	0.269–0.307
SD of the local spectrum	Post-Gad T1WI	0.458–0.496
		0.496–0.533
Maximum value of the local spectrum	ADC map	0.269–0.307
	Post-Gad T1WI	0.382–0.420
	T2WI	0.496–0.533

ables had classification scores ranging from 10% to 40%. Classification analysis was done on these 15 independent variables (Table 2); 62.5% of the instances were classified correctly (Table 3).

Further isolation of the high-classification percentage variables (removing the variables with a classification score of only 10%) yielded 7 significant variables (Table 4). These 7 variables correctly classified 81.3% of the tumors (Table 5). The agreement between predicted and true class (κ statistic) was 0.625 (where 0 indicates no agreement and 1 indicates complete agreement).

Table 5: BN classification results

	TP Rate	FP Rate	Precision	Recall	F-Measure	ROC Area	p53 Status
p53-Positive	0.875	0.250	0.778	0.875	0.824	0.742	Positive
p53-Negative	0.750	0.125	0.857	0.750	0.800	0.742	Negative
Weighted average	0.813	0.188	0.817	0.813	0.812	0.742	

Note:—BN indicates Bayesian network; FP, false-positive; ROC, receiver operating characteristic; TP, true-positive.

DISCUSSION

We found that MR imaging texture features could significantly ($P < .05$) differentiate HNSCC tumors by p53 status by using 7 discriminatory radial-frequency bands with 81.3% accuracy. In comparison, a recent study of p53-status detection in gliomas by using MR imaging texture analysis showed an accuracy of 65.2%.³⁷ Another recent study showed that MR imaging texture analysis could discriminate benign and malignant parotid tumors with an accuracy of up to 84.5%.³⁸ An earlier study of methylation-status prediction in glioblastoma yielded accuracies of up to 93.2%.²⁷ Other studies have shown that normal liver tissue could be differentiated from focal liver lesions with accuracies up to 88%³⁹ and that normal bladder wall could be differentiated from bladder cancer with an accuracy of 87.0%.⁴⁰

We found that texture features of the Post-Gad T1WI, T2WI, and ADC map were influential in the analysis. A possible physiologic explanation for this finding is the differences in vascularity between p53-positive and p53-negative tumors. Studies have shown a significantly higher microvessel count in p53-positive tumors than in p53-negative tumors,⁴¹ which has been associated with greater expression of vascular endothelial growth factor in p53-positive tumors.^{42,43} Differences in microvasculature would be expected to lead to differences in signal on Post-Gad T1WI (because of differences in contrast enhancement), on T2WI (because of differences in water content), and on the ADC map (because of differences in diffusivity).

At present, the clinical relevance of p53 status in HNSCC is mainly with regard to prognosis because a significant association between p53 status and survival in patients with HNSCC has been reported.¹³ In the future, p53 status in HNSCC may play a greater role in treatment selection (eg, specific vascular endothelial growth factor inhibitors may be more or less effective depending on the p53 status).

Image analysis has the potential to be complementary to tissue biopsy. On the one hand, tissue biopsy followed by immunohistochemistry analysis provides extensive genetic information, but only for a single anatomic location. On the other hand, image analysis provides biologic information such as p53 status over a large anatomic region, noninvasively. The ability to scan entire tumors, followed by quantitative analysis of image texture, may have advantages over more targeted biopsy-only techniques. Furthermore, MR imaging texture analysis has been shown to predict treatment response⁴⁴ and therefore has the potential to allow better treatment choices and potentially lead to improved patient outcomes.

Our study is limited by its small sample size, but our results indicate that image analysis is a promising tool that deserves further investigation in patients with head and neck cancer.

CONCLUSIONS

MR imaging texture analysis could differentiate p53-positive and p53-negative HNSCC tumors with 81.3% accuracy. In association with information from a tissue biopsy, this technique has the potential for better treatment choices and influencing patient outcomes.

Disclosures: Joseph C. Dort—RELATED: Support for Travel to Meetings for the Study or Other Purposes: Ohlson Research Initiative.* Comments: As executive director of the Ohlson Research Initiative, I receive some support to travel to academic meetings and other conferences. The Ohlson Research Initiative is a program embedded within the Southern Alberta Cancer Institute within the Faculty of Medicine at the University of Calgary. Funding from the Ohlson Research Initiative is administered through the University of Calgary. *Money paid to the institution.

REFERENCES

1. Parkin DM, Bray F, Ferlay J, et al. **Global cancer statistics, 2002.** *CA Cancer J Clin* 2005;55:74–108
2. Ang KK, Sturgis EM. **Human papillomavirus as a marker of the natural history and response to therapy of head and neck squamous cell carcinoma.** *Semin Radiat Oncol* 2012;22:128–42
3. American Joint Committee on Cancer. *Cancer Staging Handbook: From the AJCC Cancer Staging Manual.* Berlin: Springer-Verlag; 2010
4. Bauman JE, Michel LS, Chung CH. **New promising molecular targets in head and neck squamous cell carcinoma.** *Curr Opin Oncol* 2012;24:235–42
5. Lane DP. **Cancer: p53, guardian of the genome.** *Nature* 1992; 358:15–16
6. Levine AJ, Momand J, Finlay CA. **The p53 tumour suppressor gene.** *Nature* 1991;351:453–56
7. Levine AJ, Perry ME, Chang A, et al. **The 1993 Walter Hubert Lecture: the role of the p53 tumour-suppressor gene in tumorigenesis.** *Br J Cancer* 1994;69:409–16
8. Hollstein M, Sidransky D, Vogelstein B, et al. **p53 mutations in human cancers.** *Science* 1991;253:49–53
9. Vogelstein B. **Cancer: a deadly inheritance.** *Nature* 1990;348:681–82
10. Kozomara R, Jovic N, Magic Z, et al. **p53 mutations and human papillomavirus infection in oral squamous cell carcinomas: correlation with overall survival.** *J Craniomaxillofac Surg* 2005;33:342–48
11. Smith EM, Wang D, Rubenstein LM, et al. **Association between p53 and human papillomavirus in head and neck cancer survival.** *Cancer Epidemiol Biomarkers Prev* 2008;17:421–27
12. Soussi T, Bérout C. **Assessing TP53 status in human tumours to evaluate clinical outcome.** *Nat Rev Cancer* 2001;1:233–40
13. Poeta ML, Manola J, Goldwasser MA, et al. **TP53 mutations and survival in squamous-cell carcinoma of the head and neck.** *N Engl J Med* 2007;357:2552–61
14. Skinner HD, Sandulache VC, Ow TJ, et al. **TP53 disruptive mutations lead to head and neck cancer treatment failure through inhibition of radiation-induced senescence.** *Clin Cancer Res* 2012; 18:290–300
15. De Schepper AM, De Beuckeleer L, Vandevenne J, et al. **Magnetic resonance imaging of soft tissue tumors.** *Eur Radiol* 2000;10:213–23
16. Gielen JL, De Schepper AM, Vanhoenacker F, et al. **Accuracy of MRI in characterization of soft tissue tumors and tumor-like lesions: a prospective study in 548 patients.** *Eur Radiol* 2004;14:2320–30
17. Kransdorf MJ, Murphey MD. **Radiologic evaluation of soft-tissue masses: a current perspective.** *AJR Am J Roentgenol* 2000;175:575–87
18. Sundaram M, McGuire MH, Herbold DR. **Magnetic resonance imaging of soft tissue masses: an evaluation of fifty-three histologically proven tumors.** *Magn Reson Imaging* 1988;6:237–48
19. Mahmoud-Ghoneim D, Toussaint G, Constans JM, et al. **Three dimensional texture analysis in MRI: a preliminary evaluation in gliomas.** *Magn Reson Imaging* 2003;21:983–87
20. Zhang Y. **MRI texture analysis in multiple sclerosis.** *Int J Biomed Imaging* 2012;2012:762804
21. Chang CW, Ho CC, Chen JH. **ADHD classification by a texture analysis of anatomical brain MRI data.** *Front Syst Neurosci* 2012;6:66
22. Zhang J, Yu C, Jiang G, et al. **3D texture analysis on MRI images of Alzheimer's disease.** *Brain Imaging Behav* 2012;6:61–69
23. Weyn B, van de Wouwer G, van Daele A, et al. **Automated breast tumor diagnosis and grading based on wavelet chromatin texture description.** *Cytometry* 1998;33:32–40
24. Schilling T, Mirosław L, Glab G, et al. **Towards rapid cervical cancer diagnosis: automated detection and classification of pathologic cells in phase-contrast images.** *Int J Gynecol Cancer* 2007;17:118–26
25. Brown R, Zlatescu M, Sijben A, et al. **The use of magnetic resonance imaging to noninvasively detect genetic signatures in oligodendroglioma.** *Clin Cancer Res* 2008;14:2357–62
26. Eoli M, Menghi F, Bruzzone MG, et al. **Methylation of O6-methylguanine DNA methyltransferase and loss of heterozygosity on 19q and/or 17p are overlapping features of secondary glioblastomas with prolonged survival.** *Clin Cancer Res* 2007;13:2606–13
27. Levner I, Drabycz S, Roldan G, et al. **Predicting MGMT methylation status of glioblastomas from MRI texture.** *Med Image Comput Comput Assist Interv* 2009;12:522–30
28. Drabycz S, Stockwell RG, Mitchell JR. **Image texture characterization using the discrete orthonormal S-transform.** *J Digit Imaging* 2009;22:696–708
29. Yu H, Caldwell C, Mah K, et al. **Coregistered FDG PET/CT-based textural characterization of head and neck cancer for radiation treatment planning.** *IEEE Trans Med Imaging* 2009;28:374–83
30. Neologica. DICOM Anonymizer Pro. <http://www.neologica.it/eng/DICOMAnonymPro.php>. Accessed September 12, 2012
31. Cheng CH, Mitchell JR. **Fast Time-Frequency Transform in 2D (FTFT-2D).** *IET Signal Processing* 2014;8:360–72
32. Frank E, Hall M, Trigg L, et al. **Data mining in bioinformatics using Weka.** *Bioinformatics* 2004;20:2479–81
33. Gutlein M, Frank E, Hall M, et al. **Large-scale attribute selection using wrappers.** In: *Proceedings of IEEE Symposium on Computational Intelligence and Data Mining*, Nashville, Tennessee. March 30 to April 2, 2009. Washington: IEEE Computer Society; 2009:332–39
34. Cheng J, Greiner R. **Comparing Bayesian network classifiers.** In: *Proceedings of the Fifteenth Conference on Uncertainty in Artificial Intelligence*, Stockholm, Sweden. July 30–31, 1999:101–08
35. Heckerman D. **Bayesian networks for data mining.** *Data Mining and Knowledge Discovery* 1997;1:79–119
36. Hruschka ER Jr, Hruschka ER, Ebecken NF. **Bayesian networks for imputation in classification problems.** *Journal of Intelligent Information Systems* 2007;29:231–52
37. Liu C, Zhang H, Pan Y, et al. **Towards MIB-1 and p53 detection in glioma magnetic resonance image: a novel computational image analysis method.** *Phys Med Biol* 2012;57:8393–404
38. Fruehwald-Pallamar J, Czerny C, Holzer-Fruehwald L, et al. **Texture-based and diffusion-weighted discrimination of parotid gland lesions on MR images at 3.0 Tesla.** *NMR Biomed* 2013;26:1372–79
39. Mayerhoefer ME, Schima W, Trattnig S, et al. **Texture-based classification of focal liver lesions on MRI at 3.0 Tesla: a feasibility study in cysts and hemangiomas.** *J Magn Reson Imaging* 2010;32:352–59
40. Shi Z, Yang Z, Zhang G, et al. **Characterization of texture features of bladder carcinoma and the bladder wall on MRI: initial experience.** *Acad Radiol* 2013;20:930–38
41. Guo R, Li Q, Meng L, et al. **P53 and vascular endothelial growth factor expressions are two important indices for prognosis in gastric carcinoma.** *West Indian Med J* 2008;57:2–6
42. Riedel F, Götte K, Schwalb J, et al. **Vascular endothelial growth factor expression correlates with p53 mutation and angiogenesis in squamous cell carcinoma of the head and neck.** *Acta Otolaryngol* 2000;120:105–11
43. Uchida S, Shimada Y, Watanabe G, et al. **In oesophageal squamous cell carcinoma vascular endothelial growth factor is associated with p53 mutation, advanced stage and poor prognosis.** *Br J Cancer* 1998;77:1704–09
44. Ahmed A, Gibbs P, Pickles M, et al. **Texture analysis in assessment and prediction of chemotherapy response in breast cancer.** *J Magn Reson Imaging* 2013;38:89–101

Incomplete Endochondral Ossification of the Otic Capsule, A Variation in Children: Evaluation of Its Prevalence and Extent in Children with and without Sensorineural Hearing Loss

S.E. Sanverdi, B. Ozgen, A. Dolgun, and S. Sarac

ABSTRACT

BACKGROUND AND PURPOSE: Endochondral ossification of the otic capsule is a process that continues postnatally; hence, incomplete endochondral ossification is seen as pericochlear hypoattenuation on temporal bone CT scans of children. We determined the prevalence and extent of this entity in a large series and assessed its relation to age and underlying sensorineural hearing loss.

MATERIALS AND METHODS: Initially, temporal bone CTs of 40 children with sensorineural hearing loss were retrospectively assessed and compared with those of a control group scanned for non-sensorineural hearing loss reasons to assess any difference in the prevalence or extent of incomplete endochondral ossification. Then the CT scans of 510 children (age range, 17 days to 17 years) were retrospectively reviewed, and any observed endochondral ossification areas were classified as mild, moderate, or extensive, according to their extent.

RESULTS: Neither the presence nor degree of incomplete endochondral ossification had any significant correlation with the presence of sensorineural hearing loss ($P = .08$ and $P = .1$, respectively). Incomplete endochondral ossification was more frequently seen (62% of cases) than complete ossification. There was no statistically significant correlation between incomplete endochondral ossification and sex ($P = .8$), but an inverse correlation was found between the presence of incomplete endochondral ossification and increasing age ($P < .001$). Overall, mild incomplete endochondral ossification was the most frequent involvement pattern (44.4%).

CONCLUSIONS: The pericochlear hypoattenuation in the otic capsule representing incomplete endochondral ossification is a normal finding in children and can be seen as a marked curvilinear hypoattenuation at younger ages in the absence of any clinical disorder.

ABBREVIATIONS: FAF = fissula ante fenestram; iEO = incomplete endochondral ossification; OC = otic capsule; SNHL = sensorineural hearing loss

CT of the temporal bone is widely used for the evaluation of the anatomic details and diseases of the ear, in both adults and children.¹ The accurate interpretation of this study requires both a precise knowledge of the complex temporal bone anatomy and a familiarity with the imaging appearance of various pathologic processes involving this area. It is especially important to be aware of potential developmental variations mimicking disease, such as “pericochlear CT hypoattenuation.”²⁻⁵ This hypoattenuation, especially seen in children and most frequently in the region of the fissula ante fenestram (FAF), has been reported to occur in 32%–41% of imaged children without any accompanying symptoms.^{2,5}

The otic capsule (OC) hypoattenuated foci are presumed to be a normal variant due to an incomplete endochondral ossification (iEO) of the OC during its developmental process. Focal bony hypoattenuations in the OC are also seen in pathologic conditions such as otosclerosis and osteogenesis imperfecta, however. Otosclerosis, though rare in young children, is known to have hypoattenuation at this same FAF area as an early and relatively sensitive CT finding.⁶⁻¹¹ It is thus crucial for the radiologist reporting temporal bone cases to recognize this variation of a developmental stage and its extent, to prevent unnecessary medical or surgical treatment, especially in cases with equivocal clinical and audiometric findings.

Although a few studies have investigated the presence of OC hypoattenuated foci in temporal bone CT in children, their extent was not specified in any previous study. Furthermore, the relation of the OC hypoattenuation to underlying sensorineural hearing loss (SNHL) or a radiologically evident inner ear anomaly has not been thoroughly evaluated, to our knowledge. We thus aimed to determine the prevalence of this entity and its extent in a large group of children and to assess its relation to age and underlying SNHL.

Received August 23, 2012; accepted July 9, 2014.

From the Departments of Radiology (S.E.S., B.O.), Biostatistics (A.D.), and Otolaryngology (S.S.), Hacettepe University, School of Medicine, Ankara, Turkey.

Paper previously presented at: American Society of Neuroradiology Annual Meeting and the Foundation of the ASNR Symposium, April 21–26, 2012; New York, New York.

Please address correspondence to Burce Ozgen, MD, Hacettepe University, School of Medicine, Department of Radiology, 06100 Sıhhiye, Ankara, Turkey; e-mail: burce@hacettepe.edu.tr

<http://dx.doi.org/10.3174/ajnr.A4128>

MATERIALS AND METHODS

Patients

The study was performed in 2 phases. In the first part, the temporal bone CTs of patients with and without SNHL were compared to assess any difference in the prevalence of incomplete endochondral ossification in these 2 groups. For this purpose, temporal bone CT scans of 40 patients with SNHL and temporal bone CTs of age-compatible patients scanned for reasons other than SNHL were assessed with respect to the presence and extent of hypoattenuated foci of the OC. The images were retrieved from the PACS data base in a randomized manner. The indication for the scan in the control group included auricular atresia in 5 patients, middle ear infection in 18 patients, and conductive hearing loss in 17 patients. None of these patients had evidence of SNHL on their audiologic tests, and they did not have any inner ear abnormality on CT. The children scanned for conductive hearing loss had no clinical or audiologic findings suggestive of otosclerosis. The mean age for the patient group with SNHL was 4.9 ± 3.3 years (range, 17 days to 17 years), while for the control group the mean age was 8.1 ± 4.5 years (range, 10 months to 17 years).

For the second phase of the study, the CT scans of 1020 temporal bones of 510 children (younger than 18 years of age) archived the hospital and radiology data base system of our institution (hospital information system and radiology information system, respectively) between January 2005 and May 2014 were reviewed. The patient ages ranged from 17 days to 17 years (mean age, 5.2 ± 4.3 years; female/male ratio, 254:256). The study protocol was approved by the institutional review board. Patient charts and audiologic tests were assessed by an experienced otolaryngologist in selected relevant cases.

Imaging

All CT studies of the temporal bone were performed with thin sections, on the same 4-channel multidetector CT scanner (Somatom Plus 4/Volume Zoom; Siemens, Erlangen, Germany). The images were obtained by using the pediatric temporal bone protocol, with 0.5-mm collimation, 0.5-mm thickness, 100 mA, and 120 kV(peak). Subsequently, axial reformatted images parallel to the lateral semicircular canal were obtained. Coronal reformatted images were created perpendicular to the axial reformats. Images with extensive motion or implant artifacts ($n = 21$ children) were excluded from the study. Images without extensive motion or implant artifacts were included in the patient group. Mild motion and/or implant artifacts were observed in 14 temporal bones (1%, 14/1020) but did not prevent the evaluation of the otic capsule.

Image Evaluation

Two neuroradiologists experienced in head and neck imaging (B.O., S.E.S.) retrospectively and simultaneously evaluated the images. Hypoattenuated foci consistent with iEO areas in the OC were defined and classified as mild, moderate, or extensive according to the extent of focal hypoattenuation. Because there were no studies in the literature that had a specific grading system for OC hypoattenuation, we graded it according to the embryologic ossification order from the latest to the earliest. Mild iEO was defined as a focal hypoattenuated area in the FAF region (Fig 1). Moderate iEO was defined as a focal hypoattenuated area extend-

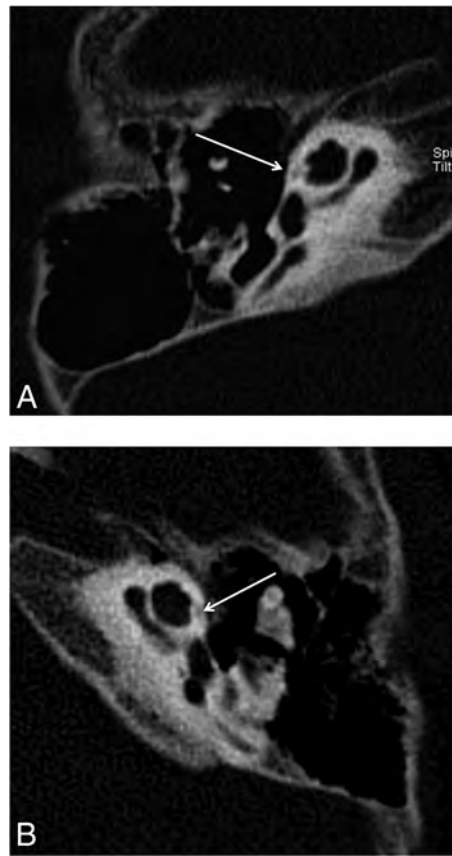


FIG 1. Reformatted axial CT image of the right (A) and the left (B) temporal bones of a 13-year-old girl with SNHL. Note linear hypoattenuation in the region of the FAF (arrows), consistent with mild incomplete ossification.

ing from the FAF to the anterior aspect of the cochlea (Fig 2). Finally, extensive iEO was defined as a large curvilinear hypoattenuated area extending to the posteromedial aspect of the cochlea in an arc-like pattern (Fig 3).

Statistical Analysis

All statistical analyses were performed by using SPSS, Version 15.0 for Windows (IBM, Armonk, New York). The relationships among EO and sex and SNHL were analyzed by using the χ^2 test. Because the ages of patients followed a normal distribution, 1-way analysis of variance was used to determine the relationship between the EO grades and age. Independent *t* tests were used to analyze the relationships between age and both EO and SNHL. The χ^2 test was also used to determine the relationship between the presence and grade of the EO in the patients with SNHL compared with the control group. The level of significance was set at $P < .05$.

RESULTS

For the cases included in the first phase of the study, iEO was seen in 62% of patients with SNHL and in 57.5% of the control group. Neither the presence nor degree of iEO had any significant correlation with the presence of SNHL by the χ^2 test ($P = .08$ and $P = .1$, respectively).

For the cases included in the second phase, the temporal bone CT imaging in patients with SNHL revealed normal findings in

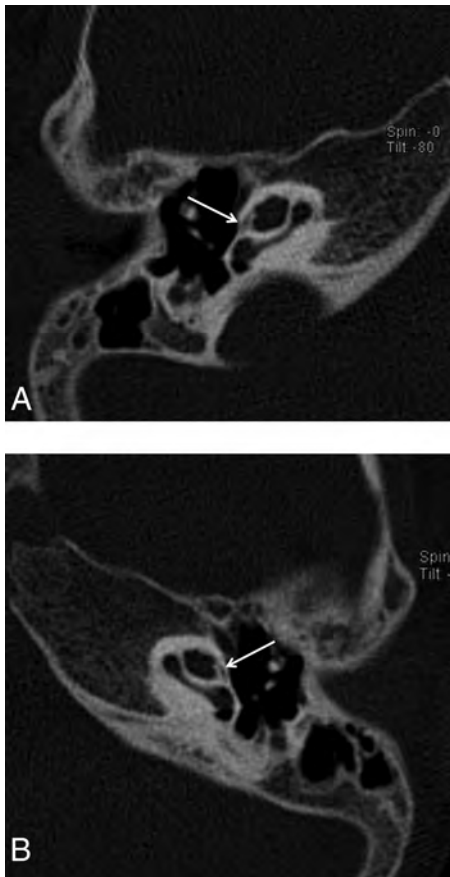


FIG 2. Reformatted axial CT images of the right (A) and the left (B) temporal bones of a 6-year-old girl with SNHL. Note hypoattenuation in the region of the FAF extending slightly to the anterior aspect of the cochlea (arrows), consistent with moderate incomplete ossification.



FIG 3. Axial CT images of the right temporal bone of a 1-year-old boy with SNHL. A hypoattenuated curvilinear line surrounds the cochlea, consistent with extensive incomplete ossification (arrows).

Frequency and age distribution of the different levels of otic capsule endochondral ossification

EO of the Otic Capsule	No. of Temporal Bones (%)	Mean Age (yr) (Range)
Complete	387 (38%)	7.9 ± 4.6 (8 months to 17 years)
Incomplete	633 (62%)	2.8 ± 2.4 (17 days to 15 years)
Mild	453 (71.6%)	3.7 ± 3.1 (5 months to 15 years)
Moderate	118 (18.6%)	2.5 ± 1.9 (4 months to 12 years)
Extensive	62 (9.8%)	1.1 ± 0.8 (17 days to 6 years)

Note:—EO indicates endochondral ossification.

846 temporal bones (83%). Various inner ear abnormalities were observed in 174 temporal bones (17%). The most common inner ear abnormality was the enlargement of the vestibular aqueduct ($n = 50$, 28.7%). In a descending order of frequency, other inner ear abnormalities included incomplete partition abnormality type 2 (31.15%), incomplete partition abnormality type 1 (22.95%), cochlear hypoplasia (19.67%), internal auditory canal stenosis (18.85%), cochlear aperture stenosis (9.8%), isolated vestibular dysplasia (6.56%), common cystic deformity (5.74%), isolated enlarged vestibular aqueduct (4.92%), complete labyrinthine aplasia (3.28%), rudimentary otocyst (1.64%), and cochlear aplasia (0.82%). There was no statistically significant correlation between the presence of iEO and radiologically detected inner ear abnormality ($P = .2$).

iEO was seen in 62% of all the evaluated cases and thus was more frequent than complete ossification (38% of the cases) in our series. The mean age for the iEO group was 2.8 ± 2.4 years (range, 17 days to 17 years), and for complete ossification, the mean age was 7.9 ± 4.6 years (range, 8 months to 17 years). There was no statistically significant correlation between iEO and sex ($P = .8$). However, an inverse correlation was found between the presence of iEO and increasing age by an independent t test ($P < .001$).

In the iEO group ($n = 633$), mild iEO was the most frequent involvement pattern ($n = 453$, 71.6%). Moderate iEO was found in 118 temporal bones (18.6%), while extensive iEO was found bilaterally in 62 temporal bones (9.8%). The mean ages for the mild, moderate, and extensive iEO groups were 3.7 ± 3.1 (range, 5 months to 15 years), 2.5 ± 1.9 (range, 4 months to 12 years), and 1.1 ± 0.8 years (range, 17 days to 6 years), respectively (Table). The age range and the mean age of mild and moderate iEO groups were quite similar. However, the mean age showed statistically significant differences between the mild and moderate iEO groups ($P = .005$). The youngest patient population was seen in the extensive iEO group (mean age, 1.1 ± 0.8 years). Additionally, 80% of patients having extensive iEO were younger than 1 year of age, and 65.5% were younger than 6 months of age. Extensive iEO was thus much more frequent in infants compared with older children. However, a cutoff age limit could not be defined to differentiate the extensive iEO group from mild/moderate iEO groups ($P = .2$, $P = 1$, respectively). The charts of cases presenting with extensive iEO were reviewed, but no clinical or audiologic manifestations suggestive of otospongiosis and osteogenesis imperfecta were found (Fig 4).

The pattern of iEO involvement (defined by the grade) was asymmetric between the 2 ears of the same patient in 37 cases (7.5%). In most patients with asymmetric iEO involvement (23 patients), EO was complete in one ear, while the other ear presented mild iEO. In the remaining 14 patients, the asymmetric

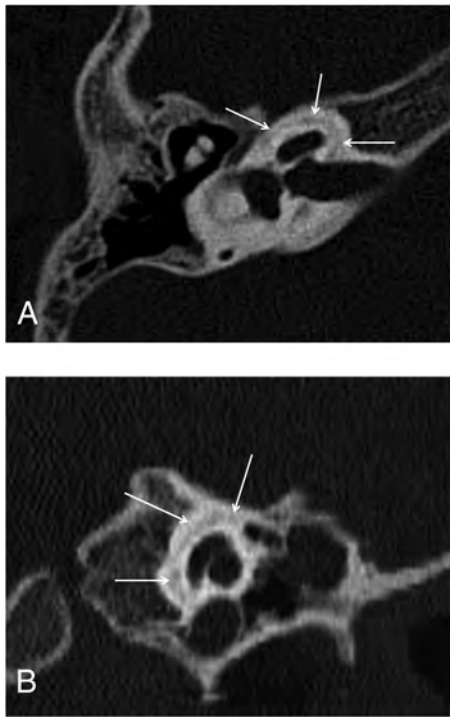


FIG 4. Axial (A) and coronal (B) CT images of the right temporal bone of a 6-year-old boy with SNHL who had been treated with corticosteroids for 3 years due to congenital adrenogenital syndrome. Hypoattenuation surrounding the cochlea, consistent with extensive incomplete ossification, is again noted (arrows).

ossification pattern was mild iEO in one ear and moderate in the contralateral ear. In 17 of 74 patients presenting with asymmetric EO, various inner ear abnormalities were found. Inner ear structures were radiologically normal in the remaining 57 ears with the asymmetric ossification pattern. The asymmetric pattern did not have a statistically significant correlation with the underlying inner ear abnormality ($P = .2$). The presence of an asymmetric enchondral ossification pattern showed reverse correlation with age ($P = .03$).

DISCUSSION

The temporal bone has highly complex anatomy, and its embryonic development is reported to be one of the most complicated examples of cellular morphogenesis in any biologic system. The initial step in the formation of the ear is the differentiation of the otic placode, which will form the membranous labyrinth. Through a complicated embryogenesis influenced by numerous autocrine and paracrine factors, the surrounding mesenchyme undergoes chondrogenesis, which will eventually form the bony capsule that encircles the membranous labyrinth.¹²⁻¹⁵ The mechanism of ossification of the OC is mainly by EO, with intrachondral bone ossification predominating in some stages.¹⁶ Histologically, the ossifying OC has 3 layers: a thin inner (endosteal) layer, a middle layer composed of a combination of endochondral and intrachondral bone, and an outer (periosteal) layer. The endosteal layer of bone surrounding the otic capsule ossifies at midgestation and does not change after birth; the middle layer, however, is partly calcified in the near-term fetus but then is rapidly replaced by bone.⁴ EO is completed finally in the region of the FAF, which

is a cleft between the inner and middle layers just anterior to the oval window.⁵ Fibrocartilage may persist at the FAF even in adults; this region is also a site of predilection for otosclerosis (probably due to the presence of specific cartilage constituents targeted by autoimmune reactions).¹⁷

Because ossification is first completed in the inner and outer layers and the middle layer containing bone marrow is the last portion to ossify, the FAF region, which has mainly a middle layer, might remain as an incompletely ossified area even in adults and can be seen as a focal hypoattenuation on CT images even in adults.⁵ In our series, CT revealed focal hypoattenuation in the region of the FAF in most children (633 cases, 62%). The incidence in our study is higher than that in previously reported series with incidences in the range of 32%–41%. This difference may be partly due to technical factors because our study acquired very thin sections (the section thickness of the scans in the prior studies were as follows: 0.5–1.5 mm in the study by Pekkola et al,⁵ 0.5–0.75 mm in the study by de Brito et al,³ and this information was not given in the study by Chadwell et al²). The mean age of our study was similar to the one in the series by Pekkola et al⁵ and thus could not provide an explanation for the difference in incidences (the mean age was not given in the other 2 studies).

In the development of the inner ear, different inner ear structures are known to induce each other. In addition, EO is not completed until the membranous inner ear structures have completed and reached their adult size. One might expect that the EO could be affected by pathologies of the inner ear (radiologically silent or detected). However, we found no correlation between the presence of SNHL and the level of EO. De Brito et al³ compared the incidence of hypoattenuated foci in patients with and without SNHL and similarly found no correlation. We diagnosed radiologic inner ear abnormalities in 174 (17%) of all the imaged temporal bones, but those cases had degrees of EO similar to those in the cases with normal-appearing inner ears. We thus suggest that the presence of hypoattenuated foci in the OC is independent of the membranous and bony labyrinth development.

In this study, the iEO was similar among the 2 sexes but, as expected, had an inverse correlation with age. This finding is in agreement with previously mentioned series reporting that the OC ossification is correlated with the age of the individual rather than the sex but is somewhat controversial due to the established knowledge of delayed bone maturation in males,¹⁸ and our results may be because the area of concern is very small and minor differences are difficult to detect. Asymmetric EO among the contralateral ears was found in 74 patients without a sex or age predilection ($P = .8$ and $P = 1$, respectively). As suggested in previous studies, inherent variations in the developmental process might play a role in these minor asymmetries.

In a CT study evaluating ossification features of the OC,⁴ it has been shown that incomplete ossification of the entire middle otic layer in a neonate skull specimen was seen as a hypoattenuated halo surrounding the cochlea (Fig 4 in the article by Moser et al⁴). This appearance is similar to that in our cases labeled extensive iEO; thus, extensive iEO probably reflects the earliest appearance of a completely nonossified middle layer. In our study, 31 patients had extensive iEO. Patients included in the extensive iEO group were younger

in comparison with the 2 other iEO groups, and 65.5% of the patients with extensive iEO were 6 months of age or younger.

The mean age for the mild iEO group was higher (3.7 ± 3.1 years) than that of the moderate and extensive iEO groups. Although the mean ages for different grades of iEO (mild, moderate, and extensive) were numerically close to one another, there was a direct correlation of age with the degree of ossification of the OC. These findings lead us to think that in most cases, extensive iEO subsequently does convert to moderate and mild iEO with increasing age. In a single patient in our series who had subsequent imaging a year later, we found that extensive iEO had upgraded to moderate iEO in the follow-up study the next year. Although it was not the aim of this study, it would be interesting to see, in a separate study, the evolution of the iEO with time for individual patients (eg, with a retrospective data base search of children who had multiple temporal bone studies).

Although the mean age of the patients was significantly different between the mild and moderate iEO groups ($P = .005$), this significance could not be reached when comparing the mean age values of moderate iEO and extensive iEO groups. Overlapping age ranges between the iEO groups might have influenced these statistical results. However, more important, the small number of patients with extensive iEO and the presence of older children, which has caused an increase in the mean age in the group with extensive iEO, are probably the main reasons for statistical insignificance. The lower number of patients with extensive iEO in our series could be because very small children and infants do not frequently undergo CT imaging and they tend to be imaged preferentially with MR imaging due to radiation concerns.

In the extensive iEO group, only 1 patient (a 6-year-old boy) had a history of corticosteroid administration for 3 years due to congenital adrenogenital syndrome. Except for this 1 case, we did not find any underlying pathologic condition in children with extensive iEO who were older than 1 year of age to explain a delay in ossification, such as vitamin D deficiency or other metabolic abnormalities. Because the patients with extensive iEO in our series did not undergo histopathologic evaluation of their otic capsule, it is still unclear whether the imaging findings are due to an individual variation or are a result of delayed bone maturation. Similarly, an underlying genetic abnormality was not sought but cannot be ruled out.

The small size of the control group is the main limitation of our study. Because SNHL is the prominent type of hearing loss in childhood and for this young age group CT of the temporal bone is mainly undertaken to identify possible inner ear abnormalities, it is difficult to obtain a large control group of patients without SNHL or inner ear abnormalities. Patients with extensive iEO were only evaluated for radiologic mimics such as osteogenesis imperfecta and otosclerosis and were not investigated further for genetic and/or laboratory abnormalities; however, as of today, no significant scientific data suggest a specific underlying cause for delayed/abnormal endochondral ossification besides osteogenesis imperfecta and otosclerosis. Further studies with histopathologic correlation and investigations comparing temporal bone maturation with systemic bone development are necessary to resolve this issue.

CONCLUSIONS

The presence of focal hypoattenuation in the OC can be accepted as a normal finding in young children. Mild forms of incomplete endosteal ossification can be seen in children up to 15 years of age and can have asymmetric involvement between the 2 ears of the same individual. At younger ages (especially in the first 6 months of life), excessive hypoattenuation reaching the anterior OC can be seen without any clinical evidence of otosclerosis/osteogenesis imperfecta. This hypoattenuation most likely represents incomplete endochondral ossification, a process that seems to proceed independent of the development of the inner ear.

REFERENCES

1. Krombach GA, Honnef D, Westhofen M, et al. **Imaging of congenital anomalies and acquired lesions of the inner ear.** *Eur Radiol* 2008;18:319–30
2. Chadwell JB, Halsted MJ, Choo DI, et al. **The cochlear cleft.** *AJNR Am J Neuroradiol* 2004;25:21–14
3. de Brito P, Metais JP, Lescanne E, et al. **Pericochlear hypodensity on CT: normal variant in childhood** [in French]. *J Radiol* 2006;87(6 pt 1):655–59
4. Moser T, Veillon F, Sick H, et al. **The hypodense focus in the petrous apex: a potential pitfall on multidetector CT imaging of the temporal bone.** *AJNR Am J Neuroradiol* 2008;29:35–39
5. Pekkola J, Pitkaranta A, Jappel A, et al. **Localized pericochlear hypoattenuating foci at temporal-bone thin-section CT in pediatric patients: nonpathologic differential diagnostic entity?** *Radiology* 2004;230:88–92
6. d'Archangeau O, Parizel PM, Koekelkoren E, et al. **CT diagnosis and differential diagnosis of otodystrophic lesions of the temporal bone.** *Eur J Radiol* 1990;11:22–30
7. Lescanne E, Bakhos D, Metais JP, et al. **Otosclerosis in children and adolescents: a clinical and CT-scan survey with review of the literature.** *Int J Pediatr Otorhinolaryngol* 2008;72:147–52
8. Mafee MF, Henrikson GC, Deitch RL, et al. **Use of CT in stapedial otosclerosis.** *Radiology* 1985;156:709–14
9. Mafee MF, Valvassori GE, Deitch RL, et al. **Use of CT in the evaluation of cochlear otosclerosis.** *Radiology* 1985;156:703–08
10. Rovsing H. **Otosclerosis: fenestral and cochlear.** *Radiol Clin North Am* 1974;12:505–15
11. Swartz JD, Mandell DW, Berman SE, et al. **Cochlear otosclerosis (otospongiosis): CT analysis with audiometric correlation.** *Radiology* 1985;155:147–50
12. Groves A. **The induction of the otic placode.** In: Kelley M, Wu D, Fay RR, eds. *Development of the Inner Ear: Springer Handbook of Auditory Research.* Vol. 26. New York: Springer-Verlag; 2005:10–42
13. Kelly M, Wu D. **Developmental neurobiology of the ear: current status and future directions.** In: Kelly M, Wu D, Fay RR, eds. *Development of the Inner Ear: Springer Handbook of Auditory Research.* Vol. 26. New York: Springer-Verlag; 2005:1–9
14. Mansour S, Schoenwolf G. **Morphogenesis of the inner ear.** In: Kelly M, Wu D, Fay RR, eds. *Development of the Inner Ear: Springer Handbook of Auditory Research.* Vol. 26. New York: Springer-Verlag; 2005:43–84
15. Nemzek WR, Brodie HA, Chong BW, et al. **Imaging findings of the developing temporal bone in fetal specimens.** *AJNR Am J Neuroradiol* 1996;17:1467–77
16. Sperber GH. *Craniofacial Embryology.* London: Wright; 1989
17. Huang CC, Yi ZX, Abramson M. **Type II collagen-induced otospongiosis-like lesions in rats.** *Am J Otolaryngol* 1986;7:258–66
18. Ballabriga A. **Morphological and physiological changes during growth: an update.** *Eur J Clin Nutr* 2000;54(suppl 1):S1–6

High-Resolution CT Findings in Children with a Normal Pinna or Grade I Microtia and Unilateral Mild Stenosis of the External Auditory Canal

R. Jacob, S. Gupta, B. Isaacson, J.W. Kutz Jr, P. Roland, Y. Xi, and T.N. Booth

ABSTRACT

SUMMARY: A subset of patients presents with unilateral conductive hearing loss, a normal pinna or grade I microtia, and mild external auditory canal stenosis. The physical findings of microtia and a small external canal are commonly absent or subtle in this group of patients, who are being commonly referred for imaging to evaluate isolated conductive hearing loss. We present a case series of patients with unilateral conductive hearing loss and characteristic ossicular abnormalities, commonly anterior fixation of the malleus. All patients had a significantly increased distance from the cochlear promontory to the handle of the malleus and an abnormal incudostapedial angle, indicative of an abnormal ossicular position and/or morphology. Successful surgical reconstruction of the ossicular chain was attempted and accomplished in 3 patients.

ABBREVIATIONS: CHL = conductive hearing loss; EAC = external auditory canal; HRCT = high-resolution CT

Congenital hearing loss affects 1–3 per 1000 children.¹ Hearing loss can be due to central auditory dysfunction, conductive, sensorineural, or a combination.² Congenital conductive hearing loss (CHL) may be related to an isolated anomaly of the middle ear without associated anomalies of the external ear or canal.³ More commonly, anomalies of the middle ear are linked to congenital anomalies of the pinna, which has an incidence of approximately 1 in 11,000 children. These patients present with conductive hearing loss related to stenosis or atresia of the external auditory canal (EAC).⁴ Ossicular anomalies such as absence, fixation, and abnormal fusion have been described in children with or without EAC stenosis or atresia. External auditory canal stenosis or atresia in the absence of anomalies of the pinna is uncommon but has been described in nonsyndromic children and children with chromosome 18q deletion.⁵ The absence or subtle nature of external ear anomalies in this patient population could potentially lead to delay in identification of the etiology of hearing loss. High-resolution CT (HRCT) is beneficial in elucidating the

etiology of congenital CHL and guides surgical management in these patients.⁴

We describe the clinical presentation and audiometric and HRCT findings in a group of patients with unilateral CHL and a normal or minimally abnormal pinna associated with mild stenosis of the EAC.

Case Series

Patients. This was a Health Insurance Portability and Accountability Act–compliant retrospective case series performed after approval from the institutional review board at a tertiary referral center. A PACS search was performed with the Boolean function combining “external canal,” “external auditory canal” AND “stenosis,” or “stenotic” for identifying relevant cases of CT of the temporal bones performed during a 5-year period (2009–2013). The inclusion criteria were patients with unilateral congenital EAC stenosis of <50% diameter on CT, a normal pinna or grade I microtia, and a diagnostic temporal bone HRCT. Children with syndromes associated with temporal bone abnormalities were excluded. Grade I microtia is characterized by a hypoplastic auricle with all the identifiable landmarks, grade II microtia consists of an abnormal auricle without some identifiable landmarks, grade III microtia is recognized by a very small auricular tag, and anotia is classified as grade IV.^{6,7}

The electronic medical records were reviewed for the presence or absence of an abnormal pinna. Audiograms were reviewed for the severity of conductive hearing loss, and the pure tone average was graded as mild (20–40 dB), moderate (40–60 dB), or severe/

Received May 6, 2014; accepted after revision June 22.

From the Departments of Radiology (R.J., Y.X., T.N.B.) and Otolaryngology (S.G., B.I., J.W.K., P.R.), Children’s Medical Center of Dallas, University of Texas, Southwestern Medical Center, Dallas, Texas.

Paper previously presented at: Annual Meeting of the American Society of Neuro-radiology and the Foundation of the ASNR Symposium, May 17–22, 2014; Montreal, Quebec, Canada.

Please address correspondence to Timothy N. Booth, MD, Department of Radiology, Children’s Medical Center of Dallas, 1935 Medical District Dr, Dallas, TX 75235; e-mail: tim.booth@childrens.com

<http://dx.doi.org/10.3174/ajnr.A4067>

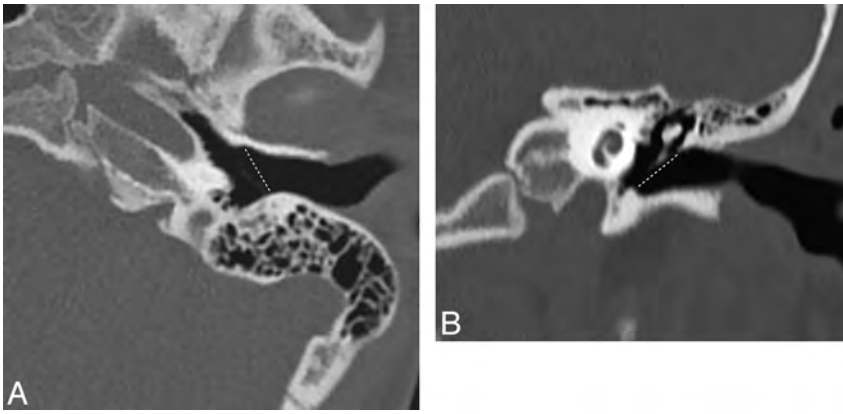


FIG 1. Measurement method for the EAC diameter. Axial and coronal temporal bones at the level of the EAC. The left EAC is measured obliquely along the most medial aspect, parallel to the tympanic membrane (*dotted line*) in both the axial and coronal planes.

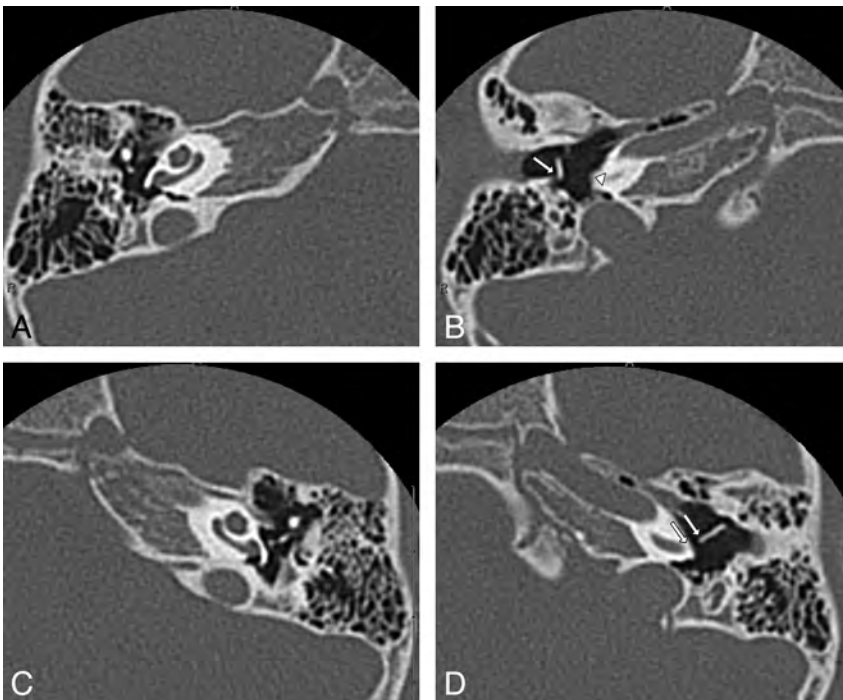


FIG 2. Abnormal orientation of the handle of the malleus in a 4-year-old girl with right-sided CHL (patient 6). Axial HRCT of the temporal bone, superior-to-inferior. *A* and *B*, Superior image shows a normal ossicular position. Inferiorly, abnormal orientation of the handle of the right malleus along with posterior fixation of the handle of the malleus (*arrow*) is present. There is asymmetric widening of the distance between the cochlear promontory (*arrowhead*) and the handle of the malleus. *C* and *D*, Normal ossicular anatomy is present superiorly. Inferiorly, normal orientation of the handle of the left malleus and a normal distance from the promontory to the handle (between *arrows*) are seen.

profound (≥ 60 dB). HRCT studies were reviewed by a pediatric neuroradiologist with 17 years of experience and a pediatric neuroradiology fellow.

Imaging Analysis

HRCT studies were performed with a reconstruction thickness of 0.5–0.8 mm. Targeted magnified reconstructions were performed for each ear in the plane of the lateral semicircular canal, with perpendicular coronal reformats constructed at 0.2- to 0.5-mm thickness.

The external auditory canal measurement was compared with

that of the contralateral normal ear, which served as an internal standard. The EAC was measured in the axial and coronal planes, parallel to the tympanic membrane, along the medial-most aspect of the external auditory canal (Fig 1). The measurements were compared with the contralateral EAC to assess the degree of asymmetry in size. More complex methods have been described, but a single axial and coronal measurement was determined adequate due to the availability of the contralateral normal ear for comparison.⁸

HRCT of the temporal bone was evaluated for findings based on the criteria developed by Jahrsdoerfer et al⁹ for identifying suitable candidates with congenital aural atresia for surgery.^{10,11} The presence of ossicular anomalies, including fixation, abnormal position, and abnormal shape or size, was noted. Fixation was defined as the presence of an osseous bar between the ossicles and the margins of the middle ear cavity or when the ossicles were not separable from the walls of the middle ear cavity. The positions and relationships of the ossicles in the middle ear were evaluated. The distance between the cochlear promontory and the most medial portion of malleus handle was measured on the normal and abnormal sides on axial HRCT images to assess the position of the malleus. To evaluate the relationship between the incus and stapes, we measured the angle between the long process of the incus and the capitulum stapes (incudostapedial angle) on coronal images at the level of the oval window.^{10,12} The size of the Prussak space was compared with that of the contralateral normal ear. The incudomalleal and incudostapedial joints were evaluated for fusion or widening. The size of the middle ear was compared with that of the contralateral ear and subjectively evaluated as normal or mildly or severely hypoplastic.

The patency of the oval and round windows was assessed along with the status of the facial nerve. The position of the tympanic segment of the facial nerve was considered abnormal if it was inferiorly medially displaced, overlying the oval window; if the position of the posterior genu was anterior to the round window; and/or if the vertical segment of the facial canal had an anterolateral course. Inner ear structures were evaluated for the presence of cochlear or vestibular dysplasia and the size of the cochlear nerve canal (normal, >1.4 mm).¹³ Intraoperative findings, audiograms, and the success of reconstruction were reviewed by a neurotologist.

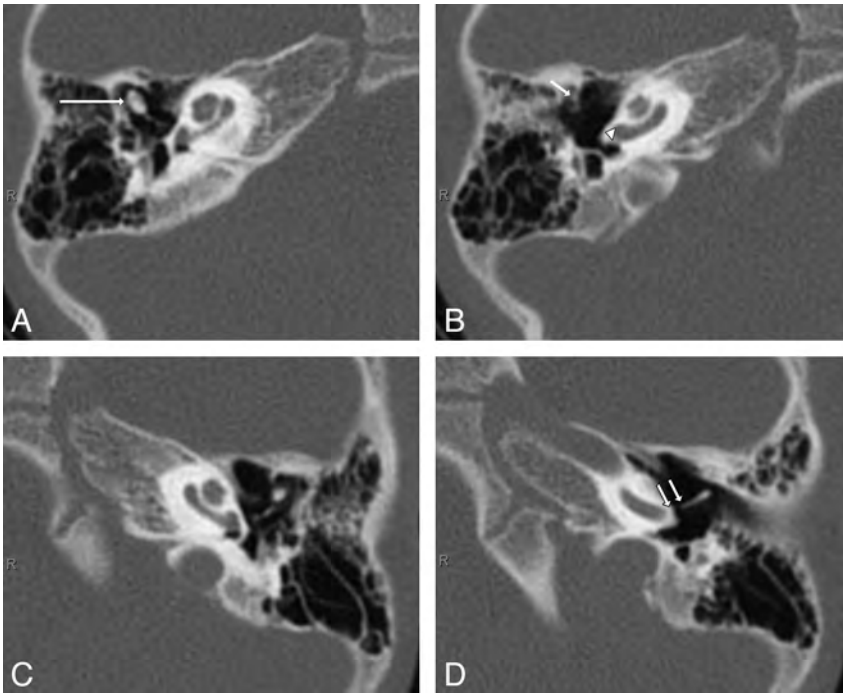


FIG 3. Abnormal fixation of the handle of the malleus along with increased distance of the handle of malleus to the cochlear promontory in a 4-year-old boy with right-sided CHL (patient 9). Axial HRCT of the temporal bones, superior-to-inferior. *A* and *B*, There is abnormal fusion of the right malleus and incus (*long arrow*) superiorly. The inferior image shows fixation of the handle of the malleus anteriorly (*short arrow*). Note an increased distance of the handle of the malleus to the cochlear promontory (*arrowhead*). *C* and *D*, Normal separation of the left ossicles is present superiorly. Inferiorly, there is a normal distance of the handle of the left malleus to the promontory in the normal ear (between *arrows*).

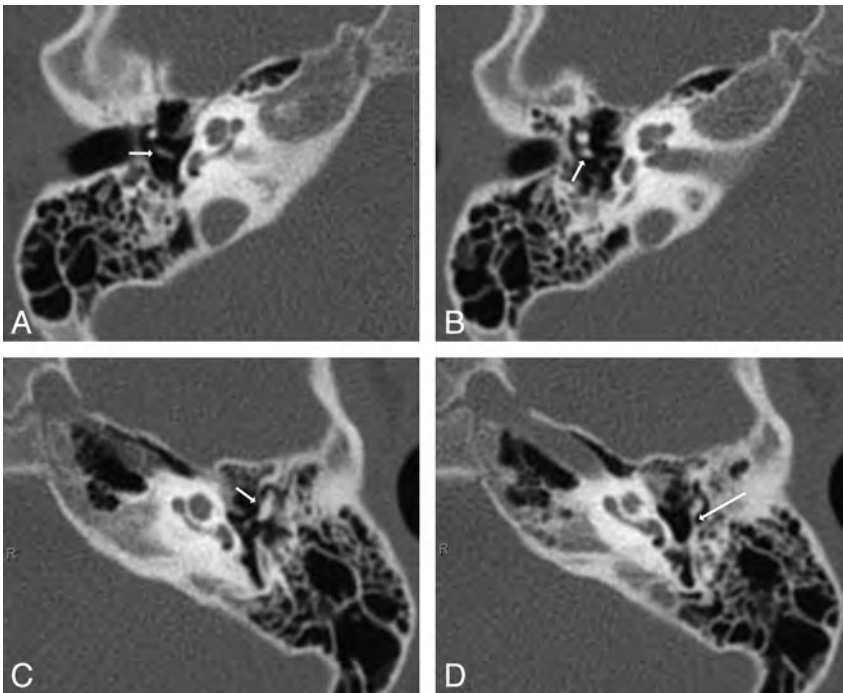


FIG 4. Abnormal fixation of the incus in a 5-year-old girl with left-sided CHL (patient 1). Axial HRCT of the temporal bone, superior-to-inferior. *A* and *B*, Superiorly, there is a normal incus with articulation with the stapes (*arrow*). Inferior image shows a normal long process of the incus with no fixation bar (*arrow*). *C* and *D*, Superiorly, there is fusion of the left malleus and incus (*arrow*). Inferior image shows a posterior fixation bar extending from the long process of the incus (*long arrow*) to the posterior wall of the tympanic cavity.

Statistical analysis was performed by using the Wilcoxon signed rank test due to the small sample size. The malleal handle to the cochlear promontory distance and the incudostapedial angle were compared with the measurements from the contralateral normal ear.

Clinical Findings

A 5-year PACS search with specified criteria revealed 9 patients. Three were excluded due to syndromic association (2 Goldenhar, 1 Down syndrome). The male/female ratio was 5:4, and the mean age was 7 years (range, 3–12 years). All patients presented with unilateral CHL. On physical examination, 5/9 patients had no abnormality of the pinna and clinically normal EACs. Four of 9 patients had grade I microtia. The mean pure tone average was 49.4 ± 14.2 dB (range, 28–68 dB), and the mean air-bone gap was 49.6 ± 12.9 dB (range, 25–65 dB). Two patients had mild CHL; 5, moderate CHL; and 2, severe CHL.

Imaging Findings

CT showed the mean EAC diameter to be 5.1/6.7 mm (axial/coronal) on the affected side and 7.7/8.7 mm (axial/coronal) in the normal-hearing ear. Fixation of the handle of the malleus to the tympanic annulus was seen anteriorly in 7/9 ears and posteriorly in 1 ear (Figs 2 and 3). Posterior fixation of the long process of the incus was present in 2/9 ears (Fig 4). Abnormal orientation of the handle of the malleus with an abnormally increased distance to the cochlear promontory was present in all ears. The mean distance between the cochlear promontory and the handle of the malleus on the normal side was 1.7 mm (range, 1–2.9 mm) and 3.9 mm (range, 3.1–4.4 mm) on the abnormal side, with the distance being increased on the abnormal side (Figs 2 and 3). These findings were found to be significant ($P = .039$, Wilcoxon signed rank test). The mean incudostapedial angle on the normal side was 82.3° (range, 66° – 96°) and 101.1° (range, 73° – 119°) on the abnormal side (Fig 5). These findings were significant ($P = .015$, Wilcoxon signed rank test). The angle was increased in all affected ears.

There was a mild subjective decrease in size in the middle ear on the affected

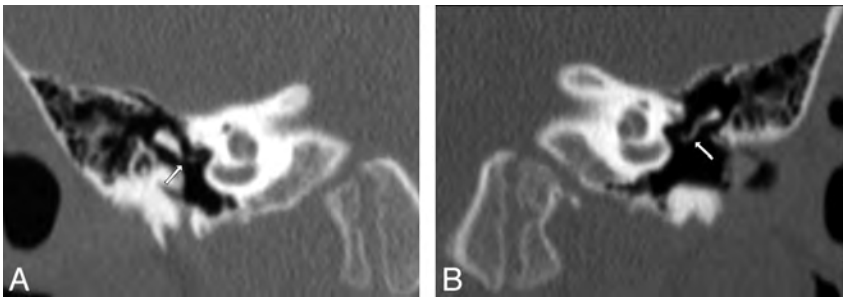


FIG 5. Abnormal asymmetric increased in the incudostapedial angle in a 3-year-old boy with right-sided CHL (patient 8). Coronal-reconstruction HRCT of the temporal bone at the level of the long process of the incus. *A*, An abnormally increased incudostapedial angle (arrow) measuring 109° is present in the right ear. *B*, The normal left ear has an incudostapedial angle measuring 93° (arrow).

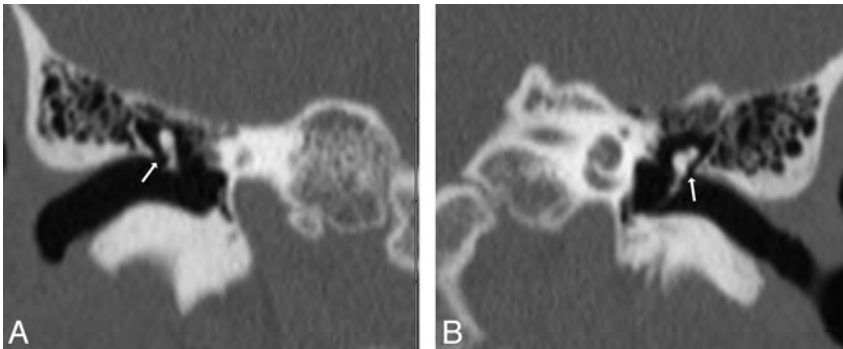


FIG 6. Asymmetric narrowing of the Prussak space in a 12-year-old boy with left-sided CHL (patient 2). Coronal-reconstruction HRCT of the temporal bone at the level of the malleus. *A*, Normal appearance of the Prussak space in the normal right ear (arrow) is present. *B*, Asymmetric narrowing of the Prussak space (arrow) in the affected left ear is present with a normal volume of the tympanic cavity.

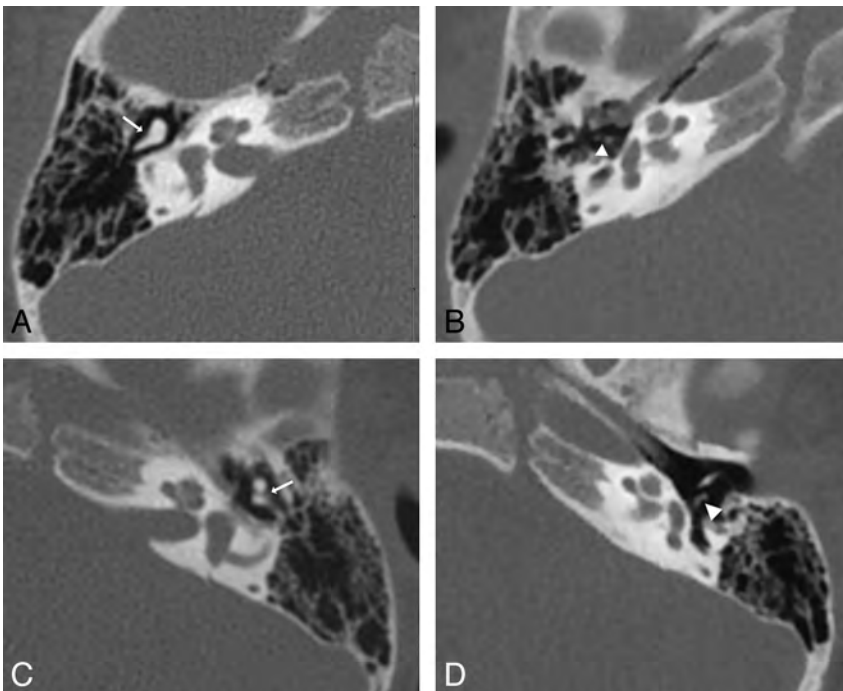


FIG 7. Abnormal incudomalleal and incudostapedial joints in a 3-year-old boy with right-sided CHL (patient 8). Axial HRCT of the temporal bone at the level of the ossicular articulations, superior-to-inferior. *A* and *B*, Superior image shows abnormal incudomalleal fusion (arrow). Inferiorly, abnormal incudostapedial widening (arrowhead) in the right ear is present. *C* and *D*, The normal left incudomalleal (arrow) and incudostapedial joints (arrowhead) are demonstrated.

side in 5 ears, and the middle ear was normal in size in 4 ears. There were no patients with severe hypoplasia of the middle ear cavity, and all ears were normally aerated without soft tissue present. A narrowed Prussak space suggested an abnormal ossicular position in 5/9 ears (Fig 6). The most common ossicular abnormalities included decreased size of the malleus head (7/9) and a narrowed or fused incudomalleal joint (7/9). Widening of the incudostapedial joint was present in 5/9 ears (Fig 7). The stapes was abnormal in 1 patient with an enlarged capitulum.

The oval and round windows were normal in all ears. The tympanic segment of the facial nerve was normally positioned and free of the oval window in all ears. The posterior genu was in the normal position at the level of or posterior to the round window in all ears. There was mild anterior displacement of the vertical segment of the facial nerve in 1 ear. No inner ear anomalies and normal cochlear nerve canals were demonstrated.

Surgical Correlation

Surgery was performed in 3 patients with agreement of most findings on HRCT. One imaging study showed a widened incudostapedial joint, which was not apparent at surgery. Tympanoplasty was performed in all those with a canaloplasty in 1 ear. Natural ossiculoplasty (mobilization of the fixed malleus head) was performed in 2 ears with malleus fixation, and an ossicular chain reconstruction (partial ossicular reconstruction prosthesis) was performed in 1 ear with incudostapedial joint separation. Significant improvement in hearing was noted in 2 patients on the postoperative audiogram (mean improvements in pure tone average of 24 dB), and 1 patient was lost to follow-up.

DISCUSSION

The auricle is derived from the first and second pharyngeal arches, and the external auditory canal is derived from the first pharyngeal cleft. The malleus and incus are derived from endochondral ossification of the cartilage of the first and second arches.⁴ Hence, abnormal development of the first and second arches can lead to auricular malformations, including microtia, external auditory canal stenosis,

and ossicular dysplasia. The early identification of unilateral conductive hearing loss can be difficult in the absence or presence of minor deformity of the external ear.⁵

Most patients in this series had normal external examination findings on the initial evaluation when unilateral CHL was the sole reason for obtaining HRCT. 3D volumetric reconstruction of the CT dataset may be useful in assessing minor external ear malformations to aid in a potential diagnosis. Bilateral EAC stenosis would be more difficult to evaluate by imaging without the contralateral ear for comparison. However, most patients, approximately two-thirds, with congenital EAC stenosis have unilateral disease, which would facilitate an imaging diagnosis.¹⁴ Patients with syndromic associations are also more commonly associated with bilateral involvement and would be identified clinically.¹⁵ Patients presenting with unilateral CHL should be evaluated for mild stenosis of the external auditory canal on HRCT, especially because anomalies of the external ear can be subtle or absent on physical examination. Development of a simple normative EAC diameter may be helpful to evaluate the child with bilateral CHL.

Middle ear and ossicular anomalies are more common in children presenting with CHL and EAC stenosis.¹⁵ The present study identified characteristic fixation abnormalities of the ossicles in this group of patients. High-resolution CT in the present study demonstrated that the malleus handle was laterally displaced from the cochlear promontory. Most commonly, this displacement appears to relate to anterior rotation of the handle with anterior fixation to the anterior tympanic annulus. Additional indirect signs such as narrowing of the Prussak space on the affected side can be very helpful in identifying ossicular anomalies if they are not readily apparent. The incudostapedial angle was also consistently increased on the affected side but remained $<120^\circ$ in all affected ears. An incudostapedial angle of $<120^\circ$ has been associated with a good surgical prognosis.¹⁶

Mayer et al¹⁰ found the oval window to be absent in one-third of the patients with EAC stenosis or atresia and noted no significant correlation with the degree of associated external ear abnormality. A main predictor of the success of ossicular reconstruction is the patency of the oval window, and all were widely patent in the present study.⁴ The limited number in our group that had surgery had excellent hearing results.

Malposition of the facial nerve has been reported in mild microtia in up to half of patients.⁹ This is typically manifested by anterior displacement of the mastoid segment. Only 1 patient in this series had a mild anteriorly positioned mastoid segment. The obstruction of access to the oval window by the anterolateral displacement of the vertical segment of the facial canal was reported in 41% of patients with atresia in the series by Dedhia et al.¹¹ The abnormal position of the facial nerve could potentially increase the risk of injury to the nerve. There were no anomalies of the tympanic segment of the facial nerve canal in this series, which would have precluded surgical access to the oval window.

Potential limitations of our study include the use of search criteria based on radiologic reports. This may significantly underestimate the incidence of such findings because the presence of mild stenosis may be difficult to subjectively appreciate. The study is also limited by the resultant small sample size and surgical correlation in only 3 patients.

CONCLUSIONS

Patients presenting with unilateral conductive hearing loss should be evaluated for mild EAC stenosis and potentially subtle but characteristic ossicular malformations. Anomalies of the pinna are commonly absent or subtle in this group of patients. Systematic evaluation of the middle ear structures is suggested with evaluation of the distance from the cochlear promontory to the handle of the malleus and the incudostapedial angle. These patients typically have favorable anatomy for ossicular reconstruction.

Disclosures: Brandon Isaacson—UNRELATED: Board Membership: Advanced Bionics, Comments: Medical Advisory Board; Consultancy, Medtronic Midas Rex Institute, Comments: consultant for drill design; Payment for Lectures (including service on Speakers Bureaus): Oticon, Comments: lectured on bone-anchored hearing aid; Travel/Accommodations/Meeting Expenses Unrelated to Activities Listed: Oticon, Comments: discussed bone-anchored hearing aids and cochlear implants in Copenhagen, Denmark and Nice, France.

REFERENCES

1. Kemper AR, Downs SM. A cost-effectiveness analysis of newborn hearing screening strategies. *Arch Pediatr Adolesc Med* 2000;154:484–88
2. Smith RJ, Shearer AE, Hildebrand MS, et al. Deafness and hereditary hearing loss overview. February 14, 1999; updated January 9, 2014. In: Pagon RA, Adam MP, Bird TD, et al, eds. *GeneReviews*. Seattle: University of Washington, Seattle; 1993–2014. <http://www.ncbi.nlm.nih.gov/books/NBK1434/>. Accessed April 21, 2014
3. Park K, Choung YH. Isolated congenital ossicular anomalies. *Acta Otolaryngol* 2009;129:419–22
4. Raz Y, Lustig L. Surgical management of conductive hearing loss in children. *Otolaryngol Clin North Am* 2002;35:853–75
5. Stewart JM, Downs MP. Congenital conductive hearing loss: the need for early identification and intervention. *Pediatrics* 1993;91:355–59
6. Marx H. Die Missbildungen des Ohres. In: Henke F, Lubarsh O, eds. *Handbuch der Spez Path Anatomie Histologie*. Berlin: Springer-Verlag; 1926:620–25
7. Ishimoto S, Ito K, Yamasoba T, et al. Correlation between microtia and temporal bone malformation evaluated using grading systems. *Arch Otolaryngol Head Neck Surg* 2005;131:326–29
8. Mahboubi H, Wu EC, Jahanbakhshi R, et al. A novel method to determine standardized anatomic dimensions of the osseous external auditory canal. *Otol Neurotol* 2012;33:715–20
9. Jahrsdoerfer RA, Yeakley JW, Aguilar EA, et al. Grading system for the selection of patients with congenital aural atresia. *Am J Otol* 1992;13:6–12
10. Mayer TE, Brueckmann H, Siegert R, et al. High-resolution CT of the temporal bone in dysplasia of the auricle and external auditory canal. *AJNR Am J Neuroradiol* 1997;18:53–65
11. Dedhia K, Yellon RF, Branstetter BF, et al. Anatomic variants on computed tomography in congenital aural atresia. *Otolaryngol Head Neck Surg* 2012;147:323–28
12. Skinner M, Honrado C, Prasad M, et al. The incudostapedial joint angle: implications for stapes surgery prosthesis selection and crimping. *Laryngoscope* 2003;113:647–53
13. Yi JS, Lim HW, Kang BC, et al. Proportion of bony cochlear nerve canal anomalies in unilateral sensorineural hearing loss in children. *Int J Pediatr Otorhinolaryngol* 2013;77:530–33
14. Gassner EM, Mallouhi A, Jaschke WR. Preoperative evaluation of external auditory canal atresia on high-resolution CT. *AJR Am J Roentgenol* 2004;182:1305–12
15. Tekes A, Ishman SL, Baugher KM, et al. Does microtia predict severity of temporal bone CT abnormalities in children with persistent conductive hearing loss? *J Neuroradiol* 2013;40:192–97
16. Kim DW, Lee JH, Song JJ, et al. Continuity of the incudostapedial joint: a novel prognostic factor in postoperative hearing outcomes in congenital aural atresia. *Acta Otolaryngol* 2011;131:701–07

Advanced Fiber Tracking in Early Acquired Brain Injury Causing Cerebral Palsy

F. Lennartsson, L. Holmström, A.-C. Eliasson, O. Flodmark, H. Forssberg, J.-D. Tournier, and B. Vollmer



ABSTRACT

BACKGROUND AND PURPOSE: Diffusion-weighted MR imaging and fiber tractography can be used to investigate alterations in white matter tracts in patients with early acquired brain lesions and cerebral palsy. Most existing studies have used diffusion tensor tractography, which is limited in areas of complex fiber structures or pathologic processes. We explored a combined normalization and probabilistic fiber-tracking method for more realistic fiber tractography in this patient group.

MATERIALS AND METHODS: This cross-sectional study included 17 children with unilateral cerebral palsy and 24 typically developing controls. DWI data were collected at 1.5T (45 directions, $b=1000$ s/mm²). Regions of interest were defined on a study-specific fractional anisotropy template and mapped onto subjects for fiber tracking. Probabilistic fiber tracking of the corticospinal tract and thalamic projections to the somatosensory cortex was performed by using constrained spherical deconvolution. Tracts were qualitatively assessed, and DTI parameters were extracted close to and distant from lesions and compared between groups.

RESULTS: The corticospinal tract and thalamic projections to the somatosensory cortex were realistically reconstructed in both groups. Structural changes to tracts were seen in the cerebral palsy group and included splits, dislocations, compaction of the tracts, or failure to delineate the tract and were associated with underlying pathology seen on conventional MR imaging. Comparisons of DTI parameters indicated primary and secondary neurodegeneration along the corticospinal tract. Corticospinal tract and thalamic projections to the somatosensory cortex showed dissimilarities in both structural changes and DTI parameters.

CONCLUSIONS: Our proposed method offers a sensitive means to explore alterations in WM tracts to further understand pathophysiologic changes following early acquired brain injury.

ABBREVIATIONS: CerPed = cerebral peduncle; CP = cerebral palsy; CSD = constrained spherical deconvolution; CST = corticospinal tract; FA = fractional anisotropy; FTA = fiber-tract assessment; M1 = primary motor cortex; MD = mean diffusivity; PLIC = posterior limb of the internal capsule; TRSI = thalamic projections to the somatosensory cortex

Cerebral palsy (CP) is a disorder of movement and posture caused by nonprogressive disturbances in the developing brain. Brain lesions that cause CP are commonly identified by visual inspection of conventional structural T1- and T2-weighted MR imaging. A range of macrostructural abnormalities has been

described.¹ However, subtle brain abnormalities may be missed on visual inspection.

Diffusion-weighted MR imaging can be used to infer the structural composition and integrity of neuronal tissue,² and white-matter fiber tractography can be used to trace fiber tracts noninvasively.³ Diffusion tensor imaging describes a single diffusion process in a voxel. However, most voxels contain multiple, often crossing, fiber populations.⁴ The use of probabilistic fiber tracking in diffusion models capable of resolving complex fiber struc-

Received February 26, 2014; accepted after revision July 5.

From the Department of Neuroradiology (F.L., O.F.), Karolinska University Hospital, Stockholm, Sweden; Departments of Clinical Neurosciences (F.L., O.F.) and Women's and Children's Health (L.H., A.-C.E., H.F., B.V.), Karolinska Institute, Stockholm, Sweden; The Florey Institute of Neuroscience and Mental Health (J.-D.T.), Melbourne, Victoria, Australia; Department of Medicine (J.-D.T.), University of Melbourne, Victoria, Australia; Centre for the Developing Brain (J.-D.T.) and Department of Biomedical Engineering (J.-D.T.), Division of Imaging Sciences and Biomedical Engineering, King's College London, London, United Kingdom; and Clinical Neurosciences, Clinical and Experimental Sciences (B.V.), Faculty of Medicine, University of Southampton, Southampton, United Kingdom.

This work was supported in part by grants from the Stockholm County Council (ALF project), the Swedish Medical Research Council, the Australian National Health and Medical Research Council, the Australian Research Council, and by a Marie Curie Fellowship for Experienced Researchers, FP6 Framework.

Please address correspondence to Finn Lennartsson, MD, Department of Neuroradiology, Karolinska University Hospital, SE-171 76 Stockholm, Sweden; e-mail: fnn.lennartsson@karolinska.se

Indicates open access to non-subscribers at www.ajnr.org

Indicates article with supplemental on-line table.

Indicates article with supplemental on-line photo.

Evidence-Based Medicine Level 2.

<http://dx.doi.org/10.3174/ajnr.A4072>

tures is likely to be beneficial when studying white matter tracts and could provide additional information about the pathophysiology of altered fiber pathways. Findings in recent studies in CP support this assumption.⁵⁻⁷

In CP, studies have shown alterations in major fiber tracts, including the corticospinal tract (CST), the corticobulbar tract, superior and posterior thalamic radiations, the superior longitudinal fasciculus, and transcallosal fibers (for a review, see Scheck et al⁸). Parametric changes include decreased fractional anisotropy (FA) and increased mean diffusivity (MD), indicating altered tract microstructure. Decreased tract volumes and fiber counts, which may be indicative of perturbations during tract development, have been described.⁸ Studies also have shown parametric changes that suggest secondary (Wallerian) neurodegeneration distant from the primary lesion site, with decreased FA and axial diffusivity (the largest tensor eigenvalue), increases in radial diffusivity (the mean of the 2 smaller tensor eigenvalues), but no changes or only slight increase in MD.^{5,9} Moreover, the overall severity of CP, measured by, for example, the Gross Motor Function Classification System,¹⁰ appears to correlate with diffusion parameters in motor^{9,11-13} and/or sensory pathways.¹⁴⁻¹⁶ In addition, correlations have been shown between diffusion measures in motor and sensory tracts and specific measures of sensory and/or motor functions.^{5-7,17-20} Some studies suggest that sensory and motor functions correlate more strongly with changes in the sensory pathways (superior and posterior thalamic radiation) than changes in the motor pathways (CST).^{6,19} These findings indicate that preservation of sensory pathways is important for motor function. However, most tractography studies in CP have used deterministic diffusion tensor tractography, which is a limitation because the algorithm cannot progress in areas where the tensor model shows a high uncertainty in the estimated fiber directions due to complex fiber architecture or pathologic changes.

In this study, we aimed to improve fiber tractography and characterization of motor and sensory fiber tracts in children with early acquired brain lesions by using a combined normalization and probabilistic fiber-tracking method. In addition, we aimed to use this method to characterize changes in gross morphology and in diffusion parameters close to and distant from the primary lesion.

MATERIALS AND METHODS

Participants

We examined a convenience sample of 17 children with unilateral spastic CP at the Gross Motor Function Classification System level I and the Manual Ability Classification System²¹ levels I–II. After we excluded poor-quality imaging data, 15 children (6 boys, 9 girls; median age, 12.4 years; range, 7.2–17 years) remained in the sample (On-line Table). Twenty-four typically developing children served as controls (9 boys, 15 girls; median age, 12.7 years; range, 8.8–17.3 years; 23 right-handed). The lesion side is referred to as the hemisphere where structural abnormalities are detected on visual inspection of conventional structural MR imaging (On-line Table). In cases of bilateral lesions, the lesion side is defined as the most affected side as assessed by visual inspection. Measures from the lesion side in the subjects with CP are com-

pared with measures in the hemisphere ipsilateral to the dominant hand in the controls.

Neuroimaging

MR imaging was performed on a 1.5T MR imaging system (Signa Excite Twinspeed; GE Healthcare, Milwaukee, Wisconsin). Conventional structural MR imaging included T1-, T2-weighted, and FLAIR images. DWI (TR/TE = 10,000/76 ms, voxel size = 2.3 mm³ reconstructed to 1.72 mm² in-plane) included 6 $b = 0$ images followed by 45 gradient directions with $b = 1000$ s/mm². Conventional structural MRIs were visually assessed for lesion type, location, and extent. All controls had normal findings on MRI, and in the group with unilateral CP, a representative spectrum of lesions was seen (On-line Table).

Preprocessing of DWI

Tools in the FSL package (Version 4.0; <http://www.fmrib.ox.ac.uk/fsl>)²² were used for distortion and motion correction and to realign the gradient directions.²³ MRtrix (<http://neuro.debian.net/pkgs/mrtrix.html>)²⁴ was used for estimation of diffusion tensors and fiber orientation distributions with constrained spherical deconvolution (CSD) to assess multiple fiber populations in every voxel. From the diffusion tensors parametric maps of MD, FA, axial diffusivity, and radial diffusivity were computed.

All sections in all diffusion volumes and FA maps were visually inspected for artifacts. In addition, for each section, the mean signal was plotted over all diffusion volumes to detect large signal changes indicating gross imaging artifacts. Two of the original 17 subjects (1 child with a cortical malformation and 1 with white matter damage of immaturity) were excluded due to artifacts.

Spatial Normalization of DWI

A study-specific FA template was created by using symmetric normalization.²⁵ A subset of 6 controls and 7 subjects (randomly selected after excluding subjects with a severe extent of WM damage and the patient with schizencephaly; On-line Table) were chosen for constructing the template. A $b=0$ template and a color-coded FA template were constructed as the average of the corresponding images mapped into template space. All control and subject FA maps were then registered to this FA template. To check the consistency of the spatial registration, we mapped the FA template onto each subject's FA map by using the inverse transform. The results showed satisfactory agreement in the central and peripheral WM.

ROI Definition in Template Space

Regions of interest in the cerebral peduncles (CerPeds), the posterior limb of the internal capsule (PLIC), the thalami, and the primary motor (M1) and somatosensory cortex were manually defined on the study template (On-line Fig).

ROI Mapping and Refinement

All ROIs in template space were mapped onto each subject's native space. Transforming a binary region-of-interest image by using a continuous deformation field generates a nonbinary image in native space; therefore, the mapped region of interest had to be thresholded. Having explored several lower thresholds (0.1–0.5),

we chose a threshold of ≥ 0.2 to ensure anatomically adequate mapping of the template ROIs. Mapped ROIs were visually inspected and manually edited when required to ensure accurate anatomic placement. In addition, to prevent tracts from entering spaces with CSF, we multiplied the fiber-orientation distribution field by a subject-specific mask of the WM. The WM mask effectively confined the tracking to WM-dominated voxels but did not exclude any voxels in the thalami, for example.

Fiber Tracking of the Cortical Spinal Tract and the Thalamic Projections to the Somatosensory Cortex

Probabilistic fiber tracking was performed on the CSD-estimated fiber orientation distribution fields with the mapped ROIs as input by using default tracking parameters. The CSTs were tracked by seeding in M1 and by using the PLIC and the cerebral peduncles on the same side as Waypoint masks. The thalamic projections to the somatosensory cortex (TRS1s) were tracked by seeding in the thalamus and by using the somatosensory cortex as a Waypoint mask. The fiber-tracking algorithm was run until 10^4 streamlines had been produced. Tracts that did not reach this number within 10^8 trials were considered to have an unrealistically low probability of connectivity and were excluded from further analysis.

Fiber tracts were converted to probability maps with voxel values equal to the fraction of the number of passing and generated streamlines. These were thresholded at 0.01 (1% of the total number of streamlines) and were considered to be the core of the fiber tracts. The ROIs for the PLIC and the cerebral peduncle were used to separate the CST probability maps into different parts: between M1 and the cerebral peduncle (CST-M1 to CerPed), between the PLIC and the cerebral peduncle (CST-PLIC to CerPed), and between M1 and the PLIC (CST-M1 to PLIC, not including PLIC-level voxels). The thalamic ROIs were used to remove thalamic voxels from the TRS1 probability maps. The complete processing from region-of-interest definition in the template space to the thresholded probability maps was performed twice in all participants by the primary study rater (F.L.) and, in a randomly selected subset of 7 subjects and 7 controls, by rater B.V., to evaluate the intra- and interrater reproducibility. To rule out partial volume effects as a confounder, we generated histograms of the MD voxel values in all probability maps; outliers were observed in only a very small proportion of voxels.

To assess diffusion parameters along CST and TRS1, we extracted the median voxel value (to minimize the influence of outliers) for FA and MD within the thresholded probability maps. In the CST-PLIC to CerPed, where the descending motor fibers are the dominating fiber population, the axial diffusivity and radial diffusivity were also extracted. For statistical comparisons, the mean of the median values for the trials of rater F.L. was used.

Qualitative Fiber-Tract Assessment

From visual inspection of the fiber tracts, 4 distinct, spatial characteristics deviating from what is normally expected were identified in lesion-affected areas: dislocation of the major branch of the tract; local, continuous splitting of the tract into 2 separate

branches; compaction of a nonsplit tract; or failure to delineate the fiber tract (as described above). A fiber tract was found to have an atypical fiber-tract assessment (FTA) if ≥ 1 of these scenarios was observed along the tract and was confirmed on the thresholded probability map (Fig 1).

Statistics

Statistical analyses were performed by using the Statistics Toolbox in Matlab (MathWorks, Natick, Massachusetts). To assess intra- and interrater reproducibility of fiber tracts, we performed pairwise comparisons of the spatial matching between the thresholded probability maps by calculating the Cohen κ coefficient.²⁶ Comparison of DTI parameters between subjects and controls was done by using the nonparametric Mann-Whitney U test (2-tailed, with $P < .05$ as the significance threshold).

Ethics

The study was granted ethics approval by the Regional Ethics Committee Stockholm North. All children and parents gave informed written consent.

RESULTS

Reproducibility of Generated Fiber Tracts

The normalization and fiber-tracking method showed high intra- and interrater reproducibility for all fiber tracts. Cohen κ values for the intrarater reproducibility were in the range of 0.88–0.98 for the controls and 0.81–0.94 for the subjects. For the interrater reproducibility, Cohen κ values were in the range of 0.84–0.91 for the controls and 0.87–0.92 for the subjects.

Applicability of the Fiber-Tracking Method in Typically Developing Controls

Both the CST and the TRS1 were successfully reconstructed in agreement with expected neuroanatomy (column 1, Fig 1). In 3 controls the CST and in another 3 controls the TRS1 had atypical FTA with minor splits. None of the splits could be explained by any abnormalities on conventional structural MR imaging.

Applicability of the Fiber-Tracking Method in Subjects with Unilateral CP

Both the CST and TRS1 were successfully reconstructed in most subjects with CP (On-line Table). On the nonlesion side, FTA for the TRS1 was typical for all subjects, whereas FTA for the CST was atypical in 1 subject having a minor split but without obvious underlying pathology (subject 5, On-line Table). In contrast, on the lesion side, the TRS1 and the CST showed atypical FTA in 7/15 and 10/15 subjects, respectively, and underlying pathologic changes were present in all these subjects (On-line Table). While atypical FTA was more frequently observed in the CST than in TRS1, in most cases, both tracts were affected simultaneously, though rarely in the same way.

DTI Parameters in Fiber Tracts

Diffusion parameters (FA, MD, axial diffusivity, and radial diffusivity) for the CST and TRS1 were compared between the subjects with CP and the controls (Fig 2).

On the nonlesion side, both the CST-M1 to CerPed and its subpart CST-M1 to PLIC showed significant increases in MD

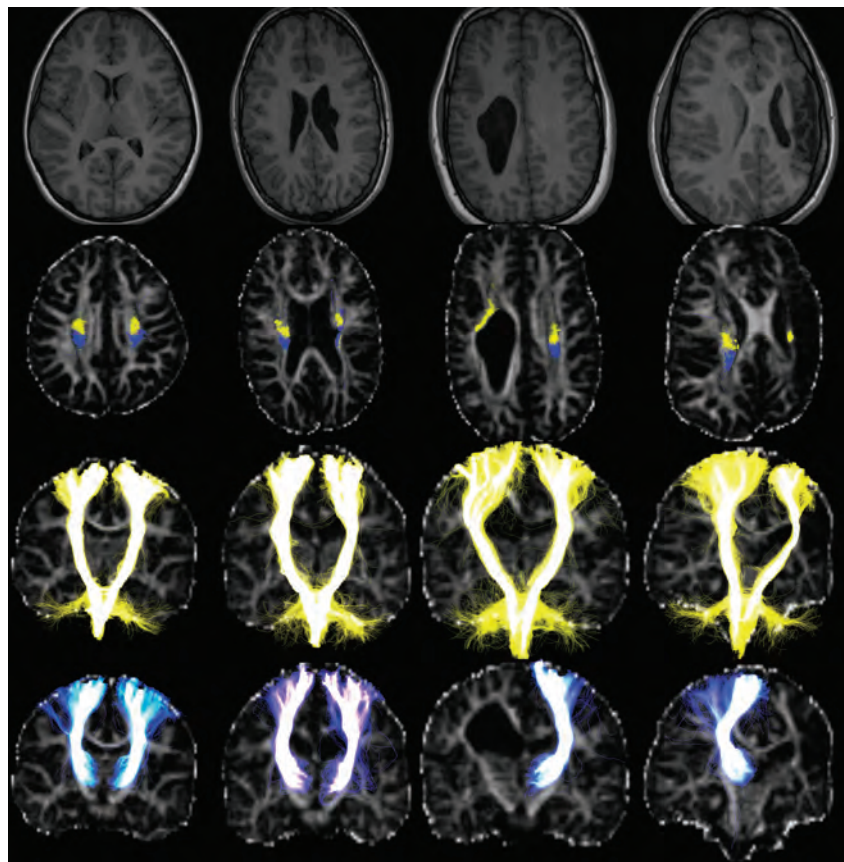


FIG 1. Tracking results of the CSTs (yellow) and the TRSIs (blue) in a healthy control (column 1) and 3 subjects with unilateral CP (columns 2–4, On-line Table). Images, shown in radiologic orientation, include T1-weighted images (row 1) and tracts superimposed on FA maps in the axial section at the level of the upper corona radiata (row 2) and entire coronal projections (rows 3–4). In the control (column 1), the CSTs are initiated from the entire M1 ROIs and follow consistent, expected paths down to the brain stem. The TRSIs are primarily initiated in the ventroposterior parts of the thalami, then travel posterior to the CSTs in the corona radiata, and spread over a large part of the somatosensory cortex ROIs. Subject 9 (column 2) has a periventricular pseudocyst at the level of corona radiata, which causes local splits to the left TRS1 and left CST, which are seen to partly share locations, and dislocate the major branch of the left CST. Subject 12 (column 3) has a large right WM lesion obstructing the anticipated courses of the TRSIs and the CSTs, making tracking of the TRS1 impossible and dislocating the right CST. Subject 14 (column 4) had a left focal infarct with extensive damage to the entire left hemisphere and severe WM damage above the PLIC, which confined the left CST to a thin sliver of WM at the level of the corona radiata and made the left TRS1 nontrackable.

($P < .05$ and $P < .05$) in the CP group compared with controls, whereas no changes in diffusion parameters were found in the subpart CST-PLIC to CerPed compared with controls. The TRS1 showed significant increase in MD ($P < .05$) in the CP group compared with controls.

On the lesion side in the CP group with successful tracking of the CST ($n = 12$), both CST-M1 to CerPed and CST-M1 to PLIC showed a significant decrease in FA ($P < .001$ and $P < .001$) and an increase in MD ($P < .001$ and $P < .001$) compared with controls. The subpart CST-PLIC to CerPed showed a significant decrease in FA ($P < .001$) and axial diffusivity ($P < .05$) and an increase in radial diffusivity ($P < .001$) compared with controls. The TRS1 ($n = 11$) showed a significant increase in MD ($P < .01$) compared with controls.

DISCUSSION

The CST and the TRS1 could be reconstructed according to expected neuroanatomy. We saw that DTI parameters varied along the CST in primary and secondary affected areas with traits consistent with primary and secondary (Wallerian) neurodegeneration. Both CST and TRS1 were affected on the lesion side; how-

ever, they showed different patterns on FTA assessment and in DTI parameters, which suggest that alterations were more pronounced in the CST than in the TRS1.

Fiber-Tracking Method

Manually drawn ROIs have been used in most existing studies in CP, either for comparing diffusion parameters or as input for fiber tractography.⁸ Often inter- and intrarater reproducibility statistics are reported, but ROIs may still not have been defined in comparable locations among subjects due to differences in section orientation. Defining ROIs on a normalized template could improve this deficiency. However, normalization of brains with lesions is difficult and has been used in few previous studies in CP.^{16,27,28} In our study, the symmetric normalization algorithm²⁵ allowed accurate registration of central GM and WM, even in subjects with large brain lesions. The cortical GM and subcortical WM were less accurately registered, most likely due to intersubject variability in cortical sulcation patterns. Thus, the native-space ROIs of M1 and the somatosensory cortex had to be edited slightly in some individuals to ensure anatomically correct placement. Our sug-

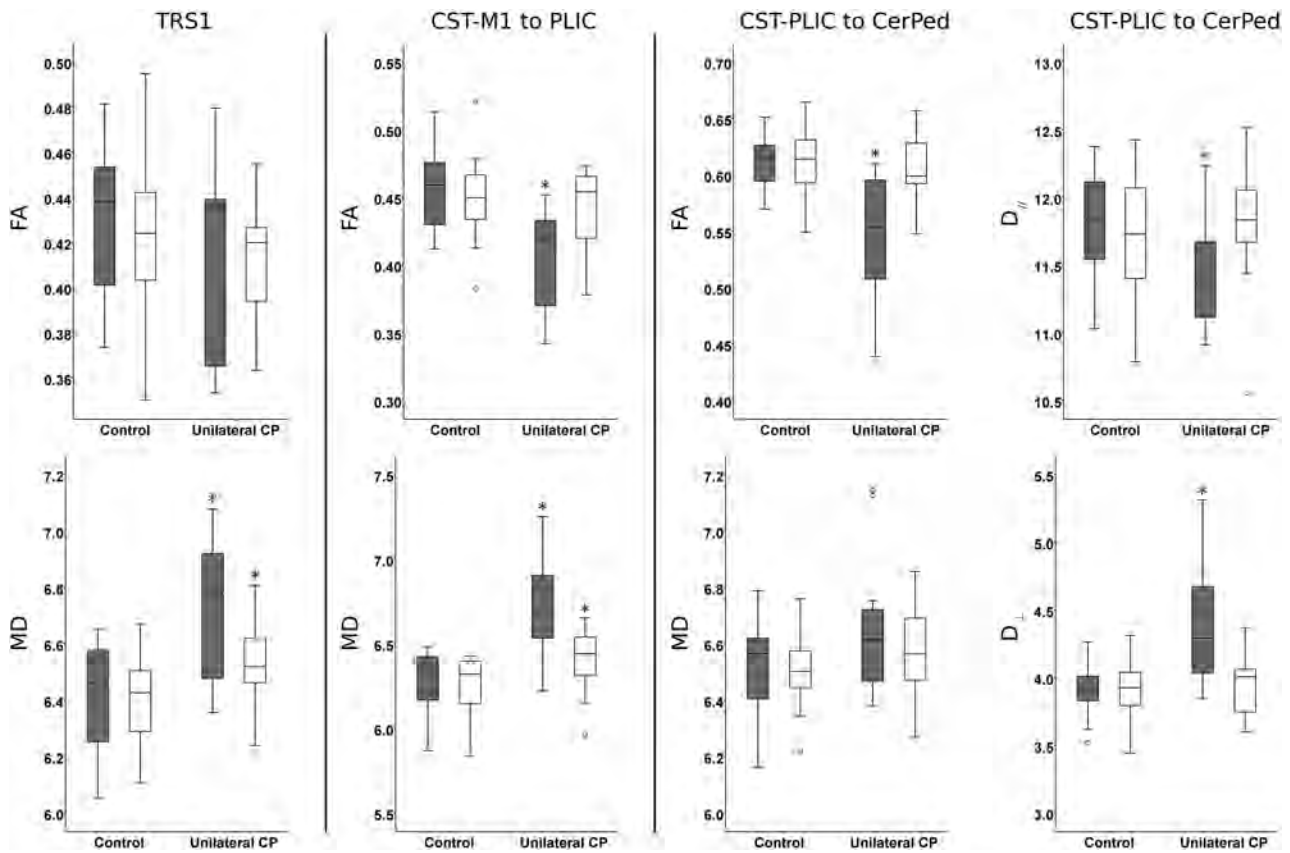


FIG 2. Boxplots of diffusion parameters in the TRS1, CST-M1 to PLIC, and CST-PLIC to CerPed in the group with unilateral CP and controls on the lesion (gray) and nonlesion (white) sides. Diffusivity is expressed as 10^{-4} mm²/s. The asterisk indicates a significant difference between the group with unilateral CP and controls by statistical comparisons using the Mann-Whitney *U* test (2-tailed; significance level, .05).

gested method showed high intra- and interrater reproducibility, indicating that the method is robust.

Probabilistic fiber tracking with CSD of the CST and the TRS1 from their assumed starting points and including distant Waypoints appears to provide reliable and anatomically accurate tracking results. This finding is supported by Rose et al⁶ and Tsao et al,⁷ who also used probabilistic CSD fiber tractography to successfully track motor and sensory pathways. An alternative could have been to define the cortical ROIs from functional data such as fMRI. Thus, parts of the motor and somatosensory strips, such as the hand areas, could be targeted separately. However, the fMRI localization of functional areas is not perfect, the resolution is relatively poor, and it is not certain that fMRI would elicit a functional response in the CP group. Moreover, in early brain lesions, there are indications of different reorganizational patterns in the motor and somatosensory systems in CP. It has been shown that somatosensory functions show mainly ipsilesional reorganization patterns, whereas the motor functions can show ipsilesional, contralesional, or mixed reorganization patterns.²⁹ Functional MR imaging activation sites may therefore not be relevant as cortical targets because we were interested in the structure of the ipsi- and contralesional CST and TRS1.

Some case reports show diffusion tensor tractograms of thalamocortical connections that are displaced by lesions but still reach cortical areas in individuals with early acquired brain lesions (eg, Staudt et al³⁰; Guzzetta et al³¹). With our method, we

observed, in several cases and in all lesion types, that both the CST and TRS1 on the lesion side have altered paths when passing lesion-affected areas. These fiber tracts showed expected distributions in their end points and displayed plausible deviations from their expected route, and both the CST and the adjacent TRS1 showed very similar but not identical behavior on FTA. Likewise, when a tract could not be delineated, the reason was, in all cases, an interruption of the tract by the lesion. At the same time, tracts on the nonlesion side followed paths consistent with those observed in the controls, indicating that the tracking method is robust.

Qualitative Fiber-Tract Assessment

We saw atypical FTA in many cases for both the CST and the TRS1 on the lesion side. The tracts that were classified as nontractable, compacted, or dislocated all corresponded with macrostructural abnormalities, but the splits detected were both plausible splits caused by the lesion and smaller splits that had no macrostructural correlate on conventional structural MR imaging. The occurrence of small splits without any macrostructural correlate might be explained by the limited performance of CSD with the current imaging protocol. Sampling more directions and using a larger b-value of 2000–3000 s/mm² would improve the ability of CSD to resolve the fiber-orientation distributions in cases of multiple fiber populations²⁴ but would make motion and eddy-current correction harder.

DTI Parameter Changes in CST and TRS1

On the nonlesion side, the CST-PLIC to CerPed did not show any changes in DTI parameters, whereas farther up, both CST-M1 to PLIC and TRS1 showed similar significant increases in MD only, which were much less pronounced than on the lesion side. DWI increases the sensitivity of detecting lesions that commonly display increased MD. Our findings are suggestive of additional subtle lesions that can be detected with analysis of DTI parameters in patients without overt bilateral lesions on visual inspection of conventional structural MR imaging. A more speculative explanation may be secondary (Wallerian) neurodegeneration in these areas of intersecting pathways,³² with involvement of transcallosal connections from the lesion side, which has been shown to be affected in CP.²⁰ In the future, it may be possible to investigate changes in the individual fiber populations in these areas by using parameters derived from multifiber models (eg, Raffelt et al³³; Dell'Acqua et al³⁴).

On the lesion side, the CST distant from the primary lesion site (CST-PLIC to CerPed) showed a pattern of diffusion measures indicative of secondary (Wallerian) neurodegeneration, whereas closer to the lesion, the CST-M1 to PLIC showed a pattern compatible with the signs of primary neurodegeneration.³² This finding is in line with the results of Thomas et al,³⁵ who showed similar changes close to and distant from the lesion, and with Glenn et al⁹ in their study of the CST between the PLIC and the cerebral peduncle. The TRS1 showed a significant increase in MD but no changes in FA, which do not indicate any specific pathologic pattern. Although the interpretation above of DTI parameters is the current prevailing view, there are several factors, both on a microscopic cellular and macroscopic architectural level, that will influence them and it is difficult to infer which factors actually account for a change.³⁶ Also, even if certain DTI changes are identified in a disease model, the inverse may not always hold; moreover, generalization of DTI changes from one disease model may not be valid in other situations. This is a potential problem in early brain lesions because we see a large spectrum of both lesions and etiologies. In our opinion, this issue remains unresolved. Many studies contain heterogeneous CP groups and/or lesion types.⁸ Nevertheless, we did show that different parts of the CST display distinct patterns in DTI parameters, and extracting parameters as averages over large parts of the tracts, as done in most studies, might be misleading. Furthermore, on the lesion side, the TRS1 and the CST-M1 to PLIC both showed similar, significant increases in MD, but only CST-M1 to PLIC showed significant change in FA. The only study to report DTI parameters in both CST and superior thalamocortical fibers in unilateral CP is Thomas et al,³⁵ who also saw this distinction between FA and MD. The CST and TRS1 are affected differently in our patient cohort, as indicated by the FTAs and DTI parameters. We cannot infer the underlying cause of this difference from the limited information provided by DTI parameters in areas with complex fiber architecture. One speculative explanation could be that we see reactive changes in the somatosensory projections, and indeed, it has been proposed that there is a greater capacity for ipsilesional reorganization in the somatosensory system than in the motor system.²⁹

Limitations

Our sample is representative regarding the spectrum of lesion types in unilateral CP; however, the lesion groups are not equally represented. The study is partly limited by the fact that on the lesion side, we could not track the CST in 3/15 and TRS1 in 4/15 subjects with CP. Hence, we could not evaluate any DTI parameters along those tracts. It may have been possible to delineate more of these tracts by using an improved DWI protocol by increasing the number of diffusion directions and the b-value.

CONCLUSIONS

We have successfully used a normalization method for improved region-of-interest definition and probabilistic CSD fiber tracking in individuals with early brain lesions and unilateral CP. Our study demonstrated structural changes in the CST and the TRS1 on the lesion side, which could be linked to underlying pathologic changes as seen on conventional structural MR imaging. Analysis of DTI parameters along the CST showed traits of primary neurodegeneration in lesion areas and distant secondary (Wallerian) neurodegeneration, emphasizing the importance of analyzing different parts of a tract separately. There were dissimilarities in both structural changes and in DTI parameters between the CST and TRS1 on the lesion side indicating differences in how a tract is affected by the injury. By providing sensitive means to, first, normalize and define ROIs and, second, to explore WM tracts in areas with complex white matter architecture, our methods improve interpretation of diffusion measures in early acquired brain lesions and, by inference, of underlying pathophysiologic changes.

Disclosures: Finn Lennartsson—*RELATED: Grant:* supported by grants provided by the Stockholm County Council (ALF project). Linda Holmström—*RELATED:* financed by one of the postgraduate programs at Karolinska Institute.* Ann-Christin Eliasson—*UNRELATED: Grants/Grants Pending:* Swedish Research Council, Karolinska Institute, *Comments:* general grants including this study; *Stock/Stock Options:* Handfast AB, *Comments:* small agency for education (does not give stock dividends). Hans Forsberg—*UNRELATED: Board Membership:* scientific foundations, *Comments:* Center for Molecular Medicine, Sunnedahls Handikappfond; *Grants/Grants Pending:* Swedish Medical Research Council,* Foundation Olle Engkvist Byggnästare,* Swedish Brain Foundation,* Foundation Frimurarna Barnhuset,* Swedish Research Council (5925),* Swedish Foundation for Strategic Research,* Berzelii Center Stockholm Brain Institute (Vinnova and Swedish Research Council),* Strategic Neuroscience Program at Karolinska Institute,* Knut and Alice Wallenberg Foundation,* and a research application to Promobilia (I MSEK) pending*;*Royalties:* Royalties are paid to me from Mac Keith Press, London, and from Studentlitteratur, Lund, for chapters in textbooks.* Jacques-Donald Tournier—*RELATED: Grant:* Australian National Health and Medical Research Council,* Australian Research Council.* Brigitte Vollmer—*RELATED: Grant:* Marie Curie Fellowship for Experienced Researchers, FP6 Framework. *Money paid to the institution.

REFERENCES

1. Bax M, Tydeman C, Flodmark O. **Clinical and MRI correlates of cerebral palsy.** *JAMA* 2006;296:1602–08
2. Beaulieu C. **The basis of anisotropic water diffusion in the nervous system: a technical review.** *NMR Biomed* 2002;15:435–55
3. Mori S, Crain BJ, Chacko VP, et al. **Three-dimensional tracking of axonal projections in the brain by magnetic resonance imaging.** *Ann Neurol* 1999;45:265–69
4. Jeurissen B, Leemans A, Tournier JD, et al. **Investigating the prevalence of complex fiber configurations in white matter tissue with diffusion magnetic resonance imaging: prevalence of multifiber voxels in WM.** *Hum Brain Mapp* 2013;34:2747–66
5. Holmström L, Lennartsson F, Eliasson AC, et al. **Diffusion MRI in**

- corticofugal fibers correlates with hand function in unilateral cerebral palsy. *Neurology* 2011;77:775–83
6. Rose S, Guzzetta A, Pannek K, et al. MRI structural connectivity, disruption of primary sensorimotor pathways, and hand function in cerebral palsy. *Brain Connect* 2011;1:309–16
 7. Tsoa H, Pannek K, Boyd RN, et al. Changes in the integrity of thalamocortical connections are associated with sensorimotor deficits in children with congenital hemiplegia. *Brain Struct Funct* 2013 Oct 22. [Epub ahead of print]
 8. Scheck SM, Boyd RN, Rose SE. New insights into the pathology of white matter tracts in cerebral palsy from diffusion magnetic resonance imaging: a systematic review. *Dev Med Child Neurol* 2012;54:684–96
 9. Glenn OA, Ludeman NA, Berman JI, et al. Diffusion tensor MR imaging tractography of the pyramidal tracts correlates with clinical motor function in children with congenital hemiparesis. *AJNR Am J Neuroradiol* 2007;28:1796–802
 10. Palisano R, Rosenbaum P, Walter S, et al. Development and reliability of a system to classify gross motor function in children with cerebral palsy. *Dev Med Child Neurol* 1997;39:214–23
 11. Kidokoro H, Kubota T, Ohe H, et al. Diffusion-weighted magnetic resonance imaging in infants with periventricular leukomalacia. *Neuropediatrics* 2008;39:233–38
 12. Murakami A, Morimoto M, Yamada K, et al. Fiber-tracking techniques can predict the degree of neurologic impairment for periventricular leukomalacia. *Pediatrics* 2008;122:500–06
 13. Rha D, Chang WH, Kim J, et al. Comparing quantitative tractography metrics of motor and sensory pathways in children with periventricular leukomalacia and different levels of gross motor function. *Neuroradiology* 2012;54:615–21
 14. Trivedi R, Agarwal S, Shah V, et al. Correlation of quantitative sensorimotor tractography with clinical grade of cerebral palsy. *Neuroradiology* 2010;52:759–65
 15. Yoshida S, Hayakawa K, Yamamoto A, et al. Quantitative diffusion tensor tractography of the motor and sensory tract in children with cerebral palsy. *Dev Med Child Neurol* 2010;52:935–40
 16. Lee JD, Park HJ, Park ES, et al. Motor pathway injury in patients with periventricular leukomalacia and spastic diplegia. *Brain* 2011;134:1199–210
 17. Bleyenheuff Y, Grandin CB, Cosnard G, et al. Corticospinal dysgenesis and upper-limb deficits in congenital hemiplegia: a diffusion tensor imaging study. *Pediatrics* 2007;120:e1502–11
 18. Ludeman NA, Berman JI, Wu YW, et al. Diffusion tensor imaging of the pyramidal tracts in infants with motor dysfunction. *Neurology* 2008;71:1676–82
 19. Hoon AH Jr, Stashinko EE, Nagae LM, et al. Sensory and motor deficits in children with cerebral palsy born preterm correlate with diffusion tensor imaging abnormalities in thalamocortical pathways. *Dev Med Child Neurol* 2009;51:697–704
 20. Weinstein M, Green D, Geva R, et al. Interhemispheric and intrahemispheric connectivity and manual skills in children with unilateral cerebral palsy. *Brain Struct Funct* 2014;219:1025–40
 21. Eliasson AC, Krumlinde-Sundholm L, Rösblad B, et al. The Manual Ability Classification System (MACS) for children with cerebral palsy: scale development and evidence of validity and reliability. *Dev Med Child Neurol* 2006;48:549–54
 22. Behrens TE, Berg HJ, Jbabdi S, et al. Probabilistic diffusion tractography with multiple fibre orientations: what can we gain? *Neuroimage* 2007;34:144–55
 23. Leemans A, Jones DK. The B-matrix must be rotated when correcting for subject motion in DTI data. *Magn Reson Med* 2009;61:1336–49
 24. Tournier JD, Calamante F, Connelly A. MRtrix: diffusion tractography in crossing fiber regions. *Int J Imaging Syst Technol* 2012;22:53–66
 25. Avants BB, Epstein CL, Grossman M, et al. Symmetric diffeomorphic image registration with cross-correlation: evaluating automated labeling of elderly and neurodegenerative brain. *Med Image Anal* 2008;12:26–41
 26. Landis JR, Koch GG. An application of hierarchical kappa-type statistics in the assessment of majority agreement among multiple observers. *Biometrics* 1977;33:363–74
 27. Faria AV, Hoon A, Stashinko E, et al. Quantitative analysis of brain pathology based on MRI and brain atlases: applications for cerebral palsy. *Neuroimage* 2011;54:1854–61
 28. Yoshida S, Faria AV, Oishi K, et al. Anatomical characterization of athetotic and spastic cerebral palsy using an atlas-based analysis: anatomical characterization of cerebral palsy. *J Magn Reson Imaging* 2013;38:288–98
 29. Guzzetta A, Bonanni P, Biagi L, et al. Reorganisation of the somatosensory system after early brain damage. *Clin Neurophysiol* 2007;118:1110–21
 30. Staudt M, Braun C, Gerloff C, et al. Developing somatosensory projections bypass periventricular brain lesions. *Neurology* 2006;67:522–25
 31. Guzzetta A, D'Acunto G, Rose S, et al. Plasticity of the visual system after early brain damage: review. *Dev Med Child Neurol* 2010;52:891–900
 32. Pierpaoli C, Barnett A, Pajevic S, et al. Water diffusion changes in Wallerian degeneration and their dependence on white matter architecture. *Neuroimage* 2001;13:1174–85
 33. Raffelt D, Tournier JD, Rose S, et al. Apparent fibre density: a novel measure for the analysis of diffusion-weighted magnetic resonance images. *Neuroimage* 2012;59:3976–94
 34. Dell'Acqua F, Simmons A, Williams SC, et al. Can spherical deconvolution provide more information than fiber orientations? Hindrance modulated orientational anisotropy, a true-tract specific index to characterize white matter diffusion. *Hum Brain Mapp* 2013;34:2464–83
 35. Thomas B, Eyssen M, Peeters R, et al. Quantitative diffusion tensor imaging in cerebral palsy due to periventricular white matter injury. *Brain* 2005;128(pt 11):2562–77
 36. Wheeler-Kingshott CA, Cercignani M. About “axial” and “radial” diffusivities. *Magn Reson Med* 2009;61:1255–60

Apparent Diffusion Coefficient Scalars Correlate with Near-Infrared Spectroscopy Markers of Cerebrovascular Autoregulation in Neonates Cooled for Perinatal Hypoxic-Ischemic Injury

A. Tekes, A. Poretti, M.M. Scheurkogel, T.A.G.M. Huisman, J.A. Howlett, E. Alqahtani, J.-H. Lee, C. Parkinson, K. Shapiro, S.-E. Chung, J.M. Jennings, M.M. Gilmore, C.W. Hogue, L.J. Martin, R.C. Koehler, F.J. Northington, and J.K. Lee



ABSTRACT

BACKGROUND AND PURPOSE: Neurologic morbidity remains high in neonates with perinatal hypoxic-ischemic injury despite therapeutic hypothermia. DTI provides qualitative and quantitative information about the microstructure of the brain, and a near-infrared spectroscopy index can assess cerebrovascular autoregulation. We hypothesized that lower ADC values would correlate with worse autoregulatory function.

MATERIALS AND METHODS: Thirty-one neonates with hypoxic-ischemic injury were enrolled. ADC scalars were measured in 27 neonates (age range, 4–15 days) in the anterior and posterior centrum semiovale, basal ganglia, thalamus, posterior limb of the internal capsule, pons, and middle cerebellar peduncle on MRI obtained after completion of therapeutic hypothermia. The blood pressure range of each neonate with the most robust autoregulation was identified by using a near-infrared spectroscopy index. Autoregulatory function was measured by blood pressure deviation below the range with optimal autoregulation.

RESULTS: In neonates who had MRI on day of life ≥ 10 , lower ADC scalars in the posterior centrum semiovale ($r = -0.87, P = .003, n = 9$) and the posterior limb of the internal capsule ($r = -0.68, P = .04, n = 9$) correlated with blood pressure deviation below the range with optimal autoregulation during hypothermia. Lower ADC scalars in the basal ganglia correlated with worse autoregulation during rewarming ($r = -0.71, P = .05, n = 8$).

CONCLUSIONS: Blood pressure deviation from the optimal autoregulatory range may be an early biomarker of injury in the posterior centrum semiovale, posterior limb of the internal capsule, and basal ganglia. Optimizing blood pressure to support autoregulation may decrease the risk of brain injury in cooled neonates with hypoxic-ischemic injury.

ABBREVIATIONS: ACS = anterior centrum semiovale; HII = hypoxic-ischemic injury; HVx = hemoglobin volume index; IQR = interquartile ranges; NIRS = near-infrared spectroscopy; MAP = mean arterial blood pressure; MAP_{OPT} = optimal MAP; PCS = posterior centrum semiovale; PLIC = posterior limb of the internal capsule; PP = putamen and globus pallidus

Neonatal hypoxic-ischemic injury (HII) may cause significant and life-long neurologic disabilities.^{1,2} Although therapeutic

hypothermia has improved overall neurologic outcomes, death and disability still occur in 30%–70% of affected neonates despite treatment.^{3–5} Early identification of brain injury and risk stratification of neonates with HII are critical for prognostication, adjuvant therapies, family counseling, and additional refinement of hypothermia protocols. Qualitative and quantitative MR imaging serves as an early biomarker of neurologic outcome in HII.^{5,6} Advanced MR imaging techniques such as DTI can detect and quantify abnormalities that may be subtle or under-recognized by conventional MR imaging alone. DTI provides information about the tissue microstructure in vivo by measuring the 3D magnitude, shape, and direction of diffusion of water molecules within the brain.⁷ ADC allows quantification of the magnitude of water dif-

Received April 14, 2014; accepted after revision July 6.

From the Division of Pediatric Radiology and Pediatric Neuroradiology (A.T., A.P., M.M.S., T.A.G.M.H., E.A.), Department of Radiology; Neurosciences Intensive Care Nursery Program (A.T., A.P., T.A.G.M.H., J.A.H., C.P., K.S., M.M.G., F.J.N., J.K.L.); Division of Neonatology, (J.A.H., C.P., K.S., M.M.G., F.J.N.), Department of Pediatrics; Department of Anesthesiology and Critical Care Medicine (J.-H.L., C.W.H., R.C.K.); Division of General Pediatrics and Adolescent Medicine (S.-E.C., J.M.J.), Department of Pediatrics; Center for Child and Community Health Research (S.-E.C., J.M.J., J.K.L.); and Division of Neuropathology (L.J.M.), Department of Pathology, Johns Hopkins University School of Medicine, Baltimore, Maryland.

This work was supported by a research grants from Covidien (Boulder, Colorado; J.K.L.); Thomas Wilson Sanitarium for Children Research Foundation (Baltimore, Maryland; J.K.L.); American Heart Association (Dallas, Texas; J.K.L.); International Anesthesia Research Society (San Francisco, California; J.K.L.); and National Institutes of Health NS060703 (Bethesda, Maryland; R.C.K.), National Institutes of Health R01HL092259 (C.W.H.), and National Institutes of Health HD070996 (F.J.N.).

Please address correspondence to Aylin Tekes, MD, Division of Pediatric Radiology and Section of Pediatric Neuroradiology, Russell H. Morgan Department of Radiology and Radiological Sciences, Johns Hopkins University School of Medicine, 1800

Orleans St, Zayed 4th floor, Room 4155, Baltimore, MD 21205; e-mail: atekes1@jhmi.edu

Indicates open access to non-subscribers at www.ajnr.org

<http://dx.doi.org/10.3174/ajnr.A4083>

fusion within the brain noninvasively. Decreased diffusion (characterized by low ADC values) is a common feature of hypoxic-ischemic injury in the acute and early subacute phases.⁸

Near-infrared spectroscopy (NIRS) is a noninvasive, bedside monitor that can estimate changes in cerebral blood flow. Ensuring stable cerebral perfusion is critical for preventing secondary brain injury after HII. Cerebrovascular autoregulation maintains steady cerebral blood flow across changes in blood pressure within a specific range of mean arterial blood pressure (MAP). The hemoglobin volume index (HVx) measures vasoreactivity (which mediates autoregulation) by correlating data derived from NIRS to MAP.^{9,10} The range of MAP with the most robust vasoreactivity and optimized autoregulation is called the “optimal MAP” (MAP_{OPT}) and can be identified with HVx.^{6,11} We hypothesized that lower ADC scalars would correlate with greater blood pressure deviation below MAP_{OPT} in neonates with HII who received therapeutic hypothermia.

MATERIALS AND METHODS

This study was approved by our institutional review board. Near-term and term neonates (35 gestational weeks and later) with moderate or severe HII were prospectively enrolled for 27 months, after obtaining written informed consent from the parents. Criteria for HII were based on the clinical trial of hypothermia in HII of the Eunice Kennedy Shriver National Institute of Child Health and Human Development Neonatal Research Network.³ All enrolled neonates had moderate-to-severe encephalopathy. The neonates’ parents had to speak English or Spanish, the languages available on the consent form. Exclusion criteria were lack of an arterial blood pressure catheter, congenital anomalies that make cooling unsafe, or coagulopathy with active bleeding.

Therapeutic Hypothermia Protocol

Clinical care was determined by the neonatology team and clinical protocol. Hypothermia was delivered with a whole-body cooling blanket (Mul-T-Blanket Hyper/Hypothermia Blanket and Mul-T-Pad Temperature Therapy Pad; Gaymar Medi-Therm III; Gaymar Industries, Orchard Park, New York) to maintain a rectal temperature of $33.5 \pm 0.5^\circ\text{C}$ for 72 hours. Rewarming was conducted during 6 hours (goal, $0.5^\circ\text{C}/\text{h}$) to normothermia (36.5°C). Sedation was provided with opiate infusions and boluses. Hemodynamic goals and the decision of whether to initiate vasopressor or pharmacologic inotropic support were determined by the clinicians. When vasoactive medications were indicated, dopamine was given followed by dobutamine, epinephrine, or milrinone as clinically indicated. Neonates were monitored with full montage electroencephalograms during hypothermia and after rewarming and with continuous amplitude-integrated electroencephalogram monitoring (Brainz BRM3 Monitor or CFM Olympic Brainz Monitor; Natus Medical, San Carlos, California) during hypothermia, rewarming, and the first 6 hours of normothermia. Phenobarbital was given for clinical or subclinical/electrographic seizures. Fosphenytoin, levetiracetam, or topiramate was added for persistent/recurrent seizures. Clinicians could view the regional cerebral oxygen saturation from the NIRS monitor, but not the HVx.

MR Imaging

MR imaging studies were performed on a 1.5T clinical scanner (Avanto; Siemens, Erlangen, Germany) by using a standard neonatal 8-channel head coil. Standard neonatal brain MRI with sagittal T1-weighted, axial T2-weighted, and axial SWI was obtained during normothermia. A single-shot, spin-echo, echo-planar axial DTI sequence with diffusion gradients along 20 noncollinear directions was acquired. An effective high b-value of $1000 \text{ s}/\text{mm}^2$ was used for each of the 20 diffusion-encoding directions. An additional measurement without diffusion weighting ($b = 0 \text{ s}/\text{mm}^2$) was performed. For the acquisition of the DTI data, we used the following parameters: TR, 8500 ms; TE, 86 ms; section thickness, 2.0 mm; FOV, $192 \times 192 \text{ mm}$; and matrix size, 96×96 (reconstructed as 192×192 with zero-filled interpolation). A parallel imaging integrated parallel acquisition technique factor 2 with generalized auto-calibrating partial parallel acquisition reconstruction was used. The acquisition was repeated twice to enhance the SNR. ADC maps were automatically calculated by the vendor-specific software in the MR imaging scanner.

Image analysis was performed on the PACS workstation. ADC scalars were measured by region-of-interest analysis on the PACS workstation. ROIs were manually drawn in 7 anatomic regions in each cerebral hemisphere: anterior centrum semiovale (ACS), posterior centrum semiovale (PCS), posterior limb of the internal capsule (PLIC), putamen and globus pallidus (PP), and the entire thalamus, pons, and middle cerebellar peduncle. Additionally, a region of interest was drawn to cover the entire middle pons. To guarantee correct positioning of the ROIs, we correlated ADC maps with the matching fractional anisotropy maps when necessary (eg, PLIC). Otherwise, the remainder of the anatomic areas was identified on the ADC maps (Fig 1). Each region of interest was measured in 3 contiguous axial sections, and the mean of the 3 values was used as the ADC measure for each anatomic region in each cerebral hemisphere. The radiologist was unaware of the patients’ HVx, blood pressures, clinical histories, and conventional MR imaging findings.

Autoregulation Monitoring

Neonatal cerebral oximetry probes (INVOS; Covidien, Mansfield, Massachusetts) were placed bilaterally on the patient’s forehead. NIRS signals and arterial blood pressure data from the bedside monitor (Marquette MAC 500; GE Healthcare, Milwaukee, Wisconsin) were synchronously sampled at 100 Hz and processed with an analog-to-digital converter (DT9804; Data Translation, Marlboro, Massachusetts) by using ICM+ software (Cambridge Enterprises, Cambridge, United Kingdom).^{6,12} Signal artifacts in the MAP and NIRS data (eg, arterial line flushes) were manually removed, and data that accounted for <1% of the recording period were excluded as an additional measure to remove artifacts.⁶

The HVx was calculated by using a continuous, moving correlation coefficient between MAP and the relative total tissue hemoglobin attenuation, which is a surrogate measure of cerebral blood volume obtained by NIRS.^{9,10} The relative total tissue hemoglobin attenuation is obtained by NIRS by using light with a wavelength of 805 nm. Because this wavelength is isosbestic to both oxygenated and deoxygenated hemoglobin, relative tissue hemoglobin is not affected by changes in cerebral oxygen satura-

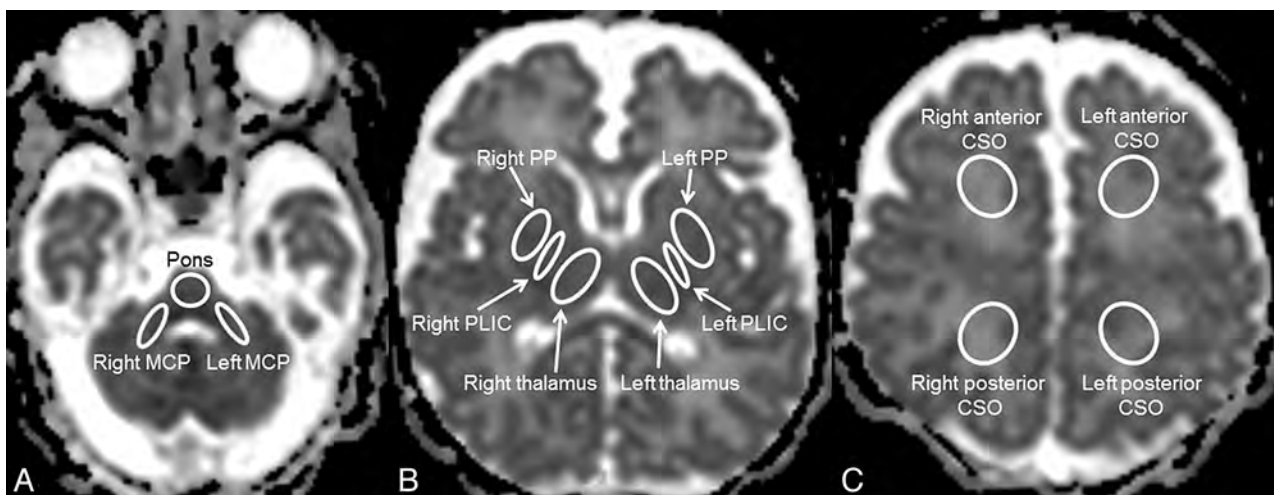


FIG 1. Axial ADC maps at the level of the posterior fossa (A), deep gray matter nuclei (B), and centrum semiovale (C) showing the position of the manually drawn ROIs in 7 anatomic regions: the pons (A), MCPs (A), thalami (B), PLICs (B), PPs (B), and ACS and PCS bilaterally (C). MCP indicates middle cerebellar peduncle

tion. Therefore, HVx can be used to measure autoregulatory vasoreactivity during conditions that affect the relative proportions of oxygenated-to-deoxygenated hemoglobin, such as therapeutic hypothermia (which may affect the cerebral metabolic rate and cardiac output). The use of HVx has been validated in HII piglets undergoing hypothermia and rewarming.^{10,13} Consecutive, paired, 10-second averaged values from a 300-second duration were used for each calculation, thereby incorporating 30 data points for each HVx calculation.¹² HVx is a continuous variable that ranges from -1 to $+1$. When vasoreactivity is functional (and autoregulation is therefore intact), the cerebral blood volume and MAP either do not correlate or are negatively correlated. This result generates a near-zero or a negative HVx. When vasoreactivity and autoregulation become impaired, the cerebral blood volume and MAP correlate and the HVx becomes positive and approaches $+1$.^{6,9,10}

Right and left HVx values were averaged and sorted into 5-mm Hg bins of MAP to generate bar graphs. MAP_{OPT} was defined as the bin with the most negative HVx when the graph showed a trend toward increasing index values as MAP deviated from this nadir.⁶ The MAP_{OPT} was identified during hypothermia, rewarming, and the first 6 hours of normothermia by 2 physicians independently (J.K.L. and C.W.H.), who were unaware of the patient history and MR imaging results. Both physicians had to agree on the MAP_{OPT} to include the neonate in the analysis. Worse autoregulatory function was indicated by spending greater time with blood pressure below MAP_{OPT} and greater blood pressure deviation below MAP_{OPT}.⁶

Autoregulation was analyzed by using 3 methods within each period (hypothermia, rewarming, and the first 6 hours of normothermia). First, the amount of time the neonate spent with blood pressure below MAP_{OPT} was calculated. Time with blood pressure below MAP_{OPT} was then analyzed as a percentage of the autoregulation monitoring period. Second, the maximum blood pressure deviation below MAP_{OPT} was determined. Third, the area under the curve was calculated to combine the amount of time spent with blood pressure below MAP_{OPT} and the extent of blood pressure deviation below MAP_{OPT}. To cal-

culate the area under the curve, we analyzed time as the absolute duration of autoregulation monitoring. The area under the curve (minimum \times millimeter of mercury/hour) for time (minutes) spent with blood pressure below MAP_{OPT} and blood pressure deviation (millimeter of mercury) below MAP_{OPT} was normalized for monitoring the duration (hours).¹⁴

Statistical Analysis

Data were analyzed with SAS, Version 9.2 (SAS Institute, Cary, North Carolina). Graphs were generated with GraphPad Prism (Version 5.03; GraphPad Software, San Diego, California). Data are reported as means with SDs and medians with interquartile ranges (IQRs) when appropriate. A 2-sided P value $\leq .05$ was considered significant. The lowest mean ADC scalar between the right and left cerebral hemispheres was taken as the representative ADC scalar of that anatomic region for the analysis.

ADC scalars in each anatomic region were compared with the percentage of time spent with blood pressure below MAP_{OPT}, the maximal blood pressure deviation below MAP_{OPT}, and the area under the curve below MAP_{OPT} in each period using Spearman correlations. In addition, the data were stratified for separate analyses of neonates who received their MR imaging before day of life 10 and neonates who received their MR imaging on day of life 10 or later to account for delayed pseudonormalization of ADC in cooled neonates with HII.¹⁵

RESULTS

Fifty-six neonates with HII were identified. Twenty-five neonates could not be enrolled in the study due to refusal of consent (8), lack of arterial cannulae (7), withdrawal of care or death soon after birth (4), language barrier (1), known intracranial hemorrhage (1), congenital heart disease (1), extracorporeal membrane support (1), abandonment (1), and inadequate resources (1). Consequently, 31 neonates were enrolled in the study. Autoregulation monitoring could not be accomplished in 1 neonate due to technical problems, and 3 had motion artifacts on MR imaging. Therefore, data were analyzed for 27 neonates (12 females and 15 males).

Apparent Diffusion Coefficient Scalars

Brain MRI were obtained on median day of life 8 (range, 4–15 days). Mean ADC scalars between the right and left cerebral hemispheres were similar in the PCS ($P = .82$), PP ($P = .39$), PLIC ($P = .47$), and middle cerebellar peduncle ($P = .35$). There were differences in mean ADC measures between the right and left hemispheres in the ACS ($P = .04$) and thalamus ($P = .04$).

Autoregulation

Autoregulation was monitored in 27/27 (100%) neonates during hypothermia, 25/27 (93%) during rewarming, and 24/27 (89%) during normothermia. Reasons for early cessation of monitoring included transfer to the pediatric intensive care unit for extracorporeal membrane support (1 neonate) and removal of the arterial blood pressure cannula (2 neonates). The median duration of monitoring was 31 hours (IQR, 23–45 hours) during hypothermia, 6 hours (IQR, 5–8 hours) during rewarming, and 6 hours (IQR, 6–6 hours) during normothermia. The neonates' blood pressures are illustrated in Fig 2. MAP_{OPT} was identified in 23/27 (85%) neonates during hypothermia, 24/25 (96%) during rewarming, and 19/24 (79%) during normothermia. Median MAP_{OPT} values were 50 (IQR, 45–55) during hypothermia, 50 (IQR, 45–55) during rewarming, and 50 (IQR, 45–60) during normothermia.

Apparent Diffusion Coefficient Scalars and Autoregulation

When all neonates were analyzed together, ADC scalars did not correlate to time spent with blood pressure below MAP_{OPT} , maximum blood pressure deviation below MAP_{OPT} , or area under the curve below MAP_{OPT} in any period ($P > .08$ during hypothermia [$n = 23$], $P > .07$ during rewarming [$n = 24$], and $P > .10$ during normothermia [$n = 19$]). Among neonates who had MRI obtained on day of life ≥ 10 , lower ADC scalars in PCS negatively correlated to time spent with blood pressure below MAP_{OPT} ($P < .006$), blood pressure deviation below MAP_{OPT} ($P = .03$), and area under the curve ($P = .003$; $n = 9$) during hypothermia. Lower ADC in the PLIC negatively correlated to blood pressure deviation below MAP_{OPT} during hypothermia ($P = .04$, $n = 9$) (Table 1). Lower ADC scalars in PP negatively correlated to blood pressure deviation below MAP_{OPT} during rewarming ($P = .05$, $n = 8$). ADC in the middle cerebellar peduncle correlated to maximal blood pressure deviation below MAP_{OPT} during rewarming ($P = .02$, $n = 8$) (Table 2). Blood pressure and ADC did not correlate during normothermia (Table 3). ADC and blood pressure did not correlate during any period among neonates who underwent MRI on day of life < 10 .

DISCUSSION

Severe neurologic disabilities persist in survivors of HII despite therapeutic hypothermia.^{1,2} HII is characterized by a period of reduced blood flow (ischemia) and oxygen delivery (hypoxia) followed by reperfusion with transient energy recovery and then secondary energy failure.¹⁶ Therapeutic hypothermia aims to prevent the events that initiate with reperfusion and culminate in cell death. Although hypothermia was initially thought to decrease both mortality and disability rates, recent long-term outcome studies show significance

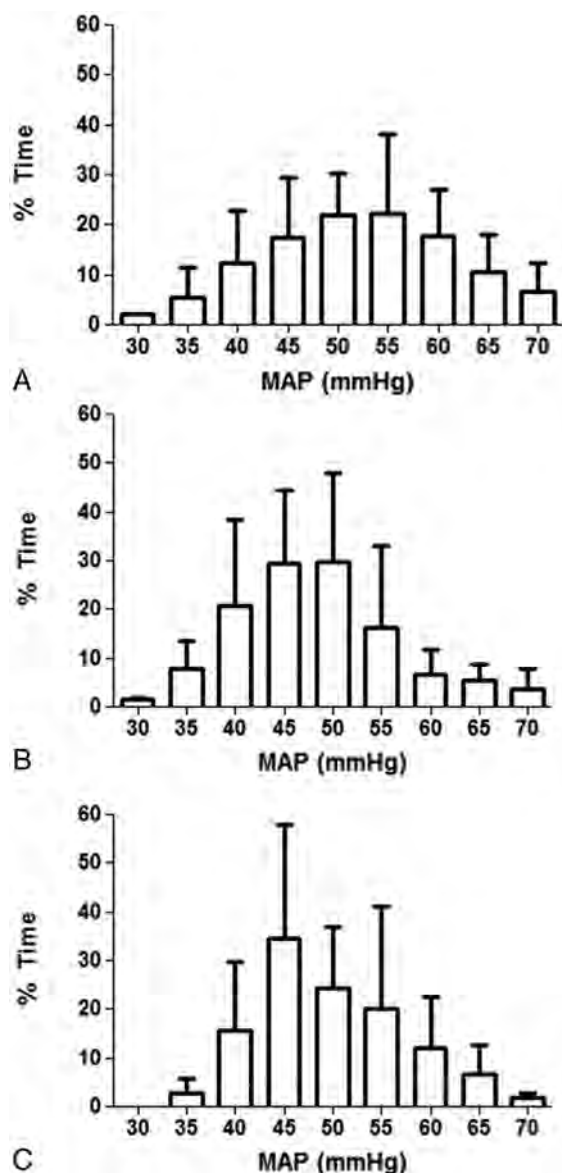


FIG 2. The percentage of the autoregulation monitoring period that neonates spent at each mean arterial blood pressure during hypothermia ($n = 27$) (A), rewarming ($n = 25$) (B), and the first 6 hours of normothermia ($n = 24$) (C). Data are shown as means with SDs. The neonates' blood pressures were similar across time periods.

only for decreased mortality.^{17,18} Research to better define which patients would benefit most from therapeutic hypothermia and the optimal duration of hypothermia is needed. Moreover, neonates who do not fit the current inclusion criteria for HII in clinical trials might still benefit from therapeutic hypothermia.^{18,19} Thus, there is an urgent need to better define the effects of cooling and rewarming on the brain in neonates with HII.

Advanced MR imaging techniques, including DTI and MR spectroscopy, serve as biomarkers of brain injury in HII.^{20,21} However, MR imaging is usually done after the completion of hypothermia and when the child is hemodynamically stable. Autoregulation monitoring with HVx can be used continuously at the bedside and during hypothermia. By identifying the MAP range that optimizes autoregulation with HVx, clinicians could target neuroprotective hemodynamic goals that reduce the risk of ischemia.

Table 1: Correlation of ADC scalars and blood pressure in relation to MAP_{OPT} during therapeutic hypothermia^a

	Maximum MAP		
	% Time below MAP _{OPT} (r) (P Value)	Deviation below MAP _{OPT} (r) (P Value)	AUC below MAP _{OPT} (r) (P Value)
DOL <10 (n = 14)			
ACS	0.31 (.28)	0.36 (.20)	0.38 (.19)
PCS	0.12 (.67)	0.25 (.39)	0.21 (.47)
PP	-0.07 (.81)	0.06 (.84)	-0.04 (.90)
Thalamus	0.01 (.97)	0.13 (.67)	0.05 (.85)
PLIC	0.10 (.74)	0.19 (.51)	0.18 (.55)
Pons	0.44 (.12)	0.40 (.16)	0.45 (.11)
MCP	-0.32 (.27)	-0.10 (.74)	-0.25 (.39)
DOL ≥10 (n = 9)			
ACS	-0.58 (.10)	-0.34 (.38)	-0.58 (.10)
PCS	-0.83 (.006) ^b	-0.71 (.03) ^b	-0.87 (.003) ^b
PP	-0.47 (.20)	-0.19 (.62)	-0.35 (.36)
Thalamus	-0.44 (.23)	-0.43 (.25)	-0.47 (.21)
PLIC	-0.61 (.08)	-0.68 (.04) ^b	-0.57 (.12)
Pons	-0.05 (.90)	0.07 (.86)	0.03 (.93)
MCP	-0.08 (.85)	-0.16 (.68)	-0.08 (.83)

Note:—DOL indicates day of life; MCP, middle cerebellar peduncle; AUC, area under the curve.

^a Autoregulation measurements are the following: the percentage of time spent with blood pressure below MAP_{OPT}, maximal blood pressure deviation below MAP_{OPT}, and AUC below MAP_{OPT}. Data were analyzed by Spearman correlations.

^b P ≤ .05.

Table 2: Correlation of ADC scalars and blood pressure in relation to MAP_{OPT} during rewarming^a

	Maximum MAP		
	% Time below MAP _{OPT} (r) (P Value)	Deviation below MAP _{OPT} (r) (P Value)	AUC below MAP _{OPT} (r) (P Value)
DOL <10 (n = 16)			
ACS	-0.25 (.36)	-0.06 (.83)	-0.23 (.40)
PCS	-0.14 (.59)	0.005 (.99)	-0.09 (.75)
PP	-0.02 (.93)	-0.10 (.71)	-0.07 (.79)
Thalamus	-0.22 (.42)	-0.15 (.58)	-0.24 (.38)
PLIC	-0.22 (.41)	0.05 (.86)	-0.19 (.49)
Pons	-0.13 (.64)	0.14 (.62)	-0.03 (.91)
MCP	-0.20 (.46)	-0.22 (.42)	-0.18 (.50)
DOL ≥10 (n = 8)			
ACS	-0.55 (.16)	-0.18 (.68)	-0.45 (.26)
PCS	-0.21 (.61)	0.24 (.57)	-0.10 (.82)
PP	-0.64 (.09)	-0.35 (.39)	-0.71 (.05) ^b
Thalamus	0.24 (.57)	0.42 (.31)	-0.10 (.82)
PLIC	0.14 (.74)	0	-0.05 (.91)
Pons	-0.14 (.74)	0.01 (.98)	0.17 (.69)
MCP	0.57 (.14)	0.79 (.02) ^b	-0.48 (.23)

Note:—DOL indicates day of life; MCP, middle cerebellar peduncle; AUC, area under the curve.

^a Autoregulation measurements are the following: the percentage of time spent with blood pressure below MAP_{OPT}, maximal blood pressure deviation below MAP_{OPT}, and AUC below MAP_{OPT}. Data were analyzed by Spearman correlations.

^b P ≤ .05.

In our study, lower ADC scalars in the PCS, PLIC, and PP correlated with blood pressure deviation below MAP_{OPT} during hypothermia and rewarming in neonates who had MRI on day of life ≥10. An association between qualitative MR imaging measures of injury in the PP and thalamus and blood pressure below MAP_{OPT} during rewarming was previously reported in HII.⁶ Here, we identified additional correlations between hypoxic-ischemic injury to the PCS and PLIC and blood pressure autoregulation. This reflects the added value of quantitative ADC measurements as opposed to qualitative/

Table 3: Correlation of ADC scalars and blood pressure in relation to MAP_{OPT} during the first 6 hours of normothermia^a

	Maximum MAP		
	% Time below MAP _{OPT} (r) (P Value)	Deviation below MAP _{OPT} (r) (P Value)	AUC below MAP _{OPT} (r) (P Value)
DOL <10 (n = 12)			
ACS	0.05 (.87)	0.22 (.50)	0.07 (.82)
PCS	0.16 (.62)	0.46 (.13)	0.20 (.53)
PP	-0.30 (.34)	-0.20 (.54)	-0.13 (.69)
Thalamus	0.02 (.95)	0.11 (.74)	0.21 (.50)
PLIC	0.11 (.74)	0.36 (.25)	0.18 (.59)
Pons	0.46 (.13)	0.48 (.11)	0.49 (.10)
MCP	-0.11 (.73)	0.15 (.64)	0.02 (.94)
DOL ≥10 (n = 7)			
ACS	0.18 (.70)	0.40 (.37)	0.04 (.94)
PCS	0.18 (.70)	0.11 (.81)	-0.04 (.94)
PP	-0.14 (.76)	0.46 (.30)	-0.21 (.64)
Thalamus	0.54 (.22)	0.61 (.15)	0.05 (.25)
PLIC	0	0.09 (.84)	-0.18 (.70)
Pons	-0.14 (.76)	-0.48 (.28)	-0.32 (.48)
MCP	0.39 (.38)	0.40 (.37)	0.46 (.29)

Note:—DOL indicates day of life; MCP, middle cerebellar peduncle; AUC, area under the curve.

^a Autoregulation measurements are the following: the percentage of time spent with blood pressure below MAP_{OPT}, maximal blood pressure deviation below MAP_{OPT}, and AUC below MAP_{OPT}. Data were analyzed by Spearman correlations.

subjective MR imaging analysis alone. Thalamic ADC scalars did not correlate with HVx in this study, possibly because the entire thalamus was included in our region of interest and we did not have the precision to delineate subcompartments of the thalamus that show differential vulnerability to HII.

Correlation between lower ADC scalars and worse autoregulation was observed in the PCS but not in the ACS. The absence of an association between ADC scalars in ACS and autoregulation is surprising and could reflect differences in the effects of HII on the anterior-versus-posterior circulations. In the posterior fossa, no correlation was observed in the pons, but a positive correlation between ADC and blood pressure occurred in the middle cerebellar peduncle. Measures of autoregulation obtained over the frontal cortex may not be relevant to ischemia in the posterior fossa. These findings emphasize the complex relationships among HII, regional ischemic injury, and autoregulation measurements by using NIRS technology.

The temporal cascade of events that take place during HII is quite complex, and the impact of cooling adds another piece to this puzzle. Although we had a variation in timing of brain MR imaging, this variation enabled us to factor in delayed pseudonormalization in our analysis. ADC scalars and blood pressure only correlated in neonates who received MRI on day of life ≥10. Pseudonormalization of ADC values is delayed in cooled neonates through 10 days of age.¹⁵ Our study included neonates with moderate or severe HII, and we did not further score the degree of disease severity. Future studies are needed to determine whether more severely injured neonates may have more or less delay in ADC pseudonormalization.

The lowest mean ADC scalar from the right or left cerebral hemisphere was used as the representative measure for that anatomic region. With the exception of the ACS and thalamus, ADC values were similar between the right and left sides in all anatomic regions, including the PCS, PLIC, and PP, where significant correlations between ADC and blood pressure autoregulation were identified. ADC scalars in the ACS and thalamus did not correlate to blood pressure.

Therefore, using the lowest ADC value between hemispheres to assess regional ischemic injury was a reasonable approach.

HVx assesses autoregulatory vasoreactivity by measuring total tissue hemoglobin attenuation in the superficial frontal cortex. It does not directly measure deep brain regions. Techniques to continuously measure cerebral blood flow autoregulation in deep regions of the brain are not clinically available for neonates. Whether vascular responses to changes in blood pressure are different in deep brain regions compared with the cortex after global HII and therapeutic hypothermia remains unclear. Nonetheless, the association between MAP_{OPT} and ischemia measured by ADC in the PCS, PLIC, and PP suggests that superficial autoregulation measurements may identify blood pressure goals that protect deeper brain regions, as well.

There were several limitations in this study. The sample size was small. The severity of ischemic brain injury or degree of encephalopathy could not be controlled for in the analysis. Whether maintaining blood pressure close to MAP_{OPT} to optimize autoregulation decreases the risk of brain injury cannot be determined in this observational study. The blood pressure and autoregulation measurements were obtained during the neonates' first few days of life during hypothermia, rewarming, and the beginning of normothermia, whereas the brain MRI was obtained after normothermia was attained. Moreover, autoregulation monitoring could only begin once an arterial blood pressure cannula was placed and informed consent was obtained. Therefore, disturbances in autoregulation that may have occurred before the start of monitoring were not accounted for in the analysis.

CONCLUSIONS

This study identified several findings relevant to the treatment of HII. In neonates cooled for HII, lower ADC scalars in the PCS, PLIC, and PP correlated to greater blood pressure deviation below the range with optimal autoregulation. It remains unclear to what extent the ADC changes are attributable to the primary hypoxic ischemic injury versus secondary impaired autoregulation, or a combination of all complex events that take place during the injury and therapeutic hypothermia. Although a causal relationship could not be identified in this observational study, these data suggest that minimizing blood pressure deviation below MAP_{OPT} may minimize ischemic injury in these brain regions.

Disclosures: Maureen M. Gilmore—UNRELATED: Grants/Grants Pending: Covidien,* Comments: Covidien previously provided grant funding to Jennifer Lee, MD, the primary investigator leading our group in the autoregulation studies we perform with term and near-term babies with hypoxic-ischemic encephalopathy; Payment for Development of Educational Presentations: eNeonatal Review, Comments: I received an honorarium as the Course Director for this on-line educational literature review of neonatology-related topics. Charles W. Hogue—RELATED: Grant: National Institutes of Health ROI HL 092259*; UNRELATED: Consultancy: CLS Behring (DSMB), Ornim (Advisory Board), Covidien (served as advisor, but not in past 12 months); Expert Testimony: Dr Hogue has consulted on legal matters, serving as an expert witness in medical litigation in September 2013; Grants/Grants Pending: Covidien.* Raymond C. Koehler—RELATED: Grant: National Institutes of Health.* Jennifer K. Lee—RELATED: Grant: Covidien,* Thomas Wilson Sanitarium for Children, research grant.* American Heart Association*; UNRELATED: Grants/Grants Pending: Covidien.* Frances J. Northington—RELATED: Grant: National Institutes of Health—Eunice Kennedy Shriver National Institute of Child Health and Human Development,* Covidien*; UNRELATED: Grants/Grants Pending: National Institutes of Health—Eunice Kennedy Shriver National Institute of Child Health and Human Development,* Covidien*; Payment for Lectures (including service on Speakers Bureaus): American Academy of Pediatrics (honorarium); Travel/Accommodations/

Meeting Expenses Unrelated to Activities Listed: American Academy of Pediatrics (accommodations and travel), National Institutes of Health (travel to study section). *Money paid to the institution.

REFERENCES

1. Dilenge ME, Majnemer A, Shevell MI. **Long-term developmental outcome of asphyxiated term neonates.** *J Child Neurol* 2001;16:781–92
2. Nelson KB. **Neonatal encephalopathy: etiology and outcome.** *Dev Med Child Neurol* 2005;47:292
3. Shankaran S, Laptook AR, Ehrenkranz RA, et al. **Whole-body hypothermia for neonates with hypoxic-ischemic encephalopathy.** *N Engl J Med* 2005;353:1574–84
4. Gluckman PD, Wyatt JS, Azzopardi D, et al. **Selective head cooling with mild systemic hypothermia after neonatal encephalopathy: multicentre randomised trial.** *Lancet* 2005;365:663–70
5. Azzopardi D, Strohm B, Edwards AD, et al. **Treatment of asphyxiated newborns with moderate hypothermia in routine clinical practice: how cooling is managed in the UK outside a clinical trial.** *Arch Dis Child Fetal Neonatal Ed* 2009;94:F260–64
6. Howlett JA, Northington FJ, Gilmore MM, et al. **Cerebrovascular autoregulation and neurologic injury in neonatal hypoxic-ischemic encephalopathy.** *Pediatr Res* 2013;74:525–35
7. Poretti A, Meoded A, Rossi A, et al. **Diffusion tensor imaging and fiber tractography in brain malformations.** *Pediatr Radiol* 2013;43:28–54
8. Brissaud O, Amirault M, Villega F, et al. **Efficiency of fractional anisotropy and apparent diffusion coefficient on diffusion tensor imaging in prognosis of neonates with hypoxic-ischemic encephalopathy: a methodologic prospective pilot study.** *AJNR Am J Neuroradiol* 2010;31:282–87
9. Lee JK, Kibler KK, Benni PB, et al. **Cerebrovascular reactivity measured by near-infrared spectroscopy.** *Stroke* 2009;40:1820–26
10. Lee JK, Brady KM, Mytar JO, et al. **Cerebral blood flow and cerebrovascular autoregulation in a swine model of pediatric cardiac arrest and hypothermia.** *Crit Care Med* 2011;39:2337–45
11. Zweifel C, Castellani G, Czosnyka M, et al. **Noninvasive monitoring of cerebrovascular reactivity with near infrared spectroscopy in head-injured patients.** *J Neurotrauma* 2010;27:1951–58
12. Brady K, Joshi B, Zweifel C, et al. **Real-time continuous monitoring of cerebral blood flow autoregulation using near-infrared spectroscopy in patients undergoing cardiopulmonary bypass.** *Stroke* 2010;41:1951–56
13. Larson AC, Jamrogowicz JL, Kulikowicz E, et al. **Cerebrovascular autoregulation after rewarming from hypothermia in a neonatal swine model of asphyxial brain injury.** *J Appl Physiol* (1985) 2013;115:1433–42
14. Aronson S, Dyke CM, Levy JH, et al. **Does perioperative systolic blood pressure variability predict mortality after cardiac surgery? An exploratory analysis of the ECLIPSE trials.** *Anesth Analg* 2011;113:19–30
15. Bednarek N, Mathur A, Inder T, et al. **Impact of therapeutic hypothermia on MRI diffusion changes in neonatal encephalopathy.** *Neurology* 2012;78:1420–27
16. Ferriero DM. **Neonatal brain injury.** *N Engl J Med* 2004;351:1985–95
17. Shankaran S, Pappas A, McDonald SA, et al. **Childhood outcomes after hypothermia for neonatal encephalopathy.** *N Engl J Med* 2012;366:2085–92
18. Jacobs SE, Berg M, Hunt R, et al. **Cooling for newborns with hypoxic ischaemic encephalopathy.** *Cochrane Database Syst Rev* 2013;1:CD003311
19. Gancia P, Pomero G. **Therapeutic hypothermia in the prevention of hypoxic-ischaemic encephalopathy: new categories to be enrolled.** *J Matern Fetal Neonatal Med* 2012;25(suppl 4):94–96
20. Bonifacio SL, Saporta A, Glass HC, et al. **Therapeutic hypothermia for neonatal encephalopathy results in improved microstructure and metabolism in the deep gray nuclei.** *AJNR Am J Neuroradiol* 2012;33:2050–55
21. Massaro AN, Jeromin A, Kadom N, et al. **Serum biomarkers of MRI brain injury in neonatal hypoxic ischemic encephalopathy treated with whole-body hypothermia: a pilot study.** *Pediatr Crit Care Med* 2013;14:310–17

MRI Characteristics of Globus Pallidus Infarcts in Isolated Methylmalonic Acidemia

E.H. Baker, J.L. Sloan, N.S. Hauser, A.L. Gropman, D.R. Adams, C. Toro, I. Manoli, and C.P. Venditti



ABSTRACT

BACKGROUND: Bilateral infarcts confined to the globus pallidus are unusual and occur in conjunction with only a few disorders, including isolated methylmalonic acidemia, a heterogeneous inborn error of metabolism. On the basis of neuroradiographic features of metabolic strokes observed in a large cohort of patients with methylmalonic acidemia, we have devised a staging system for methylmalonic acidemia–related globus pallidus infarcts.

MATERIALS AND METHODS: Forty patients with isolated methylmalonic acidemia and neurologic symptoms underwent clinical brain MR imaging studies, which included 3D-T1WI. Infarcted globus pallidus segments were neuroanatomically characterized, and infarct volumes were measured.

RESULTS: Globus pallidus infarcts were present in 19 patients; all were bilateral, and most were left-dominant. A neuroanatomic scoring system based on the infarct patterns was devised; this revealed a 5-stage hierarchical susceptibility to metabolic infarct, with the posterior portion of the globus pallidus externa being the most vulnerable. Globus pallidus infarct prevalence by methylmalonic acidemia class was the following: *cbIA* (5/7, 71%), *cbIB* (3/7, 43%), *mut^o* (10/22, 45%), and *mut⁻* (1/4, 25%). Tiny lacunar infarcts in the pars reticulata of the substantia nigra, previously unrecognized in methylmalonic acidemia, were found in 17 patients, 13 of whom also had a globus pallidus infarct.

CONCLUSIONS: The staged pattern of globus pallidus infarcts in isolated methylmalonic acidemia suggests a nonuniform, regionally specific cellular susceptibility to metabolic injury, even for patients having milder biochemical phenotypes. In support of this hypothesis, the delineation of lacunar infarcts in the pars reticulata of the substantia nigra, a tissue functionally and histologically identical to the globus pallidus interna, supports the concept of cell-specific pathology.

ABBREVIATIONS: bFFE = balanced fast-field echo; GP = globus pallidus; GPe = globus pallidus externa; GPI = globus pallidus interna; MMA = methylmalonic acidemia; MUT = methylmalonyl-coenzyme A mutase; SNr = pars reticulata of the substantia nigra

Isolated methylmalonic acidemia (MMA) is a group of autosomal recessive inborn errors of metabolism caused by impaired activity of methylmalonyl-coenzyme A mutase (MUT).¹⁻⁴

This cobalamin-dependent enzyme isomerizes methylmalonyl-coenzyme A into succinyl-coenzyme A, a critical Krebs cycle intermediate. Mutations in the gene encoding MUT result in an inactive (*mut^o*) or partially active (*mut⁻*)^{3,5} enzyme, the most common cause of isolated MMA. Impaired biosynthesis and transfer of the cofactor 5'-deoxyadenosylcobalamin to the MUT enzyme (*cbIA* and *cbIB*) or defective transport of cobalamin into the mitochondrion (*cbID*) also impairs the action of the MUT enzyme. These defects result in massive accumulation of methylmalonic acid and propionyl-coenzyme A–derived metabolites such as 2-methylcitrate.⁶

MMA treatment strategies vary^{4,7,8} but generally involve adherence to a low-protein diet to restrict the intake of amino acids that are oxidized to propionyl-coenzyme A (isoleucine, valine, threonine, methionine), hydroxocobalamin injections for cobalamin-responsive patients, carnitine supplementation to relieve acyl-coenzyme A accretion in the mitochondrion, and a high-

Received May 15, 2014; accepted after revision June 26.

From the Department of Radiology and Imaging Sciences (E.H.B.), Clinical Center, and Genetics and Molecular Biology Branch (J.L.S., I.M., C.P.V.), Medical Genetics Branch (D.R.A.), and Undiagnosed Diseases Program (C.T.), National Human Genome Research Institute, National Institutes of Health, Bethesda, Maryland; Medical Genetics and Metabolism Department (N.S.H.), Children's Hospital Central California, Madera, California; and Department of Neurology (A.L.G.), Children's National Medical Center, Washington, DC.

This work was supported by the Intramural Research Program of the National Human Genome Research Institute (National Institutes of Health protocol 04-HG-0127 "Clinical and Basic Investigations of Methylmalonic Acidemia and Related Disorders," clinicaltrials.gov identifier NCT00078078).

Please address correspondence to Eva H. Baker, MD, PhD, 10 Center Dr, MSC 1074, Bethesda, MD 20892-1074; e-mail: bakere@mail.nih.gov

Indicates open access to non-subscribers at www.ajnr.org

<http://dx.doi.org/10.3174/ajnr.A4087>

energy diet to prevent catabolism. Despite vigilant dietary and metabolic management, patients with MMA experience multisystem disease, including metabolic instability, pancreatitis,⁹ renal failure,^{9,10} intellectual impairment,^{9,11} growth retardation,⁹ optic nerve atrophy,⁹ and acute injury to the globus pallidus.¹²⁻²² Some patients eventually require liver and/or kidney transplantation.

Most globus pallidus (GP) strokes are unilateral lacunar infarcts resulting from thromboembolic occlusion of a lenticulostriate artery; therefore, their margins reflect the vascular territory rather than the anatomic boundaries of the GP. In contrast, metabolic GP infarcts are typically bilateral, and infarct margins are constrained by neuroanatomic boundaries. Diseases that can cause GP infarction, with or without infarction of other basal ganglia, include propionic acidemia, some variants of Leigh disease, carbon monoxide poisoning, and cyanide poisoning.¹⁵ Isolated bilateral GP infarcts, never involving other structures, have been reported only in MMA. GP injury is a well-known complication of isolated MMA, classically occurring during severe decompensation or acute illness, and can result in an incapacitating movement disorder characterized by choreoathetosis and dystonia.^{15,16} The largest previously reported series that counted GP infarcts in patients with isolated MMA revealed GP infarcts in 4 of 23 patients (17%).⁹

In this article, we describe the patterns of the GP infarcts found in patients with isolated MMA and further characterize the GP infarcts by volumetric measurements. Our analyses revealed that the lesions follow a characteristic progression; therefore, we propose a staging system for MMA-related GP infarcts. We also established that patients with certain classes of isolated MMA are more likely to develop GP infarcts than others. Furthermore, we identified a novel imaging finding suggesting small defects in the cerebral peduncles, which we propose are produced by the same toxic or metabolic mechanism as the GP infarcts, also affecting the histologically²³ and functionally²⁴ identical cells that compose the pars reticulata of the substantia nigra (SNr).

MATERIALS AND METHODS

Patient studies were approved by the institutional review board of our institution and were performed in compliance with the Helsinki Declaration. Patients were evaluated between 2004 and 2013. There was no recruitment strategy on the basis of race, sex, nutritional status, or disease severity. Long-term care of these patients was managed by their referring physicians.

During the period covered by this analysis, 64 patients having a variant of isolated MMA were evaluated by our clinic. All were classified by cellular enzymology and/or molecular genetics. Many patients had neurologic symptoms including movement disorders, hearing impairment, visual loss, and developmental delay.¹¹ Neurologic evaluation (performed by a neurologist familiar with MMA) was particularly directed toward detecting signs of a GP stroke, such as movement disorders, weakness, and asymmetric motor findings. Many patients had follow-up neurologic examinations to check for progression and to detect strokes occurring in the absence of a sentinel clinical event.

Because our protocol did not allow MR imaging solely for research purposes, patients were selected for MR imaging on the basis of clinical indications. The most common reasons for MR

imaging were for work-up of a movement disorder, for progression of symptoms, and as part of the initial diagnosis. Follow-up imaging was also performed for clinical indications, and 10 patients had ≥ 1 follow-up MR imaging during the study period. There were 25 patients (younger children and some adults with movement disorders) who required sedation with propofol. Patients scanned at our institution had a basic clinical brain MR imaging without gadolinium-based contrast material. MRIs performed at our institution all included 3D-T1WI (mostly MPRAGE, some 3D-fast-field echo). In addition to 3D-T1WI, some examinations included high-resolution balanced fast-field echo (bFFE) images. At our institution, MRIs were performed on a 3T Achieva (Philips Healthcare, Best, the Netherlands) scanner by using a sensitivity encoding head coil. Parameters used were the following: for MPRAGE, TE = 6.6 ms, TR = 11.6 ms, flip angle = 6°, FOV = 220 mm, acquisition matrix = 256 × 131, reconstruction matrix = 256 × 256, section thickness = 1.0 mm, NEX = 2; for 3D-fast-field echo, TE = 2.2 ms, TR = 5.0 ms, flip angle = 15°, FOV = 240 mm, acquisition matrix = 256 × 244, reconstruction matrix = 256 × 256, section thickness = 1.0 mm, NEX = 1; for bFFE, TE = 2.1 ms, TR = 5.1 ms, flip angle = 45°, FOV = 220 mm, acquisition matrix = 384 × 367, reconstruction matrix = 384 × 384, section thickness = 1.0 mm, NEX = 1. Six patients had scans performed outside our institution; these images were obtained with a variety of scan protocols.

MR imaging scans were reviewed by a single neuroradiologist to determine whether GP infarcts were present. Putative infarcts were carefully assessed to distinguish small infarcts from prominent perivascular spaces, a nonpathologic phenomenon that can also occur in the basal ganglia with a similar appearance on MR imaging. Perivascular spaces have a linear or branching appearance when examined in 3D and can traverse anatomic boundaries; metabolic infarcts are rounded or crescent and are confined by the anatomic boundaries of the GP. bFFE images are particularly helpful in clarifying the difference. If an infarct was present, the involved segments of the GP were recorded. Images were also evaluated for potential lacunar infarcts in the SNr; the number and location of SNr infarcts were recorded. Again, findings having a linear or branching appearance that would indicate a prominent perivascular space rather than an infarct were excluded.

MPRAGE or 3D-fast-field echo images of GP infarcts were exported to the MIPAV image analysis software (National Institutes of Health, Bethesda, Maryland; <http://mipav.cit.nih.gov>).²⁵ A gray-level tracking tool was used for automated detection of infarct margins; gray-level tracking starts from a seed pixel and attempts to find all connected pixels having the same signal intensity, interpolating when necessary. The resulting boundary contours were manually edited as needed to remove (or add) pixels included (or omitted) due to issues such as image noise and artifacts. Volumes enclosed by the boundary contours were then calculated. Measurements of SNr infarct volumes were not attempted due to their small size relative to the image resolution.

RESULTS

Demographics

Forty patients (25 males, 15 females) with isolated MMA had MR imaging scans. The mean age at the first scan as part of our study

Demographics of infarcts in isolated MMA^a

MMA Class	No.	GP Infarct	SNr Infarct	GP+SNr Infarct	Isolated GP Infarct	Isolated SNr Infarct
<i>cblA</i>	7	5 (71%)	5 (71%)	4	1	1
<i>cblB</i>	7	3 (43%)	3 (43%)	2	1	1
All <i>mut</i> subtypes	26	11 (42%)	9 (34%)	7	4	2
<i>mut-</i>	4	1 (25%)	0 (0%)	0	1	0
<i>mut^o</i>	22	10 (45%)	9 (41%)	7	3	2
All patients	40	19 (48%)	17 (43%)	13	6	4

^a Of 40 patients scanned, 16 had both 3D-T1WI and bFFE images (most sensitive for detection of SNr infarcts), 22 had 3D-T1WI without bFFE images (less sensitive), and 2 had only 2D-T1WI (least sensitive). SNr infarcts were detected at a higher rate among patients with bFFE images (56%) than those without them (36%); therefore, SNr infarcts are probably under-reported.

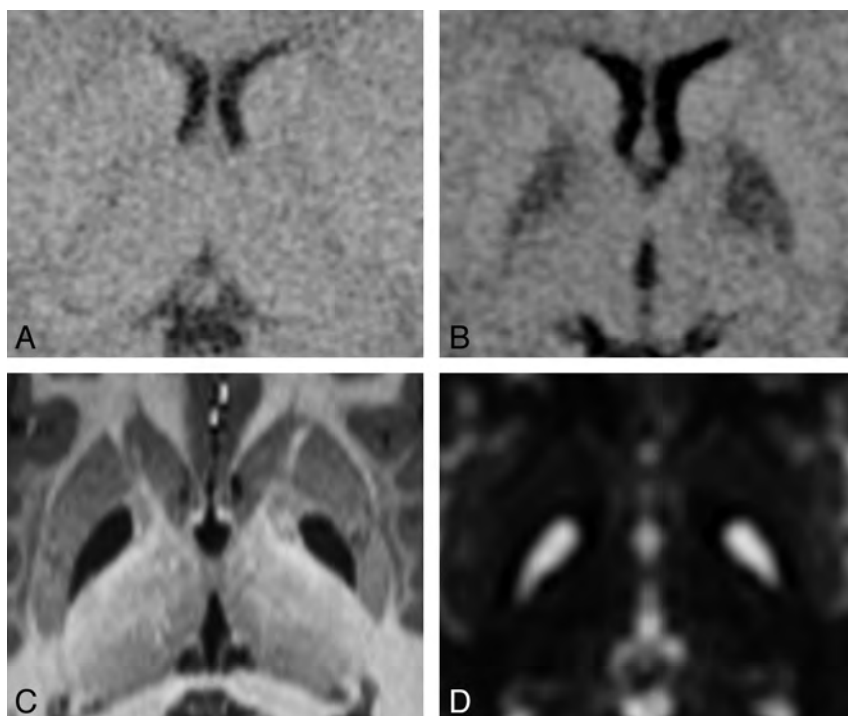


FIG 1. Progression of a GP infarct. This 16-month-old patient was known to have MMA due to the *cblB* defect that had been diagnosed 6 months previously. Within 24 hours after onset of symptoms from gastroenteritis, she became lethargic and was taken to the emergency department. *A*, CT at the time of admission to the hospital appears to have normal findings. *B*, CT scan 35 hours later shows distinct hypoattenuating abnormalities involving the entirety of each GP. DWI performed 1 week later showed restricted diffusion in each GP (image not available). *C*, High-resolution MPRAGE image and *D*, T2-weighted image ($b=0$ image from DTI) acquired 7.5 years later demonstrate bilateral complete GP infarcts.

was 17 years (median, 18 years; range, 2 weeks to 35.5 years). Of these patients, 19 (48%) were found to have GP infarcts, 6 of which had been present at the time of diagnosis. Treatments of the patients whose infarcts were discovered subsequent to diagnosis included diet modification ($n = 13$), carnitine supplements ($n = 13$), hydroxocobalamin injection ($n = 6$), liver and kidney transplantation ($n = 5$), and kidney transplantation ($n = 4$).

GP infarct prevalence by MMA class was as follows: *cblA* (5/7, 71%), *cblB* (3/7, 43%), *mut^o* (10/22, 45%), and *mut-* (1/4, 25%). If both subtypes of the *mut* class were taken together, the rate for all patients with *mut* was 11/26 (42%). Lacunar SNr infarcts were detected in 17 patients. Thirteen patients had both GP and SNr infarcts, while 4 patients had only SNr infarcts and another 6 had only GP infarcts. Of particular interest, 1 patient initially had only SNr infarcts but subsequently developed GP infarcts. This patient

was re-imaged at an interval of 5 years due to clinical progression. The other 9 patients who had follow-up imaging during the time frame of the study demonstrated no discernible changes in their GP. Infarct demographics are summarized in the Table.

Laterality of Infarcts

All GP infarcts were bilateral. It is presumed that the infarcts were synchronous, as illustrated by the example in Fig 1. However, most of the GP infarcts were not symmetrical (Fig 2). A laterality index was computed as $(R - L) / (R + L)$; thus, right-dominant cases are represented by positive numbers; left-dominant cases, by negative numbers; and symmetrical cases, by values near zero. Most GP infarcts (12/19) were left-dominant, 5 were nearly symmetrical (within $\pm 10\%$), and 2 were right-dominant. The range of laterality indexes was -0.47 to $+0.48$, the mean was -0.13 , and the median was -0.17 .

In most patients (10/17), SNr infarcts were bilateral; SNr infarcts were detected only on the right in 5 patients and only on the left in 2 patients. SNr infarct sizes were not necessarily symmetrical, but there did not appear to be systematic lateralization, either in size or number. Patients had ≤ 3 infarcts per side. The total count of SNr infarcts was 17 per side.

GP Infarct Volumes

GP infarct volumes ranged from 9 to 1021 μL (Fig 3). Although the ranges overlapped, volumes for *mut* variants (*mut-* and *mut^o*) were smaller on average than volumes for *cblA* and *cblB*. Application of a *t* test suggested that there is a statistically significant difference in infarct size between the 2 *mut* subtypes together, the 2 *cbl* variants together ($P = .01$), and the *mut^o* subtype alone versus the 2 *cbl* classes together ($P = .02$). There was a statistically significant difference between the *mut-* subtype alone and each of the other categories ($P = .01$ versus *mut^o*, $P < .01$ versus *cblA*, and $P = .02$ versus *cblB*). A paired *t* test showed statistically significant lateralization within the *cblA* class ($P = .04$).

GP Infarct Staging

On review of the GP infarcts as a group, it became apparent that the infarct pattern was not random and that some segments of the GP infarcted more often than others. The 5 infarct-delineated segments are shown in Fig 4. There appear to be 3 distinct segments in the globus pallidus externa (GPe) and 2 distinct segments in the globus pallidus interna (GPi). When the affected

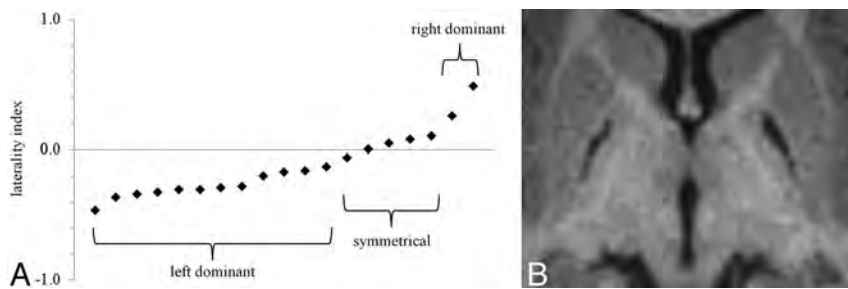


FIG 2. Laterality of GP infarcts. *A*, Most GP infarcts were left-dominant. A few were nearly symmetrical (5 were within $\pm 10\%$), and 2 were right-dominant. The average laterality index was -0.13 , and the median was -0.17 . *B*, An example of a left-dominant infarct. The laterality index in this case is -0.20 .

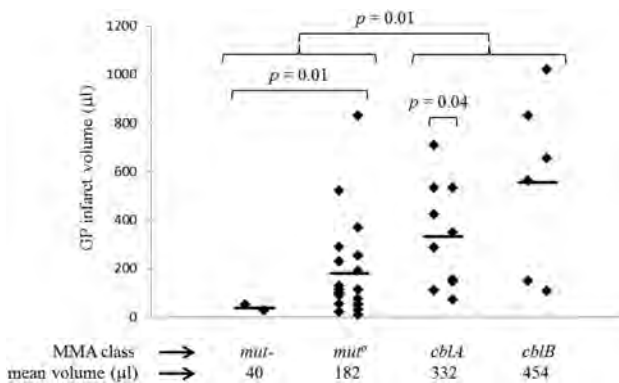


FIG 3. Volume of GP infarcts. The range of GP infarct volumes is $9\text{--}1021\ \mu\text{L}$. Laterality of the infarcts is apparent when infarcts are segregated into left and right columns for each of the MMA classes. Group means (indicated by the heavy bar) differ between classes. Application of a *t* test suggests that there is a statistically significant difference in infarct size between the 2 *mut* subtypes together (*mut*⁻ and *mut*^o), the 2 *cbl* classes together (*cblA* and *cblB*) ($P = .01$), and the *mut*^o subtype alone versus the 2 *cbl* classes together ($P = .02$). There was a statistically significant difference between the *mut*⁻ subtype alone and each of the other categories ($P = .01$ versus *mut*^o, $P < .01$ versus *cblA*, and $P = .02$ versus *cblB*). There was a statistically significant difference between the left and right for the *cblA* class ($P = .04$).

segments were all displayed as a group (Fig 5), it appeared that the segments were affected sequentially, with a few exceptions (5 of 38 infarcts in 3 of 19 patients). This observation suggested a staging system, in which the infarct stage is determined by counting the number of affected segments. According to this staging system, we observed 10 stage 1 infarcts, 7 stage 2 infarcts, 7 stage 3 infarcts, 3 stage 4 infarcts, and 11 stage 5 infarcts. In 3 patients, the right and left stages were discordant.

The GPe appeared to be more vulnerable to metabolic infarct than the GPi. In fact, only 1 infarct had any part of the GPi involved without involving the entire GPe. Within the GPe, vulnerability appeared highest in the most posterior segment and lowest in the most anterior segment, though there were 4 exceptions to that pattern. GPi vulnerability would seem to be fairly homogeneous, though there were 2 exceptions in which only half of the GPi was infarcted; in one case, only the posterior half was involved, and in the other case, only the anterior half was involved.

Distribution of SNr Infarcts

We observed that SNr infarcts were not randomly distributed but segregated into 3 distinct locations, which we have named accord-

ing to their relative positions, as shown in Fig 6. The anterior location was most common (20 infarcts). There were 9 infarcts in the posterior location and 5 infarcts in the middle location. Unlike the GP lesions, there was no clear hierarchy of SNr infarct locations. Among patients with *cblA*, 6 of 7 SNr infarcts were in the anterior location, but there did not seem to be a preferred location for any other type of MMA. Location and laterality of the SNr infarcts did not appear to correlate with GP infarct volume, stage, or laterality.

The demographics of SNr infarcts relative to GP infarcts does not suggest a clear difference between these locations in sensitivity to the toxic agent because we saw 4 cases of patients who had isolated SNr infarcts, 6 who had isolated GP infarcts, and 13 who had both types of infarcts. Examination of the demographics of the SNr infarcts (Table) demonstrated that the prevalence of SNr infarcts in each MMA class is similar to the prevalence of GP infarcts.

Detection of SNr Infarcts

We observed a difference in sensitivity for the detection of SNr infarcts related to the type of imaging performed. Among patients for whom bFFE images were available, SNr infarcts were detected in 9 of 16 (56%). However, among patients who had only 3D-T1WI, SNr infarcts were detected in 8 of 22 (36%). No SNr infarcts were detected for the 2 patients scanned outside our institution without any 3D imaging sequences. When both types of images were available, no SNr infarcts were detected on the 3D-T1WI that were not also detected on the bFFE images. Availability of bFFE images was determined by the date of the examination, rather than by any patient-related factors because this sequence was added to our scan protocol partway through the study. We expect that had the bFFE images been obtained in all patients, more SNr infarcts would have been detected.

DISCUSSION

The occurrence of bilateral isolated infarcts of the GP in patients who have isolated MMA has been previously reported.¹²⁻²¹ However, the analysis presented here is the first systematic study of GP imaging findings in a large group of patients with MMA, to our knowledge. This analysis also identified the previously unrecognized association of lacunar infarcts in the SNr with isolated MMA.

The staged pattern of MMA-related infarcts in the GP suggests that there are groups of cells in the GP that have differing vulnerability to metabolic stress and/or toxic metabolites. If there are neurons in certain locations in the GP and SNr that exist in a more tenuous balance between energy demands and blood supply, then this feature may also contribute to the staged pattern we observed. It is certainly possible that energy demands vary across the GP because the nuclei demonstrate somatotopic organization²⁶; therefore, some neurons within these nuclei are more frequently or intensely active than others. In humans and other primates, the

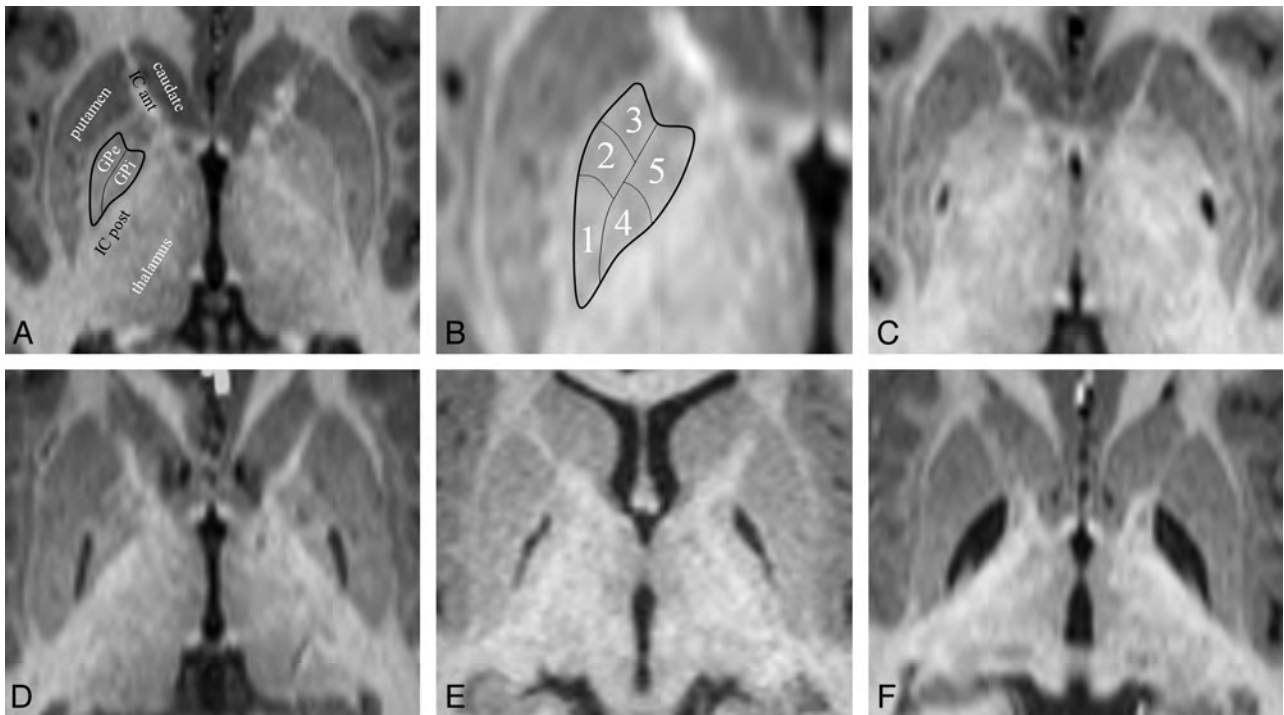


FIG 4. GP infarct segments. A, Normal anatomy of the dorsal pallidum, also known as the globus pallidus. The *thin line* indicates the medial medullary lamina; the *thick line*, the boundary of the globus pallidus. Surrounding structures include the anterior limb of the internal capsule (IC ant) and the posterior limb of the internal capsule (IC post). The putamen, thalamus, and head of the caudate nucleus are also labeled. The external medullary lamina separates the putamen from the GPe. B, Infarct segments 1–5. Segment 1 seems to be the most sensitive to metabolic infarct in MMA, followed by segment 2, then segment 3; segments 4 and 5 are the least sensitive and usually infarct together. C, An example of a segment 1 infarct (posterior GPe). D, An example of an infarct of segments 1 + 2 (posterior and middle GPe). E, An example of an infarct of segments 1 + 2 + 3 (whole GPe). F, An example of an infarct of segments 1 + 2 + 3 + 4 + 5 (complete GP, both externa and interna). Note that the medial medullary lamina (a white matter tract) remains intact and can be seen separating the GPe and GPi.

SNr is functionally part of the GPi and is composed of histologically identical cells.²⁴ In most nonprimate mammals, the GPi is not located adjacent to the GPe but rather exists as a separate nucleus called the “entopeduncular nucleus” that is embedded within the internal capsule.²⁴

In the initial analyses of GP infarcts in our patient cohort, we noted what appeared to be small defects in the cerebral peduncles in the vicinity of the substantia nigra. These changes were initially interpreted as secondary degeneration of the substantia nigra, as has been reported in cases of patients with vascular-origin strokes obliterating the ipsilateral basal ganglia.^{27,28} However, careful review revealed that this phenomenon occurs even in patients who have no GP infarcts; thus, this finding could not represent secondary degeneration. Given that cells of the SNr are histologically and functionally identical to cells of the GPi, it seems logical that they are susceptible to the same toxic and metabolic phenomena; therefore, we propose that these tiny lesions represent infarcts. While we lack histologic evidence that the lesions are located in the pars reticulata of the substantia nigra, as opposed to the pars compacta of the substantia nigra, the SNr location is consistent with a toxic/metabolic mechanism model due to the histologic and functional similarity to the GPi that is lacking in the dopaminergic portion of the substantia nigra (the pars compacta). There is 1 case report of isolated bilateral SNr lacunar infarcts (of unknown cause) in the literature.²⁹ It confirmed histologically that the lacunar infarct was in the SNr; the location of the infarct in the

case report encompasses the location that we have described as “anterior SNr” in Fig 6.

The relative sensitivity of GPe and GPi segments to toxicity in MMA seems fairly clear from the results presented in this report, but the relative sensitivity of the SNr remains less certain. One possible scenario is that the SNr is more sensitive to toxic injury in MMA than is the GPe and that few GPe infarcts occur without a preceding (or synchronous) SNr infarct, but that our detection of SNr infarcts is poor due to contrast and resolution considerations. If this scenario is accurate, then acquiring even higher resolution bFFE images of the midbrain in future patients with MMA should reveal additional SNr infarcts and should demonstrate that patients with GP infarcts are a subset of the patients with SNr infarcts. Another possible scenario would be that the sensitivity of the SNr to injury in MMA may actually be different from that in the GP; if so, the pattern we found in the current study should hold up even if higher resolution images are acquired in the future.

Given the somatotopy of the GP, one would expect that selective infarction of portions of the GPe and GPi would manifest neurologic symptoms that are specific to the site of the infarct. Experimental lesion studies in African green monkeys^{30,31} demonstrated that lesions in the posterior GPe produce dyskinesia, lesions in the middle GPe produce attention deficit disorder, and anterior-inferior GPe lesions produce stereotypical behaviors. This finding corresponds to the primary motor, supplementary

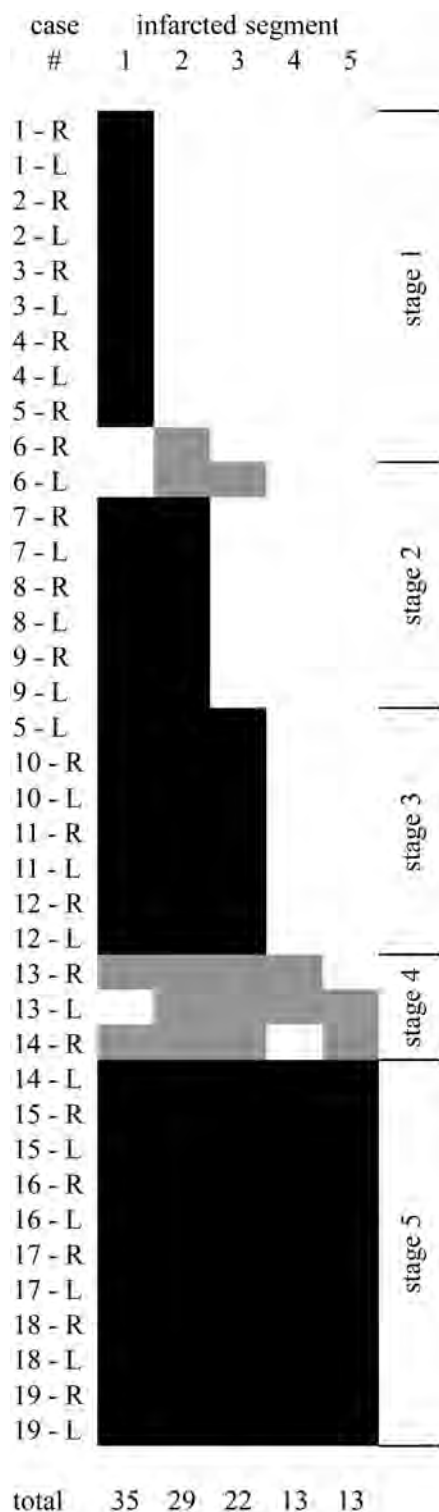


FIG 5. Graphic depiction of all 38 GP infarcts. Infarcted segments are shown in black (follows the rule) or gray (exception to the rule). The segments appear to follow a rule in which the likelihood of infarct is $1 > 2 > 3 > 4 = 5$. Five infarcts (in 3 different patients) do not follow the segment-ordering rule. Infarcts can be staged by counting the number of infarcted segments, regardless of the order. In 16 of 19 patients, right and left infarcts are of the same stage, even if the volumes differ (as described in Fig 2). The location of the segments is shown in Fig 4.

motor, and limbic zones of the GPe. Somatotopy of the GPI is parallel to that in the GPe²⁶ and ought to produce a similar profile of symptoms, except for the functions that are handled by the SNr. Isolated SNr infarcts ought to specifically produce orofacial motor symptoms. One might also expect that infarct volume and/or stage would correlate with overall symptom severity and that infarct laterality would correlate with lateralization of symptoms. The patients in our study underwent detailed neurologic examinations, and correlations between movement syndromes and infarct spatial patterns will be the subject of another article.

The laterality of GP infarct volumes is consistent with a previously reported asymmetric GP size in humans.³² In most people, the left GP is larger than the right, so our finding that most of the infarcts are larger on the left is consistent. Although we did not have enough left-handed patients with infarcts to determine whether preinfarct handedness had any influence on GP infarct laterality, we did observe 1 patient who appeared to change handedness (from right to left) following a large bilateral GP infarct (bilateral stage 5, right volume = 656 μ L, left volume = 562 μ L, laterality index = 0.08) and a tiny bilateral SNr infarct.

Among the various classes of isolated MMA, we found differences in both prevalence and size of GP infarcts and parallel differences in the prevalence of SNr infarcts. The relatively lower prevalence of both GP and SNr infarcts in patients with *mut* compared with other variants suggests that partial activity of the MUT enzyme has a protective effect, likely because patients with *mut* typically have lower concentrations of abnormal metabolites and less severe mitochondrial dysfunction.⁹ Although patients with *cblA* (and occasional patients with *cblB*) can be responsive to hydroxocobalamin supplementation, we found that their average stroke volume was significantly larger compared with patients with *mut*. The reasons for this finding are unclear, and it is possible that factors not directly related to the disease mechanism contribute. For example, the patients chosen for imaging in this study were selected, in part, on the basis of clinical suspicion of stroke, creating an ascertainment bias for more severe phenotypes in patients with normally milder biochemical defects (such as *cblA*); this choice would tend to skew our measurements toward larger and more symptomatic infarcts than we might have found had we imaged all patients being followed in our clinic. Another possibility would be that because so many of the infarcts were not associated with an abrupt change in symptoms, very few were detected in the acute phase; therefore, in most cases, we know neither the age of the patient at the time of the infarct nor the age of the infarct at the time of imaging. Potentially, the patients with *cblA* and *cblB* were older (and therefore larger) than the patients with *mut* at the time of the GP infarction because we know that some patients with *cblA* and *cblB* were not diagnosed with MMA until they presented in crisis later in childhood. If patients having different types of MMA typically have GP infarcts at different ages, when their brains are different sizes, there is the possibility that we would see a difference in infarct size even if the same fraction of the GP is infarcted, or perhaps infarcts imaged after a longer delay become larger as a result of atrophy of adjacent tissues. Normalizing the infarct volume as a fraction of the total GP volume could potentially correct some of these considerations, but de-

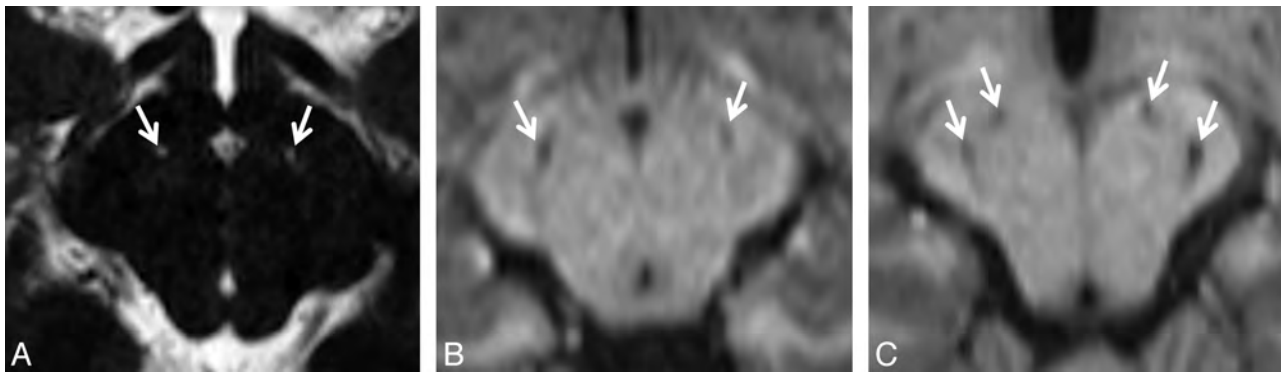


FIG 6. Lacunar infarcts of the SNr. Due to the small size of the cell clusters that form the SNr (near or below the lower limit of MR imaging resolution), detection of these infarcts can be difficult. *A*, Tiny bilateral infarcts of the SNr are seen on a bFFE image. The resolution of this image is $0.6 \times 0.6 \times 1.0$ mm per voxel. The infarcts measure approximately 1 mm. Both are found in the anterior location. *B*, Slightly larger bilateral infarcts of the SNr are seen on an MPRAGE image with a resolution of $0.9 \times 0.9 \times 1.0$ mm per voxel. These infarcts are in the middle location. *C*, Bilateral infarcts at 2 sites (anterior and posterior) in the SNr are seen on an MPRAGE image. SNr infarcts were found in only 3 distinct locations, which we are designating by their relative positions; the anterior location was the most common (20 infarcts), followed by the posterior location (9 infarcts). The middle location was the least common (5 infarcts).

fining the exact margins of the healthy portion of the GP, even manually, is difficult in practice due to the low contrast-to-noise ratio.

An additional limitation of this study is that we were unable to test for correlations relating infarct size, stage, and prevalence to factors such as prescribed treatments, compliance with treatment, and patient age (equivalent to duration of the disease). Unfortunately, the uncertainty in dating the infarcts precluded this type of analysis, and this uncertainty will remain an issue until presymptomatic and longitudinal brain imaging become part of the routine clinical management of MMA.

CONCLUSIONS

In summary, we examined patterns of GP infarction in patients with isolated MMA. We found a hierarchical pattern involving distinct segments of the GP, suggesting nonuniform sensitivity to the mechanism of infarct and suggesting a staging system. We found that the prevalence and size of the infarcts varied according to the class of isolated MMA and that the laterality of infarct volumes is similar to previously reported anatomic variation of the GP. We also noted small defects in the cerebral peduncles that we believe represent tiny lacunar infarcts in the SNr that are produced by the same toxic or metabolic mechanism as the GP infarcts but appear to arise as independent events.

ACKNOWLEDGMENTS

We thank the MR imaging technologists who acquired the images for this project, particularly Mastaneh Owahdi, Betty Wise, and Bonita Damaska. We also thank the patients (and their families) who participated in this study, the National Human Genome Research Institute medical and biochemical genetics fellows who helped evaluate the patients, and the physicians who referred their patients to our study.

Disclosures: Andrea L. Gropman—RELATED: Fees for Participation in Review Activities such as Data Monitoring Boards, Statistical Analysis, Endpoint Committees, and the Like: I am on a Data and Safety Monitoring Board for a Neuronal Ceroid Lipofuscinosis study; UNRELATED: Consultancy: I do consulting work for GeneDX, for the epilepsies; Expert Testimony: I have done some medical-legal work, usually 1 case per year; Grants/Grants Pending: Subproject of a U54 was awarded to my institu-

tion, but the topic is neuroimaging in Urea Cycle Disorders, not MMA*; Payment for Lectures (including service on Speakers Bureaus): I was reimbursed for a Grand Rounds at Rutgers; Payment for Development of Educational Presentations: I developed a basic neuroimaging introduction course for Shire Human Genetic Therapies; Travel/Accommodations/Meeting Expenses Unrelated to Activities Listed: I presented at the American College of Medical Genetics on Imaging in Neurogenetics but did not talk about MMA.

REFERENCES

- Manoli I, Venditti CP. *Methylmalonic Acidemia*. In: Pagon RA, Adam MP, Bird TD, et al, eds. *GeneReviews*. Seattle: University of Washington, Seattle; 2005
- Rosenberg LE, Lilljeqvist AC, Hsia YE. **Methylmalonic aciduria: an inborn error leading to metabolic acidosis, long-chain ketonuria and intermittent hyperglycinemia.** *N Engl J Med* 1968;278:1319–22
- Matsui SM, Mahoney MJ, Rosenberg LE. **The natural history of the inherited methylmalonic acidemias.** *N Engl J Med* 1983;308:857–61
- Fenton WA, Gravel RA, Rosenblatt DS. *Disorders of Propionate and Methylmalonate Metabolism*. New York: McGraw-Hill; 2013
- Willard HF, Rosenberg LE. **Inherited methylmalonyl CoA mutase apoenzyme deficiency in human fibroblasts: evidence for allelic heterogeneity, genetic compounds, and codominant expression.** *J Clin Invest* 1980;65:690–98
- Ando T, Rasmussen K, Wright JM, et al. **Isolation and identification of methylcitrate, a major metabolic product of propionate in patients with propionic acidemia.** *J Biol Chem* 1972;247:2200–04
- Hauser NS, Manoli I, Graf JC, et al. **Variable dietary management of methylmalonic acidemia: metabolic and energetic correlations.** *Am J Clin Nutr* 2011;93:47–56
- Touati G, Valayannopoulos V, Mention K, et al. **Methylmalonic and propionic acidurias: management without or with a few supplements of specific amino acid mixture.** *J Inherit Metab Dis* 2006;29:288–98
- Hörster F, Baumgartner MR, Viardot C, et al. **Long-term outcome in methylmalonic acidurias is influenced by the underlying defect (mut^o, mut⁻, cblA, cblB).** *Pediatr Res* 2007;62:225–30
- Kruszka PS, Manoli I, Sloan JL, et al. **Renal growth in isolated methylmalonic acidemia.** *Genet Med* 2013;15:990–96
- O’Shea CJ, Sloan JL, Wiggs EA, et al. **Neurocognitive phenotype of isolated methylmalonic acidemia.** *Pediatrics* 2012;129:e1541–51
- Bindu PS, Kovoov JM, Christopher R. **Teaching neuroimages: MRI in methylmalonic acidemia.** *Neurology* 2010;74:e14
- Campeau PM, Valayannopoulos V, Touati G, et al. **Management of West syndrome in a patient with methylmalonic aciduria.** *J Child Neurol* 2010;25:94–97
- de Sousa C, Piesowicz AT, Brett EM, et al. **Focal changes in the globi**

- pallidi associated with neurological dysfunction in methylmalonic acidemia. *Neuropediatrics* 1989;20:199–201
15. Heidenreich R, Natowicz M, Hainline BE, et al. **Acute extrapyramidal syndrome in methylmalonic acidemia: “metabolic stroke” involving the globus pallidus.** *J Pediatr* 1988;113:1022–27
 16. Korf B, Wallman JK, Levy HL. **Bilateral lucency of the globus pallidus complicating methylmalonic acidemia.** *Ann Neurol* 1986;20:364–66
 17. Larnaout A, Mongalgi MA, Kaabachi N, et al. **Methylmalonic acidemia with bilateral globus pallidus involvement: a neuropathological study.** *J Inherit Metab Dis* 1998;21:639–44
 18. Michel SJ, Given CA 2nd, Robertson WC Jr. **Imaging of the brain, including diffusion-weighted imaging in methylmalonic acidemia.** *Pediatr Radiol* 2004;34:580–82
 19. Roodhooft AM, Baumgartner ER, Martin JJ, et al. **Symmetrical necrosis of the basal ganglia in methylmalonic acidemia.** *Eur J Pediatr* 1990;149:582–84
 20. Trinh BC, Melhem ER, Barker PB. **Multi-slice proton MR spectroscopy and diffusion-weighted imaging in methylmalonic acidemia: report of two cases and review of the literature.** *AJNR Am J Neuroradiol* 2001;22:831–33
 21. Yeşildağ A, Ayata A, Baykal B, et al. **Magnetic resonance imaging and diffusion-weighted imaging in methylmalonic acidemia.** *Acta Radiol* 2005;46:101–03
 22. Işıkay S, Temel L, Keskin M. **Imaging findings associated with methylmalonic aciduria.** *Pediatr Neurol* 2014;50:435–36
 23. Sousa R, Hrinya Tannery N, Lafer EM. **Two new monoclonal antibodies provide immunohistochemical evidence for the unique biochemical similarity of the mouse globus pallidus, entopeduncular nucleus and substantia nigra pars reticulata.** *Neuroscience* 1990;34:403–10
 24. Nambu A. **Globus pallidus internal segment.** *Prog Brain Res* 2007;160:135–50
 25. McAuliffe M, Lalonde FM, McGarry D, et al. **Medical image processing, analysis and visualization in clinical research.** In: *Proceedings of the 14th IEEE Symposium on Computer-Based Medical Systems*, Washington, DC. July 26–27, 2001:381–86
 26. Nambu A. **Somatotopic organization of the primate basal ganglia.** *Front Neuroanat* 2011;5:26
 27. Forno LS. **Reaction of the substantia nigra to massive basal ganglia infarction.** *Acta Neuropathol* 1983;62:96–102
 28. Nakane M, Teraoka A, Asato R, et al. **Degeneration of the ipsilateral substantia nigra following cerebral infarction in the striatum.** *Stroke* 1992;23:328–32
 29. McKee AC, Levine DN, Kowall NW, et al. **Peduncular hallucinosis associated with isolated infarction of the substantia nigra pars reticulata.** *Ann Neurol* 1990;27:500–04
 30. François C, Grabli D, McCairn K, et al. **Behavioural disorders induced by external globus pallidus dysfunction in primates. II. Anatomical study.** *Brain* 2004;127:2055–70
 31. Grabli D, McCairn K, Hirsch EC, et al. **Behavioural disorders induced by external globus pallidus dysfunction in primates. I. Behavioural study.** *Brain* 2004;127:2039–54
 32. Kooistra CA, Heilman KM. **Motor dominance and lateral asymmetry of the globus pallidus.** *Neurology* 1988;38:388–90

Diffusivity Measurements Differentiate Benign from Malignant Lesions in Patients with Peripheral Neuropathy or Plexopathy

E.L. Yuh, S. Jain Palrecha, G.M. Lagemann, M. Kliot, P.R. Weinstein, N.M. Barbaro, and C.T. Chin



ABSTRACT

BACKGROUND AND PURPOSE: Peripheral nerve disorders caused by benign and malignant primary nerve sheath tumors, infiltration or compression of nerves by metastatic disease, and postradiation neuritis demonstrate overlapping features on conventional MR imaging but require vastly different therapeutic approaches. We characterize and compare diffusivities of peripheral nerve lesions in patients undergoing MR neurography for peripheral neuropathy or brachial or lumbosacral plexopathy.

MATERIALS AND METHODS: Twenty-three patients, referred for MR neurography at our institution between 2003 and 2009 for a peripheral mononeuropathy or brachial or lumbosacral plexopathy and whose examinations included DWI, received a definitive diagnosis, based on biopsy results or clinical and imaging follow-up, for a masslike or infiltrative peripheral nerve or plexus lesion suspicious for tumor. Mean ADC values were determined within each lesion and compared across 3 groups (benign lesions, malignant lesions, and postradiation changes).

RESULTS: Both ANOVA and Kruskal-Wallis tests demonstrated a statistically significant difference in ADC values across the 3 groups ($P = .000023$, $P = .00056$, respectively). Post hoc pair-wise comparisons showed that the ADC within malignant tumors differed significantly from that within benign tumors and postradiation changes. ADC within benign tumors and postradiation changes did not differ significantly from each other.

CONCLUSIONS: DWI may be highly effective for the differentiation of benign from malignant peripheral nerve masslike or infiltrative lesions.

Peripheral neuropathies can be divided into mononeuropathies, polyneuropathies, and plexopathies. Patients present with pain, sensory symptoms, and/or motor deficits in the distribution of a single peripheral nerve, multiple peripheral nerves, or a nerve plexus. Mononeuropathies affect a single peripheral nerve. Polyneuropathies affect multiple peripheral nerves. In plexopathies, symptoms are localized to the brachial or lumbosacral plexus.

Polyneuropathies are generally attributable to systemic diseases (eg, diabetes and vitamin deficiencies), while mononeuropathies are most often due to trauma, nerve compression syndromes that occur at a few characteristic anatomic locations, or mass lesions. History and physical examination, supplemented in a subset of cases by laboratory studies, electrodiagnostic studies, and neuroimaging, are the main tools for diagnostic evaluation. In patients with a classic compression mononeuropathy, such as median nerve compression at the carpal tunnel, the diagnosis can often be made clinically and corroborated by needle electromyography, nerve conduction, and/or imaging studies.¹⁻⁴ For mononeuropathies involving nerves not typically susceptible to compression syndromes, imaging can play an essential role in identifying the lesion and guiding management.

Plexopathies give rise to motor and/or sensory deficits in an extremity. Most brachial plexopathies (75%) are attributable to postradiation changes, primary and metastatic lung cancer, or metastatic breast cancer.⁵ Common causes of lumbosacral plexopathy are primary and metastatic tumor, including cervical, endometrial, ovarian, prostate, testicular, and colorectal cancer;

Received February 22, 2014; accepted after revision June 23.

From the Departments of Radiology and Biomedical Imaging (E.L.Y., C.T.C.) and Neurological Surgery (P.R.W.), University of California at San Francisco, San Francisco, California; San Leandro Medical Center (S.J.P.), The Permanente Medical Group, San Leandro, California; Department of Radiology (G.M.L.), University of Pittsburgh, Pittsburgh, Pennsylvania; Department of Neurosurgery (M.K.), Northwestern University Feinberg School of Medicine, Chicago, Illinois; and Goodman Campbell Brain and Spine (N.M.B.) and Department of Neurological Surgery (N.M.B.), Indiana University, Indianapolis, Indiana. E.L. Yuh and S. Jain Palrecha contributed equally to this work.

Please address correspondence to Cynthia T. Chin, MD, Department of Radiology and Biomedical Imaging, University of California at San Francisco, 505 Parnassus Ave, Box 0628, San Francisco, CA 94143-0628; e-mail: cynthia.t.chin@ucsf.edu



Indicates article with supplemental on-line table.

<http://dx.doi.org/10.3174/ajnr.A4080>

postradiation changes; and diabetes.⁶ For patients with a history of radiation for malignancy, recurrent tumor with nerve invasion must be distinguished from radiation plexopathy; both can develop months to years following therapy and can have similar clinical presentations.⁶

Although benign and malignant primary nerve sheath tumors, infiltration of nerves by metastatic disease, and postradiation neuritis require different therapeutic approaches, they also demonstrate overlapping features on MR imaging, including T2 hyperintensity, focal enlargement, and enhancement.^{7,8} Diffusivity measurements from DWI may be helpful in differentiating distinct pathologic entities. In prior studies, DWI was useful in differentiating malignant and benign peripheral nerve sheath tumors,⁹ retroperitoneal masses,¹⁰ head and neck tumors,^{11,12} and lymph nodes.^{13,14} Other studies have demonstrated differences in the diffusivities of adult¹⁵ or pediatric brain tumors¹⁶ that correlate with tumor grade and/or histologic type. In this study, we focus on masslike or infiltrative lesions of the peripheral nerves detected by MR imaging in patients presenting clinically with a peripheral mononeuropathy or plexopathy. We characterize and compare the diffusivities of these lesions and demonstrate significant differences among benign and malignant peripheral nerve tumors and postradiation changes.

MATERIALS AND METHODS

Study Population

Twenty-three patients referred for MR neurography at our institution between 2003 and 2009 by neurologists, neurosurgeons, and oncologists for a clinical indication of a peripheral mononeuropathy or brachial or lumbosacral plexopathy and who received a definitive diagnosis of a masslike or infiltrative nerve lesion based on biopsy results, long-term clinical and imaging follow-up, or intermediate-term follow-up supplemented by PET, neurologic examination, and/or nerve conduction studies were included in the study population. We included patients with noncystic “mass”-like lesions, defined as noncystic lesions with a diameter at least 50% larger than that of the apparent nerve of origin as well as patients with more infiltrative lesions consisting of more subtle nerve thickening and/or effacement of normally visualized interfascicular and surrounding fat planes without the presence of a well-defined “mass.” Study participants were divided into 3 groups according to the final most likely pathologic diagnosis. Group 1 ($n = 10$) consisted of benign lesions; Group 2 ($n = 7$), malignant tumors; and Group 3 ($n = 6$), postradiation changes, without evidence of residual tumor.

MR Neurography

MR imaging sequences performed at 1.5T (Gyrosan Intera 1.5T; Philips Healthcare, Best, the Netherlands) included axial and coronal STIR (TR = 2200 ms, TE = 20 ms, TI = 160 ms, NEX = 4, FOV = 22, matrix = 256 × 192, slice thickness/gap = 3/0.3 mm), T1 and fat-saturated postgadolinium T1-weighted spin-echo (TR = 500, TE = 14, NEX = 3), and DWI (single-shot echoplanar imaging, 6 directions, TR = 2 ms × pulse-pulse interval, TE = 15 ms, FOV = 22, matrix = 256 × 144, slice thickness/gap = 5.0/0.5 mm, b-value = 400 s/mm²). ADC maps were cal-

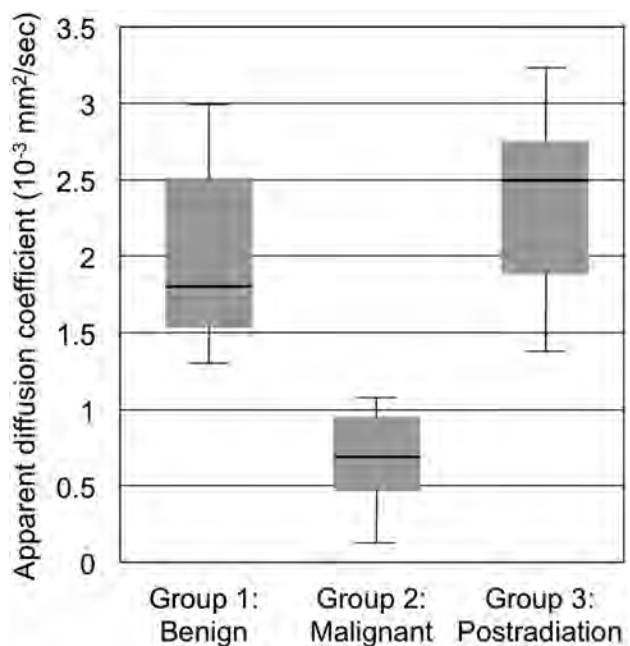


FIG 1. Boxplot shows median (thick horizontal lines within boxes), interquartile range (heights of boxes), and smallest and largest (lines protruding from boxes) ADC values within Group 1 (benign masses), Group 2 (malignant lesions), and Group 3 (postradiation changes). Group 1 ($n = 10$) included schwannomas and neurofibromas; Group 2 ($n = 7$) included 1 rhabdomyosarcoma, 1 malignant peripheral nerve sheath tumor, 2 cases of metastatic breast cancer, 1 case of metastatic renal cell carcinoma, 1 diffuse large B-cell lymphoma, and 1 case of acute lymphoblastic leukemia. Group 3 ($n = 6$) consisted of postradiation changes with no evidence for residual tumor. Group 3 (postradiation changes) demonstrated the highest median ADC value of $2.50 \times 10^{-3} \text{ mm}^2/\text{s}$ (interquartile range = $0.87 \times 10^{-3} \text{ mm}^2/\text{s}$, minimum = $1.39 \times 10^{-3} \text{ mm}^2/\text{s}$, maximum = $3.22 \times 10^{-3} \text{ mm}^2/\text{s}$), followed closely by benign lesions (Group 1) with a median ADC value of $1.81 \times 10^{-3} \text{ mm}^2/\text{s}$ (interquartile range = $0.98 \times 10^{-3} \text{ mm}^2/\text{s}$, minimum = $1.30 \times 10^{-3} \text{ mm}^2/\text{s}$, maximum = $2.97 \times 10^{-3} \text{ mm}^2/\text{s}$). Malignant lesions (Group 2) recorded the lowest median ADC value of $0.69 \times 10^{-3} \text{ mm}^2/\text{s}$ (interquartile range = $0.49 \times 10^{-3} \text{ mm}^2/\text{s}$, minimum = $0.26 \times 10^{-3} \text{ mm}^2/\text{s}$, maximum = $1.08 \times 10^{-3} \text{ mm}^2/\text{s}$).

culated using the Philips vendor software on the MR imaging scanner console immediately after acquisition of DWI data.

Mean and SD of ADC values within approximately 1-cm ROIs drawn within the lesions were determined independently by 2 board-certified radiologists. Each radiologist drew multiple ROIs for lesions that exceeded 3 cm and averaged the means within these ROIs, to avoid limited regional sampling of spatially heterogeneous lesions. Nonenhancing T2 hyperintense areas suspicious for cystic or necrotic areas were not included within any ROI. Volumes of masslike lesions were approximated by using the volume formula for an ellipsoid; volume = $(4/3) \times \pi \times a \times b \times c$, where a, b, and c were orthogonal linear dimensions of the lesion measured by one radiologist. (Volume measurements were not performed on infiltrative lesions that consisted of more subtle nerve thickening without a well-defined mass with a diameter at least 50% larger than that of the nerve of origin.)

Statistical Analysis

Intrarater reliability for ADC measurements was determined through calculation of the Pearson correlation coefficient be-

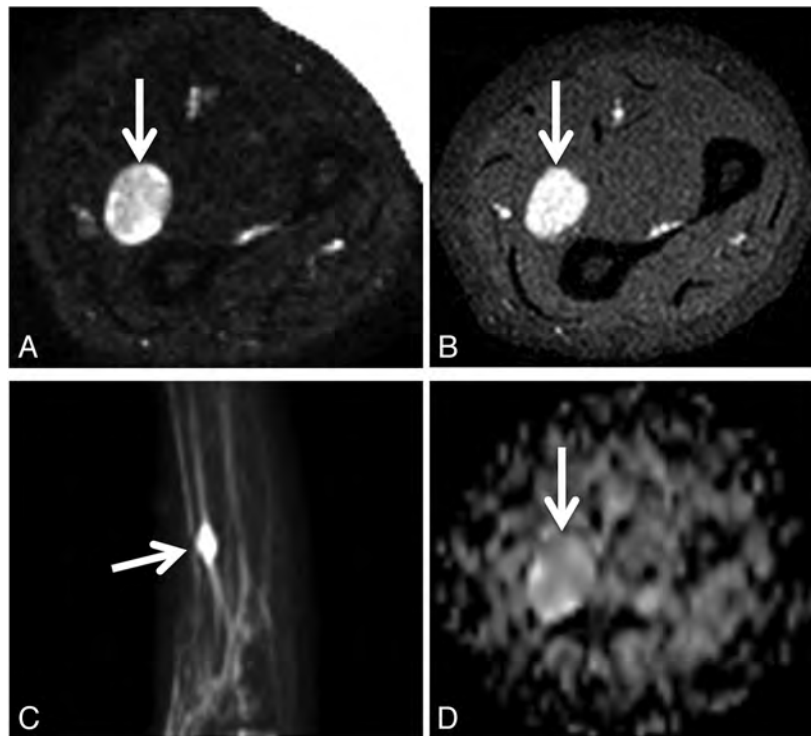


FIG 2. Biopsy-proven schwannoma of the left median nerve in a 48-year-old woman presenting with left upper extremity pain and paresthesias. Axial fat-suppressed T2 (A), axial fat-saturated postgadolinium T1 (B), maximum-intensity-projection DWI (C), and axial ADC (D) demonstrate a vividly enhancing, heterogeneously T2 hyperintense mass (*arrows*) along the median nerve. The ADC value within the mass was $2.1 \pm 0.36 \times 10^{-3}$ mm²/s. The lesion was resected due to progressive symptoms.

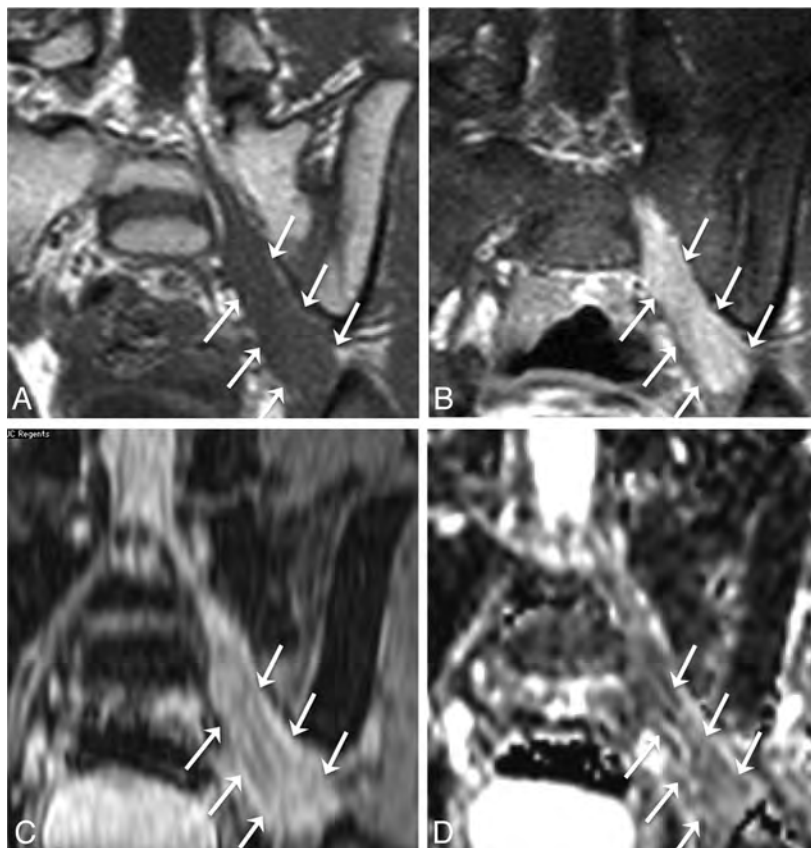


FIG 3. Biopsy-proven neurofibroma of the left S1 and sciatic nerves in a 6-year-old boy with left foot drop. Coronal T1 (A), coronal fat-saturated postgadolinium T1 (B), oblique reformatted coronal STIR (C), and coronal ADC (D) demonstrate enhancing masslike T2 hyperintense soft tissue (*arrows*) along the left S1 nerve and left sciatic nerve. The lesion was treated with radiation therapy.

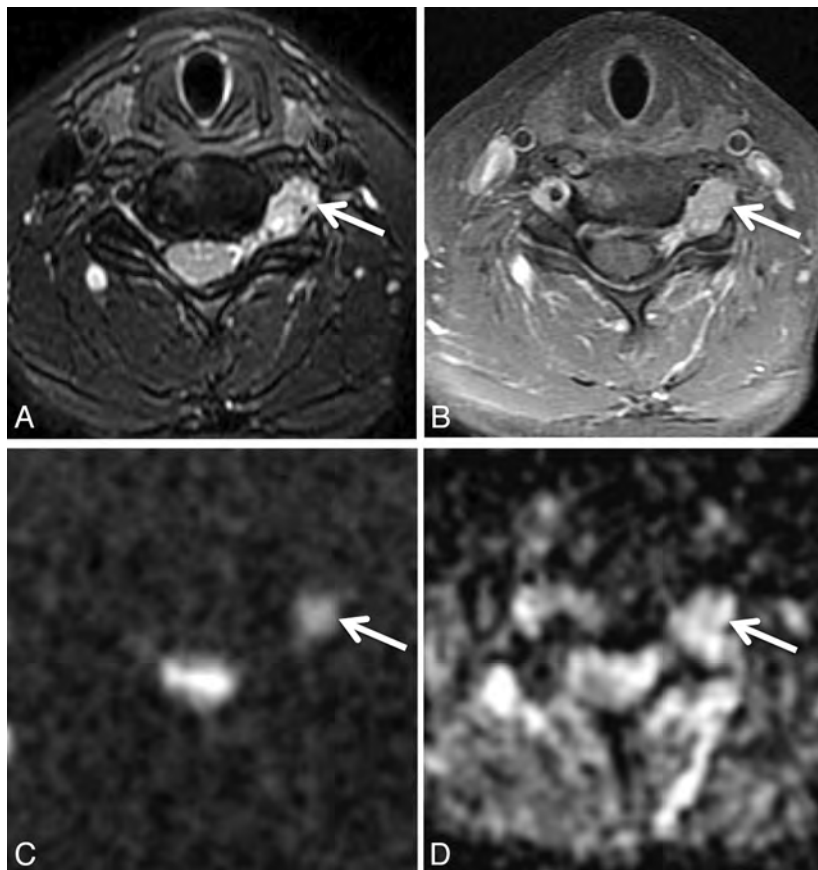


FIG 4. Metastatic renal cell carcinoma in a 46-year-old woman with left arm weakness. Axial STIR (A), axial fat-saturated postgadolinium T1 (B), axial DWI (C), and axial ADC (D) demonstrate a T2 hyperintense, enhancing mass (arrows) along the left C6 nerve just outside the left C5–C6 neural foramen. ADC within the mass was $1.08 \pm 0.09 \times 10^{-3} \text{ mm}^2/\text{s}$. The mass was subtotally resected and irradiated.

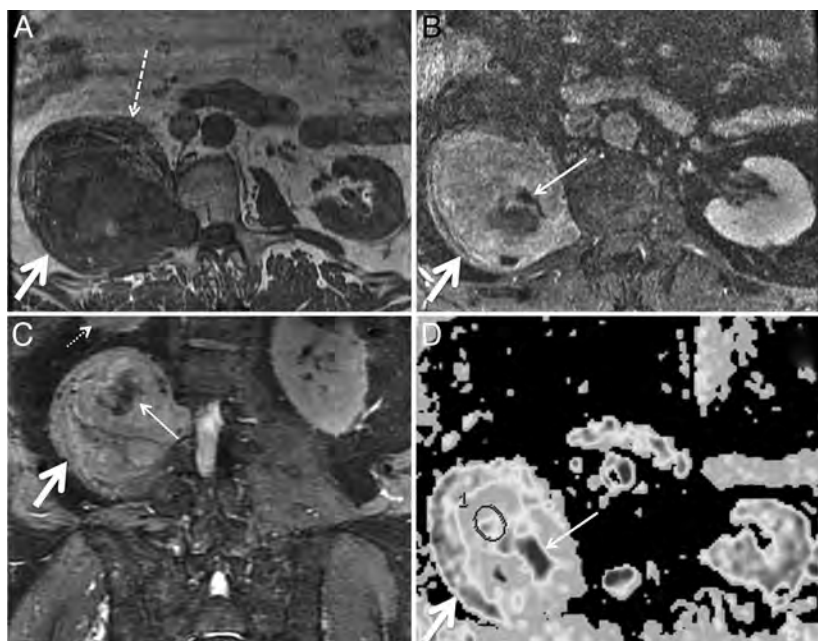


FIG 5. Malignant peripheral nerve sheath tumor in a 69-year-old man with several years of right lower extremity pain and anterior thigh numbness. Percutaneous biopsy several years earlier had demonstrated benign schwannoma. Gross total resection was performed for presumed schwannoma, with areas of necrosis attributed to the large size of the mass and outgrowth of blood supply. Final pathologic diagnosis was malignant peripheral nerve sheath tumor. Axial T1 (A), axial fat-saturated postgadolinium T1 (B), coronal STIR (C), and axial ADC (D) demonstrate a large mass (thick arrows) extending from a widened right L2–L3 neural foramen along the expected course of the right femoral nerve at the posterior aspect of the right psoas muscle. The right psoas muscle (dashed arrow) is draped and elongated over the anterior aspect of the mass. The right kidney (small dotted arrow) is displaced superiorly. D, ADC ROIs (circle) were selected to avoid nonenhancing areas (thin solid arrows in B–D) thought to represent necrosis. The mean ADC within nonnecrotic regions in the mass was $0.26 \times 10^{-3} \text{ mm}^2/\text{s}$.

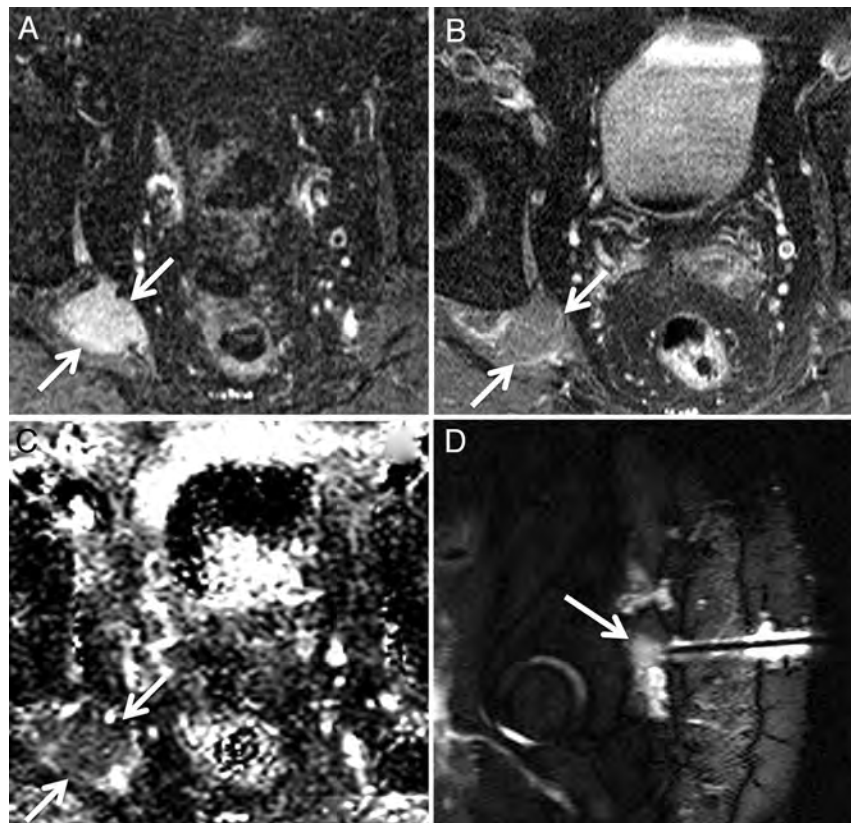


FIG 6. Biopsy-proven non-Hodgkin lymphoma infiltrating the right sciatic nerve. Axial STIR (A), axial fat-saturated postgadolinium T1 (B), and axial ADC map (C) demonstrate a T2 hyperintense minimally enhancing soft-tissue mass (arrows) along the right sciatic nerve at the greater sciatic foramen. ADC within the mass was $0.69 \pm 0.33 \times 10^{-3} \text{ mm}^2/\text{s}$. CT-guided biopsy was nondiagnostic. D, MR imaging-guided biopsy was performed, yielding a pathologic diagnosis of diffuse large B-cell lymphoma. The patient underwent chemotherapy and radiation to the mass.

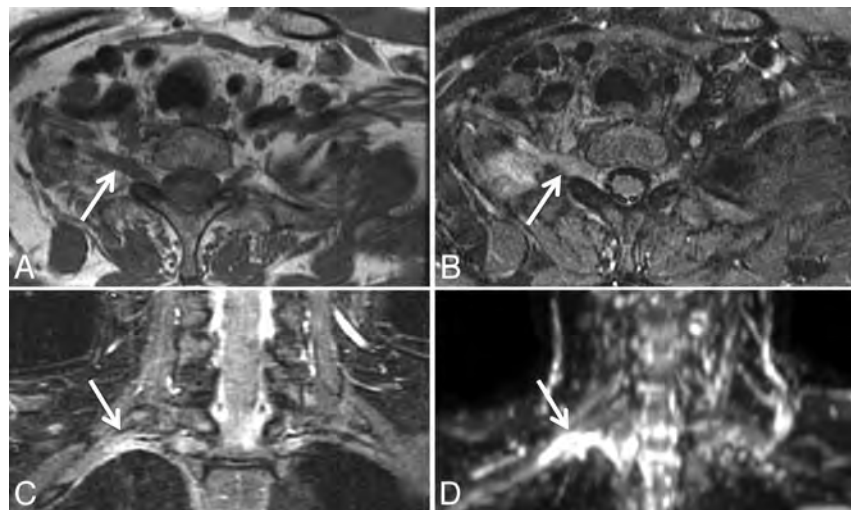


FIG 7. Biopsy-proven metastatic breast cancer infiltrating the right brachial plexus in a 53-year-old woman with right upper extremity pain. Axial T1 (A) and axial STIR (B) images demonstrate a thickened, T2 hyperintense right first thoracic nerve (arrows) with effacement of the fascicular structure normally visible on T1-weighted images. Coronal STIR (C) and maximum-intensity-projection DWI (D) demonstrate asymmetrically increased DWI signal in the right T1 nerve and inferior trunk of the right brachial plexus (arrows), with a corresponding mean ADC of $0.95 \pm 0.05 \times 10^{-3} \text{ mm}^2/\text{s}$. The patient underwent palliative radiation therapy.

tween separate measurements performed for each lesion by a single radiologist. Interrater reliability was determined through the Pearson correlation coefficient between measurements performed on each lesion by the 2 different radiologists.

One-way between-groups ANOVA was performed to assess for a statistically significant difference in ADC values among the 3 groups (benign lesions, malignant lesions, and postradiation changes) at $P < .05$. Post hoc pair-wise comparisons were

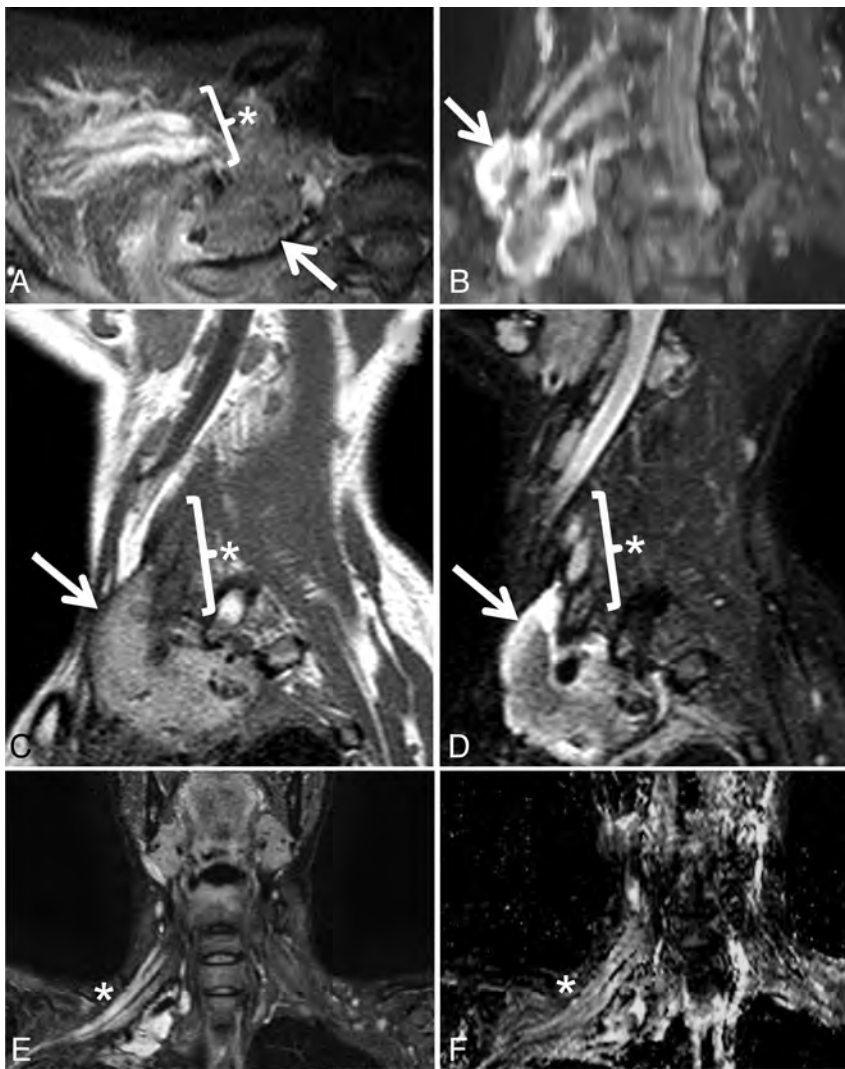


FIG 8. Postradiation brachial plexopathy in a 42-year-old woman with progressive right upper extremity weakness, beginning in the hand and progressing proximally. She had undergone resection and radiation therapy 12 years earlier for high-grade round cell sarcoma of the right brachial plexus. Axial STIR (A), maximum-intensity-projection coronal oblique STIR (B), sagittal T1 (C), sagittal STIR (D), coronal STIR (E), and coronal ADC (F) demonstrate a soft-tissue mass (arrows) and a thickened, T2 hyperintense right brachial plexus (asterisks) with an average ADC of $2.59 \pm 0.16 \times 10^{-3} \text{ mm}^2/\text{s}$. Although symptoms persisted, the appearance of the mass and the enhancing, T2 hyperintense brachial plexus were unchanged over multiple follow-up MR imaging examinations over 60 months, and a final diagnosis of postradiation brachial plexopathy was made. The soft-tissue mass likely represents fibrosis related to surgical resection of the mass and subsequent radiation.

then performed using the Tukey test to assess for statistically significant pair-wise differences between pairs of groups at $P < .05$.

Although ADC values within each group satisfied the Shapiro-Wilk test for normality, the sensitivity of this test for nonnormality may be reduced for small sample sizes.¹⁷ The nonparametric Kruskal-Wallis test was also performed on the ADC values to assess for a statistically significant difference across groups at $P < .05$. Post hoc nonparametric pair-wise comparisons were performed using Mann-Whitney *U* tests to assess for statistically significant differences between pairs of groups at $P < .05$. All statistical analyses were performed using SPSS, Version 19 (IBM, Armonk, New York).

This study was approved by the institutional committee on human subjects research. All patient data stored for the purpose of this research study were anonymized by using accession numbers to identify each case.

RESULTS

The On-line Table shows diagnoses in 23 patients divided into 3 groups on the basis of biopsy results ($n = 10$); long-term clinical and imaging follow-up ($n = 10$; mean follow-up, 40 ± 31 months); or intermediate-term follow-up supplemented by PET, neurologic examination, and/or nerve conduction studies ($n = 3$, mean follow-up, 4 ± 1 months). Group 1 ($n = 10$) consisted of benign masses, including 4 biopsy-proven schwannomas, 1 biopsy-proven neurofibroma, and 5 peripheral nerve masses that demonstrated both long-term stability in size and conventional MR imaging features characteristic of a benign primary nerve sheath tumor. Group 2 ($n = 7$), malignant tumors, consisted of 1 biopsy-proven malignant peripheral nerve sheath tumor, 1 biopsy-proven rhabdomyosarcoma, 2 cases of metastatic breast cancer involving the brachial plexus (biopsy-proven) or the sacral nerves, 1 case of biopsy-proven metastatic renal cell carcinoma involving a cervical nerve, 1 case of biopsy-proven non-Hodgkin lymphoma involving the sciatic nerve, and 1 case of acute lymphoblastic leukemia involving the brachial plexus. Group 3 ($n = 6$) consisted of postradiation changes without evidence of residual tumor in 6 cases of previously irradiated malignancies, including 3 cases of breast cancer, 1 high-grade sarcoma, 1 case of Hodgkin lymphoma, and 1 case of oral squamous cell carcinoma. Lesion volumes ranged

from 1 to 5530 cm^3 (median, 37 cm^3 ; 25th percentile, 14 cm^3 ; 75th percentile, 122 cm^3).

Fig 1 demonstrates ADC values within Groups 1–3. Postradiation changes without evidence of residual tumor (Group 3) demonstrated the highest median ADC value of $2.50 \times 10^{-3} \text{ mm}^2/\text{s}$ (interquartile range = $0.87 \times 10^{-3} \text{ mm}^2/\text{s}$, minimum = $1.39 \times 10^{-3} \text{ mm}^2/\text{s}$, maximum = $3.22 \times 10^{-3} \text{ mm}^2/\text{s}$, mean ADC = $2.37 \times 10^{-3} \text{ mm}^2/\text{s}$, SD = $0.61 \times 10^{-3} \text{ mm}^2/\text{s}$), followed closely by benign lesions (Group 1) with a median ADC value of $1.81 \times 10^{-3} \text{ mm}^2/\text{s}$ (interquartile range = $0.98 \times 10^{-3} \text{ mm}^2/\text{s}$, minimum = $1.30 \times 10^{-3} \text{ mm}^2/\text{s}$, maximum = $2.97 \times 10^{-3} \text{ mm}^2/\text{s}$, mean ADC = $1.99 \times 10^{-3} \text{ mm}^2/\text{s}$, SD = $0.60 \times 10^{-3} \text{ mm}^2/\text{s}$). Malignant lesions (Group 2) recorded the lowest median ADC

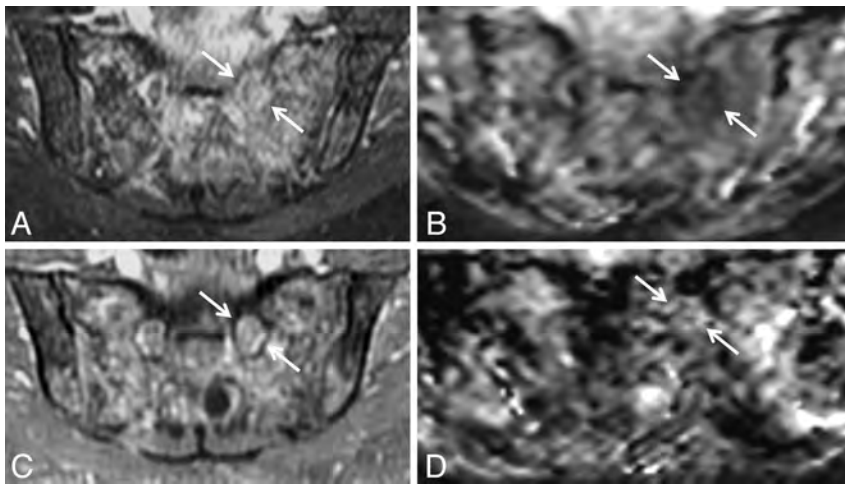


FIG 9. Marked increase in diffusivity following radiation therapy for metastatic breast cancer in a 47-year-old woman with pain in the left L4 through S2 distribution. Axial fat-saturated post-gadolinium T1 and ADC before (A and B) and 4 months following completion of radiation therapy (C and D). Initial images (A and B) demonstrate metastatic disease throughout the sacrum and infiltrating the left S1 nerve (arrows). B, Before radiation, ADC within the diseased left S1 nerve was $0.78 \pm 0.15 \times 10^{-3} \text{ mm}^2/\text{s}$. D, Four months later, following completion of radiation therapy, ADC within the nerve had markedly increased to $1.39 \pm 0.23 \times 10^{-3} \text{ mm}^2/\text{s}$.

value of $0.69 \times 10^{-3} \text{ mm}^2/\text{s}$ (interquartile range = $0.49 \times 10^{-3} \text{ mm}^2/\text{s}$, minimum = $0.26 \times 10^{-3} \text{ mm}^2/\text{s}$, maximum = $1.08 \times 10^{-3} \text{ mm}^2/\text{s}$, mean ADC = $0.69 \times 10^{-3} \text{ mm}^2/\text{s}$, SD = $0.28 \times 10^{-3} \text{ mm}^2/\text{s}$). Intrarater and interrater reliability for ADC measurements, characterized by the Pearson correlation coefficient r , were $r = 0.98$ ($P = 7.0 \times 10^{-7}$) for intrarater reliability and $r = 0.88$ ($P = .0011$) for interrater reliability.

One-way between-groups ANOVA demonstrated a statistically significant difference in ADC values across the 3 groups: F ($df_1 = 2, df_2 = 20$) = 19.0, $P = .000023$. Post hoc pair-wise comparisons using the Tukey test showed that the mean ADC values for Group 1 ($1.99 \times 10^{-3} \text{ mm}^2/\text{s}$) and Group 2 ($0.69 \times 10^{-3} \text{ mm}^2/\text{s}$) were significantly different at $P = .0002$ and mean ADC values for Group 2 ($0.69 \times 10^{-3} \text{ mm}^2/\text{s}$) and Group 3 ($2.37 \times 10^{-3} \text{ mm}^2/\text{s}$) were significantly different at $P = .000039$. The ADC for Groups 1 and 3 did not differ significantly from each other ($P = .36$).

The nonparametric Kruskal-Wallis test also showed a statistically significant difference in ADC across the 3 groups, with χ^2 ($df = 2, 23$ subjects) = 15.0 and $P = .00056$. Finally, post hoc nonparametric pair-wise comparisons using the Mann-Whitney U test showed a statistically significant difference in ADC between Groups 1 and 2 ($P = .00010$) and between Groups 2 and 3 ($P = .0012$), but no statistically significant difference between Groups 1 and 3 ($P = .97$).

Figs 2–9 demonstrate MR images of representative cases from each of the 3 groups (benign lesions, malignant lesions, and post-radiation changes).

DISCUSSION

Peripheral polyneuropathies affect multiple peripheral nerves and are generally caused by systemic diseases, most commonly diabetes, and vitamin deficiency related to alcohol use or pernicious anemia, in the United States and Europe. Polyneuropathies

are usually diagnosed through clinical history, physical examination, laboratory studies, nerve conduction studies, and needle electromyography.^{6,18} Unlike polyneuropathies, mononeuropathies and plexopathies are most often due to trauma, nerve compression syndromes at characteristic anatomic locations, mass lesions, and post-radiation changes; and imaging can play a decisive role in diagnosis. In a study of MR imaging of symptomatic nontraumatic brachial plexopathy, post-radiation change was the most common cause, accounting for 31% of cases, with metastatic breast cancer and primary or metastatic lung cancer accounting for 24% and 19% of cases, respectively. The remaining 26% of cases were caused by a wide variety of benign and malignant tumors.⁵ Unlike many cases of diffuse polyneuropathy, patients with brachial or lumbosacral plexopathy frequently undergo MR imaging due to the localized

distribution of symptoms and presumed localized extent of the pathologic findings.^{19,20}

We characterized the diffusivity of masslike or infiltrative lesions of the peripheral nerves discovered on MR imaging performed for a clinical indication of peripheral mononeuropathy or brachial or lumbosacral plexopathy. We demonstrated a statistically significant difference among the diffusivities of benign and malignant tumors and post-radiation changes. This result is compatible with other studies that have demonstrated diffusivity to be generally inversely correlated with tumor cellularity and tumor grade in several contexts, including adult and pediatric brain tumors, head and neck masses, lymph nodes, retroperitoneal soft-tissue masses,^{10-16,21} and MR neurography.⁹ Our results are also consistent with a prior study⁹ in which a statistically significant difference in ADC values between benign ($1.85 \pm 0.40 \times 10^{-3} \text{ mm}^2/\text{s}$) and malignant ($0.90 \pm 0.25 \times 10^{-3} \text{ mm}^2/\text{s}$) peripheral nerve tumors and tumorlike masses was reported ($P < .001$). In the current study, we extended the analysis to include infiltrative post-radiation changes of the peripheral nerves that were not included in that previous study. We report a complete separation of ADC values between benign and malignant lesions, with malignant lesions demonstrating $\text{ADC} \leq 1.08 \times 10^{-3} \text{ mm}^2/\text{s}$, and benign lesions demonstrating $\text{ADC} \geq 1.30 \times 10^{-3} \text{ mm}^2/\text{s}$.

The apparent diffusion coefficient is a measure of the diffusivity, or microscopic mobility, of water protons in tissue. The difference in ADC values of the lesions in our study was likely due to factors such as tumor cellularity, integrity of cell membranes, nuclear-to-cytoplasmic ratio, and the water content of the extracellular matrix. These have been postulated to account for low diffusivity within malignant solid tumors in prior studies.^{10-16,21} A study of benign and malignant extracranial soft-tissue tumors in children showed an inverse relationship between ADC measurements and cellular density derived from histologic analysis, but correlation was only moderate ($R^2 = 0.54$), and it was postulated

that additional factors such as extracellular water content also influence the ADC.²² Myxoid matrix is known to be abundant in both schwannomas and neurofibromas. Schwannomas, particularly Antoni B tissue within schwannomas, contain a high water content, due to low cellularity and high mucin and low collagen content,²³ and this likely accounts for their high diffusivity.

Limitations of this study include the lack of biopsy-proven diagnoses for all patients, the likelihood that diffusion characteristics of postradiation changes evolve with time, and the need for validation in a larger study population. Some malignant peripheral nerve sheath tumors, which may arise either de novo or from malignant degeneration of plexiform neurofibromas, have been shown to have a significant myxoid content; one prior study of soft-tissue masses reported that ADC failed to differentiate benign from malignant myxoid soft-tissue tumors, though only one malignant peripheral nerve sheath tumor was included in that study.²¹ ADC values in postradiation change are likely to be affected by features such as edema, fibrous-inflammatory reaction, and vascular permeability that are temporally dynamic, particularly in the first few months after treatment. Long-term follow-up imaging rather than biopsy was more often performed for lesions with benign features on conventional imaging, introducing a bias, because biopsy was performed on all lesions that ultimately received a malignant diagnosis but on only a subset of lesions receiving a benign diagnosis. Finally, rare entities such as perineuroma²⁴ and posttraumatic neuroma appear as mass lesions of the peripheral nerves, but were not included within our study population.

CONCLUSIONS

We demonstrate a statistically significant difference in diffusivity between biopsy-proven malignant lesions, and lesions with either biopsy-proven benign histology or stable size and benign features on follow-up imaging. Although our results need to be validated in a larger study population, the pattern of diffusivity values within benign and malignant lesions described here may be helpful in selecting patients for percutaneous tissue sampling, debulking versus en bloc total resection, and/or short-term clinical and imaging follow-up.

Disclosures: Nicholas M. Barbaro—UNRELATED: Grants/Grants Pending: National Institute of Neurological Disorders and Stroke.* Elekta.* *Money paid to the institution.

REFERENCES

- Spinner RJ. **Outcomes for peripheral nerve entrapment syndromes.** *Clin Neurosurg* 2006;53:285–94
- Britz GW, Haynor DR, Kuntz C, et al. **Carpal tunnel syndrome: correlation of magnetic resonance imaging, clinical, electrodiagnostic, and intraoperative findings.** *Neurosurgery* 1995;37:1097–103
- Guggenberger R, Markovic D, Eppenberger P, et al. **Assessment of median nerve with MR neurography by using diffusion-tensor imaging: normative and pathologic diffusion values.** *Radiology* 2012;265:194–203
- Keen NN, Chin CT, Engstrom JW, et al. **Diagnosing ulnar neuropathy at the elbow using magnetic resonance neurography.** *Skeletal Radiol* 2012;41:401–07
- Wittenberg KH, Adkins MC. **MR imaging of nontraumatic brachial plexopathies: frequency and spectrum of findings.** *Radiographics* 2000;20:1023–32
- Amato AA, Barohn RJ. **Peripheral neuropathy.** In: Longo DL, Fauci AS, Kasper DL, et al, eds. *Harrison's Principles of Internal Medicine*. 18th ed. New York: McGraw-Hill; 2011:3448–72
- Stoll G, Bendszus M, Perez J, et al. **Magnetic resonance imaging of the peripheral nerves.** *J Neurol* 2009;256:1043–51
- Li CS, Huang GS, Wu HD, et al. **Differentiation of soft tissue benign and malignant peripheral nerve sheath tumors with magnetic resonance imaging.** *Clin Imaging* 2008;32:121–27
- Chhabra A, Thakkar RS, Andreisek G, et al. **Anatomic MR imaging and functional diffusion tensor imaging of peripheral nerve tumors and tumorlike conditions.** *AJNR Am J Neuroradiol* 2013;34:802–07
- Nakayama T, Yoshimitsu K, Irie H, et al. **Usefulness of the calculated apparent diffusion coefficient value in the differential diagnosis of retroperitoneal masses.** *J Magn Reson Imaging* 2004;20:735–42
- Thoeny HC, De Keyser F, King AD. **Diffusion-weighted MR imaging in the head and neck.** *Radiology* 2012;263:19–32
- Abdel Razek AA, Kandeel AY, Soliman N, et al. **Role of diffusion-weighted echo-planar MR imaging in differentiation of residual or recurrent head and neck tumors and posttreatment changes.** *AJNR Am J Neuroradiol* 2007;28:1146–52
- Fornasa F, Nesoti MV, Bovo C, et al. **Diffusion-weighted magnetic resonance imaging in the characterization of axillary lymph nodes in patients with breast cancer.** *J Magn Reson Imaging* 2012;36:858–64
- Koşucu P, Tekinbas C, Erol M, et al. **Mediastinal lymph nodes: assessment with diffusion-weighted MR imaging.** *J Magn Reson Imaging* 2009;30:292–97
- Yamasaki F, Kurisu K, Satoh K, et al. **Apparent diffusion coefficient of human brain tumors at MR imaging.** *Radiology* 2005;235:985–91
- Kan P, Liu JK, Hedlund G, et al. **The role of diffusion-weighted magnetic resonance imaging in pediatric brain tumors.** *Childs Nerv Syst* 2006;22:1435–39
- Shapiro SS, Wilk MB, Chen HJ. **A comparative study of various tests for normality.** *J Am Statist Assoc* 1968;63:1343–72
- England JD, Asbury AK. **Peripheral neuropathy.** *Lancet* 2004;363:2151–61
- Grant GA, Britz GW, Goodkin R, et al. **The utility of magnetic resonance imaging in evaluating peripheral nerve disorders.** *Muscle Nerve* 2002;25:314–31
- Thyagarajan D, Cascino T, Harms G. **Magnetic resonance imaging in brachial plexopathy of cancer.** *Neurology* 1995;45:421–27
- Nagata S, Nishimura H, Uchida M, et al. **Diffusion-weighted imaging of soft tissue tumors: usefulness of the apparent diffusion coefficient for differential diagnosis.** *Radiat Med* 2008;26:287–95
- Humphries PD, Sebire NJ, Siegel MJ, et al. **Tumors in pediatric patients at diffusion-weighted MR imaging.** *Radiology* 2007;245:848–54
- Wippold FJ, Lubner M, Perrin RJ, et al. **Neuropathology for the neuroradiologist: Antoni A and Antoni B tissue patterns.** *AJNR Am J Neuroradiol* 2007;28:1633–38
- Merlini L, Viallon M, De Coulon G, et al. **MRI neurography and diffusion tensor imaging of a sciatic perineuroma in a child.** *Pediatr Radiol* 2008;38:1009–12

Vertebral Augmentation for Neoplastic Lesions with Posterior Wall Erosion and Epidural Mass

A. Cianfoni, E. Raz, S. Mauri, S. Di Lascio, M. Reinert, G. Pesce, and G. Bonaldi

ABSTRACT

BACKGROUND AND PURPOSE: The presence of a cortical erosion of the posterior wall or an epidural mass is commonly considered a contraindication to performing a vertebral augmentation, considering the perceived increased risk of an epidural cement leak. Our aim was to assess technical and clinical complications of vertebral augmentation procedures performed for pain palliation and/or stabilization of neoplastic lytic vertebral body lesions, with cortical erosion of the posterior wall, often associated with a soft-tissue epidural mass.

MATERIALS AND METHODS: In 48 patients, we performed retrospective vertebral augmentation assessment on 70 consecutive levels with cortical erosion of the posterior wall, as demonstrated by preprocedural CT/MR imaging. An epidural mass was present in 31/70 (44.3%) levels. Cavity creation was performed with Coblation Wands before cement injection in 59/70 levels. Injection of high-viscosity polymethylmethacrylate was performed under real-time continuous fluoroscopic control. Postprocedural CT of the treated levels was performed in all cases. Clinical follow-up was performed at 1 and 4 weeks postprocedurally.

RESULTS: In 65/70 (92.8%) levels, the vertebral augmentation resulted in satisfactory polymethylmethacrylate filling of the lytic cavity and adjacent trabecular spaces in the anterior half of the vertebral body. An epidural leak of polymethylmethacrylate occurred in 10/70 (14.2%) levels, causing radicular pain in 3 patients, which spontaneously resolved within 1 week in 2 patients, while 1 patient with a T1–T2 foraminal leak developed severe weakness of the intrinsic hand muscles and a permanent motor deficit.

CONCLUSIONS: In our series of vertebral augmentation of neoplastic lytic vertebral lesions performed for palliation of pain and/or stabilization, we observed a polymethylmethacrylate epidural leak in only 14.2% of levels, despite the presence of cortical erosion of the posterior wall and an epidural mass, with an extremely low rate of clinical complications. Our data seem to justify use of vertebral augmentation in patients with intractable pain or those at risk for vertebral collapse.

ABBREVIATIONS: CE-PW = cortical erosion of the posterior wall; EM = epidural mass; PMMA = polymethylmethacrylate; VA = vertebral augmentation

Spinal metastases, which are present in approximately 5% of patients with systemic cancer,^{1,2} are often associated with severe pain and reduced quality of life and can lead to potential catastrophic complications linked to spinal cord compression.³

Vertebroplasty, first described in 1987,⁴ and, in more general terms, vertebral augmentation (VA) procedures are widely performed, especially for osteoporotic fractures⁵ but also as palliative treatment for painful or at-risk-of-collapse neoplastic lytic vertebral

body lesions.⁶ The intent of the procedure is to relieve pain and/or stabilize the vertebral body to arrest a developing fracture or prevent a new one.^{7–9} Multiple recent studies have shown a significant improvement in clinical outcomes (including pain) by using percutaneous vertebroplasty with or without kyphoplasty.^{10–12} The presence of a cortical erosion of the posterior wall (CE-PW) or an epidural mass (EM) is commonly considered a contraindication to performing VA, considering the perceived increased risk of an epidural polymethylmethacrylate (PMMA) cement leak.¹³ A PMMA epidural leak carries the risk of compression of the spinal cord and/or the nerve roots. The cement may also displace the tumor posteriorly, through a dehiscence posterior wall into the spinal canal; this event may be an even more dangerous complication, given the lack of control and visualization under fluoroscopy.¹³

The recently introduced controlled ablation (Coblation; ArthroCare, Austin, Texas) is a technique that allows the destruction of the tumor by placing a radiofrequency “wand” through the

Received May 6, 2014; accepted after revision June 26.

From the Departments of Neuroradiology (A.C., E.R.) and Neurosurgery (M.R.), Neurocenter of Southern Switzerland, Lugano, Switzerland; Department of Radiology (E.R.) New York University Langone Medical Center, New York, New York; Department of Neurology and Psychiatry (E.R.), Sapienza University of Rome, Rome, Italy; Oncology Institute of Italian Switzerland (S.M., S.D.L., G.P.), Bellinzona, Switzerland; and Department of Neuroradiology (G.B.), Papa Giovanni XXIII Hospital, Bergamo, Italy.

Please address correspondence to Eytan Raz, MD, Department of Radiology, NYU Langone Medical Center, 660 First Ave, 7th floor, 10016 New York, NY; e-mail: eytan.raz@gmail.com

<http://dx.doi.org/10.3174/ajnr.A4096>

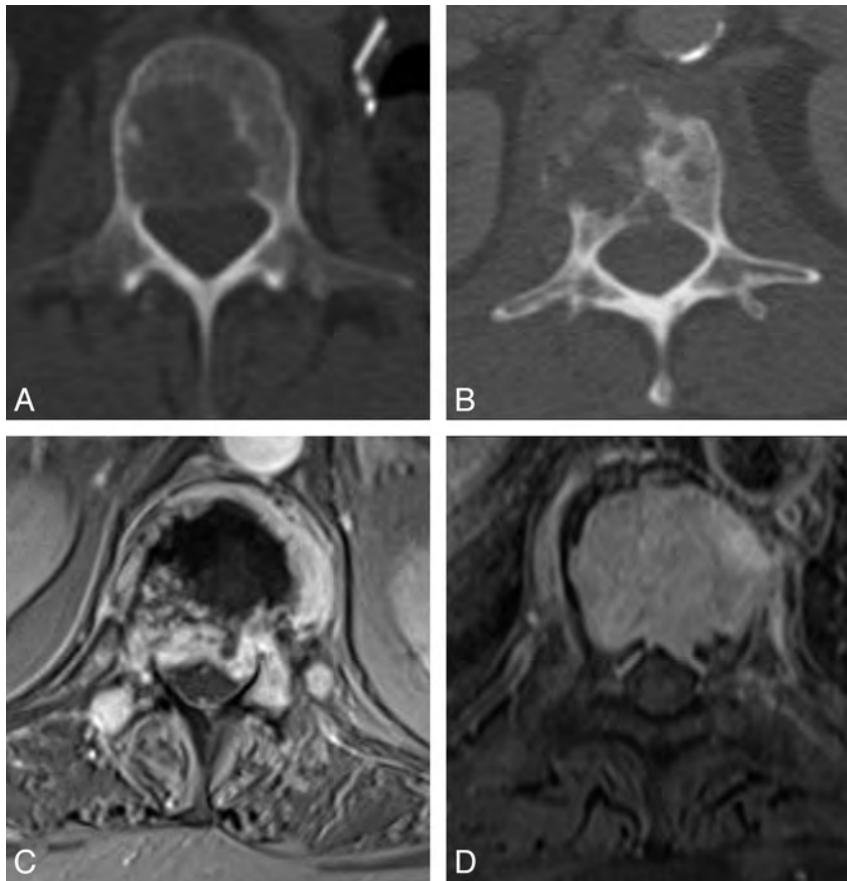


FIG 1. Preprocedural imaging. All patients had preprocedural CT to detect the presence of lytic cortical erosion of the posterior wall of the vertebral body, which was dichotomized into 2 main patterns: large defect (A) and permeative erosive defect (B). All patients had preprocedural MR imaging of the spine at the target levels to detect extraosseous neoplastic epidural soft tissue, dichotomized into large and convex (C) and small and concave (D).

vertebroplasty needle and uses the activation of a plasma field to vaporize the neoplastic soft tissue and create a cavity¹⁴; this cavity can then be filled more precisely and with low-pressure injection with PMMA, with a reduced risk of cement leak and posterior tumor displacement.^{15,16} The use of high-viscosity PMMA has a rationale in the treatment of such lesions, having been reported to help reduce the rate of extravertebral cement leak in benign and malignant fractures.¹⁷

The aim of this work was to assess technical and clinical complications of VA, performed for pain palliation and/or stabilization of neoplastic lytic vertebral body lesions, in a cohort of patients with CE-PW with or without associated soft-tissue EM.

MATERIALS AND METHODS

Patients

Patients were eligible for this retrospective, institutional review board–approved study if they were treated with VA between March 2011 and December 2012. At the time of treatment, patients were entered into a prospectively maintained data base. Additional data were collected by reviewing charts and reports and by analyzing all radiologic images available. For this analysis, we selected the subgroup of patients treated for a malignant vertebral lytic lesion with CE-PW. Indications for treatment were pain palliation and/or stabilization of neoplastic lytic vertebral

body lesions. All patients underwent preprocedural CT and gadolinium-enhanced MR imaging of the spine at the target level.

Two neuroradiologists evaluated, in consensus, the preprocedural CT to determine the presence or absence of CE-PW and the preprocedural MR imaging to determine the presence of EM. The study population was, hence, a series of procedures on 70 consecutive vertebral levels in 48 patients. The mean age of the included patients was 64 years (range, 36–84 years; 20 men and 28 women). We recorded the following lesion characteristics: primary tumor, vertebral level, presence of an EM, dichotomic differentiation of the cortical erosion as “large” or “permeative,” dichotomic differentiation of the EM as “large and convex” or “small and concave” (Fig 1), and the presence of compression of neural structures.

The VA procedures were variably performed before, during, or after radiation treatment and/or chemotherapy, following a multidisciplinary shared individualized clinical decision among a neuroradiologist, neuro-oncologist, radiation oncologist, and neurosurgeon.

Percutaneous VA Procedure and Follow-Up

All procedures were performed by the same operator, with variable participation of trainees under supervision. All patients were under monitor-assisted-care intravenous sedation and local anesthesia or under general anesthesia. The procedural technique was individualized and varied for different patients, at the operator’s discretion, depending on the morphology, extent, consistency, and level of the vertebral lesions (Fig 2). The VA procedures were all performed under fluoroscopic guidance and control by using single-plane equipment. Combined additional CT guidance was used for some procedures to assist in accurate needle placement, mainly in the presence of extensive lytic changes involving the pedicles. In those cases, a C-arm fluoroscope was positioned in a lateral view, just adjacent to the CT gantry, to monitor PMMA injection in real-time. Intraoperative myelography was used during treatment of some vertebrae in the lumbar or thoracolumbar junction areas in the presence of a large soft-tissue EM projecting into the spinal canal (Fig 3).

Beveled 15-, 10-, or 8-ga bone needles were inserted into the vertebral body under fluoroscopic guidance. A unilateral or bilateral transpedicular or parapedicular approach was used in the thoracolumbar spine. In the cervical spine, the anterolateral approach was used for C4–C7 levels, while a transoral approach was used for C2–C3 levels and a posterolateral CT-guided approach

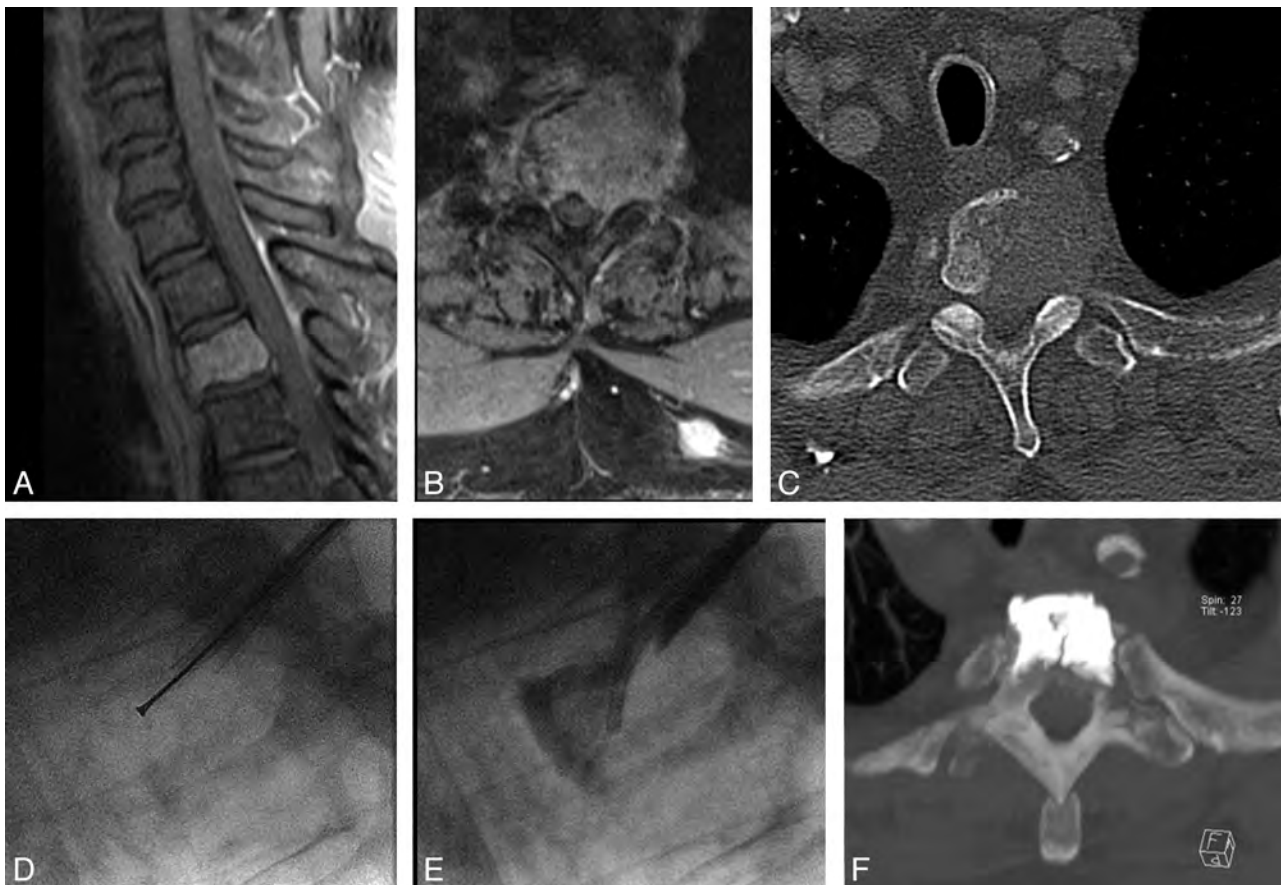


FIG 2. Cement augmentation of the weight-bearing portion of the vertebral body. Extensive lung cancer metastatic lytic destruction of the T2 vertebral body, with large cortical erosion of the posterior wall and a small concave epidural mass (A–C) at risk of impending collapse. After cavity creation with Coblant (D), we performed cement augmentation by injecting high-viscosity PMMA with a coaxial, curved, directional cannula (E) to achieve cement distribution in the anterior two-thirds of the vertebral body, spanning superior-to-inferior disk endplates and preventing epidural leaks (E–F). The cement filling was deemed excellent and appropriate for providing structural stability.

was used for the C1 level.¹⁸ Coaxially, several devices were variably inserted into the vertebral body. Plasma-field-activated radiofrequency Coblant Wands (ArthroCare), osteotomes, and curettes were used for cavity creation within the anterior two-thirds of the vertebral body when deemed necessary and appropriate, especially for solid tumors, before cement injection, following the technique already described in the literature.¹⁹ When vertebral height restoration seemed desirable, in an attempt to reduce vertebral collapse, kyphoplasty balloons (Kyphon; Medtronic, Minneapolis, Minnesota) were used (Fig 3A–D). Finally, high-viscosity PMMA (Vertaplex HV; Stryker, Kalamazoo, Michigan) was injected in variable amounts under real-time continuous fluoroscopic control, until satisfactory filling of the lytic cavity and interdigitation in adjacent trabecular bone in the anterior two-thirds of the vertebral body were achieved. The aim was to obtain cement deposition in the portion of the vertebra at risk of collapse, namely the anterior two-thirds of the vertebral body, possibly spanning from superior-to-inferior endplates across the midline.

PMMA injection was halted if radiopaque cement approached the central canal or visibly tended to leak outside the vertebra, in the soft tissues, or in vascular structures. Control nonenhanced helical CT of the treated spinal segments was performed in every patient within 24 hours postprocedurally to assess PMMA leaks in

the epidural space and foramina and to evaluate the PMMA filling of lytic cavities and adjacent trabecular spaces. CT datasets were reconstructed with a bone algorithm with 3-mm-thick multiplanar reformatted and 10-mm MIP images in the axial, sagittal, and coronal planes and were reviewed in consensus by 2 neuroradiologists. Clinical follow-up was performed at 1 week over the phone by a specialized nurse and at 4 weeks by a physician in consultation, to evaluate treatment-related clinical complications. The Visual Analog Scale pain score (range, 0–20) was measured before, 1 week after, and 1 month after treatment. Our clinical practice included plain film follow-up at 1 month post-procedure of the target spinal segment for those patients with nonsatisfactory (poor) cement filling, to rule out increased or newly developed vertebral collapse.

Statistics

The data are expressed as mean \pm SD or as median and range. A Fisher exact test to compare categorical data was performed. A Pearson correlation coefficient was used for any correlation among the outcome, complications, and age of the patient. A *P* value $< .05$ was considered statistically significant. Statistics were calculated by using SPSS (Version 21.0; IBM, Armonk, New York).

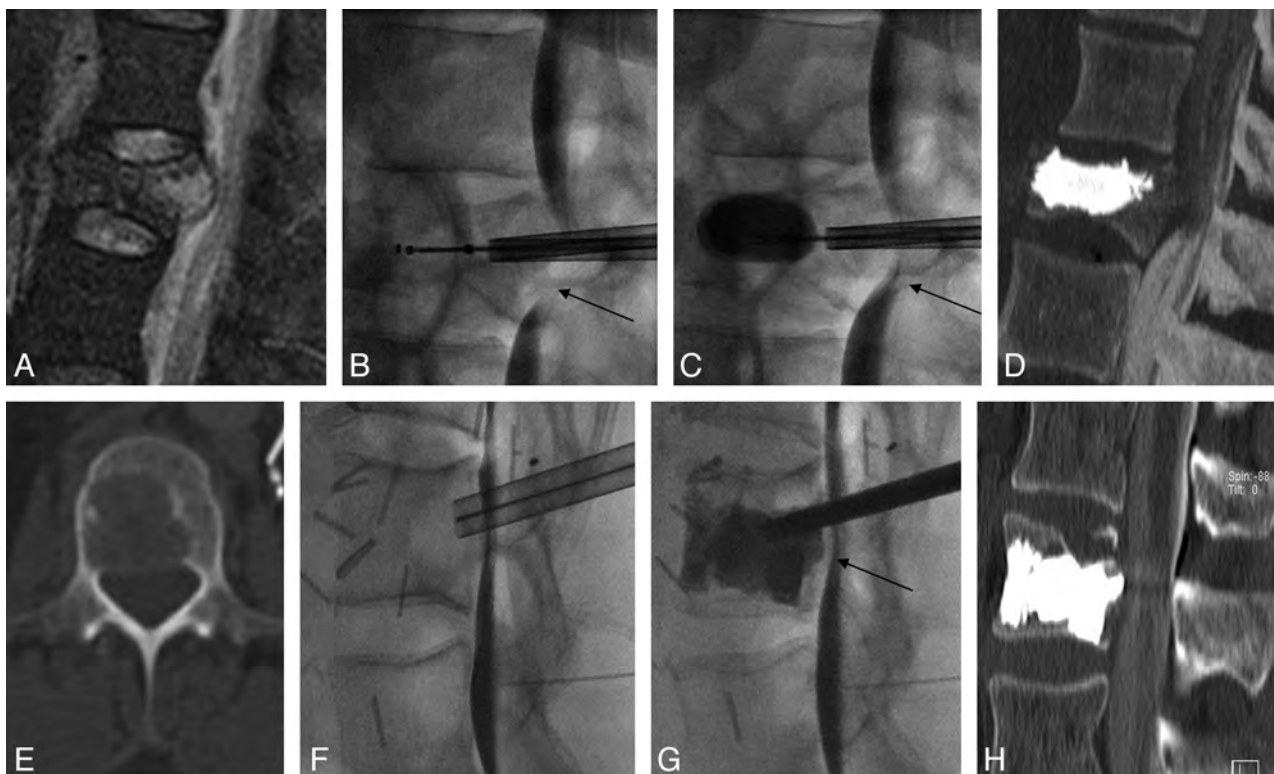


FIG 3. Two cases of the use of intraoperative myelography. *A–D*, Case 1 has a pathologic fracture of L1 related to a renal cell cancer metastatic lytic lesion, characterized by a large posterior wall cortical erosion and a convex epidural mass (*A*). The intraoperative myelographic images (*B–C*) show fracture reduction and widening of the central canal during balloon inflation (*C*), with reduced evidence of myelographic block (compare arrows on *B* and *C*). *D*, Post-cement augmentation reformatted sagittal CT image. *E–H*, Case 2 has a lytic lung cancer metastatic lesion of the L2 vertebral body with a large cortical erosion of the posterior wall (*E*). Intraoperative myelographic images (*F–G*) show progressive retropulsion of the posterior aspect of the tumor toward the epidural space, with a posteriorly displaced tumor-contrast interface (arrow on *G*) during cement injection in the vertebral body, which prompted halting cement injection. *H*, Final results on CT.

Table 1: Demographic data, imaging characteristics, and vertebral levels treated in 48 patients

Data	Total
Patients (No.)	48
Age (yr) (mean) (\pm SD)	64 (14.8)
Primary cancer (No.)	
Solid tumors	51
Multiple myeloma	17
Lymphoma	2
Cortical erosion (No.)	70
Large	43
Permeative	27
Epidural mass (No.)	31
Large and convex	18
Small and concave	13

RESULTS

Demographic data, tumor histotype, treated levels, and imaging characteristics of the patients of our series are shown in Table 1.

We treated 8 cervical (11.4%), 38 thoracic (54.3%), and 24 lumbosacral levels (34.3%). The mean number of treated levels per patient was 1.45 (range = 1–5; median = 1). Thirty patients had 1 level treated, 11 patients had 2 levels treated, 3 patients had 3 levels treated, and 1 patient each had 4 and 5 levels treated during 1 procedure. Compression of neural structures was seen preoperatively in 16/70 (22.8%) levels. Of the 45 patients treated, only 18 presented with pain resistant to conservative mea-

asures and reasonably attributable to the target lesions that were subsequently treated; in 15 cases, the pain appeared more diffuse and less easily linkable to the target lesions, while in 38 cases stabilization was an exclusive or additional indication to the VA treatment.

No patients in this series had a neurologic deficit attributable to compression of neural structures preoperatively. An MR imaging–proved EM was present in 31/70 (44.2%) levels; in 18/31 (58%) cases, the EM was large, with a posterior convex profile, while in 13/31 (41.9%) cases, it was small, with a posterior concave profile. Combined fluoroscopic/CT guidance was used in 9/70 (12.8%) levels, while intraoperative myelography was used in 6/70 (8.5%) levels. Balloon kyphoplasty was performed in 7/70 (10%) levels. Cavity creation with plasma-field-activated radio-frequency (Coblation) wands was used in 59/70 (84.2%) levels before cement injection. Cement filling of the lytic cavity and adjacent trabecular spaces was desired and attempted, especially in the weight-bearing anterior two-thirds of the vertebral body. According to previously described criteria,⁹ the PMMA filling, as seen on postprocedural CT, was deemed excellent (percentage of filling = 67%–100%) in 40 levels (57.1%), good (percentage of filling = 34%–66%) in 25 levels (35.7%), and poor (percentage of filling = 0%–33%) in 5 levels (7.1%). As a whole, in 65/70 levels (92.8%), satisfactory PMMA filling (excellent and good) of the lytic cavity and adjacent trabecular spaces was obtained.

An epidural leak of PMMA occurred in 10/70 levels (14.2%)

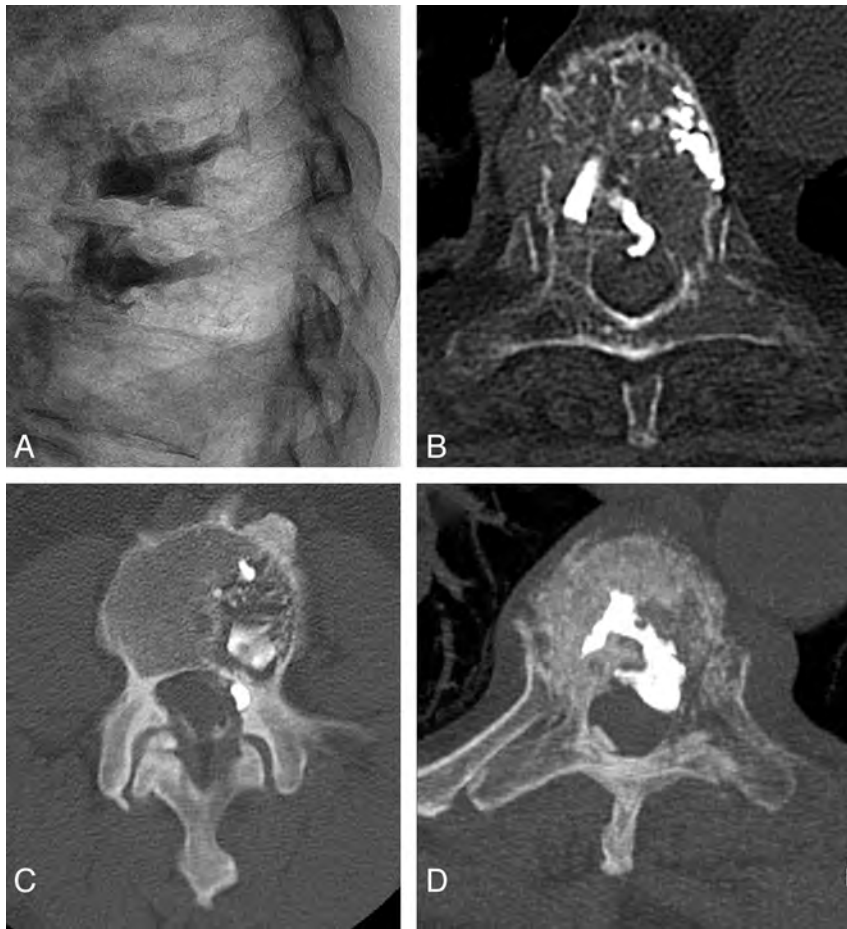


FIG 4. Examples of epidural leaks in our series. *A* and *B*, A central ventral epidural leak at T6 in a multiple myeloma vertebral cement augmentation, which was asymptomatic. *C*, A small lateral foraminal epidural leak, causing a transient, self-resolving radicular pain. *D*, A quite large ventral epidural leak that required stopping the cement injection, resulting in technically unsatisfactory cement filling of the vertebral body. The leak was otherwise clinically silent.

Table 2: Contingency table (2 × 2) showing the lack of correlation between epidural leak and type of cortical erosion, large or permeative^a

	Epidural Leak+	Epidural Leak-	Total
Large CE	7	36	43
Permeative CE	3	24	27
Total	10	60	70

Note:—CE indicates cortical erosion.

^a Fisher exact test. Two-tailed $P = .730$.

Table 3: Contingency table (2 × 2) showing the lack of correlation between epidural leak and presence of epidural mass^a

	Epidural Leak+	Epidural Leak-	Total
Epidural mass+	4	27	31
Epidural mass-	6	33	39
Total	10	60	70

^a Fisher exact test. Two-tailed $P = 1$.

(Fig 4). In 4/10 leaks (40%), the patients had an associated EM. No correlation was found between the occurrence of an epidural leak and a permeative or large pattern of cortical erosion (Fisher exact test, $P = .73$) (Table 2), between the occurrence of an epidural leak and the presence of an EM (Fisher exact test, $P = 1$) (Table 3), or between the occurrence of an epidural leak and the

type of EM (Fisher exact test, $P = .28$) (Table 4). No significant correlation was observed between leak occurrence and tumor histotype (χ^2 test, $P = .805$).

In 3/10 cases with epidural leak, the leak was in the neural foramen; 2 of these patients experienced ipsilateral radicular pain, which spontaneously resolved within 1 week. In 1 case with T1–T2 foraminal leak (Fig 5), the patient developed severe weakness of the right intrinsic hand muscles (myotome T1) without pain; the patient declined decompressive surgery and was treated with oral steroids. The motor deficit partially improved but was nevertheless persistent (M3/5) at 1 month. In the other 7 patients, the epidural leak was in the ventral median and ventral lateral epidural space; no new radicular pain or neurologic deficit occurred postprocedurally or at follow-up.

No patient developed a neurologic deficit related to spinal cord compression. At 1-week and 4-week follow-up, no patients had worsened back or radicular pain attributable to the procedure. In the subgroup of patients with pain judged related to the target level ($n = 18$), the mean Visual Analog Scale pain score before treatment was 16.3 ± 2.5 (range, 12–20) versus 7.4 ± 4.1 (range, 1–17) at 1 week versus 6.1 ± 5.2 (range, 1–14) at 1 month postprocedurally. One patient who had poor filling at 2 weeks

postprocedurally presented with new onset of back pain; imaging revealed increased vertebral collapse at the treated level. This patient underwent a new VA procedure, which was uneventful and successful in obtaining satisfactory PMMA filling and pain resolution (this second procedure was not counted in this series, being a retreatment). In the remaining 4 patients with poor filling reported, no new symptoms were attributable to a clinically significant new or progressive vertebral fracture and their imaging follow-up revealed no increased collapse at 1 month.

DISCUSSION

In our series of VA procedures in neoplastic lytic vertebral lesions with CE-PW performed for palliation of pain and/or for stabilization, 92.8% of procedures were technically successful. We observed a cement epidural leak in only 14% of levels, despite the presence of the CE-PW in all patients of the cohort by definition of the inclusion criteria. The rate of transient clinical complications was extremely low (4.2%), but 1 (1.4%) clinical complication with permanent disability, likely from radicular injury related to a PMMA foraminal leak, did occur. Notably, none of the patients developed a neurologic deficit related to spinal cord com-

pression. We also found that the presence of an MR imaging-improved EM did not represent a risk factor for epidural leak.

Treatment Indications

The aim of the VA procedure was pain palliation and/or stabilization in fractured or at-risk-of-collapse vertebral bodies. The indication to treat with VA was presented for each individual patient in the setting of a multidisciplinary discussion (Spine Tumor Board), where conservative, medical, radiation, surgical, and interventional radiology therapeutic options were discussed. Whenever stability was a concern but surgery was contraindicated by the general condition of the patient or by the indication not to delay radiation treatment or by local specific conditions (ie, multilevel metastatic involvement), either reasonable stabilization was deemed obtainable by a less invasive percutaneous cement augmentation procedure or VA was favored as a first-line therapeutic approach.

Table 4: Contingency table (2 × 2) showing the lack of correlation between of epidural leak and type of epidural mass, “large convex” or “small concave”^a

	Epidural Leak+	Epidural Leak-	Total
Epidural mass S CV	3	10	13
Epidural mass L CX	1	17	18
Total	4	27	31

Note:—S CV indicates small concave; L CX, large convex.

^a Fisher exact test. Two-tailed $P = .283$.

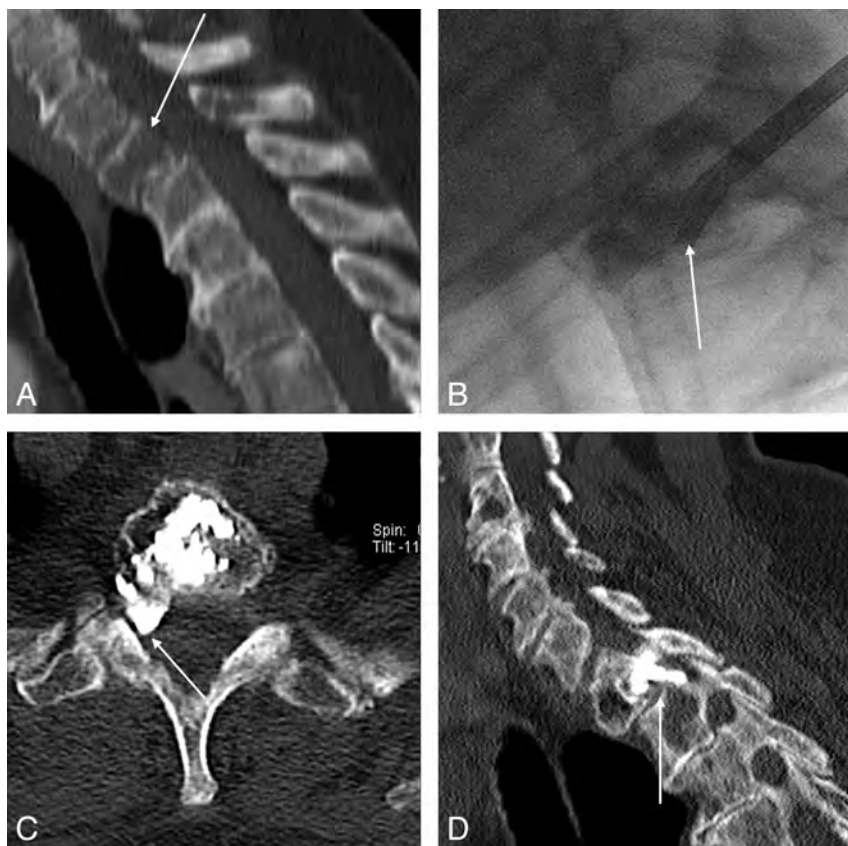


FIG 5. Symptomatic T1–T2 foraminal cement leak. Extensive breast cancer metastatic lytic lesion of the T1 vertebral body with a large cortical erosion of the posterior wall (arrow on A). Vertebral augmentation was performed under fluoroscopic guidance (B); despite inherently poor visibility in the lateral view of the cervicothoracic junction, the epidural leak was promptly recognized (arrow on B) and cement injection was halted. Nevertheless, the strategically located right foraminal PMMA leak (arrows on C and D) caused a permanent motor deficit of the T1 myotome.

In patients with multilevel involvement, selection of levels to treat to prevent a fracture was based on the extent and location of the lytic lesions suggesting biomechanical risk of collapse as described by Krishnaney et al²⁰ and Taneichi et al²¹ and by the Spinal Instability Neoplastic Score criteria.¹¹ In patients with pain and multilevel vertebral neoplastic involvement, identifying the lesion or the cause of the symptoms is often not possible with certainty. In such cases, the selection of levels to treat with VA was based on clinical judgment, in some cases aided by physical examination under fluoroscopy.

Worldwide, radiation therapy is still the criterion standard for spinal metastases. Nevertheless, there are non-radiation-sensitive tumors, >20%–30% of patients with painful bone metastasis are nonresponders, and radiation therapy may not be an option because of high radiation doses previously delivered. Moreover, radiation treatment requires a 2- to 4-week delay to achieve maximum effect; and following radiation, there might be a phase of increased vertebral fragility and risk of fracture.²² VA can be included in the multimodal treatment of spinal metastases with a role complementary to radiation therapy, offering prompt pain relief and immediate stabilization of the anterior column. In selected cases, if VA is successful in relieving pain and/or offering stability and if there is no real curative goal, radiation therapy can be avoided or the dose exposure spared for a later time. Hirsch et al²³ reported no difference in pain outcomes with regard to sequencing of radiation therapy and the VA procedure.

In addition, clinical use of radiation against neoplastic disease is not affected by the presence of PMMA, and the characteristics of PMMA are not affected by the level of the radiation dose in clinical use. At our institution, the presence of neurologic deficits due to compression of nerve structures does not absolutely preclude VA, but radiation treatment or decompressive surgery or both are rather considered as first-line treatments and VA is sometimes performed in conjunction or as a second-line stabilization or pain-palliation measure. In this series, none of the treated patients presented with neurologic deficits due to spinal cord compression before the procedure.

Procedure Efficacy

The aim of the VA procedure was to fill the lytic areas in the weight-bearing portions of the vertebral body with PMMA, namely the anterior two-thirds, also to obtain cement interdigitation in the non-lytic adjacent trabecular bone, whenever possible.

Because some patients included in this study did not present with pain and underwent the VA procedure exclu-

sively for stabilization, we did not assess pain levels as a measure of efficacy of the procedure. Nevertheless, in the subgroup of patients presenting with pain and a correlated target lesion, VA resulted in significant pain reduction at 1 week and 1 month, reproducing known results from the literature.¹⁰⁻¹³ Because the study is retrospective and the patients were not specifically selected for inclusion on the basis of pain symptoms only and because individual patients received different pain pharmacologic regimens and different oncologic treatment regimens, the reported results on pain might reflect confusing effects from other factors not assessed in this study. As a measure of the efficacy of the procedure, we focused rather on the degree of PMMA filling and the rate of technical and clinical complications related to the procedure. Cement leakage into the spinal canal or neuroforamina (Figs 4 and 5), one of the most feared technical complications of VA in neoplastic vertebral lesions due to its potential for nerve damage, was assessed by technical and clinical complications of the procedure. We did not perform imaging follow-up of those levels in which we achieved good or excellent cement filling. The efficacy of the stabilization procedure in arresting or preventing clinically significant vertebral collapse was rather inferred by the absence of new clinical symptoms at the target levels. In patients with poor filling who underwent the 1-month plain film follow-up, no new collapse was detected. Only 1 patient among those with poor PMMA filling presented within 1 month postprocedurally with new back pain, prompting imaging assessment that disclosed increased collapse at the treated level.

VA Technique

Due to the highly variable characteristics of the vertebral lesions requiring treatment, each posing specific technical challenges, the VA procedures in this series have been performed by using different techniques, imaging-guidance modalities, tools, and devices, individualized for each case.

Fluoroscopy was the imaging-guidance technique of choice, invariably used to have real-time control of PMMA injection, but in cases with extensive lytic disruption of the pedicles or poor fluoroscopic visibility of bony landmarks, CT guidance was used to place the needles and to intermittently control PMMA spread. When posterior wall retropulsion or a large EM was encroaching on the spinal canal, intraoperative myelography allowed indirect visualization of the posterior vertebral body margins and depicted intraprocedural worsening of retropulsion. This technique was applicable only at the lumbar and lower thoracic levels, where the contrast agent injected intrathecally would form a stable and visible contrast-tumor interface in the prone patient. Intraoperative myelography increased operator comfort and confidence in such challenging cases, and in only 1 case did it actually show a progressive mild retropulsion of soft-tissue tumor during cement injection (Fig 3E-H). This observation led to halting the cement injection; the cement filling was already satisfactory and no clinical consequences ensued. In no other case was an evident soft-tissue-mass posterior displacement noted as an immediate consequence of the procedure.

Every effort was made to allow the most optimal and precise fluoroscopic projections and visualization throughout each phase

of the VA procedure; we think this effort is crucial in such challenging cases.

All the VA procedures used high-viscosity PMMA, with a working time of approximately 18 minutes. PMMA injection was performed very slowly, starting as anterior as possible in the vertebral body, with mandatory real-time continuous fluoroscopic control in the lateral projection and intermittent anteroposterior checks. The use of high-viscosity cement reduces the rate of extravertebral leaks.¹⁷ The volumes of injected PMMA varied widely; this variation reflected differences in the size of lytic lesions, trabecular compliance, and injected cement distribution.²⁴

Cavity Creation

In most cases in our series, due to the presence of CE-PW, cavity creation in the anterior two-thirds of the vertebral body was performed before cement injection, to favor optimal PMMA filling of the lytic cavity while minimizing the risks of epidural PMMA leak or displacement of solid tumoral tissue through the dehiscence posterior wall.²⁵ Cavity creation in the vertebral body was performed with Coblation Wands (Fig 2), as previously reported by other authors,^{19,26,27} in 59/70 levels. The decision not to use Coblation was made intraprocedurally when the advancement of the trocar cannulas through the lytic area did not reveal typical soft-tissue consistency, but rather fluid consistency, such as in markedly necrotic tumors or in some multiple myeloma lesions.

Coblation is a form of radiofrequency energy that, through a controlled, non-heat-driven process, excites the electrolytes in a conductive medium, such as saline solution.²⁸ The energized particles cause tissue to dissolve into gas at relatively low temperatures with volumetric removal of target tissue with minimal damage and minimal heating of the surrounding tissue.²⁹ Dissolution through vaporization of soft tissues in close proximity of the tip of the Coblation Wand, with a modest temperature rise, represents a theoretic advantage over conventional thermal radiofrequency tumor ablation, also used in combination with VA in metastatic lesions of the spine.²⁶ Radiofrequency kills the tumor tissue without dissolving it, therefore without truly creating a cavity; moreover, radiofrequency causes a significant rise in the temperature of the soft tissues and renders neural structures at risk of heat lesions, especially when the posterior wall cortex is defective.²⁶ The creation of a cavity by tissue dissolution also represents a theoretic advantage over a cavity created by mechanical tissue displacement, as in kyphoplasty. We used kyphoplasty in 7 cases, not for cavity creation but always after the cavity was created with Coblation, in an attempt to obtain height restoration and reduction of posterior wall retropulsion (Fig 3A-D), exploiting the tension of the posterior longitudinal ligament (ligamentotaxis).³⁰

Complications

CE-PW is thought to be a risk factor for epidural PMMA leak, which has potential for nerve structure compression and neurologic injury and might require decompression surgery. Furthermore, a leak occurring early during injection would prompt the early interruption of the procedure, limiting the desired filling of the vertebral body. Despite the potential for nerve damage, in most cases, the leakage is asymptomatic or manifests as transient

radicular pain,⁹ which is due to PMMA-related heating rather than compressive damage.

In the only patient in our series who reported a permanent clinical complication related to the procedure, a foraminal PMMA leak occurred at T1–T2 (Fig 5). It was a breast cancer metastasis involving the T1 vertebra. Coblation-assisted cavity creation was performed. Despite the inherent relatively poor fluoroscopic visibility of the cervicothoracic junction on lateral-view fluoroscopy during the PMMA injection, the posterior cement leak was promptly recognized and cement injection was stopped. The patient presented a few hours later with a radicular T1 motor deficit. No spinal cord compression was noted. Conservative-versus-decompressive surgery measures were discussed, and the patient elected not to undergo surgery.

The occurrence of cement leakage in our series (14%) only in patients with CE-PW was not larger than that in other published series on neoplastic lytic lesions,^{9,13,17} and it is well-recognized in the literature that the depiction of PMMA leaks is much higher when CT is used as a postprocedural imaging follow-up compared with fluoroscopy or plain films. Similarly, the notably low rate of clinical complication (3 cases, [4.2%], 2 of which were transient) obtained in our study is the result of multiple factors. We believe that creation of a well-sized cavity by using Coblation allows low-pressure injection, makes the distribution of PMMA more predictable, and can effectively limit the chance of posterior cement leakage in this subcategory of patients. Use of high-viscosity PMMA, optimal fluoroscopic visualization of the field, and appropriate knowledge of radiographic and cross-sectional spinal anatomy are key factors. To validate the results of this single-center single-operator study, a larger, multicenter study with a larger cohort and longer follow-up may be useful.

A limitation of our study is the retrospective nature, even though this cohort is the result of a prospectively established data base and all the cases performed were included. Lack of a control group and lack of long-term imaging or clinical follow-up to assess durability in all patients were other limitations.

CONCLUSIONS

Our data seem to justify the use of percutaneous vertebral augmentation in neoplastic lytic vertebral lesions with cortical erosion of the posterior wall, performed for palliation of pain and/or for stabilization in case of risk of vertebral collapse. Adequate skills levels; state-of-the-art equipment, devices, and materials; and individualized technical adjustments are critical for keeping complication rates low.

Disclosures: Michal Reinert—UNRELATED: Grants/Grants Pending: Oxygen Biotherapeutics,* Comments: severe head injury studies. *Money paid to the institution.

REFERENCES

- Jacobs WB, Perrin RG. Evaluation and treatment of spinal metastases: an overview. *Neurosurg* 2001;11:e10
- Jemal A, Thun MJ, Ries LA, et al. Annual report to the nation on the status of cancer, 1975–2005, featuring trends in lung cancer, tobacco use, and tobacco control. *J Natl Cancer Inst* 2008;100:1672–94
- Kassamali RH, Ganeshan A, Hoey ET, et al. Pain management in spinal metastases: the role of percutaneous vertebral augmentation. *Ann Oncol* 2011;22:782–86
- Galibert P, Deramond H, Rosat P, et al. Preliminary note on the treatment of vertebral angioma by percutaneous acrylic vertebroplasty [in French]. *Neurochirurgie* 1987;33:166–68
- Chiras J, Barragán-Campos HM, Cormier E, et al. Vertebroplasty: state of the art [in French]. *J Radiol* 2007;88:1255–60
- Tancioni F, Lorenzetti MA, Navarra P, et al. Percutaneous vertebral augmentation in metastatic disease: state of the art. *J Support Oncol* 2011;9:4–10
- Weill A, Chiras J, Simon JM, et al. Spinal metastases: indications for and results of percutaneous injection of acrylic surgical cement. *Radiology* 1996;199:241–47
- Deramond H, Depriester C, Galibert P, et al. Percutaneous vertebroplasty with polymethylmethacrylate: technique, indications, and results. *Radiol Clin North Am* 1998;36:533–46
- Barragán-Campos HM, Vallee JN, Lo D, et al. Percutaneous vertebroplasty for spinal metastases: complications. *Radiology* 2006;238:354–62
- Dudeny S, Lieberman IH, Reinhardt MK, et al. Kyphoplasty in the treatment of osteolytic vertebral compression fractures as a result of multiple myeloma. *J Clin Oncol* 2002;20:2382–87
- Fourney DR, Schomer DF, Nader R, et al. Percutaneous vertebroplasty and kyphoplasty for painful vertebral body fractures in cancer patients. *J Neurosurg* 2003;98:21–30
- Berenson J, Pflugmacher R, Jarzem P, et al. Balloon kyphoplasty versus non-surgical fracture management for treatment of painful vertebral body compression fractures in patients with cancer: a multicentre, randomised controlled trial. *Lancet Oncol* 2011;12:225–35
- van der Linden E, Kroft LJ, Dijkstra PD. Treatment of vertebral tumor with posterior wall defect using image-guided radiofrequency ablation combined with vertebroplasty: preliminary results in 12 patients. *J Vasc Interv Radiol* 2007;18:741–47
- Trial C, Brancati A, Marnet O, et al. Coblation technology for surgical wound debridement: principle, experimental data, and technical data. *Int J Low Extrem Wounds* 2012;11:286–92
- Gerszten PC, Monaco EA 3rd. Complete percutaneous treatment of vertebral body tumors causing spinal canal compromise using a transpedicular cavitation, cement augmentation, and radiosurgical technique. *Neurosurg Focus* 2009;27:E9
- Wilson DJ, Owen S, Corkill RA. Coblation vertebroplasty for complex vertebral insufficiency fractures. *Eur Radiol* 2013;23:1785–90
- Anselmetti GC, Zoarski G, Manca A, et al. Percutaneous vertebroplasty and bone cement leakage: clinical experience with a new high-viscosity bone cement and delivery system for vertebral augmentation in benign and malignant compression fractures. *Cardiovasc Intervent Radiol* 2008;31:937–47
- Boulter DJ, Rumboldt Z, Bonaldi G, et al. Tilting the gantry for CT-guided spine procedures. *Radiol Med* 2014;119:750–57
- Georgy BA, Wong W. Plasma-mediated radiofrequency ablation assisted percutaneous cement injection for treating advanced malignant vertebral compression fractures. *AJNR Am J Neuroradiol* 2007;28:700–05
- Krishnaney AA, Steinmetz MP, Benzel EC. Biomechanics of metastatic spine cancer. *Neurosurg Clin North Am* 2004;15:375–80
- Taneichi H, Kaneda K, Takeda N, et al. Risk factors and probability of vertebral body collapse in metastases of the thoracic and lumbar spine. *Spine* 1997;22:239–45
- Rose PS, Laufer I, Boland PJ, et al. Risk of fracture after single fraction image-guided intensity-modulated radiation therapy to spinal metastases. *J Clin Oncol* 2009;27:5075–79
- Hirsch AE, Jha RM, Yoo AJ, et al. The use of vertebral augmentation and external beam radiation therapy in the multimodal management of malignant vertebral compression fractures. *Pain Physician* 2011;14:447–58
- Tschirhart CE, Finkelstein JA, Whyne CM. Optimization of tumor volume reduction and cement augmentation in percutaneous vertebroplasty for prophylactic treatment of spinal metastases. *J Spinal Disord Tech* 2006;19:584–90

25. Ahn H, Mousavi P, Chin L, et al. **The effect of pre-vertebroplasty tumor ablation using laser-induced thermotherapy on biomechanical stability and cement fill in the metastatic spine.** *Eur Spine J* 2007;16:1171–78
26. Georgy BA. **Bone cement deposition patterns with plasma-mediated radio-frequency ablation and cement augmentation for advanced metastatic spine lesions.** *AJNR Am J Neuroradiol* 2009;30:1197–202
27. Groetz SF, Birnbaum K, Meyer C, et al. **Thermometry during coblation and radiofrequency ablation of vertebral metastases: a cadaver study.** *Eur Spine J* 2013;22:1389–93
28. Bortnick DP, Plastic Surgery Educational Foundation DATA Committee. **Coblation: an emerging technology and new technique for soft-tissue surgery.** *Plast Reconstr Surg* 2001;107:614–15
29. Chen YC, Lee SH, Saenz Y, et al. **Histologic findings of disc, end plate and neural elements after coblation of nucleus pulposus: an experimental nucleoplasty study.** *Spine J* 2003;3:466–70
30. Bonaldi G, Cianfoni A. **Percutaneous treatment of lumbar compression fracture with canal stenosis and neurogenic intermittent claudication: combining kyphoplasty and interspinous spacer.** *J Vasc Interv Radiol* 2012;23:1437–41

Double Inversion Recovery Sequence of the Cervical Spinal Cord in Multiple Sclerosis and Related Inflammatory Diseases

I. Riederer, D.C. Karampinos, M. Settles, C. Preibisch, J.S. Bauer, J.F. Kleine, M. Mühlau, and C. Zimmer



ABSTRACT

BACKGROUND AND PURPOSE: MR imaging plays an important role in diagnosing MS and other related inflammatory diseases; however, imaging of the spinal cord is still challenging. We hypothesized that a 3D double inversion recovery sequence for cervical spinal cord imaging would be more sensitive in detecting inflammatory lesions than a conventional 2D T2-weighted TSE sequence at 3T.

MATERIALS AND METHODS: On a 3T MR imaging scanner, we examined 30 patients with suspected or established MS (MS, $n = 16$; clinically isolated syndrome, $n = 12$; isolated myelitis, $n = 2$) and 10 healthy controls. Newly developed 3D double inversion recovery and conventional 2D axial and sagittal T2-weighted TSE images of the cervical spinal cord were acquired. Two blinded neuroradiologists independently assessed the scans in pseudorandomized order for lesion numbers and rated lesion visibility and overall image quality on 5-point scales. A subsequent consensus reading delivered definite lesion counts. Standardized contrast-to-noise ratios were calculated in representative lesions of each patient.

RESULTS: Overall, 28% more lesions could be detected with 3D double inversion recovery than with conventional T2WI (119 versus 93, $P < .002$). On average, the standardized contrast-to-noise ratio was significantly higher ($P < .001$) in double inversion recovery than in T2WI. Lesion visibility was rated significantly higher ($P < .001$) in double inversion recovery compared with T2WI despite lower image quality.

CONCLUSIONS: The novel 3D double inversion recovery sequence allowed better detection of lesions in MS and related inflammatory diseases of the cervical spinal cord, compared with conventional 2D T2WI.

ABBREVIATIONS: DIR = double inversion recovery sequence; sCNR = standardized contrast-to-noise ratio

Among the inflammatory CNS diseases, spinal cord lesions can most frequently be found in multiple sclerosis, though they are very uncommon in other neurologic diseases.¹ MR imaging of the brain and spinal cord plays a major role not only for establishing the diagnosis of MS but also for evaluating its individual course.^{2,3} The following sequences are recommended in the standard MS spinal cord imaging protocol: 2D (sagittal and axial) proton-attenuation/T2-weighted images, sagittal T1-weighted images pre- and postcontrast, and axial T1-weighted images postcontrast through suspicious lesions.⁴ MR imaging of the spinal cord, however, is still challenging because of technical difficulties

due to the small size of the spinal cord and its lesions and artifacts caused by deglutition, respiration, and cardiac pulsation. This challenge often leads to uncertainty during assessment of the images. Numerous studies have compared different sequences, such as STIR, which provides high lesion contrast, with this standard protocol in MS.⁵⁻⁷ Other studies compared T2*-weighted gradient recalled-echo sequences with and without a magnetization transfer prepulse with axial T2 FSE and sagittal STIR images.⁸ In inflammatory spine diseases with a diffuse pattern, such as neuromyelitis optica, diffusion tensor imaging has recently been used to measure fractional anisotropy with great success.^{9,10}

The double inversion recovery (DIR) sequence was first described by Redpath and Smith in 1994.^{11,12} In this sequence, the signals from both the CSF and normal white matter are suppressed simultaneously, while inflammatory lesions remain unsuppressed and appear hyperintense. The fast spin-echo version of DIR was introduced 1998 by Bedell and Narayana.¹³ Several studies have shown that this sequence is very sensitive to MS lesions in the brain, especially with respect to intracortical le-

Received May 13, 2014; accepted after revision July 10.

From the Departments of Diagnostic and Interventional Neuroradiology (I.R., C.P., J.S.B., J.F.K., C.Z.) and Diagnostic and Interventional Radiology (D.C.K., M.S.), Neuroimaging Center at the Technische Universität München (C.P., M.M.), and Department of Neurology (M.M.), Klinikum rechts der Isar, Technische Universität München, Munich, Germany.

Please address correspondence to Isabelle Riederer, MD, Department of Diagnostic and Interventional Neuroradiology, Klinikum rechts der Isar, Technische Universität München, Ismaninger Str 22, 81675 Munich, Germany; e-mail: Isabelle.riederer@tum.de

<http://dx.doi.org/10.3174/ajnr.A4093>

MRI acquisition parameters of the 3D DIR and axial and sagittal T2WI TSE sequences

Sequence	3D DIR	2D T2WI TSE	
Imaging plane	Sagittal	Sagittal	Axial
Acquisition matrix	208 × 208 × 300	212 × 233	308 × 207
Acquisition voxel size (mm ³)	1.2 × 1.2 × 1.3	0.94 × 1.18 × 2	0.65 × 0.88 × 4
TR (ms)	5500	3071	4238
TE (ms)	287	100	100
TSE factor	173	29	25
IR delays (ms)	2550/450		
Flip/refocusing angle	T2prep with TE = 125 ms and 4 refocusing pulses	90°/120°	90°/120°
Acquisition time	7 min 36 sec	3 min 47 sec	3 min 15 sec
Sections	300	15	28

Note:—IR indicates inversion recovery; T2prep, preparation pulse to ensure T2 weighting.

sions.¹⁴⁻¹⁶ An analogous DIR sequence for spinal cord imaging, however, has not yet been established in clinical practice and research. To the best of our knowledge, the only published material on spinal DIR imaging is a vendor demonstration of a DIR sequence of the cervical spinal cord.¹⁷

The aim of our study was, therefore, to compare a newly established cervical spinal 3D DIR sequence with the conventional axial and sagittal T2WI TSE sequences at 3T regarding image quality and lesion detectability. Because the DIR sequence improves the detection of lesions in the brain, especially in the cortex,¹⁴⁻¹⁶ we hypothesized that the spinal 3D DIR sequence would also be a more sensitive tool for the examination of the spinal cord in inflammatory diseases, especially in patients with suspected or established MS.

MATERIALS AND METHODS

Patients and Healthy Volunteers

In 33 patients and 10 healthy volunteers, a DIR sequence was acquired from the cervical spinal cord according to techniques described below. Three of the patients were excluded because of inadequate image quality in 3D DIR (but not in the conventional T2WI TSE) images. Poor image quality in these cases was caused by aliasing artifacts and magnetic field inhomogeneities presumably caused by adiposity (body mass index of >35 in all 3 patients). None of the 10 healthy volunteers (4 women; mean age, 33 ± 4 years; range, 27–41 years) had to be excluded. In the remaining 30 patients (17 women, mean age, 39 ± 11 years; range, 20–57 years), 12 had a prior diagnosis of definite MS, whereas MR imaging was performed in the remaining 18 patients to establish the primary diagnosis. The patients were examined due to a new clinical attack compatible with myelitis or for routine follow-up. Of note, although image data were collected prospectively with the intent of subsequent blinded scientific evaluation, all images were available to clinicians for routine clinical purposes and radiologic reporting immediately after acquisition and, hence, could have impacted clinical diagnoses and decision-making. The final diagnoses were MS ($n = 16$; 11 relapsing-remitting, 2 primary-progressive, and 3 secondary-progressive), clinically isolated syndrome ($n = 12$), and isolated myelitis of unknown etiology ($n = 2$). The median Expanded Disability Status Scale score was 2.45 (range, 0–7).

Patients were recruited consecutively at the department of neurology at the Klinikum rechts der Isar (Technische Universität München, Munich, Germany), which runs a dedicated center for

MS and related disorders with a high volume of stationary and ambulatory patients. Diagnoses were made by the treating neurologists, experienced experts in MS and inflammatory CNS diseases. The study was conducted in accordance with the 1964 Declaration of Helsinki, and the study protocol was approved by the local ethics committee.

MR Imaging Acquisition

Scans were performed on a 3T scanner (Ingenia; Philips Healthcare, Best, the Netherlands). Our standard protocol

consists of multisection sagittal and axial T2-weighted images, sagittal T1-weighted images pre- and postcontrast, and axial T1-weighted images postcontrast. In this study, we additionally acquired a 3D fat-saturated double inversion recovery sequence with suppression of the CSF and normal white matter. The acquired voxel sizes were 1.2 × 1.2 × 1.3 mm in the DIR sequence and 0.94 × 1.18 × 2 mm and 0.65 × 0.88 × 4 mm the sagittal and axial T2WI TSE sequences, respectively. The DIR sequence was interpolated to a voxel size of 1.2 × 1.2 × 0.65 mm by zero-filling of the k -space. It was then reformatted with section thicknesses of 2 (sagittal) and 4 mm (axial) for a better comparison with the 2D sequences. The acquisition times were 7:36 minutes (DIR) and 7:02 minutes (T2WI: sagittal, 3:47 minutes; axial, 3:15 minutes). Additional parameters of the sequences are listed in the Table.

MR Imaging Analysis

Scans were assessed independently by 2 experienced neuroradiologists (I.R. and J.F.K., with 2.5 and 9 years of experience, respectively), blinded to diagnoses and clinical symptoms, on a standard PACS workstation. The 3D DIR and T2WI TSE image series were assessed separately, each in pseudorandomized order, with a temporal delay of at least 2 weeks to exclude biases by memory effects. A lesion was defined as a focal hyperintensity surrounded by a normal isointense spinal cord. Confluent lesions with no distinct delineation in between were counted as 1 lesion. Spinal cord lesions between the top of the C2 and the bottom of the C7 vertebral body levels were counted. To assure comparable conditions with the 2D T2WI TSE sequence, we counted lesions in the sagittal and axial reconstructions of the 3D DIR sequence. Additionally, DIR and T2 images were independently rated by the 2 neuroradiologists on 5-point scales in terms of overall image quality, lesion visibility (5, excellent; 4, good; 3, average; 2, poor; 1, not diagnostic) and artifacts (5, none; 4, mild, not affecting diagnostic value; 3, moderate, minor impact expected on diagnostic value; 2, pronounced, major impact on diagnostic value; 1, severe, no diagnostic value). A definite lesion count was derived from an additional consensus reading held after a delay of at least 1 week by both neuroradiologists, by using the thin-sectioned raw data and coronal reconstructions in addition to the axial and sagittal reconstructions.

The contrast-to-noise ratio comparison between 2 sequences with identical voxel sizes and acquisition durations is traditionally

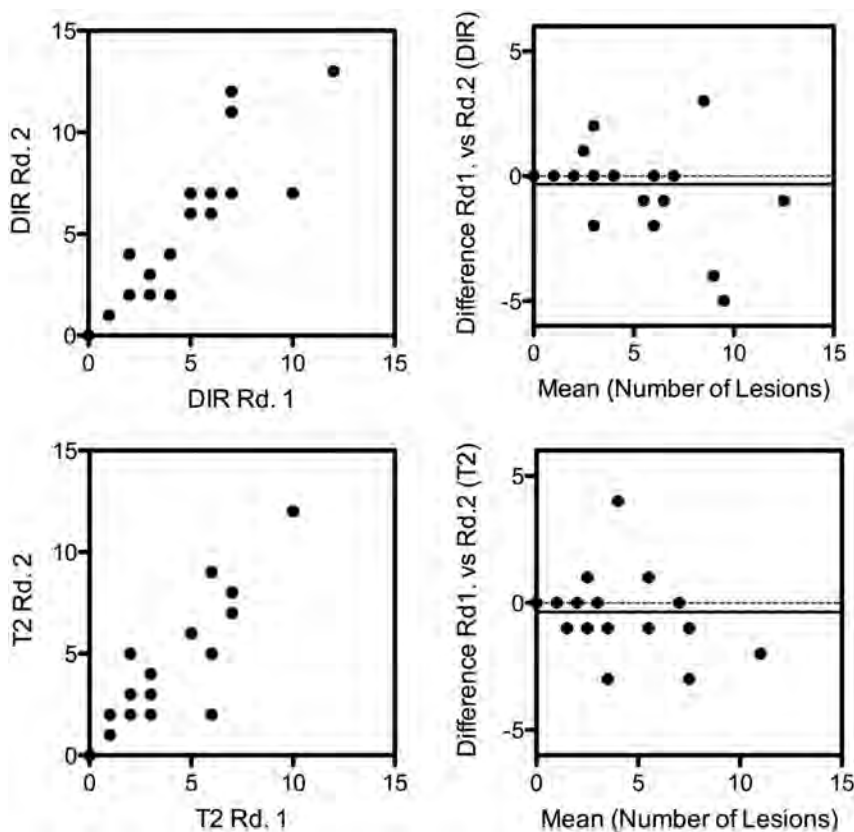


FIG 1. Bland-Altman analysis of the lesion counts of reader 1 and 2 for the DIR sequence (*upper row*) and the T2WI TSE sequence (*lower row*). There was an almost identical, nonsignificant bias in both techniques, with reader 2 counting on average 0.33 more lesions on DIR images and 0.37 more lesions on T2 images than reader 1 (95% CI, -3.2 – 2.6 ; correlation coefficient, $r = 0.97$; and -2.8 – 2.1 , $r = 0.94$, respectively).

performed on the basis of the ratio of the signal difference between the 2 tissues of interest over the SD of noise. However, as signal noise decreases and contrast-to-noise ratio increases with increasing voxel size and acquisition time, it is questionable to compare (nonstandardized) contrast-to-noise ratios of sequences that are, in these respects, different, as is the case for the 2D T2WI TSE and 3D DIR sequences used. According to Edelstein et al,¹⁸ the contrast-to-noise ratio is proportional to the acquisition voxel volume and the square root of the total sampling time. To account for this dependency and establish comparability for the 2 sequences, we defined a “standardized” contrast-to-noise ratio (sCNR) according to

$$sCNR = \frac{S_{lesion} - S_{spinal\ cord}}{SD_{background} \times V_{voxel} \times \sqrt{t_{acq}}}$$

where S_{lesion} and $S_{spinal\ cord}$ denote the mean signal in a region of interest in the lesion and normal spinal cord tissue, respectively. $SD_{background}$ is the SD of noise in a region of interest selected in the background, V_{voxel} is the voxel size, and t_{acq} the acquisition time in seconds. Calculation and measurement of the mean values were performed with standard tools of the PACS workstation. To calculate the average signal intensity of lesions, we placed circular ROIs in the largest lesion of each patient that was easily discernible in both the T2WI TSE and DIR images. The ROIs for the mean signal intensities of healthy spinal cord tissue were placed in

regions with normal signal without any hyperintensities nearby. The noise region was placed in the background in a region without signal and noticeable artifacts.

Statistical Analysis

Differences in lesion number, sCNR, and image quality were analyzed by using a 2-sided Student *t* test for paired samples. The level of significance was set to $P < .01$ for the whole study. The interobserver agreement was calculated by using the Lin concordance (concordance correlation coefficient).¹⁹ Bland-Altman analysis was performed to assess agreement between the 2 different radiologists for each of the sequences.

RESULTS

Lesion Detectability

In the independent readings, both raters detected substantially more lesions in the reformatted DIR images than in the conventional T2WI TSE images (115 versus 96, $P = .097$, and 105 versus 85, $P = .004$). The slightly higher lesion counts of the more experienced reader were reflected in the Bland-Altman analysis, which showed a similarly small, nonsignificant bias of -0.37 and -0.33 between radiologist 1 and radiologist 2 on T2WI TSE and DIR images, respectively (Fig 1, 95% CI, -2.8 – 2.1 and -3.2 – 2.6 , respectively).

The concordance between radiologists was similar for both the DIR and T2WI TSE sequence (both, concordance correlation coefficient = 0.91).

In the consensus reading, differences in lesion counts between the DIR and T2WI TSE sequences occurred in 13 patients, always favoring the DIR images. All lesions apparent in the T2WI TSE images were also detected in the DIR images, but not vice versa (Fig 2). Overall, 28% more lesions could be detected with the 3D DIR sequence than with the conventional 2D T2WI TSE sequence (119 versus 93, $P < .002$). On average, 4 lesions per patient were detectable in the DIR sequence, compared with 3 in the conventional T2WI TSE sequence (range, 0–13 [DIR], 0–11 [T2WI TSE]; mean, 3.97 ± 3.85 [DIR], 3.10 ± 3.00 [T2WI TSE]; $P < .01$; Fig 3).

Image Quality

The sCNR was significantly higher in the 3D DIR sequence compared with the standard 2D T2WI TSE sequence (0.36 ± 0.14 versus 0.26 ± 0.14 , $P < .001$); thus, the visibility of the lesions was clearly improved in the 3D DIR sequence (Fig 4). On a 5-point-scale, lesion visibility was rated significantly higher in the DIR sequence compared with the T2WI TSE sequence (4.8 versus 3.3 on a 5-point scale, $P < .001$), despite lower overall image quality (3.7 versus 4.8, $P < .001$).

The DIR sequence seems to be more prone to motion artifacts



FIG 2. Examples of 2 patients with lesions visible only in the DIR images and not in the T2WI TSE images. Sagittal (A and F) and axial (D and H) T2WI TSE images; sagittal (B and G), coronal (C), and axial (E and I) reconstructions of the 3D DIR sequence of the spinal cord. The group of images on the left (I, A–E) shows the cervical spinal cord of a 52-year-old female patient. Note the lesion in the spinal cord at the C4 vertebral body level, which is only visible in the DIR sequence. This patient indicated pain in her left shoulder, weakness of her left arm, and tingling in her left palm. In T2WI TSE images, 1 lesion was visible in the cervical spinal cord at the C2/C3 level with discrete contrast enhancement (not shown in the image). At first, the differential diagnosis included neoplasm and inflammation. Due to the cervical 3D DIR sequence, another small lesion was detected at the C4 lateral level on the right (arrow), favoring the diagnosis of cervical myelitis. The group of images on the right (II, F–I) shows the spinal cord of a 49-year-old patient with clinically isolated syndrome. Note the lesion in the spinal cord at the C7 vertebral body level, which is only visible in the DIR sequence.

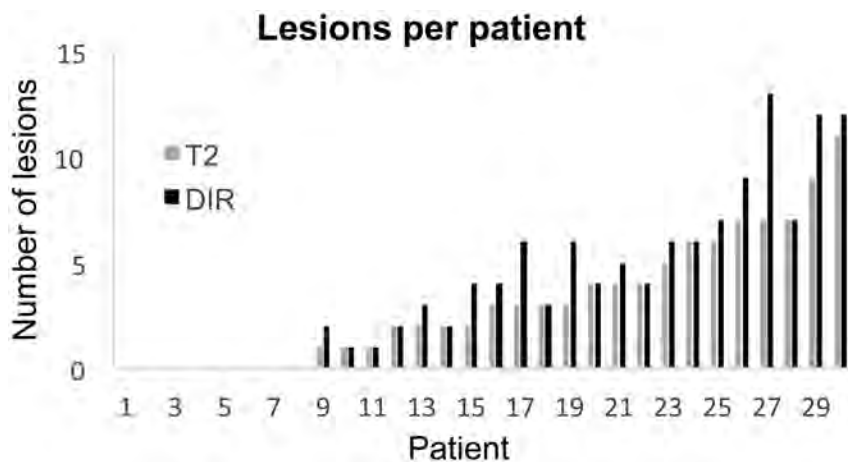


FIG 3. The number of lesions per patient according to the consensus reading of both radiologists in the T2WI TSE and DIR sequences. Volunteers are not included. Range, 0–13 (DIR), 0–11 (T2WI TSE); mean, 3.97 ± 3.85 (DIR), 3.10 ± 3.00 (T2WI TSE); $P < .01$.

such as swallowing. Eight T2WI TSE images but only 2 DIR images were rated as completely free of artifacts (4.5 versus 3.8, $P < .001$). Furthermore, image quality of the DIR sequence was restricted in 3 patients due to aliasing artifacts and B1 inhomogeneities due to obesity. Therefore, these patients were excluded from

the study. No false-positive lesions of the spinal cord were found in the control group in any of the sequences.

DISCUSSION

The present study demonstrates that the DIR sequence, which has been shown to improve visibility of MS-related inflammatory lesions, in particular of intracortical lesions in the brain,^{14,15} can be adapted for imaging of the cervical spinal cord. The newly developed spinal 3D DIR sequence is more sensitive than conventional T2WI TSE sequences for inflammatory lesions in patients with suspected or definite MS. This sensitivity can be attributed to the higher sCNR of the 3D DIR sequence and the correspondingly enhanced lesion visibility.

Early attempts to improve spinal cord imaging in MS strived to establish a spinal version of the fluid-attenuated inversion recovery sequence, trying to take advantage of the high sensitivity of the FLAIR sequence for MS lesions in the brain.^{6,20,21} However, due to poor contrast between lesions and healthy spinal cord, the sensitivity of the spinal FLAIR sequence was actually lower compared with conventional T2-weighted images.²⁰



FIG 4. Sagittal T2WI TSE (A and C) and DIR (B and D) images of the cervical spinal cord of 2 patients. A and B, Two lesions in the spinal cord at the C4 vertebral body level of a 22-year-old female patient with clinically isolated syndrome. C and D, A diffuse myelitis of an 18-year-old female patient with MS. The lesion-to-background contrast sCNR in DIR images is remarkably higher.

More recently, alternative techniques, such as classic T2WI STIR, a modified T1WI STIR, and a 3D gradient recalled-echo sequence, have been applied to spinal cord imaging in MS. Although these sequences yielded promising results, comparing favorably with T2WI TSE sequences,^{5–8} current guidelines still include the conventional proton-attenuation/T2WI TSE sequence as part of the spinal cord imaging protocol in MS,⁴ which we therefore chose as a reference. However, future studies need to directly compare these sequences, all of which appear to be candidate techniques to replace or supplement conventional T2WI TSE sequences in future standard MS imaging protocols.

At present, the diagnosis of MS is usually based on the McDonald criteria, as revised in 2010,²² which conceptually rely on the demonstration of lesion dissemination in both space and time. Both dissemination in space and dissemination in time can be evidenced by clinical findings and history, but also by MR imaging,²² following the simplified MR imaging criteria developed by Swanton et al.²³ Herein, the detection of at least 1 lesion on spinal cord MR imaging in addition to at least 1 cerebral lesion will fulfill the criterion of dissemination in space, and the detection of any novel spinal lesion in follow-up MR imaging will fulfill the criterion of dissemination in time.

Hence, current diagnostic criteria for MS rely heavily on the detection of spatially segregated or novel lesions. Therefore, we focused on lesion counts to compare the sensitivities of 3D DIR and T2WI TSE imaging. Notwithstanding the authoritative role of the McDonald criteria in MS however, lesion numbers alone have limited informative value. Other parameters such as the lesion location, the overall volume of lesions, and the clinical impact are important and will influence patient management. Moreover, novel MR imaging–based techniques, including diffusion tensor, magnetization transfer, and “tissue-specific” imaging, may provide estimates of the degree of tissue damage in lesions;

reveal abnormalities in healthy-appearing tissue, as shown in neuromyelitis optica; and help differentiate lesions with distinct pathologic substrates (demyelination, inflammation, edema, gliosis, remyelination) but similar intrinsic signal in T2WI sequences.^{9,10,24,25} Such techniques may provide valuable information beyond mere lesion visualization, and this may well be incorporated into future diagnostic guidelines.

Current diagnostic criteria, however, warrant the assessment of lesion-detection rates to compare imaging techniques in MS. Their clinical relevance is highlighted by 2 of the 18 (11%) patients in our study, in whom a definite diagnosis had not been established before imaging. In 1 patient with a prominent lesion in the cervical cord, detection of a second lesion (conspicuous only in the 3D DIR image) largely ruled out a neoplastic process and favored the diagnosis of an inflammatory disease. In the other patient, several spinal lesions, revealed only by the 3D DIR sequence, completed the criterion of dissemination in space, changing the diagnosis from “possible” to “definite” MS.

In addition, the benefits of the 3D DIR sequence are likely not to be confined to improved lesion-detection rates. The high sCNR, in combination with high isotropic spatial resolution and the possibility of generating multiplanar reconstructions from a 3D dataset (eg, coronal planes, which are not commonly acquired in routine spinal MR imaging of patients with MS), may allow a more precise delineation of lesion borders, in particular of complex, elongated lesions and small lesions adjacent to the CSF (Fig 5). As one consequence, we would expect the 3D DIR sequence to provide a more precise tool for volumetric measurements than conventional 2D T2WI TSE sequences, which are prone to inaccuracies due to partial volume effects and lower contrast. This expectation, however, needs to be confirmed by additional studies.

We acknowledge limitations of our study. Most important, the

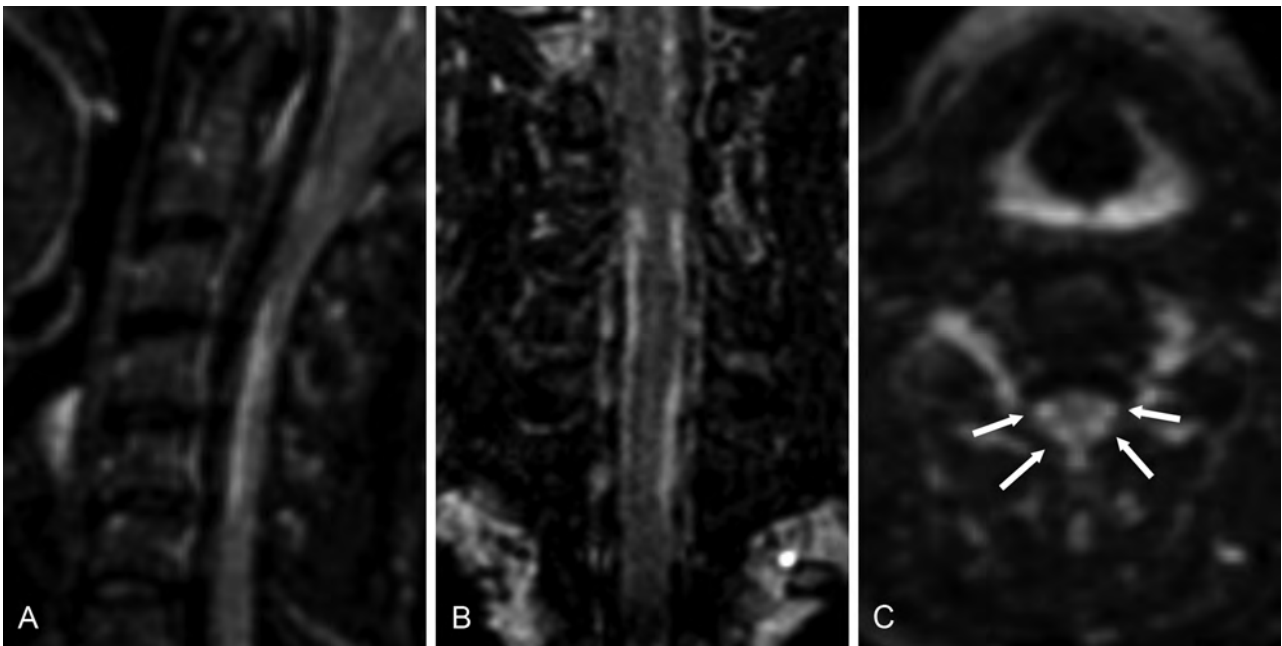


FIG 5. Sagittal (A), coronal (B), and axial (C) reconstructions of 3D DIR images of the cervical spinal cord of a 42-year-old female patient with primary-progressive MS. Elongated lesions in the lateral spinal cord are visible on both sides (*arrow*).

spinal 3D DIR sequence was more strongly affected by artifacts and magnetic field inhomogeneities than conventional 2D T2WI TSE sequences. Overall, these were outweighed by still higher sCNR and consequently improved lesion-detection rates but led to unacceptable image quality in 3 patients with marked obesity. Moreover, the 3D DIR sequence of the thoracic spinal cord is technically even more challenging because of large magnetic susceptibility differences of adjacent tissues (lungs versus abdominal organs) and motion artifacts caused by cardiac pulsation and respiration. Preliminary studies of the thoracic spinal cord with a modified 3D DIR sequence yielded results comparable with those in the cervical spinal cord in selected patients (Fig 6). Nevertheless, at present, routine clinical application of the spinal 3D DIR sequence is confined to the cervical spinal cord, and further optimization is required to improve its stability to make it suitable for the lower part of the spinal cord as well. Furthermore, follow-up examinations were not available to determine whether lesions conspicuous only with the 3D DIR sequence would also become visible in conventional T2WI TSE images after some time. Finally, hyperintensities visible in the 3D DIR sequence are not specific for MS lesions, but this feature also holds true for conventional T2WI TSE sequences. One study correlating a postmortem 3D DIR sequence and histopathology showed the high specificity of the 3D DIR sequence for lesions in the cerebral cortex of patients with MS.²⁶ A similar MR imaging-to-histopathology correlation would be desirable for the spinal 3D DIR sequence but was not possible in the present study. However, no abnormalities were detected in the healthy volunteers in blinded analysis, so the risk of false-positive findings in the spinal 3D DIR sequence is likely to be very low.

CONCLUSIONS

The 3D DIR sequence allowed better detection of lesions in MS and related inflammatory diseases of the cervical spinal cord in

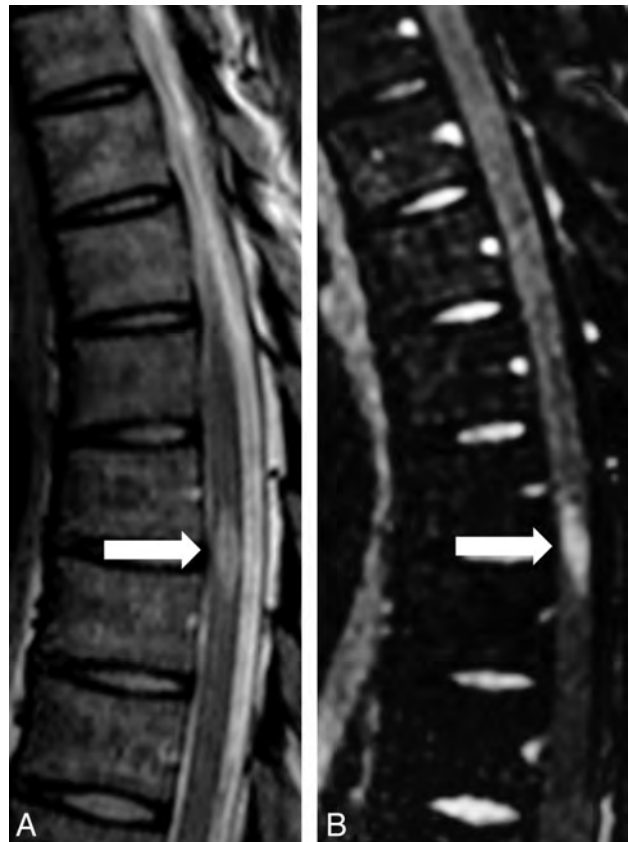


FIG 6. Sagittal T2WI TSE (A) and DIR (B) sequence of the thoracic spinal cord of a 35-year-old female patient with clinically isolated syndrome. On both sequences, a hyperintense lesion is visible in the spinal cord at the T7 level (*arrow*).

comparison with conventional 2D T2WI TSE sequences. Currently, we recommend acquiring the 3D DIR sequence of the cervical spinal cord, especially in doubtful cases.

ACKNOWLEDGMENTS

We thank Hendrik Kooijman (Philips Healthcare, Hamburg, Germany) for his support in establishing the 3D DIR sequence. Furthermore, we are grateful to all patients and volunteers who participated in this study.

Disclosures: Dimitrios C. Karampinos—UNRELATED: Grants/Grants Pending: Philips Healthcare.* Jan S. Bauer—UNRELATED: Grants/Grants Pending: German Research Foundation (DFG BA 4085 1/2)*; Travel/Accommodations/Meeting Expenses Unrelated to Activities Listed: meeting expenses covered by Terumo/MicroVenton, United States.* Mark Mühlau—UNRELATED: Payment for Lectures (including service on Speakers Bureaus); Merck Serono*; Travel/Accommodations/Meeting Expenses Unrelated to Activities Listed: Bayer, Merck Serono. *Money paid to the institution.

REFERENCES

1. Bot JC, Barkhof F, Lycklama A, et al. **Differentiation of multiple sclerosis from other inflammatory disorders and cerebrovascular disease: value of spinal MR imaging.** *Radiology* 2002;223:46–56
2. Lukas C, Sombekke MH, Bellenberg B, et al. **Relevance of spinal cord abnormalities to clinical disability in multiple sclerosis: MR imaging findings in a large cohort of patients.** *Radiology* 2013;269:542–52
3. Sombekke MH, Wattjes MP, Balk LJ, et al. **Spinal cord lesions in patients with clinically isolated syndrome: a powerful tool in diagnosis and prognosis.** *Neurology* 2013;80:69–75
4. Simon JH, Li D, Traboulsee A, et al. **Standardized MR imaging protocol for multiple sclerosis: consortium of MS Centers Consensus Guidelines.** *AJNR Am J Neuroradiol* 2006;27:455–61
5. Bot JC, Barkhof F, Lycklama A, et al. **Comparison of a conventional cardiac-triggered dual spin-echo and a fast STIR sequence in detection of spinal cord lesions in multiple sclerosis.** *Eur Radiol* 2000;10:753–58
6. Hittmair K, Mallek R, Prayer D, et al. **Spinal cord lesions in patients with multiple sclerosis: comparison of MR pulse sequences.** *AJNR Am J Neuroradiol* 1996;17:1555–65
7. Thorpe JW, MacManus DG, Kendall BE, et al. **Short tau inversion recovery fast spin-echo (fast STIR) imaging of the spinal cord in multiple sclerosis.** *Magn Reson Imaging* 1994;12:983–89
8. Ozturk A, Aygun N, Smith SA, et al. **Axial 3D gradient-echo imaging for improved multiple sclerosis lesion detection in the cervical spinal cord at 3T.** *Neuroradiology* 2013;55:431–39
9. Rivero RL, Oliveira EM, Bichuetti DB, et al. **Diffusion tensor imaging of the cervical spinal cord of patients with neuromyelitis optica.** *Magn Reson Imaging* 2014;32:457–63
10. Naismith RT, Xu J, Klawiter EC, et al. **Spinal cord tract diffusion tensor imaging reveals disability substrate in demyelinating disease.** *Neurology* 2013;80:2201–09
11. Redpath TW, Smith FW. **Imaging gray brain matter with a double-inversion pulse sequence to suppress CSF and white matter signals.** *MAGMA* 1994;2:451–55
12. Redpath TW, Smith FW. **Technical note: use of a double inversion recovery pulse sequence to image selectively grey or white brain matter.** *Br J Radiol* 1994;67:1258–63
13. Bedell BJ, Narayana PA. **Implementation and evaluation of a new pulse sequence for rapid acquisition of double inversion recovery images for simultaneous suppression of white matter and CSF.** *J Magn Reson Imaging* 1998;8:544–47
14. Calabrese M, De Stefano N, Atzori M, et al. **Detection of cortical inflammatory lesions by double inversion recovery magnetic resonance imaging in patients with multiple sclerosis.** *Arch Neurol* 2007;64:1416–22
15. Geurts JJ, Pouwels PJ, Uitdehaag BM, et al. **Intracortical lesions in multiple sclerosis: improved detection with 3D double inversion-recovery MR imaging.** *Radiology* 2005;236:254–60
16. Wattjes MP, Lutterbey GG, Gieseke J, et al. **Double inversion recovery brain imaging at 3T: diagnostic value in the detection of multiple sclerosis lesions.** *AJNR Am J Neuroradiol* 2007;28:54–59
17. Shipp D. **Case report: cervical spine 3D double inversion recovery (DIR) in demyelination.** *MAGNETOM Flash* 2012:49–50. www.siemens.com/magnetom-world. Accessed October 10, 2013
18. Edelstein WA, Glover GH, Hardy CJ, et al. **The intrinsic signal-to-noise ratio in NMR imaging.** *Magn Reson Med* 1986;3:604–18
19. Lin LI. **A concordance correlation coefficient to evaluate reproducibility.** *Biometrics* 1989;45:255–68
20. Keiper MD, Grossman RI, Brunson JC, et al. **The low sensitivity of fluid-attenuated inversion-recovery MR in the detection of multiple sclerosis of the spinal cord.** *AJNR Am J Neuroradiol* 1997;18:1035–39
21. Thomas DJ, Pennock JM, Hajnal JV, et al. **Magnetic resonance imaging of spinal cord in multiple sclerosis by fluid-attenuated inversion recovery.** *Lancet* 1993;341:593–94
22. Polman CH, Reingold SC, Banwell B, et al. **Diagnostic criteria for multiple sclerosis: 2010 revisions to the McDonald criteria.** *Ann Neurol* 2011;69:292–302
23. Swanton JK, Rovira A, Tintore M, et al. **MRI criteria for multiple sclerosis in patients presenting with clinically isolated syndromes: a multicentre retrospective study.** *Lancet Neurol* 2007;6:677–86
24. Bagnato F, Ikonomidou VN, van Gelderen P, et al. **Lesions by tissue specific imaging characterize multiple sclerosis patients with more advanced disease.** *Mult Scler* 2011;17:1424–31
25. Rovira A. **Tissue-specific MR imaging in multiple sclerosis.** *AJNR Am J Neuroradiol* 2009;30:1277–78
26. Seewann A, Kooi EJ, Roosendaal SD, et al. **Postmortem verification of MS cortical lesion detection with 3D DIR.** *Neurology* 2012;78:302–08



Trevo[®] XP

PROVUE RETRIEVER

Take Control. Capture More.

The newly designed Trevo[®] XP ProVue Retriever takes proven Trevo Retriever performance to new levels for **easy delivery**, **easy placement**, and **easy visualization**.

When you're in control, it's amazing what you can capture.

stryker[®]
Neurovascular

MR CLEAN: Expanding Clinical Evidence for Stent Retrievers

stryker[®]
Neurovascular

Stryker Neurovascular congratulates the MR CLEAN Investigators¹

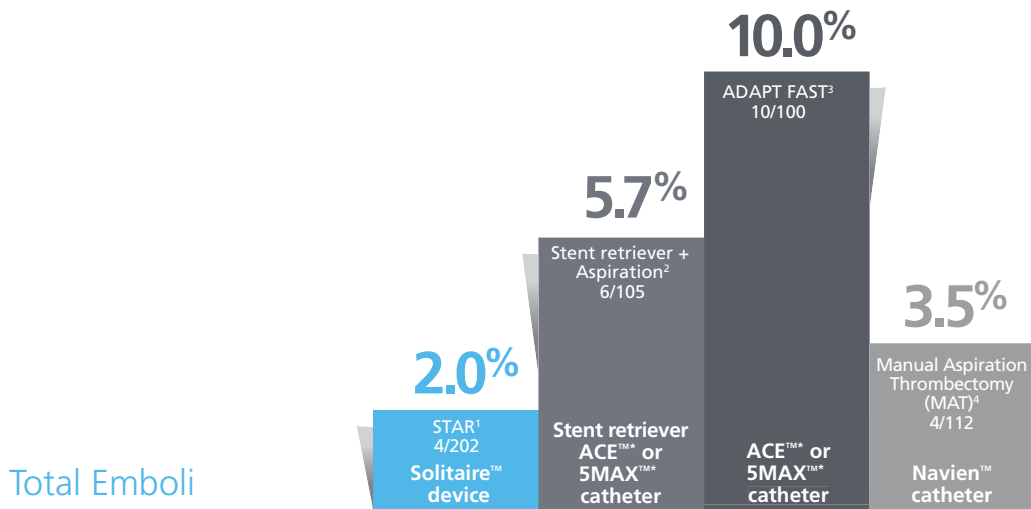
Full study protocol is available at www.mrclean-trial.org

1. Results of the Multicenter Randomized Clinical trial of Endovascular treatment for Acute ischemic stroke in the Netherlands, as presented at the 9th Annual World Stroke Congress, October 25, 2014.

Copyright © 2014 Stryker
NV00012181.AB

Complete  Care[®]

Stroke: *Our Only Focus. Our Ongoing Promise.*



Total Emboli

Numbers don't lie.

Using the Solitaire™ device first results in the lowest recorded instances of distal emboli, especially when compared to ADAPT.



For you, and your acute ischemic stroke patients, outcomes make all the difference. That's why evaluating and understanding the differences in the data, across multiple clinical studies, is so important to delivering the best possible outcomes and quality of life after stroke.

The Solitaire™ revascularization device has been more rigorously tested¹⁻⁶ than any other mechanical thrombectomy device. With consistent results showing significantly lower total emboli¹⁻⁴, unrivaled* neurological outcomes¹⁻⁷, and the lowest observed mortality¹⁻⁷, **the Solitaire™ device is demonstrably the fastest route to better outcomes.**

Solitaire™ Revascularization Device



* mRS ≤ 2 over 50% in a published study.

REFERENCES 1. Pereira V, Gralla J, Davalos A, et al. Prospective, Multicenter, Single-Arm Study of Mechanical Thrombectomy Using Solitaire Flow Restoration in Acute Ischemic Stroke. *Stroke*. 2013;44:2802-2807. 2. Humphries W, Hoyt D, Doss VT, et al. *J NeuroIntervent Surg*. doi:10.1136/neurintsurg-2013-010986. Data self reported. 3. Turk AS, Frei D, Fiorella D, et al. *J NeuroIntervent Surg*. doi:10.1136/neurintsurg-2014-011125. Data self reported. 4. Jankowitz B, Grandhi R, Horev A, et al. *J NeuroIntervent Surg*. doi:10.1136/neurintsurg-2013-011024. Data self reported. 5. Saver JL, Jahan R, Levy EI, et al. SWIFT Trialists. Solitaire flow restoration device versus the Merci Retriever in patients with acute ischemic stroke (SWIFT): a randomized, parallel-group, non-inferiority trial. *Lancet*. 2012;380(9849):1241-1249. 6. Jahan R, Liebeskind D, Nogueira R, et al. For SWIFT Investigators. Abstract 163: TIC1 success rates in SWIFT: comparison between randomized arms and correlation to 90 day neurologic outcome. *Stroke*. 2013;44:A163. 7. Dávalos A, Pereira VM, Chapot R, et al. Solitaire Group. Retrospective multicenter study of Solitaire FR for revascularization in the treatment of acute ischemic stroke. *Stroke*. 2012;43(10):2699-2705.

The Solitaire™ revascularization device is intended to restore blood flow by removing thrombus from a large intracranial vessel in patients experiencing ischemic stroke within 8 hours of symptom onset. Patients who are ineligible for intravenous tissue plasminogen activator (IV t-PA) or who fail IV t-PA therapy are candidates for treatment. Indications, contraindications, warnings and instructions for use can be found on the product labeling supplied with each device. CAUTION: Federal (USA) law restricts this device to sale by or on the order of a physician.

COVIDIEN, COVIDIEN with Logo, and Covidien Logo are US and internationally registered trademarks of Covidien AG. TM* Trademark of its respective owner. Other brands are trademarks of a Covidien company. ©2014 Covidien. MK1138072014A